https://ntrs.nasa.gov/search.jsp?R=19840025332 2020-03-20T20:55:26+00:00Z

NASA-CR-159,389

NASA-CR-159389
19840025332

A Reproduced Copy

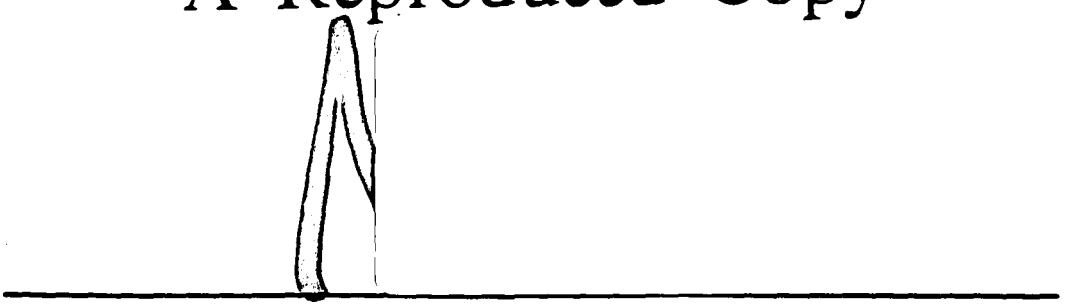

Reproduced for NASA

by the

Center for AeroSpace Information

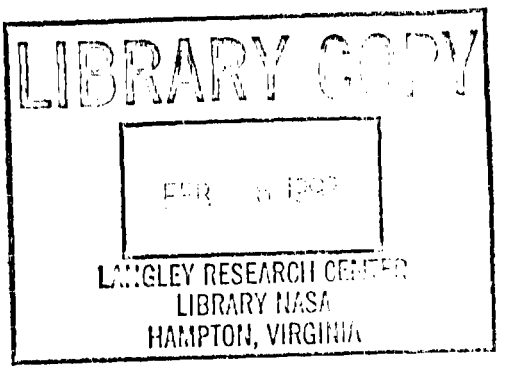

3 1176 01357 3689

NASA Contractor Report 159389

(NASA-CR-159389) RESULTS OF DESIGN STUDIES AND WIND TUNNEL TESTS OF AN ADVANCED HIGH LIFT SYSTEM FOR AN ENERGY EFFICIENT TRANSPORT (Douglas Aircraft Co., Inc.) 373 p HC A16/MF A01 CSCL 01C G3/05

N84-33403

Unclas 24033

Results of Design Studies and Wind Tunnel Tests of an Advanced High Lift System for an Energy Efficient Transport

Wayne R. Oliver

McDonnell Douglas Corporation
Douglas Aircraft Company
Long Beach, California 90846

CONTRACT NAS1-14744
DECEMBER 1980

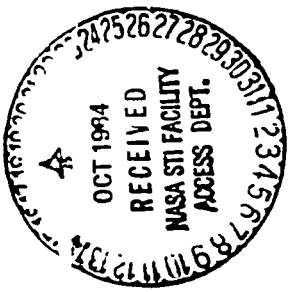

NASA

Langley Research Center

REVIEW FOR GENERAL RELEASE ON DECEMBER 31, 1982

N84-33403#

NASA Contractor Report 159389

Results of Design Studies and Wind Tunnel Tests of an Advanced High Lift System for an Energy Efficient Transport

Wayne R. Oliver
Douglas Aircraft Company
McDonnell Douglas Corporation
Long Beach, California 90846

Prepared for
Langley Research Center
under Contract NAS1-14744

NASA

Langley Research Center

FOREWORD

This document presents the results of a contract study performed for the National Aeronautics and Space Administration (NASA) by the Douglas Aircraft Company, McDonnell Douglas Corporation. This work was part of Phase I of the Energy Efficient Transport (EET) project of the Aircraft Energy Efficiency (ACEE) program. Specifically, the study was one task in the contract Selected Advanced Aerodynamic and Active Control Concepts Development. The activity included the design and testing of a low-speed, high lift wind tunnel model incorporating a high aspect ratio supercritical wing and advanced high lift system. The model included variable camber Krueger and slat leading edge devices, and two-segment and single-slot flap configurations. Optimization of these components, as well as effects of nacelles and pylons, landing gear, aileron, spoilers, and horizontal tail were studied experimentally.

Acknowledgements for their support and guidance are given to the NASA technical monitor for the contract, Mr. D.L. Maiden of the Energy Efficient Transport Project Office at the Langley Research Center and Mr. J.N. Tulinius, the on-site NASA representative; also to Dr. R.T. Whitcomb of the Langley Research Center for his concept of the supercritical wing.

Acknowledgements are also given to the director and staff of the NASA Ames and Langley Research Centers, at which facilities the test programs were conducted. The cooperation and discussions concerning high lift development for high aspect ratio supercritical wings of Mr. R.J. Margason and H.L. Morgan of the NASA Langley STAD Low-Speed Aerodynamics Branch was greatly appreciated.

The Douglas personnel who made significant contributions to this work were:

M. Klotzsche	ACEE Program Manager
A.B. Taylor	EET Project Manager
J.G. Callaghan	Branch Chief, Configuration Design and Development, Aerodynamics Subdivision

J.T. Callaghan	Aerodynamics Project Engineer - EET
D.E. Ellison	Section Chief, Stability, Control, and Flying Qualities, Aerodynamics Subdivision
W.R. Oliver	Task Manager, Aerodynamic Design (Report Author)
B.K. Bergman	Aerodynamic Design
J.W. Humphreys	Aerodynamic Design
D.G. MacWilkinson	Unit Chief, Advanced Commercial Programs, Aerodynamic Design
P.M. Minor	Aerodynamic Design
G.G. Myers	Aerodynanic Design
L.A. Spacht	Aerodynamic Design
N.F. Wasson	Aerodynamic Design
J.D. Cadwell	Branch Chief, Aerodynamics Wind Tunnel Model Group
F.B. Baugh	Aerodynamics Wind Tunnel Model Group
D.H. Broderson	Aerodynamics Wind Tunnel Model Group
L.B. Scherer	Aerodynamics Wind Tunnel Model Group
A.P. Morgan	Aerodynamic Design (Secretary)

TABLE OF CONTENTS

TABLE OF CONTENTS - continued

ILLUSTRATIONS

LIST OF TABLES

SUMMARY

This report presents the results of the design, evaluation, and wind-tunnel testing of a low-speed high-lift model of a fuel-efficient advanced technology aircraft. This aircraft, derived from detailed system studies for a medium-range wide-body transport, incorporated an advanced technology high-lift system. The results presented include: design trade studies, design and analysis techniques, and results and analysis of the wind tunnel data. The experimental results included the first low-speed high Reynolds number wind tunnel test for such an advanced transport. Experimental data include the effects on the low-speed aerodynamic characteristics of slat and variable camber Krueger (VCK) leading-edge devices, two-segment and single-slot trailing-edge flaps, nacelles, pylons, aileron, spoilers, horizontal tail, and landing gear. Both Mach and Reynolds number effects were also studied for selected configurations.

The trade studies indicated significant improvement in takeoff field length, takeoff and landing lift-to-drag ratio, and maximum lift coefficient for a configuration incorporating the advanced high lift systems compared with a conventional high lift system. A reduction in fuel burned was also obtained for the advanced configuration. Comparisons of the estimated performance of the selected configuration with existing aircraft, indicated reduced fuel burned (per seat-mile), improved payload capacity for hot/high operations, reduced takeoff and landing noise levels, and reduced (per-seat) operating costs.

The experimental program confirmed most of the estimated low-speed aerodynamic performance parameters. The cruise wing achieved a trimmed maximum lift coefficient of 1.5 and a lift-to-drag ratio of 15.0. For the high lift configurations, the values of maximum lift coefficient were significantly improved when compared to current aircraft values. Typical trimmed maximum lift coefficients for takeoff and landing configurations were 2.58 and 3.00 (for the VCK with two-segment flap configuration). Corresponding lift-to-drag ratios for the takeoff and landing configurations were 10.2 and 8.7. The landing configuration lift-to-drag ratio is a

significant improvement over the previous generation aircraft values. The slat leading edge device achieved maximum lift and lift-to-drag ratios superior to the VCK. Pitching moment trends for the VCK were superior to those obtained with the slat.

From an optimization standpoint, results of the experimental program indicated the leading edge components were more performance sensitive than the trailing edge devices. Experimental data obtained for the leading edge device retracted configuration indicated the leading edge device was of crucial importance to the attainment of large maximum lift values. Without the leading edge device, only small gains in maximum lift coefficient could be obtained with the trailing edge flaps. As expected, the two-segment flap was superior in maximum lift coefficient and flap lift increment. Trimmed polar comparisons indicated equivalent lift-to-drag envelopes for the takeoff flap settings. For equivalent values of approach speed, the lift-to-drag ratio for the two-segment flap was superior to the corresponding single-slot flap value.

Aileron studies indicated that, for all flap settings, negative deflections (trailing-edge-up) were more effective than positive (trailing-edge-down) deflections. The effect of spoiler deflection on roll characteristics indicated improved effectiveness as the flap deflection was increased. Symmetrical spoiler deflections, for takeoff and landing flap deflection, showed the spoilers to be very effective in reducing lift and increasing drag. The drag for the landing gear was essentially the same for the takeoff and landing configurations. The landing gear caused a slight reduction in maximum lift coefficient for the landing configuration.

Comparisons of experimental data with estimated values were generally in good agreement, lending confidence to the results of the trade studies. Analysis of the data has highlighted areas where continued efforts could result in further improvements. These areas include lift-to-drag ratio for takeoff configurations, pitching moment for the high lift configurations, and ground-effect characteristics. Specific test items are suggested for this continued development.

SYMBOLS

The longitudinal aerodynamic characteristics presented in this paper are referred to the stability-axis system. Force data were reduced to coefficient form based on the trapezoidal wing area. All dimensional values are given in both International System of Units (SI) and U.S. Customary Units, the principal measurements and calculations using the latter.

Coefficients and symbols used herein are defined as follows:

AR	wing aspect ratio
b	wing span
C_D	drag coefficient
C_{D_p}	zero-lift profile drag (coefficient)
$C_{D_{PARASITE\ FLAP\ +\ L.E.}}$	combined flap and leading edge device parasite drag (coefficient)
C_L	lift coefficient
$C_{L_{MAX}}$	maximum lift coefficient
$C_{L_{TO}}$	tail-off lift coefficient
$C_{L_{TRIM}}$	trimmed lift coefficient
$C_{L_{\alpha=0}}$	lift coefficient at zero degrees angle of attack
C_l	rolling moment coefficient
$c_{l_{2-D}}$	two-dimensional sectional lift coefficient
$c_{l_{3-D}}$	three-dimensional sectional lift coefficient
C_m	pitching moment coefficient
C_P	pressure coefficient
$C_{P_{CRIT}}$	pressure coefficient corresponding to local flow Mach number equal to 1.0
$C_{P_{MIN}}$	minimum pressure coefficient

DOC	direct operating cost
e	induced drag efficiency factor
FCK	fixed camber Krueger (flap)
FRP	fuselage reference plane
H	shape factor for boundary layer profile
H_{MAC}	mean aerodynamic chord of the horizontal tail
i_H	incidence angle between the hozizontal tail and the fuselage reference plane, positive trailing edge down (deg)
L/D	lift-to-drag ratio
$(L/D)_{MAX}$	maximum lift-to-drag ratio
$(L/D)_{TRIM}$	trimmed lift-to-drag ratio
MAC	mean aerodynamic chord
MADAAM	multielement airfoil design and analysis method
O.H.	overhang
$R_{N_{MAC}}$	Reynolds number based on MAC
RSS	relaxed static stability
S	wing area
$V_{APPROACH}$	approach speed
VCK	variable camber Krueger (flap)
V_{LO}	Lift-off Speed - the speed at which the airplane first becomes airborne
V_{MAC}	mean aerodynamic chord of the vertical tail
V_{MC}	Air Minimum Control Speed - the minimum flight speed at which, when the critical engine is suddenly made inoperative, it is possible to recover control of the airplane and maintain straight flight either with zero yaw or with an angle of bank of not more than five degrees
V_{MU}	Minimum Unstick Speed - the speed at and above which the airplane can safely lift off the ground and continue the takeoff
V_R	Rotation Speed - the speed at which the pilot begins to rotate the airplane to the lift-off altitude
V_S	Stalling Speed - the minimum steady flight speed at which the airplane is controllable

V_{ef}	Engine Failure Speed - the speed at which the critical engine is assumed to fail
V_1	Takeoff Decision Speed - the speed which the pilot uses as a reference in deciding whether to continue the takeoff or to abort
V_2	Takeoff Safety Speed - the speed at 35-foot height with one engine inoperative
WPP	wing reference plane
WUSS	wing under slat surface
X_i	spanwise wing station
Y_i	chordwise wing station
$\alpha_{C_{L_{MAX}}}$	angle of attack at $C_{L_{MAX}}$
α_{FRP}	angle of attack of the fuselage reference plane, positive nose up (deg)
α_{l_0}	angle of attack at zero lift
Γ	dihedral angle
$\Delta C_{D_{\substack{\text{INDUCED} \\ \text{FLAP}}}}$	induced drag increment due to flap (coefficient)
$\Delta C_{D_{\substack{\text{INDUCED} \\ \text{NACELLE}}}}$	induced drag increment due to nacelle (coefficient)
$\Delta C_{D_{MISC}}$	miscellaneous drag increment (coefficient)
$\Delta C_{D_{TRIM}}$	trim drag increment (coefficient)
$\Delta C_{L_{MAX}}$	maximum lift increment due to flap (coefficient)
$\Delta C_{L_{\substack{MAX \\ \text{INTERFERENCE}}}}$	maximum lift increment due to interference (coefficient)
$\Delta C_{L_{TRIM}}$	increment in lift due to trim (coefficient)
$\Delta C_{l_{max_{FLAP}}}$	two-dimensional maximum lift increment due to flap (coefficient)
$\Delta C_{l_{max_{L.E.}}}$	two-dimensional maximum lift increment due to leading edge device (coefficient)
$\Delta C_{l_{\alpha=0}}$	two-dimensional lift increment at zero angle of attack (coefficient)

δ^*	boundary layer displacement thickness
$\delta_{F_{AFT}}$	aft flap deflection angle, positive for trailing edge down (deg)
$\delta_{F_{EFF}}$	effective flap deflection ($\delta_{F_{MAIN}} + 0.5\ \delta_{F_{AFT}}$) angle
$\delta_{F_{FLAPERON}}$	flaperon deflection angle, positive for trailing edge down (deg)
$\delta_{F_{MAIN}}$	main flap deflection angle, positive for trailing edge down (deg)
δ_{SP}	spoiler deflection angle (symmetrical), negative for trailing edge up (deg)
$\delta_{SP_{LH}}$	left-hand spoiler deflection angle, negative for trailing edge up (deg)
$\delta_{a_{LH}}$	left-hand aileron deflection angle, positive for trailing edge down (deg)

INTRODUCTION

One of the latest technological advances to be used in current aircraft design studies is the supercritical airfoil conceived by Dr. R. T. Whitcomb of the National Aeronautics and Space Administration. The research on supercritical wings over the past few years by NASA and the industry has shown that definite performance advantages are to be gained by applying this technology to future transport aircraft. Accordingly, the Douglas Aircraft Company, under the Energy-Efficient Transport (EET) component of the NASA Aircraft Energy Efficiency (ACEE) program, has been studying the supercritical wing in connection with the DC-X-200, a 200-passenger, wide-body, medium-range transport. The results of a systematic wing development study for the DC-X-200 are presented in Reference 1. While much development work still remains to be done to refine the high-speed characteristics, the comparisons of the available experimental data with analytical predictions establish confidence in the high-speed design concepts. On the other hand, no equivalent data base exists for high lift configurations. Moreover, establishing the true potential of the high lift system for an aircraft like the DC-X-200 requires significant experimental optimization. This requires leading- and trailing-edge position and deflection studies involving a rather complex wind tunnel model and an extensive test program.

The purpose of this report is to present the results of an initial study, made under the EET Program, to develop the high-lift system for an advanced transport aircraft with a high-aspect-ratio supercritical wing. It presents the results of Douglas-sponsored trade studies made to define the advantages that an advanced high-lift system could bring to aircraft like the DC-X-200. It then describes the design and wind tunnel tests of a model to develop the advanced high-lift system. The wind tunnel tests were made using a 4.7 percent scale model of the DC-X-200 having a 10.5 aspect-ratio supercritical wing, representing an advanced design developed in the high-speed studies of Reference 1. The model was tested with a variety of leading- and trailing-edge devices including a leading-edge slat, variable-camber Krueqers, a trailing-edge two-segment flap, a conventional vane flap, and a plain flap. Spoiler and aileron effectiveness and the effects of engine nacelles, pylons, and landing gear

were also investigated. The tests were made in the Ames 12-foot tunnel at Mach numbers from 0.20 to 0.32 and Reynolds numbers, based on wing mean aerodynamic chord, from 2.89 million to 5.12 million. Six-component forces and moments and static pressure distributions were obtained. Flow-visualization photographs using flouresoent mini-tufts were also obtained.

PRELIMINARY TRADE STUDIES

Background

At the time the NASA Aircraft Energy Efficient Transport program (ACEE) and its Energy-Efficient Transport (EET) component was initiated, the Douglas Aircraft Company was studying the DC-X-200, a 200-passenger, wide-body, medium-range transport. The environment in which these studies were being made included rapid inflation, concern over escalating fuel prices and decreasing availability, increasingly stringent noise regulations, and deregulation of the airline industry by government. The influences of these factors on the new design were:

1. Due to increased costs of producing new aircraft, advanced technologies would be required to obtain, from the standpoint of economics, performance superior to older, less expensive designs.

2. The rapidly escalating fuel prices and uncertain availability required that fuel-efficient vehicles would be required rather than those exhibiting increased speed.

3. Greater aerodynamic performance in terms of low-speed lift/drag would be required to supplement engine technology in meeting new noise requirements.

4. Improved route flexibility through better takeoff and landing performance would be required to meet the potential government deregulation of the airline industry.

As a result of these considerations the DC-X-200 family was configured to employ a high-aspect-ratio supercritical wing (Reference 1), and incorporated an advanced high lift system. The configuration also employed relaxed static stability (RSS) to further improve the fuel efficiency and economics (Reference 2). In this report, a particular version of this family of aircraft (DC-X-200 Model D969N-21) was selected for low-speed experimental studies and is referred to as the Advanced Commercial Aircraft (ACA) in other portions of this report. Other technology development programs related to advanced transports are currently being studied at Douglas under the ACEE program and are reported in Reference 3.

Fundamentally, the supercritical airfoil can be used to generate greater lift for a given thickness and drag than a conventional airfoil. Due to the emphasis on fuel-efficiency and direct operating cost (DOC), the manner in which the added benefits of supercritical airfoil technology have been utilized are, basically, to increase wing-thickness-to-chord ratio and aspect ratio. The increase in thickness-to-chord ratio results in a more efficient wing structural system, which, in turn, offsets the weight of the higher aspect ratio. Within these ground rules, however, many other design variables must be considered, which, almost without exception, have both favorable and unfavorable aspects when considering the total aircraft design. To introduce the differences in low-speed characteristics resulting from this application of supercritical airfoil technology, Figure 1 presents a comparison of the low-speed performance of a current wide body transport and one of the advanced configurations of the design studies. The former aircraft incorporated a conventional wing with an aspect ratio of 6.8, and a high lift system composed of a slat and vane-flap components. The advanced configuration used supercritical airfoils in the manner previously discussed, with an aspect ratio of 12, and an advanced high lift system

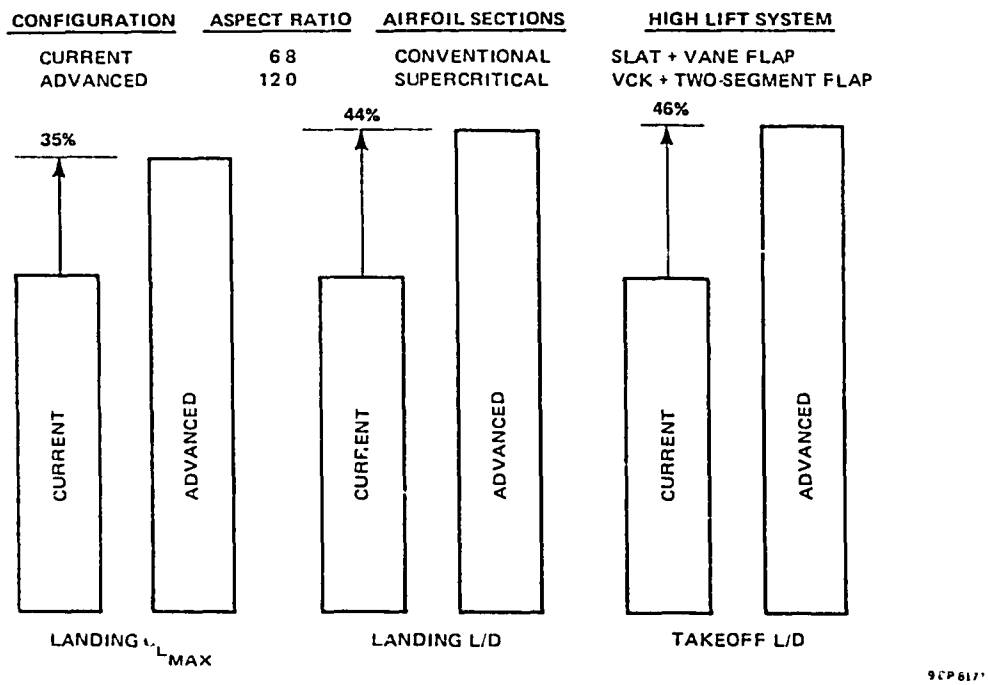

FIGURE 1. COMPARISON OF LOW-SPEED CHARACTERISTICS FOR CURRENT AND ADVANCED TRANSPORTS

composed of a variable camber Krueger (VCK) and large-chord, high-extension, two-segment, flap system. This combination represents the upper bound in low-speed performance for the configurations studies and shows that significant improvements are predicted for the advanced configuration.

High Speed Wing Parameters

Naturally, the parameters related to the high-speed design problem are very significant for this class of aircraft and closely affect the low-speed characterisitcs. The high speed design and wind tunnel development of the high aspect ratio supercritical wing development is reported in Reference 1. The most important design considerations from this reference are given below.

Spanwise Distribution of Lift, or Span Loading

Although an elliptical span loading offers the lowest induced drag, the optimum loading, considering the combined aerodynamic and structural characteristics, is usually one which has some degree of washout. Since, at cruise Mach number, the initial separation which determines buffet onset usually occurs on the outboard wing panel, it is undesirable to allow the local velocities in this region to become too high. Thinning the outboard wing can alleviate this situation, but at the expense of a penalty in weight. In the final analysis the choice of span loading is a function of not only induced drag but also wing weight, and low-speed and high-speed clean wing separation characteristics (i.e., stall progression and buffet boundary).

Spanwise Distribution of Thickness

For the same upper surface pressure distribution, modifications in the thickness result in changes to the section lift values. The decisions on the distribution of lift must be made in conjunction with the decisions on thickness. On the inboard wing the thickness near the root is affected by such considerations as the depth required for the landing gear, and the volume needed for fuel. In addition, the choice of the spanwise distribution of thickness considers not only the combination of lift and thickness required to meet the cruise performance, but also the impact of the distribution on low-speed performance in both the clean and high lift

modes. Since, for a given planform, the weight of the wing box is largely a function of the lift and the thickness-to-chord ratio, the aerodynamic and weight characteristics must be considered in unison before a final decision can be reached.

Airfoil Characteristics

The choice of chordwise and spanwise airfoil characteristics introduces many other variables. For the basic outboard airfoil, decisions must be made regarding the leading edge radius and the amount of aft camber. Blunt leading edges are desirable from the standpoint of supercritical development at cruise, and maximum lift at low speeds. They are undesirable from the standpoint of drag creep and, in some cases, lift loss at stall for low speed conditions. The latter trend can result from the rapid change in curvature near the leading edge associated with a large nose radius and a lack of nose chamber. Large adverse pressure gradients aft of the suction peak can induce a rapid change from a trailing edge separation to a leading edge separation. Highly aft-cambered airfoils are desirable from the standpoint of achieving good cruise characteristics at high lift coefficients, but they have high negative pitching moments which, for some configurations, can result in excessively high trim drag. Low lift coefficient (dive) characteristics at very high Mach numbers can also be unacceptable with too much aft camber, particularly where outboard lateral control devices are used. The spanwise distribution of aft camber also presents a design challenge as it is difficult to carry a large amount of lift aft on the chord near the root and, at the same time, counteract the root effect to maintain satisfactory inboard isobar characteristics.

Factors Influencing Selection of High Lift Systems

If the aircraft's wing area is sized by a low speed requirement, for example, approach speed, the wing area may vary by hundreds of square feet depending on the utilization of simple or advanced high lift systems. If an advanced high lift system is utilized, the resulting wing area can be relatively smaller and a resulting weight advantage should be achieved.

The low speed characteristics are also influenced by the planform effects of the supercritical wing. A small, high aspect ratio wing has a relatively

small root chord which requires significant extension in order to house the landing gear. The use of relaxed static stability (RSS), which moves the required gear position further aft relative to the wing, further aggravates the problem of available inboard flap chord. This results in a need for an advanced inboard high lift flap system. The large trailing edge extension unsweeps a significant portion of the inboard wing. This makes the job of the high-speed designer more difficult in terms of eliminating root effect, and maintaining sweep effectiveness. One method of achieving proper root characteristics at high speed under these conditions is to increase the leading edge sweep in this area. This impacts the low speed characteristics by effectively reducing inboard flap-chord/wing-chord ratio and tends to reduce local lift curve slope making higher inboard stalling angles at low speed.

The basic airfoil section also impacts the high lift system. A comparison of the supercritical and conventional airfoils, shown in Figure 2, indicates significant differences in airfoil shape. Accordingly, the high lift systems compatible with these two airfoil shapes have different design implications. For the same ratio of wing chord to flap chord, an examination of the trailing edge region shows that a flap system for the supercritical airfoil will be thinner and possess a significant amount of "built-in" camber. At the leading edge, the increased nose radius of the supercritical airfoil will yield larger maximum lift coefficients at low speeds than those of the conventional section. Consequently, larger maximum lift values can be obtained with the high lift system deflected.

In addition to wing geometric parameters there are a number of other factors that influence the selection of a high lift system for an advanced commercial transport. These are shown in Figure 3. The most fundamental requirements are those of the operator. Of primary concern to the airline is the

FIGURE 2 SUPERCRITICAL AND CONVENTIONAL AIRFOIL COMPARISON

capability of an economically profitable operation over its route structure with realistic passenger and cargo capacities. In the low speed area, the resulting requirements include takeoff and landing field lengths, and in some cases a specified approach speed for the design mission. Naturally, for a given class of transport aircraft, not all airlines have similar requirements concerning low speed performance. This adds another dimension to the selection of the high lift system in that acceptable low speed performance must be achieved for as many potential airline customers as possible.

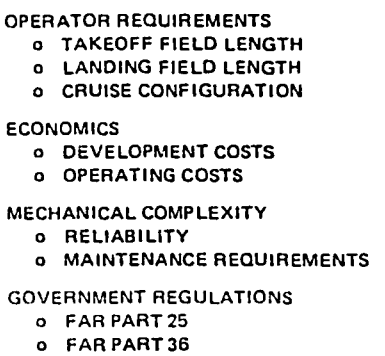

FIGURE 3. FACTORS INFLUENCING HIGH LIFT SYSTEM DEFINITION

The economic factors influence not only the airlines in terms of DOC, but also the manufacturer in terms of the development costs of new hardware and technology. Improved high lift systems can also influence fuel efficiency which, in these days of escalating oil prices, has a significant impact on airline profitability.

Reliability and maintenance requirements also influence the high lift system definition. The desired high lift mechanical system must be lightweight, have a high degree of reliability and a minimum of in-service maintenance.

Another significant factor in high lift system selection is the government regulations concerning transport aircraft. Two important documents which specify requirements for the low speed operation of transport aircraft are Federal Air Regulations (FAR) Part 25 and 36. FAR Part 25 is concerned with the operational factors (i.e., critical speeds, distances, flying qualities etc.) and FAR Part 36 specifies rules concerning acceptable noise characteristics during takeoff and landing.

ORIGINAL PAGE IS
OF POOR QUALITY

Figure 4 presents the speed definitions pertinent to the takeoff profile. Also shown in Figure 5 is one definition of takeoff field length. This is the critical engine-out takeoff distance and is the distance from the start of takeoff to a point 35-feet above the runway at the V_2 speed, assuming an engine failure to be recognized at the decision speed, V_1. The other definition of takeoff distance is 115 percent of the horizontal distance from the start of takeoff to the point at which the airplane is 35-feet above the takeoff surface with all engines operating. The final takeoff distance is specified to be the greater of the two defined takeoff distances.

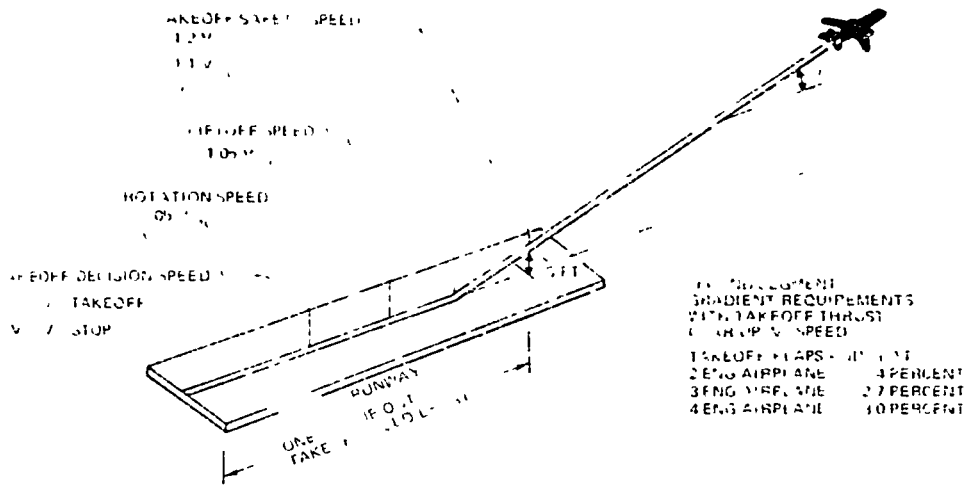

FIGURE 4. TAKEOFF DEFINITIONS

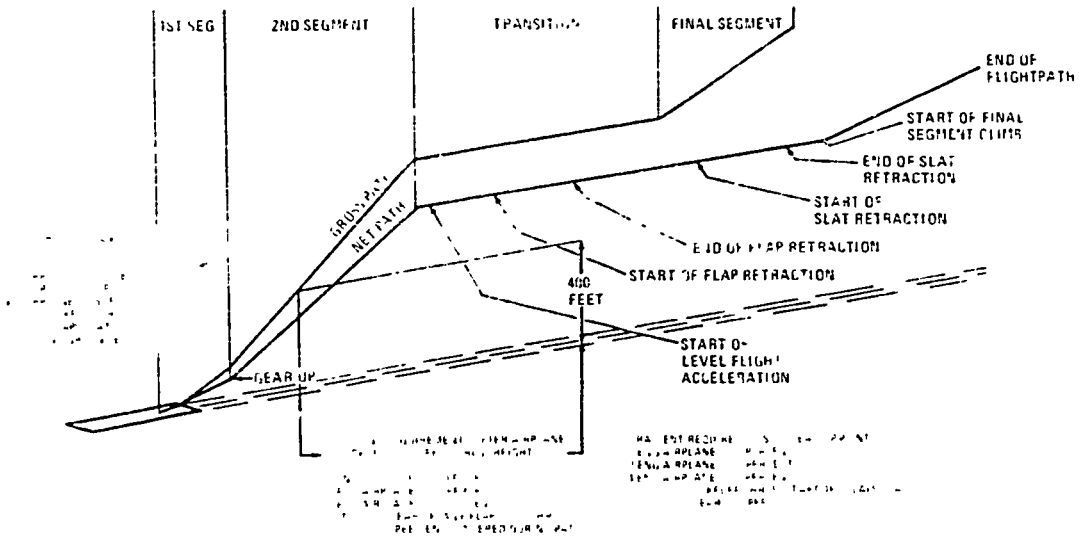

FIGURE 5. TAKEOFF FLIGHTPATH PROFILE

ORIGINAL PAGE
OF POOR QUALITY

The values required for the various takeoff climb gradients are summarized in Figure 5. Also shown in Figure 6 is the net path. This corresponds to a reduction in gradient of 0.8, 0.9, and 1.0 percent for two, three, and four engine aircraft, respectively. Figure 7 presents not only the takeoff, but also, the approach and landing climb requirements. Also shown in Figure 6, are the corresponding configurations for trailing edge flaps, leading edge device, landing gear, appropriate speed, thrust setting, and the number of engines inoperative.

CONFIGURATION	REQUIRED GRADIENTS			FLAPS	SLATS	GEAR	SPEED	THRUST SETTING	NUMBER OF ENGINES INOPERATIVE
	2 ENGINE AIRCRAFT (PERCENT)	3-ENGINE AIRCRAFT (PERCENT)	4 ENGINE AIRCRAFT (PERCENT)						
TAKEOFF FIRST SEGMENT	POSITIVE	0 3	0 5	TAKEOFF	TAKEOFF	DOWN	V_{LO}	TO	1
TAKEOFF SECOND SEGMENT	2 4	2 7	3 0	TAKEOFF	TAKEOFF	UP	V_2	TO	1
TAKEOFF FINAL SEGMENT	1 2	1 5	1 7	RETRACTED	RETRACTED	UP	$\geq 1.25\ V_S$	MAX CONTINUOUS	1
APPROACH CLIMB	2 1	2 4	2 7	APPROACH	APPROACH	UP	$1.5\ V_S$	TO	1
LANDING CLIMB	3 2	3 2	3 2	LANDING	LANDING	DOWN	$\geq 1.3\ V_S$	TO	0

FIGURE 6. CLIMB GRADIENT SUMMARY

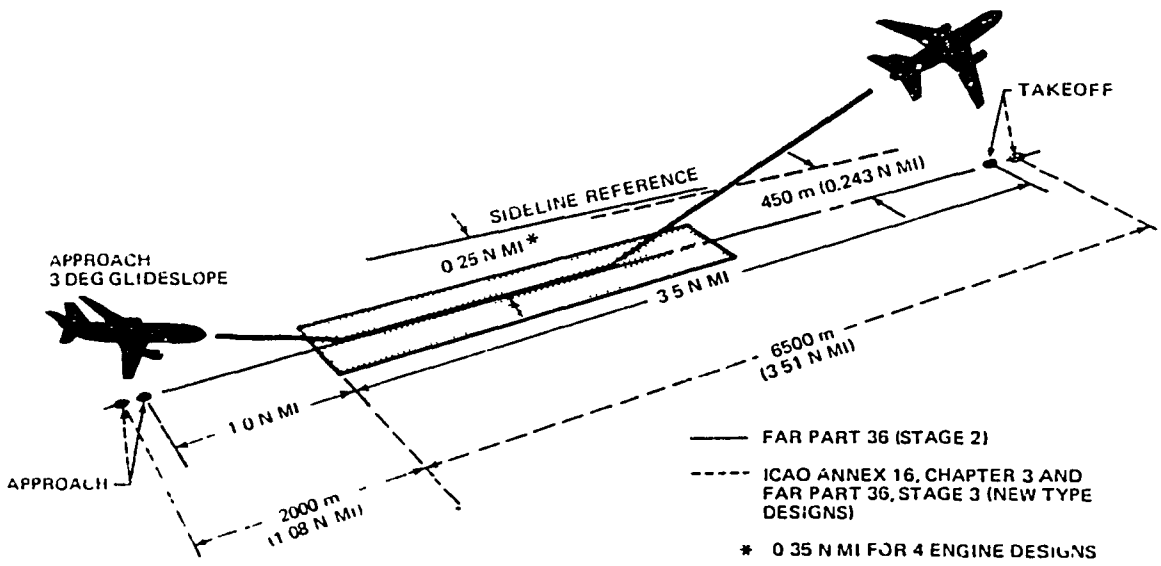

FIGURE 7. AIRCRAFT NOISE CERTIFICATION REFERENCE LOCATIONS

The landing distance requirements at the intended destination or alternate airport are also defined in the FAR, Part 25. Other more general requirements are also contained in FAR 25 which impact the low speed requirements. These are related to controllability, maneuverability, trim, stability, and stalling characteristics.

The Federal Aviation Regulations Part 36 establish noise limits for three different reference locations as shown in Figure 7. The requirement for FAA Stage 2 limits (for derivative aircraft) and the more stringent limits specified by ICAO Annex 16, Chapter 3 and FAR Part 36, Stage 3 for new transport designs are shown in Figure 8.

The takeoff and landing performance has a strong sensitivity to the pertinent low speed lift and drag characteristics. In addition to reducing takeoff and landing field lengths, reductions in takeoff, approach, and landing speeds are directly related to increased aircraft lift coefficient (C_L) at a given attitude and to increased aircraft maximum lift coefficient ($C_{L_{MAX}}$). The climb gradient is strongly dependent on the lift-to-drag ratio (L/D) for the climbout configuration. Aircraft noise levels are directly related to the thrust required, which is in turn related to the drag level of the aircraft. During takeoff, at a given climb gradient, the larger values of L/D result in reduced noise levels for the surrounding airport community. Due to the lower noise levels operational flexibility for the airline could be increased, since the aircraft could operate profitably out of more noise-critical airports.

Trade Studies

As a basis for the contract work, Douglas funded trade studies were performed and included variations of: airfoil section (conventional versus supercritical), aspect ratio, high lift system capability and type, wing sweep, twist, camber, thickness, planform, and various degrees of RSS.

Related to the preceding studies, an EET funded study was conducted to evaluate the effect of an advanced high lift system on an aircraft typical of this class of transport aircraft. The study was concerned with low speed

ORIGINAL PAGE
OF POOR QUALITY

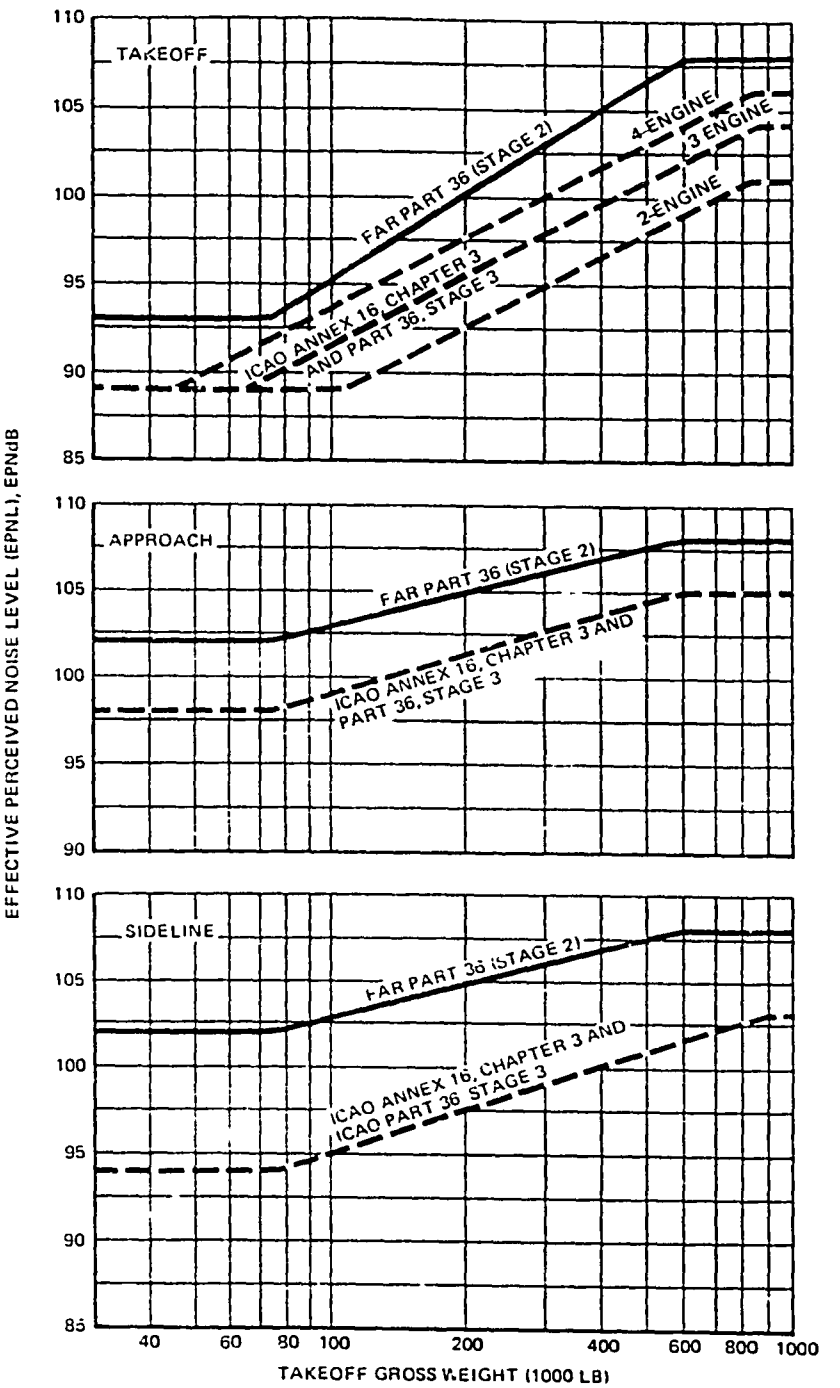

FIGURE 8. FAR PART 36, ICAO ANNEX 16, CHAPTER 3 (NEW DESIGNS) NOISE LEVEL REQUIREMENTS

OF POOR QUALITY

performance and fuel efficiency. For this study the aspect ratio (AR) was 12. Figure 9 presents the configurations assessed in this trade study. Mission requirements for this study were: a range of 5,556 km (3,000 n.mi), a payload of 20,085 kg (44,250 lb), initial cruise altitude of 10,363 m (34,000 ft), a cruise Mach number of 0.78, a $V_{APPROACH}$ of not more than 64.8 m/s (126 kt) and a takeoff field length of not more than 2438 m (8,000 ft). For the advanced and conventional high lift systems the location of the rear spar was held constant resulting in similar chord ratios for the trailing edge flap system.

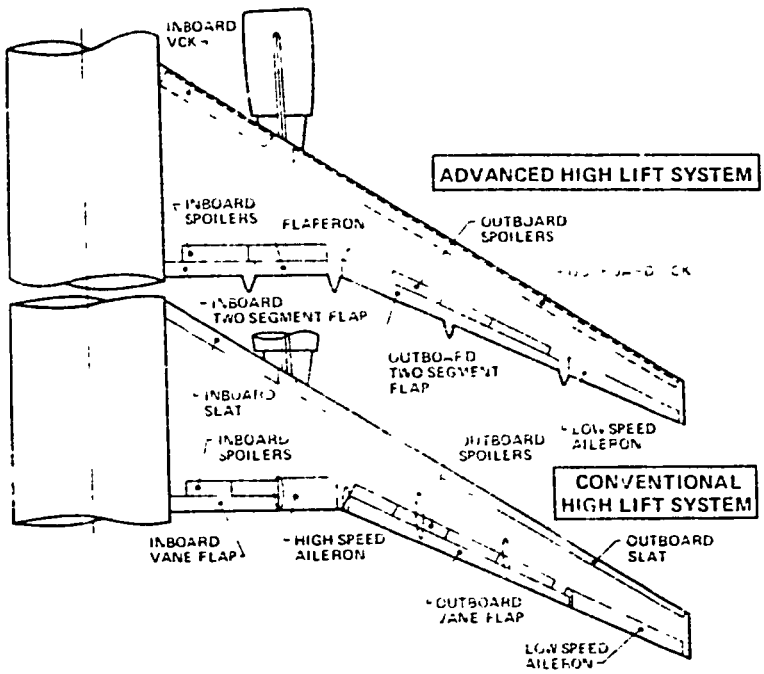

FIGURE 9 HIGH LIFT SYSTEM CONFIGURATION COMPARISON

The conventional high lift system incorporates a circular arc motion vane flap configuration. The inboard and outboard flaps are separated by a high speed aileron which is undeflected in the high lift mode. The leading edge device consists of an inboard and outboard slat, with appropriate takeoff and landing positions.

The advanced high lift system has an inboard and outboard two-segment flap system with large extension capability. A flaperon, which is deflected

during takeoff and landing, is located between the inboard and outboard flaps. The flaperon translates in the same manner as the main flap element of the inboard and outboard two-segment flap system. The leading edge device consists of a VCK for the inboard and outboard portion of the wing.

The results of the sizing study are presented in Figure 10. The conventional high lift configuration was sized by the approach speed requirement. The resulting initial cruise altitude is slightly higher than the mission requirement of 34,000 feet.

	ADVANCED		CONVENTIONAL	
WING AREA	202 99 m^2	(2,185 SQ FT)	205 32 m^2	(2,210 SQ FT)
TOGW	137,393 kg	(302,900 LB)	138,073 kg	(304,400 LB)
OEW	81,627 kg	(179,956 LB)	82,135 kg	(181,077 LB)
INITIAL CRUISE ALTITUDE	10 363 m	(34,000 FT)	10,424 m	(34,200 FT)
$V_{APPROACH}$	61 9 m/S	(120 4 KEAS)	64 8 m/S	(126 KEAS)
TOFL	1,768 m	(5,800 FT)	2 179 m	(7,150 FT)

FIGURE 10. CONVENTIONAL AND ADVANCED HIGH LIFT SYSTEM STUDY CONFIGURATIONS

The wing for the configuration with the advanced high lift system was sized by the initial cruise altitude requirement. A smaller wing area was determined for the advanced configuration. The configuration incorporating the advanced high lift system has a significantly reduced takeoff field length. Moreover, the improved L/D characteristics would reduce noise levels for takeoff and landing operations.

The effect of the advanced configuration on fuel burned over various range missions is shown in Figure 11. For the shorter range missions, the performance calculations included determination of the most favorable initial cruise altitude for the corresponding reduced initial cruise weight.

At the design range, fuel savings of 0.6 percent were obtained. However, average stage lengths for aircraft of this class would be expected to be of the order of 750 to 1000 nautical miles. At these reduced range values, fuel savings of the order of 1.6 to 1.3 percent of fuel burned were indicated.

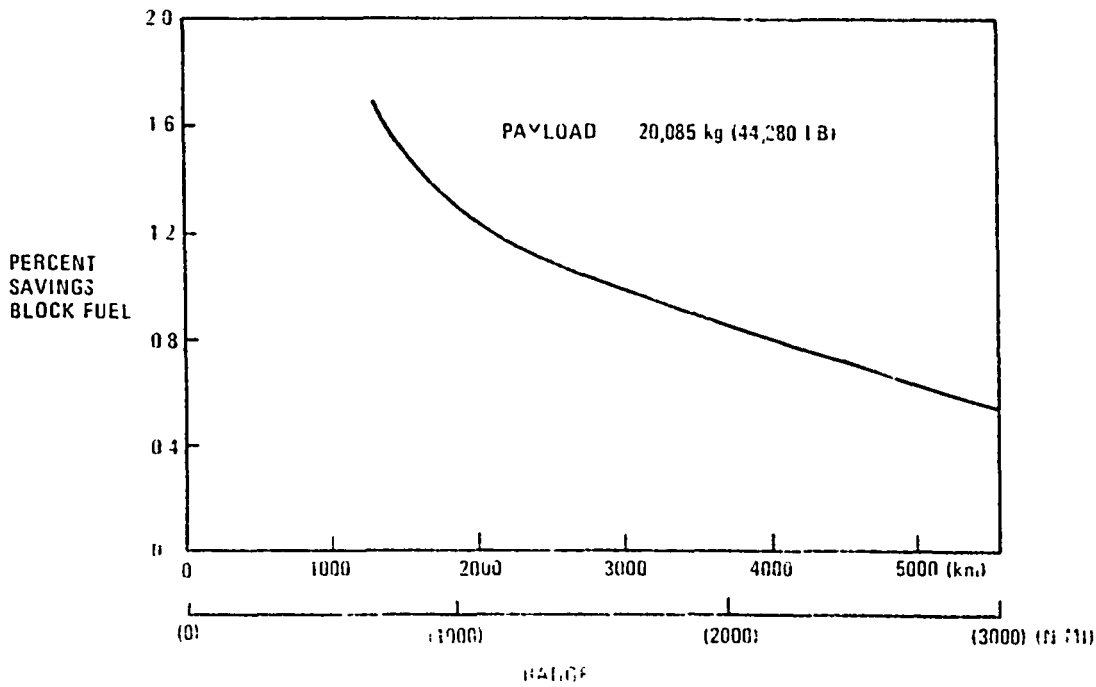

FIGURE 11 EFFECT OF ADVANCED HIGH LIFT SYSTEM ON FUEL BURNED

The distribution of fuel burned with different range missions is presented in Figure 12. As the range is increased, more fuel was burned during cruise. Since the sized configurations had similar wing areas, the fuel burned during cruise is not significantly different. The remaining fuel burned was a small percentage of the total, such that the impact of the percentage differences due to the high lift system was reduced. At the smaller ranges, the fuel burned during takeoff and approach was a larger portion of the fuel burned, and the differences due to the high lift system became more significant as the previous figures indicated.

The takeoff field length performance comparison, shown in Figure 13, at maximum takeoff gross weight, indicates a 19-percent reduction in field length due to the advanced configuration. Increased operational flexibility could therefore be obtained. For a given field length, longer range missions or increased payload for a given range could be achieved with the advanced configuration.

ORIGINAL PAGE IS
OF POOR QUALITY

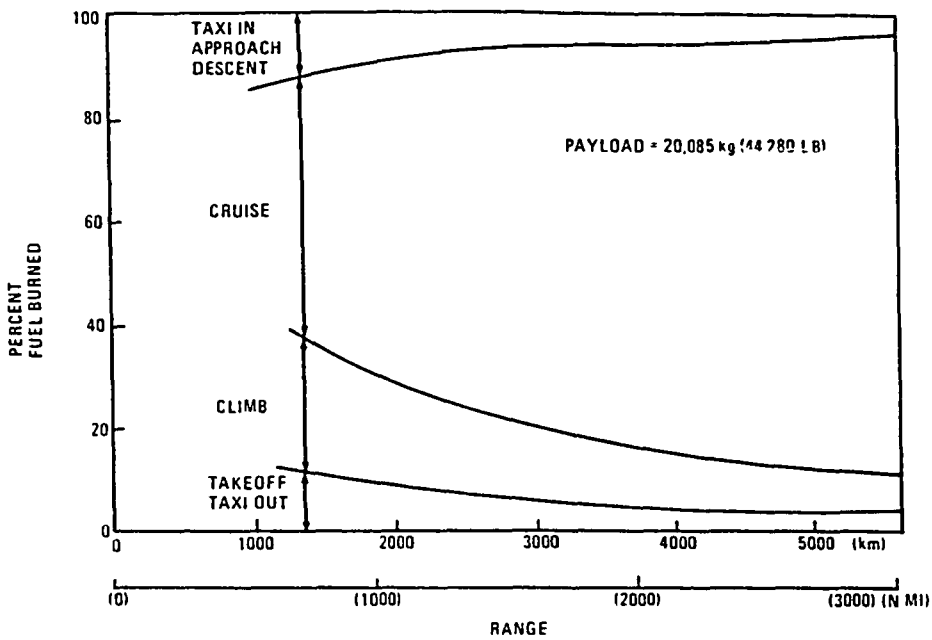

FIGURE 12. ADVANCED HIGH LIFT SYSTEM FUEL-BURNED COMPONENTS

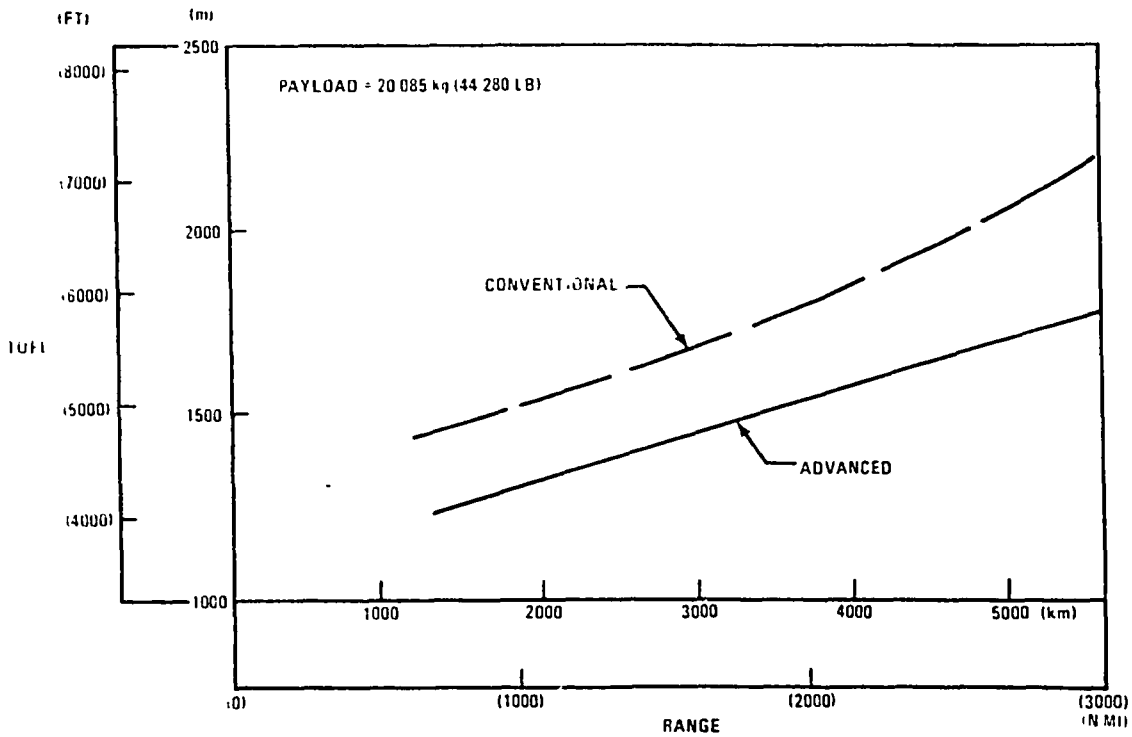

FIGURE 13. CONVENTIONAL AND ADVANCED HIGH LIFT SYSTEM TAKEOFF FIELD LENGTH PERFORMANCE

ORIGINAL PAGE IS
OF POOR QUALITY

A summary of the low speed performance results of the trade study for the mission requirements specified, is shown in Figure 14. The improved $C_{L_{MAX}}$ is due to the airfoil shape, VCK, two-segment flap, and flaperon. The 18-percent improvement in landing L/D would result in a reduction in approach noise. A more uniform spanload distribution due to the flaperon, and the improved drag characteristics of the trailing edge flap system were the sources of the increased L/D. The takeoff field length was reduced due to increased $C_{L_{MAX}}$ at takeoff flap settings and the improved L/D characteristics.

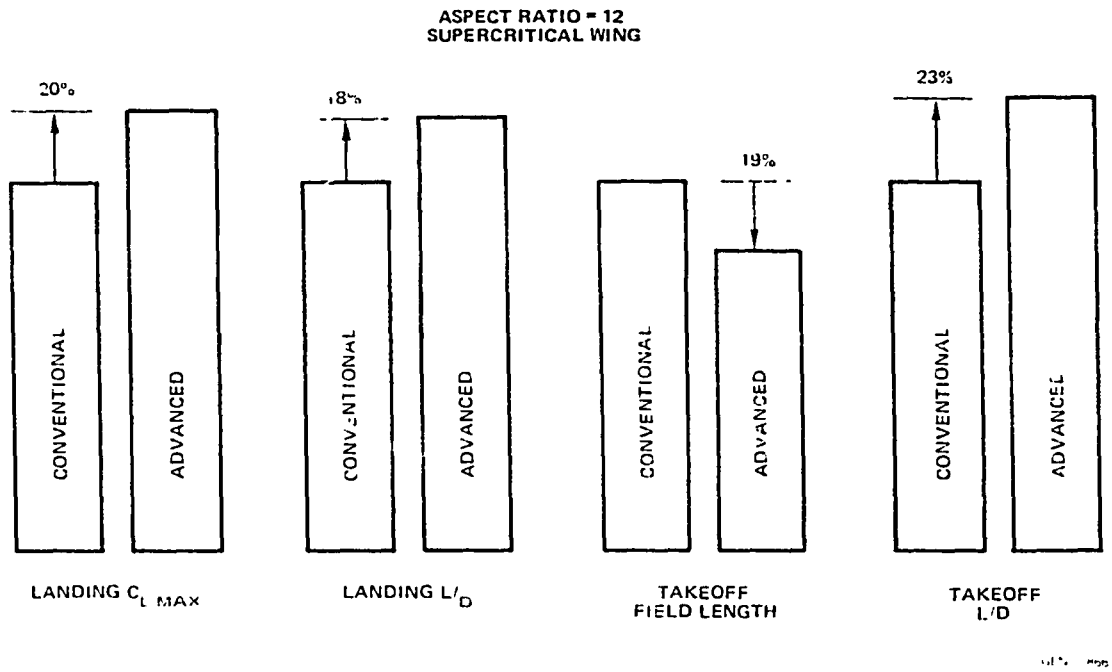

FIGURE 14. CONVENTIONAL VERSUS ADVANCED HIGH LIFT SYSTEM COMPARISON

High Lift Component Studies

During the DC-X-200 studies, full span slat and VCK configurations as well as an inboard fixed camber krueger (FCK) with VCK outboard, and slat inboard and VCK outboard were evaluated. The largest estimated $C_{L_{MAX}}$ was achieved with the full span VCK. Early weight evaluations indicated a weight advantage for the VCK compared to the slat, although as the design studies

ORIGINAL PAGE IS
OF POOR QUALITY

progress, the magnitude of this difference was reduced. A two-percent improvement in DOC was being shown for the final full span VCK configurations. The VCK was chosen as the primary leading edge device based on these results and previous experimental two-dimensional wind tunnel programs for both supercritical and conventional airfoil geometries. These tests had indicated that the VCK had the potential of superior $C_{L_{MAX}}$, and also drag levels approaching that of the slat. Figure 15 shows the VCK configuration of the Douglas-funded mechanical system studies for the retracted and extended positions. This contour-changing surface, was supported by the front spar and stowed in the lower leading edge of the wing, formed the lower surface of the leading edge prior to deployment. It extended from near the fuselage side to the wing tip, interrupted only in the area near the pylon. When the VCK was deployed, its contour was modified by a mechanical linkage during the actuation sequence so that the desired shape was attained when the surface was fully extended. Various methods of VCK drive systems were evaluated and included: open torque tube, closed loop torque tube, cable drive, and hydraulic actuators. For the torque tube systems, both jackscrew and rotary gear box drive systems were evaluated. The final mechanical system selected was a rotary gear box drive for the closed loop torque tube system. The torque tube is driven by two

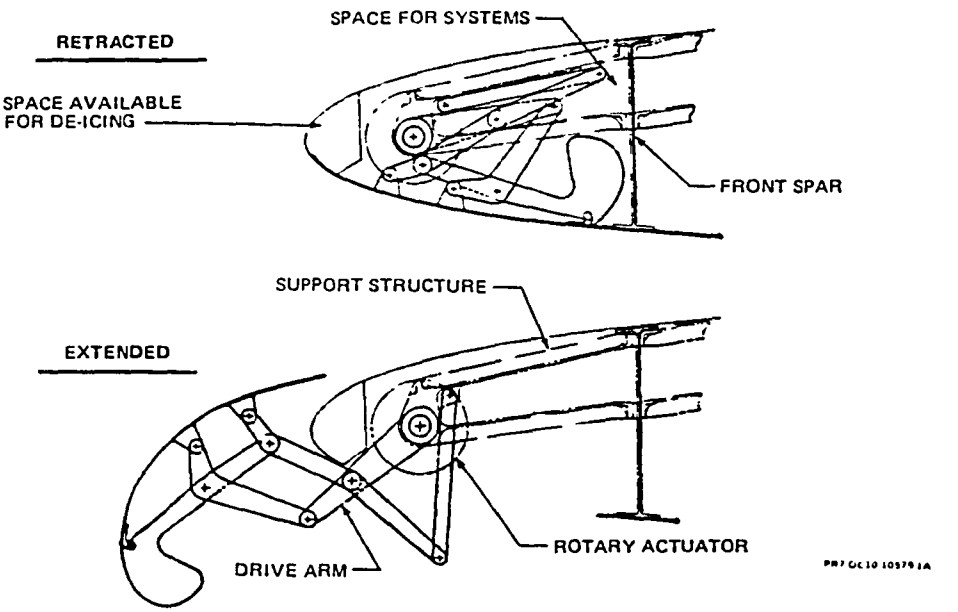

FIGURE 15. VARIABLE CAMBER KRUEGER LEADING EDGE

hydraulic motors each driven by a separate hydraulic system. Besides being lighter and more compact, this system requires no asymmetry system, will operated under a single failure, and syncronizes the VCK by the action of the torque tube. The full span slat was chosen for the secondary leading edge configuration for the high lift wind tunnel model due to the reduced drag levels associated with multi-positioning capability, which already has been demonstrated on current transport aircraft.

Trailing edge system studies included the effect of circular-arc-motion vane-flap, track-motion two-segment flaps with very large chord extension, and finally, double four-bar linkage systems for a two-segment flap with reduced chord ratio.

Previous experimental data (both two- and three-dimensional) had shown increased performance benefits for large chord vane-flap and two-segment flap configurations when compared to the circular-arc-motion flap. An alternate two-segment flap configuration was also evaluated in the Douglas funded system studies. This trailing edge high lift system had reduced chord and aft extension. The original two-segment flap was a 35-percent chord ratio two-segment system with a chord extension of 25-percent (over the outboard span). The alternate two-segment flap had a 30-percent chord ratio and a 15-percent chord extension for the same region of the wing. This flap geometry and motion was compatible with a linkage support system which offered significant advantages in cruise drag (due to smaller support farings), in structural weight, and in maintainability when compared to the large chord high-extension track system. These studies indicated the impact of the linkage system was to burn 1.7-percent less fuel and have a reduced direct operating cost of 1.2 percent compared with the track system. The operating empty weight was also reduced. All of these factors were determined at identical payload range, takeoff field length, cruise Mach number, and approach speed.

Based on these studies, the reduced flap chord linkage motion was selected for the primary trailing edge system. Figure 16 shows the trailing edge flap system selected from the design studies. The flap system consists of double-slotted two-segment type flaps for the inboard and outboard flaps.

ORIGINAL PAGE IS
OF POOR QUALITY

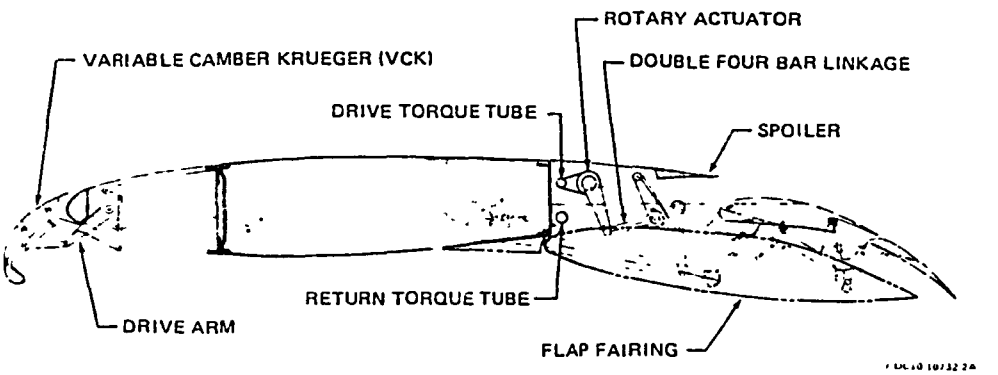

FIGURE 16. HIGH LIFT SYSTEM

Between these was a flaperon (single-slot flap) which translated in the same manner as the main flap of the inboard and outboard flap system. The inboard and outboard trailing edge flaps are mounted on double four-bar linkages which are actuated by redundant torque tubes (closed loop) extending from the center of the aircraft. Dual hydrualic motors, powered by separate hydraulic systems, drive the torque tubes, and one system alone can operate the flaps at a reduced rate. The advantages of this system were similar to those of the VCK system. A linkage supported single-slot flap system was selected for the secondary-trailing-edge high lift configuration. The experimental evaluation of this system could be accomplished with very little additional expense by retracting the aft flap of the two-segment configuration.

Final Configuration Studies

The Douglas funded system studies, which resulted in the configuration selected for the wind tunnel program, are presented in this section. Naturally, the high speed requirements determined the primary design variables for the cruise wing. Since the cruise wing geometry was the starting point for the high lift system design, and directly impacted the low speed characteristics, the selection of the more basic parameters are reviewed (see also Reference 1). Also presented is the wing sizing for the configuration with the selected high lift system and comparisons of estimated performance of the current configuration and other existing transports to illustrate the gains obtained by use of the application of the advanced technologies. As stated previously, the basic configuration was a

medium range wide-body transport capable of replacing the previous generation of narrow-body aircraft. The design goals for this aircraft relative to today's transports were improved economics, lower fuel consumption, reduced noise and expanded cargo capability. Design emphasis was placed on employing advanced technologies that improved aircraft operational economics. The principal advanced technology incorporated in this design was a high aspect ratio supercritical wing; other advanced technologies included an advanced high lift system consisting of VCK and two-segment flaps, longitudinal stability augmentation, use of composite structure for selected components, a short core-cowl nacelle for the wing mounted engines, and significant advances in digital electronic systems.

The DC-X-200 Model D969M-21 was designed for one-stop transcontinental range capability with inherent growth potential for nonstop transcontinental flight, or a significant increase in capacity. The required configuration performance included: lower fuel consumption per seat-mile than any current turbofan powered transport, excellent hot/high airfield performance, noise levels substantially below expected mandatory levels (with adequate margins for airplane growth), and excellent seat-mile and airplane-mile operating economics. A three view of the resulting configuration, which used DC-10 fuselage components, is shown in Figure 17.

Early in the system studies, cruise Mach numbers of 0.78 (M = .78) and M = 0.80 were chosen, the former to favor fuel burned, and the latter for minimum direct operating cost. Figure 18 illustrates the variation of several of the important operational parameters with cruise Mach number. While the DOC values are minimized in the region of M=0.79 to 0.81, the block fuel burned was minimum at some Mach number less than 0.78. These two considerations were of paramount concern in the selection of cruise Mach number. Other operational factors were also taken into account but to a lesser extent.

The basic wing geometry was selected after studying the effects of wing area, thickness to chord ratio, sweep, and aspect ratio on direct operating cost, fuel burned, and other economic indicators. Figure 19 illustrates results of a variation of wing sweep on DOC. With an average thickness-to-chord ratio of 0.125, a minimum value of DOC was achieved at

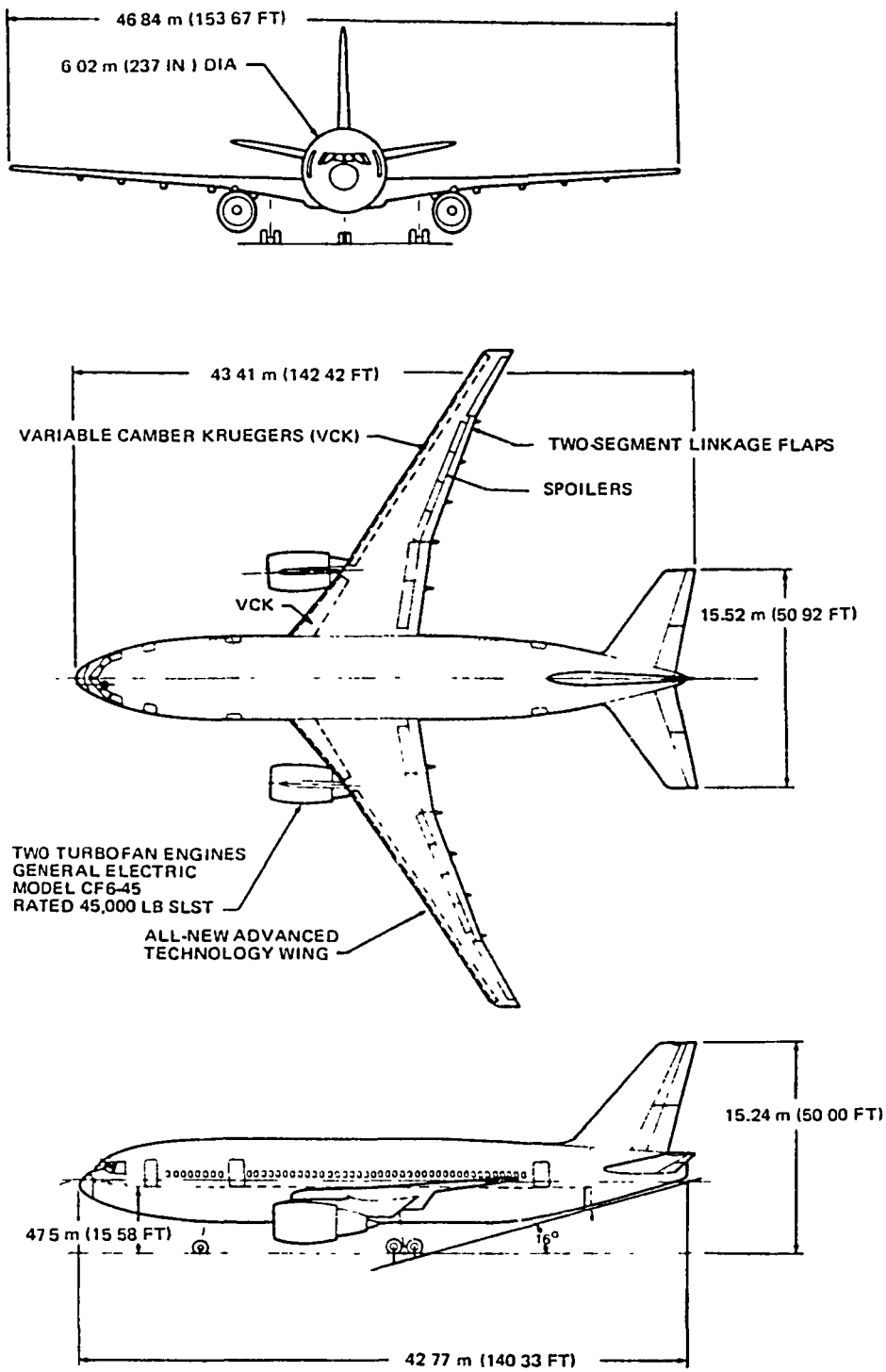

FIGURE 17. DC-X-200 GENERAL ARRANGEMENT

ORIGINAL PAGE IS
OF POOR QUALITY

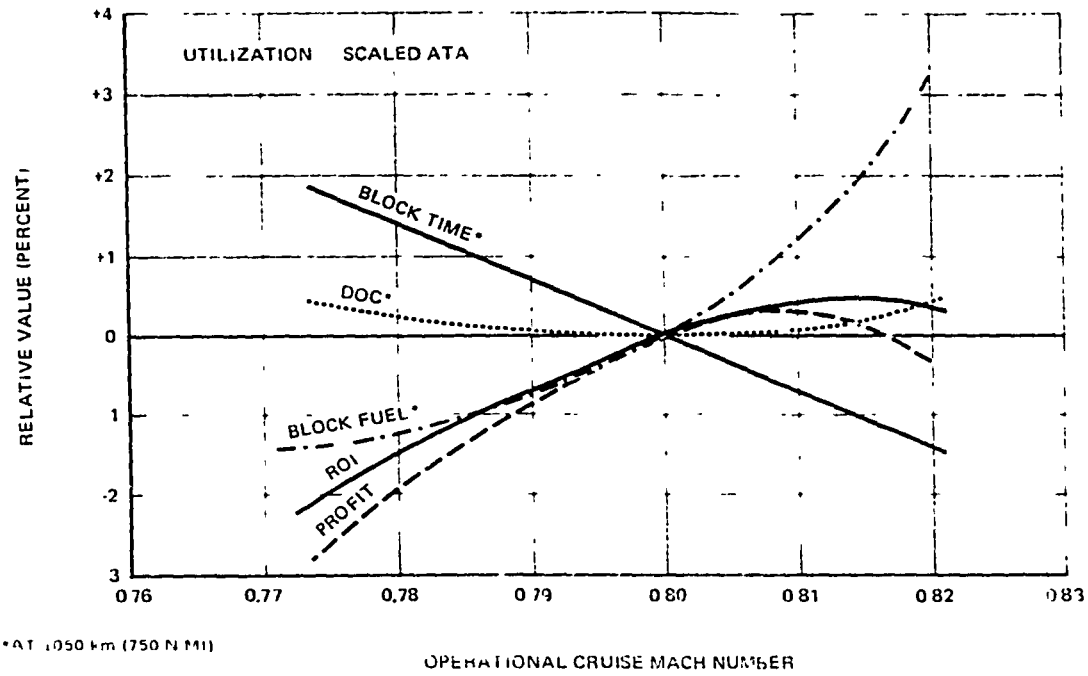

FIGURE 18. FACTORS WEIGHED IN DETERMINING OPTIMUM CRUISE SPEED

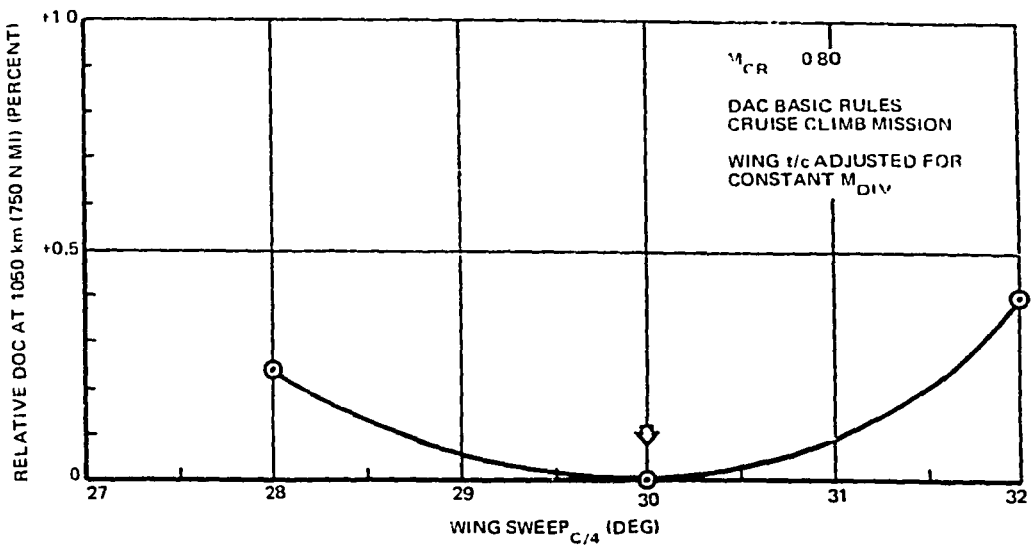

FIGURE 19. EFFECT OF WING SWEEP ON DIRECT OPERATING COST

ORIGINAL
OF POOR

30-degrees sweep. Aspect ratio effects on economic parameters and fuel burned are presented in Figures 20 and 21. The higher aspect ratios show significant improvements. Considering the results of these studies, their impact on the noise characteristics of the aircraft in low-speed operation, and the risk factors associated with higher aspect ratio, an aspect ratio of 10.0 based on adjusted wing area was selected.

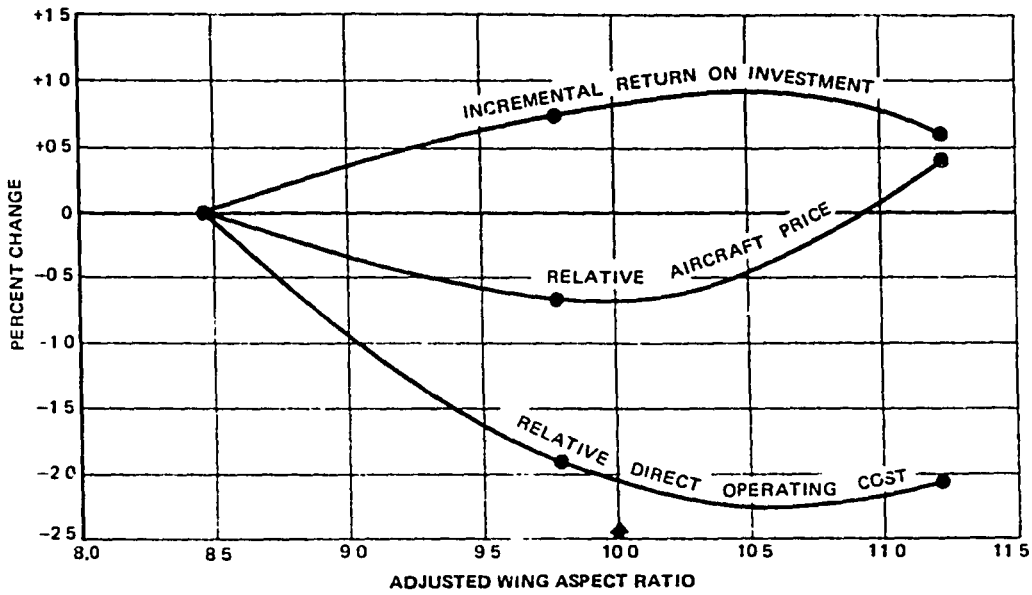

FIGURE 20. EFFECT OF ASPECT RATIO ON ECONOMIC PARAMETERS

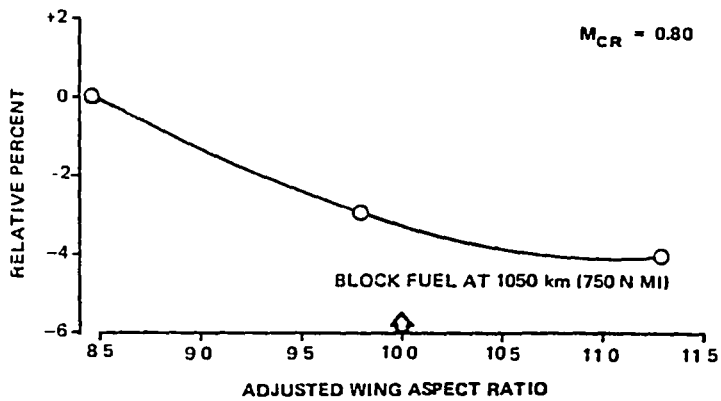

FIGURE 21. EFFECT OF ASPECT RATIO ON BLOCK FUEL

ORIGINAL
OF POOR QUALITY

Wing area study results are shown in Figure 22. Because of terminal compatibility, it was desirable that the wing span for the high aspect ratio wing not exceed that of the DC-10-30. This requirement, together with fuel usage, DOC, an initial cruise altitude capability of 10,400 m (34,000 ft), an approach speed no greater than 182 km/h (130 k+) with 30 degrees of flap deflection, resulted in a wing area of slightly under 220 M^2 (2400 sq ft).

With the sweep, thickness, aspect ratio, wing area, and high lift system defined, the resulting comparisons of aircraft performance, geometry, and other aircraft characteristics, are shown in Figures 23 through 33. Figure 23 is a performance summary illustrating payload range, takeoff field length, and altitude capability. Takeoff field length capabilities of the DC-X-200 show the effects of this configuration and high lift system. At maximum gross weights, the field length at sea level for a 29°C (84°F) day is only 2173 m (7130 ft).

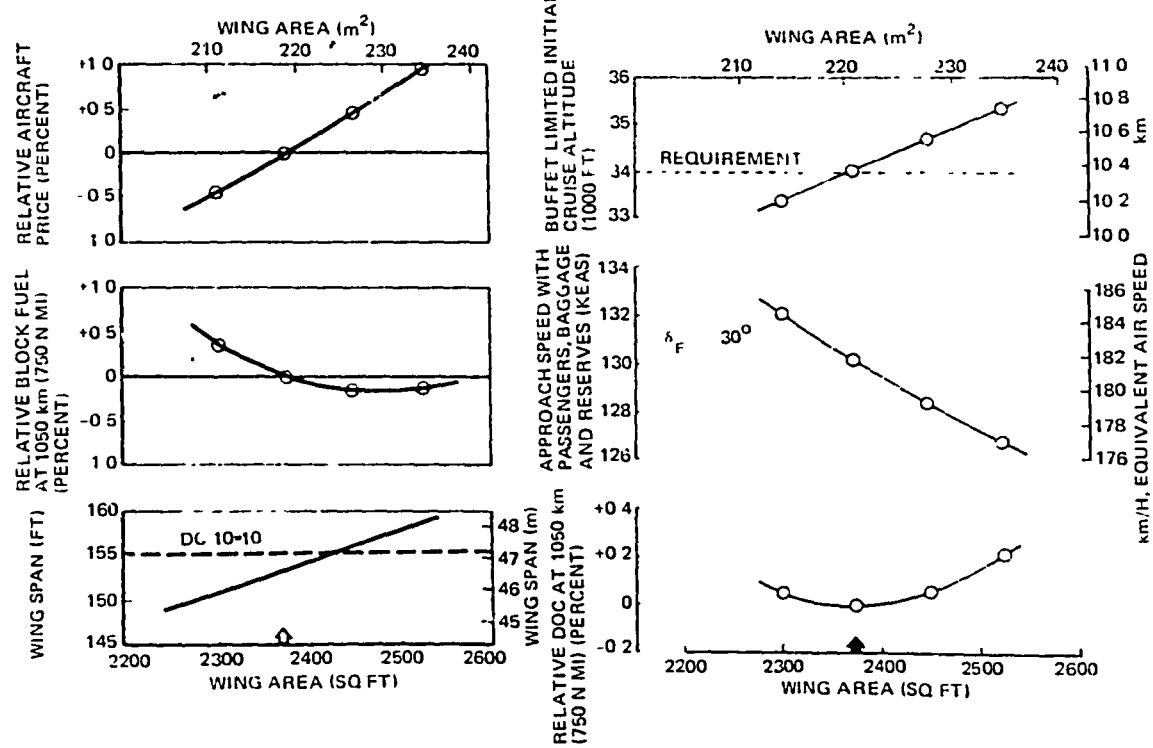

FIGURE 22. WING AREA STUDY RESULTS

ORIGINAL PAGE IS
OF POOR QUALITY

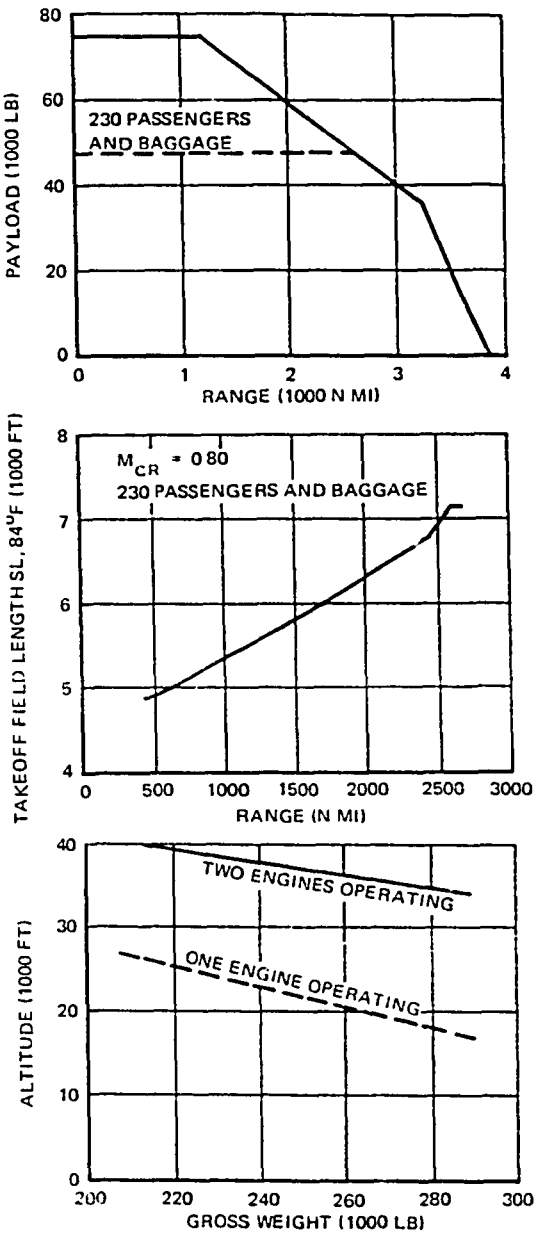

FIGURE 23. AIRCRAFT PERFORMANCE SUMMARY

The takeoff field performance at hot, high altitude airports is typified by the takeoff weight capability of 127,006 kg (280,000 lb) out of Denver on a 33°C (92°F) day. This would be sufficient to transport a full passenger load with more than 4,536 kg (10,000 lb) of cargo from Denver to major East coast cities.

ORIGINAL PAGE IS
OF POOR QUALITY

Because of the emphasis on economics and fuel efficiency, the supercritical airfoil technology was applied to the DC-X-200 to increase wing thickness while still achieving some benefits in buffet boundary. The latter is translated into cruise lift. Figure 24 illustrates these trends. The resulting wing thickness provides a structural weight advantage and the airfoil shape results in an increase in takeoff and landing $C_{L_{MAX}}$. Part of the weight reduction has been utilized to increase the wing aspect ratio in order to improve aerodynamic efficiency. Figure 25 shows a nine-percent improvement in the cruise ratio L/D when compared to the DC-10-10.

For the low speed characteristics, the wing and high lift system provide a high landing $C_{L_{MAX}}$ capability with a maximum flap deflection of only 30 degrees. The small required flap deflection at landing results in a significant improvement (70 percent) in the approach L/D over the comparable values for the DC-10-10 (see Figure 26). The takeoff L/D is improved 30 percent and the maximum lift coefficient is increased by 17 percent.

Related noise characteristics are shown in Figures 27 through 29. Figure 27 indicates that the estimated DC-X-200 levels, resulting from the high aspect ratio supercritical wing, advanced high lift systems, high-bypass ratio

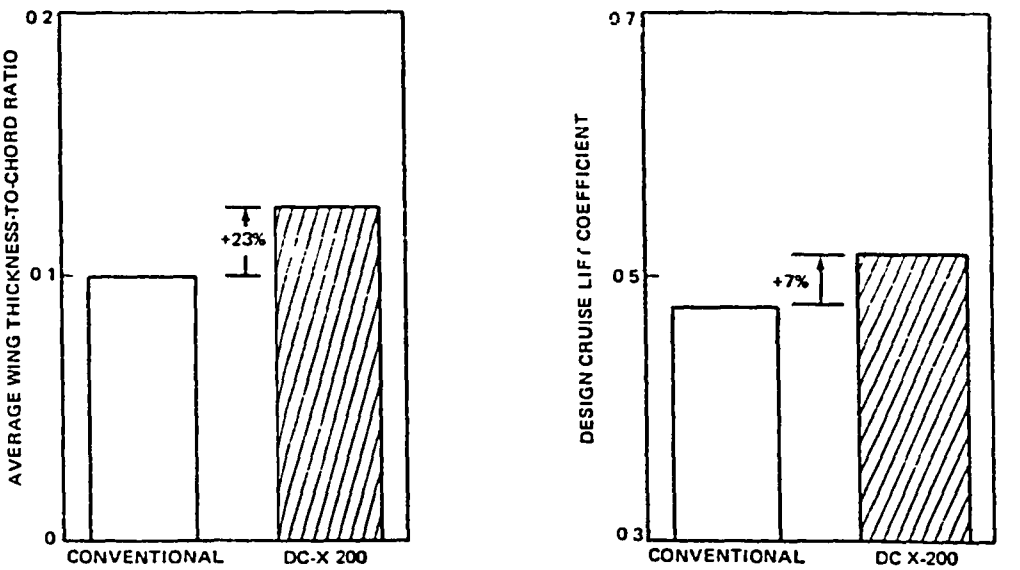

FIGURE 24. COMPARISON OF THICKNESS AND CRUISE LIFT COEFFICIENTS ~ CONVENTIONAL TRANSPORT AND DC-X-200

ORIGINAL PAGE
OF POOR QUALITY

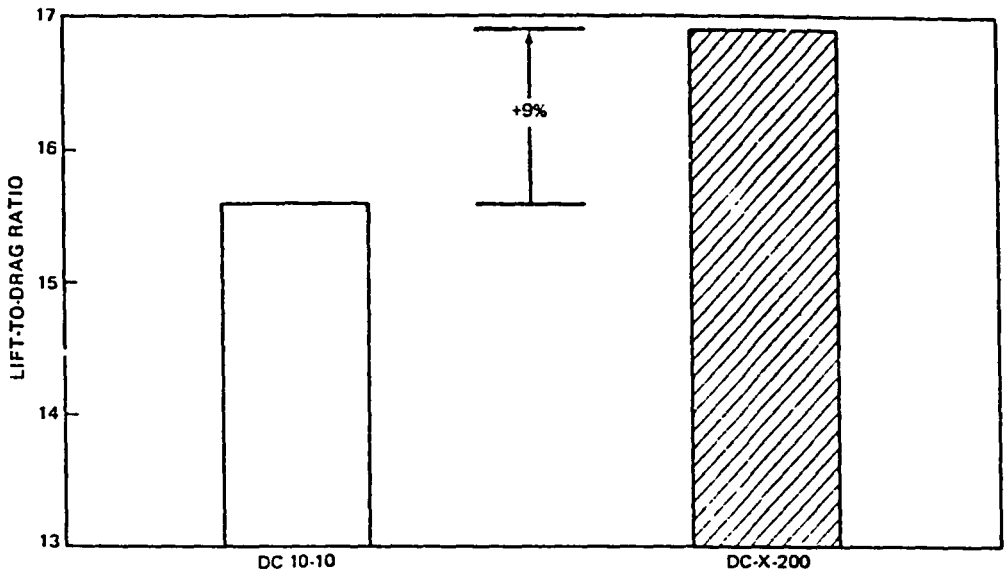

FIGURE 25. IMPROVEMENT IN CRUISE LIFT-TO-DRAG RATIO FOR ADVANCED HIGH ASPECT RATIO WING

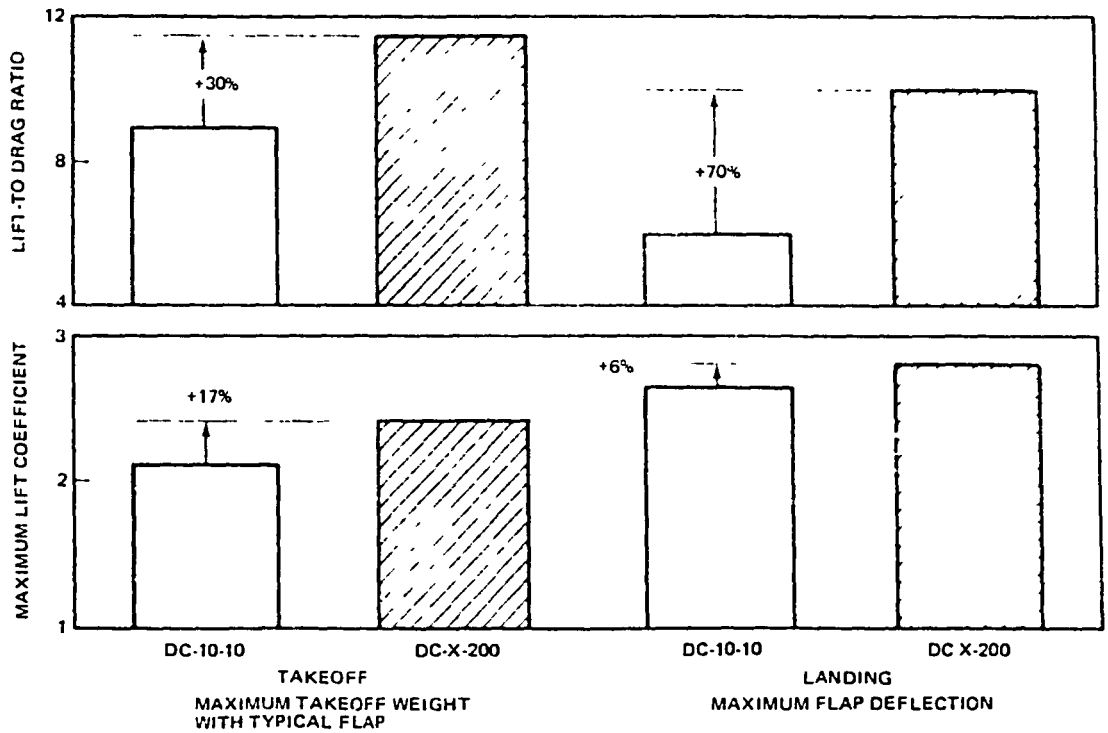

FIGURE 26. IMPROVEMENTS IN LOW-SPEED PERFORMANCE FOR ADVANCED TECHNOLOGY CONFIGURATION

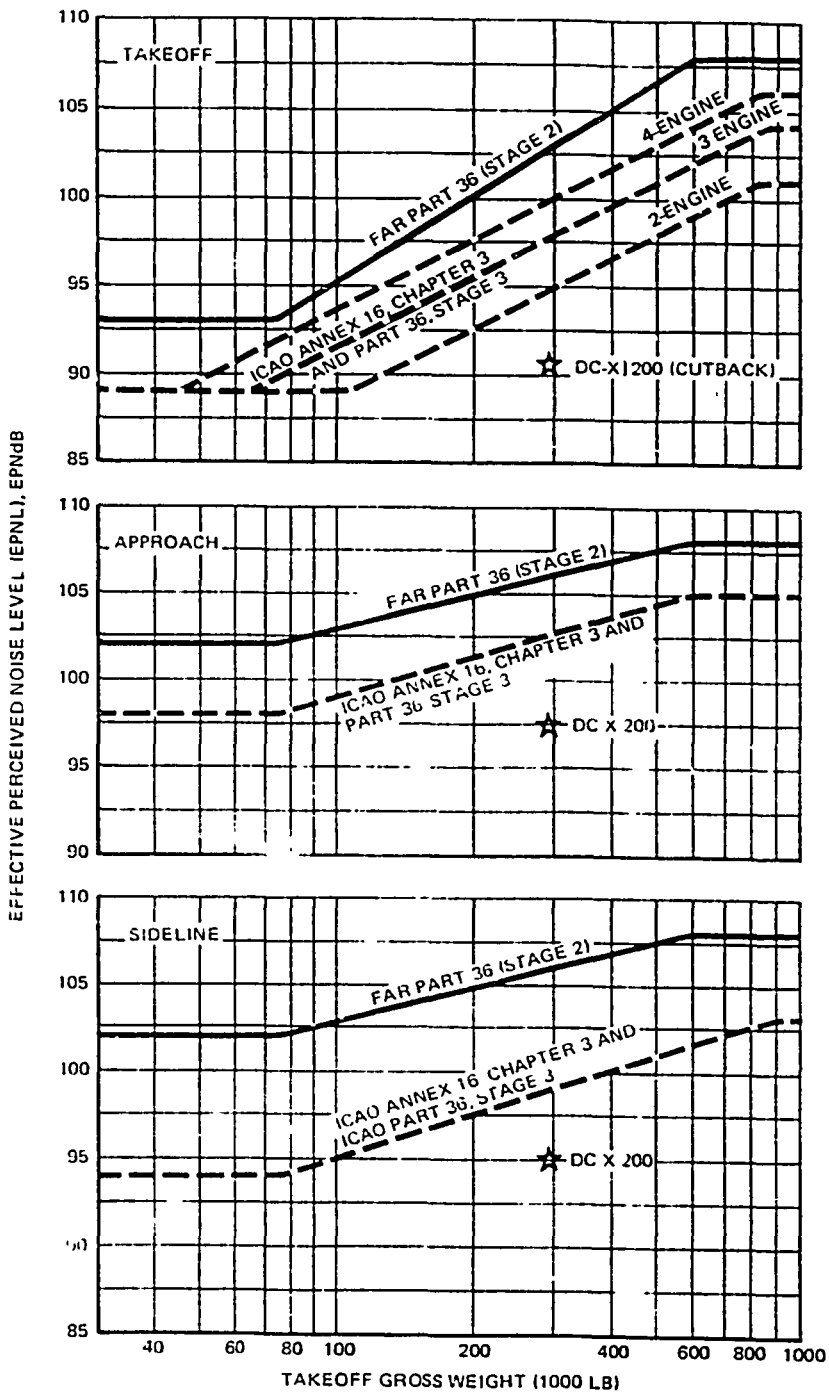

FIGURE 27. FAR PART 36; ICAO ANNEX 16, CHAPTER 3 (NEW DESIGNS) NOISE LEVEL REQUIREMENTS AND ESTIMATED DC-X-200 VALUES

engine, contain significant margins with even the most stringent noise requirements. One attribute of the low noise values for the DC-X-200 is presented in Figure 28. Estimated 100 EPNdB noise contours produced by the DC-X-200 during approach and takeoff are compared in Figure 28 with those of contemporary commercial aircraft for similar operational conditions (1000 mile trip/100-percent passenger loading and the new takeoff procedure of the Air Transport Association). The land area encompassed by the 100 EPNdB contour for the DC-X-200 is one-fifth or less than the area for the older generation of transport aircraft. Thus, the areas now exposed to annoying aircraft generated noise could be drastically reduced. This could permit operation out of noise-critical airports, increasing the utilization and route structure for the airlines. This can be a significant factor in today's "deregulation" of airline operations. Figure 29 compares the flyover noise levels of existing aircraft with the estimated values for the DC-X-200 configuration. Very low relative values are obtained for sideline and takeoff, with superior values being shown for the approach condition.

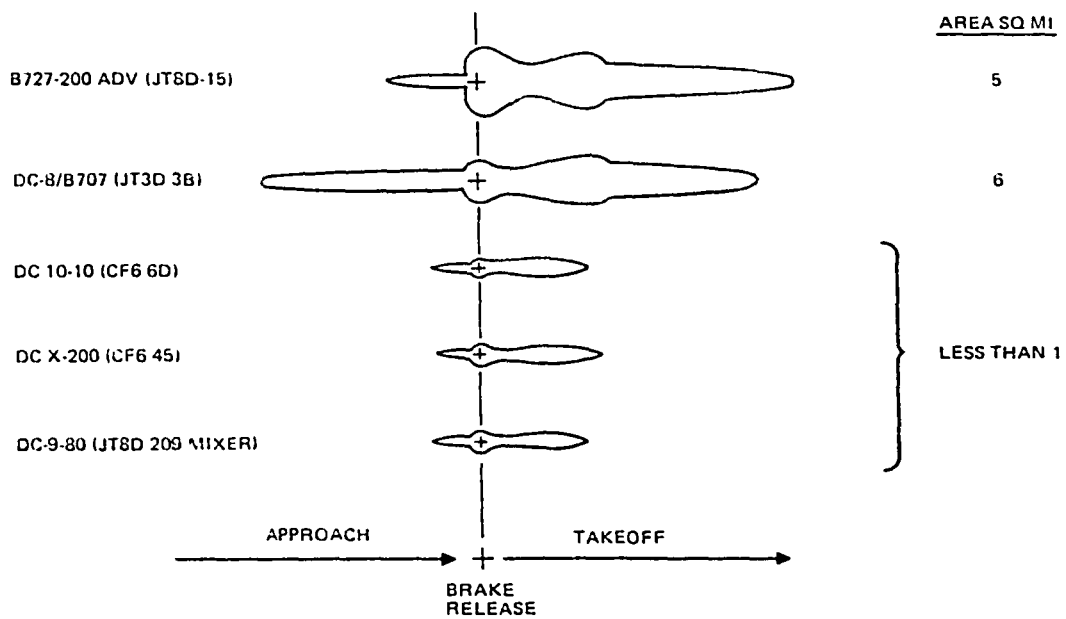

FIGURE 28 ESTIMATED 100-EPNdB APPROACH AND TAKEOFF NOISE CONTOURS (1000-STATUTE-MILE TRIP)

ORIGINAL PAGE IS
OF POOR QUALITY

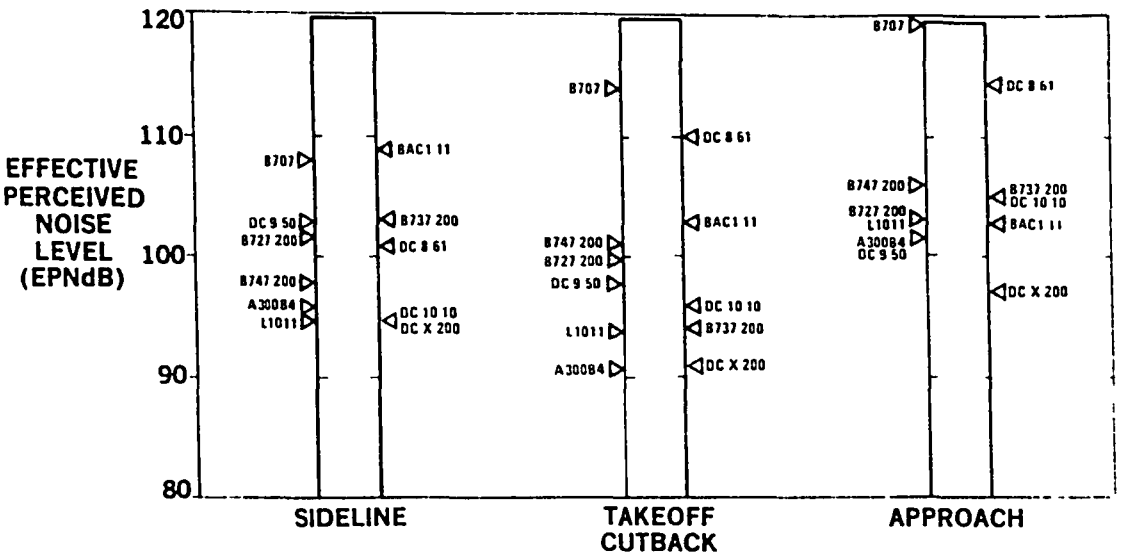

FIGURE 29. FAR PART 36 FLYOVER NOISE LEVELS

In order to evaluate the impact of the sum of the advanced technologies on fuel burned and DOC, a comparison of the DC-X-200 and existing operational aircraft was performed. The comparable characteristics are shown in Figure 30. The results are shown in Figure 31 where a comparison is made with the DC-10-10 as a base, of the relative fuel burned per seat-mile as a function of fuel burned per mile. Relative direct operating cost per 1050 km (750 n.mi) trip and per seat are shown in Figure 32. The estimated values for the 727-200 aircraft are the base for this comparison.

The DC-X-200 configuration was also compared to a configuration with a large wing area, an aspect ratio closer to the first generation jet transport aircraft, and a high lift system consisting of a slat and single-slot flap. The performance comparison was performed at 1050 km (750 n.mi). This range is more typical of the average distance over which this class of aircraft would operate. Results of this study are shown in Figure 33. Significant improvement in fuel burned and DOC are indicated for the configuration optimized for the domestic operations.

Since the overall configuration contains other advanced technology features, Figure 34 presents the breakdown of the impact of these features on DOC and profitability. The supercritical wing and high lift features are a significant portion of the total.

ORIGINAL
OF POOR

	B727-200 ADV	DC-X 200 (N-21)	A300B-4	DC 10-10
ENGINES NUMBER AND TYPE	3, JT8D 15	2, CF6-45	2, CF6 50C	3 CF6 6D
THRUST PER ENGINE, KN (LB)	68 95 (15,500)	200 17 (45,000)	226.86 (51,000)	178 37 (40,100)
NUMBER OF MIXED CLASS SEATS	140	230	257	295
CARGO VOLUME, M^3 (CU FT)	32 31 (1,141)	94 97 (3,354)	105 5 (3,725)	130 77 (4 618)
WING AREA, M^2 (SQ FT)	149 6 (1,610)	220 2 (2,370)	245 7 (2,645)	343 3 (3,695)
MAXIMUM TAKEOFF WEIGHT, KG (LB)	86,409 (190,500)	132,902 (293,000)	150 002 (330,700)	195 044 (430 000)
OPERATOR'S EMPTY WEIGHT, KG (LB)	47,368 (104 430)	79,038 (174,250)	90,945 (200 500)	110,236 (243,030)
DESIGN RANGE, KM (N MI)	2,769 (1,980)	3,636 (2,600)	2,769 (1,980)	4,349 (3,110)
CRUISE MACH NUMBER	0 81	0 80	0.80	0 83
TAKEOFF FIELD LENGTH, MTOGW, SL, 29°C (84°F), M (FT)	2 630 (8,630)	2,173 (7,130)	2 103 (6 900)	2,825 (9,270)
APPROACH SPEED WITH FULL PSGR, BAGGAGE AND RESERVES KM/H EQUIV (KEAS)	182 (130)	183 (131)	183 (131)	182 (130)
PAYLOAD FROM DEN–JFK 33°C (92°F) DAY, AIRLINE RULES [PSGR/KG (LB) CARGO]	84/0	230/3,946 (8,700)	169/0	246/0
FUEL BURNED AT 1389 KM (750 N MI), KG (LB)	7,902 (17,420)	8 160 (17,990)	11,122 (24,520)	12 374 (27 280)
RELATIVE AIRCRAFT STUDY PRICE (PERCENT)	38	79	85	100*

*1977 $30 4M

FIGURE 30. COMPARATIVE CHARACTERISTICS

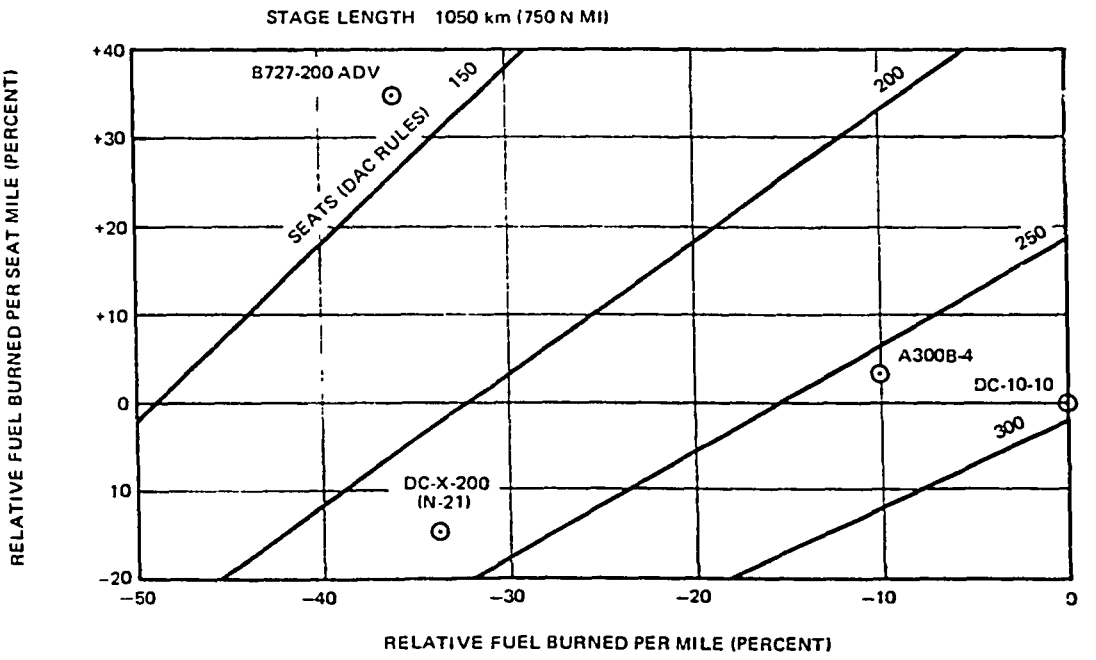

FIGURE 31. RELATIVE FUEL BURNED

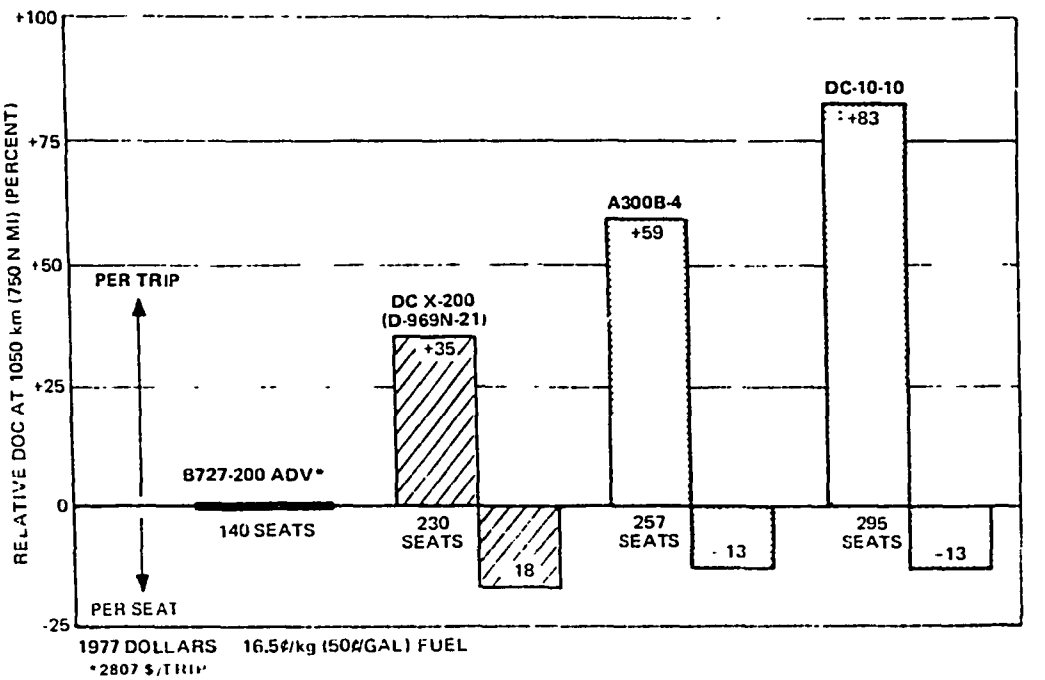

FIGURE 32. RELATIVE DIRECT OPERATING COSTS FOR CONVENTIONAL AND ADVANCED CONFIGURATIONS

DESIGN OBJECTIVE	OPTIMIZED FOR DOMESTIC OPERATIONS	COMPROMISE FOR INTERNATIONAL AND DOMESTIC OPERATIONS
WING GEOMETRY AREA	SMALL	LARGE
ASPECT RATIO	HIGH	LOW
SPAN	MEDIUM	MEDIUM
HIGH LIFT SYSTEM	VCK PLUS TWO-SLOT FLAPS	SLAT PLUS ONE SLOT FLAPS
RELATIVE FUEL BURNED	0	6 0 PERCENT
RELATIVE DIRECT OPERATING COSTS	0	2 6 PERCENT

9 DP 8155

FIGURE 33 WING GEOMETRY CHOICE

ADVANCED FEATURE	DOC (%)	INCREMENTAL* OPERATIONAL PROFIT (%)
SUPERCRITICAL WING (CONSTANT AR)	−3 5	+58
HIGH ASPECT RATIO WING	−2.0	+10
VARIABLE CAMBER KRUEGER	−1 9	+32
LONGITUDINAL STABILITY AUGMENTATION	−0 5	+5
COMPOSITE FLOOR BEAMS AND STRUTS	−0 2	+1
COMPOSITE CONTROL SURFACES/FAIRINGS/WING FIXED TRAILING EDGE	−0 2	+2
AUTOMATIC REVERSE THRUST	−0 2	+2
ELECTRICALLY SIGNALED SPOILERS	−0 1	+2
SHORTENED ENGINE CORE COWL (NO PRIMARY REV)	−0 7	+10
DIGITAL FLIGHT GUIDANCE AND CONTROL	−0 3	+6
TOTALS	−9 6	+130

*RELATIVE TO ALTERNATIVE INVESTMENTS AT 8 5% ANNUAL INTEREST

FIGURE 34. ADVANCED FEATURES ECONOMIC ASSESSMENT

Application of supercritical wing technology for the medium range transport has shown significant potential benefits from both economic, fuel usage and social aspects (noise). Increased confidence in these predicted improvements is aided by a substantiation of the performance level for each of the disciplines which are involved in the configuration definition. The current EET studies of the supercritical wing high- and low-speed aerodynamic characteristics, have aided in this substantiation, and also highlighted areas for further development.

ORIGINAL PAGE
OF POOR QUALITY

HIGH LIFT AERODYNAMIC DESIGN PROCESS

General Design Constraints

The aerodynamic design process for the high lift system is quite complex and involves the interaction of many disciplines. A primary design constraint is, of course, the requirement of high lift system compatibility with the cruise wing shape and structure. This compatibility is influenced directly by the spanwise variation of the available chord ratio for the high lift system components, as well as the shape of specific portions of these high lift devices.

Figure 35 illustrates the regions determined by the cruise configuration and those surfaces which are at the discretion of the high lift designer. Further, these latter surfaces are also influenced by structural considerations. For example, in Figure 35 the slat high lift device and its associated wing under slat surface (WUSS) are influenced by local chord constraints and slat trailing edge thickness and closure angle. A VCK concept allows more aerodynamic freedom for the basic shape definition resulting in increased lift capability. Other factors which can influence the leading edge device aerodynamic definition include front spar location, anti-icing ducting requirements, actuation system, fuel, and hydraulic line space requirements.

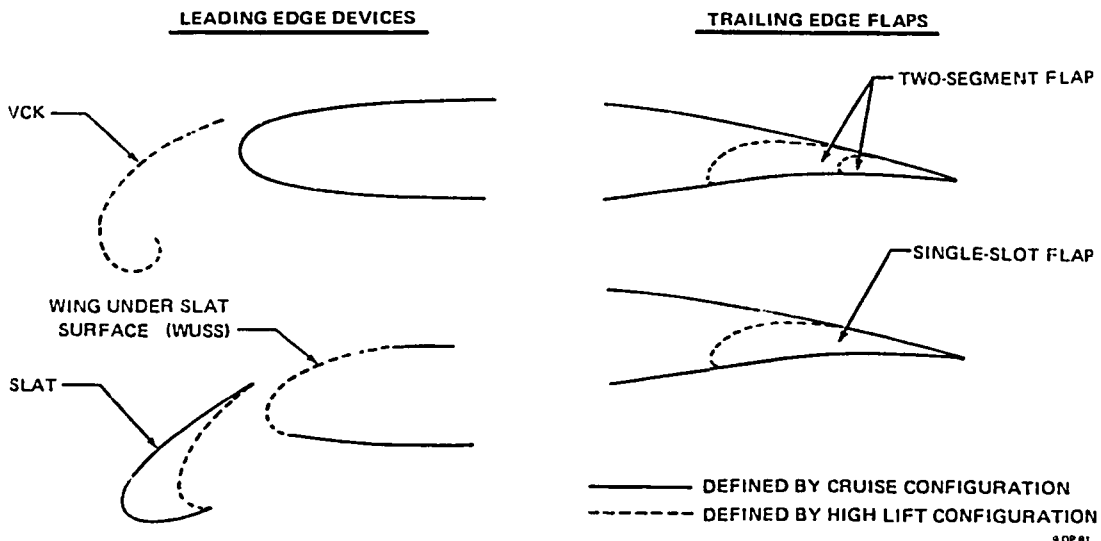

FIGURE 35. SURFACES DEFINED BY CRUISE AND HIGH LIFT CONSIDERATIONS

OR
OF POO

The trailing edge high lift system is influenced by rear spar location, the spoiler actuation system, the spoiler trailing edge chordwise position, and the spoiler closure angle and thickness. Relaxed static stability adversely affects the inboard flap chord, due to the further aft placement of the landing gear and related structure. In addition, due to lateral stability and control requirements, spoiler chord and span as well as aileron location, influence the trailing edge flap definition.

High Lift Design Methods

With the high lift concepts selected and the guidelines for the related structural constraints defined by the results of in-house studies, the detailed aerodynamic design process indicated in Figure 36 was used to define the high lift systems for the wind tunnel model. The design function consists of four basic parts: the experimental data base, two-dimensional (2-D) analytical studies, two-dimensional to three-dimensional (2-D to 3-D) concepts and the three-dimensional lifting surface calculations.

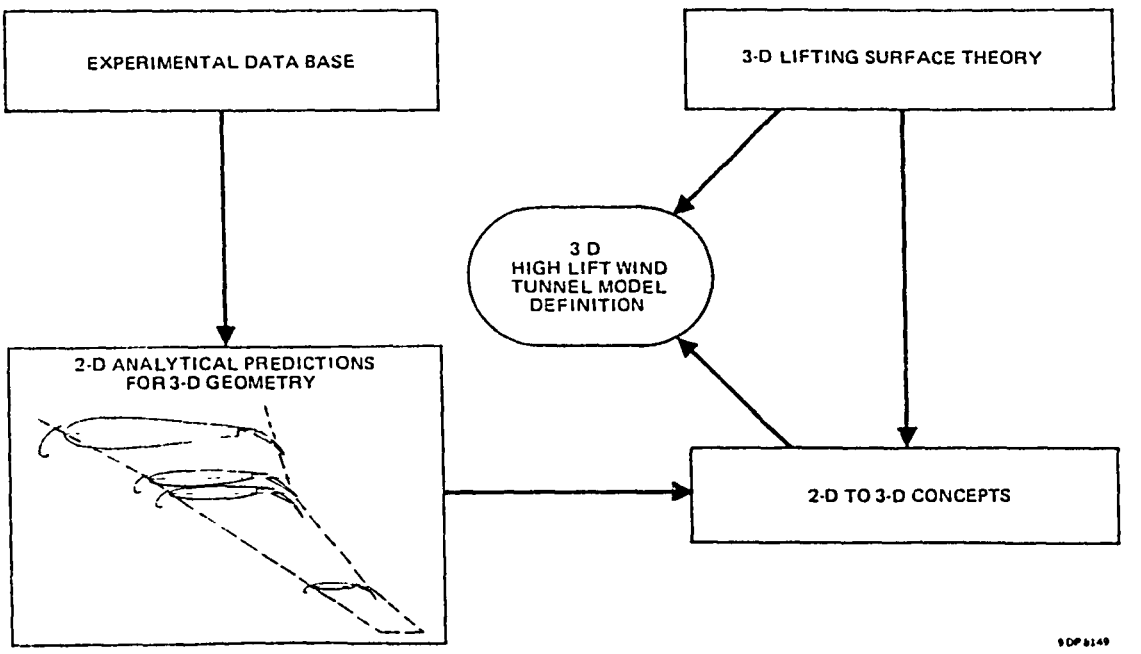

FIGURE 36. HIGH LIFT AERODYNAMIC DESIGN PROCESS

Experimental Data Base

An extensive experimental two-dimensional data base for aerodynamic characteristics of supercritical airfoil high lift systems had been generated by previous Douglas funded studies. This data base included: effects of conventional and supercritical airfoil sections; thickness ratio; slat and VCK leading edge devices, single-slot, two-segment, and triple-slotted trailing edge devices, and optimization of the position and deflection of these systems. Detailed wake and boundary layer measurements for selected configurations had also been generated to provide a more fundamental understanding of supercritical airfoil high lift systems.

This experimental data, on conventional and supercritical high lift configurations, was used in the design of the high lift system for the current three-dimensional high lift model. Various Krueger leading edge shapes were evaluated with respect to $c_{\ell_{max}}$ and profile drag characteristics. Two-dimensional values of such parameters as flap lift increment, $(\Delta c_{\ell_{\alpha=0}})$, flap maximum lift increment, $(\Delta c_{\ell_{max_{flap}}})$, and leading edge device maximum lift increment $\Delta c_{\ell_{max_{L.E.}}}$ were also utilized in the generation of the estimated characteristics for the wind tunnel model. In addition to the evaluation of various high lift concepts, another significant use of the 2-D experimental data in the design process was the determination of key design criteria by means of theoretical calculations for the experimentally optimized configurations. The design criteria included suction peaks, pressure gradients, and calculated separation locations and were used for the design and element position studies on the equivalent three-dimensional model components.

The Multielement Airfoil Design and Analysis Method (MADAAM) theoretical method (Reference 4) was used to generate the theoretical calculations. This computer program can compute the high lift characteristics of multielement airfoils of arbitrary shape for a viscous incompressible fluid in the absence of flow separation. The program combines a geometry definition routine, a potential flow solution based on a surface source distribution, and a finite-difference boundary layer routine to accomplish the analysis. The geometry routine can smooth and space the body coordinates for input to the potential flow program. After the potential flow distribution has been calculated the boundary layer characteristics are

ORIGINAL PAGE IS
OF POOR QUALITY

calculated and an equivalent inviscid body is formed by the addition of the boundary layer displacement thickness to the original geoemtry. These coordinates are used to calculate a new pressure distribution for the equivalent body. Figure 37 illustrates the computational process.

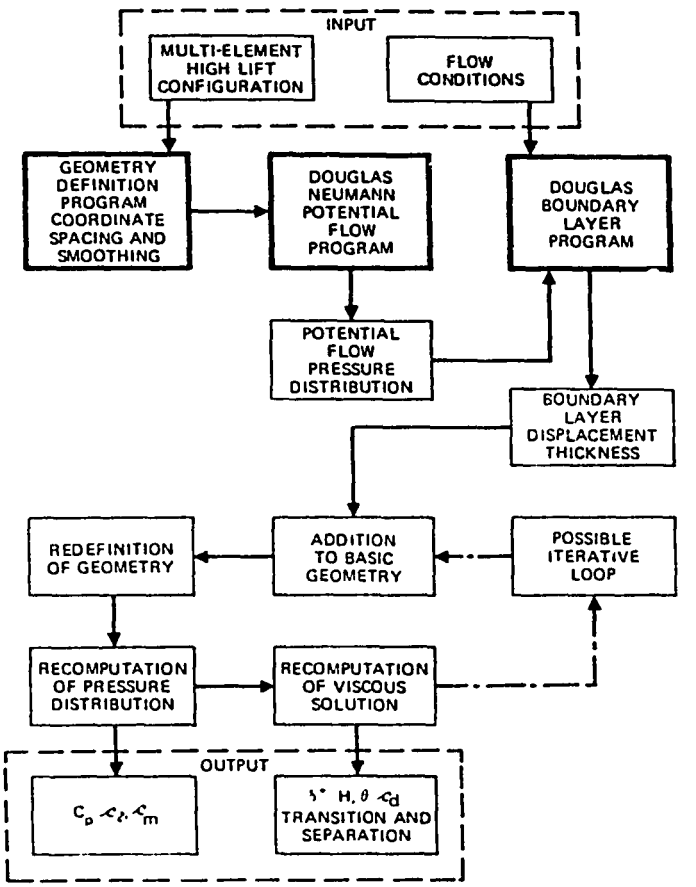

FIGURE 37. FLOW DIAGRAM OF COMPUTER PROGRAM FOR MULTI-ELEMENT AIRFOIL DESIGN AND ANALYSIS METHOD (MADAAM)

A comparison of a representative calculated pressure distribution from the MADAAM program and the multielement experimental data for a thick supercritical high lift system is presented in Figure 38. Theoretical predictions included both the potential and viscous flow capabilties of the program.

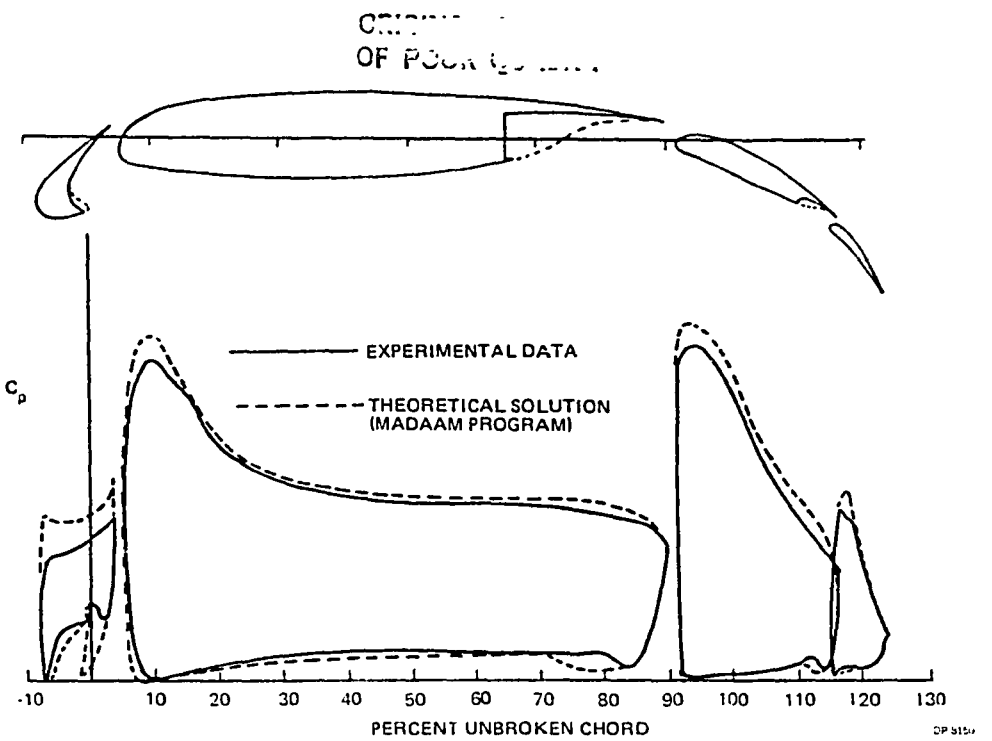

FIGURE 38. COMPARISON BETWEEN EXPERIMENTAL AND ANALYTICAL PRESSURE DISTRIBUTIONS FOR MULTI-ELEMENT AIRFOIL

2-D Analytical Prediction for 3-D Geometry

For the selected high lift concepts, values of such basic parameters as airfoil thickness and camber, flap chord, and spoiler trailing edge location varied from the existing experimental data base. Moreover, significant variations in these basic parameters occurred over the span of the three-dimensional wing. In order to account for these effects, theoretical analysis of various spanwise stations of the wing were carried out by means of the MADAAM program. Extensive use of this program was required to define the flap leading edge shape and positions relative to adjacent elements. This was due to the relatively thin trailing edge shape of the outboard supercritical wing, and the basically uncambered trailing edge region and short flap chord near the wing root. Figure 39 presents typical calculations for three spanwise positions. The configurations shown include a VCK and two-segment flap system for the inboard and outboard spanwise station, and a VCK with single-slot flap for the midspan wing position.

OF POOR

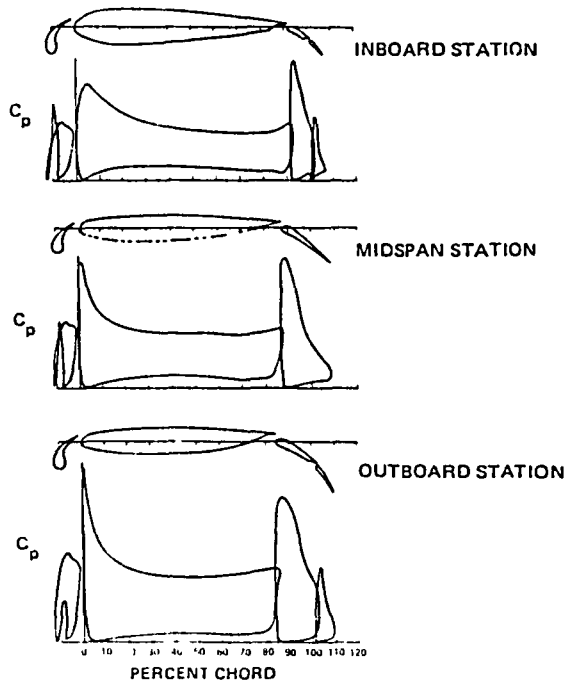

FIGURE 39. MADAAM PRESSURE DISTRIBUTIONS FOR THREE SPAN STATIONS

2-D to 3-D Concepts

The calculated 2-D results were then modified by 2-D to 3-D sweep effects. These concepts were based on previous in-house correlations of 3-D experimental multi-element pressure distributions and MADAAM program calculations. The correlations accommodate the basic sweep and taper effects of 3-D wing planforms with multi-element airfoil sections. The corresponding theoretical pressure criteria (peak pressures and gradients) established from the 2-D experimental data base were also transformed in the same manner, such that comparisons of pressure criteria and calculated 3-D pressures for the wind tunnel model could be made. All of these pressure criteria were evaluated as a function of the three-dimensional sectional lift coefficient ($c_{\ell_{3-D}}$).

3-D Lifting Surface Theory

For a given airplane lift coefficient (C_L) the section lift coefficients were evaluated by means of the Giesing Vortex Lattice program (Reference 5).

This program has been previously used to calculate $c_{\ell_{3-D}}$ for high lift configurations and good agreement between experiment and program calculations was obtained (see Reference 6). With the $c_{\ell_{3-D}}$ evaluated, the previously mentioned 2-D to 3-D pressure criteria could be evaluated for a given value of C_L.

When evaluating leading edge device, wing leading edge, or WUSS peak suction values (i.e., to determine proper VCK or slat deflection or position), one additional correction was used. The 2-D experimental data base indicated that near $c_{\ell_{max}}$ a significant reduction in flap lift was apparent. If the geometric flap deflection was used in the Giesing program near $C_{L_{MAX}}$, the $c_{\ell_{3-D}}$ distribution across the span would not be the proper variation.

Further, for a given 2-D section lift coefficient the MADAAM flap lift would be overpredicted, and a suppression of the suction peaks at the nose would result. Accordingly, the flap deflection input into the Giesing and MADAAM programs was reduced by an amount determined by the 2-D data base when evaluating suction peaks near stall for the leading edge regions previously discussed. A typical spanwise variation of calculated slat and WUSS minimum pressures is shown in Figure 40.

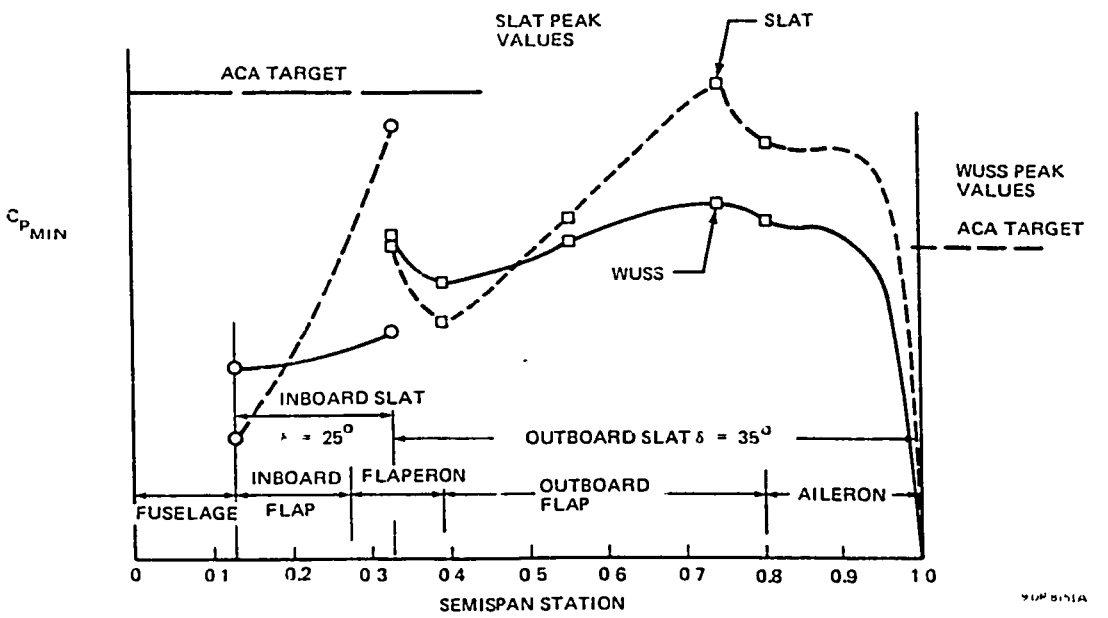

FIGURE 40. THEORETICAL SPANWISE VARIATION OF SLAT AND WUSS MINIMUM PRESSURES FOR THE LOW-SPEED WIND TUNNEL MODEL (LANDING FLAPS C_L = 3.4)

Also shown are the model target values. At each leading-edge device deflection, plots such as these were used to evaluate the basic position (gap and overhang) of the VCK or slat. Once a basic position was established, the results of the position study as calculated by the method of Figure 37, and the 2-D experimental position trends, were used to determine the alternate grid positions.

Shape Definition for Leading and Trailing Elements

The basic shape for the VCK was defined by a previously tested two-dimensional configuration. Slat and WUSS shapes were defined by application of the MADAAM program with systematic variations in WUSS chord, camber, and nose radius at a nominal slat position and deflection. Using the procedure of Figure 37, a WUSS shape was chosen for the defining stations.

The MADAAM program was also used to define the two-segment flap and flaperon shapes at the airfoil defining stations on the wing. Within the structural constraints previously discussed, flap nose radius and camber were varied and the resulting pressure distributions and separation locations were evaluated at a nominal flap setting based on previous 2-D and 3-D two-segment and single-slot flap experimental studies. The methodology of Figure 37 was again used to determine the flap shape to be tested. The ratio of main flap chord to aft flap chord was determined by previous 2-D and 3-D in-house experimental data.

OF POOR QUALITY

WIND TUNNEL MODEL DESCRIPTION

The configuration selected for the wind tunnel test program incorporated the results of the in-house studies. Additionaly, the model components allowed the testing of alternative high lift systems. Figure 41 shows the basic configuration shape. It is characterized by a high aspect ratio supercritical wing, wide-body fuselage, and wing-mounted engines. The trapezoidal wing planform, which has a quarter chord sweep of 28.5°, incorporated leading and trailing edge breaks for improved cruise characteristics. Thickness to chord ratio varied from 15 percent at the root to 11 percent at the wing tip. Near the root, the basic supercritical airfoil section changed to a symmetrical shape for improved cruise performance.

The wind tunnel model was a 4.7-percent scale representation of the DC-X-200 airplane configuration. The model was designed and fabricated for testing at high Reynolds number conditions at the NASA Ames 12-Foot Pressure Wind Tunnel. The model designation was LB-486A for the Ames test and LB-486C for the NASA Langley V/STOL test.

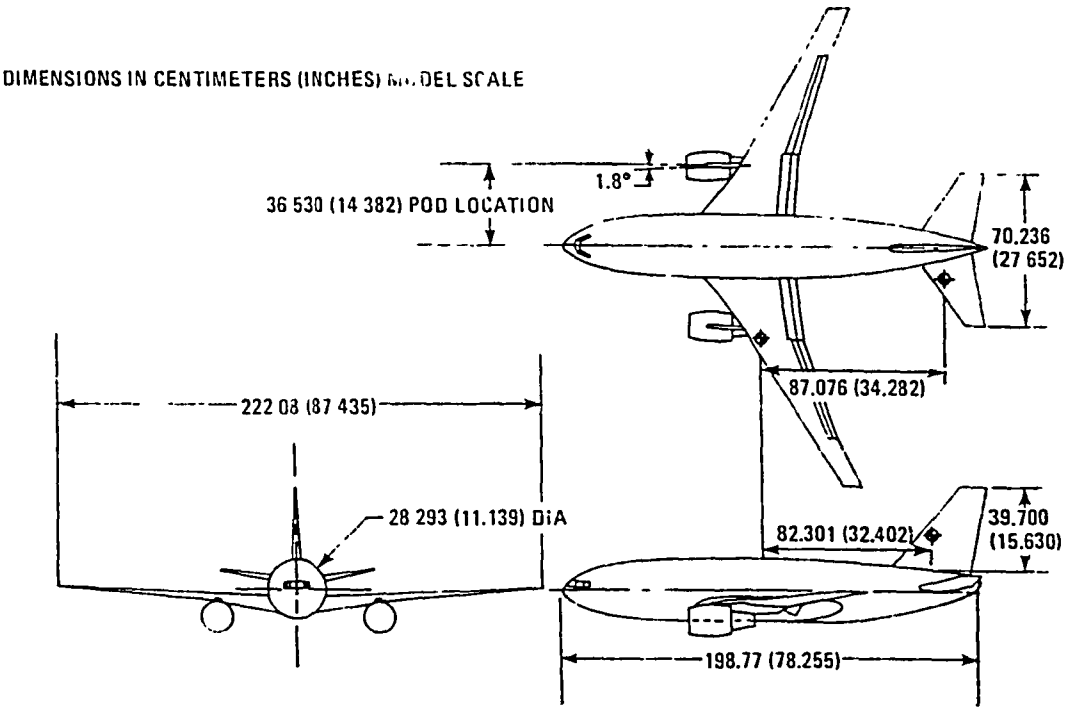

FIGURE 41. LB-486A MODEL THREE-VIEW

Figure 42 illustrates the high lift systems for the wind tunnel tests. The primary leading edge configuration was a VCK flap. While the basic configuration incorporated independent inboard and outboard segments, additional pieces were fabricated such that a continuous full span VCK extent was possible (i.e., sealed at the fuselage side and continuous across the engine pylon). Associated with this VCK were cutouts in the lower surface of the wing (VCK wells) representing the absence of a continuous lower surface when the VCK was deployed.

The secondary configuration for the leading edge was a slat. This device incorporated a sealed configuration over the engine pylon, but a gap at the fuselage side. Positioning of the inboard and outboard segments was accomplished independently. Associated with the slat was a revised leading edge contour (WUSS).

For the trailing edge high lift system, the primary configuration was an inboard and outboard two-segment flap. Between these two flaps was a device called a flaperon, which was essentially a single-slotted flap, that was articulated in the same manner as the main flap for the high lift conditions, but incorporated a high-speed short chord aileron in the retracted, or cruise configuration. At the high lift condition, the aileron was locked in an undeflected position. This permitted a continuous flap span of some 80 percent, resulting in an improved span loading for high lift conditions.

As Figure 42 shows, the secondary trailing edge configuration was a single-slot flap. On the model this configuration was obtained by simply stowing the aft flap into the main flap. The resulting configuration was an 80-percent span single-slot trailing edge flap.

In order to optimize the high lift geometry, both the leading and trailing edge devices incorporated bracketry for changing deflection and position. The model also incorporated an aileron (left wing panel only), spoilers, and remote-drive horizontal stabilizer deflection capability. The wing and high lift systems were also instrumented with static pressure orifices at the five spanwise stations. Other model components included nacelles, pylons, landing gear, and a cruise wing trailing edge (i.e., flaps retracted).

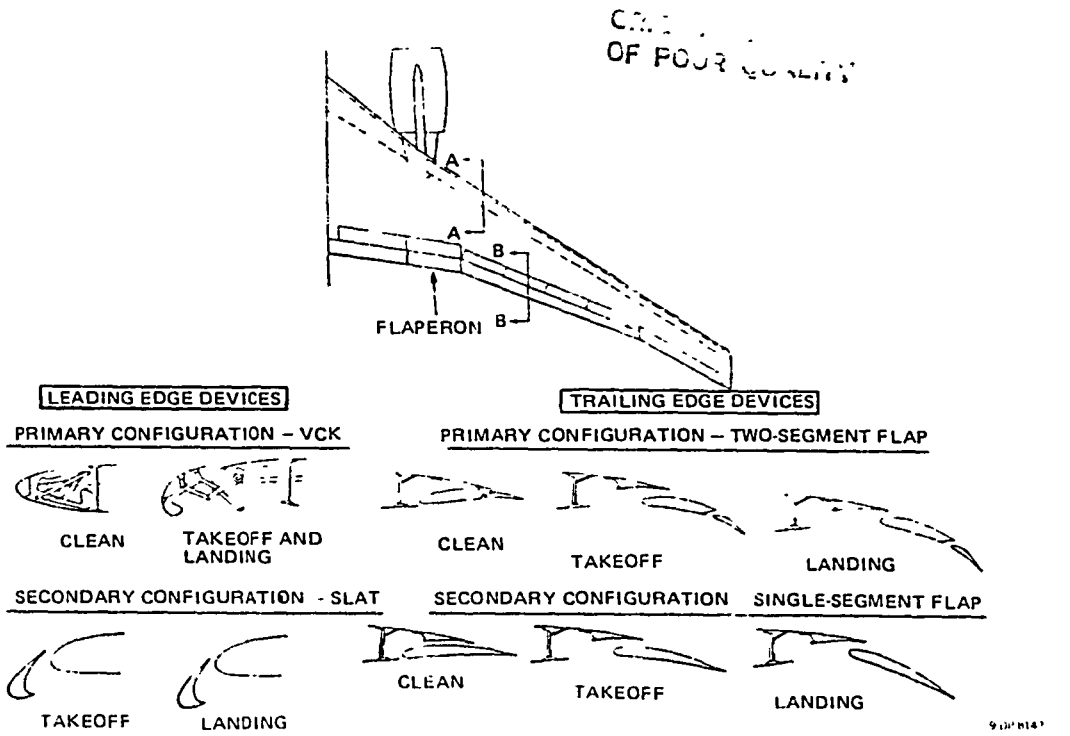

FIGURE 42. HIGH LIFT COMPONENTS EVALUATED IN EXPERIMENTAL TEST PROGRAM

The fuselage (B_{2A}) consisted of duplicated DC-10 model nose and aft fuselage shell sections, a new to[illegible] center section, and a new wing-fuselage fillet section.

An existing fuselage core was adapted for attachment of the fuselage shell sections, support of two five-module scanivalve systems, support of a bubble pack plate, and attachment of the wing, vertical, and horizontal stabilizer. An existing fuselage internal pitch system was installed in the core. This system permitted the fuselage to be pitched from $\alpha_{FRP} = 0^o$ to $+10^o$ while the internal balance remains at $\alpha_{FRP} = 0^o$. The α_{FRP} (angle of attack) is the angle which the Fuselage Reference Plane (FRP) makes with the equivalent free airstream. The other pitch angles are obtained by using the external pitch system.

The W_{3B} model wing was fabricated from Armco 17-4 steel and was lofted to simulate the airplane wing with a 1g load. The wing geometry and planform dimensions are shown on the wing diagram (Figure 43). The wing-fuselage fillet notation is X_{23}.

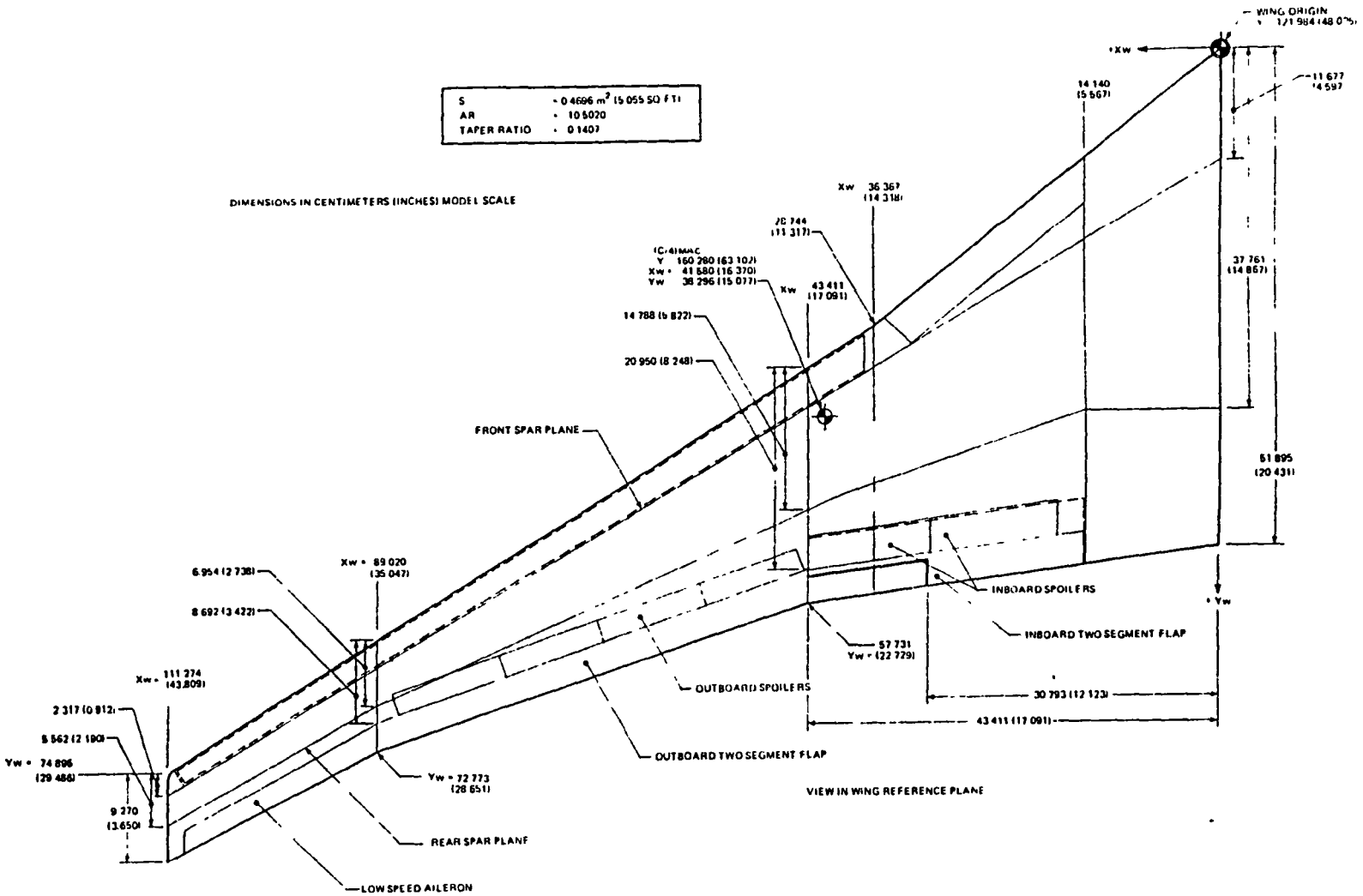

FIGURE 43. WING DIAGRAM (W_{3B})

ORIGINAL PAGE IS
OF POOR QUALITY

OF POOR QUALITY

The model wing incorporated the following features:

1) A cruise leading edge, removable at the front spar. This leading edge was tested with and without simulated VCK stowage wells. Also provided was a WUSS leading edge for the slat configuration.
2) A VCK and slat leading edge device with variable position and deflection capability.
3) A two-segment trailing edge flap supported at five deflection angles by fixed brackets simulating the airplane flap linkage. Variable position capability was provided for the main flap.
4) A manually set aileron, left side only, and spoilers, both sides.
5) Approximately 400 static pressure orifices installed in the VCK, slat, wing, and flaps.

Figure 44 presents the planform of the horizontal stabilizer as well as other geometric quantities. The horizontal stabilizer was removable for testing tail-off. The stabilizer was fabricated in one piece, each side, without elevators. An existing remote control system was adapted to vary the stabilizer incidence between +5° and -15°.

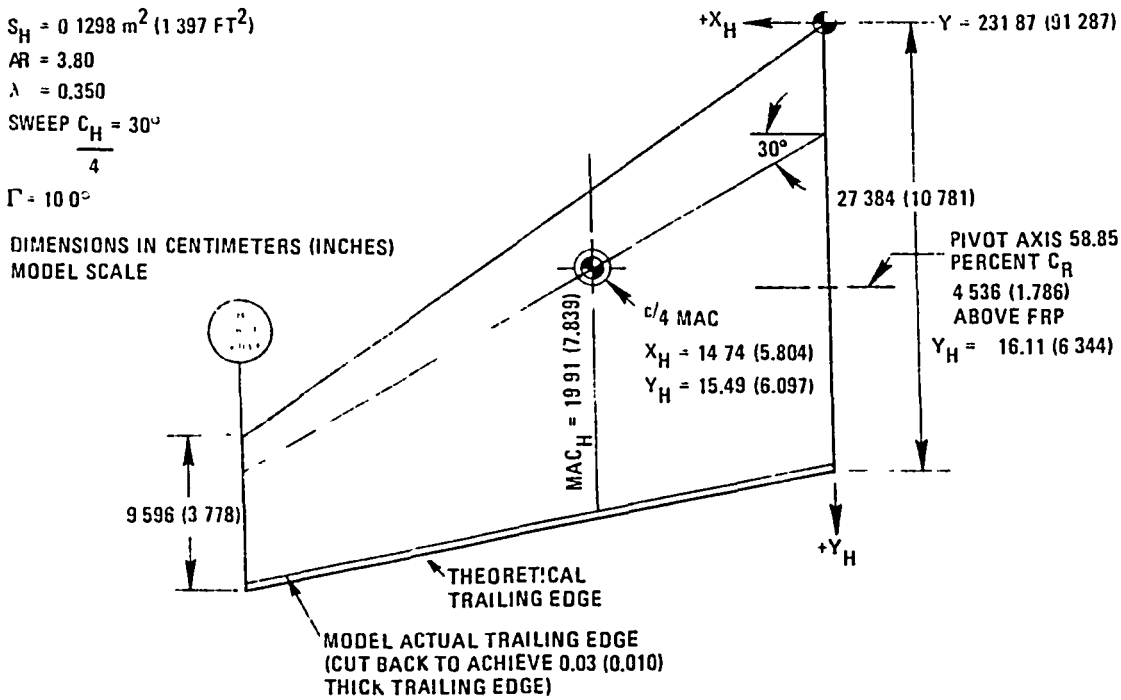

FIGURE 44. HORIZONTAL STABILIZER H_{1A} DIAGRAM

The vertical stabilizer (V_{1A}) planform is shown in Figure 45. The stabilizer was fabricated as one piece without rudders and was removable to provide a tail-off configuration.

Existing flow-through nacelles (Figure 46) from a DC-10 model were used for the subject model and designated N_{2A}. They were attached to the wing by new pylons designated P_{2A}. The pylon plane of symmetry had a 1.8° toe-in relative to the airplane plane of symmetry (measured in the FRP) and is perpendicular to the FRP with the wing in a rigged position with dihedral = 4.05°. Nacelle strakes (Z_{1A}) were attached to the nacelle for most configurations.

The nose gear simulated the DC-10 nose gear in structure and location. The main landing gear simulated the airplane gear configuration with oleos extended. Extended main gear wheel well cavities were not simulated. A

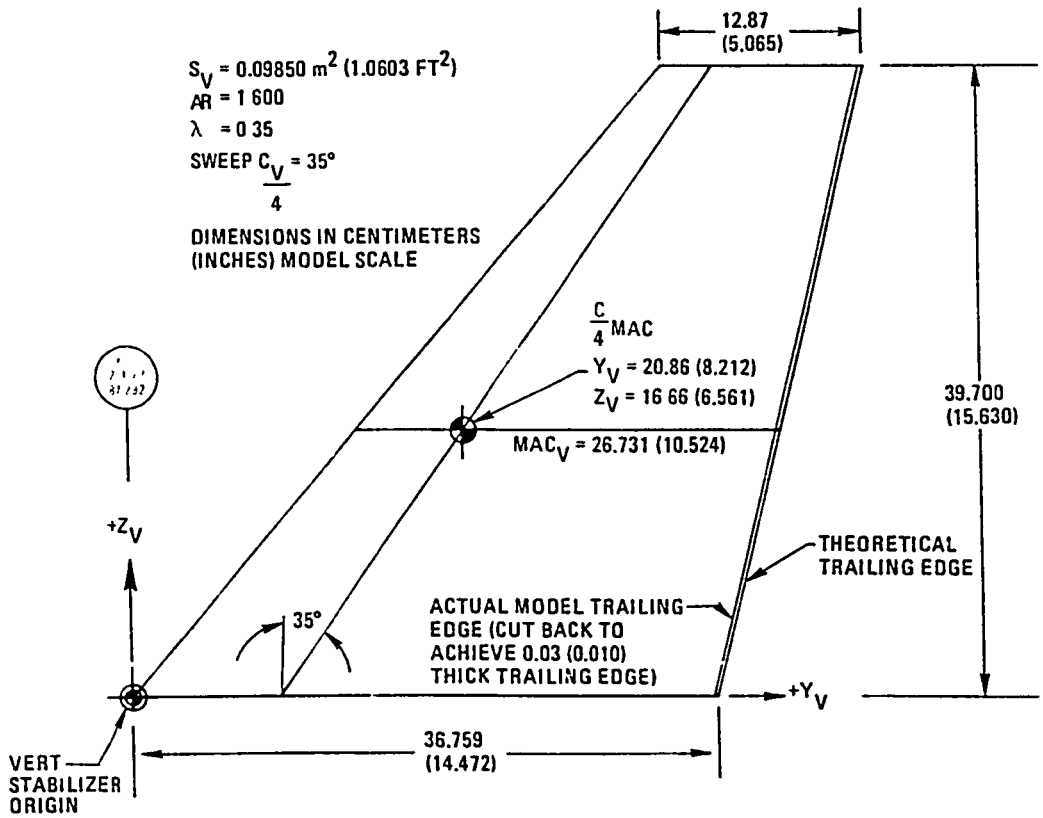

FIGURE 45. VERTICAL STABILIZER V_{1A} DIAGRAM

OF POOR QUALITY

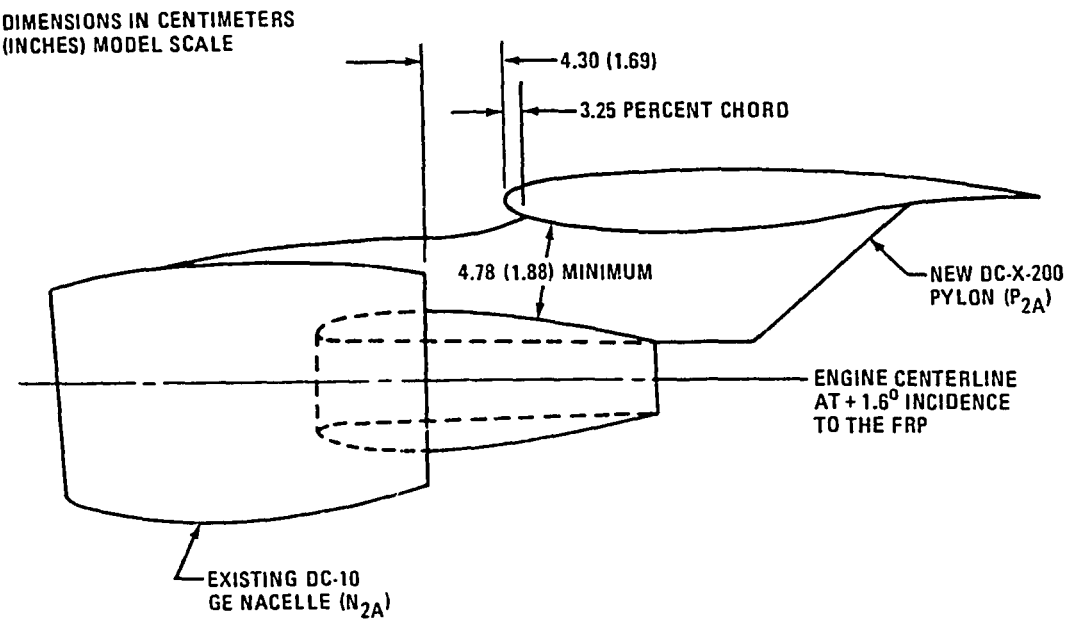

FIGURE 46. NACELLE/PYLON $N_{2A}P_{2A}$ DIAGRAM

main landing gear retracted configuration is also provided. The combined nose and main landing gear assemblies nomenclature was G_{1A}.

The outboard aileron (a_{2A}) was located in the outboard extremity of the left hand wing. The aileron incorporated a felt-type, well-gap seal and had a different upper and lower nose radius because of the vertical location of the hinge line (Figure 47).

The aileron was tested at deflection angles of 0°, ±5°, ±10°,±15°, and ±20°. The angles were measured in a plane normal to the hinge line. The aileron planform is shown in Figure 43.

Two inboard spoiler segments (f_1,f_2) and four outboard segments (f_3,f_4,f_5,f_6), both sides, could be set at deflection angles of 0°, -5°, -15°, -30°, -45°, and -60°, measured in a plane normal to the spoiler hinge line. The two inboard segments (f_1,f_2) were fabricated as separate parts while the four outboard segments (f_3,f_4,f_5,f_6) were not segmented, but were fabricated as one-piece bent plates. An individual plate was provided for each deflection angle.

ORIGINAL PAGE IS
OF POOR QUALITY

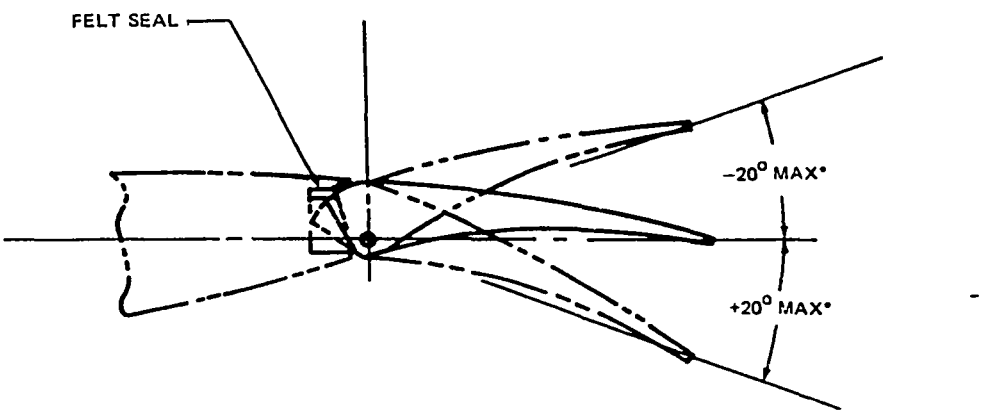

*SEE SUMMARY OF MOVABLE SURFACES (TABLE 1) FOR DEFLECTION ANGLES AVAILABLE FOR TEST

FIGURE 47. AILERON SECTION (a_{2A})

The scaled airplane spoiler trailing edge thickness would have been approximately 0.0762 cm (0.003 in.) The model spoilers deviate from these dimensions, with the lower surface of the spoiler segments modified to obtain the standard minimum trailing edge thickness of 0.0127 cm (0.005 in.) radius, while maintaining the theoretical planform trailing edge location for flap rigging purposes. The spoiler planform diagram is presented as part of Figure 43.

The definitions of gap, overhang (O.H.), and deflection used to position the leading edge high lift devices are illustrated in Figure 48. Figure 48 also shows the method of attachment to the WUSS and clean leading edge (for the slat and VCK devices respectively). As indicated for the VCK, bolts attached the device to an angle bracket and the bracket was positioned relative to the wing by means of spacers (to adjust the gap) and pin holes through the bracket into the wing for overhang positioning. An additional set of bolts fastened the bracket to the wing. Each deflection angle had separate brackets.

A full span wing leading edge slat (L_{1A},L_{2A}) with a seal at the pylon was tested. Positioning capability included three alternate positions for each of two deflection angles. The slat was fabricated in two parts, with the common boundary at station X_w = 36.367 cm (12.123 in). The inboard and outboard slat designations were L_{1A} and L_{2A}, respectively.

ORIGINAL PAGE IS
OF POOR QUALITY

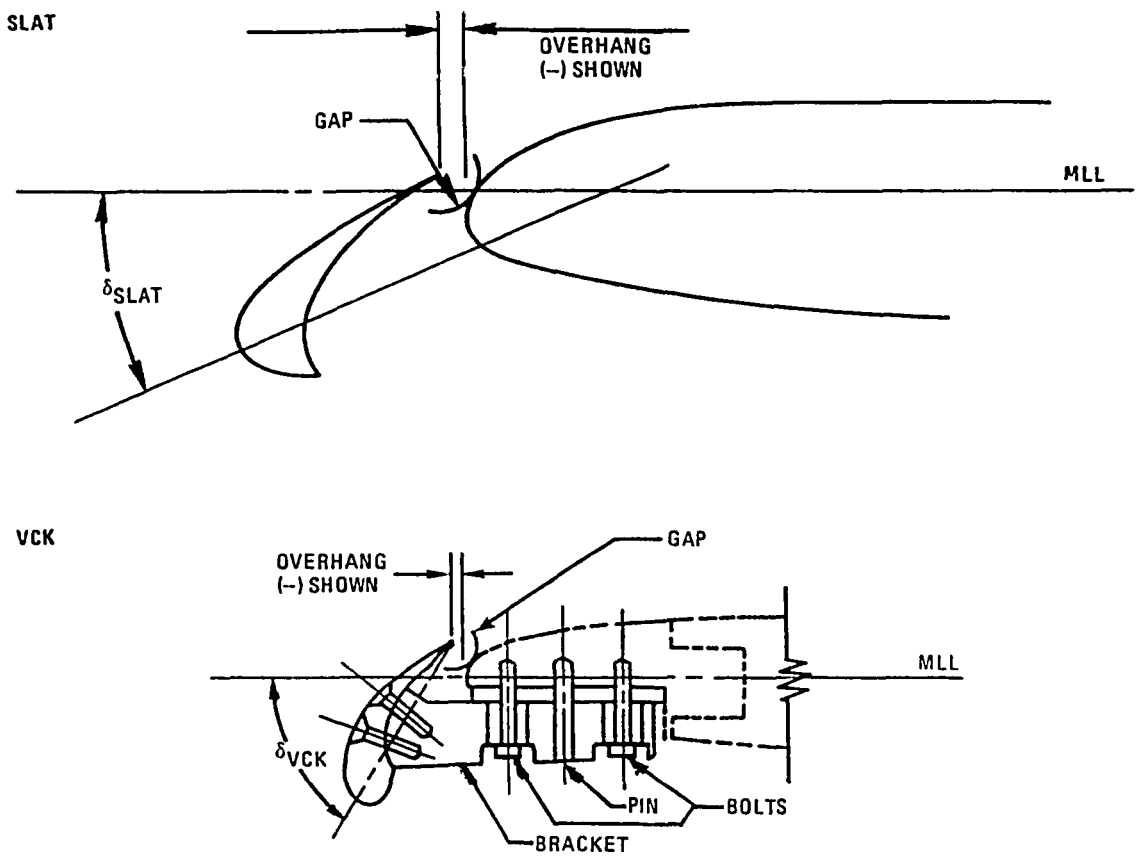

FIGURE 48. LEADING EDGE DEVICE GAP, OVERHANG, AND DEFLECTION DEFINITIONS

A WUSS component was also provided to replace the cruise leading edge. A planform diagram of the slat is shown in Figure 49.

The deflection angles were measured in a streamwise plane oriented normal to the Wing Reference Plane (WRP). The variable test positions are defined and identified in the Configuration Notations Section.

A full span VCK, with an interruption at the pylon, was designed to be installed at four alternate positions at each of two deflection angles. The VCK was supported from the cruise leading edge component which was modified for testing with and without simulated VCK stowage wells. A VCK extension to the fuselage was designated L_{5A}, and the VCK extension over the pylon was designated L_{6A}.

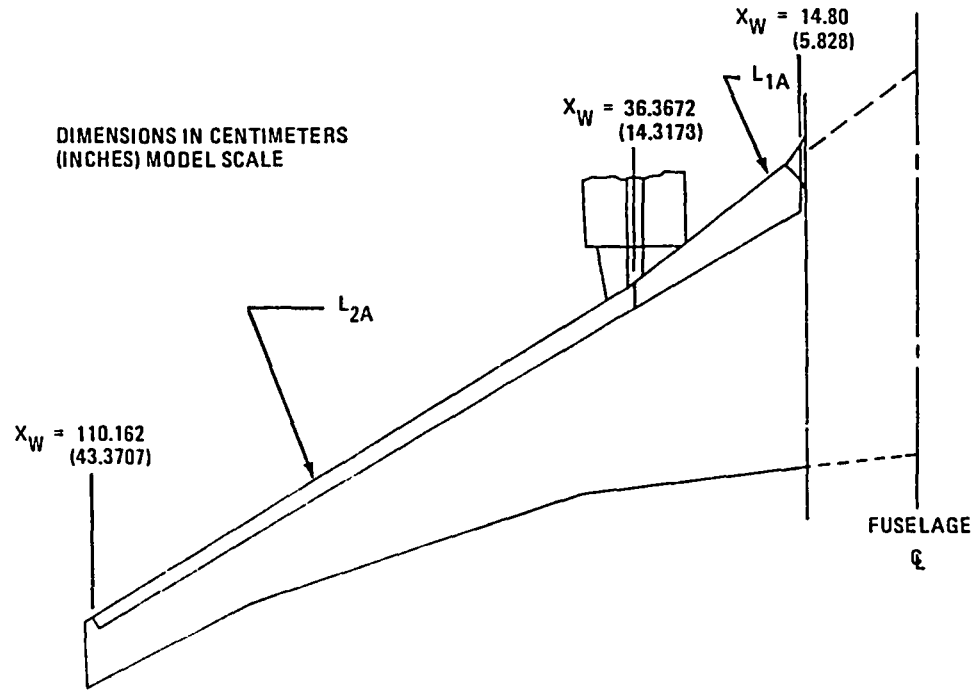

FIGURE 49. SLAT PLANFORM DIAGRAM

The VCK deflection angle was defined by the angle between the wing maximum length line and the VCK maximum length line measured in a streamwise plane normal to the WRP. The VCK planform diagram is shown in Figure 50. The variable test positions are defined and identified in the Configuration Notations Section.

Definitions for main and aft flap gap, O.H., and deflections are shown in Figure 51. The flaperon utilized the same definitions as the main flap. Figure 52 illustrates the method of attachment of the inboard and outboard flaps to each other and to the wing. As indicated for the inboard flap system, the main and aft flap were bolted to the bracket for the flap deflection required. The gap and O.H. for the main flap were varied by spacers and pin holes through the bracket into the wing surface. The flap bracket was attached to wing by another set of bolts in eccentric holes (to allow for the O.H. variation). Inboard, each combination of main and aft flap deflection was obtained by a separate bracket.

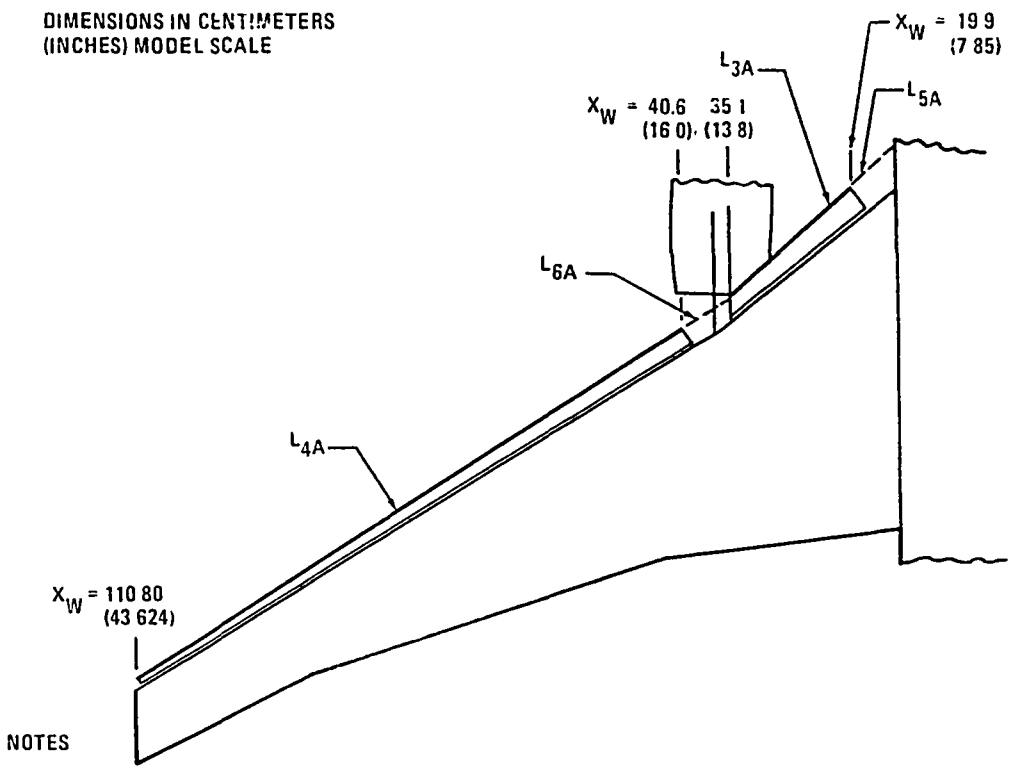

NOTES

1 VCK TRIM NORMAL TO LEADING EDGE AT X_W - 19 9 (7 85), 40 6 (16 0), 110 80 (43 674) WITH δ_{VCK} = 55°

2 TRIM AT X_W 35 1 (13 8) IS NOMINALLY AT 1 8° CANT

FIGURE 50. VCK PLANFORM DIAGRAM

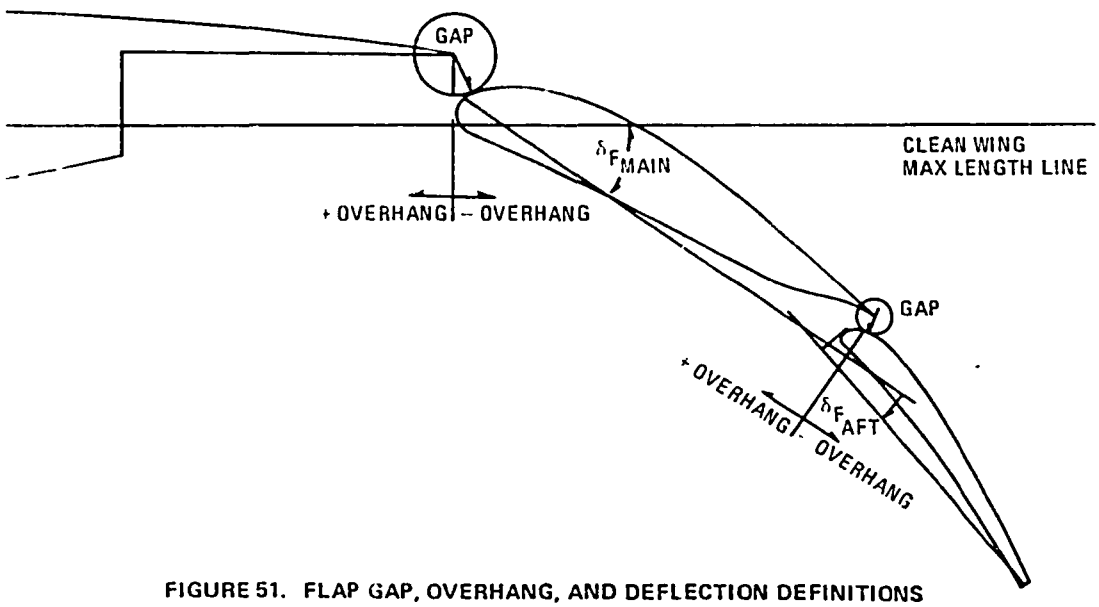

FIGURE 51. FLAP GAP, OVERHANG, AND DEFLECTION DEFINITIONS

INBOARD FLAP INSTALLATION

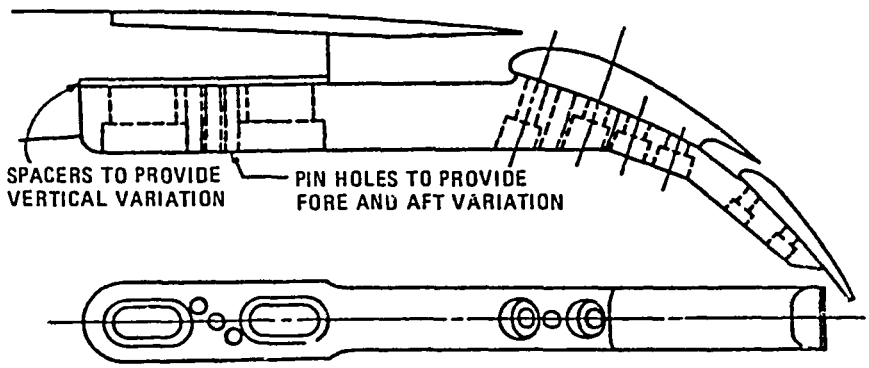

OUTBOARD FLAP INSTALLATION

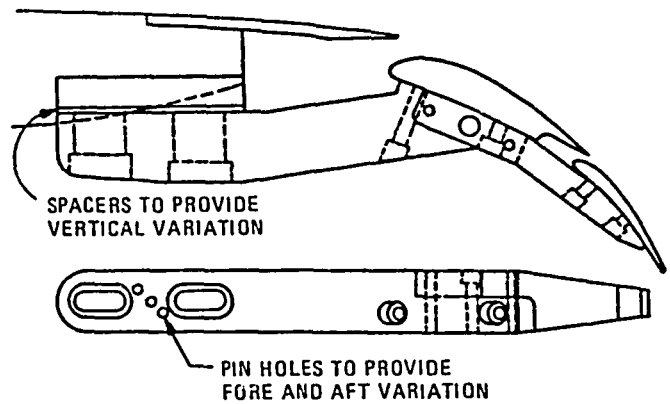

FIGURE 52. TYPICAL INBOARD AND OUTBOARD FLAP INSTALLATIONS

The outboard flap positioning was accomplished in essentially the same fashion as the inboard flap system. Various aft flap deflections were obtained by means of a separate aft bracket for each aft flap deflection (relative to the main flap).

The inboard flaps consisted of an inboard two-segment flap (F_{1A},F_{2A}) and an adjacent flaperon single-slot flap (F_{3A}).

The inboard two-segment flap was supported by brackets, simulating the airplane flap linkage, at main flap deflection angles of 0°, 5°, 15°, 25°, and 35°. Flap supports also provided four flap positions for each deflection angle. Main flap deflection angles were measured in a plane oriented streamwise and normal to the WRP. The inboard main flap was designated F_{1A}.

The aft flap of the inboard two-segment flap was supported at single positions for deflection angles of 0°, 7.5°, 10°, 12.5°, and 15°. The aft flap angles were measured in a plane oriented streamwise and normal to the WRP with the main flap at 0° deflection. The inboard aft flap was designated F_{2A}.

The flaperon single slot flap (F_{3A}) was supported by splice plates to the inboard flap on the inboard end and to the outboard flap on the outboard end for any given comparable grid position. Offset splice plates were provided to position the flaperon at the 25° nominal position while the inboard and outboard main flaps were at the 35° nominal position. The variable test positions for the inboard two-segment flap and the flaperon are defined and identified in the Configuration Notations Section.

The outboard two-segment flap was supported by external fixed brackets at main flap deflection angles of 0°, 5°, 15°, 25°, and 35°. The flap supports provided four flap test positions for each deflection angle. The support brackets approximated the airplane flap linkage. The outboard main flap was designated F_{4A}.

The main flap deflection angles were measured in a plane oriented streamwise and normal to the WRP.

The aft flap was supported at single positions for deflection angles of 0°, 7.5°, 10°, 12.5°, and 15°. The aft flap angles were measured in a plane oriented streamwise and normal to the WRP with the main flap at 0° deflection. The outboard aft flap was designated F_{5A}. The variable test positions for the outboard two-segment flap system are defined and identified in the Configuration Notation Section.

A summary of the moveable surface capabilities is presented in Table 1.

TABLE 1
SUMMARY OF MOVABLE SURFACES

MOVABLE SURFACE	DEFLECTION ANGLE (DEGREES)	GRID POSITIONS AT EACH DEFLECTION	TYPE OF CONTROL
VCK	55, 45	4	MANUAL
SLAT	INBOARD. 15, 25 OUTBOARD· 25, 35	3 3	MANUAL
FLAPS MAIN AFT	 0, 5, 15, 25, 35 0, 7 5, 10, 12 5, 15	 4 1	 MANUAL
AILERON (LEFT-HAND ONLY)	0, ±5, ± 10, ± 15, ± 20 (NORMAL TO HINGELINE)	–	MANUAL
SPOILERS	LH 0, –5, –15, –30, –45, –60 RH 0, –30, –60 (NORMAL TO HINGELINE)	–	MANUAL
HORIZONTAL STABILIZER	+5 TO –15 (NORMAL TO ROTATION AXIS)	–	REMOTE

Configuration Notation and Dimensional Data

The various configuration notation is presented in Table 2. Table 3 presents dimensional quantities related to the wind tunnel model. The various grid position notation and corresponding values for deflection, gap,and overhang are presented in Tables 4, 5, 6, and 7 for the slat, VCK, main flap and flaperon, and the aft flap, respectively.

TABLE 2

CONFIGURATION NOTATION

B_{2A}	Simulates the DC-X-200 Model D-969N-21 fuselage. Full scale dimensions: Length = 42.29 m (138.8 ft); constant section diameter = 602 cm (237 in). The aft fuselage tail cone uses the existing DC-10 model parts. The fuselage is configured for tandem strut support system.
W_{3B}	Simulates the DC-X-200 Model D-969N-21 wing and is lofted to represent the airplane wing with a 1g load. Full scale dimensions: S = 212.597 m^2 (2288.457 ft^2); b = 47.252 m (155.027 ft); aspect ratio = 10.502; λ = 0.1407; MAC = 5.351m (17.555 ft). The model wing has a removable leading edge, full span VCK flap, trailing edge two-segment flap, outboard aileron on one side, and spoilers. The wing is constructed of Armco 17.4 steel and contains five rows of pressure orifices.
X_{2B}	Wing-fuselage fillet for $B_{2A}W_{3B}$.
H_{1A}	Horizontal stabilizer for DC-X-200 (slab surface).
V_{1A}	Vertical stabilizer for DC-X-200 (slab surface).
N_{2A}	Flow-through, short core cowl nacelle configuration (2).
P_{2A}	New pylons for mating N_{2A} to wing W_{3B} (2).
Z_{1A}	Nacelle strake configuration (attaches to N_{2A}, 2 each nacelle).
G_{1A}	Main and nose landing gear defined for the DC-X-200 airplane. Main gear wheel wells with gear extended are not provided.

TABLE 2 (CONTINUED)

a_{2A}	The outboard aileron with inboard trim at X_w = 89.020 cm (35.047 in) and outboard trim at X_w = 109.480 cm (43.102 in). The hingeline is located at 75% C.
f_1, f_2	Inboard spoiler segments fabricated as individual parts. Superscript R = right side, L = left side, None = both sides.
f_{1A}, f_{2A}	f_1 and f_2 inboard 0° spoilers with sheet metal aft extension. Trailing edge step is filled with wax and faired (LB-486A). This assembly was refurbished and the T.E. step filled with potting (LB-486C).
f_3, f_4, f_5, f_6	Outboard spoiler segments fabricated as one piece.
L_{1A}	Leading edge slat inboard of X_w = 36.367cm (14.318 in) and supported at nominal gap = 2.25% C, O.H. = 2.0% C, and δ_{SLAT} = 25°.
L_{2A}	Leading edge slat outboard of X_w = 36.367 cm (14.318 in) and supported at nominal gap = 2.25% C, O.H. = -2.0% C, and δ_{SLAT} = 35°.
L_{3A}	Leading edge variable camber Krueger flap inboard of wing station X_w = 36.367 cm (14.318 in) and supported at the nominal gap = 2.82% C, O.H. = -0.725% C, δ_{VCK} = 55°.
L_{4A}	Leading edge variable camber Krueger flap outboard of wing station X_w = 36.367 cm (14.318 in) and supported at the nominal gap = 3.5% C, and O.H. = -1.0% C, δ_{VCK} = 55°.
L_{5A}	The inboard VCK extension to the fuselage.

TABLE 2 (CONTINUED)

L_{6A}	The VCK section at the pylon interruption.
F_{1A}	Inboard main flap of a two-segment flap with inboard trim at X_W = 13.868 cm (5.460 in) and outboard trim at X_W = 30.793 cm (12.123 in).
F_{2A}	Inboard aft flap of a two-segment flap trimmed to match F_{1A} and supported from F_{1A}.
F_{3A}	A single-slot flaperon with inboard trim at X_W = 30.793 cm (12.123in) and outboard trim at X_W = 43.411 cm (17.091 in).
F_{4A}	Outboard main flap of a two-segment flap with inboard trim at X_W = 43.411 cm (17.091 in) and outboard trim at X_W = 89.020 cm (35.047 in).
F_{5A}	Outboard aft flap of a two-segment flap trimmed to match F_{4A} and supported from F_{4A}.
X_W, Y_W	Wing coordinates (spanwise, chordwise).
δ_{FRP}	Angle of attack, in degrees, of the fuselage reference plane relative to the equivalent free airstream. Nose up is positive.
δ_a	Aileron deflection, in degrees. Positive deflection is trailing edge down.
$\delta_{F_{AFT}}$	Aft flap deflecltion, in degrees (see Figure 51).
$\delta_{F_{MAIN}}$	Main flap deflection, in degrees (see Figure 51).

TABLE 2 (CONCLUDED)

δ_{SLAT}	Slat deflection, in degrees (see Figure 48).
δ_{VCK}	VCK deflection, in degrees (see Figure 48).
i_H	Incidence angle, in degrees, of the horizontal stabilizer H_{1A} Positive deflection is trailing edge down.

Summary Code

S_1	$B_{2A}W_{3B}X_{2B}a_{2A}$. Body + cruise wing.
S_2	$B_{2A}W_{3B}X_{2B}N_{2A}P_{2A}Z_{1A}L_{3A}L_{4A}F_{1A}F_{2A}F_{3A}F_{4A}F_{5A}a_{2A}f_{1,2,3,4,5,6}$. Body + flapped wing + VCK leading edge device + flaps + nacelles, pylons, and nacelle strakes + VCK filler blocks.
S_3	$S_2-W_{3B}+W_{3D}$. Configuration S_2 - VCK filler blocks.
S_4	$S_2-W_{3B}+W_{3D}-f_{1,2}$ + $f_{1A}f_{2A}$. Configuration S_3 + inboard spoiler trailing edge extensions.
S_5	$B_{2A}W_{3B}X_{2B}N_{2A}P_{2A}Z_{1A}L_{1A}L_{2A}F_{1A}F_{2A}F_{3A}F_{4A}F_{5A}$ $a_{2A}f_{1A}f_{2A}f_{3}f_{4}f_{5}f_{6}$. Body + flapped wing + slat and WUSS leading edge + flaps + nacelles, pylons, and nacelle strakes.

TABLE 3
DIMENSIONAL DATA

COMPONENT	UNITS	MODEL SCALE
FUSELAGE (B_{2A})		
Length	cm (in)	198.77 (78.255)
Maximum width	cm (in)	28.293 (11.139)
Maximum height	cm (in)	28.293 (11.139)
WING (W_{3B})		
Area	m^2 (ft^2)	0.4696 (5.055)
Span	m (ft)	2.221 (7.286)
Mean Aerodynamic Chord	m (ft)	0.251 (0.825)
Root chord (trapezoidal wing)	cm (in)	37.076 (14.597)
Total root chord	cm (in)	51.895 (20.431)
Tip chord (trapezoidal wing)	cm (in)	5.217 (2.054)
Total tip chord	cm (in)	9.27 (3.65)
Aspect ratio		10.502
Taper ratio		0.1407
Spanwise station of MAC	cm (in)	41.580 (16.370)
Fuselage station of 25% MAC	cm (in)	160.28 (63.102)
Sweepback of 25% C_W	deg.	28.57
Dihedral("lg")	deg.	4.5
HORIZONTAL STABILIZER (H_{1A})		
Area	m^2 (ft^2)	0.1298 (1.397)
Span	cm (in)	70.234 (27.651)
MAC	cm (in)	19.91 (7.839)
Root chord	cm (in)	27.384 (10.781)
Tip chord	cm (in)	9.583 (3.773)
Aspect ratio		3.800
Taper ratio		0.35
Sweepback of 25% chord	deg.	30
Dihedral	deg.	10.0
Fuselage station of 25% H_{MAC}	cm (in)	247.36 (97.384)
Tail length (25% W_{MAC} to 25% H_{MAC})	cm (in)	87.076 (34.282)

TABLE 3 (CONTINUED)

COMPONENT	UNITS	MODEL SCALE
VERTICAL STABILIZER (V_{1A})		
Area	m^2 (ft^2)	0.098502 (1.0603)
Span	cm (in)	39.700 (15.630)
MAC	cm (in)	26.731 (10.524)
Root chord	cm (in)	36.759 (14.472)
Tip chord	cm (in)	12.87 (5.065)
Aspect ratio		1.6
Taper ratio		0.35
Sweepback of 25% chord	deg.	35
Tail length (25% W_{MAC} to 25% V_{MAC})	cm (in)	82.301 (32.402)
OUTBOARD AILERON (a_{2A})		
Area aft of hingeline	cm^2 (in^2)	54.4 (8.44)
Span	% b/2	18.4
Chord aft of hingeline	% C_W	25
SPOILER (f_1,f_2)		
Area (each)	cm^2 (in^2)	47.2 (7.32)
Span (each)	cm (in)	13.2 (5.18)
SPOILER (f_3,f_4,f_5,f_6)		
Area (total, one side)	cm^2 (in^2)	104.660 (16.222)
Span (total, one side)	cm (in)	43.835 (17.258)
NACELLE (N_{2A})		
Length	cm (in)	32.00 (12.60)
Maximum cowl height	cm (in)	13.7 (5.38)
Inlet diameter (fan cowl)	cm (in)	9.85 (3.88)
Exit area (gas generator)	cm^2 (in^2)	6.86 (1.06)
Incidence of thrust line to FRP	deg.	1.6
Toe in	deg.	1.8

TABLE 4
SLAT GRID NOTATION

All gaps and overhangs are percent of local wing chord

WING STATION	δ_{SLAT}	GAP	O.H.	NOTATION
X_W = 14.140 cm (5.567 in)	25°	2.25	-2.0	L_{1AA}
X_W = 36.367 cm (14.138 in)		2.25	-2.0	
X_W = 14.140 cm (5.567 in)	25°	1.50	-1.0	L_{1AB}
X_W = 36.367 cm (14.138 in)		1.50	-1.0	
X_W = 14.140 cm (5.567 in)	25°	3.25	-2.0	L_{1AC}
X_W = 36.367 cm (14.138 in)		3.25	-2.0	
X_W = 14.140 cm (5.567 in)	15°	2.25	-2.0	L_{1AD}
X_W = 36.367 cm (14.138 in)		2.25	-2.0	
X_W = 14.140 cm (5.567 in)	15°	1.50	-1.0	L_{1AE}
X_W = 36.367 cm (14.138 in)		1.50	-1.0	
X_W = 14.140 cm (5.567 in)	15°	3.25	-2.0	L_{1AF}
X_W = 36.367 cm (14.138 in)		3.25	-2.0	
X_W = 36.367 cm (14.138 in)	35°	2.25	-2.0	L_{2AA}
X_W = 89.020 cm (35.047 in)		2.25	-2.0	
X_W = 36.367 cm (14.138 in)	35°	1.50	-1.0	L_{2AB}
X_W = 89.020 cm (35.047 in)		1.50	-1.0	

TABLE 4 (CONCLUDED)

WING STATION	δ_{SLAT}	GAP	O.H.	NOTATION
X_W= 36.367 cm (14.138 in)	35°	3.25	-2.0	L_{2AC}
X_W= 89.020 cm (35.047 in)		3.25	-2.0	
X_W= 36.367 cm (14.138 in)	25°	2.25	-2.0	L_{2AD}
X_W = 89.020 cm (35.047 in)		2.25	-2.0	
X_W= 36.367 cm (14.138 in)	25°	1.50	-1.0	L_{2AE}
X_W = 89.020 cm (35.047 in)		1.50	-1.0	
X_W = 36.367 cm (14.138 in)	25°	3.25	-2.0	L_{2AF}
X_W = 89.020 cm (35.047 in)		3.25	-2.0	

TABLE 5
VCK GRID NOTATION

All gaps and overhangs are percent of local wing chord

WING STATION	δ_{VCK}	GAP	O.H.	NOTATION
X_J = 14.140 cm (5.567 in)	51.318°	2.82	-0.725	L_{3AA}
X_W = 36.367 cm (14.318 in)	55°	3.5	-1	
X_W = 14.140 cm (5.567 in)	51.318°	2,82	-1.725	L_{3AB}
X_J = 36.367 cm (14.318 in)	55°	3.5	-2	
X_W = 14.140 cm)5.567 in)	51.318°	1.82	-0.725	L_{3AC}
X_J = 36.367 cm (14.318 in)	55°	2.5	-1	
X_W = 14.140 cm (5.567 in)	51.318°	1.82	0.275	L_{3AD}
X_W = 36.367 cm (14.318 in)	55°	2.5	0	
		3.5	-1	L_{4AA}
X_W= 36.367 cm (14.318 in)	55°	3.5	-2	L_{4AB}
X_J = 111.274 cm (43.809 in)		2.5	-1	L_{4AC}
		2.5	0	L_{4AD}
X_W= 14.140 cm (5.567 in)	41.318°	282	-0.725	L_{3AE}
X_J= 36.367 cm (14.318 in)	45°	3.5	-1	
X_W = 14.140 cm (5.567 in)	41.318°	0.82	-0.725	L_{3AF}
X_J= 36.367 cm (14.318 in)	40°	.5	-1	

TABLE 5 (CONCLUDED)

WING STATION	δ_{VCK}	GAP	O.H.	NOTATION
X_w = 14.140 cm (5.567 in)	41.318°	1.82	-0.725	L_{3AG}
X_w = 36.367 cm (14.318 in)	45°	2.5	-1	
X_w = 14.140 cm (5.567 in)	41.318°	1.82	0.275	L_{3AH}
X_w = 36.367 cm (14.318 in)	45°	2.5	0	
		3.5	-1	L_{4AE}
X_w = 36.367 cm (14.318 in)	45°	1.5	-1	L_{4AF}
X_w = 111.274 cm (43.809 in)		2.5	-1	L_{4AG}
		2.5	-1	L_{4AH}

TABLE 6
MAIN FLAP GRID NOTATION

All gaps and overhangs are percent of local wing chord

Inboard Flap and Flaperon Grid

$\delta_{F_{MAIN}}$	X_w = 14.140 cm (5.567 in) GAP	X_w = 14.140 cm (5.567 in) O.H.	X_w = 43.411 cm (17.091 in) GAP	X_w = 43.411 cm (17.091 in) O.H.	NOTATION
	1.3	3.2	2.5	6.0	F_{1AA}
5°	0.8	3.2	1.5	6.0	F_{1AB}
	0.8	2.2	1.5	4.0	F_{1AC}
	1.3	2.2	2.5	4.0	F_{1AD}
	1.6	1.1	3.0	2.0	F_{1AE}
15°	1.3	2.2	2.5	4.0	F_{1AF}
	0.8	2.2	1.5	4.0	F_{1AG}
	0.8	1.1	1.5	2.0	F_{1AH}
	1.6	0.0	3.0	0.0	F_{1AJ}
25°	1.3	0.0	2.5	0.0	F_{1AK}
	1.3	0.5	2.5	1.0	F_{1AL}
	0.8	0.5	1.5	1.0	F_{1AM}
	1.9	1.1	3.5	-2.0	F_{1AN}
35°	1.3	0.0	2.5	0.0	F_{1AP}
	1.3	0.5	2.5	1.0	F_{1AR}
	1.1	0.5	2.0	1.0	F_{1AS}

TABLE 6 (CONTINUED)

OUTBOARD FLAP GRID

X_w = 43.411 cm (17.091 in) and 89.020 cm (35.047 in)

$\delta_{F_{MAIN}}$	GAP	O.H.	NOTATION
	2.5	6.0	F_{4AA}
5°	1.5	6.0	L_{4AB}
	1.5	4.0	F_{4AC}
	2.5	4.0	F_{4AD}
	3.0	2.0	F_{4AE}
15°	2.5	4.0	F_{4AF}
	1.5	4.0	F_{4AG}
	1.5	2.0	F_{4AH}
	3.0	0.0	F_{4AJ}
25°	2.5	0.0	F_{4AK}
	2.5	1.0	F_{4AL}
	1.5	1.0	F_{4AM}
	3.5	-2.0	F_{4AN}
35°	2.5	0.0	F_{4AP}
	2.5	1.0	F_{4AR}
	2.0	1.0	F_{4AS}

FLAPERON DIFFERENTIAL POSITION

X_w = 43.411 cm (17.091 in)

$\delta_{F_{FLAPERON}}$	GAP	O.H.	NOTATION
25°	2.5	1.0	F_{3AR}

TABLE 7
AFT FLAP GRID NOTATION

All gaps and overhangs are percent of local wing chord

X_w = 14.140 cm (5.567 in) X_w = 30.793 cm (12.123 in)

$\delta_{F_{AFT}}$	GAP	O.H.	GAP	O.H.	NOTATION
7.5°	0.3	0.8	0.4	1.1	F_{2AA}
10°	0.3	0.8	0.4	1.1	F_{2AB}
12.5°	0.4	0.4	0.5	0.5	F_{2AC}
15°	0.4	0.4	0.5	0.5	F_{2AD}

X_w = 43.411 cm (17.091 in) and 89.020 cm (35.047 in)

	GAP	O.H.	
7.5°	0.5	1.5	F_{5AA}
10°	0.5	1.5	F_{5AB}
12.5°	0.75	0.75	F_{5AC}
15°	0.75	0.75	F_{5AD}

Instrumentation

Aerodynamic forces on the model were measured by the Ames Task Mark II 10.16 cm (4 in.) diameter internal balance at the Ames 12-Foot Pressure Wind Tunnel (LB-486A test). For the NASA Langley V/STOL Wind Tunnel (LB-486C test), the balance used was the Langley 748 5.08 cm (2 in.) diameter internal balance.

Pressures over the model wing, outboard aileron, slat, VCK, and flap systems were measured by means of a scanivalve system installed within the fuselage nose. The spanwise position of the pressure rows is indicated in Figure 53. The wing and clean leading edge orifices were located streamwise at the percent span locations shown in Figure 53. The slat orifice rows were located streamwise with the slat deflected 25° inboard and 35° outboard. For the VCK, the orifice rows were located streamwise with the inboard and outboard leading edge device deflected 55°. The aileron orifice row was located streamwise with the aileron at 0° deflection. Main, aft flap, and flaperon orifice rows were located streamwise with 0° deflection on all flap components.

The wing chordwise pressure orifice locations are shown in Figure 54. Slat and WUSS pressure orifice locations are detailed in Figure 55. Comparable values for the VCK are presented in Figure 56. Chordwise pressure orifice

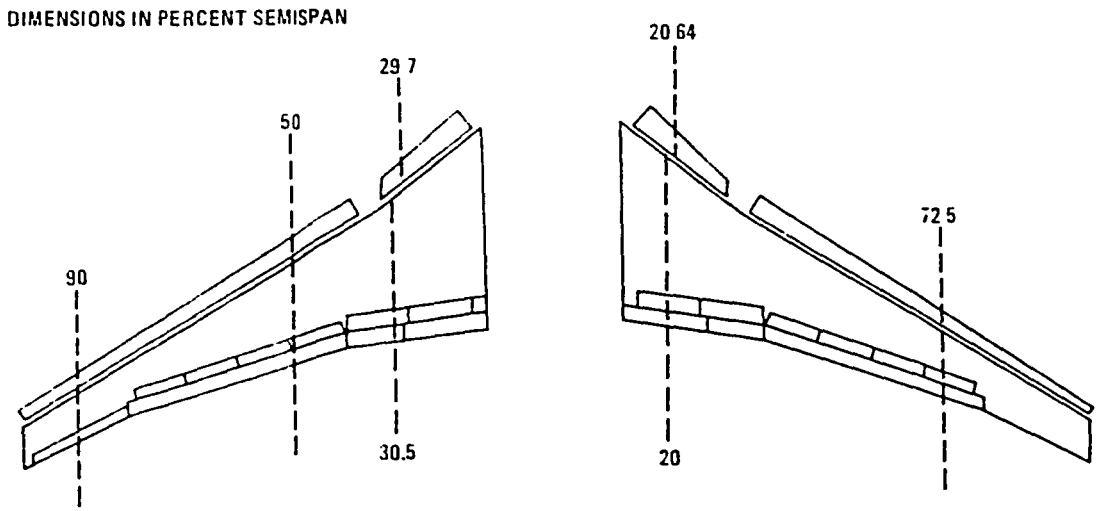

FIGURE 53. SPANWISE POSITION OF PRESSURE ORIFICE INSTRUMENTATION

ORIGINAL
OF POOR

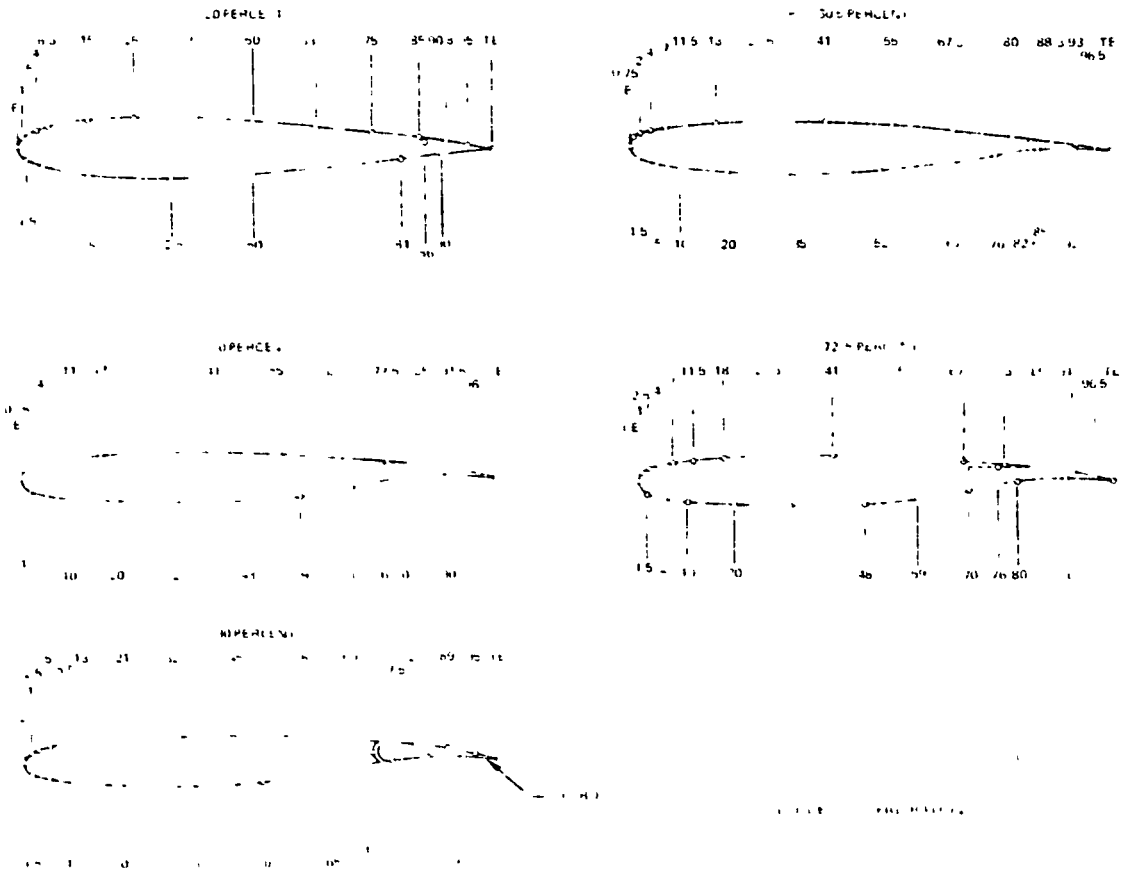

FIGURE 54. WING CHORDWISE PRESSURE ORIFICE LOCATIONS

locations for the two-segment flap system are shown in Figure 57, and for the flaperon in Figure 58.

For the Ames test, the angle of attack of the fuselage reference plane was measured by electrolytic alignment bubbles housed in the fuselage nose. From an angle of attack of -6° to 0°, the model was pitched by the external pitch drive. From 0° to +10° angle of attack, the fuselage was pitched using the fuselage internal pitch drive, while maintaining the balance at 0°. A 0° bubble on the balance housing was monitored such that 0° balance attitude was maintained. For angles of attack greater than +10°, the fuselage was pitched using the external pitch drive with a 10° angle maintained between the balance axis and the fuselage axis. For the NASA-V/STOL test, a NASA furnished electronic inclinometer was used for the determination of angle of attack.

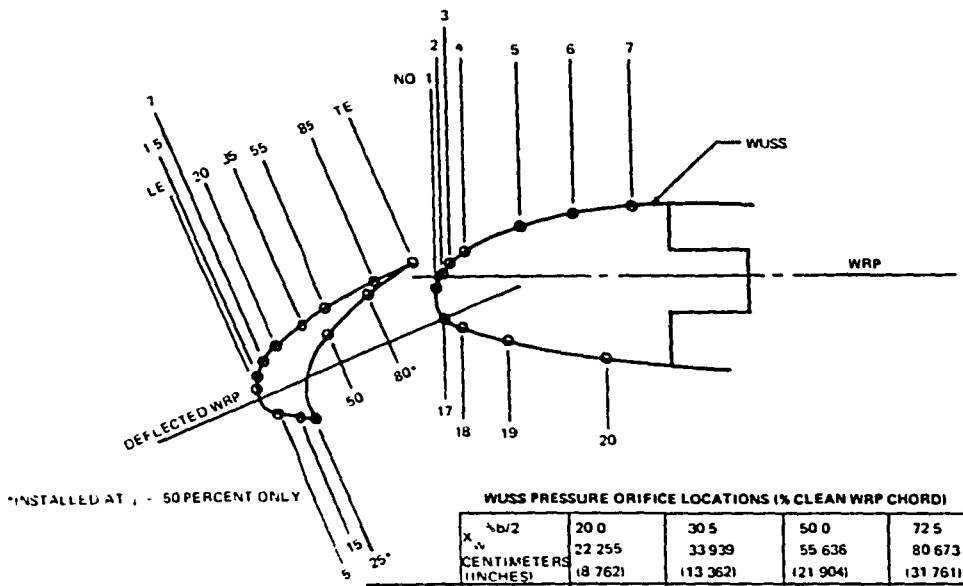

*INSTALLED AT η = 50 PERCENT ONLY

WUSS PRESSURE ORIFICE LOCATIONS (% CLEAN WRP CHORD)

	x_w/b/2	20.0	30.5	50.0	72.5	90.0
	CENTIMETERS (INCHES)	22.255 (8.762)	33.939 (13.362)	55.636 (21.904)	80.673 (31.761)	100.147 (39.428)
UPPER SURFACE	1	3.2 (LE)	3.13 (LE)	3.63 (LE)	4.47 (LE)	5.00 (LE)
	2	4.5	4.0	4.6	5.2	6.0
	3	7.0	5.5	6.0	6.5	7.5
	4	10.0	8.0	8.0	9.0	10.0
	5	14.0	11.0	10.0	12.0	14.0
	6	17.0	14.0	13.0	16.0	19.0
	7		-	16.0	20.0	22.5
LOWER SURFACE	17	4.0	4.0	5.0	5.5	6.0
	18	8.0	8.0	9.0	8.0	9.0
	19	16.0	13.0	14.0	13.0	15.0
	20	-	-	-	20.0	22.0

FIGURE 55. SLAT AND WUSS CHORDWISE PRESSURE ORIFICE LOCATIONS

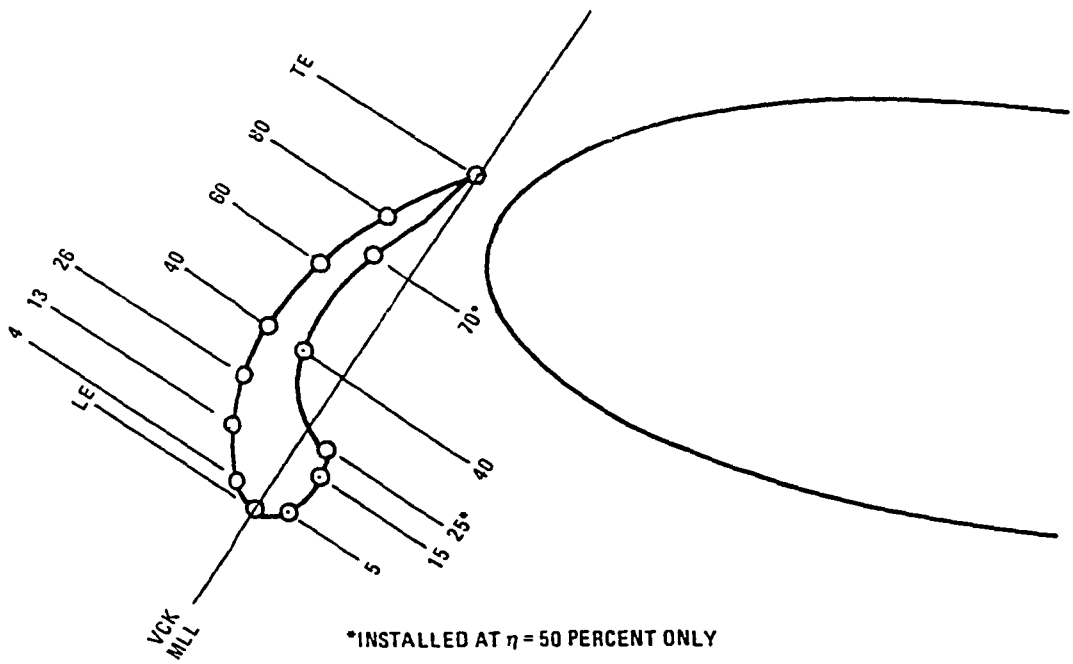

*INSTALLED AT η = 50 PERCENT ONLY

FIGURE 56. VCK CHORDWISE PRESSURE ORIFICE LOCATIONS (TYPICAL FOR ALL STATIONS EXCEPT AS NOTED)

ORIGINAL
OF POOR

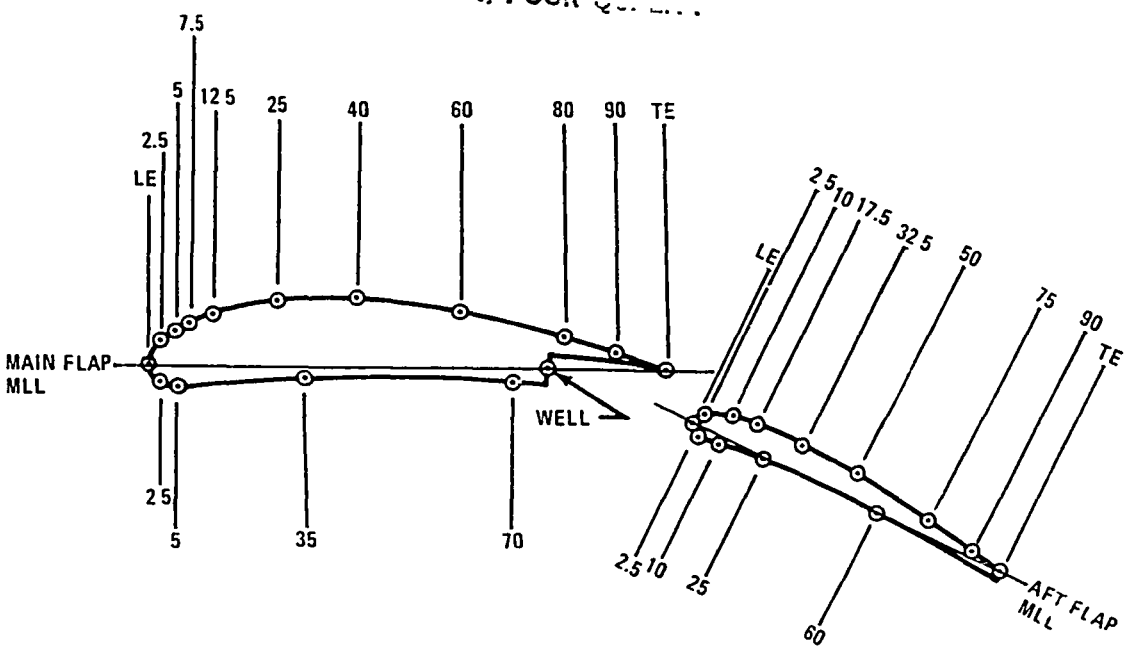

FIGURE 57. TWO-SEGMENT FLAP CHORDWISE PRESSURE ORIFICE LOCATIONS (TYPICAL FOR ROWS AT η = 20, 50, AND 72.5 PERCENT)

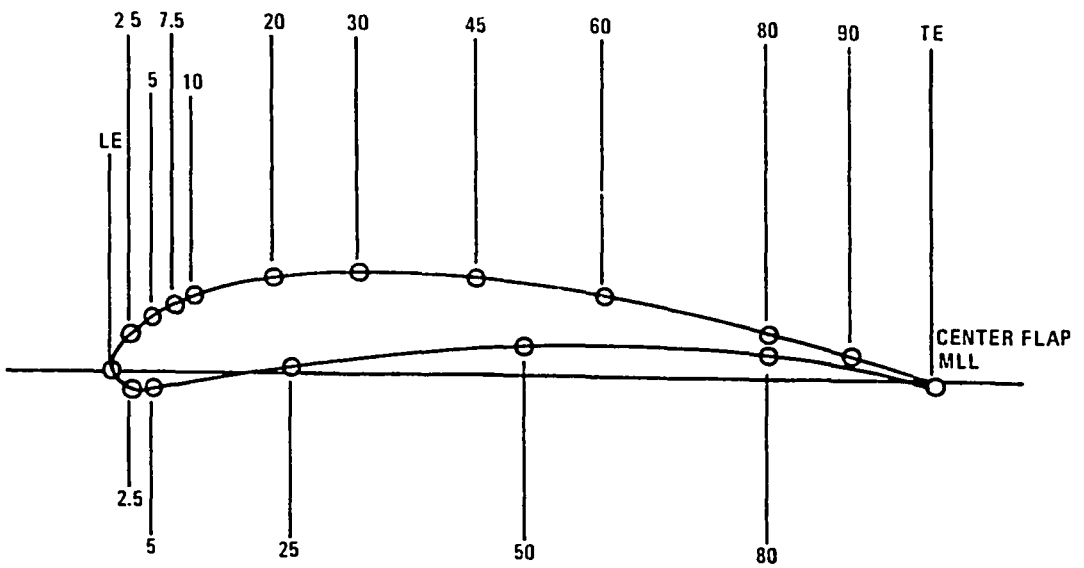

FIGURE 58. FLAPERON CHORDWISE PRESURE ORIFICE LOCATIONS (AT η = 30.5 PERCENT)

OF POOR

The horizontal stabilizer incorporated a remote drive and dual position potentiometers for tail incidence determination during a run.

Model Installation

The model was installed in the NASA Ames 12-Foot Pressure Wind Tunnel on the tandem support system shown in Figure 59. The model was pivoted about the main strut pivot point and was powered by the aft pitch strut. The entire strut system was non-metric, (i.e., air loads on the strut are not sensed by the balance). The struts entered the fuselage as far aft as practical to minimize the aerodynamic interference effects on the model.

The same support system was utilized during the NASA Langley V/STOL test program. It was adapted to the existing V/STOL tunnel structure and extensions for the main, and pitch struts were added to the basic tandem strut system. The extensions permitted the model to be located near the vertical position of the tunnel centerline (see Figure 60).

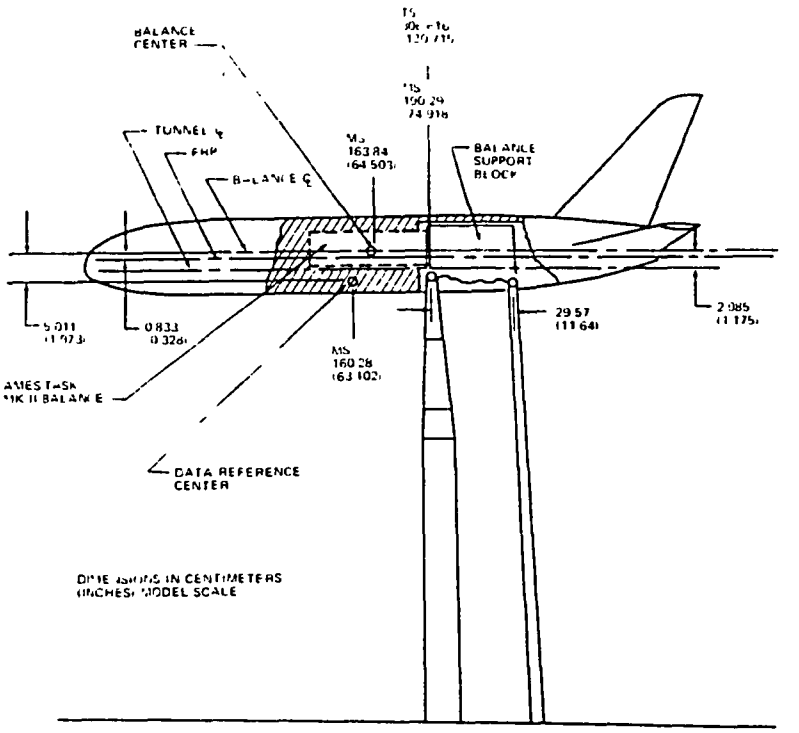

FIGURE 59. MODEL INSTALLATION IN THE NASA AMES 12-FOOT PRESSURE WIND TUNNEL

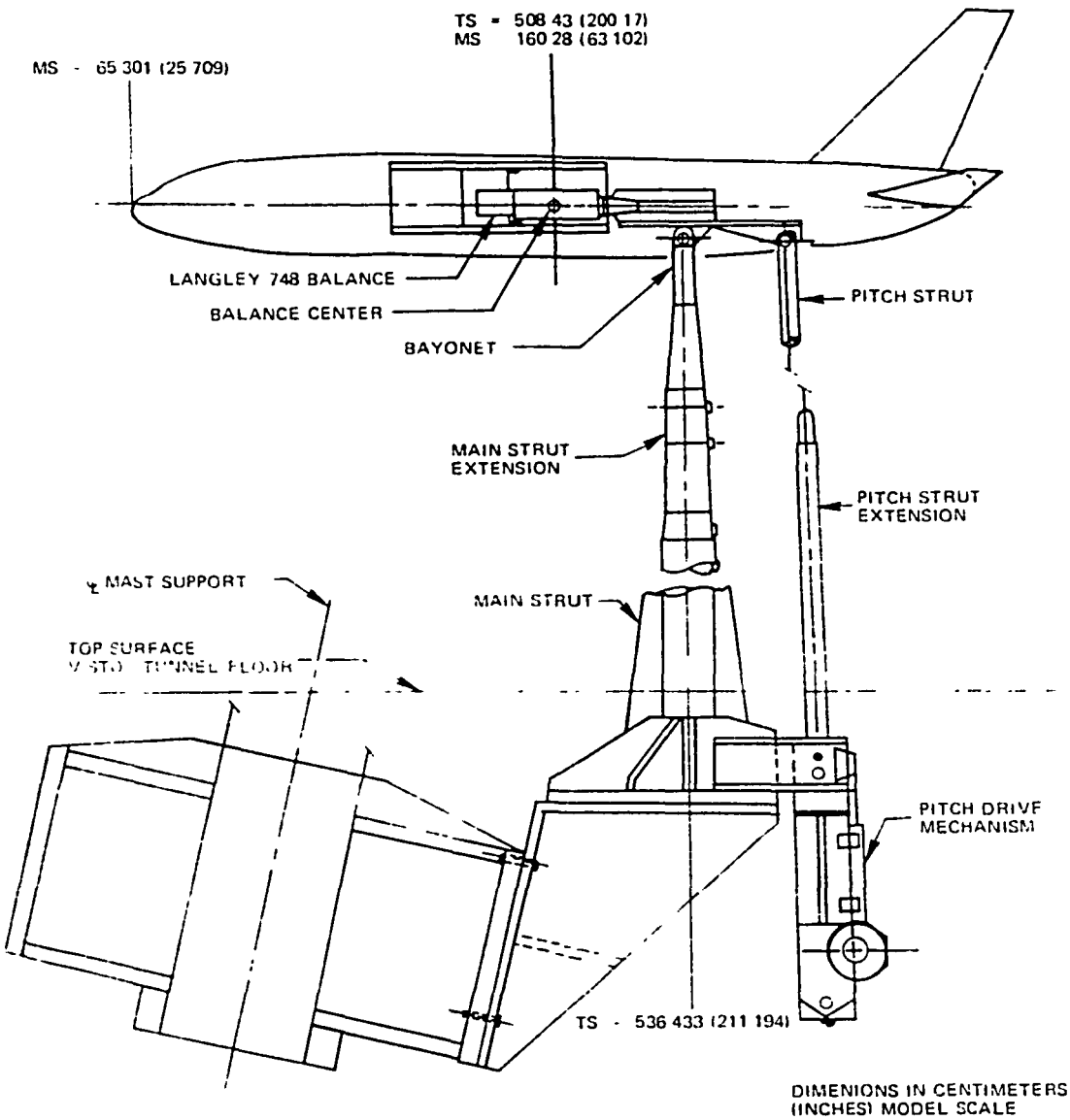

FIGURE 60. MODEL INSTALLATION IN THE NASA LANGLEY V/STOL WIND TUNNEL

PRECEDING PAGE BLANK NOT FILMED

EXPERIMENTAL RESULTS AND ANALYSIS

Test Plan and Facilities

Two wind tunnel tests were conducted between 30 November 1978 and 29 November 1979, to aid in the evaluation of the low speed characteristics of a high aspect ratio supercritical wing transport configuration. In both tests the configuration was the D-969N-21 wide-body transport with the W_{3B} wing and high lift system.

The first test (LB-486A) was conducted at the NASA Ames Research Center in the 12-Foot Pressure Wind Tunnel from 30 November 1978 through 26 January 1979. Data for various Mach and Reynolds numbers were obtained during this test for selected configurations. A majority of the configurations tested were evaluated at a high Reynolds number condition. Figure 61 presents the configurations evaluated during the Ames wind tunnel program.

The second test (LB-486C) was conducted at the NASA Langley Research Center in the V/STOL Wind Tunnel from 1 November through 29 November 1979, jointly with activities under related NASA Contract NAS1-15327. Spoiler configurations, fabricated under the current contract, were part of this test.

ESTABLISHED THREE-DIMENSIONAL HIGH LIFT CHARACTERISTICS FOR HIGH ASPECT RATIO SUPERCRITICAL WING AT HIGH REYNOLDS NUMBER

EVALUATED THE FOLLOWING AERODYNAMIC CHARACTERISTICS

- BASIC CLEAN WING
- SLAT AND VCK LEADING EDGE DEVICE OPTIMIZATION
- SINGLE AND TWO SEGMENT FLAP OPTIMIZATION
- NACELLE/PYLON AND LANDING GEAR EFFECTS
- EFFECT OF INBOARD VCK AND SLAT SPAN
- HORIZONTAL TAIL-ON CHARACTERISTICS FOR SELECTED CONFIGURATIONS
- CLEAN TRAILING EDGE CHARACTERISTICS
- CLEAN LEADING EDGE CHARACTERISTICS
- VCK WELL EFFECTS
- AILERON EVALUATION WITH HIGH LIFT SYSTEM
- EFFECT OF MINI-TUFTS ON HIGH LIFE CHARACTERISTICS
- ROLL SPOILER CHARACTERISTICS
- GROUND SPOILER CHARACTERISTICS

FIGURE 61. AMES 12-FOOT TEST RESULTS

Test Technique

The test technique and data obtained were similar for both wind tunnel facilities. Test conditions are shown in Table 8. The low values for the tip Reynolds number are noteworthy.

TABLE 8
TEST CONDITIONS

FACILITY	MACH NUMBER	$R_N/m \times 10^{-6}$	$R_N/ft \times 10^{-6}$	$R_{N_{MAC}} \times 10^{-6}$	$R_{N_{TIP}} \times 10^{-6}$
AMES 12-ft	0.20*	20.3*	6.2	5.12	1.88
AMES 12-ft	0.20	11.5	3.5	2.89	1.06
AMES 12-ft	0.20	4.53	1.38	1.14	0.42
AMES 12-ft	0.26	11.5	3.5	2.89	1.06
AMES 12-ft	0.32	11.5	3.5	2.89	1.06
LANGLEY V/STOL	0.20*	4.53*	1.38*	1.14	0.42

*normal test condition

The Ames 12-foot wind tunnel test section has a circular cross-section of 3.65m (12 ft) diameter. Flat areas on floor, ceiling, and both sides reduce this dimension to 11.3 feet. The Langley V/STOL wind tunnel has a test section height and width of 4.42m (14.50 ft) and 6.63m (21.75 ft). The model was mounted on a tandem strut system and tested through a maximum angle of attack range of -6^o to $+30^o$. For configurations without a leading edge device (i.e., cruise wing), this angle of attack range was reduced. The model was always tested with 0^o sideslip.

Fluorescent mini-tufts (Reference 7) were used in both wind tunnel tests for flow visualization of the various high lift configurations. This technique uses a very fine specially treated monofilament thread which, when struck by filtered ultraviolet light and photographed with appropriate filters, becomes readily visible on the photographic negative. The thread, being of extremely small diameter, produces little disturbance to the flow.

Unless otherwise noted, the configurations were evaluated with the nacelles, pylons, and nacelle strakes attached, and the horizontal tail off. The latter permitted the evaluation of high lift component increments in lift and drag. Tail-on characteristics were obtained for a selected number of configurations representing the better configurations resulting from the leading and trailing edge device optimization studies. Unless landing gear increments were being obtained, the cruise and takeoff configurations had the landing gear removed, and the landing configuration had the gear attached. Mini-tufts were attached to the right wing panel for most of the configurations tested.

The first test program started with the cruise wing configurations. This was followed by the VCK leading edge device study at nominal landing and takeoff flap deflections. The two-segment and single-slot flap optimization with the VCK leading edge device was evaluated next. Clean leading edge characteristics at the optimized flap positions were then evaluated, and were followed by the slat study at the previously defined flap positions. Clean trailing edge characteristics for the optimized VCK and slat positions were also obtained. Tail-on, Mach number, Reynolds number, nacelle/pylon, and aileron effects were also obtained as the appropriate configuration was being evaluated.

Wind Tunnel Test Results and Analysis

Due to the complex nomenclature associated with the high lift configurations, plotted data have been identified by a summary code (see S_1 through S_5 in Table 2). In addition, a leading edge grid position and deflection for the inboard and outboard segments has been identified for the high lift configurations. For example, 15D/25D notation for the slat, signifies that the inboard slat deflection is 15° and the grid position is AD, and for the outboard slat, the deflection is 25° and the grid position is AD. Table 4 shows the gap and O.H. to be 2.25 percent and -2.0 percent for both the inboard and outboard slat. Similar nomenclature has been used for the VCK (i.e., 45E/45G).

An example of the two-segment flap deflection, gap, and overhang nomenclature used in the plotted results is 25K/10B. The slash in this case denotes a main flap/aft flap relationship. The example signifies a 25° deflection for the main flap at position AK and an aft flap deflection of 10° at position B. Tables 6 and 7 indicate an outboard gap and O.H. of 2.5 percent and 0 percent for the main flap and 0.5 and 1.5 percent gap and overhang for the aft flap.

The single-slot flap configuration is denoted by a zero following the slash (i.e., 25K/0). By use of the configuration summary code, leading and trailing edge nomenclature, and the tables, the specific configurations in the plotted data can be obtained.

Test data presented in the following sections are without strut tare corrections. The relative performance was determined in this fashion, and selected data and final optimized configuration data were strut-tare corrected. The latter is presented in the Spoiler Deflection Effects and Summary of High Lift Characteristics sections. Strut tare corrections were based on an experimental evaluation of strut tares for a previous transport configuration, the technique being discussed in Reference 6.

The possible test variables and high lift configurations were quite numerous for this wind tunnel model. Table 9 presents a figure index for the high lift configurations and test conditions presented in this section.

Cruise Wing

The initial configuration tested was the cruise wing-body with the nacelles and pylons removed. Figure 62 illustrates this configuration installed in the NASA Ames 12-Foot Pressure Wind Tunnel. Also shown in the photograph is the tandem strut support system, and the VCK filler blocks (installed in the lower surface of the leading edge). The basic high Reynolds number characteristics (lift, pitching moment, and L/D) for the wing-body are shown in Figure 63 (see Run 22). Figure 63 indicates that $C_{L_{MAX}}$ of 1.513 was obtained at an angle of attack of 12.57°. The lift coefficient at zero degrees angle of attack was 0.4. The L/D_{MAX} for this configuration was 20.4 and at 1.2 V_S the L/D was 19.45.

TABLE 9
FIGURE INDEX FOR EXPERIMENTAL DATA PRESENTED

Model Configuration	δ_f / δ_f Main / δ_f Aux (Degrees)	Figure Index: Lift or Lift and Pitching Moment	Drag and/or L/D	Rolling Moment	Minituft Photos	Pressure Data	Section Lift Data	Reynolds Number Effects	Mach Number Effects	Horizontal Tail Effects	Reynolds Number Effects Tail on
Cruise Wing (NAP off)	0/0	63	63		66	67	68,69	70,71,72	64,65	82	83
Cruise Wing (NAP & Strakes on)	0/0	73	73	73	76	75,78,81	76,80	77	79		
VCE L E Device (Flaps Deflected)	-	-	-	-	-	-	-	-	-	-	-
VCE Optimization (Lnd)	25/12	86,88	86,88		90	91	87,89,92				
VCE Optimization (T O)	25/12	93,95	93,95		97	98	94,96,99	-	-	-	-
Two-segment Flap Optimization	-	-	-	-	-	-	-				
Main Flap (Lnd . Opt.)	25/12	100	100								
Aft Flap (Lnd . Opt.)	25/xx	101	101								
Flaperon Deflection	35/12	102	102								
Main Flap (Lnd . Opt.)	35/12	103	103								
Aft Flap (Lnd . Opt.)	35/xx	103	103								
Main Flap (T O . Opt)	15/10	104	104								
Aft Flap (T O . Opt)	15/xx	105	105								
Main Flap (T O . Opt)	5/10	106	106								
Aft Flap (T O . Opt)	5/xx	107	107								
VCE Span, NAP Effects (Lnd)	25/12	108	108								
VCE Span, NAP Effects (T O)	5/10	109	109								
VCE & Two-Segment Flap (Lnd)	25/12							110		112	113
VCE & Two-Segment Flap (T O)	5/10							111		114	
Single-Slot Flap Optimization	-	-	-	-	-	-	-	-	-	-	-
(Lnd . Opt)	25/0	115	115								
(Lnd . Opt)	35/0	116	116								
(T O . Opt)	15/0	117	117								
(T O . Opt)	5/0	118	118								
Inboard VCE Removal	25/0	119	119								
VCE & Single-Slot Flap (Lnd)	25/0							120		122	
VCE & Single-Slot Flap (T O)	15H/0							121		123	
Slat L E Device (Flaps Deflected)	-	-	-	-	-	-	-	-	-	-	-
Slat Optimization (Lnd)	25/12	125,127	125,127			129	126,128,129,130				
Slat Optimization (T O)	5/10	131	131			133	132,134				
Slat & Two-Segment Flap (Lnd)	25/12							137	135	139	140
Slat & Two-Segment Flap (T O)	5/10							138	136	141	
Slat & Single Slot Flap (Lnd)	25/0							142		145	
Slat & Single Slot Flap (T O)	15/0 & 5/0							143,144			
Clean L E (Flaps Deflected)	-	-	-	-	-	-	-	-	-	-	-
Two-Segment Flaps (Lnd & T O)	Various	146	146								
Single-Slot Flaps (Lnd & T O)	Various	147	147								
Clean T E. (L E Device Extended)	-	-	-	-	-	-	-	-	-	-	-
VCE L E Device	0/0							148			
Slat L E. Device								149		150	
Slat Trim Effects		151	151								
Aileron Characteristics	-	-	-	-	-	-	-	-	-	-	-
Cruise Wing	0/0			152							
T O Flaps (R T on)	5/10			153							
Lnd Flaps (R T on)	25/12			154							
Spoiler Characteristics	-	-	-	-	-	-	-	-	-	-	-
Cruise Wing (Roll)	0/0			155							
T O Flaps (Roll)	5/10			156							
Lnd Flaps (Roll)	25/12			157							
T O Flaps (Lift Dump)	5/10	158,160	158,161								
Lnd Flaps (Lift Dump)	25/12	159,160	159,161								
Landing Gear Effects	-	-	-	-	-	-	-	-	-	-	-
T O Flaps	5/10	162									
Lnd Flaps	25/12	162									
Strut Tare Corrected Data	-	-	-	-	-	-	-	-	-	-	-
VCE & Two-Segment Flap	Various	163,171	164					182			
Slat & Two-Segment Flap	Various	165	166					183	184		
VCE & Single Slot Flap	Various	167	168								
Slat & Single Slot Flap	Various	169	170								
Trimmed Data											
VCE & Two-Segment Flap	Various	173	174,181,182								
Slat & Two-Segment Flap	Various	175	176,181,182								
VCE & Single-Slot Flap	Various	177	178,181,182								
Slat & Single Slot Flap	Various	179	180,181,182								

ORIGINAL PAGE IS
OF POOR QUALITY

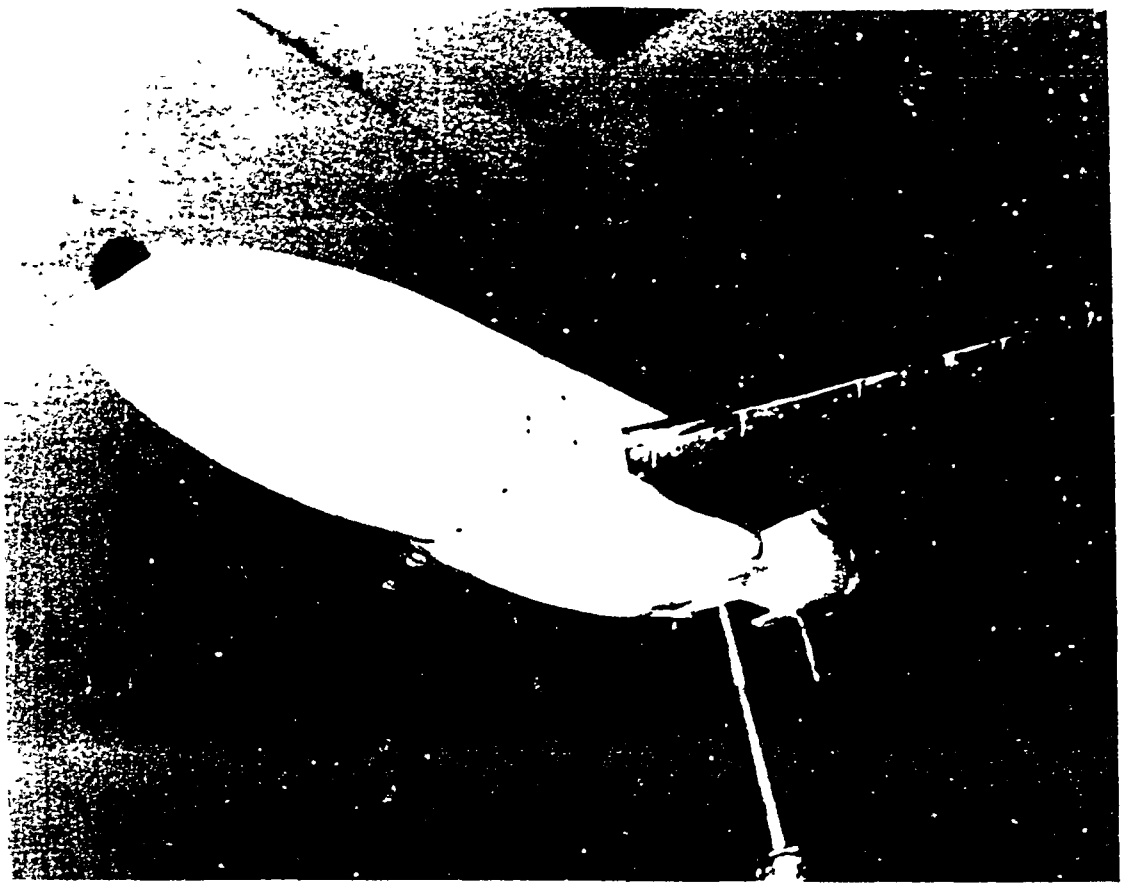

FIGURE 62. CRUISE WING CONFIGURATION IN THE AMES 12-FOOT PRESSURE WIND TUNNEL (NACELLES AND PYLON OFF)

The basic wing-body is seen to have an initial outboard stall of significant proportions in terms of the lift loss and the small angle of attack range over which this phenomenon occurs. The result of this trend is a significant reduction in wing-body stability after stall (Figure 63). Also presented in Figure 63 is a comparison of the aerodynamic characteristics with and without tufts. Good agreement in the lift and pitching moment through $C_{L_{MAX}}$ is shown. Some differences are noted in these quantities after $C_{L_{MAX}}$, but they are relatively small. The drag with the tufts on (Run 18) is seen to be lower in Figure 63 by 10 to 20 drag counts depending on the C_L, and this results in higher L/D values (Figures 63). Evaluation of the pressure data comparing Runs 18 and 22 did not indicate a significant improvement in trailing edge pressure recovery.

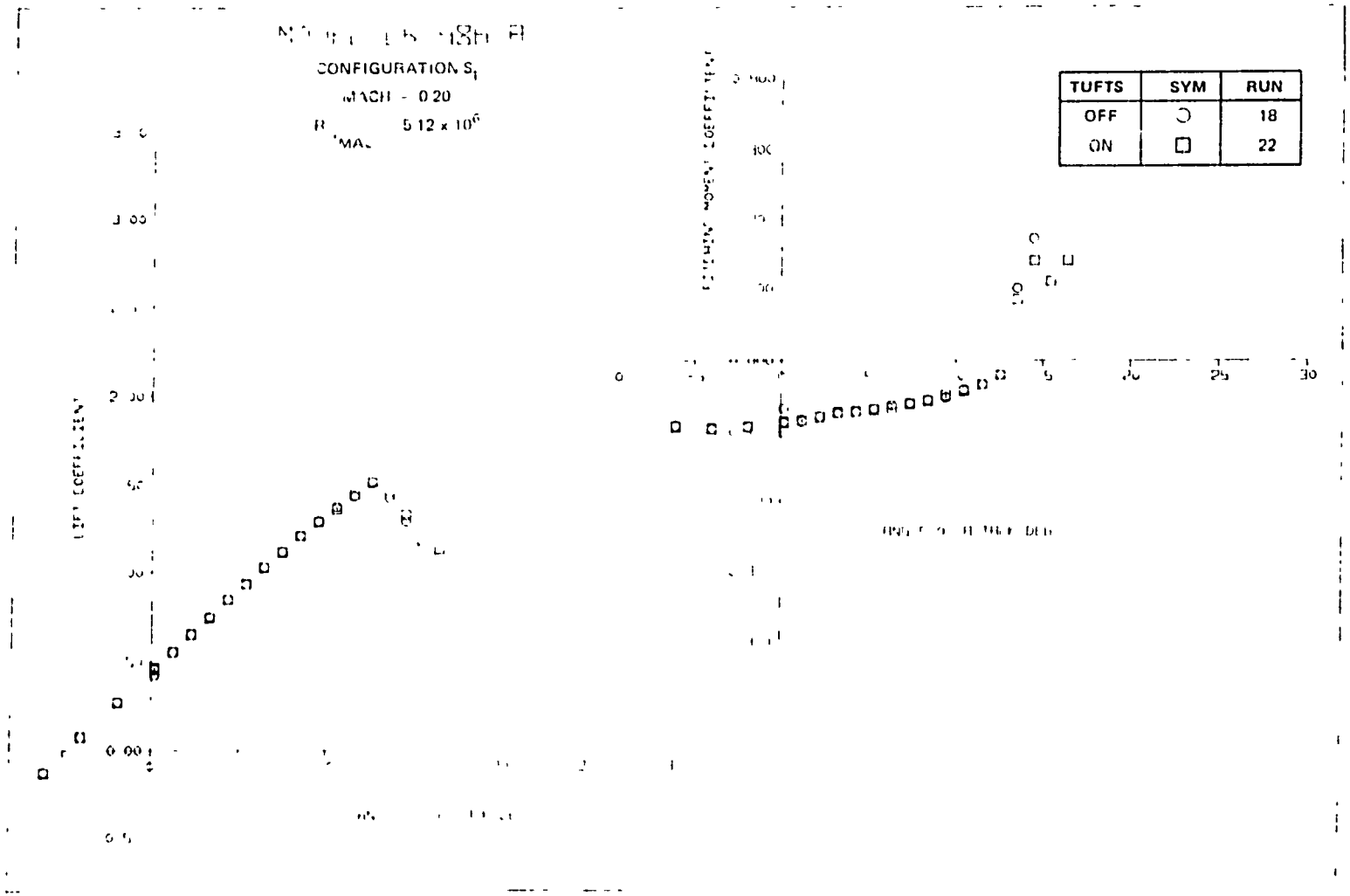

A. LIFT AND PITCHING MOMENT

FIGURE 63 AERODYNAMIC CHARACTERISTICS OF BASIC CRUISE WING-BODY AND EFFECT OF MINI-TUFTS

ORIGINAL PAGE IS
OF POOR QUALITY

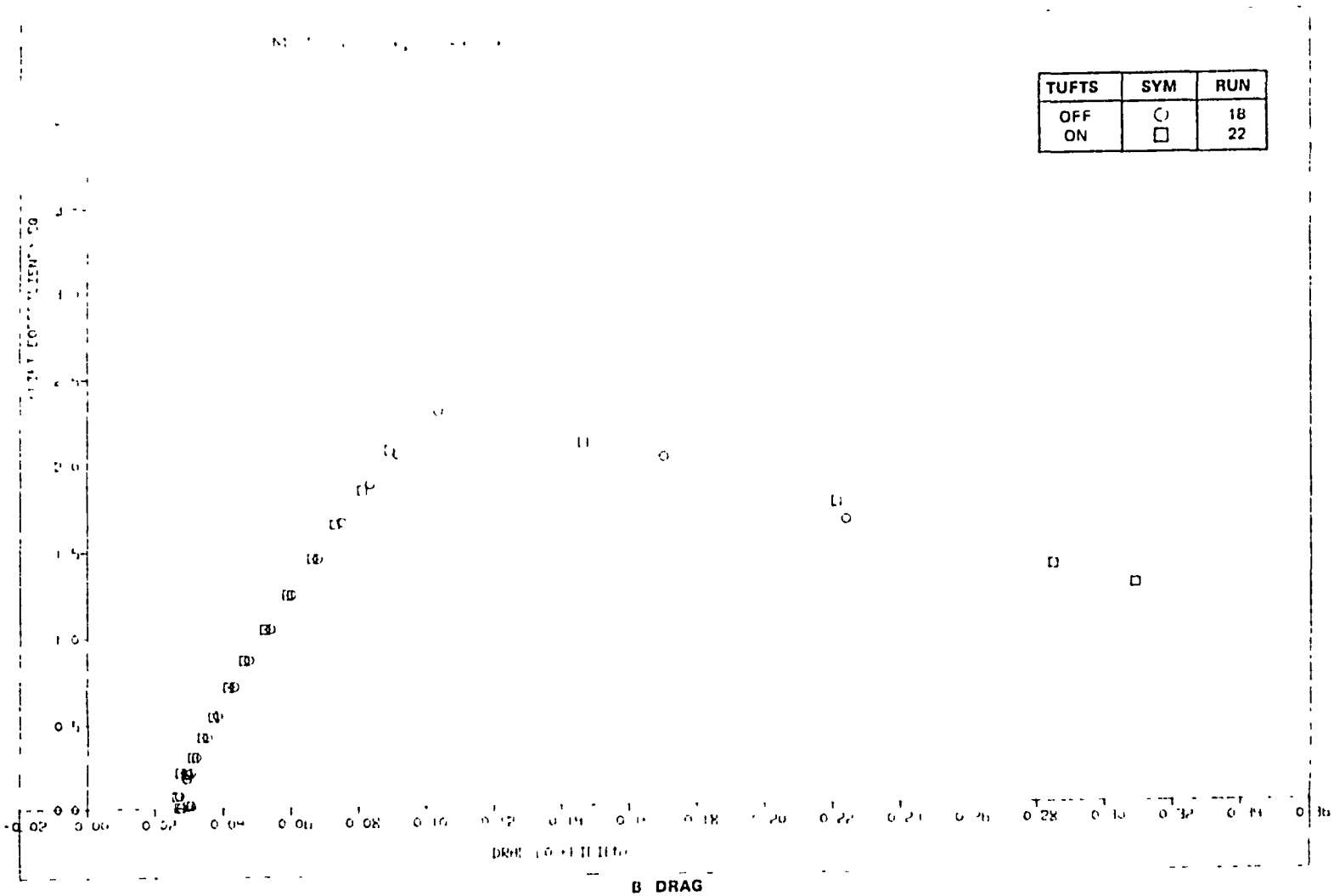

FIGURE 63 AERODYNAMIC CHARACTERISTICS OF BASIC CRUISE WING-BODY AND EFFECT OF MINI-TUFTS (CONTINUED)

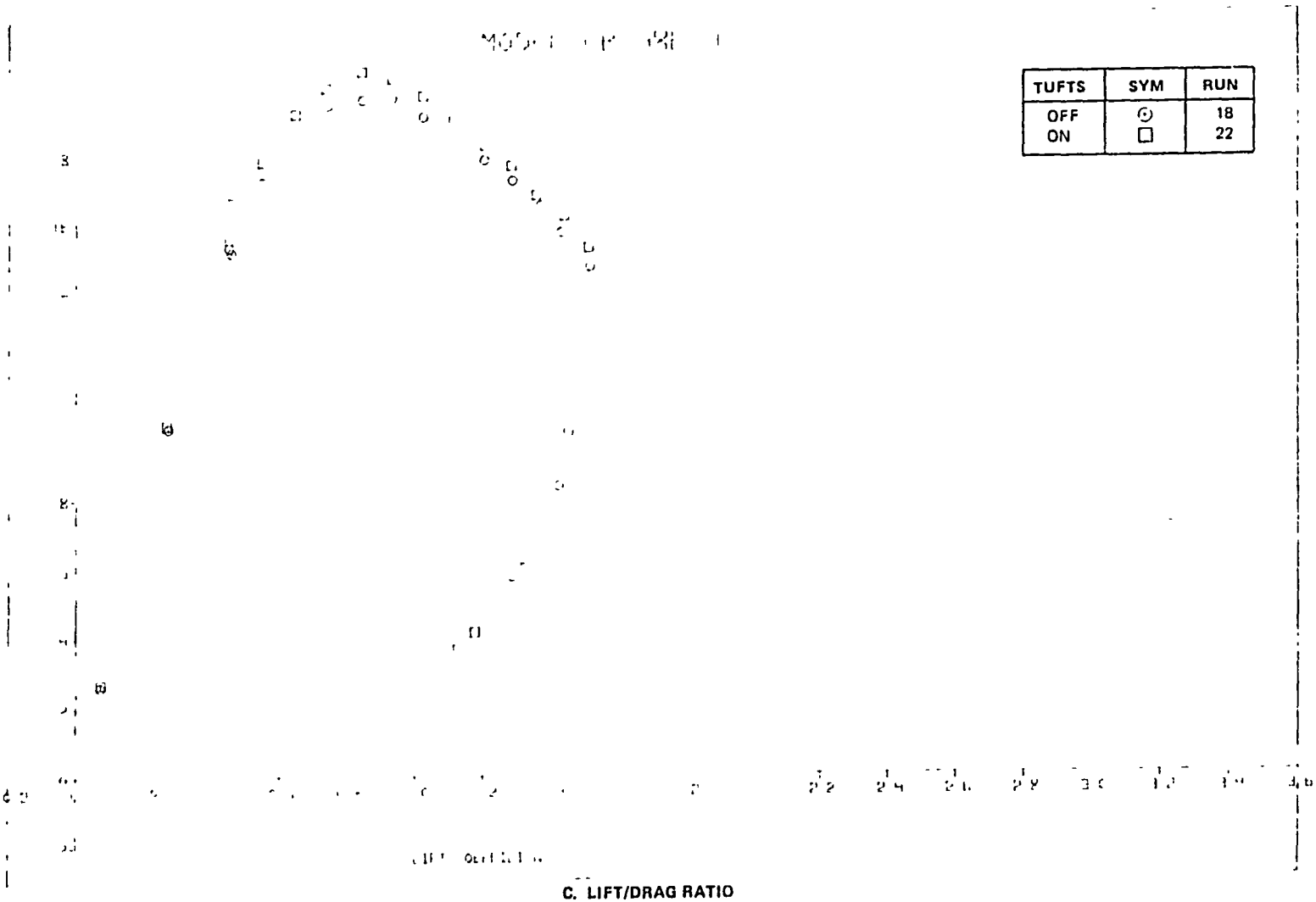

C. LIFT/DRAG RATIO

FIGURE 63. AERODYNAMIC CHARACTERISTICS OF BASIC CRUISE WING-BODY AND EFFECT OF MINI-TUFTS (CONCLUDED)

ORIGINAL PAGE IS
OF POOR QUALITY

ORIGINAL PAGE IS
OF POOR QUALITY

The cruise wing-body configuration, with the W_3 wing, had previously been tested in the Ames Research Center 11-Foot Transonic Wind Tunnel. This model was a four-percent scale model and was sting-mounted. The current data was corrected for strut tares and compared with the high-speed experimental data. Various lift parameters are compared in Figure 64. Good agreement with the high speed data is indicated for the lift quantities shown in Figure 64. The lift and drag are compared in Figure 65 for Mach numbers of 0.2 and 0.5. The lift variation shown in Figure 65 shows the expected increase in high-speed lift curve slope, and also indicates that the $C_{L_{MAX}}$ at 0.5 Mach number is influenced by compressibility effects not apparent in the low-speed data. The LB-486A Reynolds number based on the MAC was very similar to the high speed test condition at a Mach number of 0.50 and is shown in Figure 65. Good agreement in the drag is obtained for the intermediate C_L range. Compressibility effects in the high-speed data are noted for C_L^2 values above 0.6. Pitching moment comparisons were made difficult by the differences in geometry (boat-tailed configuration versus sting-mounted). Direct comparison of pitching moments indicated that for the intermediate C_L range, the low-speed values were 0.03 more positive than the high-speed data.

Mini-tuft pictures of the wing, for Mach number of 0.20, are presented in Figure 66 for angles of attack before and after $C_{L_{MAX}}$. At this point in the

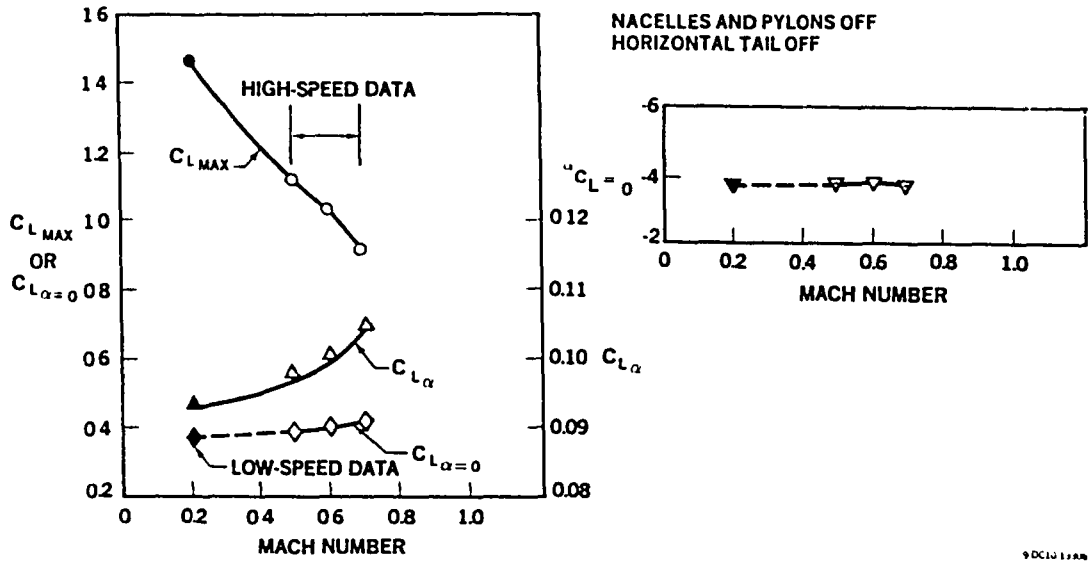

FIGURE 64. COMPARISON OF LOW- AND HIGH-SPEED CHARACTERISTICS FOR THE ACA CONFIGURATION

ORIGINAL PAGE IS
OF POOR QUALITY

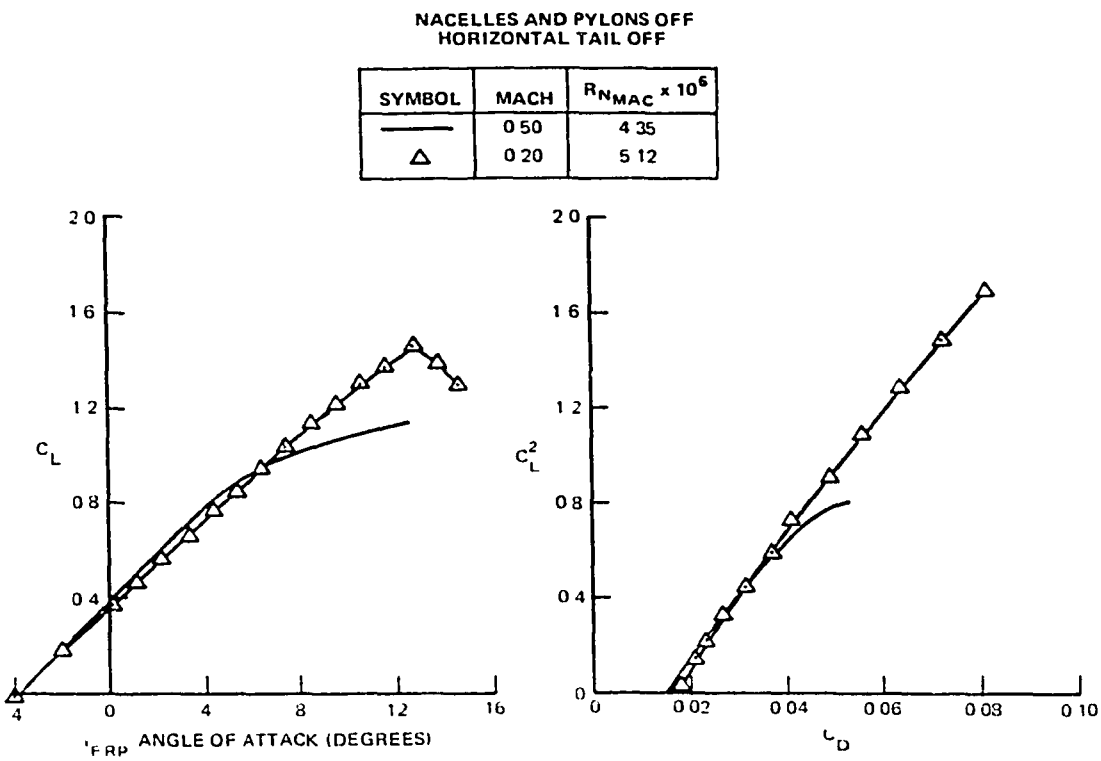

FIGURE 65. COMPARISON OF HIGH-SPEED AND LOW-SPEED LIFT AND DRAG FOR CRUISE WING CONFIGURATION

test program, the tuft length had not been lengthened to improve the readability of the pictures. Nevertheless, Figure 66 does illustrate the stall phenomena of the high aspect ratio wing at high Reynolds number conditions. Figure 67 presents the chordwise pressure distributions of the five streamwise pressure rows for $\alpha C_{L_{MAX}}$ (12.57°), and 1° and 2° past $\alpha C_{L_{MAX}}$. At $\alpha C_{L_{MAX}}$ suction peaks are evident for all spanwise locations. Slightly negative trailing edge pressure coefficients are noted for this condition at all spanwise locations except η = 20 percent. Large spanwise flow angles are indicated in the corresponding tuft photo for the trailing edge region. At α_{FRP} = 13.55° (1° past stall), the 50-percent span station indicates separation near the leading edge. The 72.5-percent span station remains attached and this is confirmed by the tuft photographs. The 90-percent span station is also separated at the leading edge. At α_{FRP} = 14.50° (2° past stall) the 50-, 72.5-, and 90-percent span stations are separated at the leading edge. On the other hand, the inboard stations are still heavily loaded. Other pressure data (not presented) indicated the 20- and 30-percent stations stalled at α_{FRP} = 15.44°.

ORIGINAL PAGE IS
OF POOR QUALITY

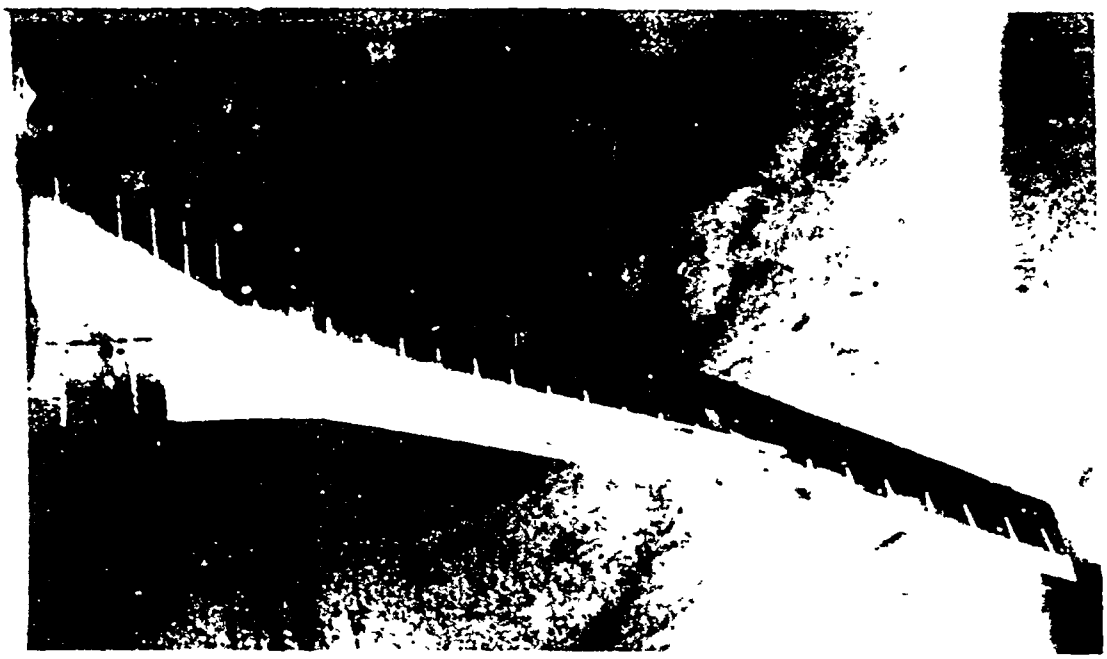

A $\alpha_{FRP} = 10.51^{\circ}$

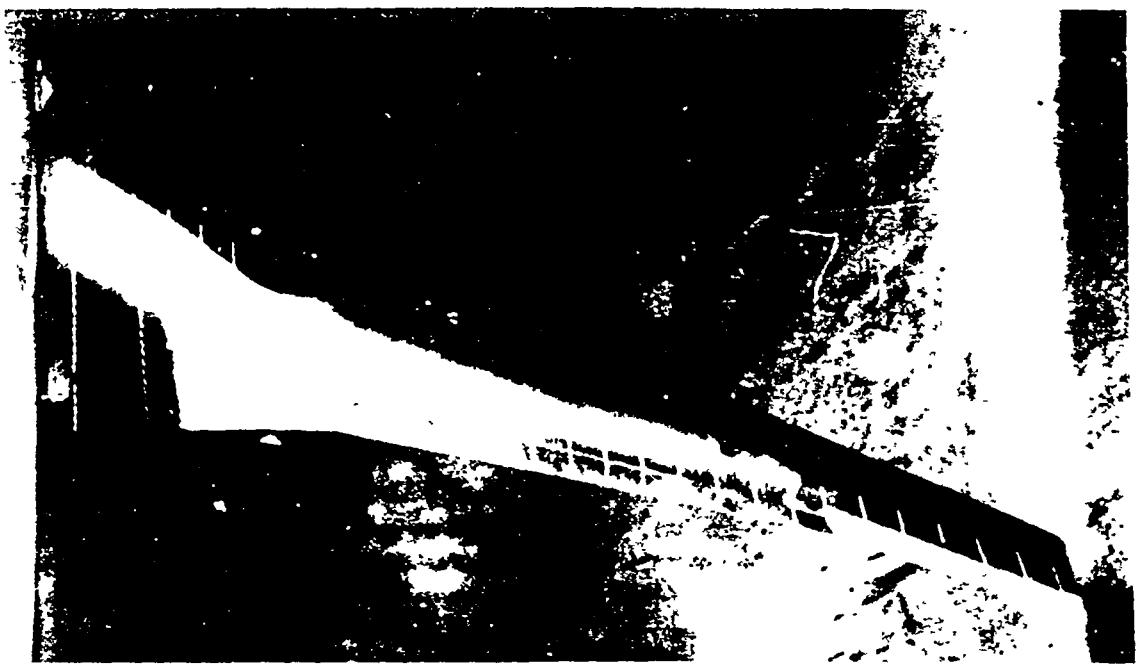

B. $\alpha_{FRP} = 12.57^{\circ}$ ($\alpha_{C_{L_{MAX}}}$)

FIGURE 66. MINI-TUFT PHOTOS FOR CRUISE WING-BODY (RUN 22)

ORIGINAL PAGE IS
OF POOR QUALITY

C $\alpha_{FRP} = 13.55^{\circ}$

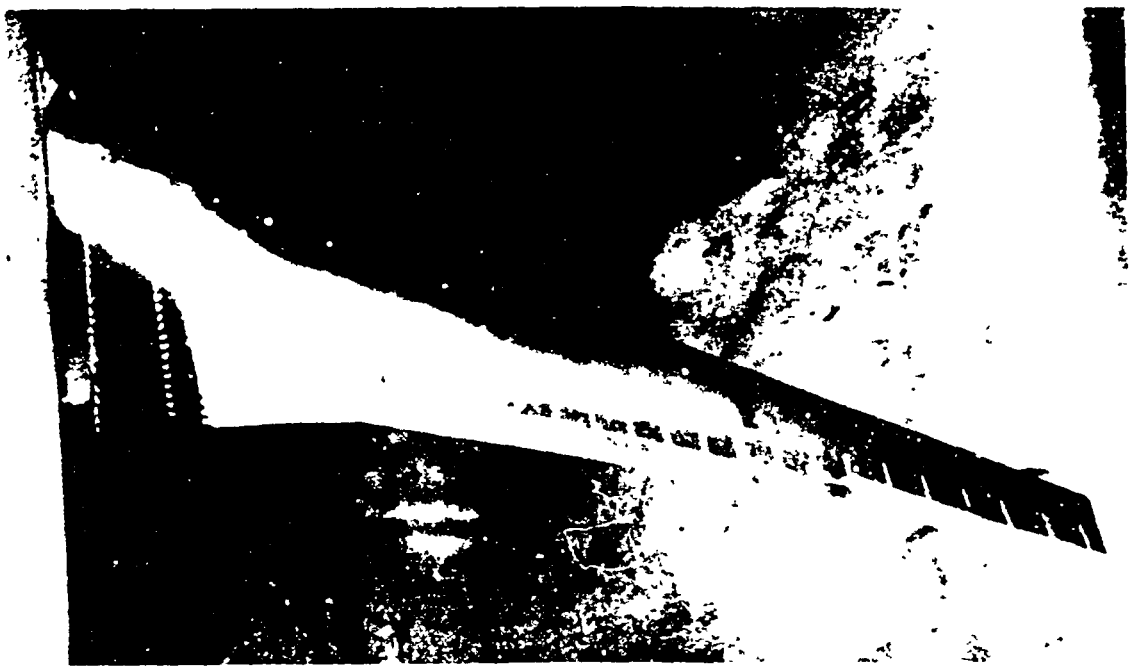

D. $\alpha_{FRP} = 15.44^{\circ}$

FIGURE 66. MINI-TUFT PHOTOS FOR CRUISE WING-BODY (CONCLUDED)

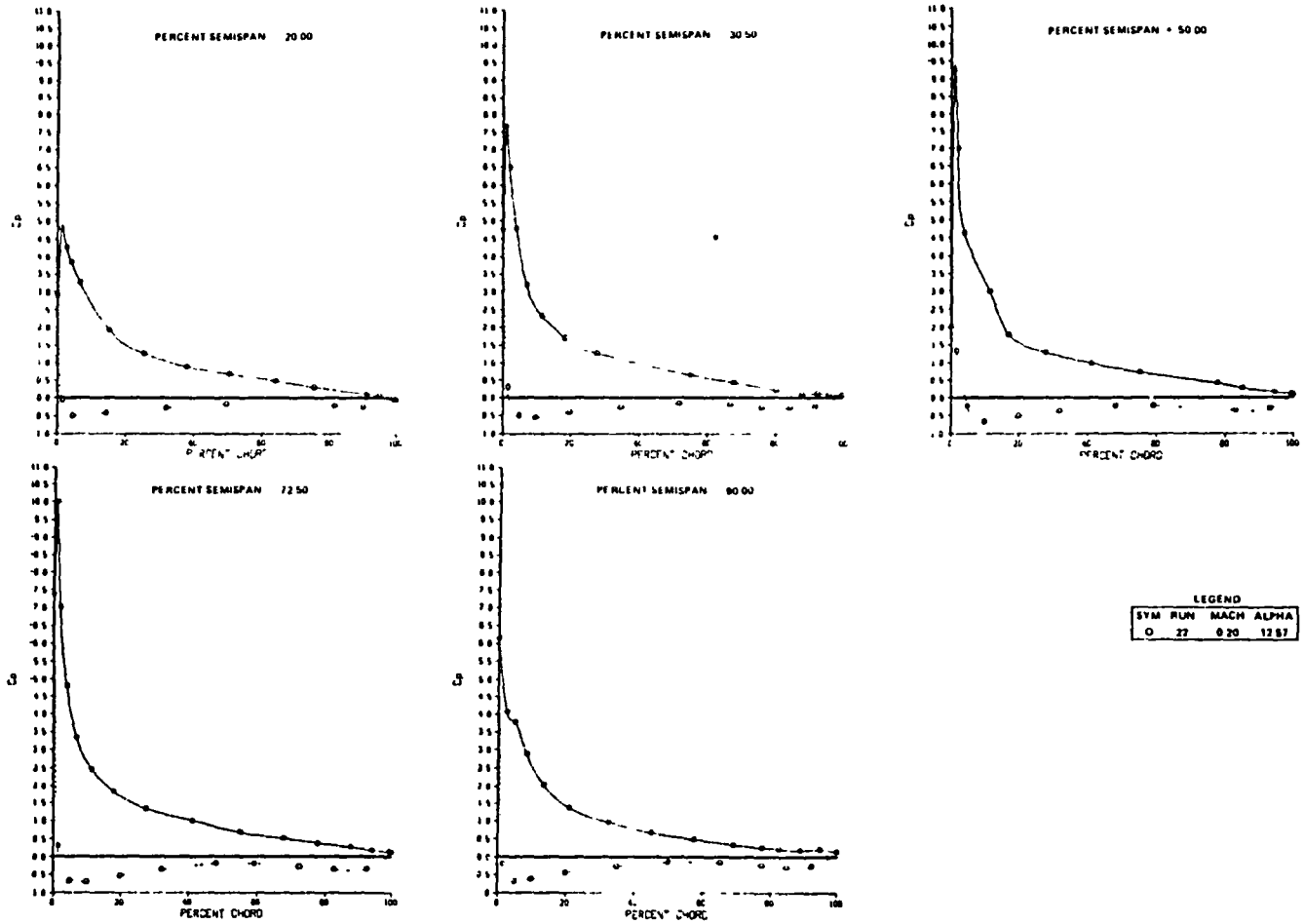

A α_{FRP} = 12.57 DEG

FIGURE 67. EXPERIMENTAL CHORDWISE PRESSURE DISTRIBUTION FOR CRUISE WING (NACELLES AND PYLONS OFF)

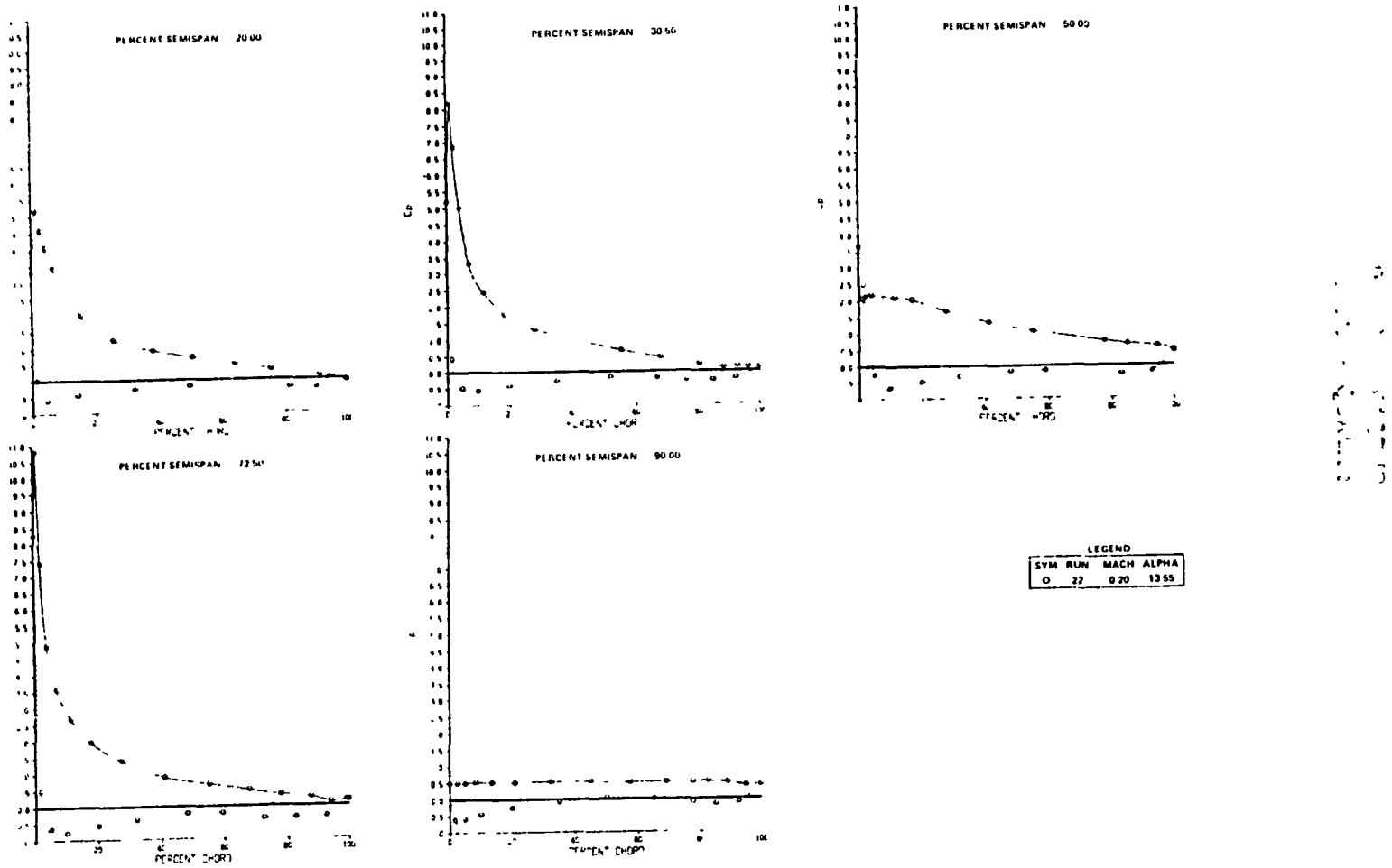

B α_{FRP} = 13.55 DEG

FIGURE 67. EXPERIMENTAL CHORDWISE PRESSURE DISTRIBUTION FOR CRUISE WING (NACELLES AND PYLONS OFF) (CONTINUED)

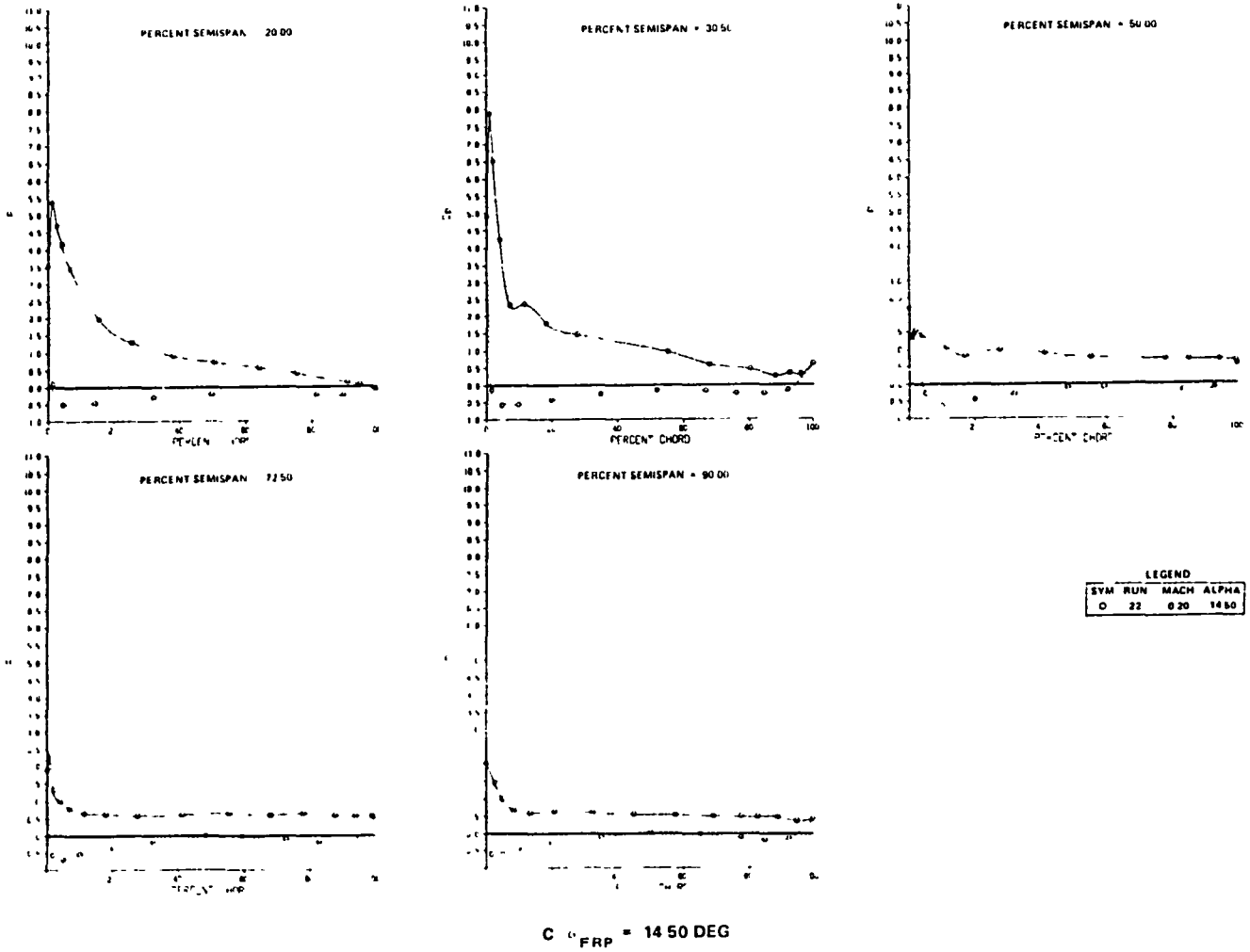

C $_{FRP}$ = 14.50 DEG

FIGURE 67. EXPERIMENTAL CHORDWISE PRESSURE DISTRIBUTION FOR CRUISE WING (NACELLES AND PYLONS OFF) (CONCLUDED)

ORIGINAL PAGE IS
OF POOR QUALITY

Figure 68 shows the variation of sectional lift, obtained from an integration of the pressures, for the five pressure rows. The large, rapid lift loss at stall for the 50-, 72.5-, and 90-percent stations is noteworthy. Figure 69 presents the spanwise variation of sectional lift. Significant variation in rolling moment for angles of attack 1^{o} or 2^{o} above ${}^{\alpha}C_{L_{MAX}}$ indicated some asymmetry in the stall pattern. Rolling moment incremental values were negative, indicating premature left wing panel stall. Flow symmetry was regained at higher angles of attack.

The basic wing-body was also tested at a Reynolds number of $R_{N_{MAC}} = 1.13 \times 10^{6}$ and a Mach number of 0.20 (atmospheric conditions for the Ames facility). The results are presented in Figures 70 through 72. A comparison of Figures 63 and 70 shows that the $C_{L_{MAX}}$ is reduced from 1.51 to 1.13, the magnitude of the post stall lift loss is decreased, and a positive Cm shift of approximately 0.02 is apparent for angles of attack prior to stall. The ${}^{\alpha}C_{L_{MAX}}$ has been reduced from 12.57^{o} to 8.43^{o}, and the configuration still exhibits the same pitch variation for the angles just after ${}^{\alpha}C_{L_{MAX}}$. The $(L/D)_{MAX}$ is reduced from 20.4 to 15.3 by the decrease in Reynolds number. Figure 71 presents the sectional lift characteristics for Run 21. Comparing Figures 68 and 71 shows the sectional lift values obtained for the 20-percent span station are the same. Significantly lower values of $C_{\ell_{MAX}}$ were obtained for the remaining stations. The 30-percent span station for the low Reynolds number has a $C_{\ell_{MAX}}$ of 1.2 and a gradual stall followed by a moderate lift loss. This is different than the high Reynolds number trend. The outboard stations (50-, 72.5-, and 90-percent) show the rapid lift loss (i.e., leading edge type separation) and lose almost half of their lift by 2^{o} after their $C_{\ell_{MAX}}$. Clearly the outboard trends are similar to the high Reynolds number data, but occur at a lower angle of attack.

It is also noteworthy that, at large angles past $C_{L_{MAX}}$, the c_{ℓ} values tend to reach similar values. A change in the type of stall (i.e., from a leading edge to a trailing edge type separation) for the flight condition would alleviate these adverse high angle-of-attack outboard wing panel lift characteristics. The large increase in the angle of attack for outboard wing panel stall, due to an increase in Reynolds number, implies that at flight conditions the outboard panel may stall later than the inboard wing.

ORIGINAL PAGE IS
OF POOR QUALITY

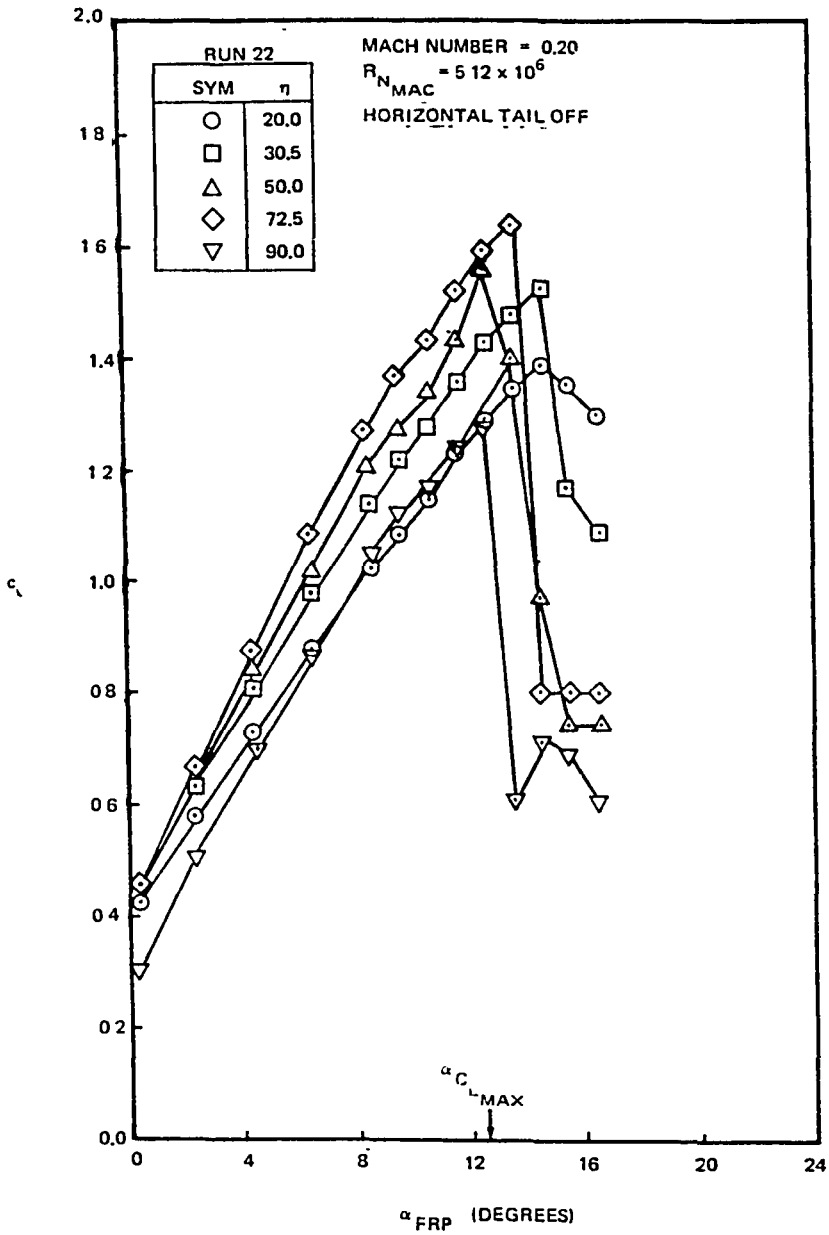

FIGURE 68. VARIATION OF SECTION LIFT COEFFICIENT FOR THE CRUISE WING (NACELLES AND PYLONS OFF, HIGH REYNOLDS NUMBER CONDITION)

ORIGINAL PAGE IS
OF POOR QUALITY

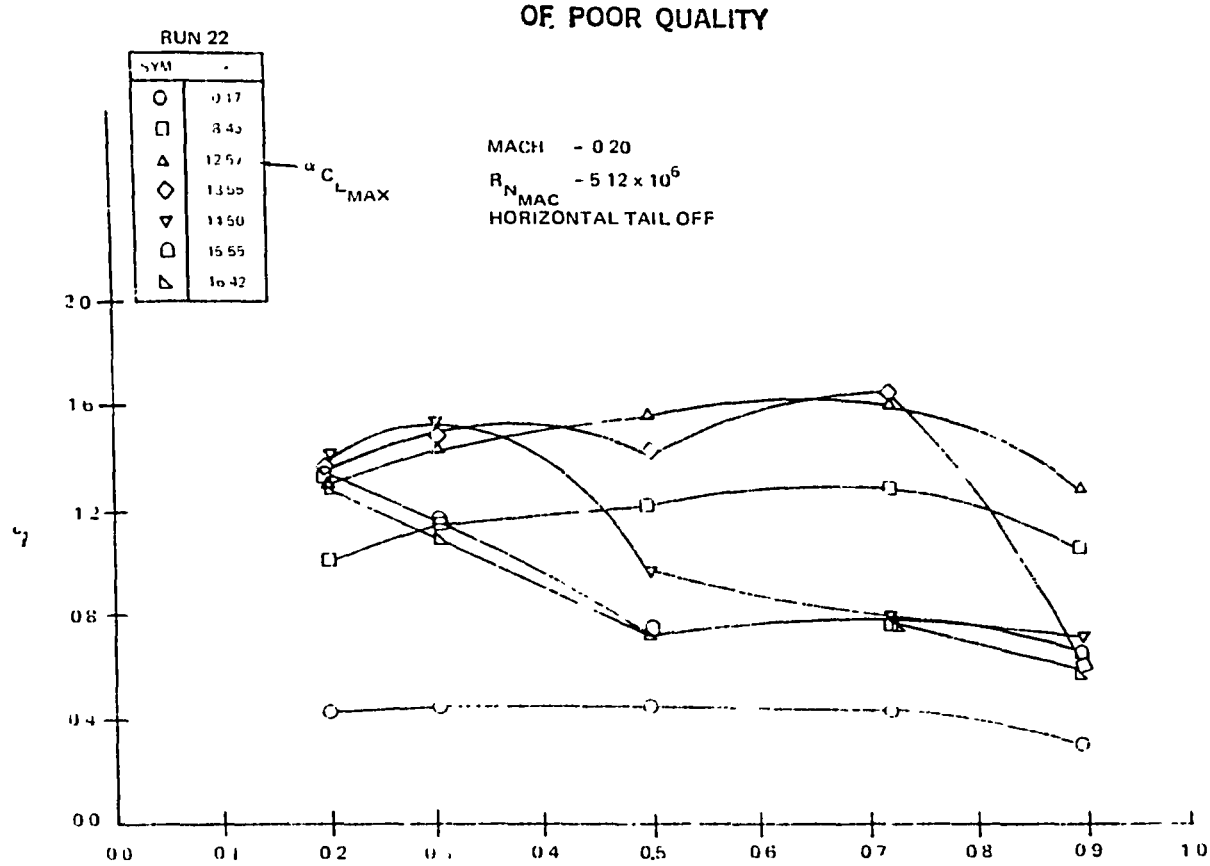

FIGURE 69. SPANWISE VARIATION OF SECTION LIFT COEFFICIENT FOR CRUISE WING (NACELLES AND PYLONS OFF, HIGH REYNOLDS NUMBER CONDITION)

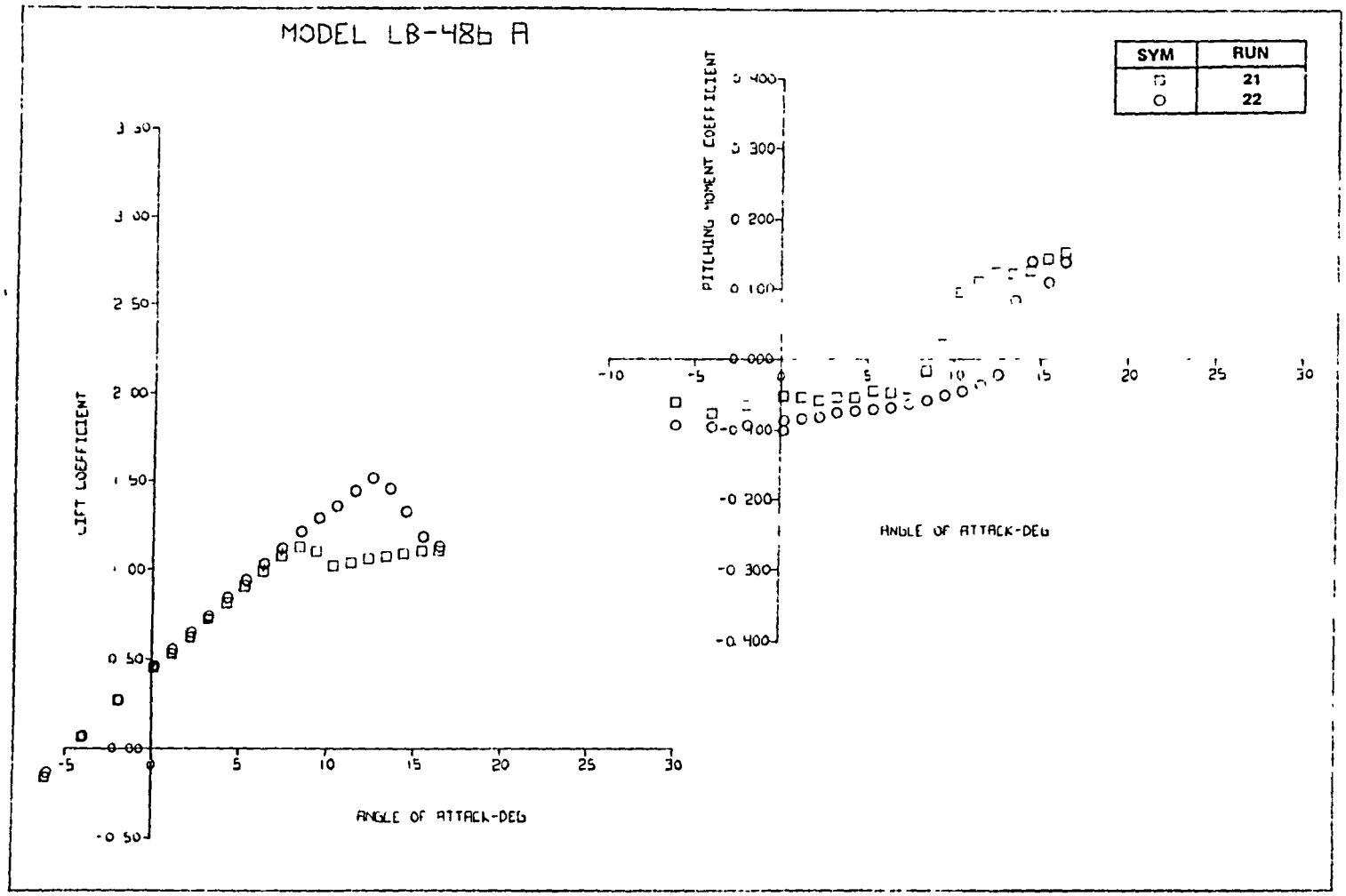

A LIFT AND PITCHING MOMENT

FIGURE 70. EFFECT OF REYNOLDS NUMBER ON AERODYNAMIC CHARACTERISTICS OF THE BASIC CRUISE WING-BODY CONFIGURATION

ORIGINAL PAGE IS
OF POOR QUALITY

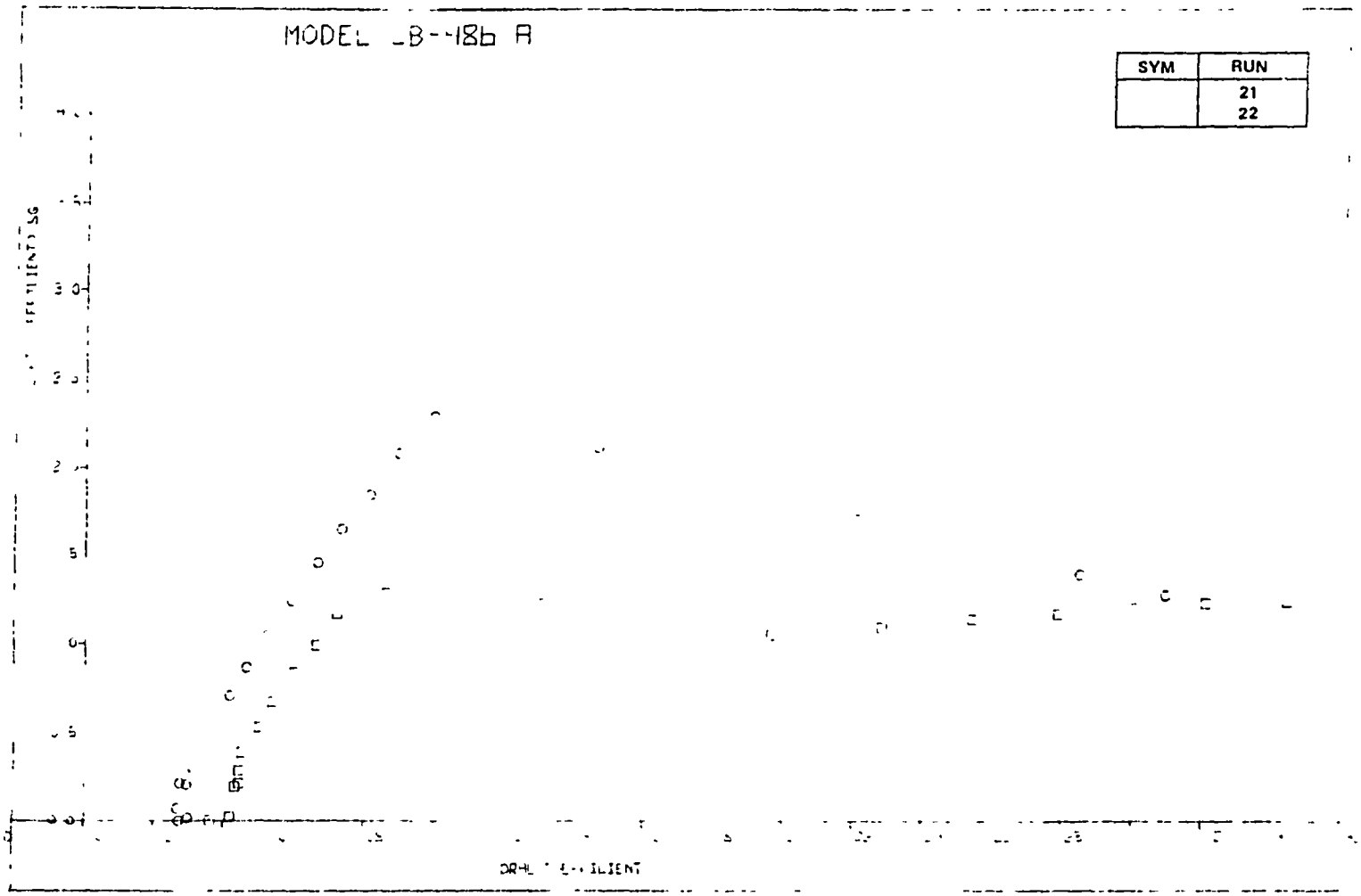

FIGURE 70 EFFECT OF REYNOLDS NUMBER ON AERODYNAMIC CHARACTERISTICS OF THE BASIC CRUISE WING-BODY CONFIGURATION (CONTINUED)

ORIGINAL PAGE IS OF POOR QUALITY

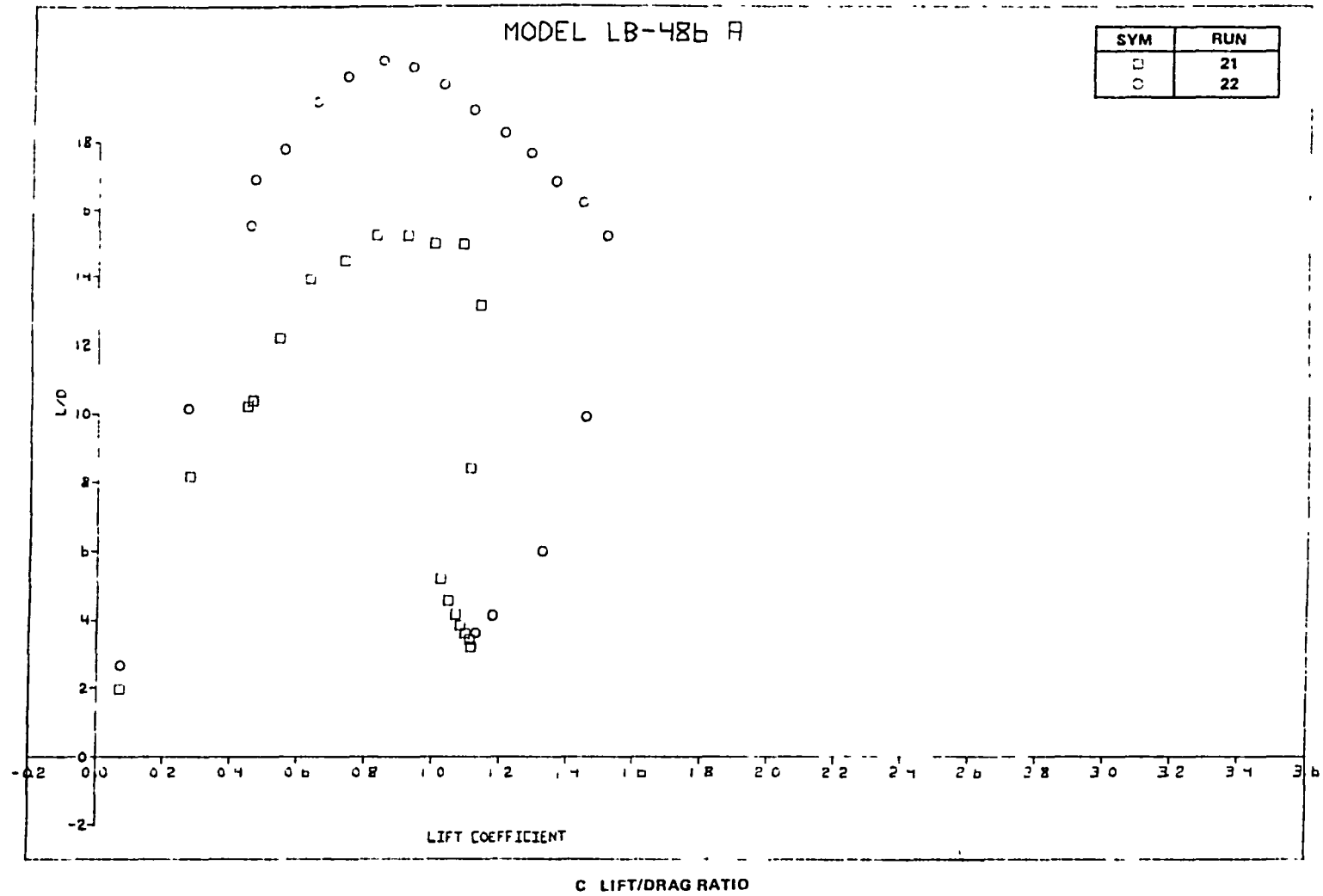

ORIGINAL PAGE IS
OF POOR QUALITY

FIGURE 70. EFFECT OF REYNOLDS NUMBER ON AERODYNAMIC CHARACTERISTICS OF THE BASIC CRUISE WING-BODY CONFIGURATION (CONCLUDED)

ORIGINAL PAGE IS
OF POOR QUALITY

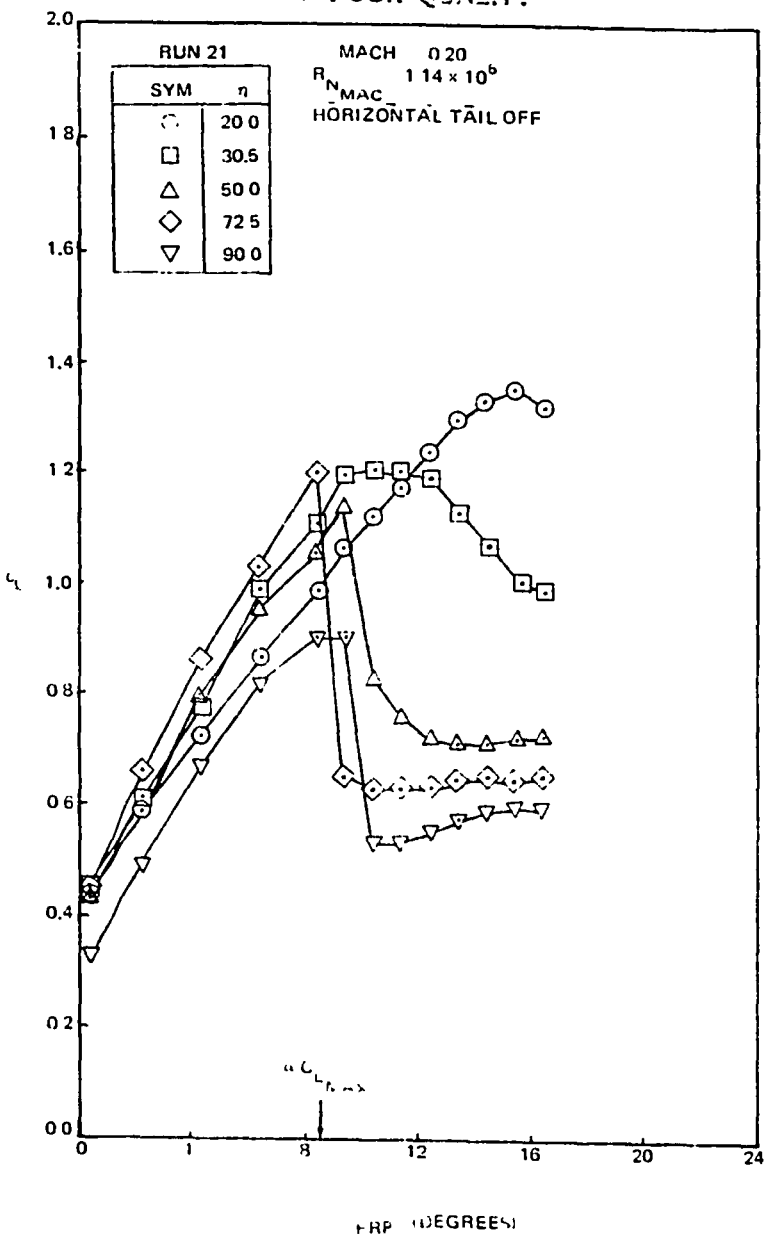

FIGURE 71 VARIATION OF SECTION LIFT COEFFICIENT FOR THE CRUISE WING (NACELLES AND PYLONS OFF, ATMOSPHERIC REYNOLDS NUMBER CONDITION)

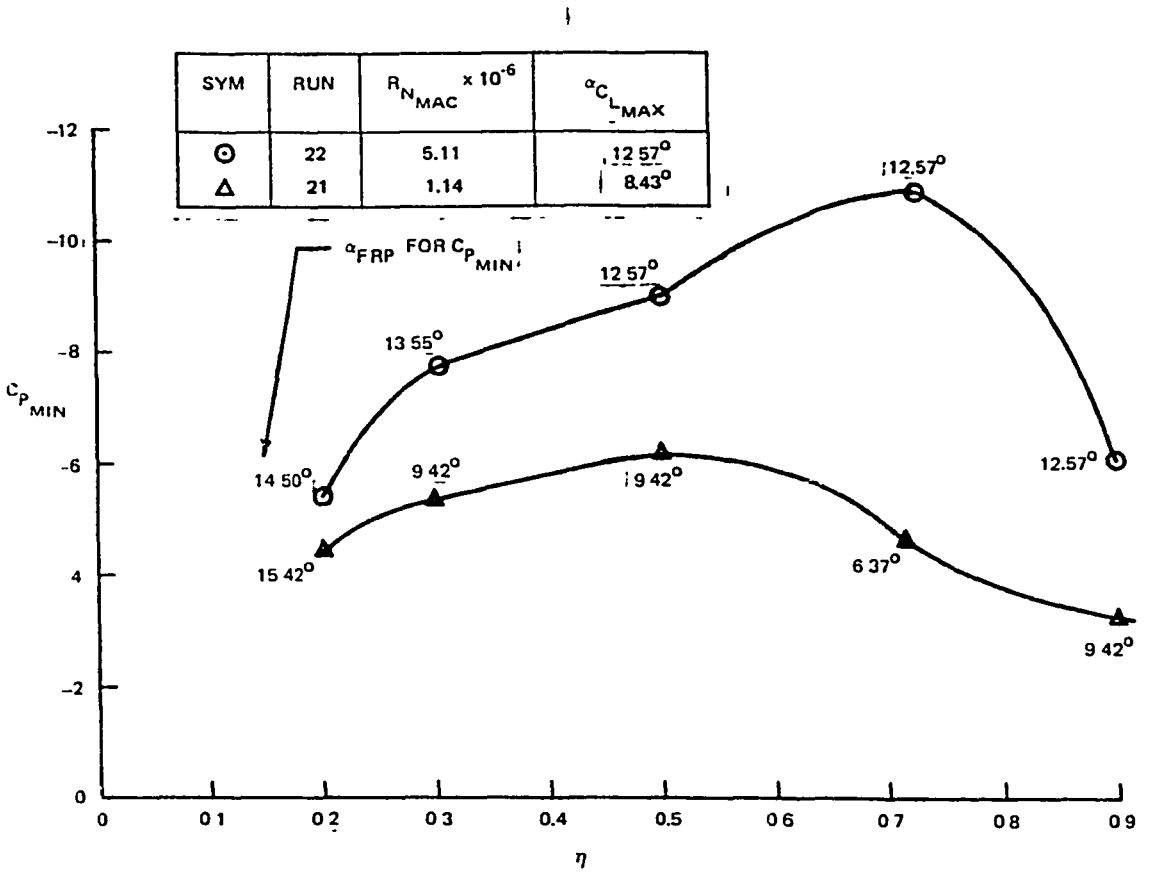

FIGURE 72. EFFECT OF REYNOLDS NUMBER ON THE SPANWISE VARIATION OF $C_{P_{MIN}}$

This would improve the pitching moment characteristics for this wing. It should be noted that the $c\ell_{MAX}$ values at the 20-percent station did not change significantly with Reynolds number. The 30-percent station $\alpha C_{L_{MAX}}$ did increase. The evaluation of the low speed supercritical airfoil stalling phenomenon at Reynolds number approaching flight conditions is thus a critical area of technology development.

It is pertinent to note that W_{3B} was one of the earlier wing geometries evaluated in the high speed development. This wing was characterized by significantly greater outboard loading than the finalized designs (see Reference 5). Future wings to be evaluated in the high speed regime have reduced outboard loadings which should alleviate the imbalance between the outboard and inboard angles of attack for stall.

Significantly lower values of minimum pressure coefficient ($C_{P_{MIN}}$) were indicated for the lower Reynolds number test condition. Figure 72 presents a comparison of the $C_{P_{MIN}}$ spanwise variation for the high and low Reynolds number condition. The differences are greatest at the 72.5-percent span station.

Nacelle/Pylon Effect on Cruise Wing. - The effects of nacelles, pylons, and nacelle strakes are shown in Figure 73. Addition of the nacelles and pylons (Run 29) resulted in essentially the same $C_{L_{MAX}}$ and lift variation after $C_{L_{MAX}}$ as the basic wing-body (Run 22). The pitching moment indicates an improved stability trend after $C_{L_{MAX}}$. Addition of the nacelles is destabilizing prior to $C_{L_{MAX}}$. The drag increment at 1.2 V_S due to the nacelle/pylon is 0.0060 and the L/D is reduced to 17.7. Rolling moment characteristics indicate the same trend (left wing stall) as the basic wing-body, but with slightly different peak rolling moment values. Addition of the nacelle strakes (Run 23) results in the same $C_{L_{MAX}}$, a reduced lift loss and similar trends of reduced stability after $C_{L_{MAX}}$ as the wing-body configuration. The drag is slightly larger (0.0005) than Run 29 values near 0.69 $C_{L_{MAX}}$. The rolling moment trends are similar to the basic wing-body values.

Mini-tuft photos for the nacelles, pylons, and strakes attached configuration are shown in Figure 74. Changes in local flow angle are evident behind the nacelle/pylon group. Comparison with Figure 66 (the cruise wing) indicates the same outboard separation phenomenon. However, the flow on the wing surface behind the nacelle is attached. Complementary flow-visualization photos for Run 29 (strakes off) indicated the area behind the nacelle is separated for the angles of attack larger than $^{\alpha}C_{L_{MAX}}$.

Chordwise pressure distribution plots for the configuration with the nacelles, pylons, and strakes attached are presented in Figure 75. The angles of attack selected were $^{\alpha}C_{L_{MAX}}$ and higher. At an α_{FRP} of 13.58°, the 50-percent span station shows a collapse of the suction peak. The corresponding flow-visualization photo, while indicating some tuft activity near the trailing edge, does not show significant tuft motion near the wing midchord region. The 50-percent pressure station is located on the left

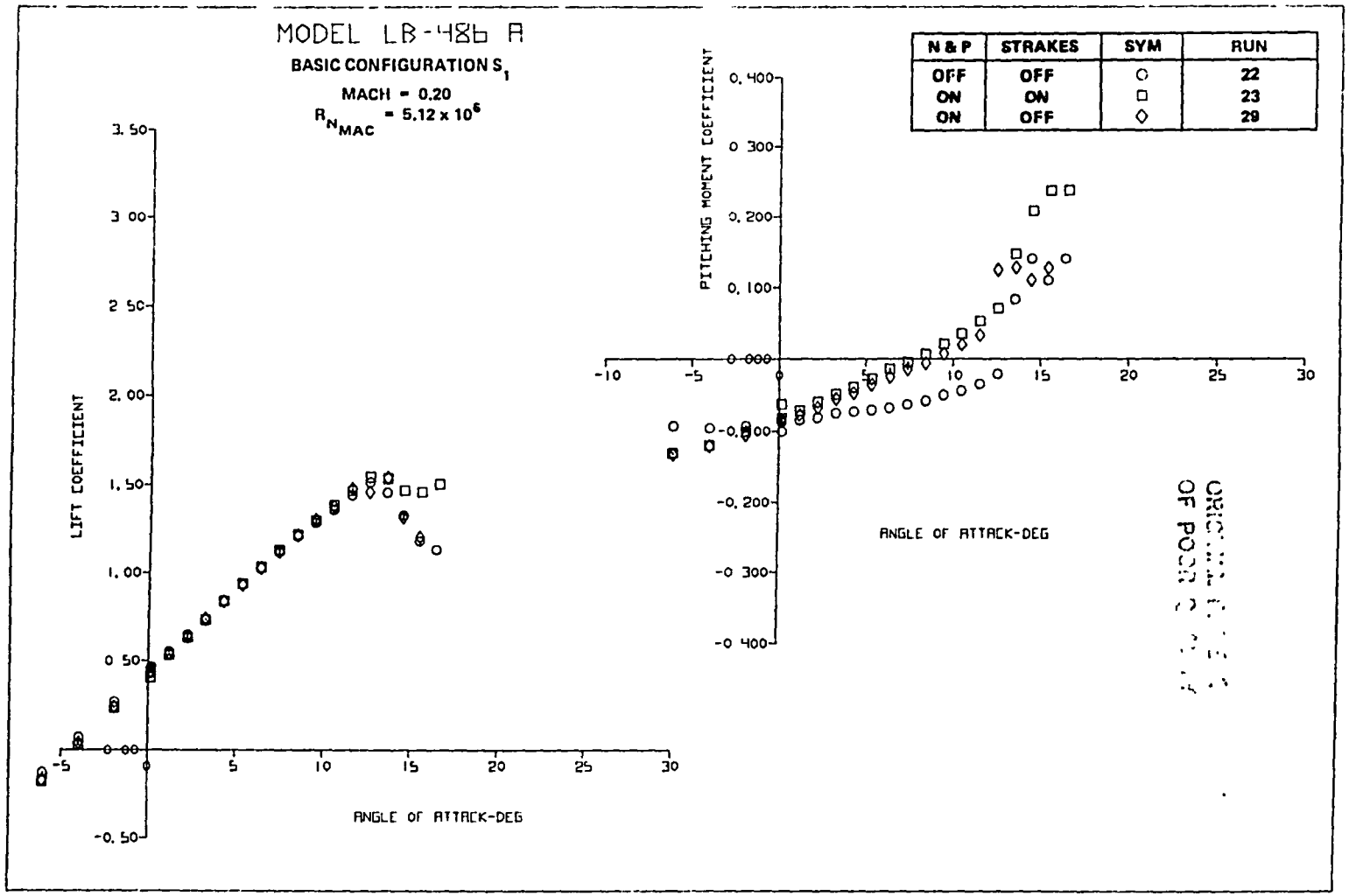

A. LIFT AND PITCHING MOMENT

FIGURE 73. EFFECT OF NACELLES, PYLONS, AND STRAKES ON AERODYNAMIC CHARACTERISTICS OF THE CRUISE WING

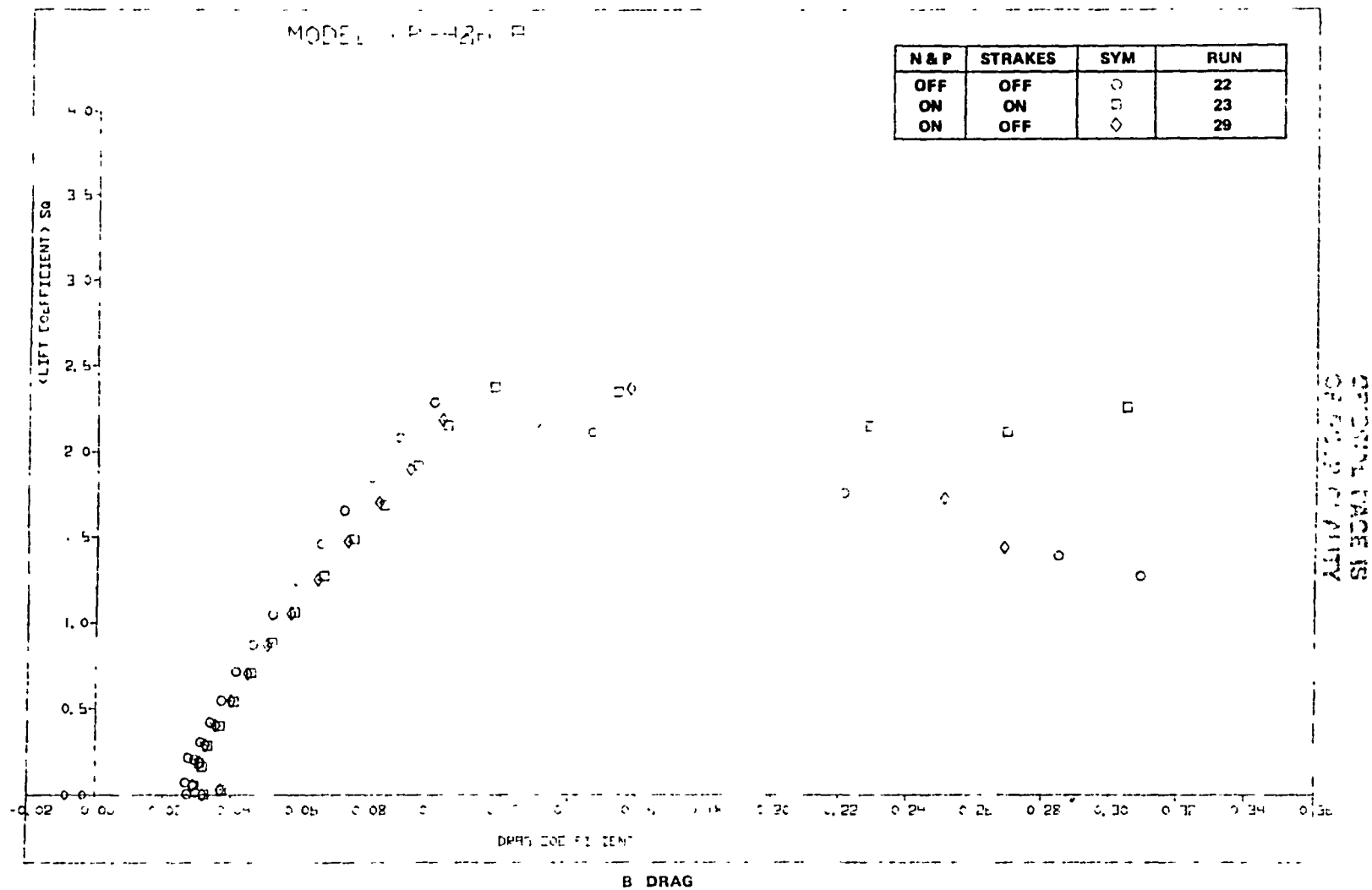

FIGURE 73. EFFECT OF NACELLES, PYLONS, AND STRAKES ON AERODYNAMIC CHARACTERISTICS OF THE CRUISE WING (CONTINUED)

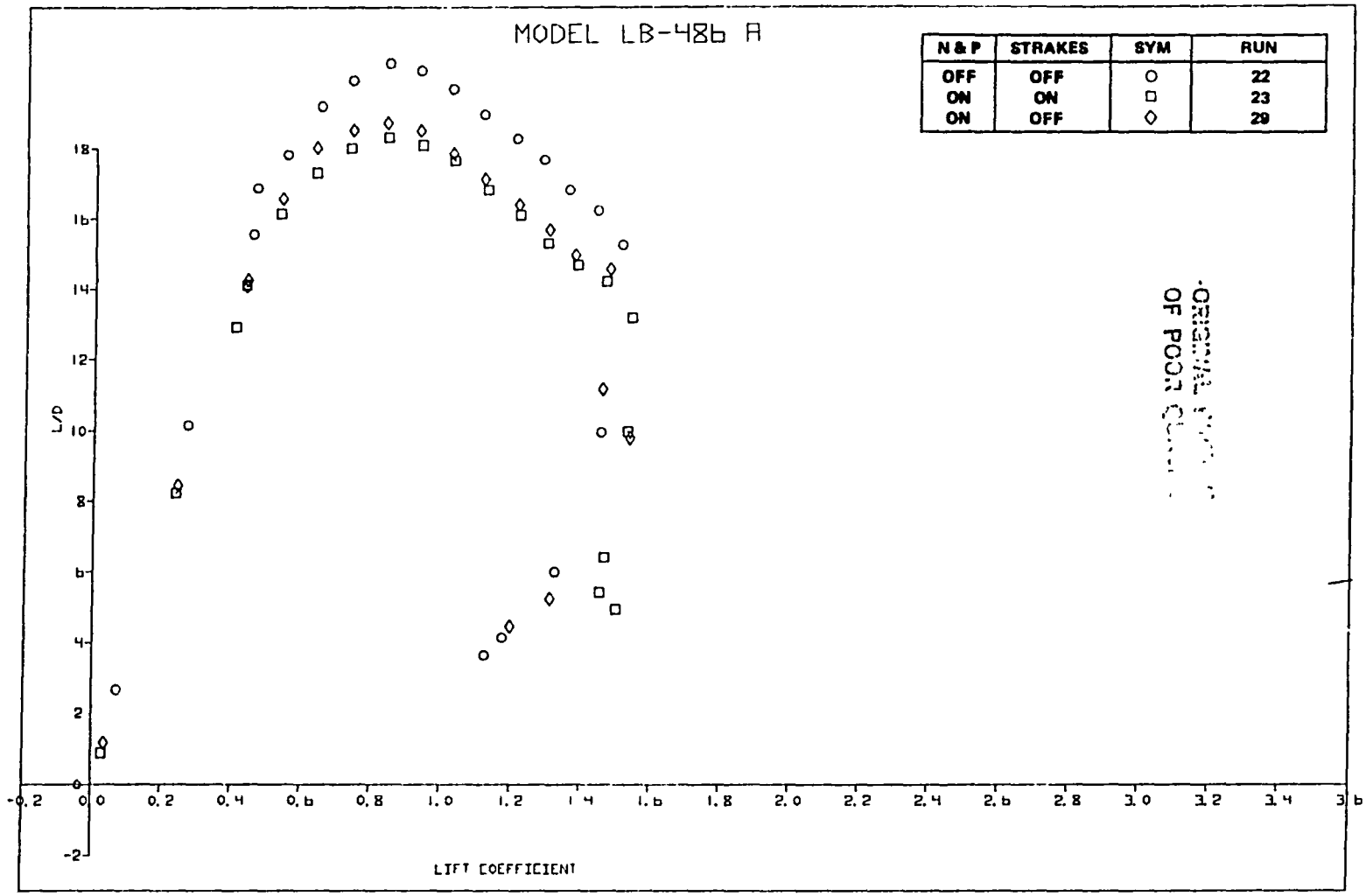

C. LIFT/DRAG RATIO

FIGURE 73. EFFECT OF NACELLES, PYLONS, AND STRAKES ON AERODYNAMIC CHARACTERISTICS OF THE CRUISE WING (CONTINUED)

CRI...
OF POOR Q...

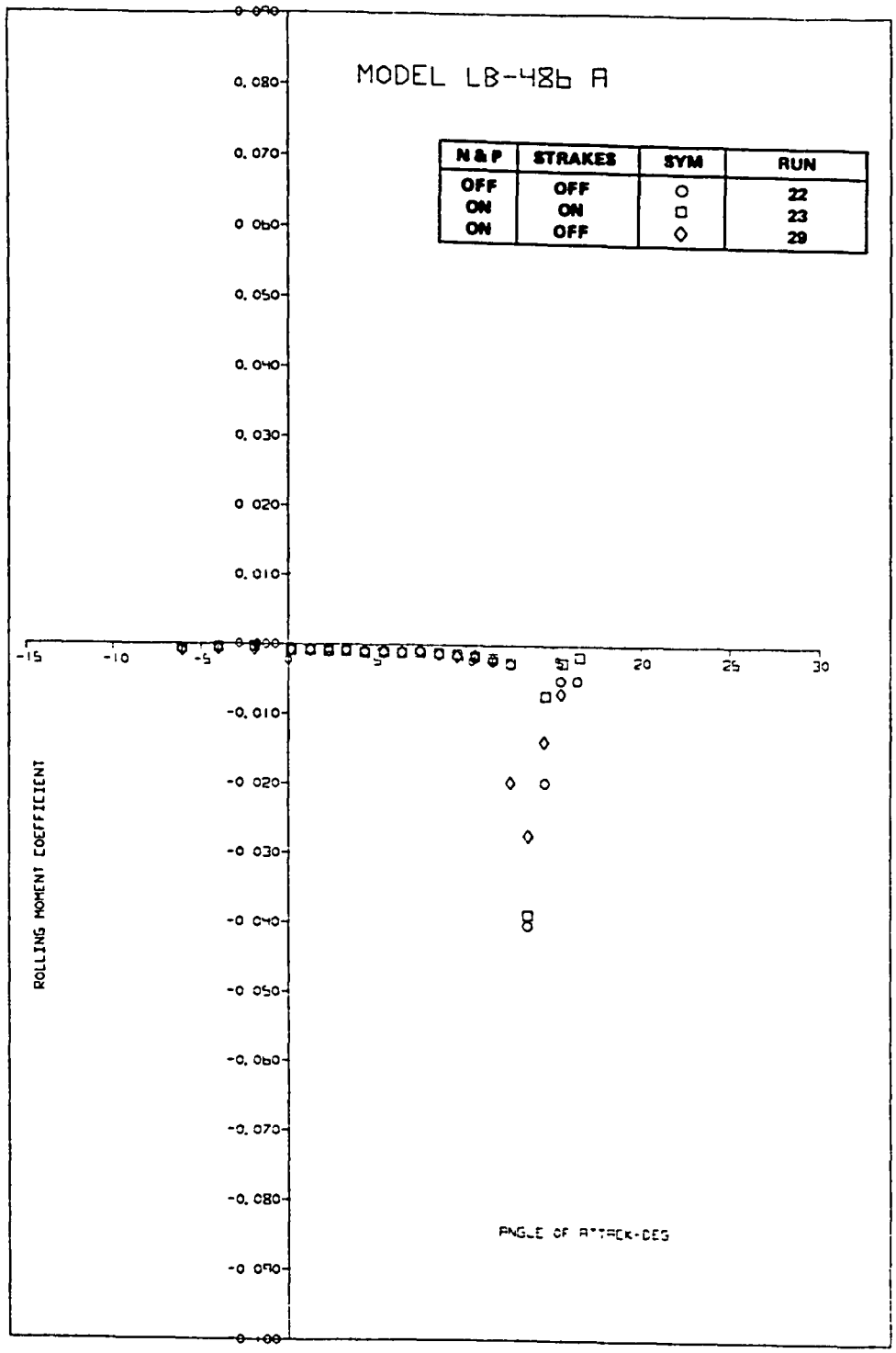

D. ROLLING MOMENT

FIGURE 73. EFFECT OF NACELLES, PYLONS, AND STRAKES ON AERODYNAMIC CHARACTERISTICS OF THE CRUISE WING (CONCLUDED)

ORIGINAL PAGE IS
OF POOR QUALITY

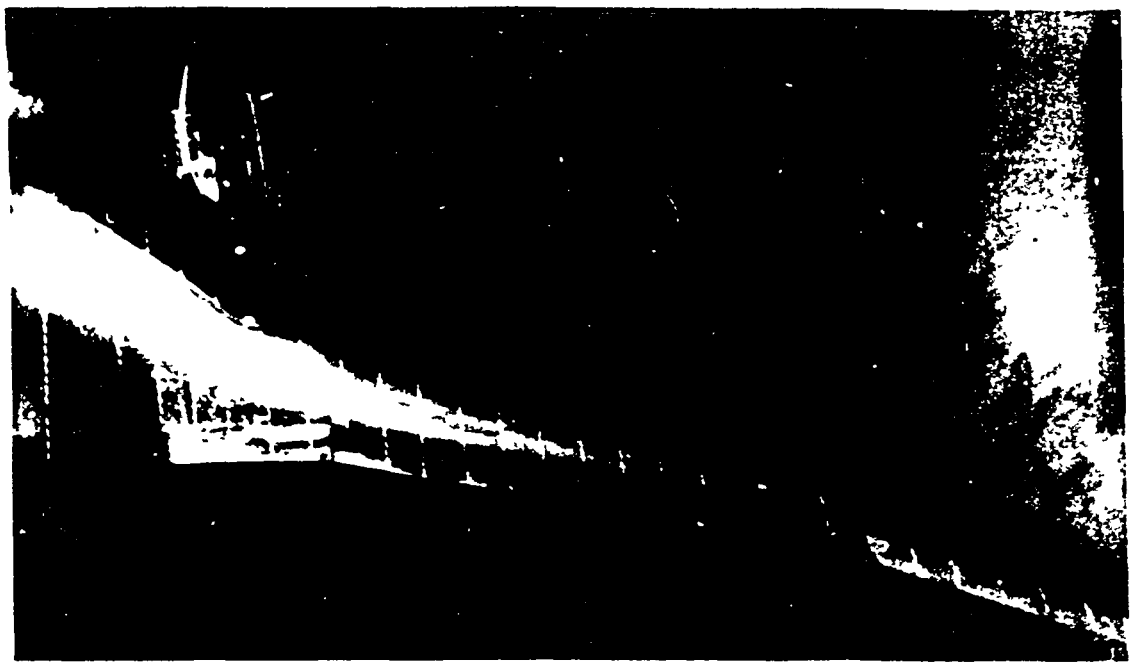

A. α_{FRP} = 12.58°

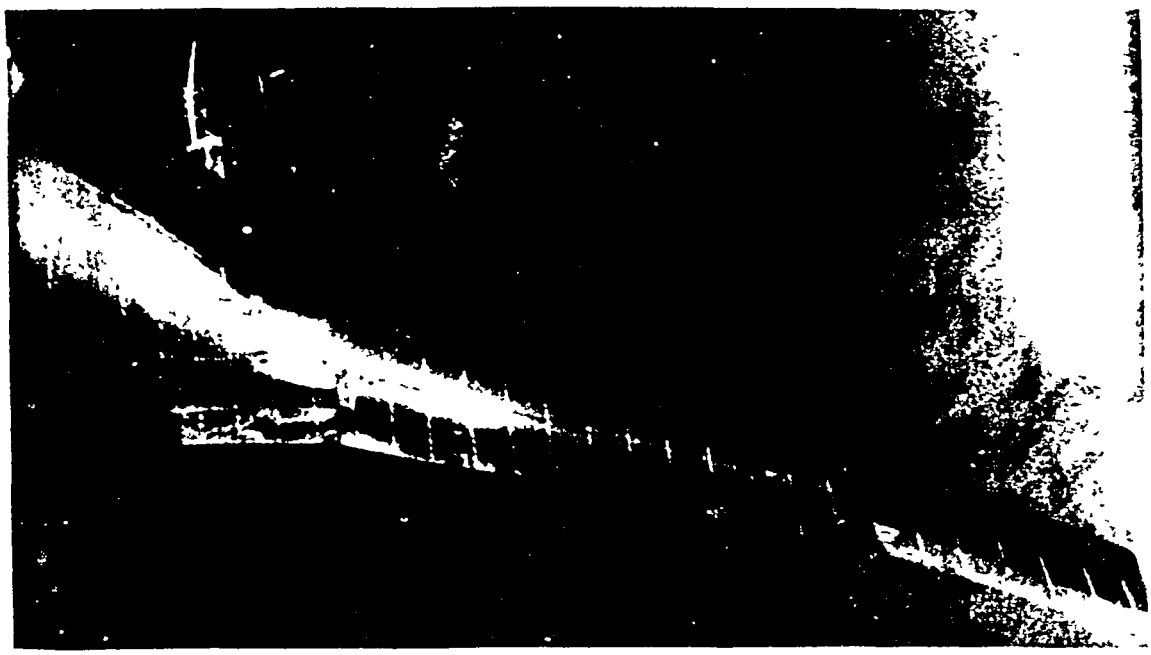

B. α_{FRP} = 13.58°

FIGURE 74. MINI-TUFT PHOTOS FOR THE CRUISE WING WITH NACELLES, PYLONS, AND STRAKES ATTACHED

ORIGINAL PAGE IS
OF POOR QUALITY

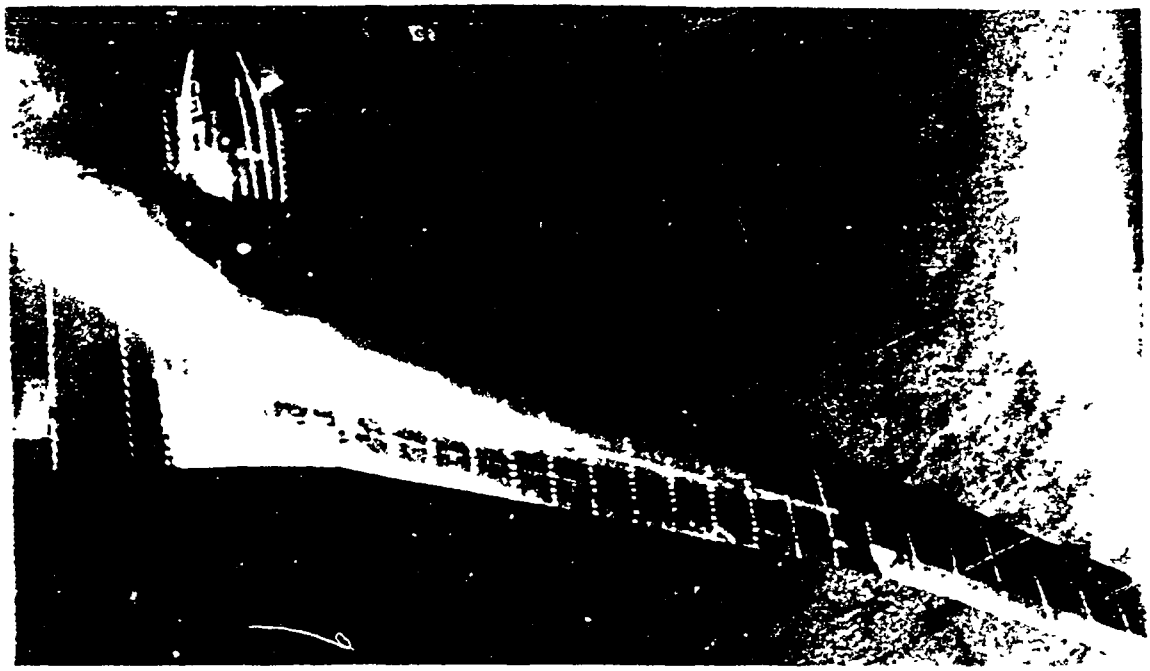

C α_{FRP} = 14.55°

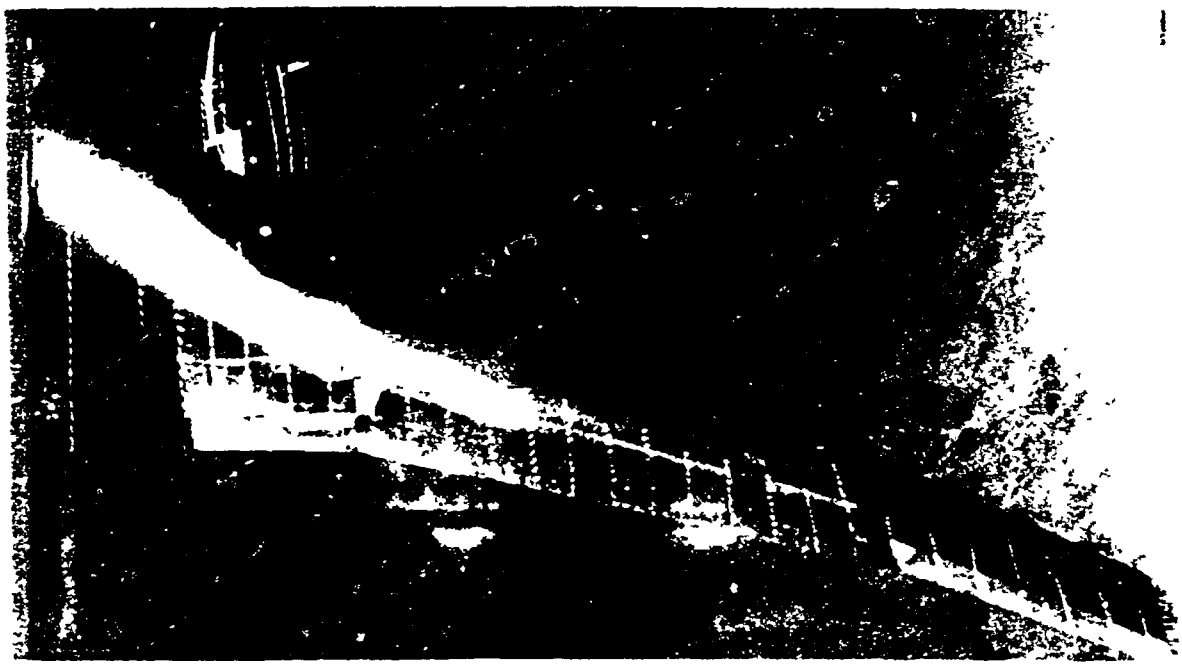

D. α_{FRP} = 16.56°

FIGURE 74. MINI-TUFT PHOTOS FOR THE CRUISE WING WITH NACELLES, PYLONS, AND STRAKES ATTACHED (CONCLUDED)

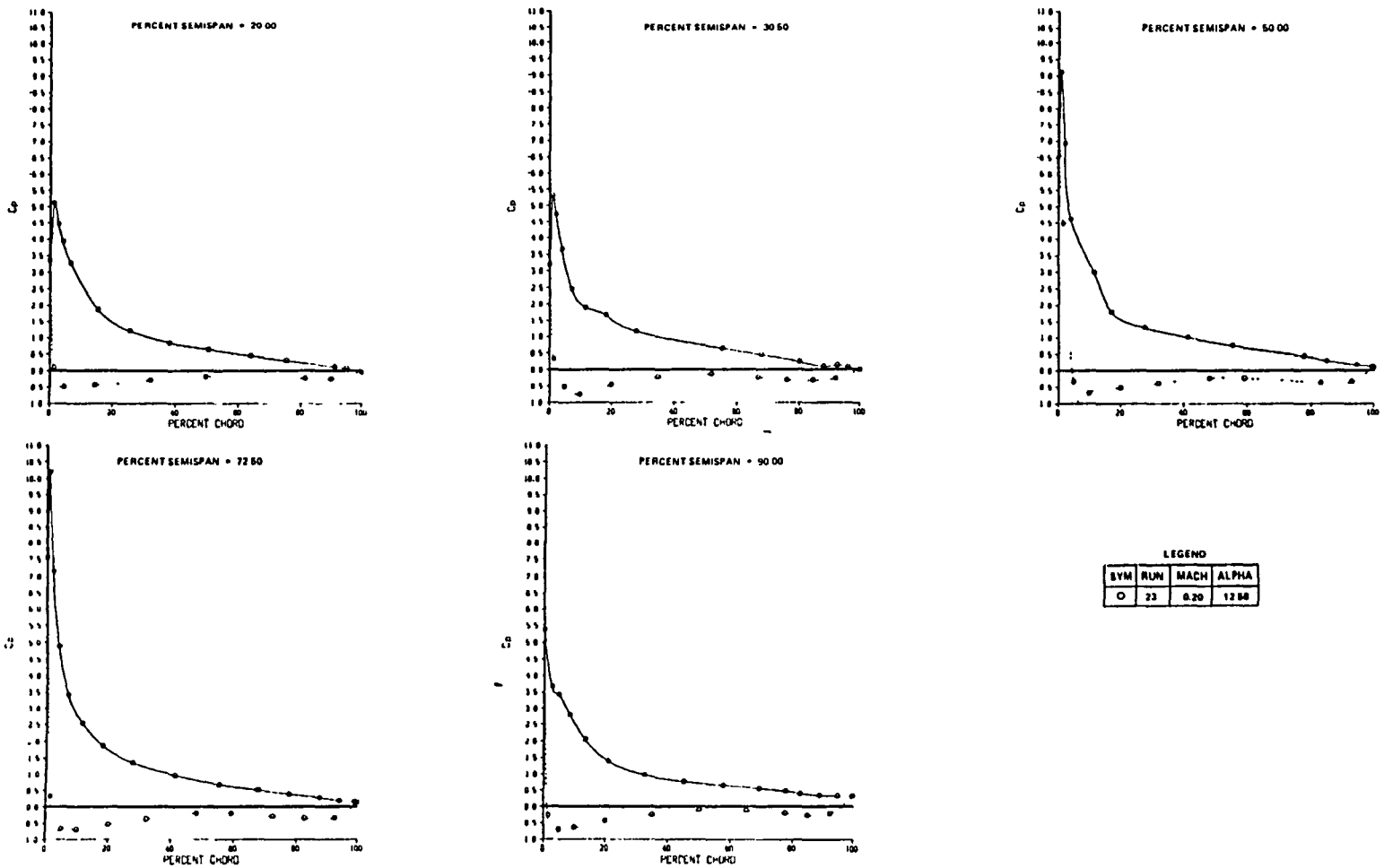

A. α_{FRP} = 12.58 DEG ($\alpha_{C_{L_{MAX}}}$)

FIGURE 75. EXPERIMENTAL CHORDWISE PRESSURE DISTRIBUTION FOR CRUISE WING (NACELLES, PYLONS, AND STRAKES ON)

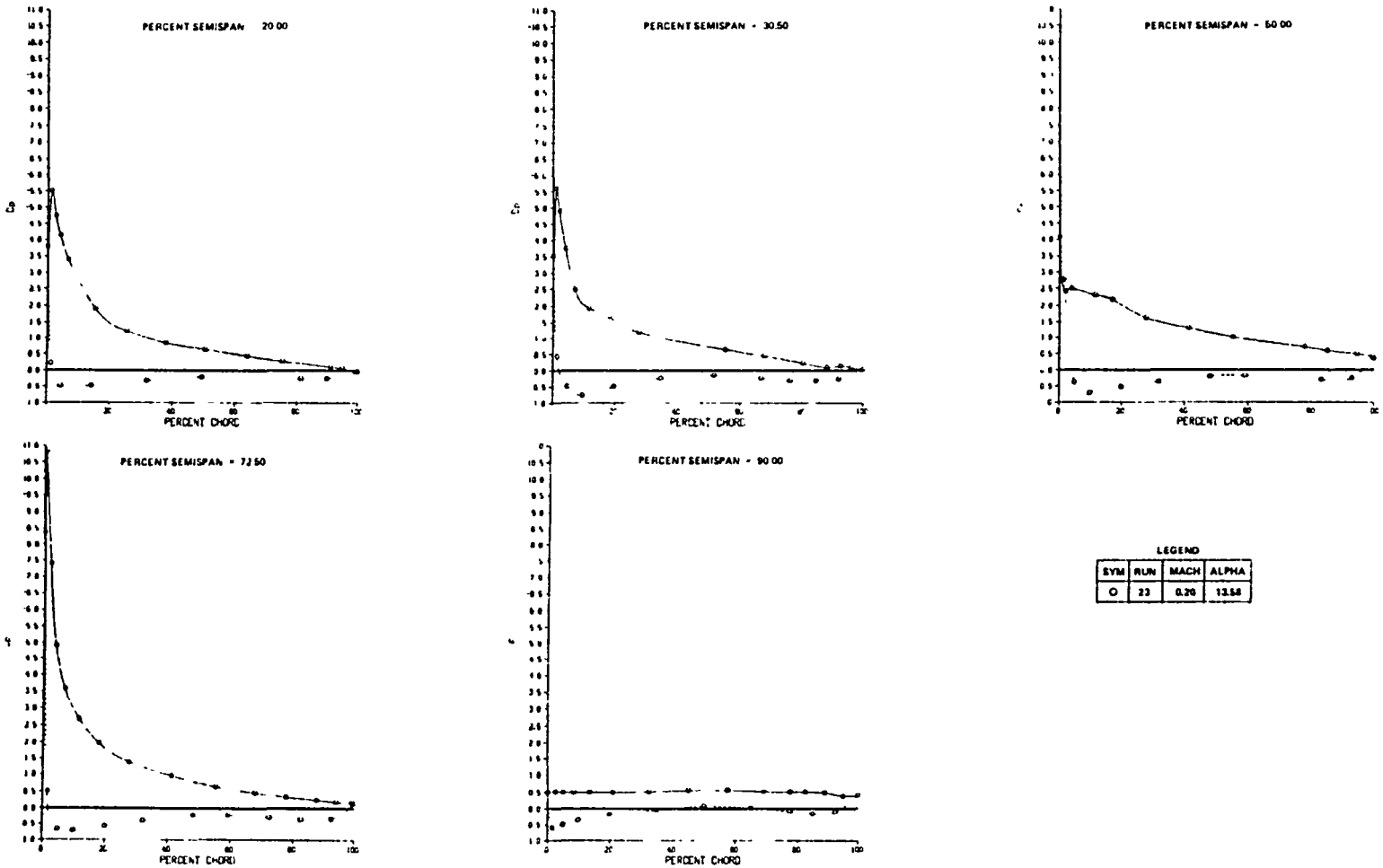

B α_{FRP} = 13 58 DEG

FIGURE 75 EXPERIMENTAL CHORDWISE PRESSURE DISTRIBUTION FOR CRUISE WING (NACELLES, PYLONS, AND STRAKES ON) (CONTINUED)

ORIGINAL PAGE IS
OF POOR QUALITY

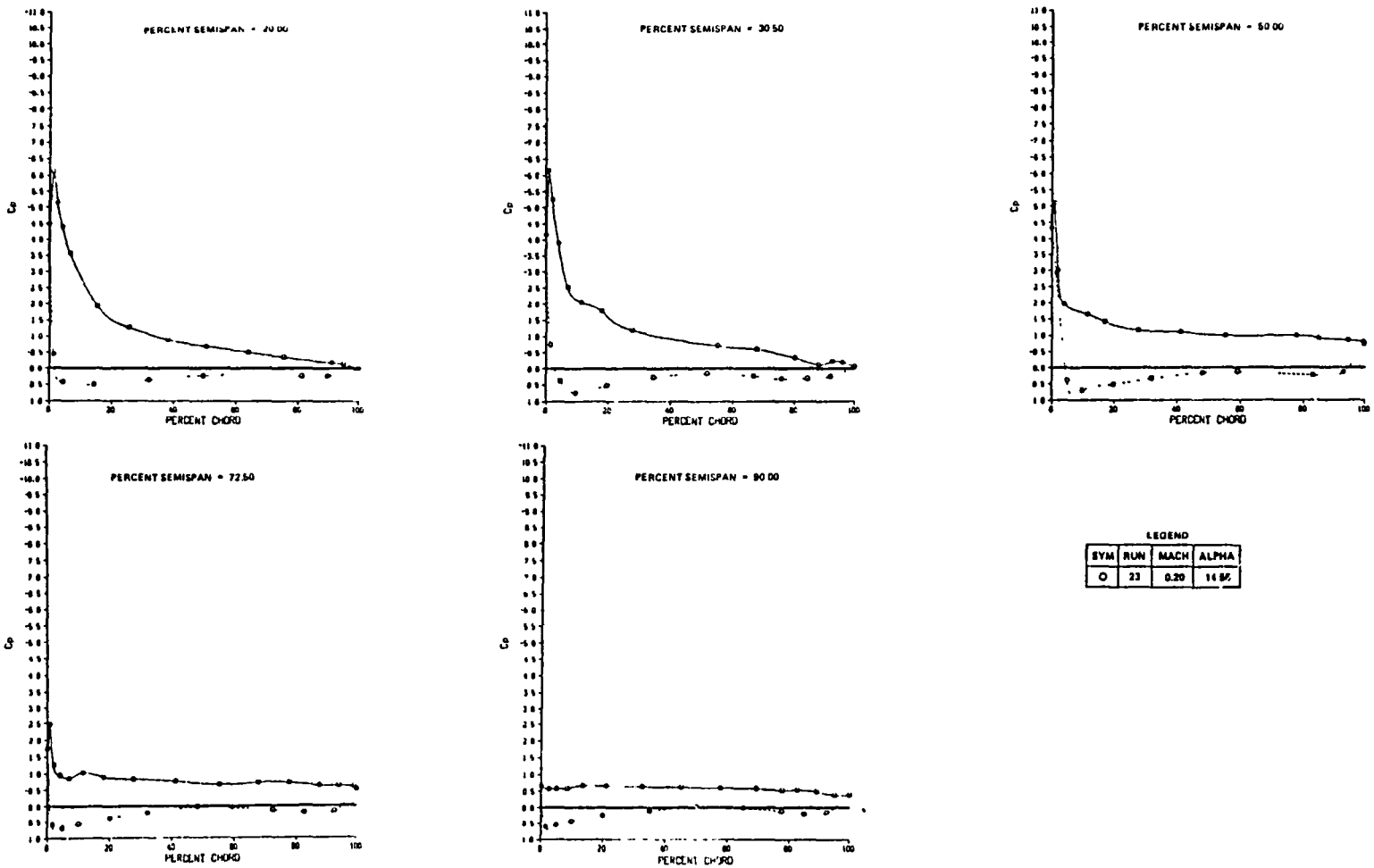

C. α_{FRP} = 14.55 DEG

FIGURE 75. EXPERIMENTAL CHORDWISE PRESSURE DISTRIBUTION FOR CRUISE WING (NACELLES, PYLONS, AND STRAKES ON) (CONTINUED)

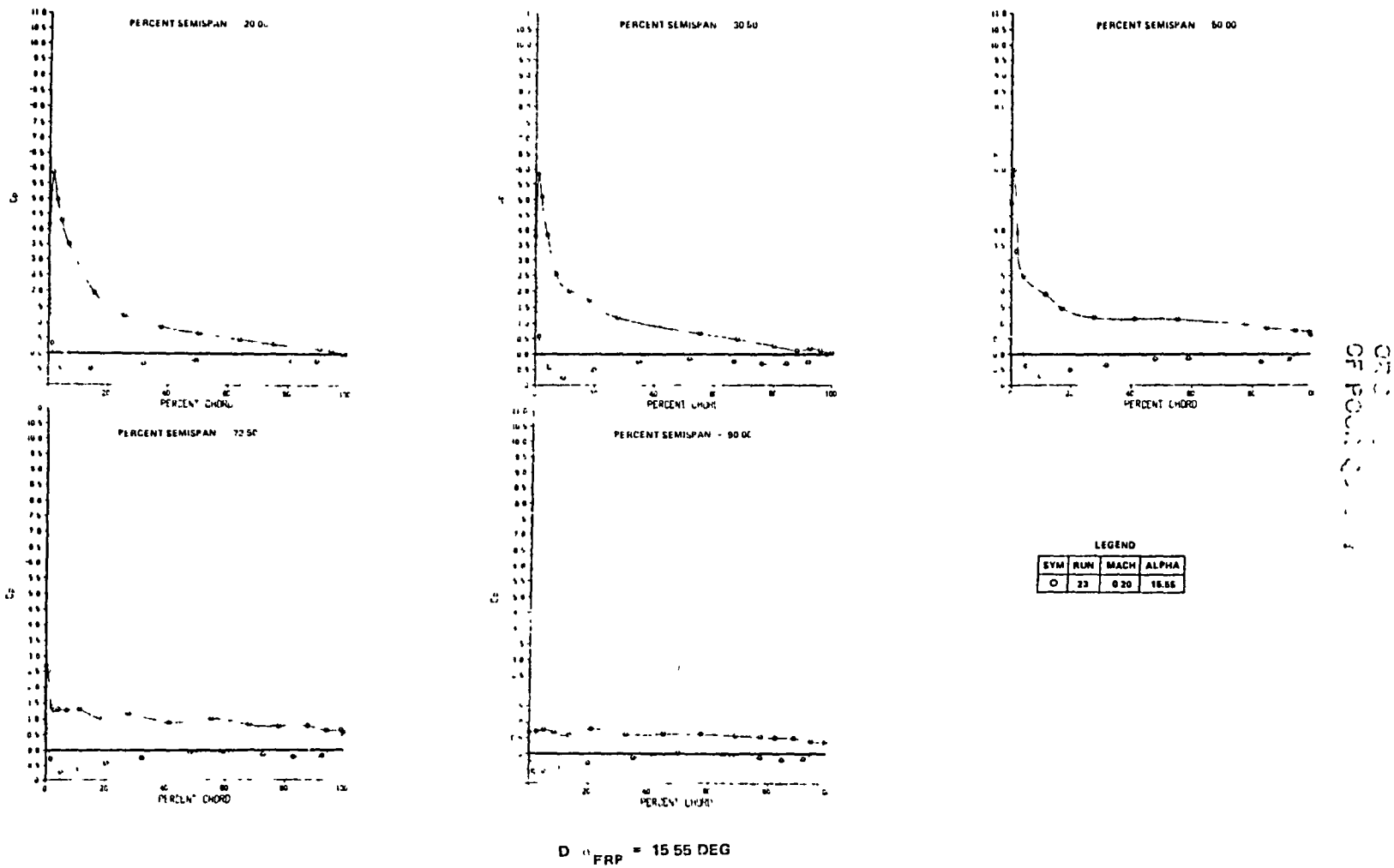

D α_{FRP} = 15.55 DEG

FIGURE 75. EXPERIMENTAL CHORDWISE PRESSURE DISTRIBUTION FOR CRUISE WING (NACELLES, PYLONS, AND STRAKES ON) (CONCLUDED)

wing, and the tufts were located on the right wing. It is possible that part of the flow-symmetry problem near stall may be located in this area of the wing. At $\alpha_{FRP} = 13.58^{o}$, the pressure distribution for the 90-percent span station indicate separated flow. The tuft photo, however, indicates only moderate trailing edge activity.

Figure 76 presents the sectional lift values for Run 23. At $\alpha_{FRP} = 13.58^{o}$, the 50- and 90-percent spanwise positions (left wing) show a lift loss. The lift loss at 90 percent semispan is more than half the $c\ell_{max}$ value. The 72.5- and 90-percent stations have the same type of lift loss at stall with the nacelles, pylons, and strakes attached. The only differences noted are reduced lift at the 30-percent span station (near the nacelle), but no stall, and a reduced lift loss at the 50-percent span station.

Reynolds Number and Mach Number Effects on Cruise Wing. - This study was performed with the nacelles, pylons, and strakes attached. Figure 77 presents the influence of Reynolds number on the aerodynamic characteristics. The angle of attack for $C_{L_{MAX}}$ and the $C_{L_{MAX}}$ attained decreased with the reduction in Reynolds number. The $C_{L_{MAX}}$ for $R_{N_{MAC}} = 5.12 \times 10^{6}$ was 1.54, and for $R_{N_{MAC}} = 1.14 \times 10^{6}$, a $C_{L_{MAX}}$ of 1.15 was obtained. A positive pitch increment after $C_{L_{MAX}}$ is apparent. The low Reynolds number data show a pitching moment level shift for most of the angle of attack range. These data also indicate a less rapid buildup of the positive pitching moment increment with angle of attack past $\alpha_{C_{L_{MAX}}}$.

Figure 78 illustrates the low Reynolds number chordwise pressure distributions for angles of attack near, and above $C_{L_{MAX}}$. The 72-percent span station suction peak has collapsed at $\alpha_{FRP} = 8.42^{o}$. At 10.42^{o} and 12.44^{o} angle of attack, the 50-, 72-, and 90-percent stations are separated at the leading edge. Although the Reynolds number has changed the angle of angle of attack for $C_{L_{MAX}}$ and the $C_{L_{MAX}}$ level, the basic trend of outboard stall is still evident.

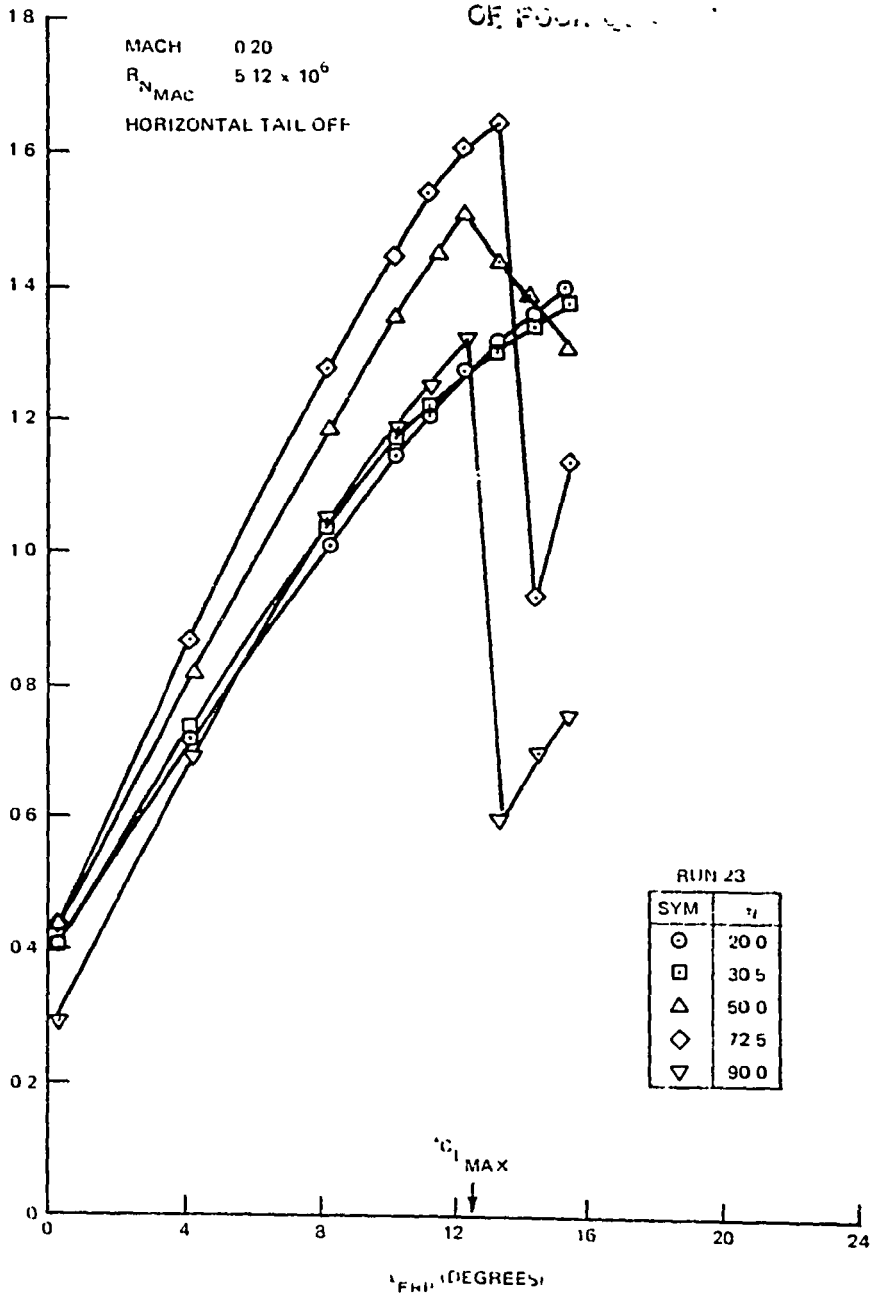

FIGURE 76. VARIATION OF SECTION LIFT COEFFICIENT FOR THE CRUISE WING, WITH NACELLES, PYLONS, AND STRAKES ATTACHED

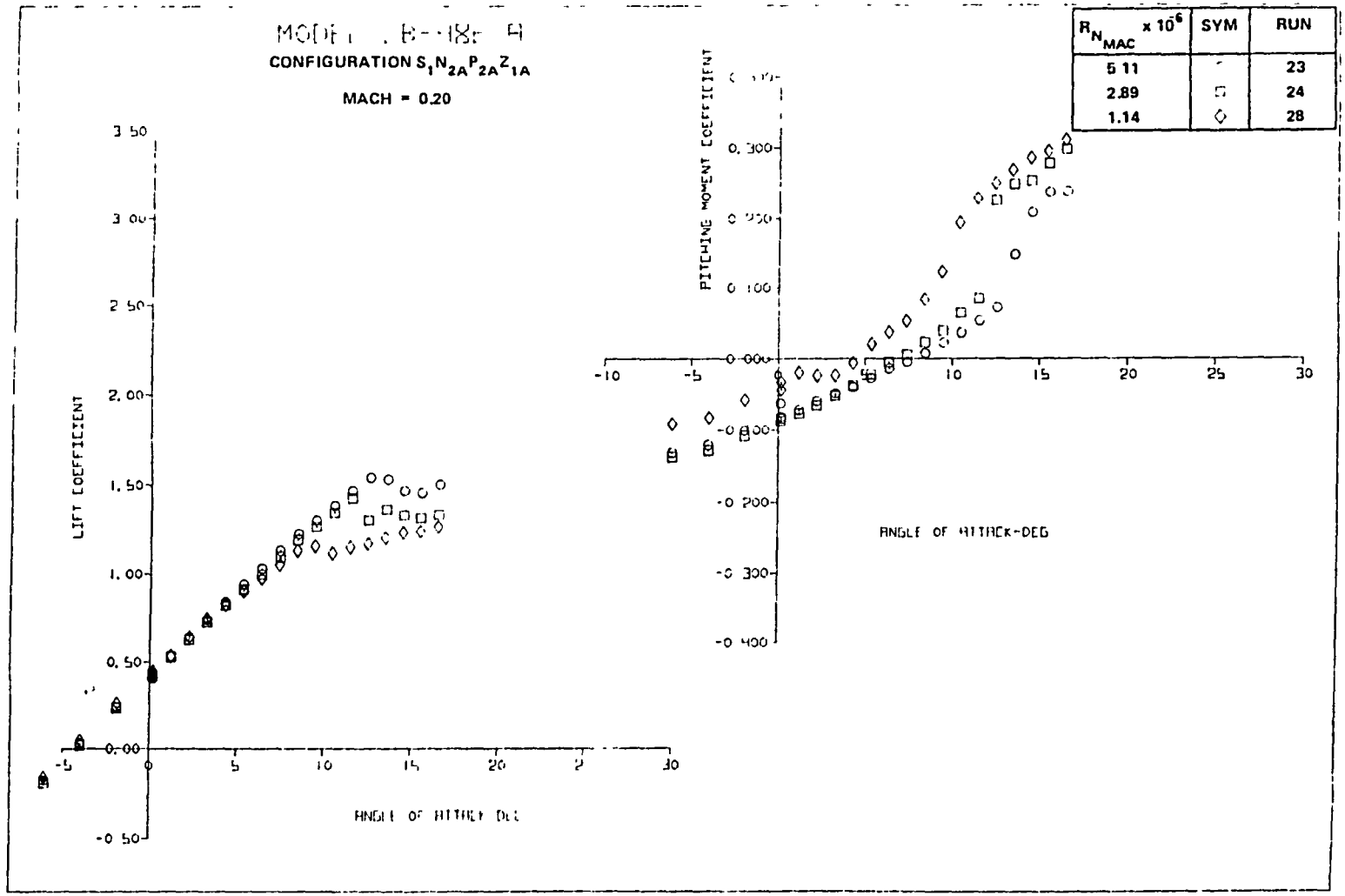

A. LIFT AND PITCHING MOMENT

FIGURE 77. EFFECT OF REYNOLDS NUMBER ON CRUISE WING WITH NACELLES, PYLONS, AND STRAKES ATTACHED

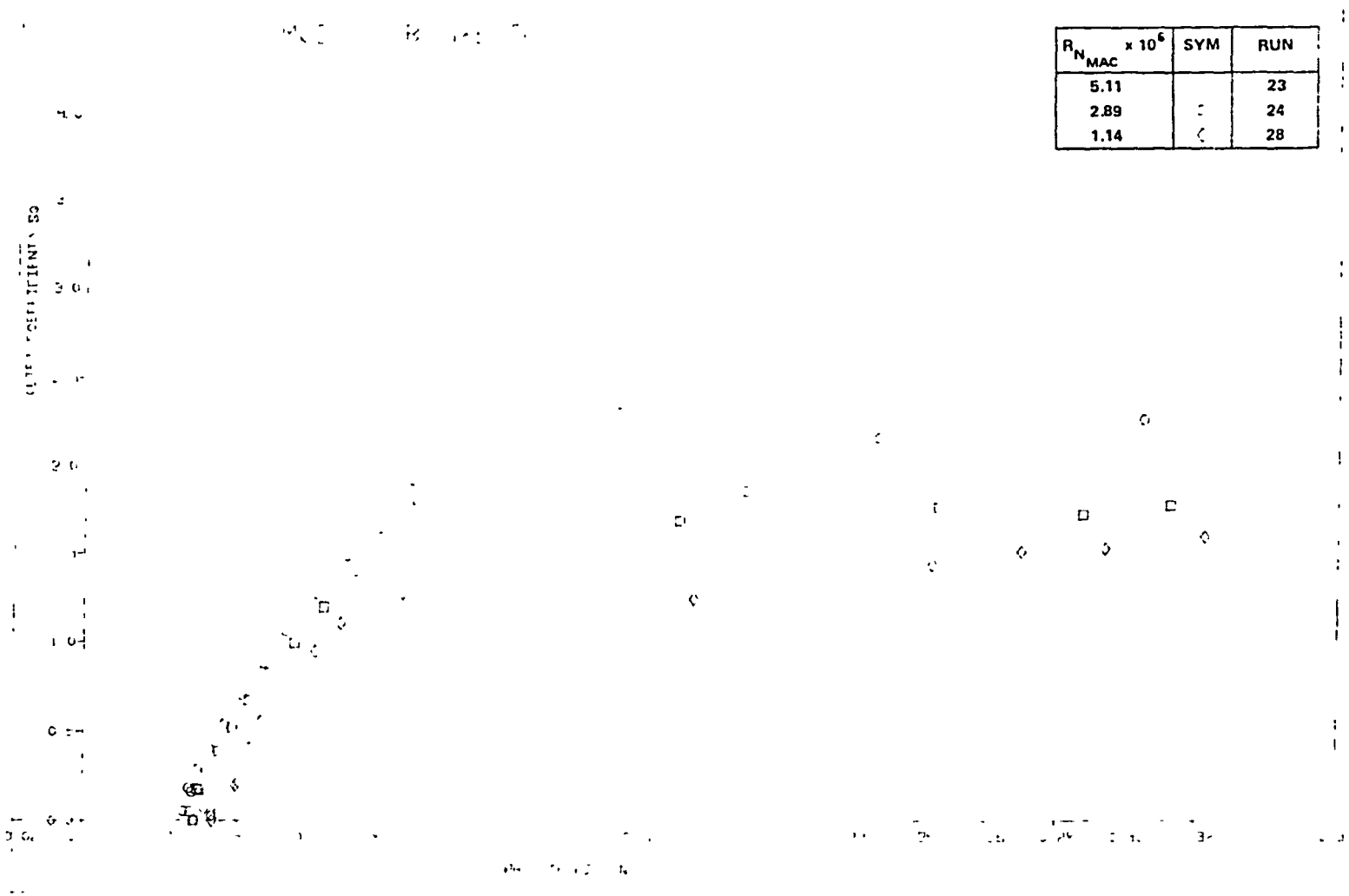

FIGURE 77. EFFECT OF REYNOLDS NUMBER ON CRUISE WING WITH NACELLES, PYLONS, AND STRAKES ATTACHED (CONTINUED)

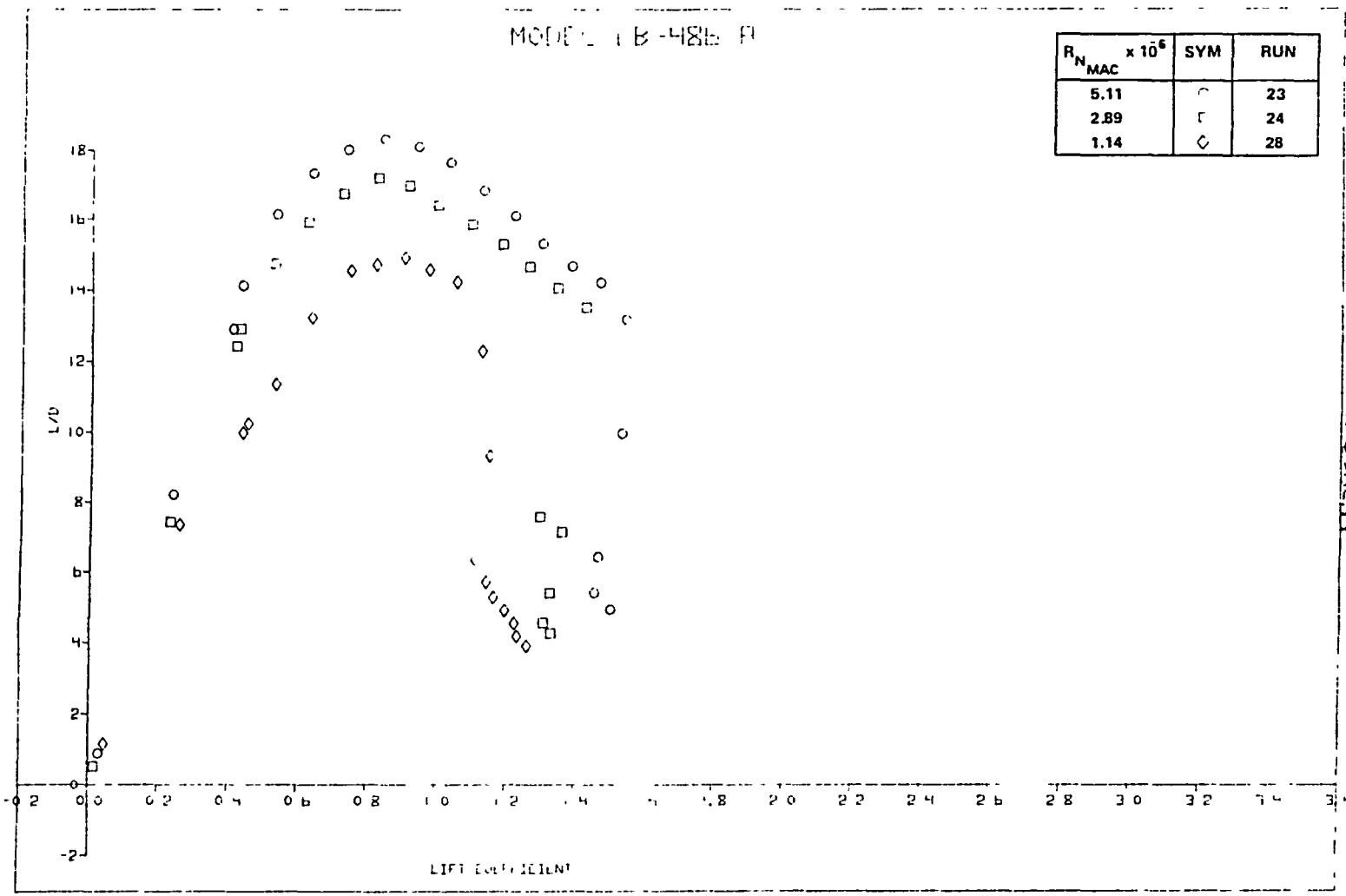

C. LIFT/DRAG RATIO

FIGURE 77. EFFECT OF REYNOLDS NUMBER ON CRUISE WING WITH NACELLES, PYLONS, AND STRAKES ATTACHED (CONCLUDED)

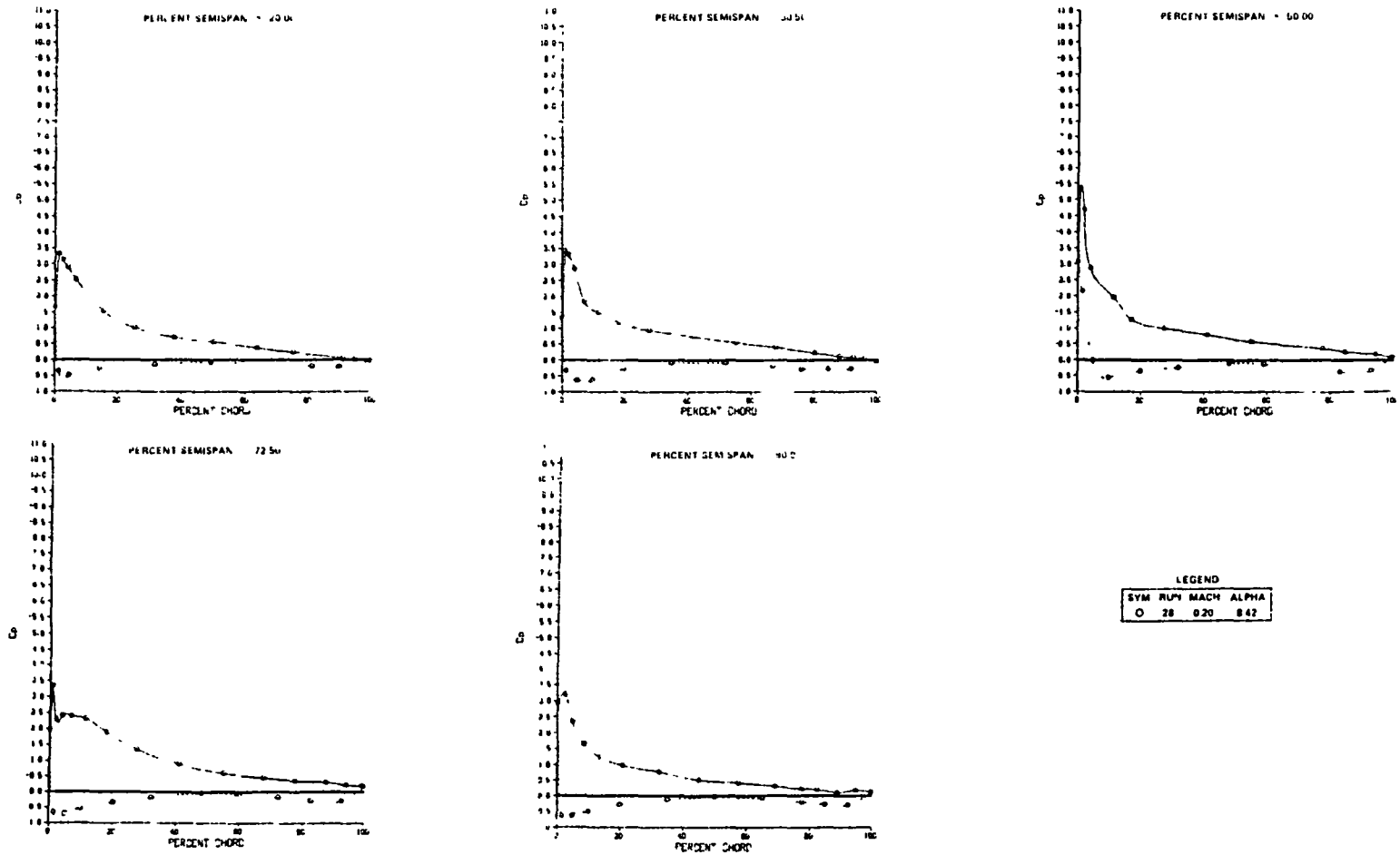

A. α_{FRP} = 8.42 DEG

FIGURE 78. EXPERIMENTAL CHORDWISE PRESSURE DISTRIBUTION FOR CRUISE WING WITH NACELLES, PYLONS, AND STRAKES ATTACHED ($R_{N_{MAC}}$ = 1.14 x 10^6)

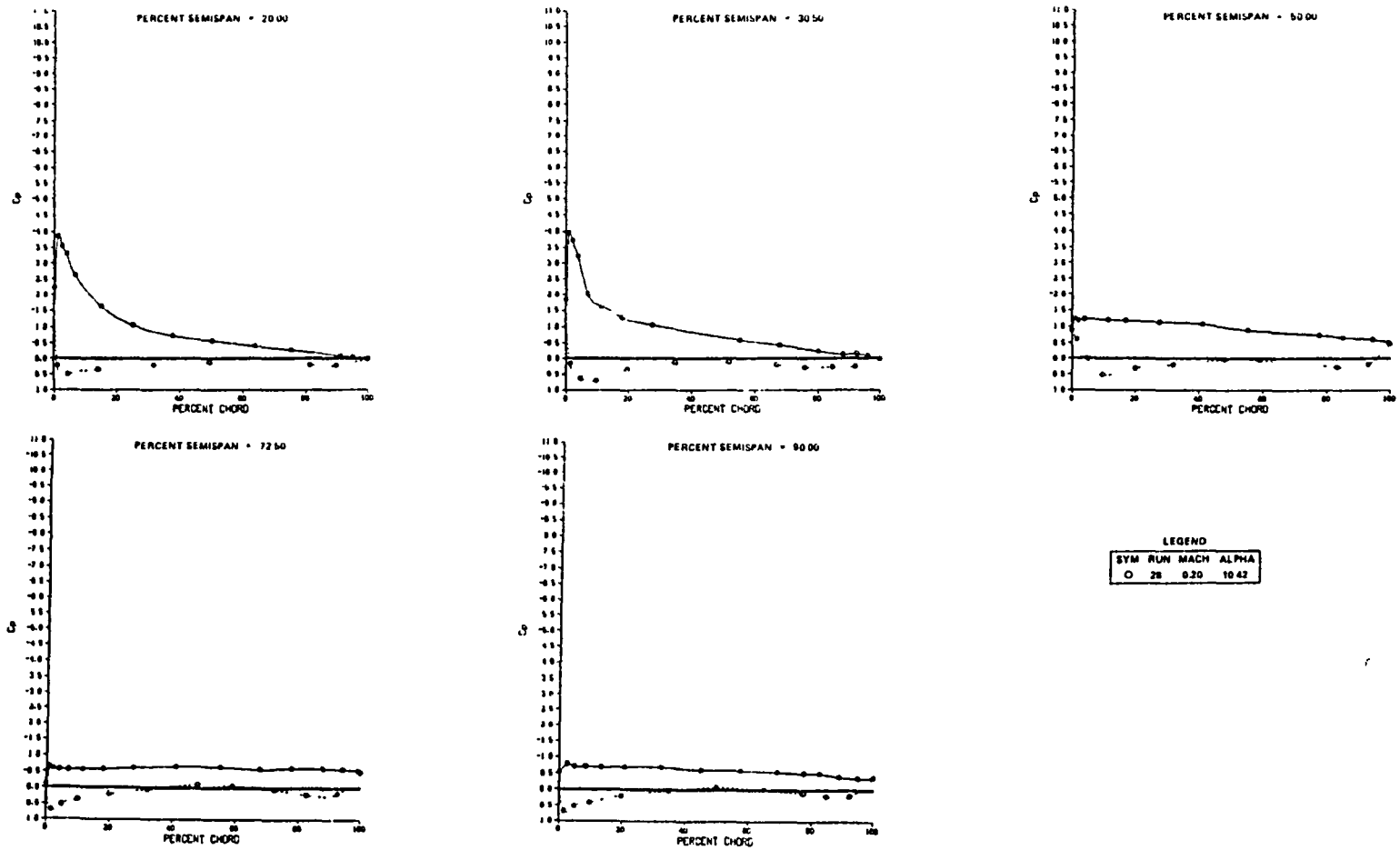

FIGURE 78. EXPERIMENTAL CHORDWISE PRESSURE DISTRIBUTION FOR CRUISE WING WITH NACELLES, PYLONS, AND STRAKES ATTACHED ($R_{N_{MAC}}$ = 1.14 x 10^6) (CONTINUED)

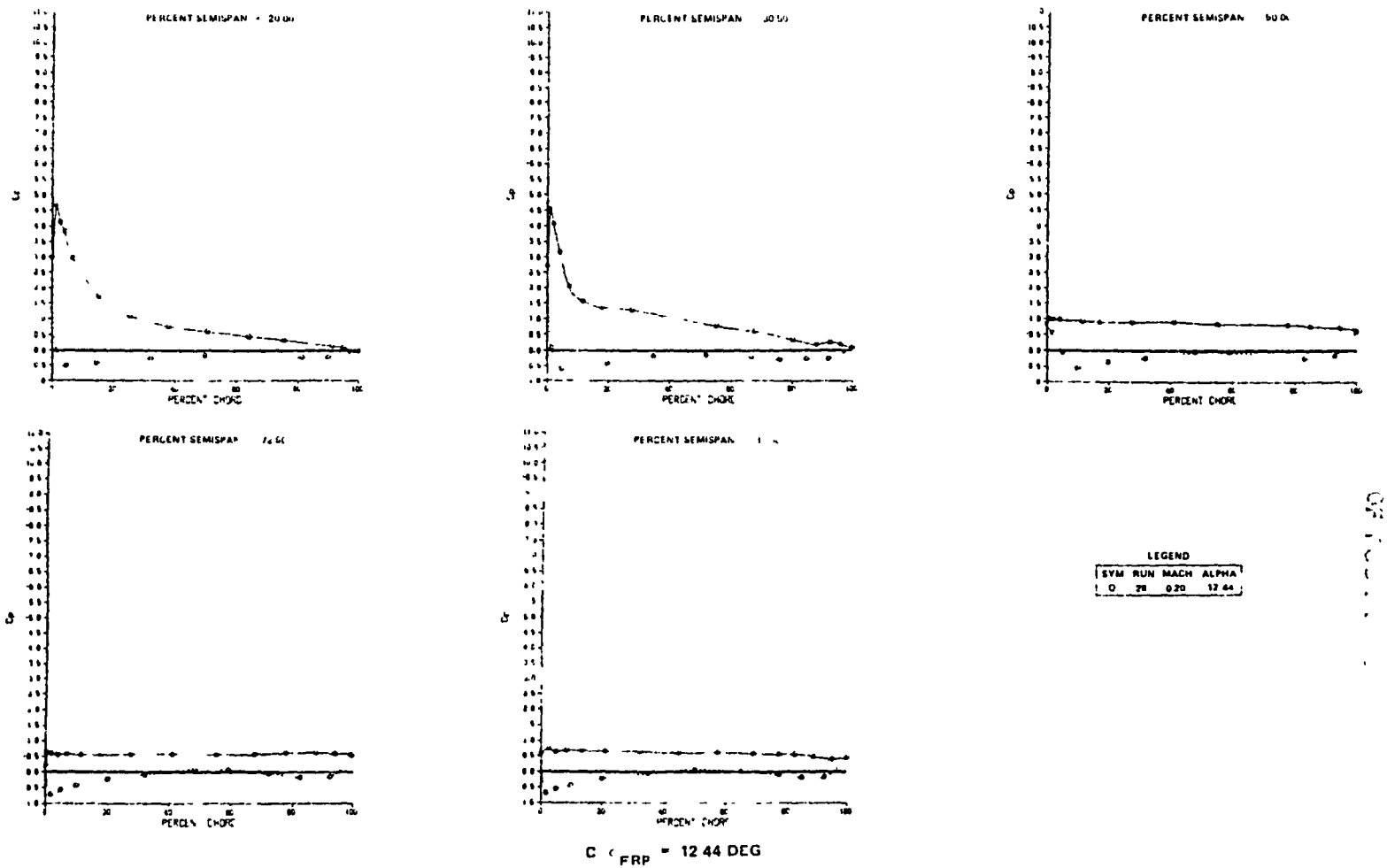

C_{FRP} = 12.44 DEG

FIGURE 78 EXPERIMENTAL CHORDWISE PRESSURE DISTRIBUTION FOR CRUISE WING WITH NACELLES, PYLONS, AND STRAKES ATTACHED ($R_{N_{MAC}}$ = 1.14 x 10^6) (CONCLUDED)

Figure 79 presents the influence of Mach number on the same configuration. These data were obtained at $^{R}N_{MAC} = 2.89 \times 10^{6}$. The effect of Mach number is to decrease $C_{L_{MAX}}$ ($C_{L_{MAX}} = 1.43$, 1.39, and 1.32 at Mach = 0.20, 0.26, and 0.32, respectively). Also, the effect of Mach number is to decrease the angle of attack for the outboard stall. At a Mach number of 0.32, the reduced stability shift has already been initiated at 9.5°. The overall shift is more gradual with angle of attack, but the basic pitch trend still remains. Maximum L/D values are indicated for a Mach number of 0.26.

Figure 80 presents the section lift coefficients for the Mach number of 0.32 (Run 26) Examination of the chordwise pressure distribution plots, indicated leading edge separation at the 50- and 72-percent span stations at an $_{FRP}$ of 10.44°. At 11.46° the three most outboard stations were separated. The outboard lift loss is apparent, as is a reduction in inboard sectional lift curve slope at an $_{FRP}$ of 11.46°. Figure 81 shows the spanwise variation of $C_{P_{MIN}}$ (minimum pressure coefficient) for the Mach number tested. Also shown for reference, is the $^{R}N_{MAC} = 5.12 \times 10^{6}$ and Mach number of 0.20 results (Run 23). $C_{P_{CRIT}}$ for the outboard leading edge region is also shown. The corresponding value at a Mach number of 0.20 would be over -16.0. Clearly, the data obtained at 0.26 and 0.32 Mach numbers indicate that the suction peaks are approaching sonic conditions. Extrapolation of the $C_{P_{MIN}}$ to the next angle of attack, for the outboard sections, would indicate supercritical flow. This was not achieved, and raises the possibility of shock-induced separation for these locations.

Cruise Wing with Horizontal Tail. - The horizontal tail-on characteristics for the cruise wing with the nacelles, pylons, strakes, and vertical tail attached is shown in Figure 82. Horizontal tail deflections of 0°, -5°, and -10° were evaluated. The pitching moment curves indicate pitch-up prior to, or at, $C_{L_{MAX}}$ for the various deflections.

Figure 83 presents the effect of Reynolds number for the tail-on configuration. $C_{L_{MAX}}$ and $^{\alpha}C_{L_{MAX}}$ are reduced at the lower Reynolds number. The lift loss after stall at the low Reynolds number is small. However, pitch-up is indicated for both Reynolds number conditions. The magnitude of the positive pitch increment is larger for the high Reynolds number

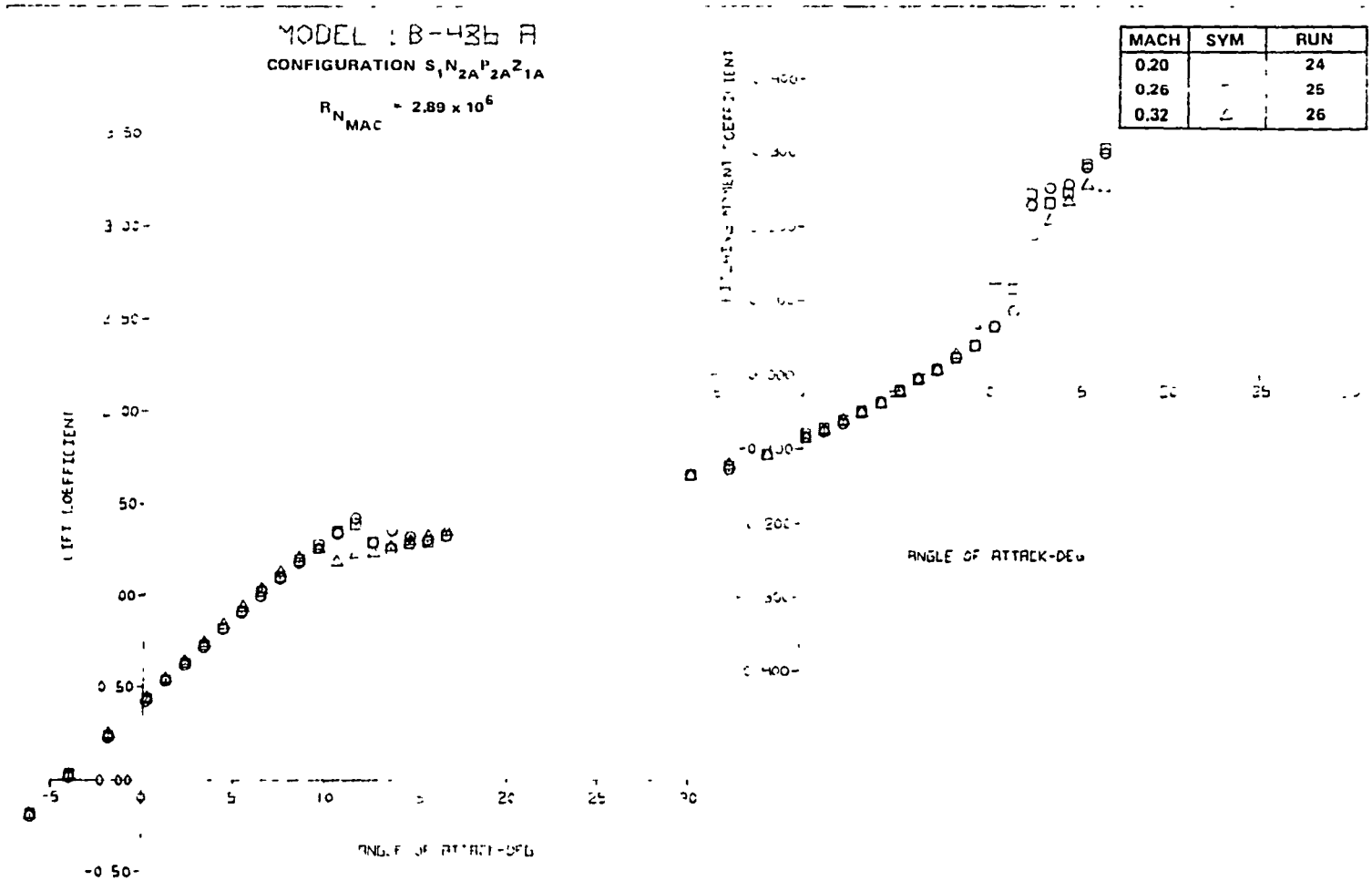

A. LIFT AND PITCHING MOMENT

FIGURE 79. EFFECT OF MACH NUMBER ON CRUISE WING WITH NACELLES, PYLONS, AND STRAKES ATTACHED

ORIGINAL PAGE IS
OF POOR QUALITY

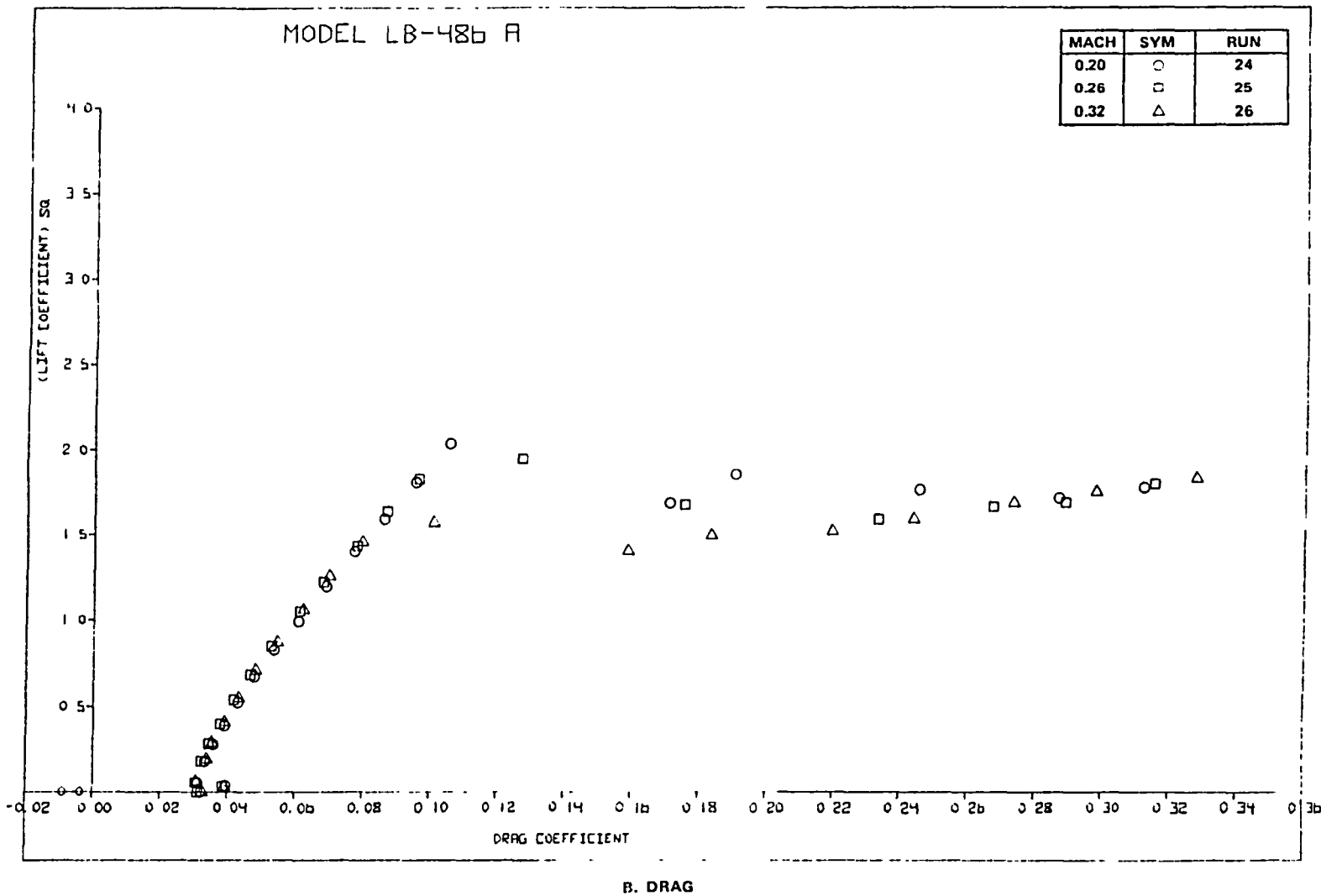

B. DRAG

FIGURE 79. EFFECT OF MACH NUMBER ON CRUISE WING WITH NACELLES, PYLONS, AND STRAKES ATTACHED (CONTINUED)

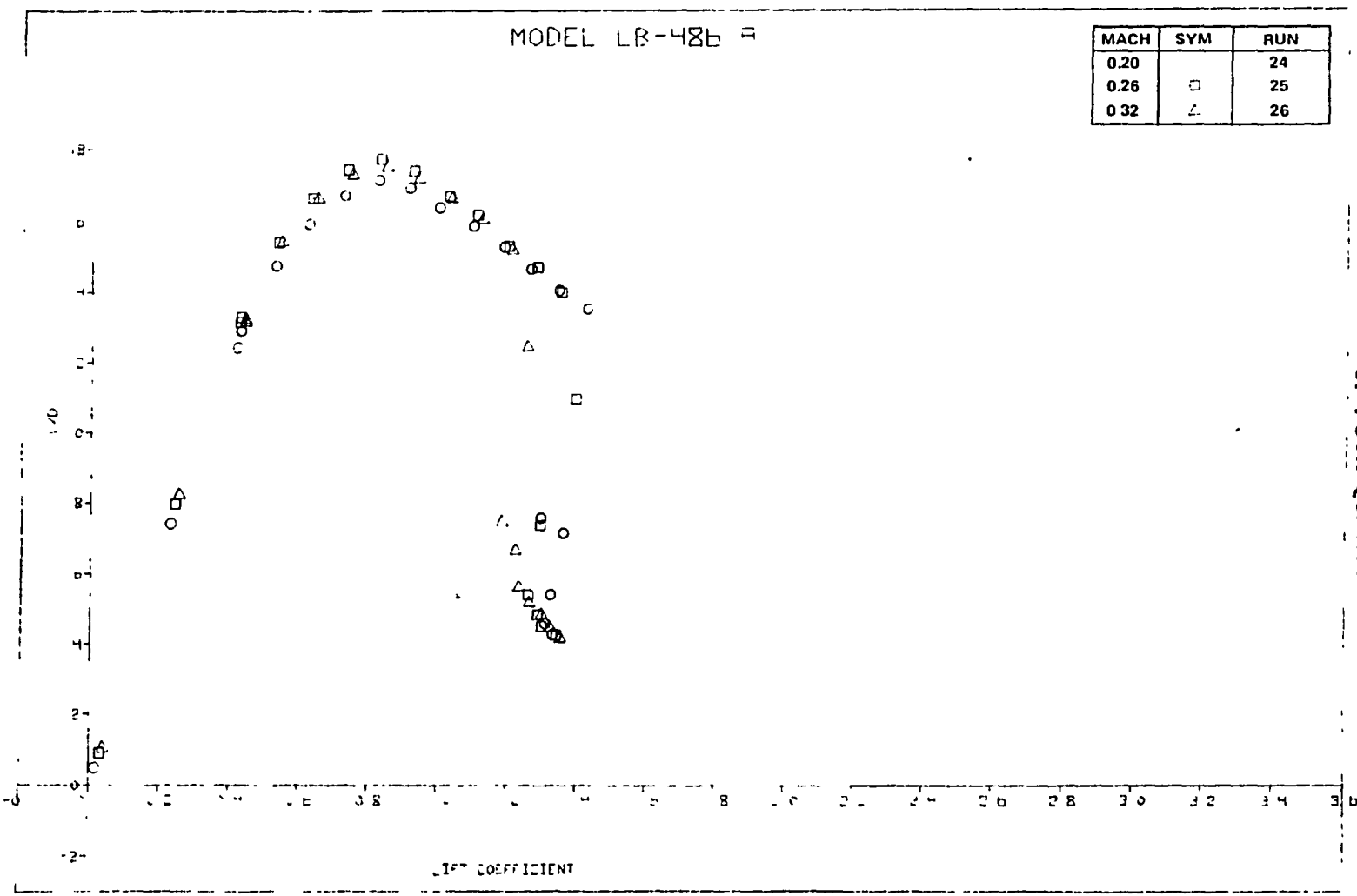

C. LIFT/DRAG RATIO

FIGURE 79. EFFECT OF MACH NUMBER ON CRUISE WING WITH NACELLES, PYLONS, AND STRAKES ATTACHED (CONCLUDED)

ORIGINAL PAGE IS
OF POOR QUALITY

ORIGINAL PAGE IS
OF POOR QUALITY

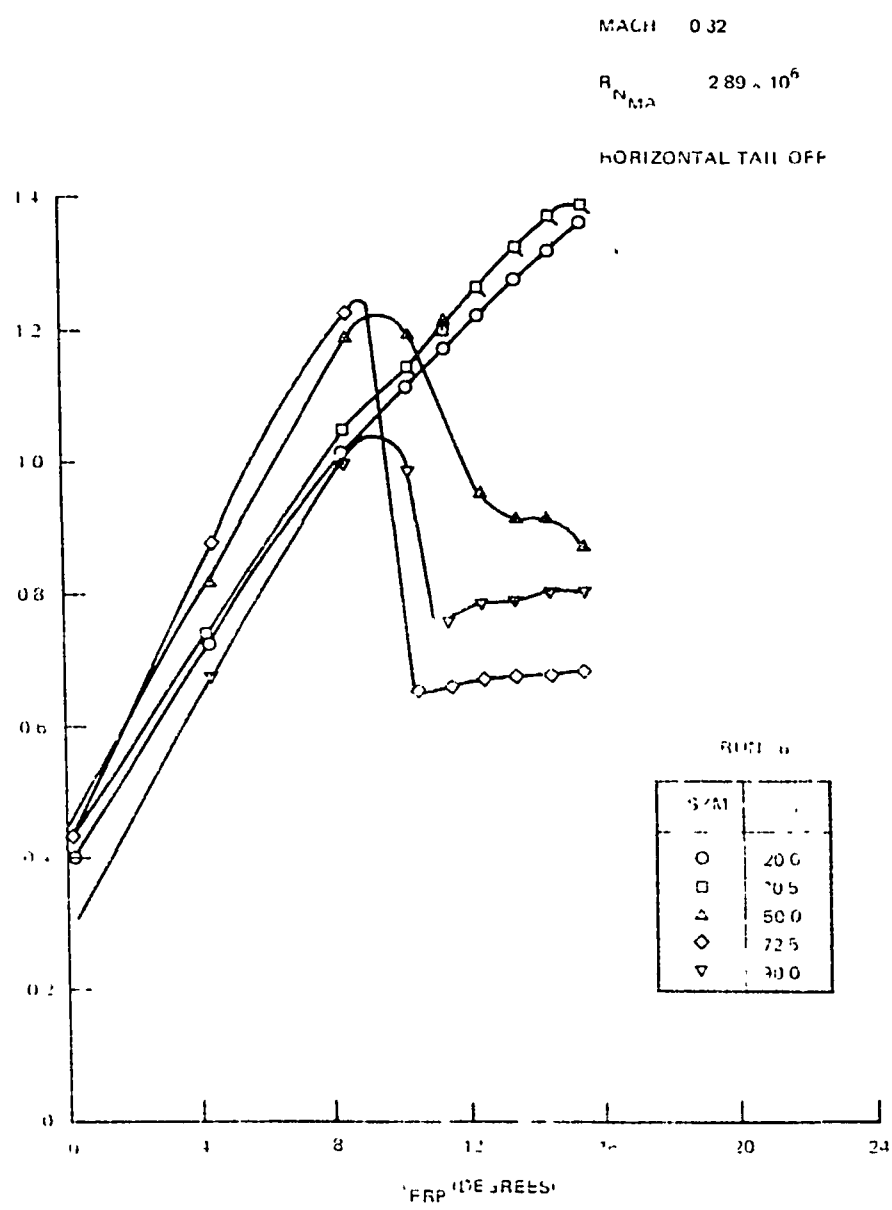

FIGURE 80 VARIATION OF SECTION LIFT COEFFICIENT FOR THE CRUISE WING WITH NACELLES, PYLONS AND STRAKES ATTACHED (MACH = 0.32)

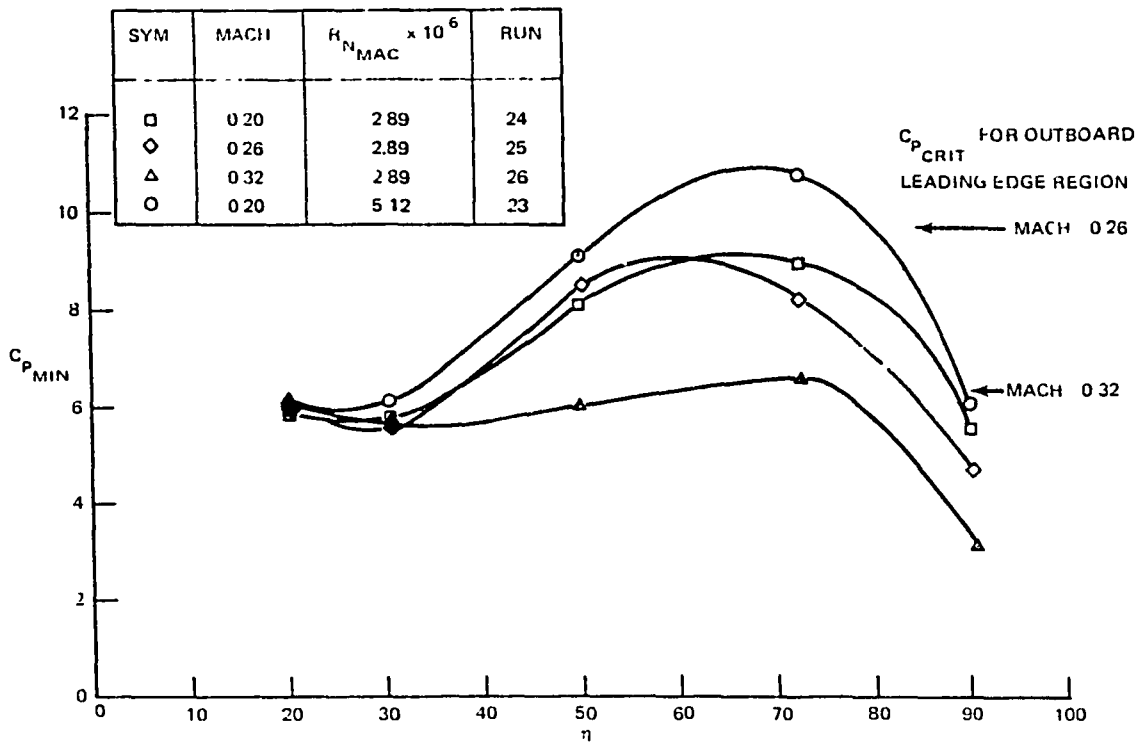

FIGURE 81 EFFECTS OF MACH AND REYNOLDS NUMBER ON CRUISE WING WITH NACELLES AND PYLON ATTACHED

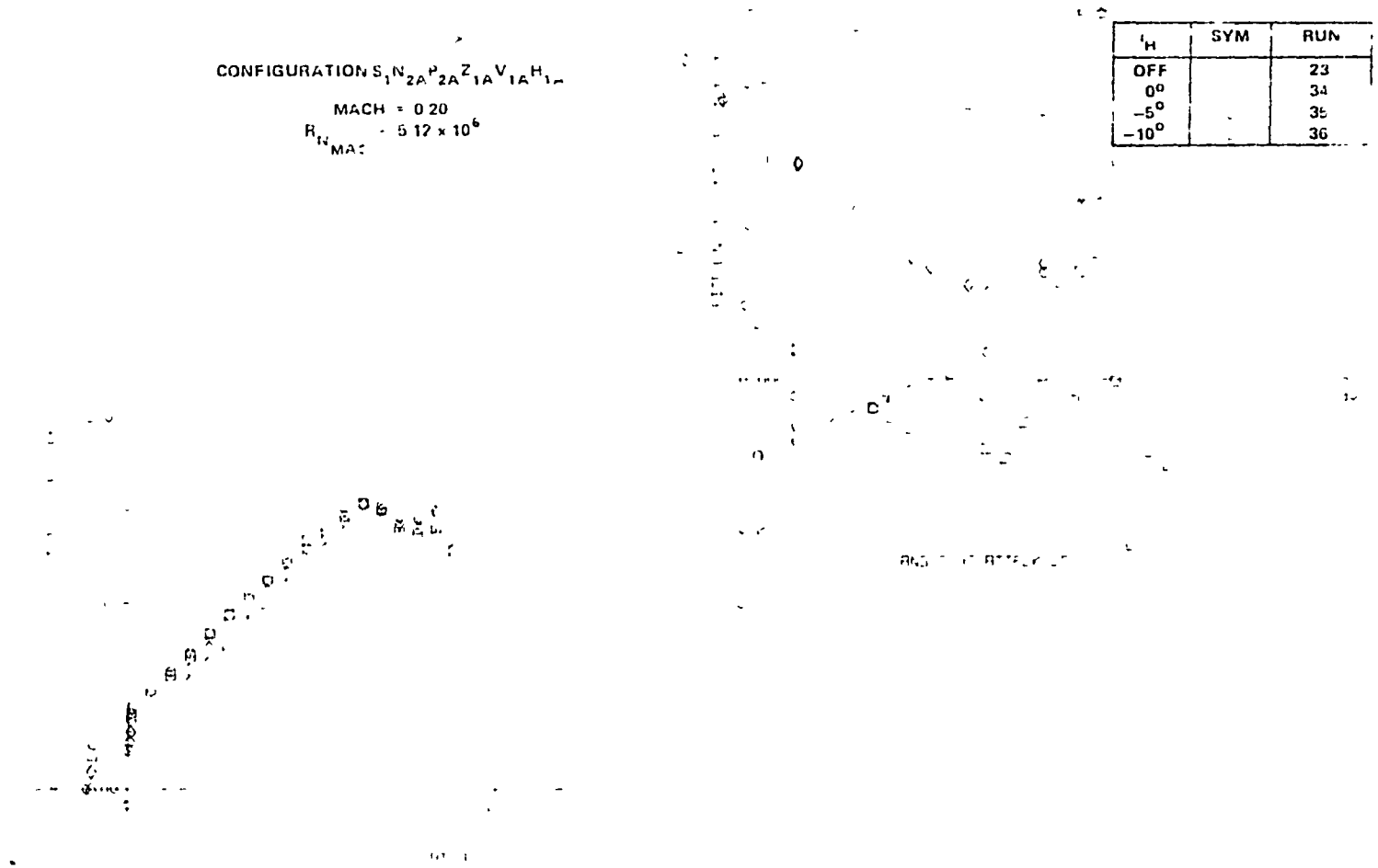

A. LIFT AND PITCHING MOMENT

FIGURE 82 TAIL-ON CHARACTERISTICS FOR THE CRUISE WING WITH NACELLES, PYLONS, AND STRAKES ATTACHED

ORIGINAL PAGE IS
OF POOR QUALITY

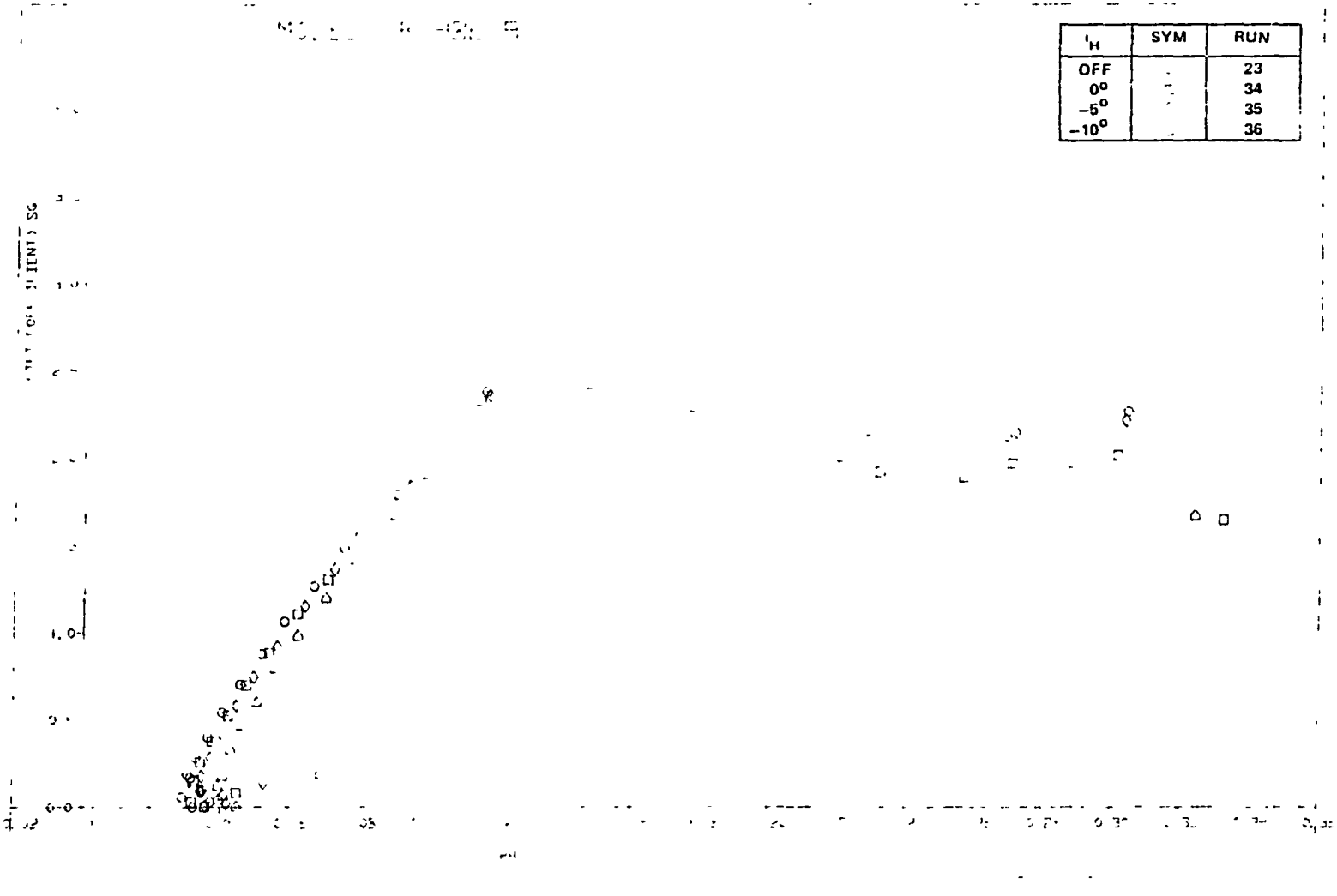

FIGURE 82. TAIL-ON CHARACTERISTICS FOR THE CRUISE WING WITH NACELLES, PYLONS, AND STRAKES ATTACHED (CONCLUDED)

ORIGINAL PAGE IS
OF POOR QUALITY

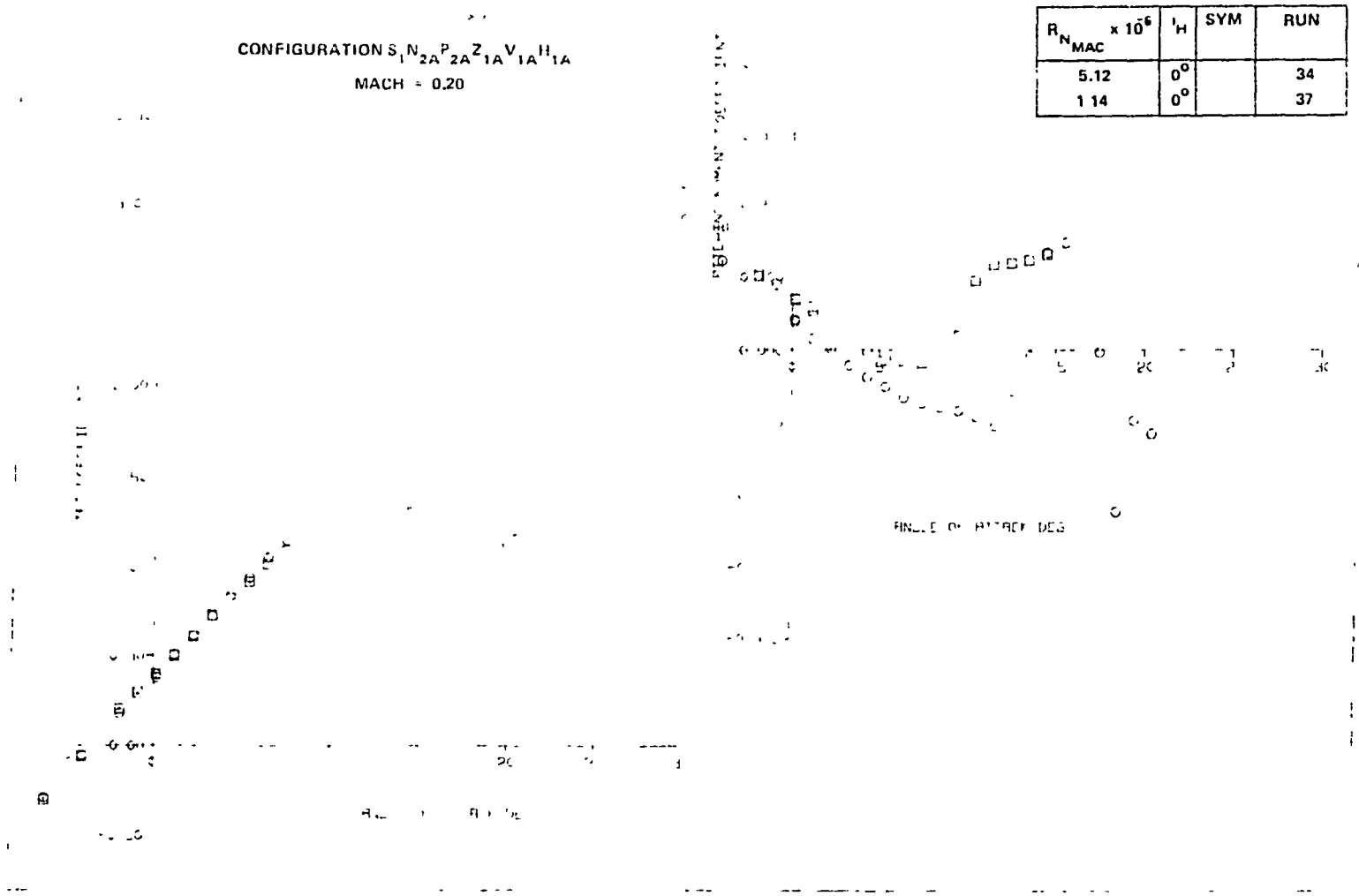

A LIFT AND PITCHING MOMENT

FIGURE 83 EFFECT OF REYNOLDS NUMBER ON CRUISE WING WITH NACELLES, PYLONS, STRAKES, AND HORIZONTAL TAIL ATTACHED

ORIGINAL PAGE IS
OF POOR QUALITY

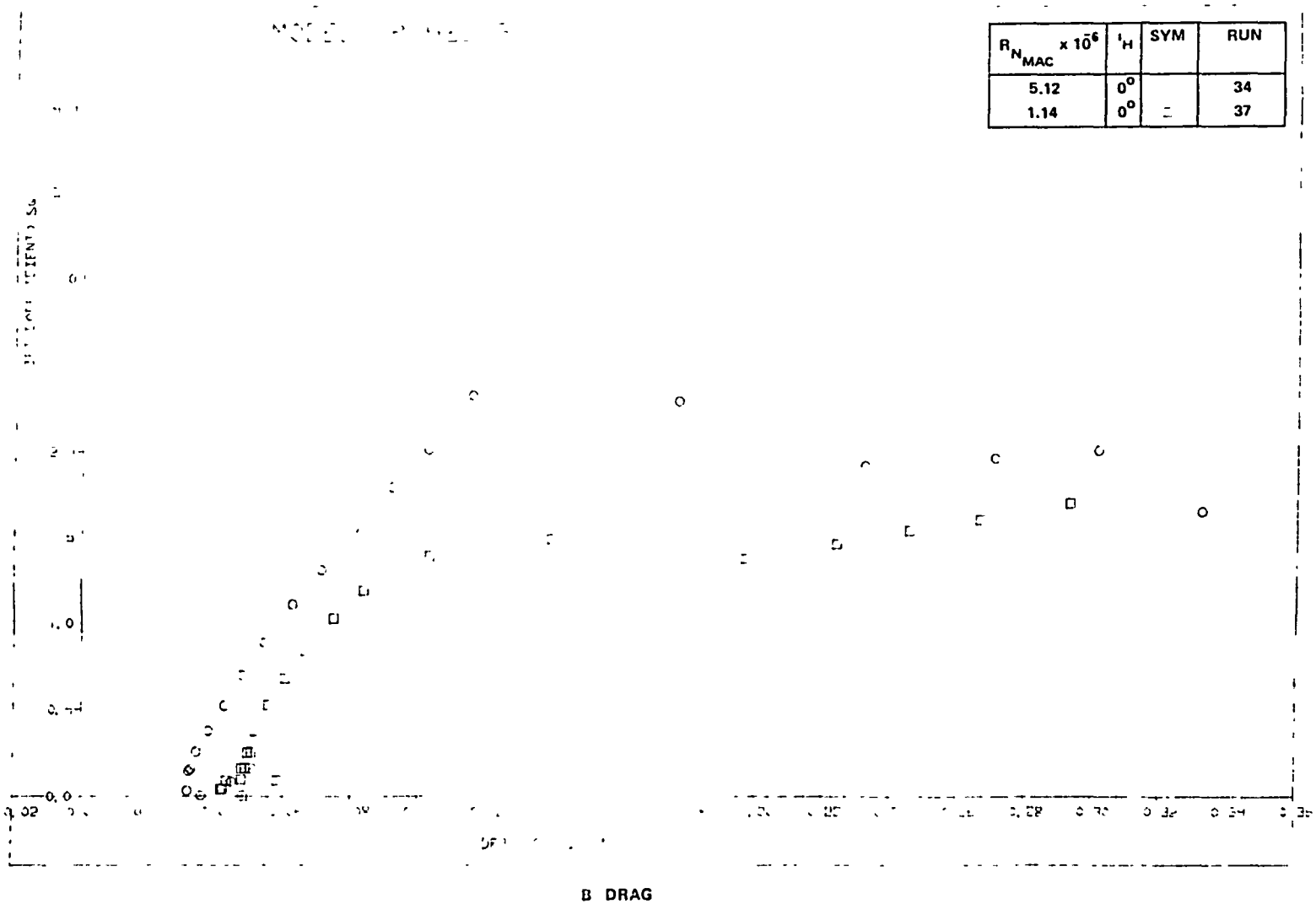

ORIGINAL PAGE IS
OF POOR QUALITY

FIGURE 83. EFFECT OF REYNOLDS NUMBER ON CRUISE WING WITH NACELLES, PYLONS, STRAKES, AND HORIZONTAL TAIL ATTACHED (CONTINUED)

ORIGINAL PAGE IS
OF POOR QUALITY

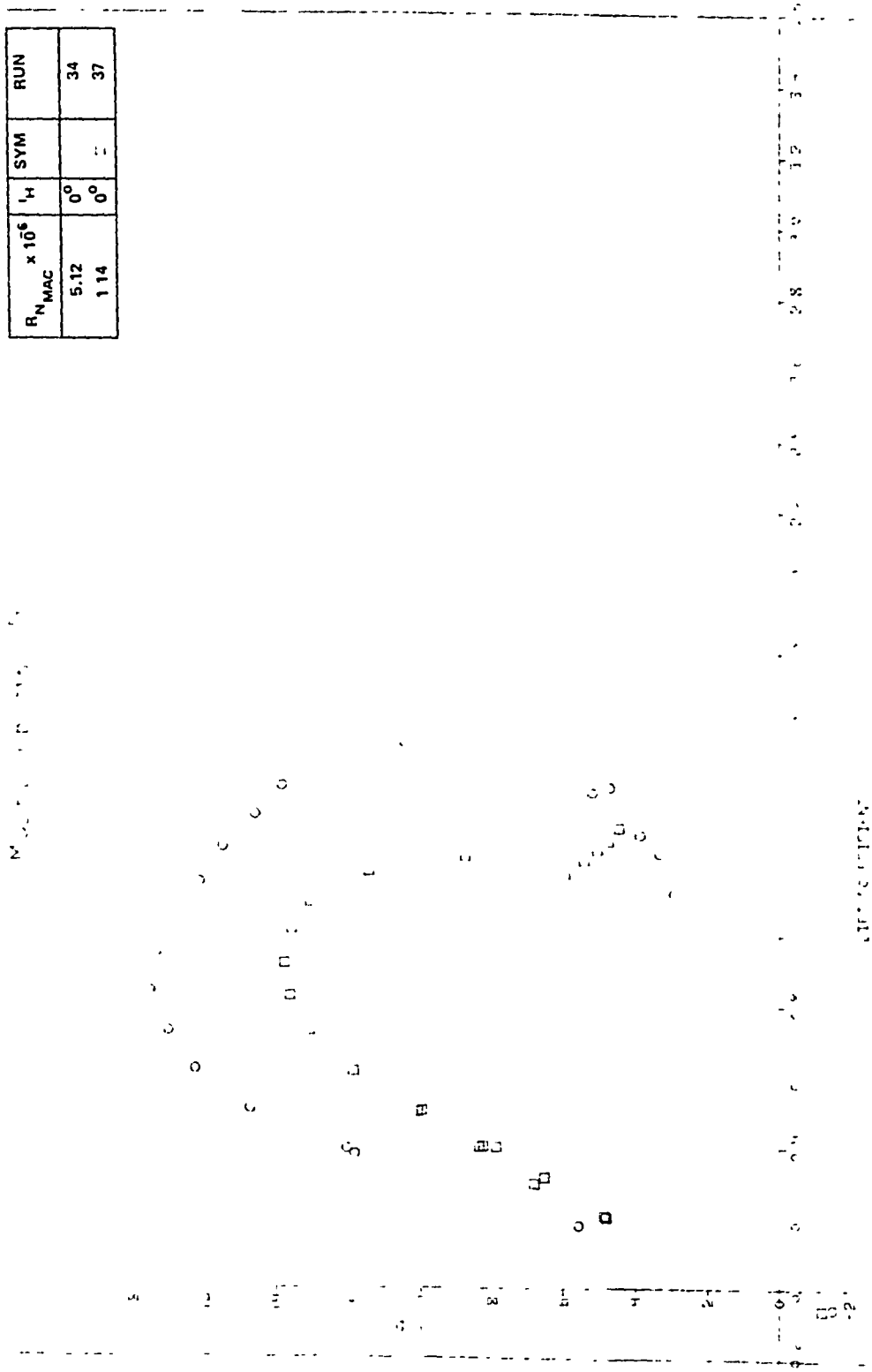

FIGURE 83. EFFECT OF REYNOLDS NUMBER ON CRUISE WING WITH NACELLES, PYLONS, STRAKES, AND HORIZONTAL TAIL ATTACHED (CONCLUDED)

condition. The L/D at 0.69 $C_{L_{MAX}}$ was reduced from 16.8 to 13.6 by the decrease in Reynolds number.

In summary, the basic cruise wing achieved a high level of $C_{L_{MAX}}$ (1.513) and L/D at 1.2 V_S (19.45). Addition of the nacelles, pylons, and strakes resulted in a neglible change in $C_{L_{MAX}}$, a reduced L/D (17.7), and improved pitch characteristics at high angles of attack. Increasing the Reynoldls number from atmospheric to the high Reynolds number test condition increased the $C_{L_{MAX}}$ significantly ($\Delta C_{L_{MAX}} = 0.39$). A Mach number increase from 0.20 to 0.32 resulted in a decrease in $C_{L_{MAX}}$ of 0.11. Test data for the cruise wing configuration with the horizontal tail indicated the low-speed pitch characteristics require improvement. It should be noted that the ongoing high-speed wing development for high aspect ratio supercritical wings has, in fact, altered the span loading which should improve the low-speed stalling behavior.

VCK Configuration

Both the VCK and slat were evaluated during the test program. The VCK was evaluated first with nominal two-segment landing and takeoff flap deflections. Before the VCK position was optimized an extension to the spoiler trailing edge in the region of the flaperon was required at the landing flap deflection. The existing spoiler length, and the resulting gap and overhang (O.H.) in this region, resulted in large flap separation. Only the most conservative flap grid position (large positive O.H. and small gap) was unseparated. The basic spoiler was extended at X_w of 36.362 cm (14.3178 in) by 0.29 cm (0.11 in). This trailing edge extension was decreased to 0.0 cm at X_w of 43.411 cm (17.091 in) and X_w of 14.800 cm (5.828 in). This resulted in a more positive O.H. of 1.29 percent at X_w of 36.362 cm (14.3178 in). The gap was also changed and, for flap position F_{1AM} a reduction of 0.3 percent resulted at the same wing station. The remainder of the test was conducted with this revised inboard spoiler configuration (f_{1A},f_{2A}). Figure 84 illustrates the VCK with two-segment flap configuration installed in the Ames 12-Foot Pressure Wind Tunnel. Before proceeding with the VCK optimization the effects due to the removal of the VCK filler blocks were evaluated. The results indicated minor changes in lift, drag, and pitching moment. The remainder of the VCK runs were accomplished with the VCK filler blocks removed (see Figure 85).

ORIGINAL PAGE IS
OF POOR QUALITY

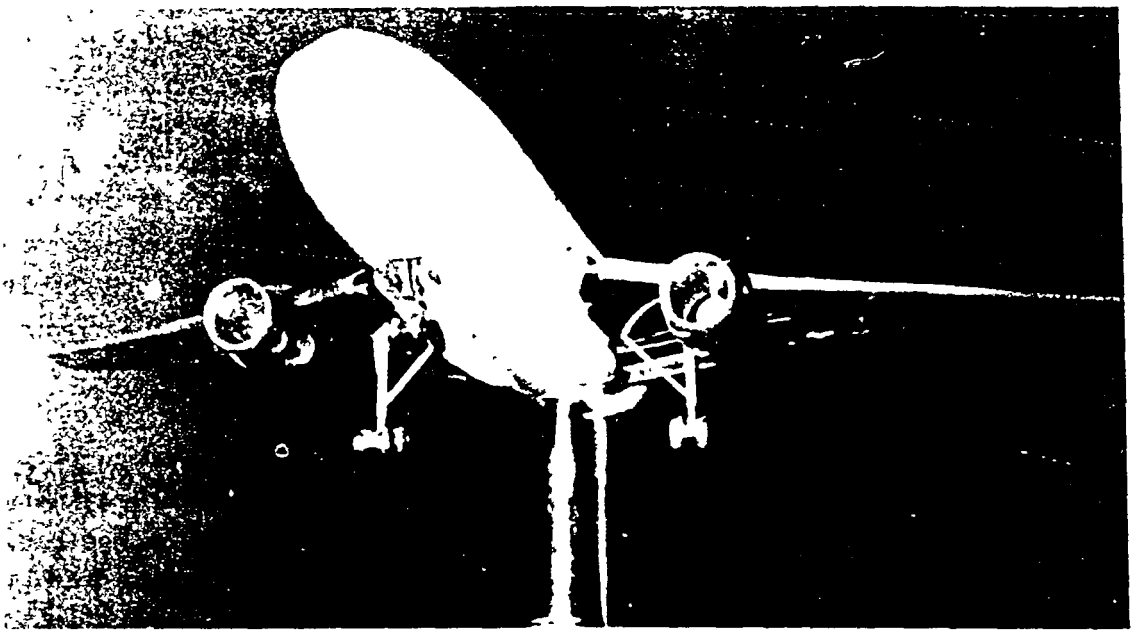

FIGURE 84. VCK AND TWO-SEGMENT FLAP CONFIGURATION IN THE AMES 12-FOOT PRESSURE WIND TUNNEL

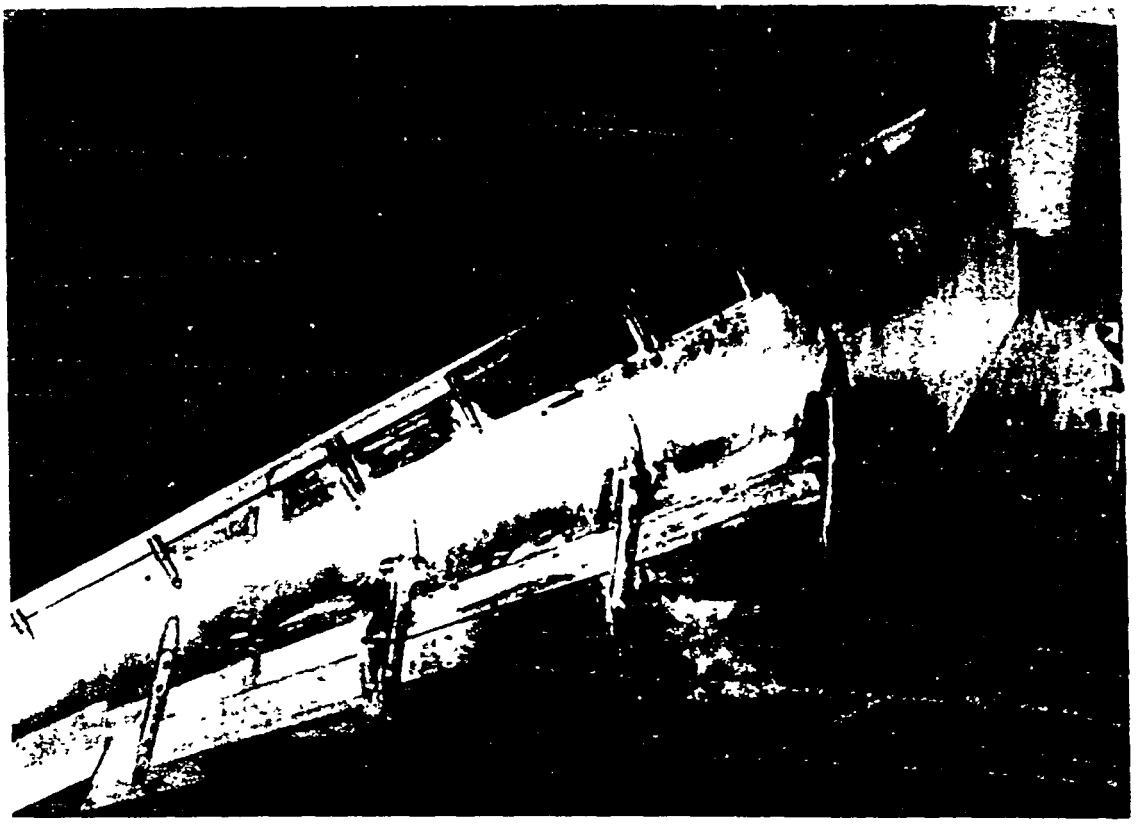

FIGURE 85. LOWER SURFACE MIDSPAN REGION OF THE VCK WITH TWO-SEGMENT FLAP CONFIGURATION

The influence of mini-tufts was also examined for the high lift configuration. As with the cruise wing configuration, the data indicated very small effects on lift and pitching moment and a slight reduction in drag ($\Delta C_D \simeq 0.002$). The change in high lift characteristics due to nacelle strakes indicated an increase in $C_{L_{MAX}}$ of 0.04, slightly more positive pitching moment, and a negligible change in drag.

VCK Landing and Takeoff Optimization. - A VCK deflection and position survey was evaluated with a nominal two-segment landing flap configuration. Figure 86 illustrates the VCK position study for 55° VCK deflection (horizontal tail-off). Significant reduction in $C_{L_{MAX}}$ and positive pitch increment is shown for the 55A/55A grid position (Gap = 3.5%, O.H. = -1%). Figure 87 presents the variation of section lift coefficient for these positions. For run 49 and 50, the 90-percent station stalls first. Run 50 indicates a rapid lift loss at the 72.5-percent station, and run 51, adverse effects due to the large gap for both 72.5- and 90-percent stations are indicated.

Figure 88 presents the position study for a VCK deflection of 45 degrees across the span. Run 52 (Gap = 1.5%), O.H. = -1%) has a significant reduction in $C_{L_{MAX}}$. Runs 66 and 67 have differential VCK grids (different inboard and outboard positions). The largest $C_{L_{MAX}}$ was obtained in Run 67 ($C_{L_{MAX}} = 3.15$). The pitching moment characteristics indicate significant variations due to the VCK position. Figure 89 presents the section lift characteristics for the position survey. Run 52 indicates that for small gap and overhang (Gap = 1.5%, O.H. = -1%) the 90- and 72.5-percent span stations achieved a large $C_{L_{MAX}}$ and gentle stall. The inboard stations, however, reached their $C_{L_{MAX}}$ values at very low angles of attack indicating premature stall inboard, and consequent loss in $C_{L_{MAX}}$. Run 53 (Gap = 2.5%, O.H. = -1%) indicates improved characteristics inboard, but increased lift loss at the 90-percent span station. The lift values for Run 54 show a reduction in inboard lift loss, and a sharp lift loss at 90 percent. The 90-percent span station is shown to have a gentle stall for Run 56 (Gap = 2.5%, O.H. = 0%). Run 66 sectional lift values indicate increased lift loss for the 50-percent station.

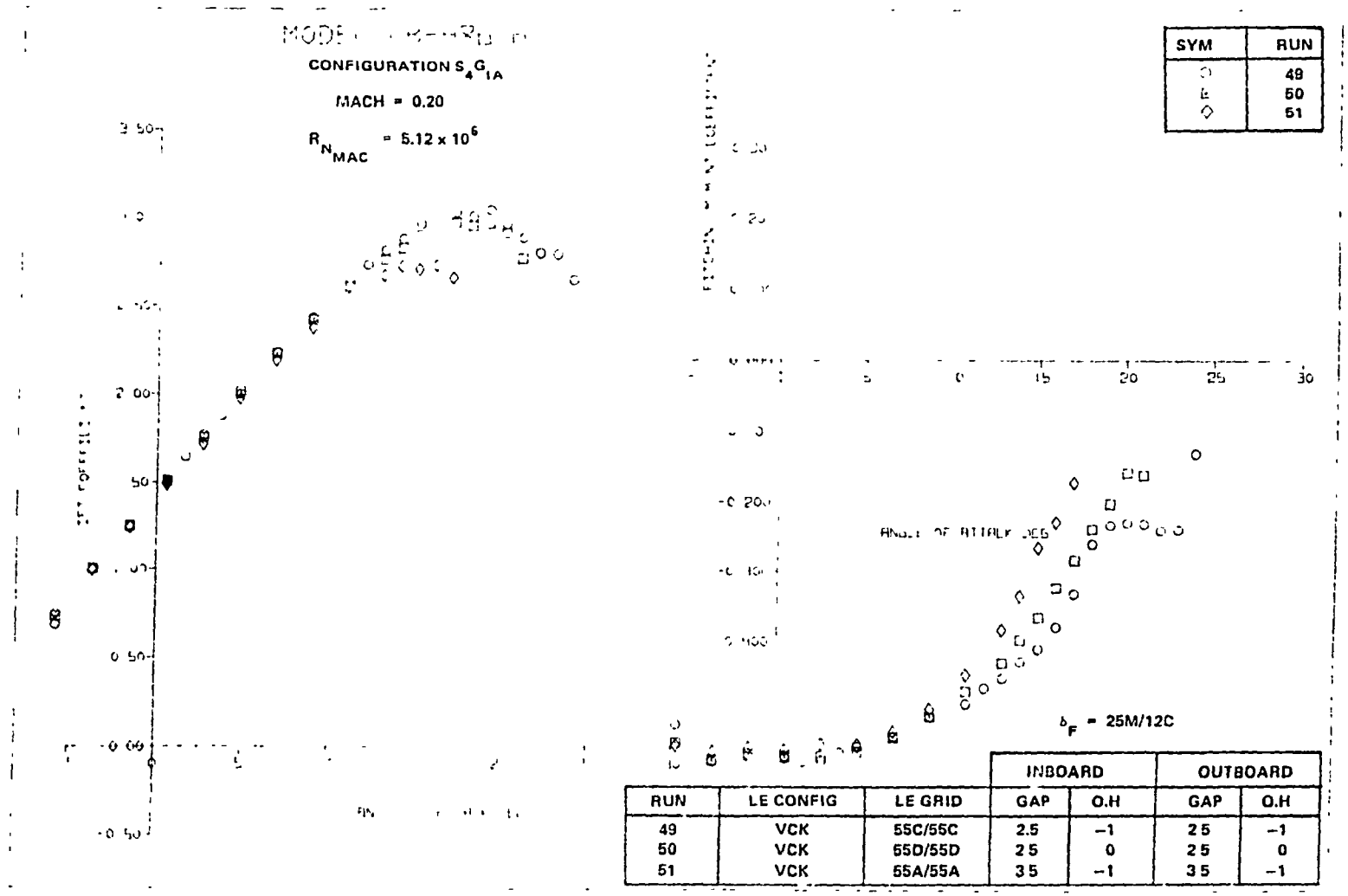

A LIFT AND PITCHING MOMENT

FIGURE 86 VCK POSITION STUDY FOR LANDING FLAPS (δ_{VCK} = 55°)

ORIGINAL PAGE IS
OF POOR QUALITY

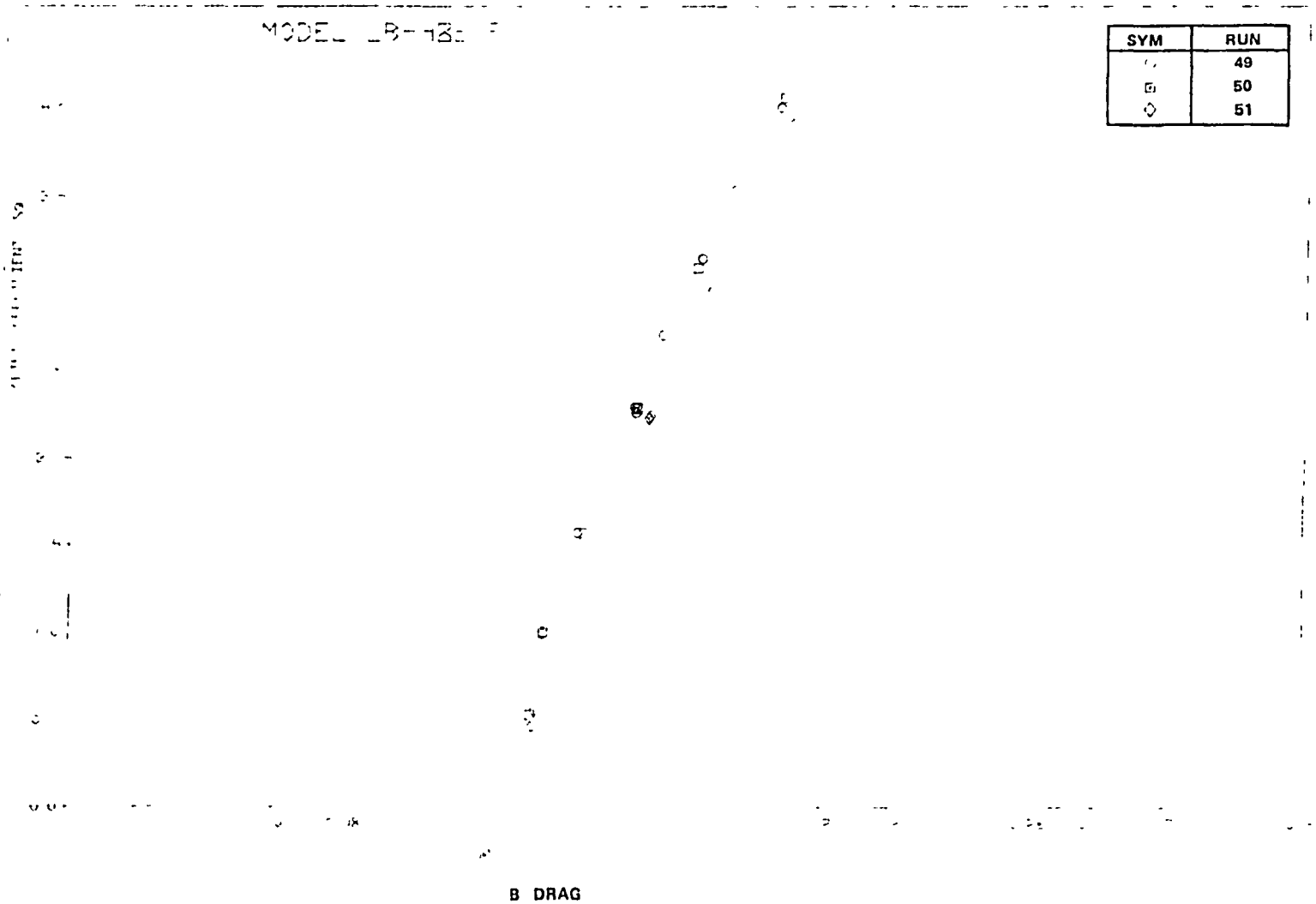

FIGURE 86. VCK POSITION STUDY FOR LANDING FLAPS (δ_{VCK} = 55°) (CONCLUDED)

ORIGINAL PAGE IS
OF POOR QUALITY

ORIGINAL P
OF POOR QUA

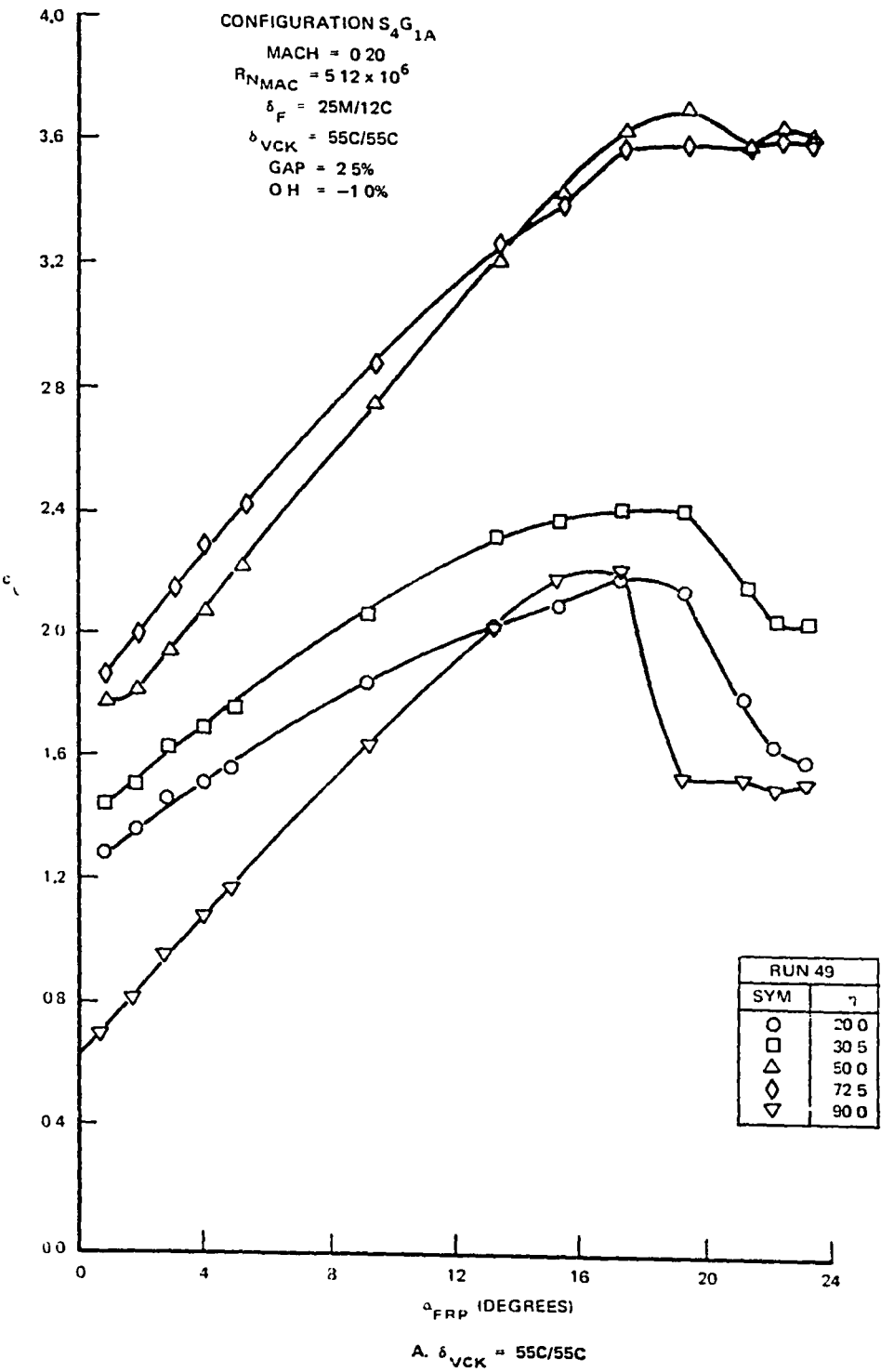

FIGURE 87 VARIATION OF SECTION LIFT COEFFICIENT FOR THE VCK WITH TWO-SEGMENT LANDING FLAPS

ORIGINAL PAGE
OF POOR QUALITY

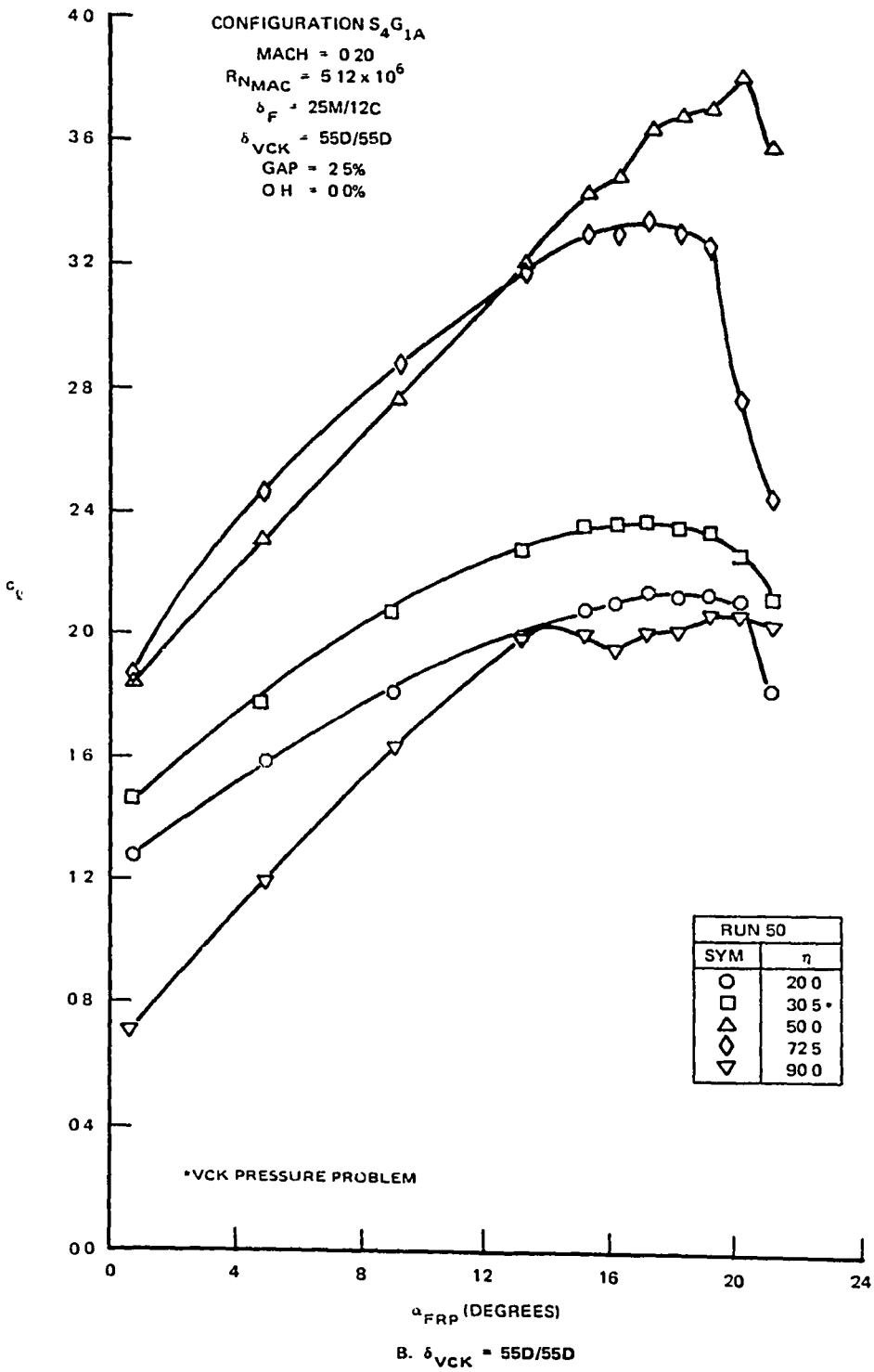

B. δ_{VCK} = 55D/55D

FIGURE 87. VARIATION OF SECTION LIFT COEFFICIENT FOR THE VCK WITH TWO-SEGMENT LANDING FLAPS (CONTINUED)

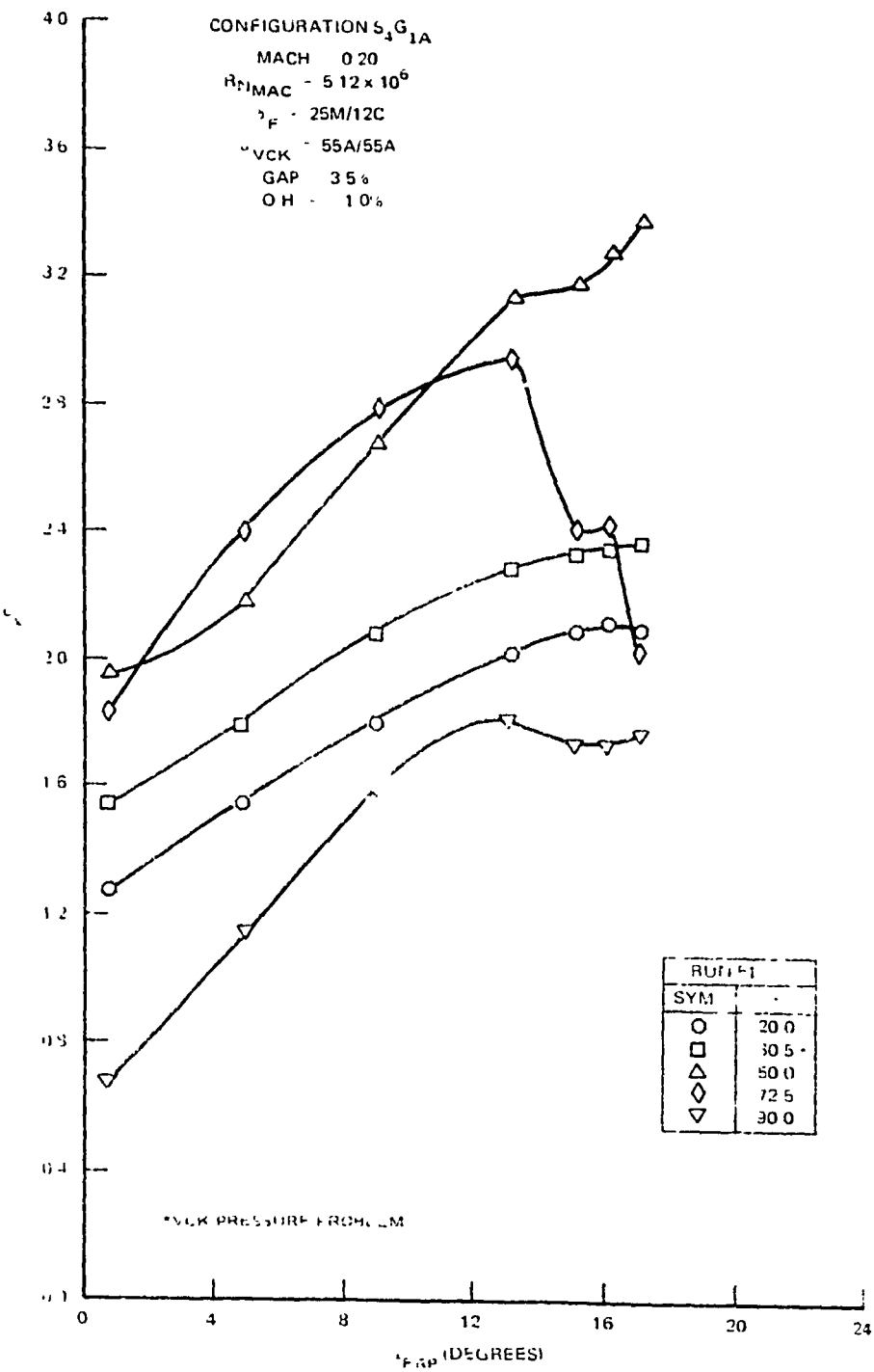

FIGURE 87 VARIATION OF SECTION LIFT COEFFICIENT FOR THE VCK WITH TWO-SEGMENT LANDING FLAPS (CONCLUDED)

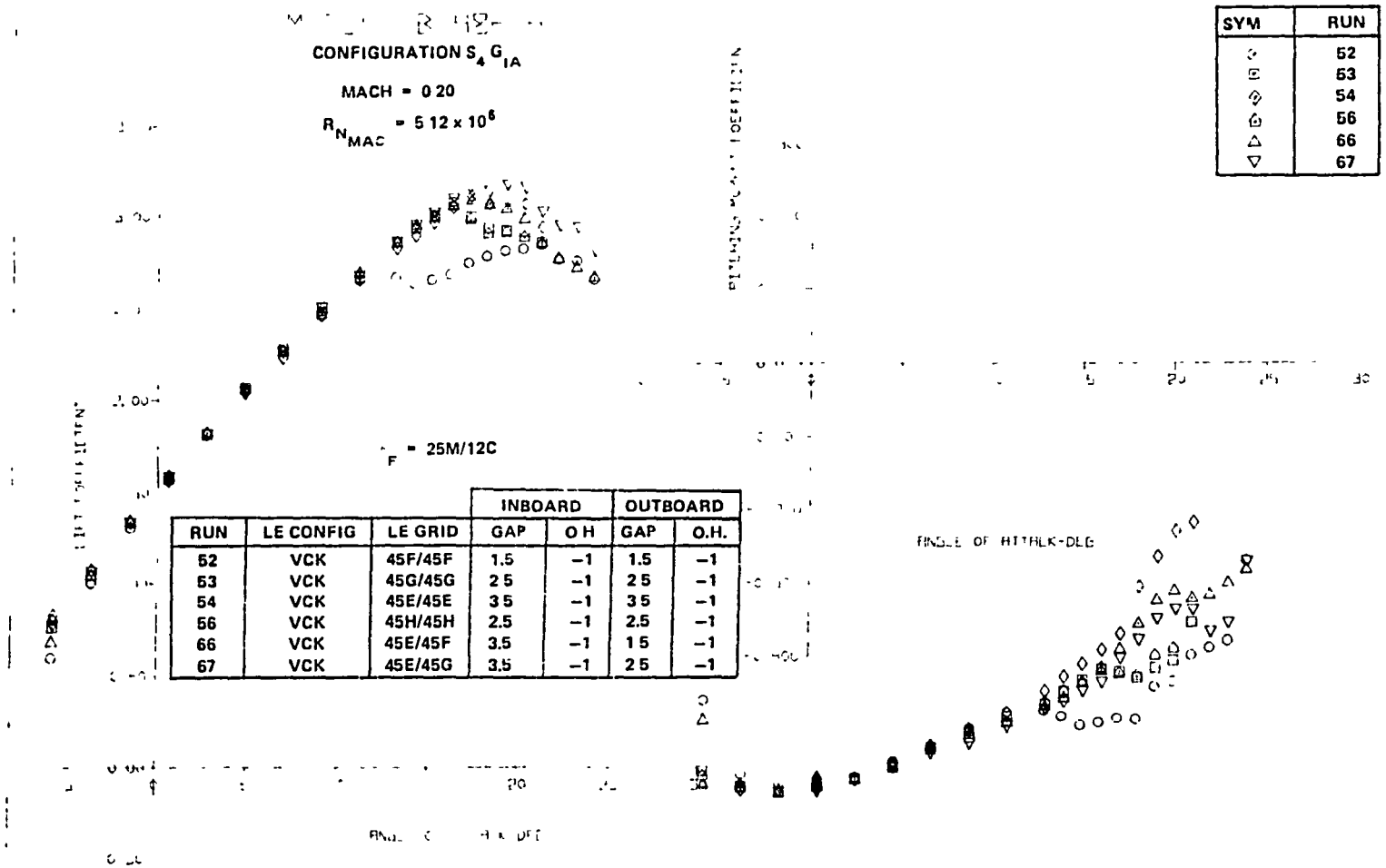

A LIFT AND PITCHING MOMENT

FIGURE 88. VCK POSITION STUDY FOR LANDING FLAPS (Λ_{VCK} = 45°)

ORIGINAL PAGE IS
OF POOR QUALITY

ORIGINAL PAGE IS
OF POOR QUALITY

SYM	RUN
•	52
○	53
△	54
◇	56
▽	66
□	67

b. DRAG

FIGURE 88 VCK POSITION STUDY FOR LANDING FLAPS (δ_{VCK} = 45°) (CONCLUDED)

ORIGINAL PAGE IS
OF POOR QUALITY

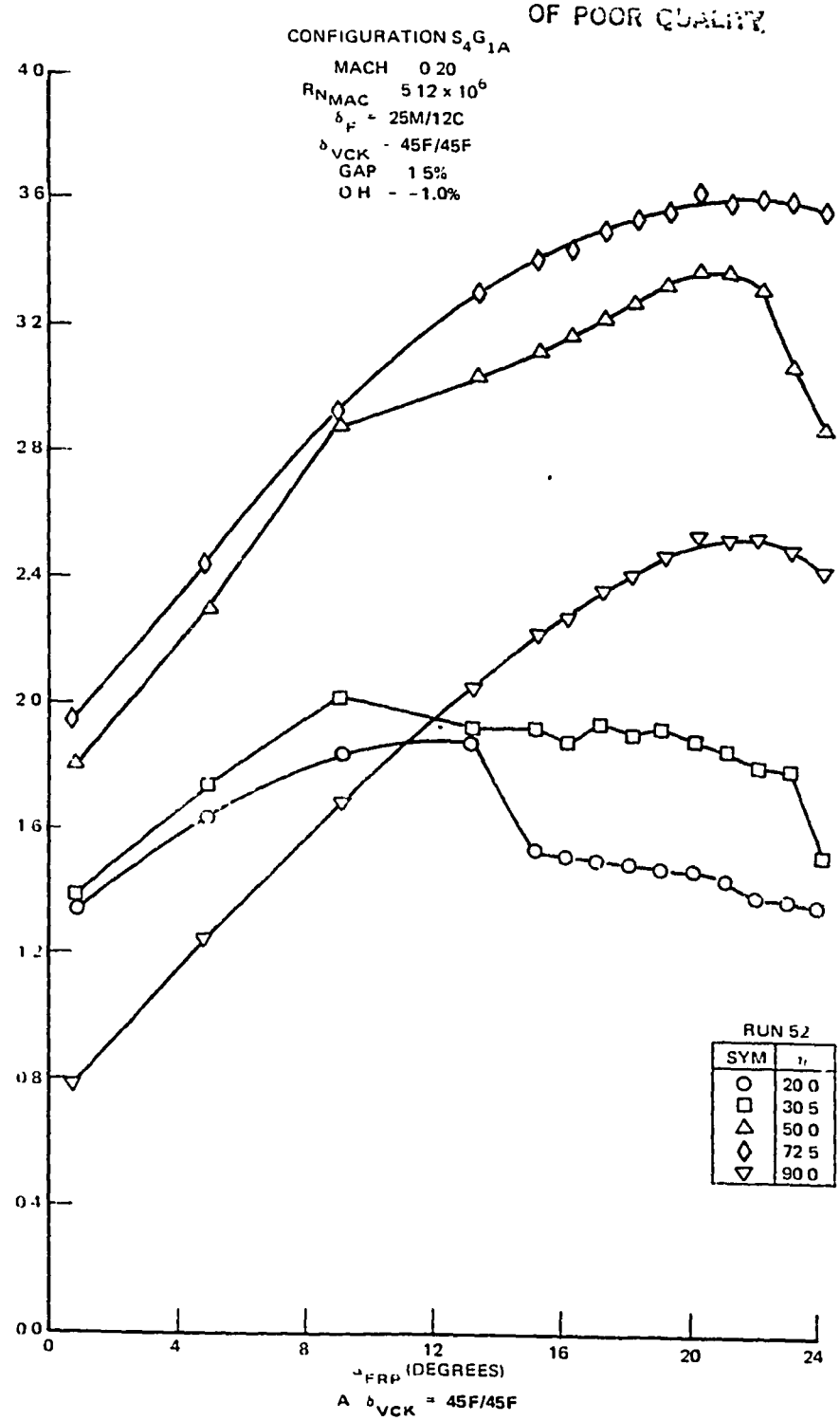

FIGURE 89 VARIATION OF SECTION LIFT COEFFICIENT FOR THE VCK WITH TWO-SEGMENT LANDING FLAPS

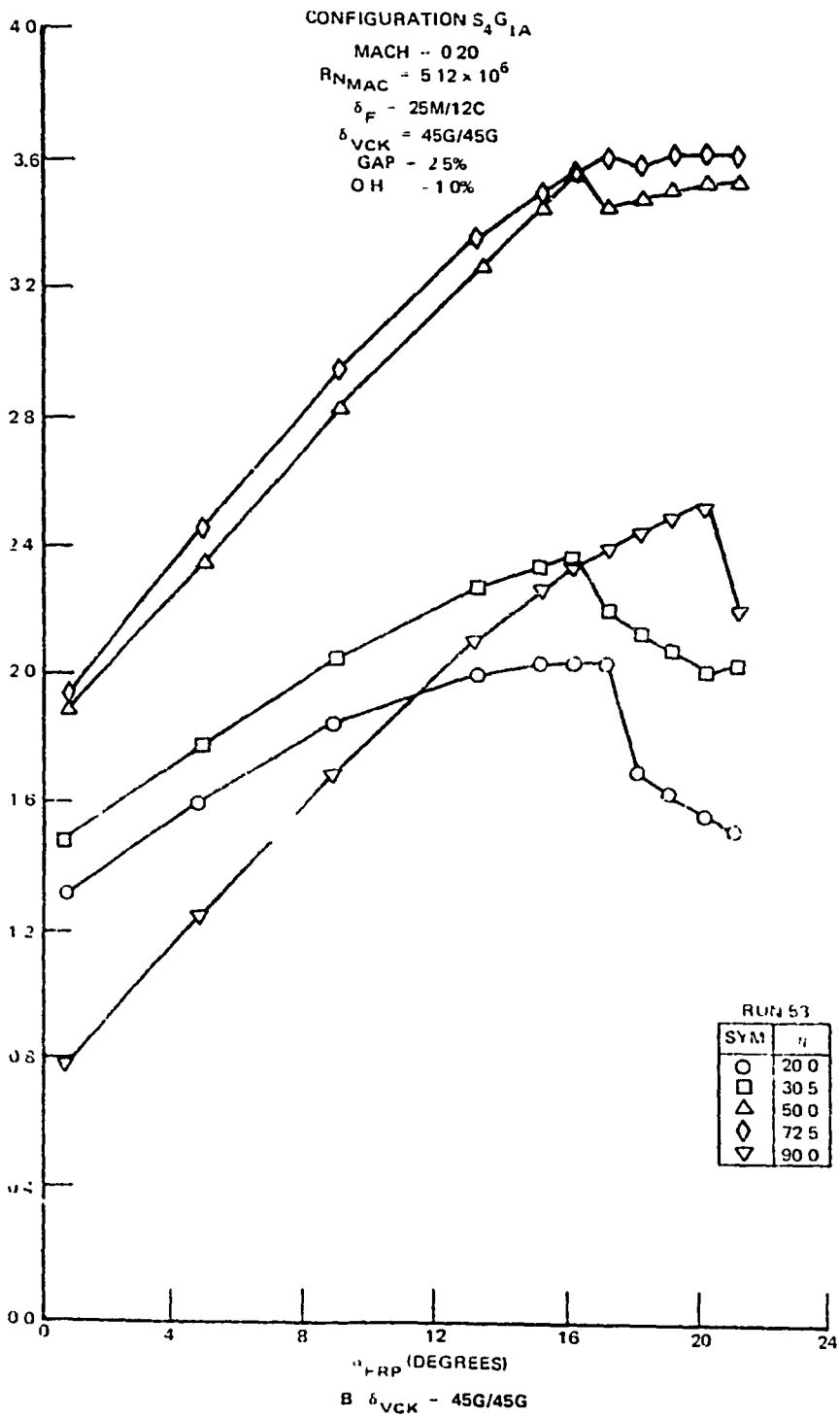

FIGURE 89. VARIATION OF SECTION LIFT COEFFICIENT FOR THE VCK WITH TWO-SEGMENT LANDING FLAPS (CONTINUED)

ORIGINAL PAGE IS
OF POOR QUALITY

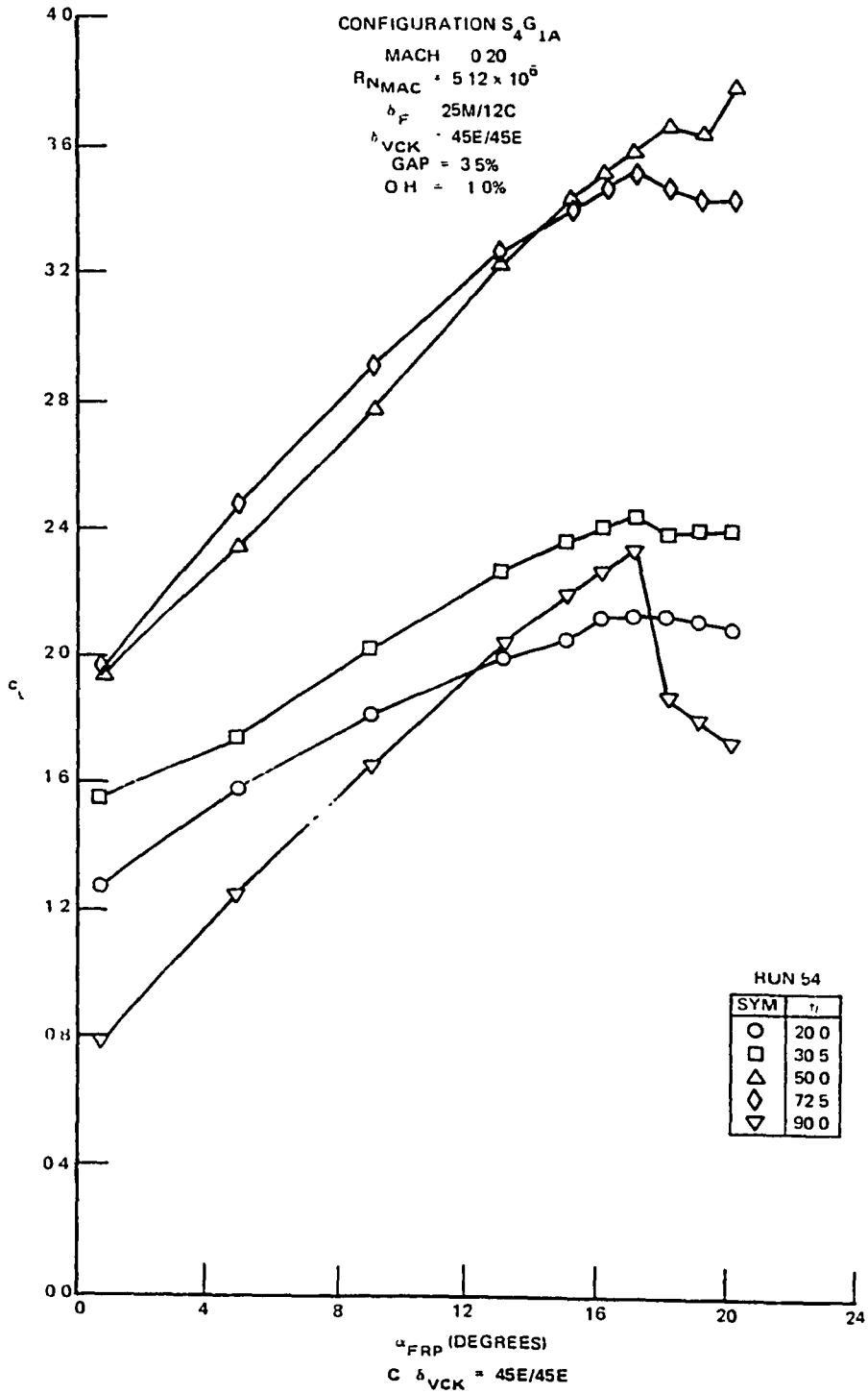

FIGURE 89. VARIATION OF SECTION LIFT COEFFICIENT FOR THE VCK WITH TWO-SEGMENT LANDING FLAPS (CONTINUED)

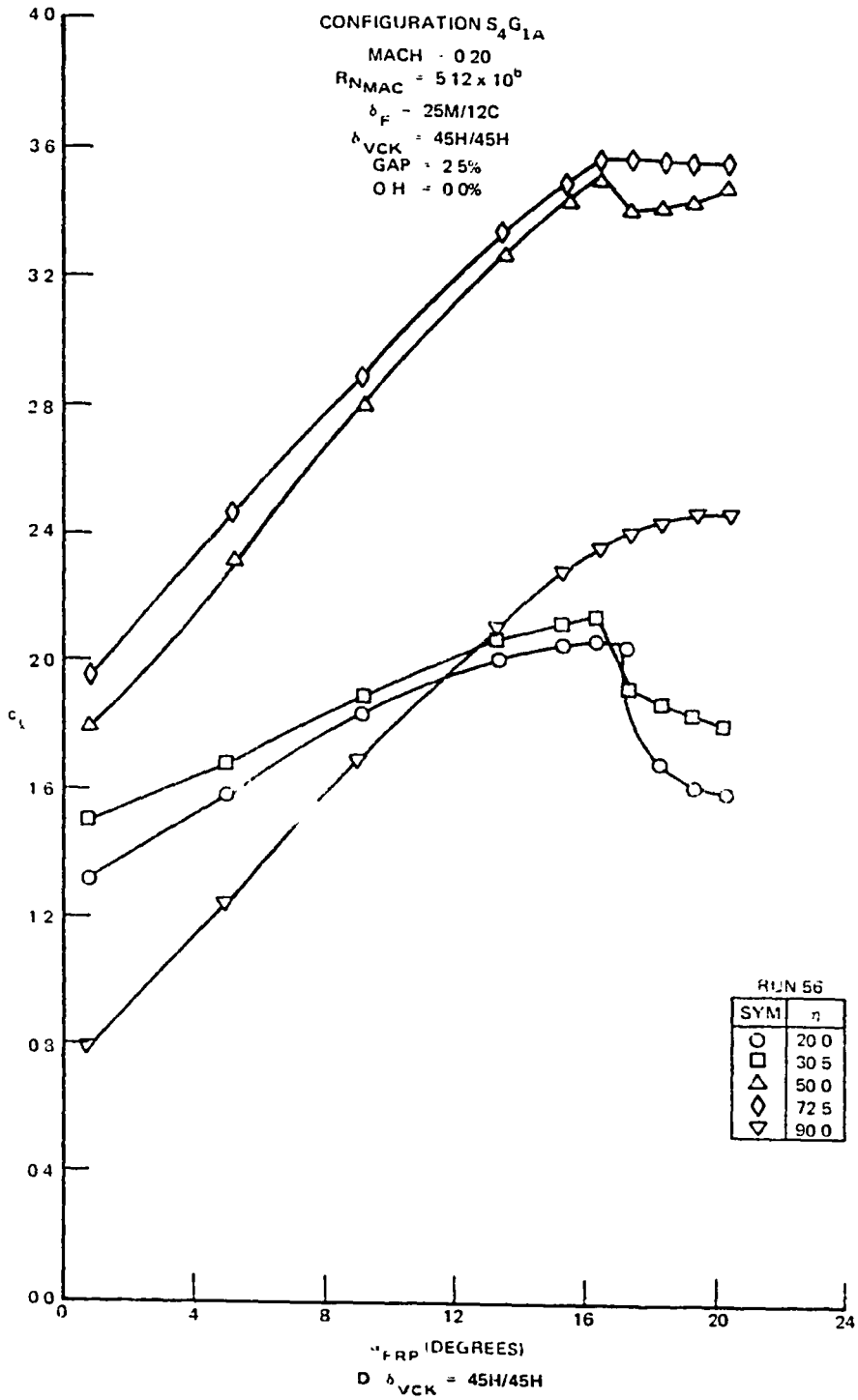

FIGURE 89. VARIATION OF SECTION LIFT COEFFICIENT FOR THE VCK WITH TWO-SEGMENT LANDING FLAPS (CONTINUED)

ORIGINAL PAGE IS
OF POOR QUALITY

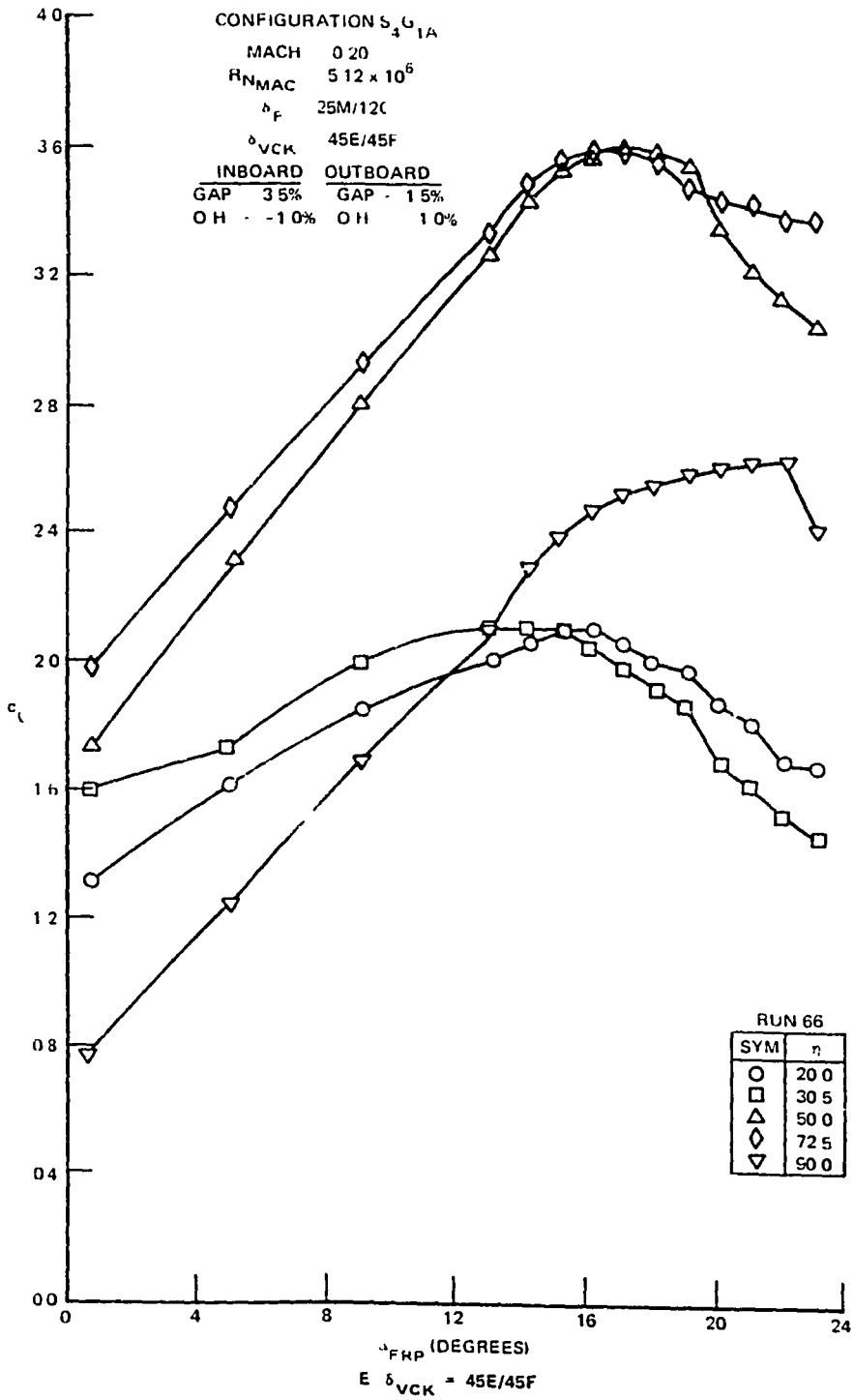

FIGURE 89. VARIATION OF SECTION LIFT COEFFICIENT FOR THE VCK WITH TWO-SEGMENT LANDING FLAPS (CONCLUDED)

Figure 90 presents mini-tuft photos for Run 67. Increasing the angle of attack past $\alpha C_{L_{MAX}}$ initiates stall on the inboard wing out to the area behind the nacelle/pylon. Some separation is also evident for the trailing edge region of the flaperon. Some trailing edge activity is noted at 90-percent span at $\alpha_{FRP} = 21.14^{o}$. As higher angles of attack are reached the separation continues over the inner region of the main wing, and at the highest angle of attack, increased tuft activity is noted at the wing tip (near the most outboard VCK support bracket). Figure 91 presents the corresponding pressure distributions. $C_{P_{MIN}}$ values of -11.25 are reached on the VCK for the outboard region of the wing. For the highest angle of attack, the pressure distribution at 90-percent span station indicates a significant reduction in c_ℓ and the resulting positive pitch increment is shown in Figure 88. Examination of the section lift characteristics in Figure 92 also indicates this trend. The section lift characteristics presented previously in Figure 89A (Gap = 1.5% and O.H. = 1%) indicates that improved characteristics could be obtained with this grid position for the outboard portion of the wing.

Figures 93 through 99 present a similar deflection and position study for a nominal two-segment takeoff flap deflection. In general the 45° VCK deflections are superior to the 55° deflections in minimizing the lift loss for the midspan and outboard sections. The stall progression shown by Figure 97, for the 45E/45G VCK grid position, is similar to that shown for the landing flap deflection. Again, at the highest angle of attack the 90-percent span station lift loss results in reduced stability for the configuration (Figure 95).

Due to mechanical complexity, a one position VCK is required (one deflected position). Comparison of the results for the landing and takeoff flap settings indicated that VCK grid position 45E/45G was the best compromise from the standpoint of $C_{L_{MAX}}$, L/D at 1.3 V_S, and pitch characteristics.

Also noted previously, a smaller gap for the VCK on the outboard region of the wing would have improved the high angle of attack pitch characteristics. The effect of reduced VCK deflection (55° versus 45°) also indicates a possible performance increase for a further reduction in VCK deflection.

ORIGINAL PAGE IS
OF POOR QUALITY

A. α_{FRP} = 0.60 DEGREES

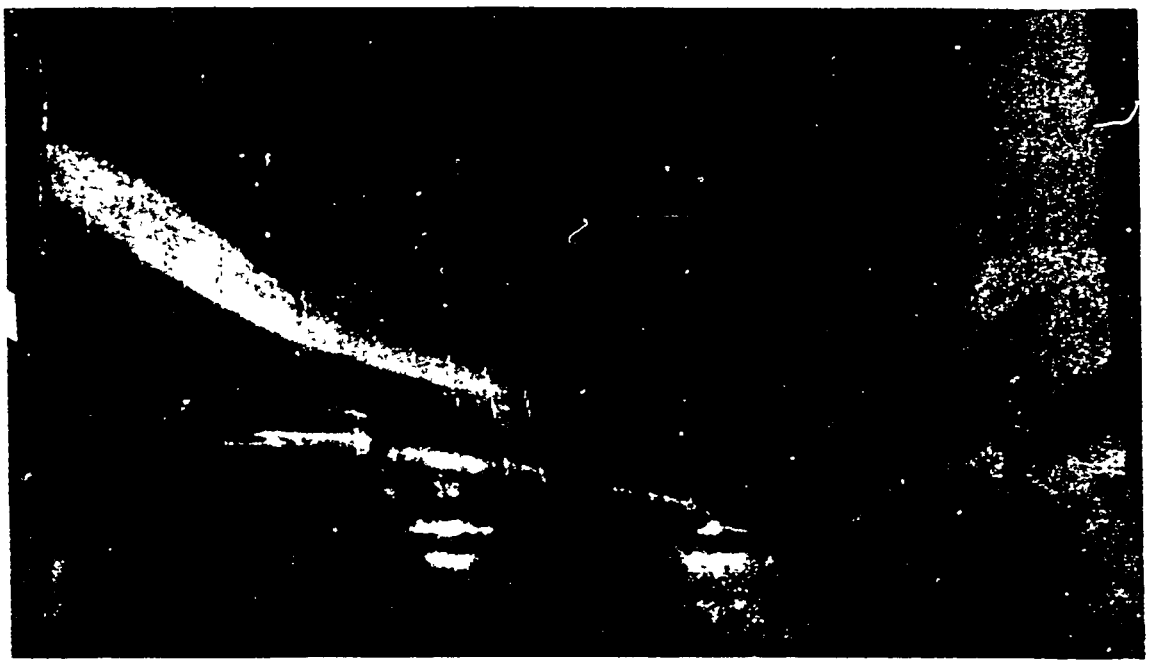

B. α_{FRP} = 17.18 DEGREES

FIGURE 90. MINI-TUFT PHOTOS FOR VCK WITH TWO-SEGMENT LANDING FLAPS (RUN 67)

ORIGINAL PAGE IS
OF POOR QUALITY

C α_{FRP} = 19.19 DEGREES ($\alpha_{C_{L_{MAX}}}$)

D. α_{FRP} = 21.14 DEGREES

FIGURE 90. MINI-TUFT PHOTOS FOR VCK WITH TWO-SEGMENT LANDING FLAPS (RUN 67) (CONTINUED)

ORIGINAL PAGE IS
OF POOR QUALITY

E α_{FRP} = 23.10 DEGREES

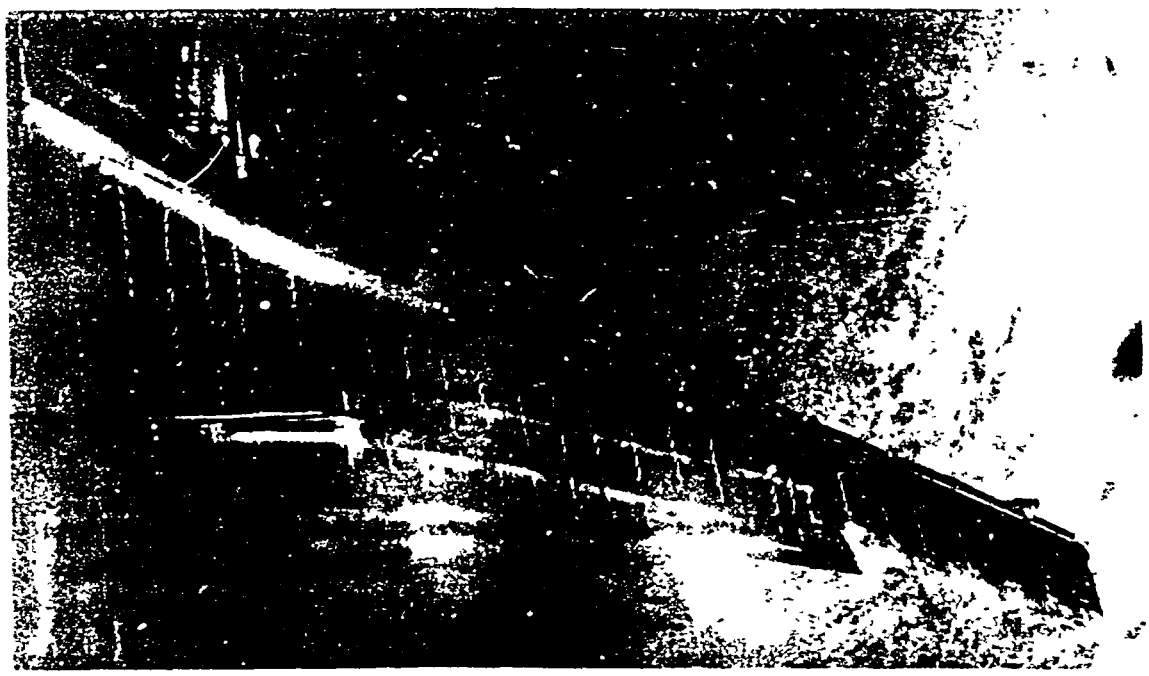

F. α_{FRP} = 24.06 DEGREES

FIGURE 90. MINI-TUFT PHOTOS FOR VCK WITH TWO-SEGMENT LANDING FLAPS (RUN 67) (CONCLUDED)

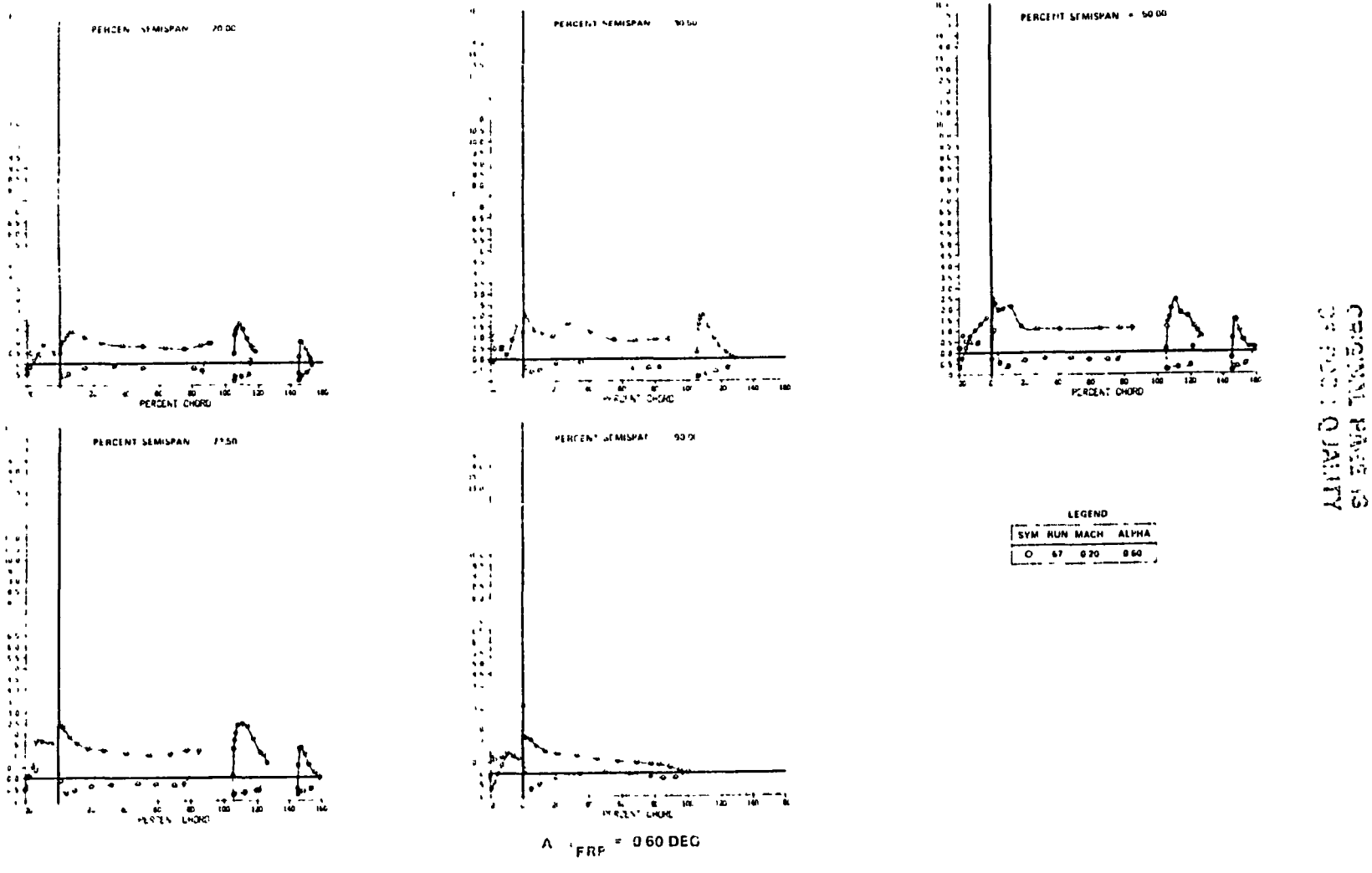

FIGURE 91. EXPERIMENTAL CHORDWISE PRESSURE DISTRIBUTION FOR VCK WITH TWO-SEGMENT LANDING FLAPS

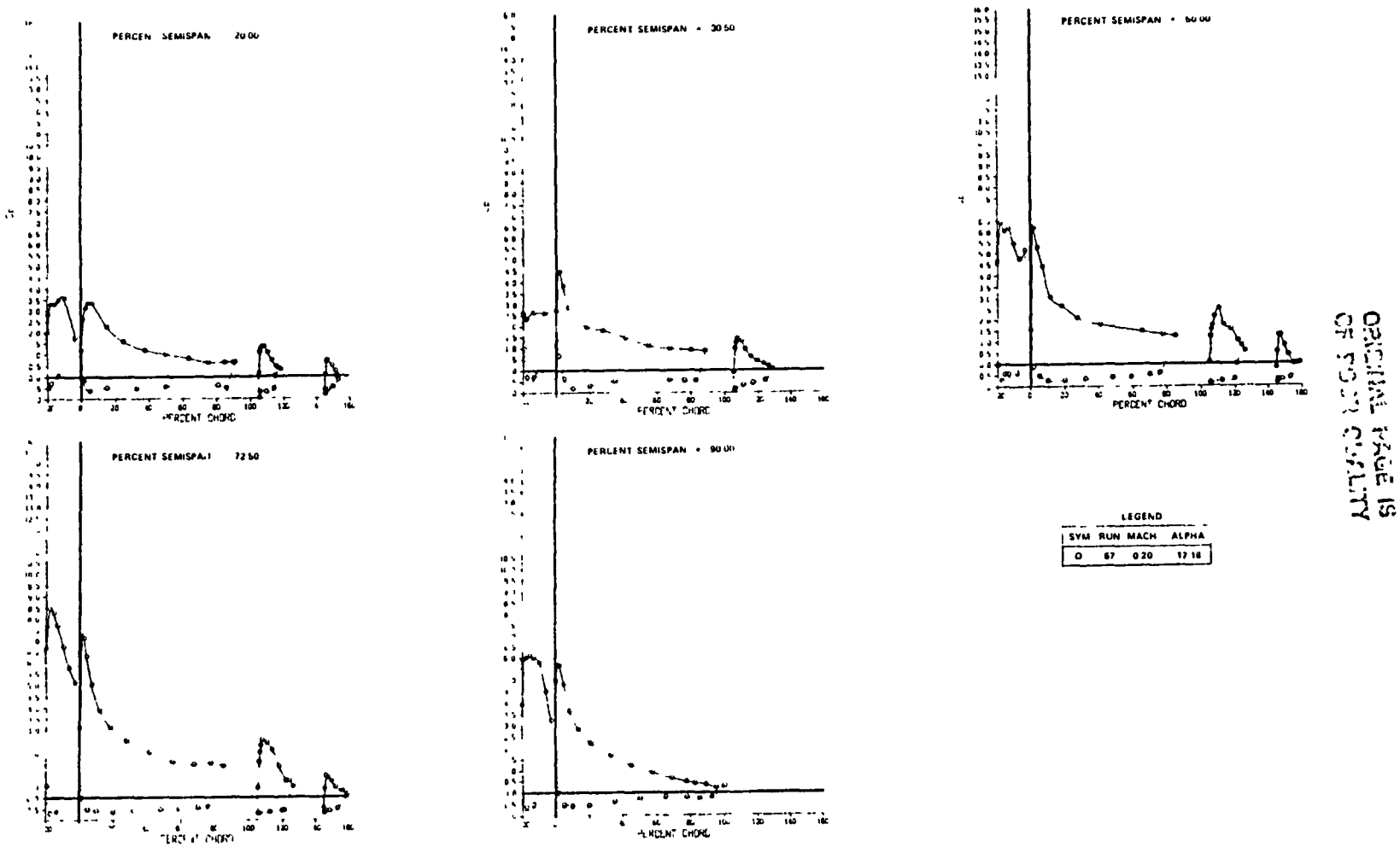

B_{FRP} = 17.18 DEG

FIGURE 91. EXPERIMENTAL CHORDWISE PRESSURE DISTRIBUTION FOR VCK WITH TWO-SEGMENT LANDING FLAPS (CONTINUED)

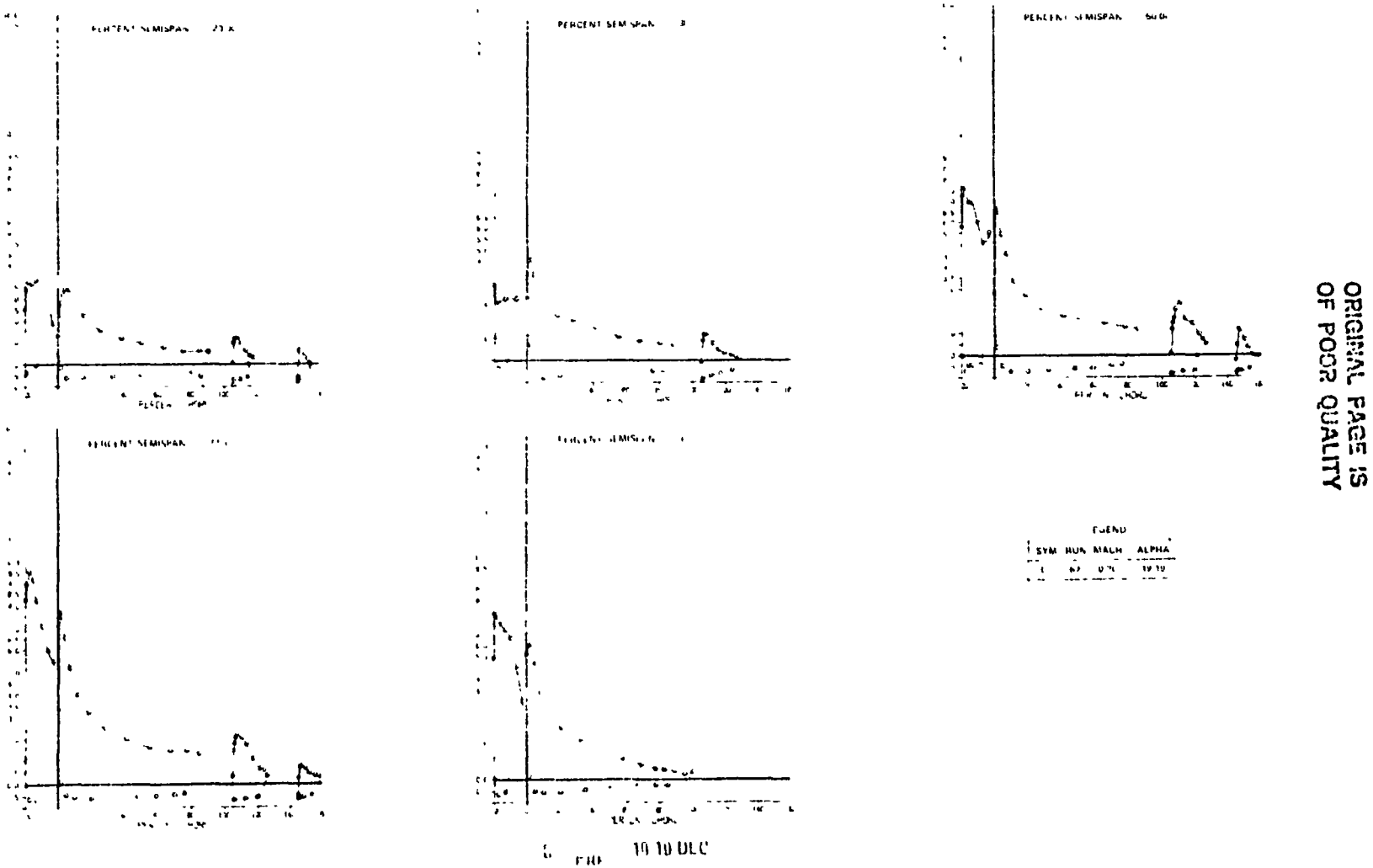

FIGURE 91 EXPERIMENTAL CHORDWISE PRESSURE DISTRIBUTION FOR VCK WITH TWO SEGMENT LANDING FLAPS (CONTINUED)

ORIGINAL PAGE IS
OF POOR QUALITY

ORIGINAL PAGE IS
OF POOR QUALITY

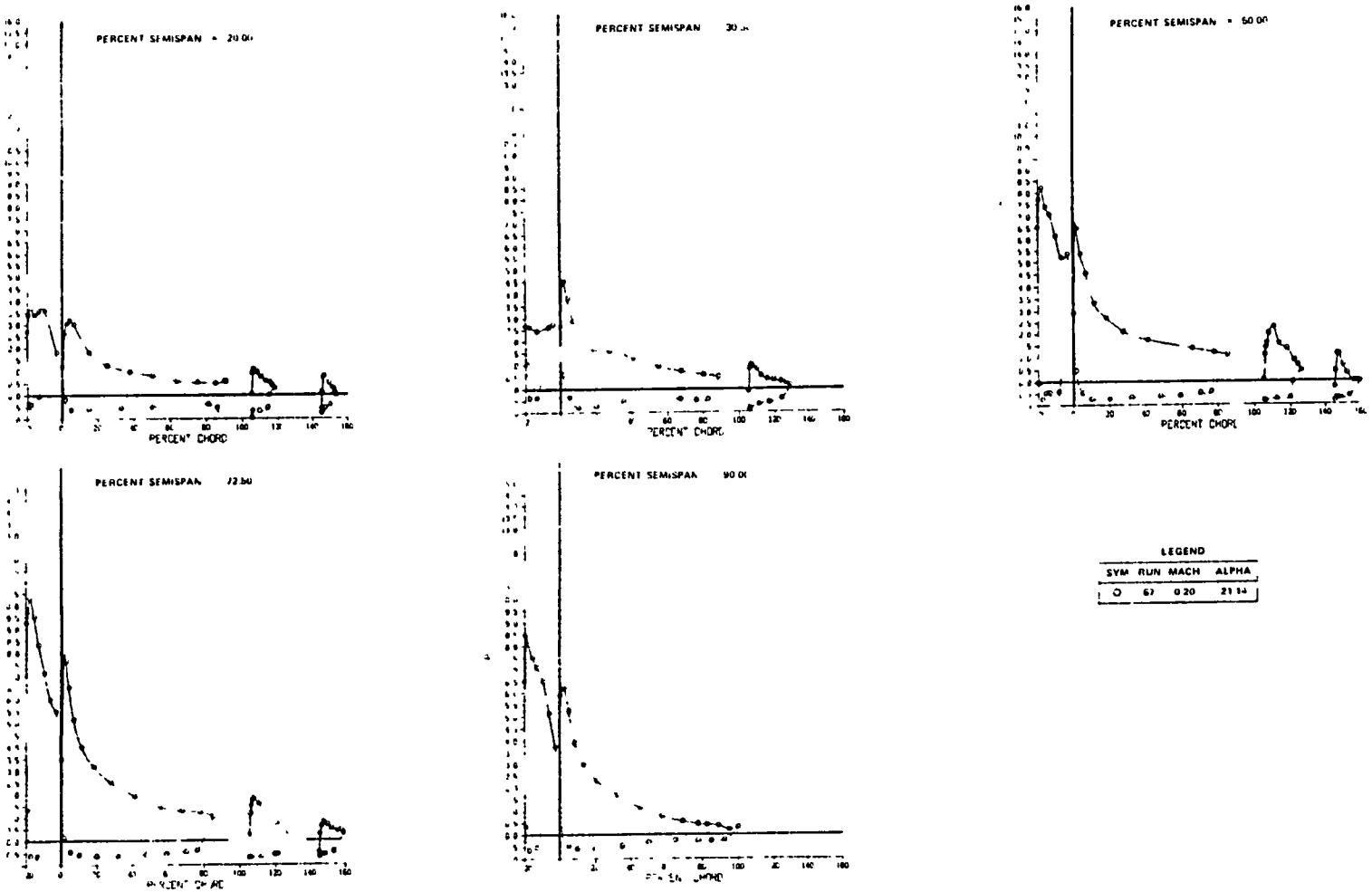

$D\ \delta_{FRP}$ = 21 14 DEG

FIGURE 21 EXPERIMENTAL CHORDWISE PRESSURE DISTRIBUTION FOR VCK WITH TWO-SEGMENT LANDING FLAPS (CONTINUED)

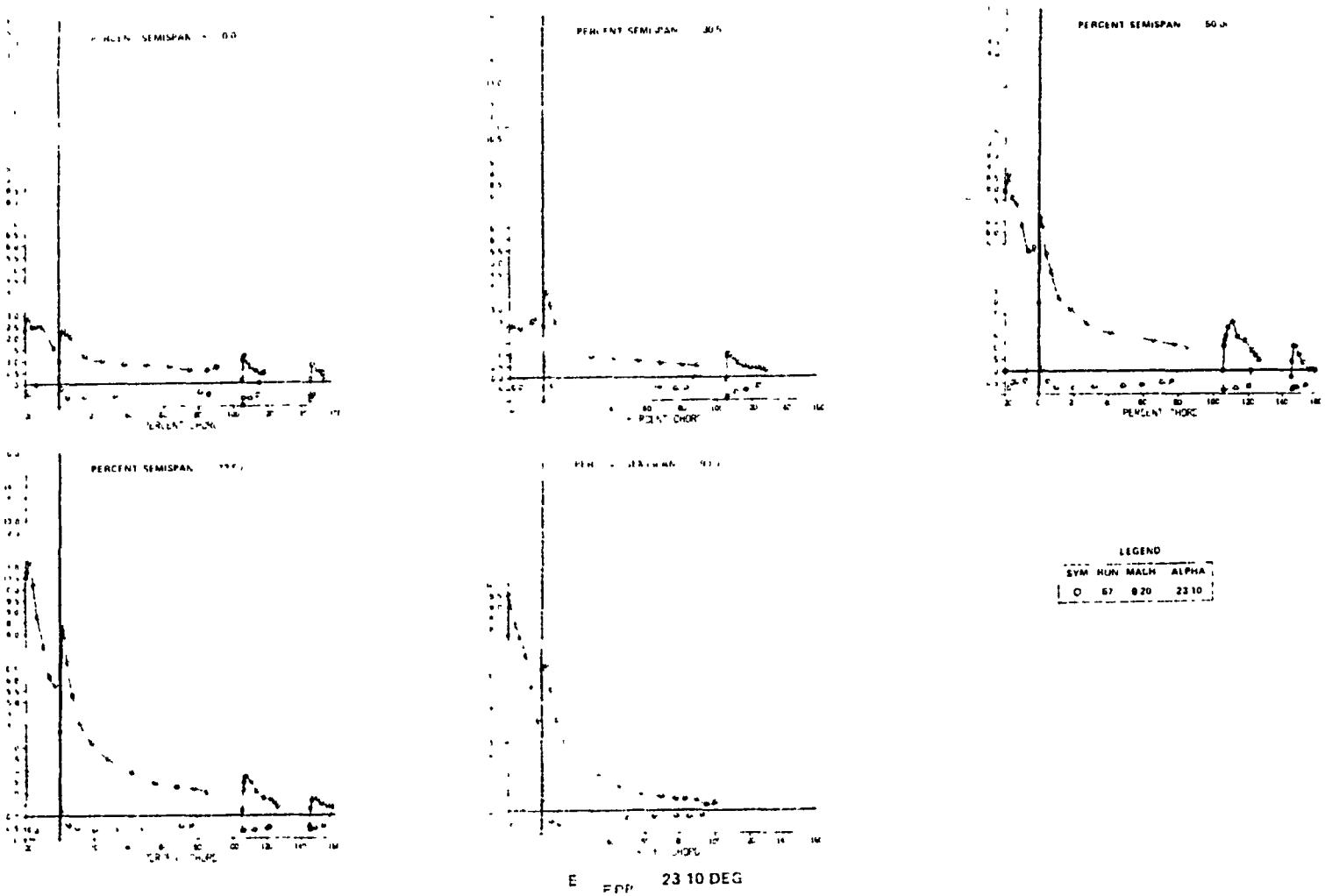

FIGURE 91 EXPERIMENTAL CHORDWISE PRESSURE DISTRIBUTION FOR VCK WITH TWO-SEGMENT LANDING FLAPS (CONTINUED)

ORIGINAL PAGE IS
OF POOR QUALITY

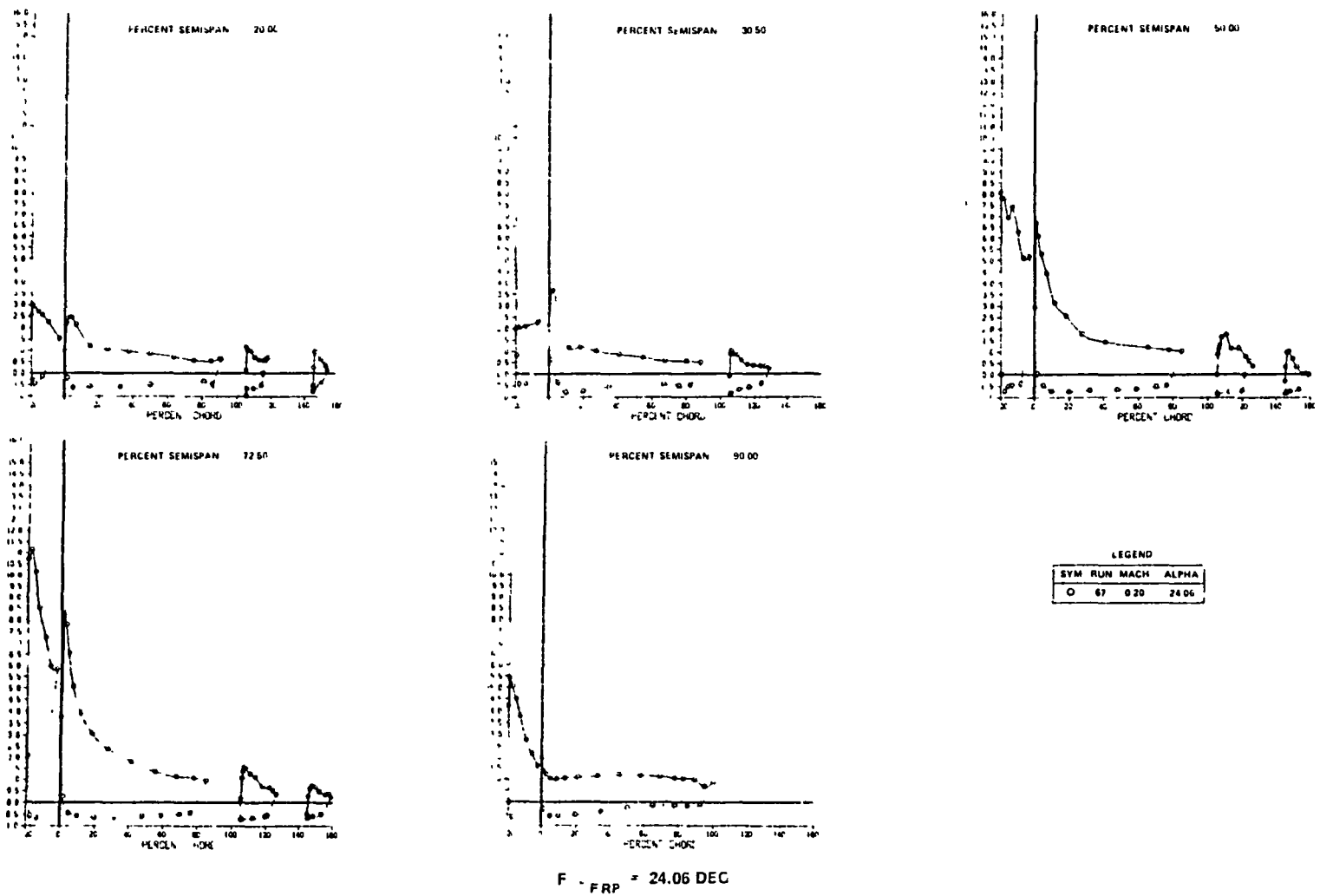

FIGURE 91. EXPERIMENTAL CHORDWISE PRESSURE DISTRIBUTION FOR VCK WITH TWO-SEGMENT LANDING FLAPS (CONCLUDED)

ORIGINAL PAGE IS
OF POOR QUALITY

OF POOR QUALITY

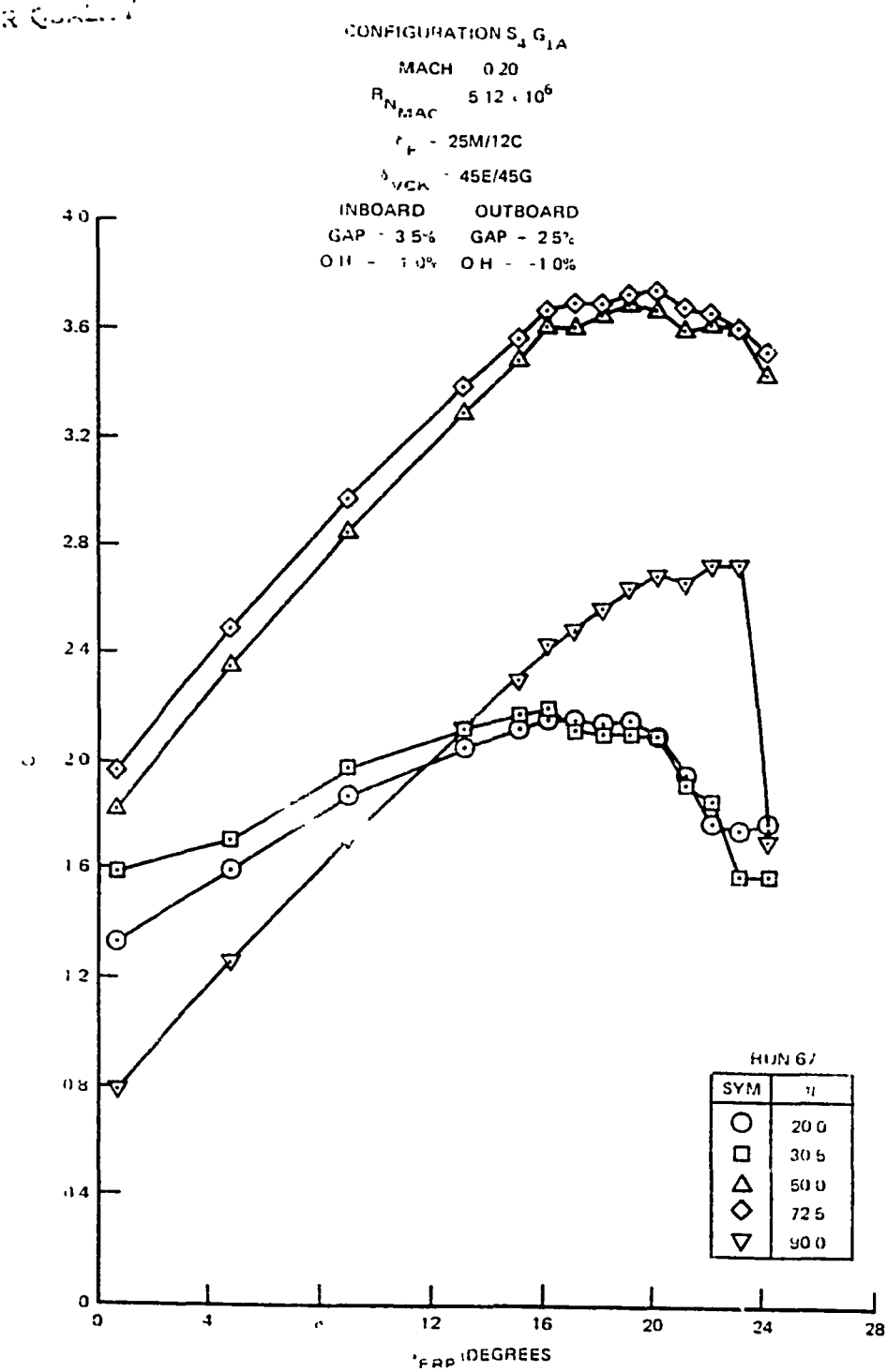

FIGURE 92. VARIATION OF SECTION LIFT COEFFICIENT FOR THE VCK WITH TWO-SEGMENT LANDING FLAPS (δ_{VCK} = 45E/45G)

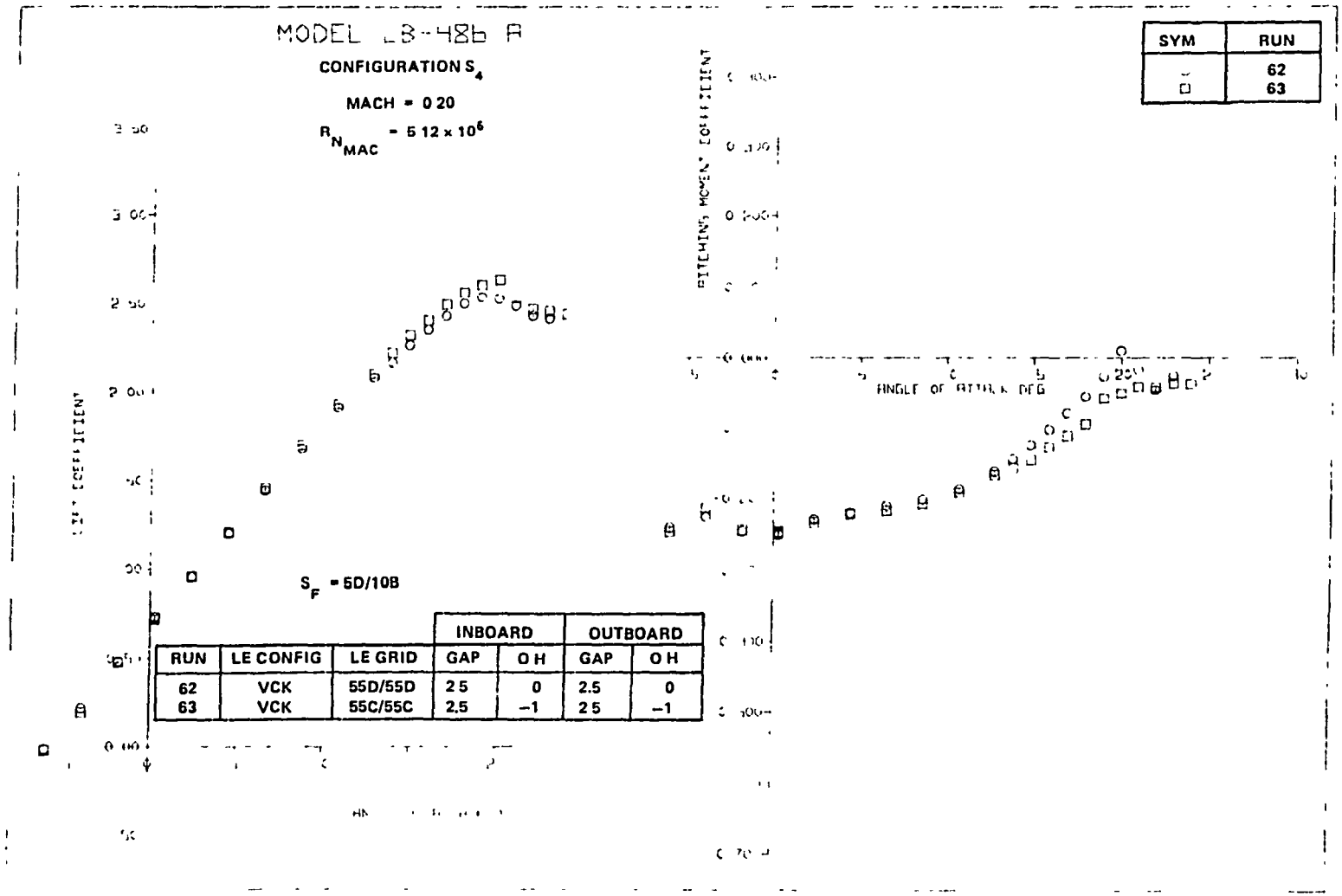

A. LIFT AND PITCHING MOMENT

FIGURE 93 VCK POSITION STUDY FOR TAKEOFF FLAPS (δ_{VCK} = 55°)

ORIGINAL PAGE IS
OF POOR QUALITY

ORIGINAL PAGE IS
OF POOR QUALITY

b. DRAG

FIGURE 93. VCK POSITION STUDY FOR TAKEOFF FLAPS ($\eta_{VCK} = 65^0$) (CONCLUDED)

ORIGINAL PAGE IS
OF POOR QUALITY

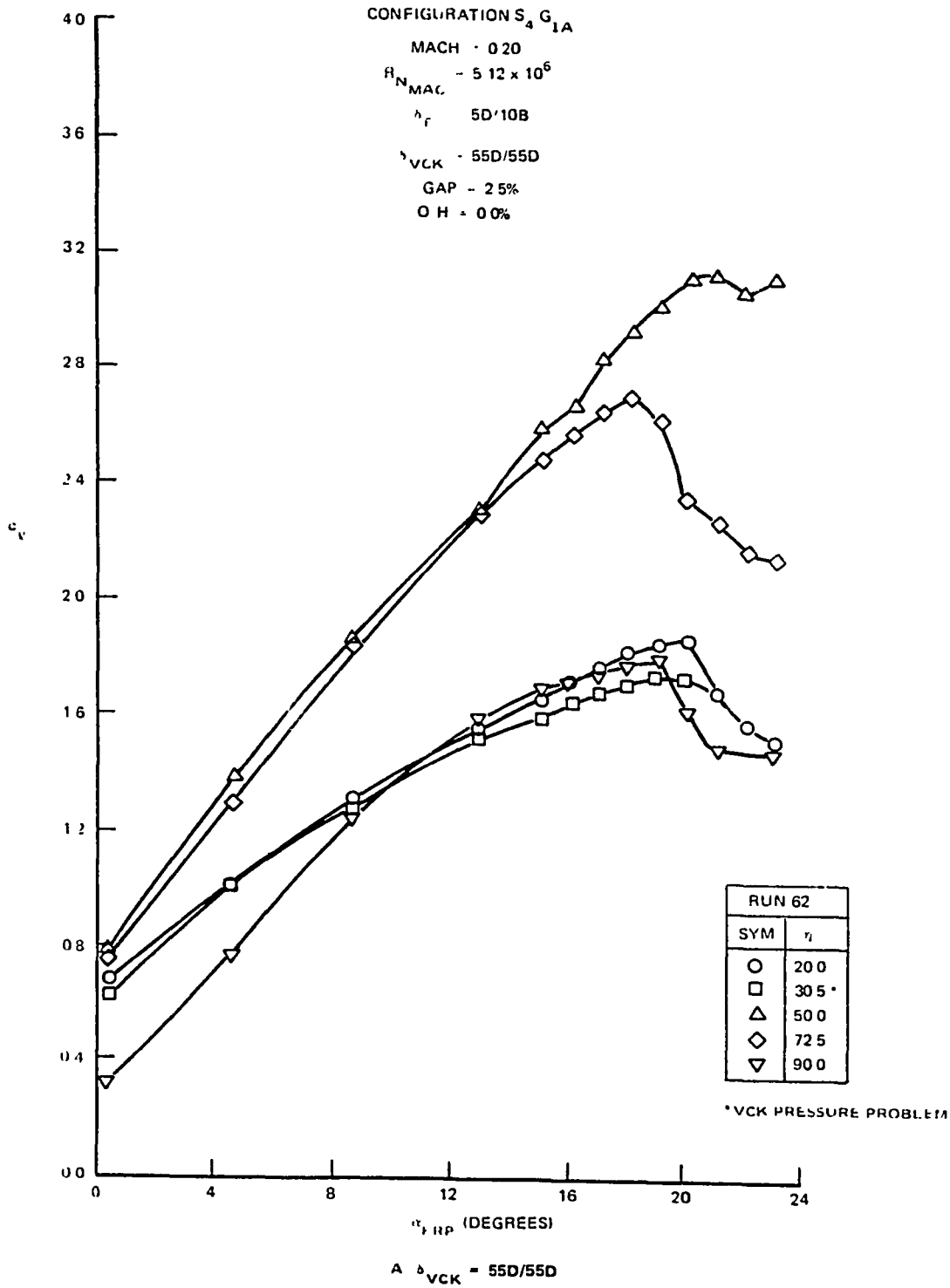

FIGURE 94. VARIATION OF SECTION LIFT COEFFICIENT FOR THE VCK WITH TWO-SEGMENT TAKEOFF FLAPS

ORIGINAL PAGE IS
OF POOR QUALITY

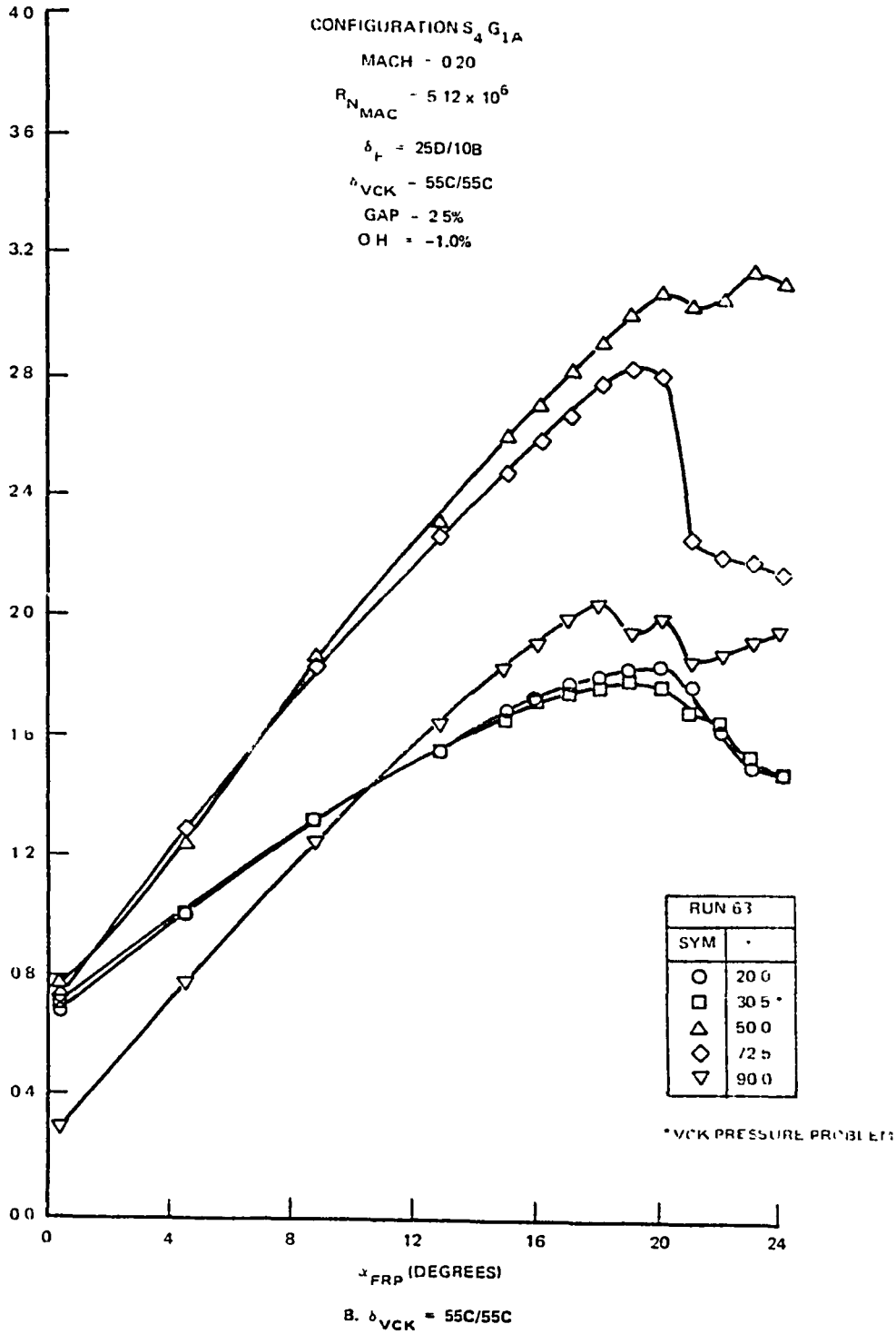

B. δ_{VCK} = 55C/55C

FIGURE 94. VARIATION OF SECTION LIFT COEFFICIENT FOR THE VCK WITH TWO-SEGMENT TAKEOFF FLAPS (CONCLUDED)

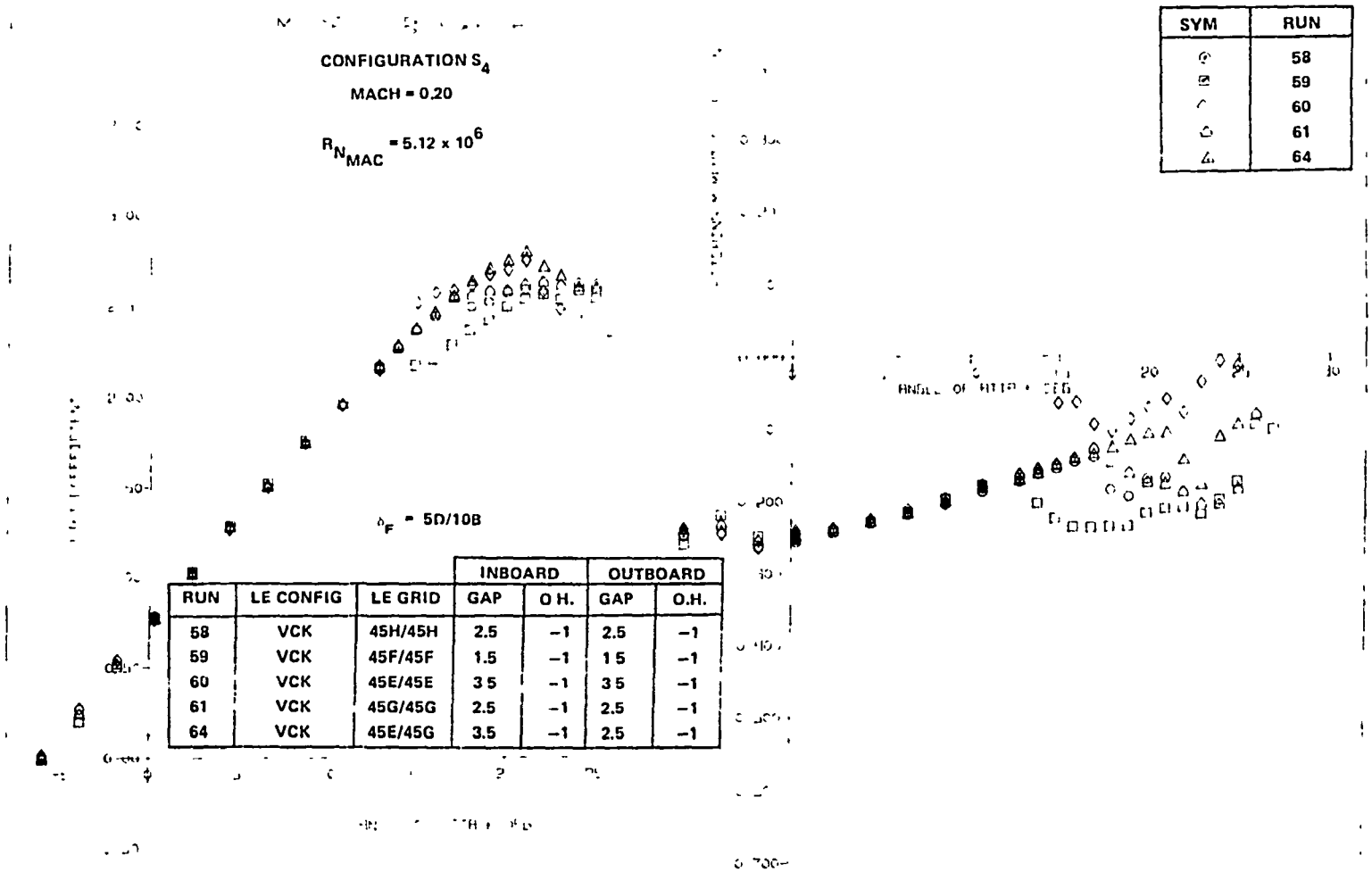

RUN	LE CONFIG	LE GRID	INBOARD GAP	INBOARD O H.	OUTBOARD GAP	OUTBOARD O.H.
58	VCK	45H/45H	2.5	−1	2.5	−1
59	VCK	45F/45F	1.5	−1	1 5	−1
60	VCK	45E/45E	3 5	−1	3 5	−1
61	VCK	45G/45G	2.5	−1	2.5	−1
64	VCK	45E/45G	3.5	−1	2.5	−1

A. LIFT AND PITCHING MOMENT

FIGURE 35. VCK POSITION STUDY FOR TAKEOFF FLAPS (δ_{VCK} = 45°)

ORIGINAL PAGE IS
OF POOR QUALITY

ORIGINAL PAGE IS
OF POOR QUALITY

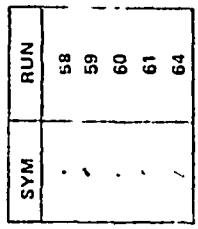

FIGURE 95. VCK POSITION STUDY FOR TAKEOFF FLAPS (δ_{VCK} = 45°) (CONCLUDED)

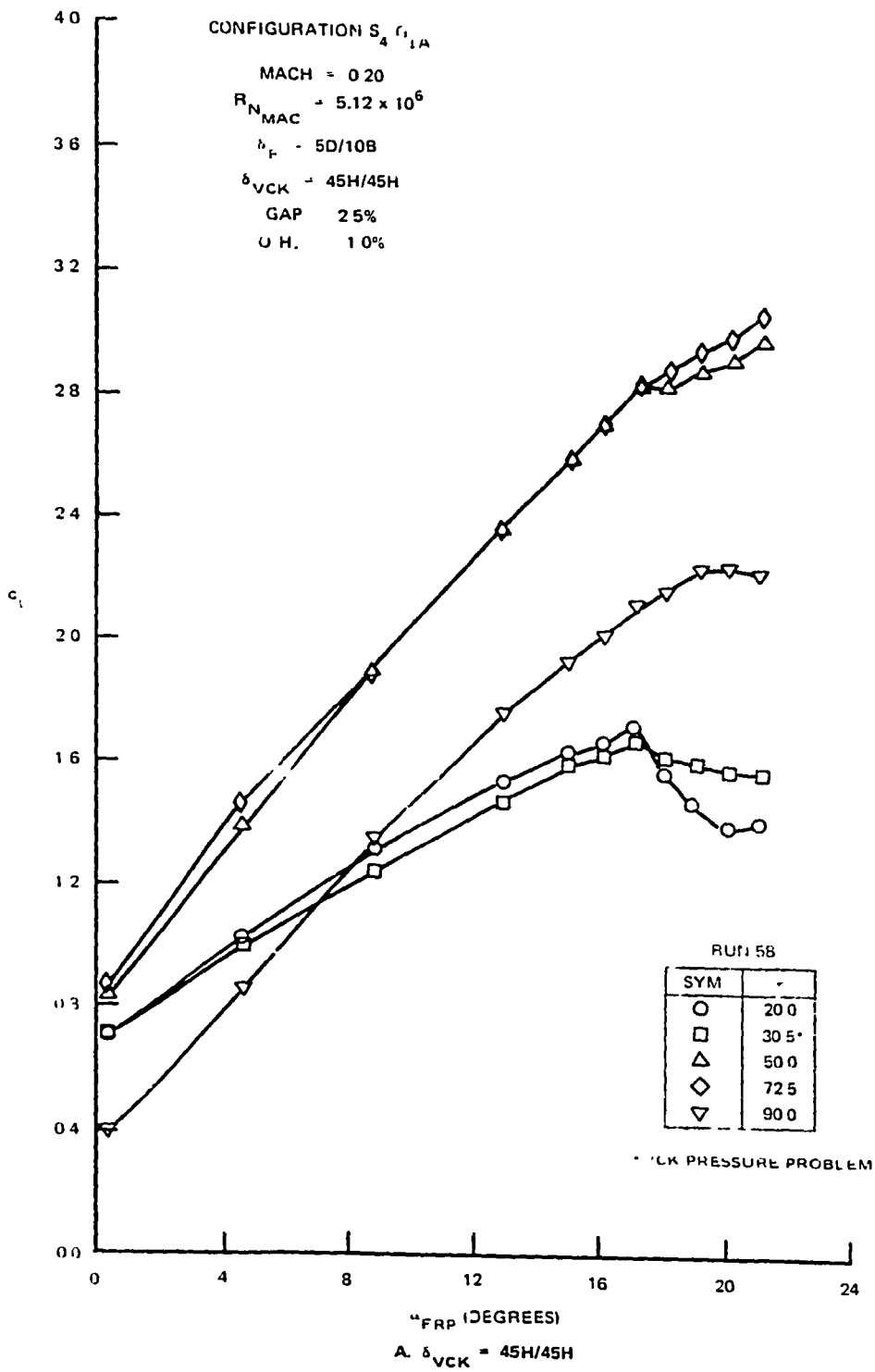

FIGURE 96. VARIATION OF SECTION LIFT COEFFICIENT FOR THE VCK WITH TWO-SEGMENT TAKEOFF FLAPS

ORIGI
OF POO

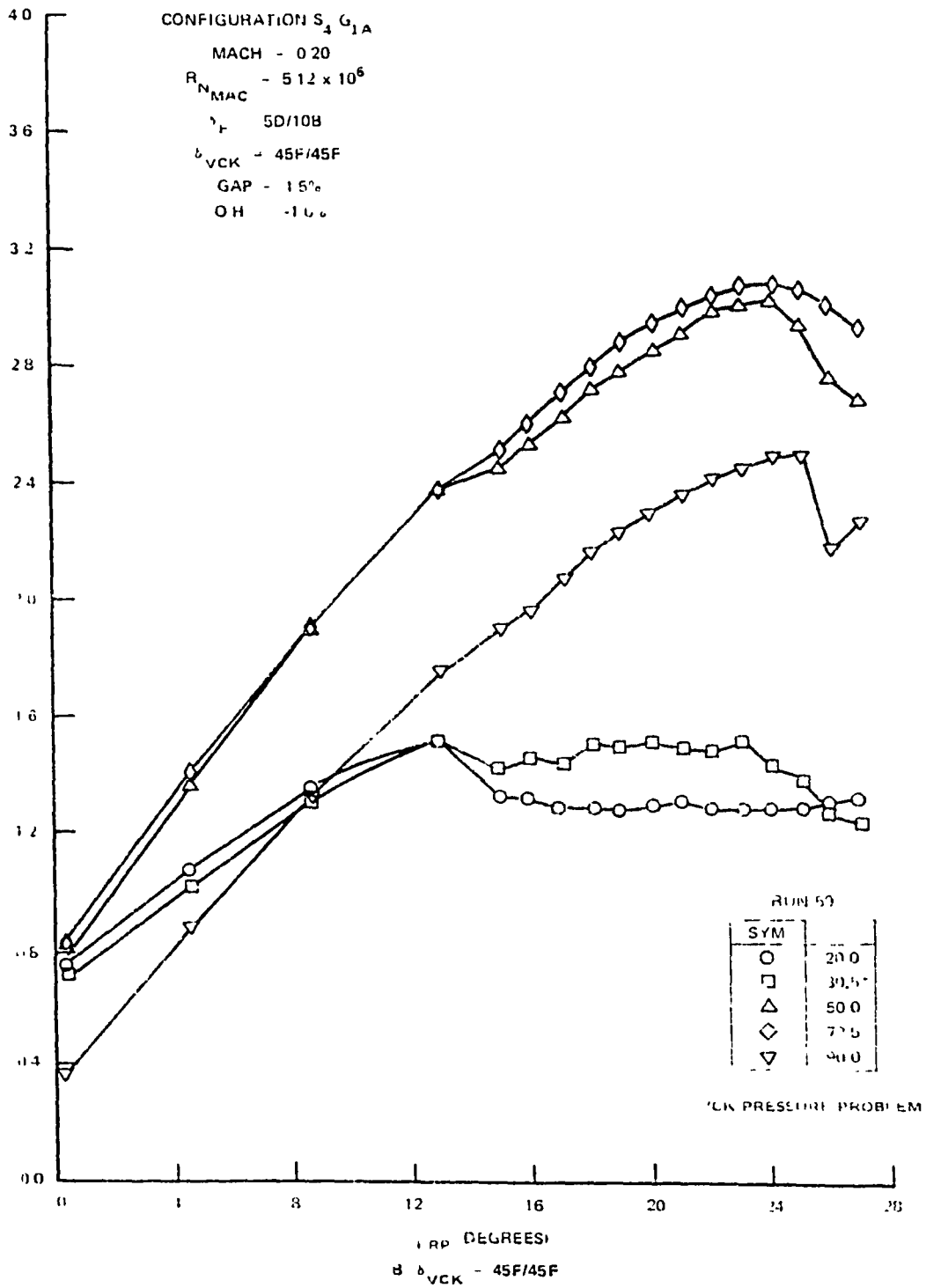

FIGURE 96. VARIATION OF SECTION LIFT COEFFICIENT FOR THE VCK WITH TWO-SEGMENT TAKEOFF FLAPS (CONTINUED)

ORIGINAL PAGE IS
OF POOR QUALITY

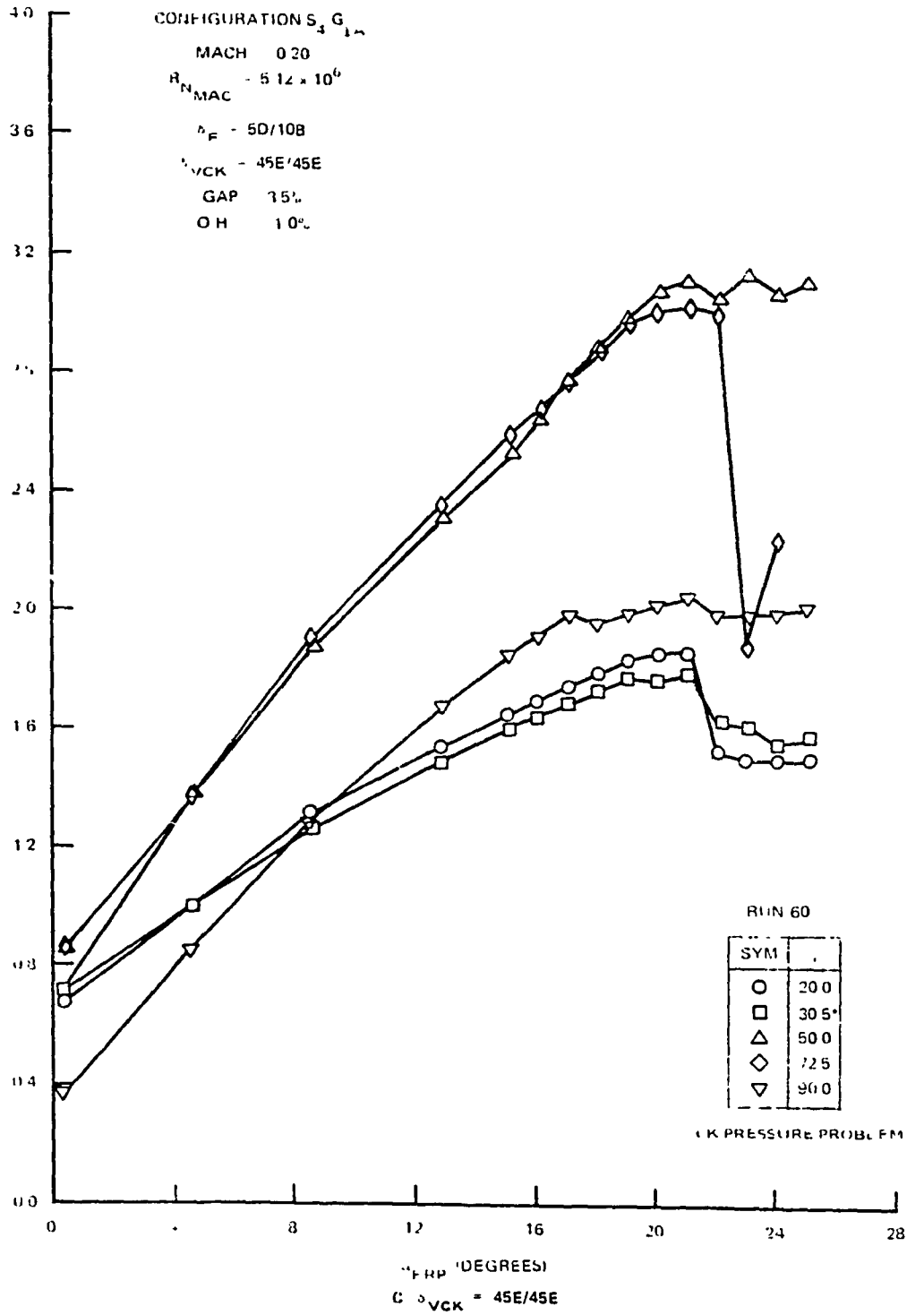

FIGURE 96 VARIATION OF SECTION LIFT COEFFICIENT FOR THE VCK WITH TWO-SEGMENT TAKEOFF FLAPS (CONTINUED)

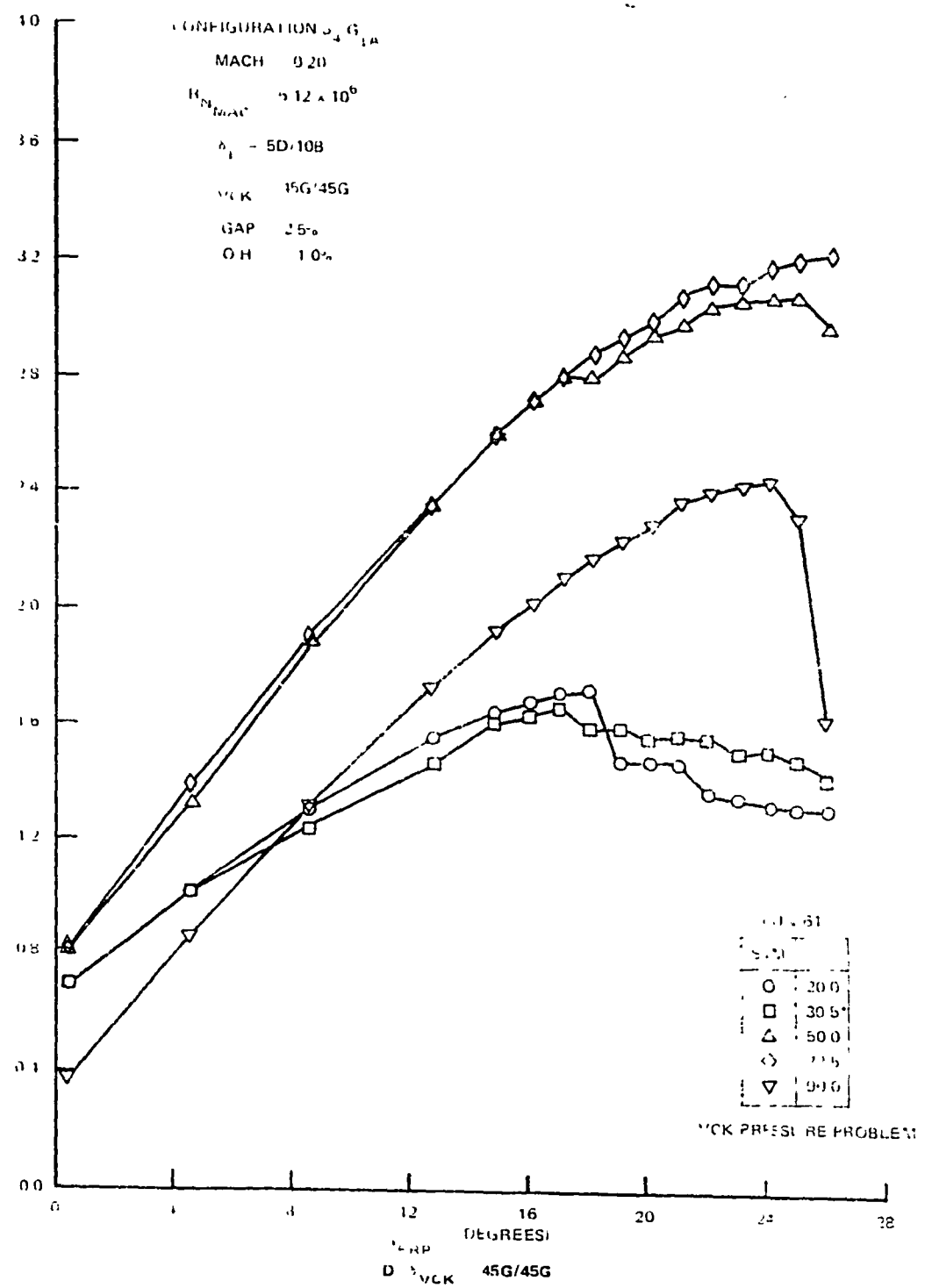

FIGURE 96. VARIATION OF SECTION LIFT COEFFICIENT FOR THE VCK WITH TWO SEGMENT TAKEOFF FLAPS (CONCLUDED)

ORIGINAL PAGE IS

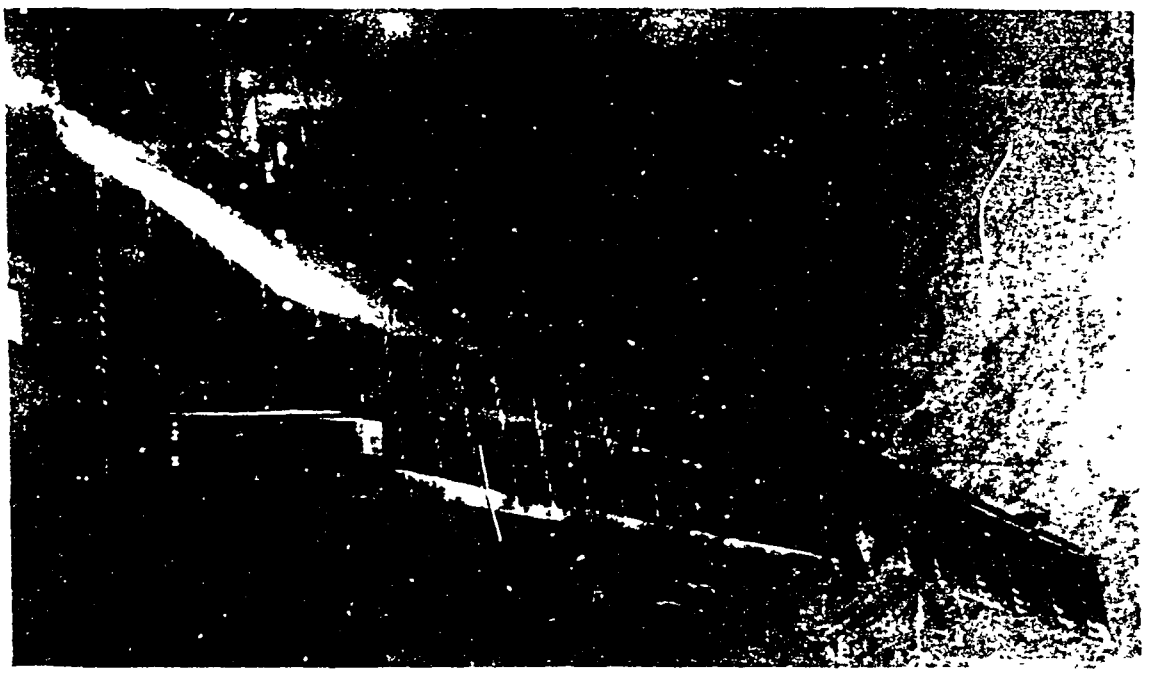

A. α_{FRP} = 21.05 ($C_{L_{MAX}}$) DEGREES

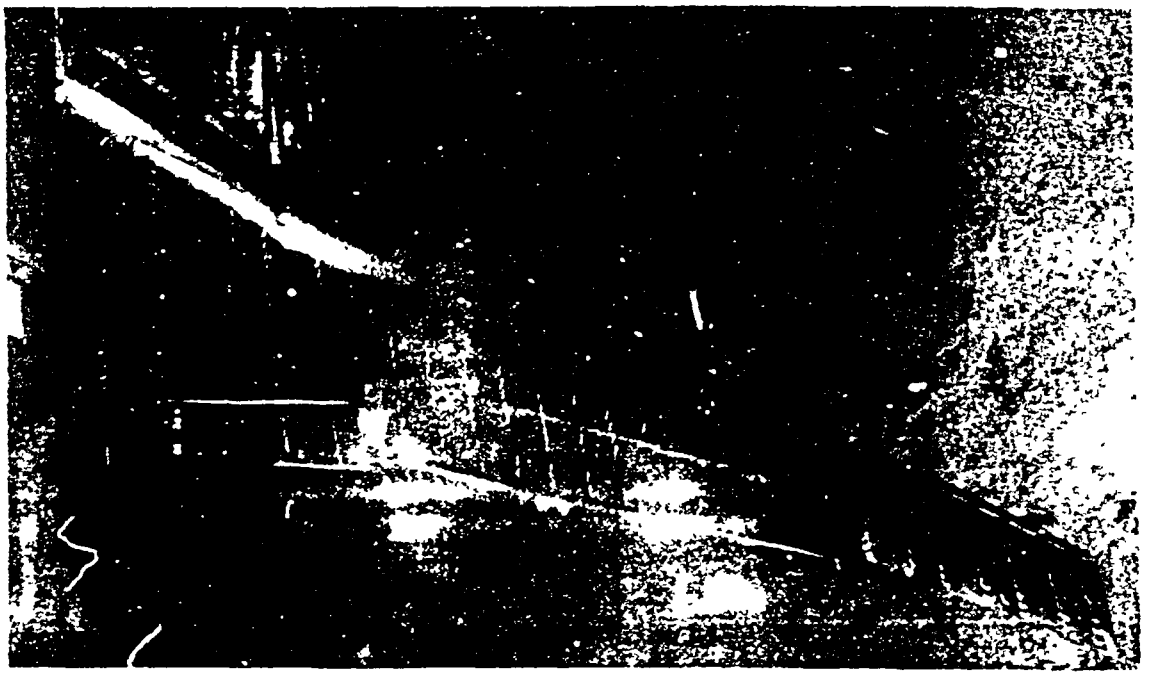

B. α_{FRP} = 23.00 DEGREES

FIGURE 97. MINI-TUFT PHOTOS FOR VCK WITH TWO-SEGMENT TAKEOFF FLAPS

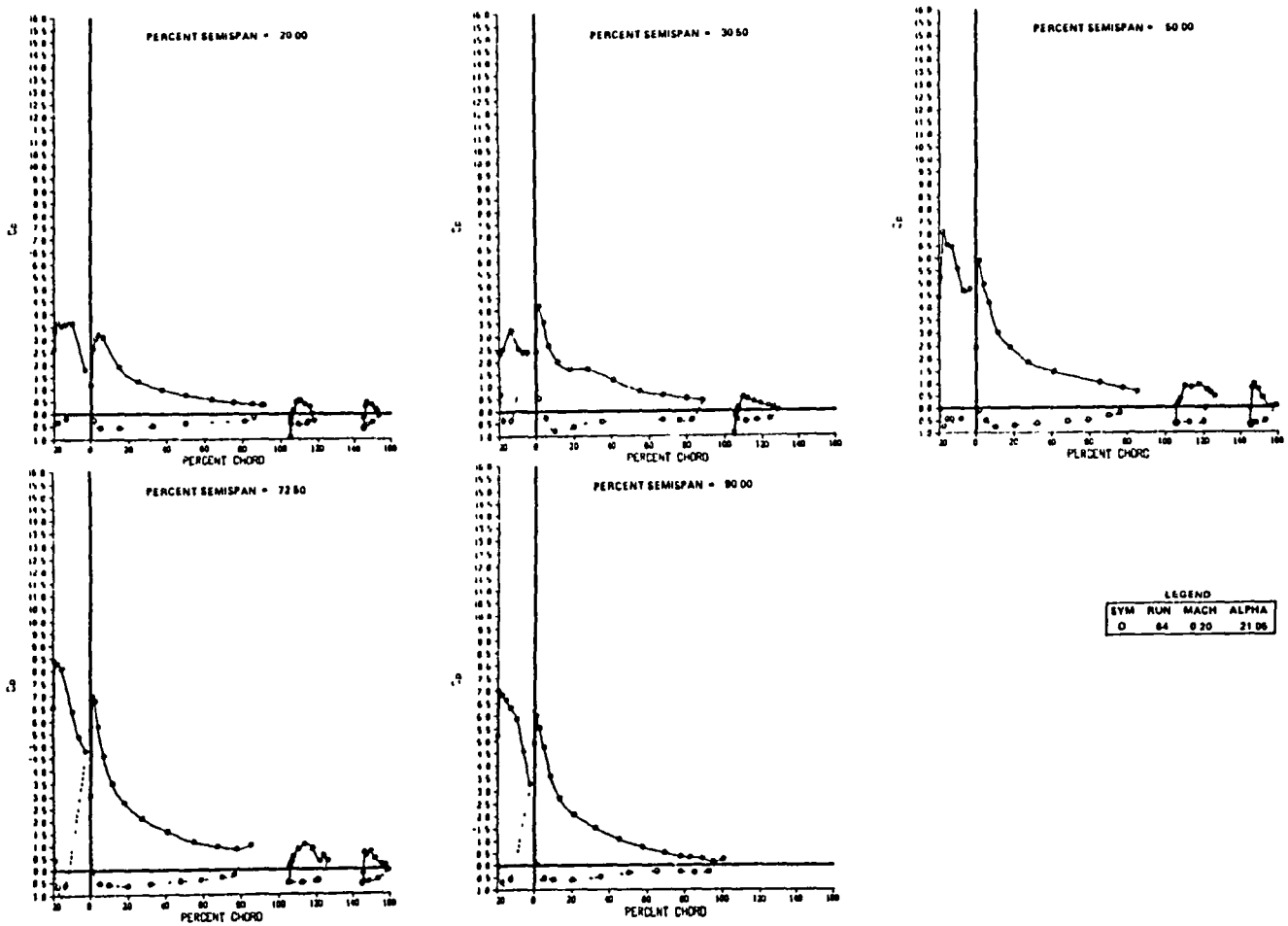

A. α_{FRP} = 21.05 DEG

FIGURE 98. EXPERIMENTAL CHORDWISE PRESSURE DISTRIBUTION FOR VCK WITH TWO-SEGMENT TAKEOFF FLAPS

ORIGINAL PAGE IS
OF POOR QUALITY

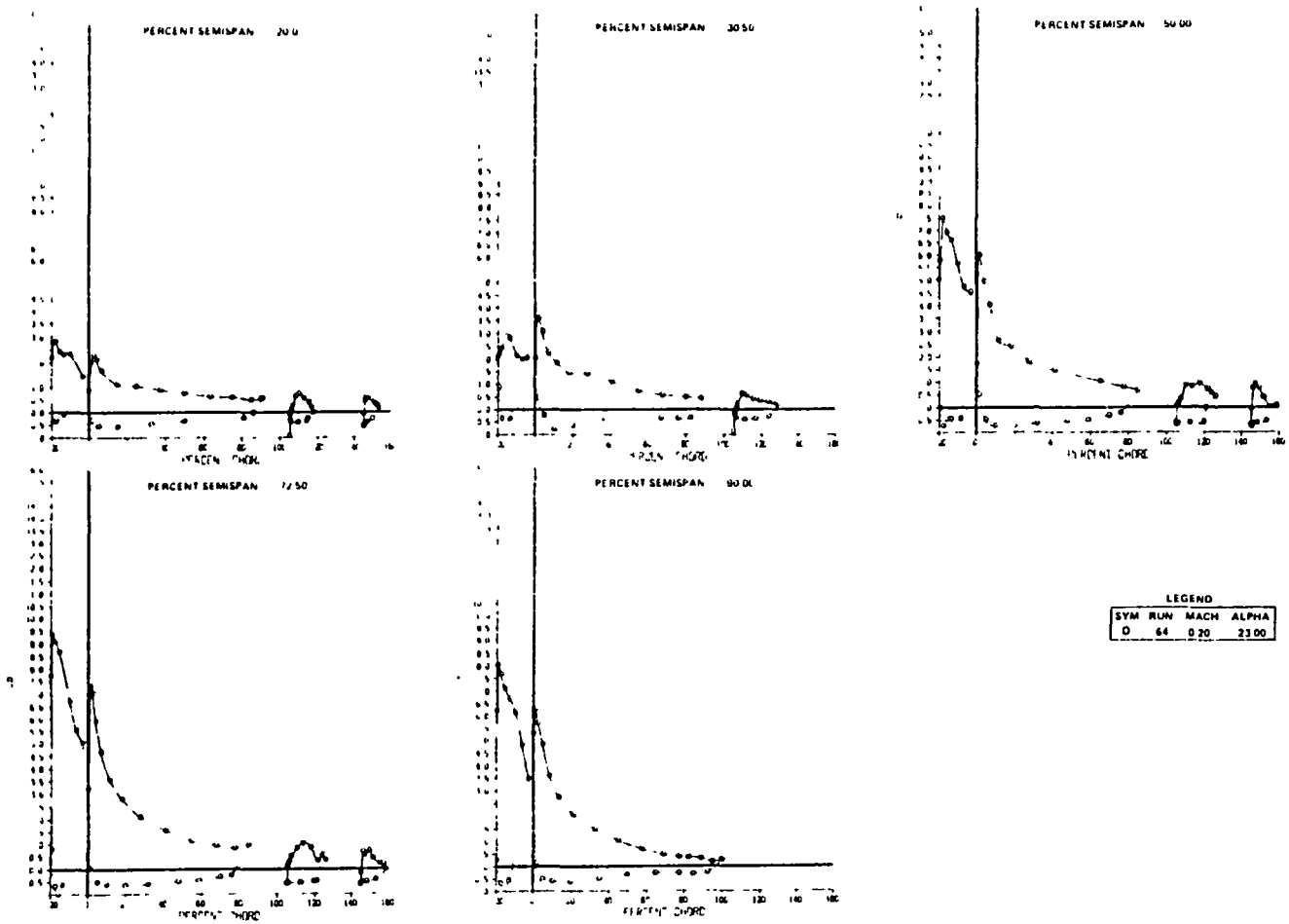

B_{FRP} - 23.00 DEG

FIGURE 98. EXPERIMENTAL CHORDWISE PRESSURE DISTRIBUTION FOR VCK WITH TWO-SEGMENT TAKEOFF FLAPS (CONCLUDED)

ORIGINAL PAGE IS
OF POOR QUALITY

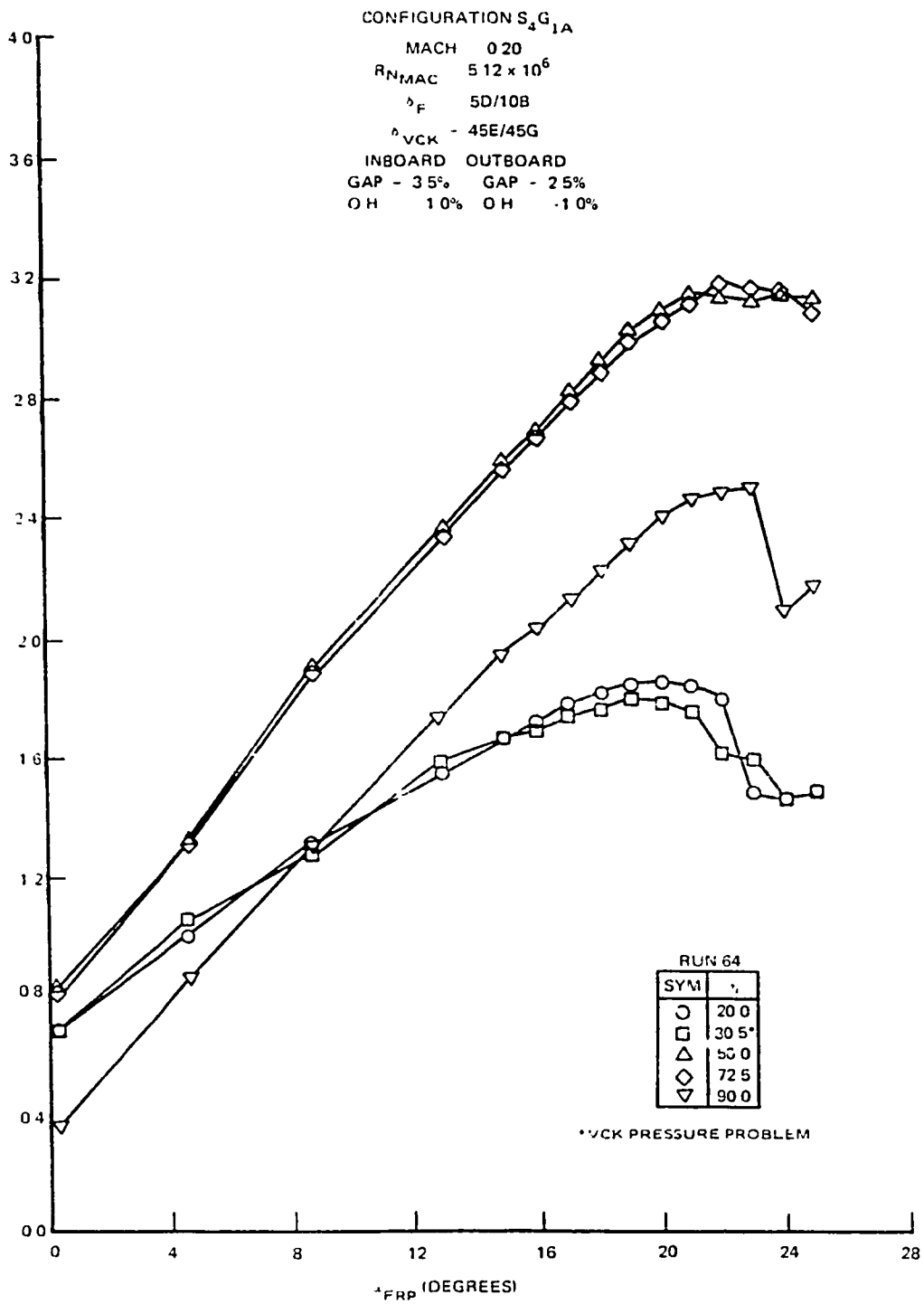

FIGURE 99 VARIATION OF SECTION LIFT COEFFICIENT FOR THE VCK WITH TWO-SEGMENT TAKEOFF FLAPS (δ_{VCK} = 45E/45G)

Two-Segment Landing and Takeoff Flap Optimization. - This was accomplished with the 45E/45G VCK position. Figures 100 through 103 present the results of the landing flap main and aft flap optimization. The data indicate, for most main flap position studies, small changes in the aerodynamic characteristics. The main flap position survey was tested first, followed by the aft flap deflection survey with the best main flap position.

For 25° of main flap deflection the 25K/12C configuration was selected as the best configuration from the standpoint of $C_{L_{MAX}}$, L/D at 1.3 V_S, and pitching moment characteristics. In Figure 102, for a flap deflection of 35R/12C, a reduction of flaperon deflection from 35° to 25° resulted in a small decrease in $C_{L_{MAX}}$, similar pitch characteristics, and decreased drag. This configuration would mechanically be very complex. 35R/12C was selected as the best compromise for this main flap deflection.

Analysis of the data for the main and aft flap survey for the 15-degree main flap (Figures 104 and 105) resulted in the selection of 15H/10B. For five degrees main flap deflection, the selected configuration was 5C/10B (see Figure 106 and 107).

VCK Span and Nacelle/Pylon Effects. - The effects of VCK span and nacelle/pylon for landing and takeoff two-segment flap deflections are shown in Figures 108 and 109. The data indicates that a $C_{L_{MAX}}$ of 3.396 was obtained for the full span VCK (nacelles and pylons off). Addition of the nacelles, pylons, and strakes, for the landing flap deflection (Figure 108) results in a positive increment in pitching moment and a small reduction in $C_{L_{MAX}}$. The pitch trends at angles of attack greater than 22 degrees are similar, but at a different level. Removal of the over-the-pylon-VCK extension (L_{6A}) resulted in a reduction in $C_{L_{MAX}}$ and improved high angle of attack pitch characteristics. Removing the fuselage seal VCK extension (L_{5A}) yielded a slight reduction in $C_{L_{MAX}}$ and a further improvement in the basic pitch characteristics. Other than the drag increase due to the nacelle/pylon and strakes the effect of VCK span was small (maximum difference in L/D at 1.3 V_S being 0.14 in L/D). A similar comparison for the takeoff flap configuration is shown in Figure 109. The reduction in $C_{L_{MAX}}$ is even larger at this flap setting. Drag comparisons (L/D at 1.2 V_S) indicated small differences due to the reduction in VCK span extent. Again, the pitch characteristics are improved with the basic VCK span extent.

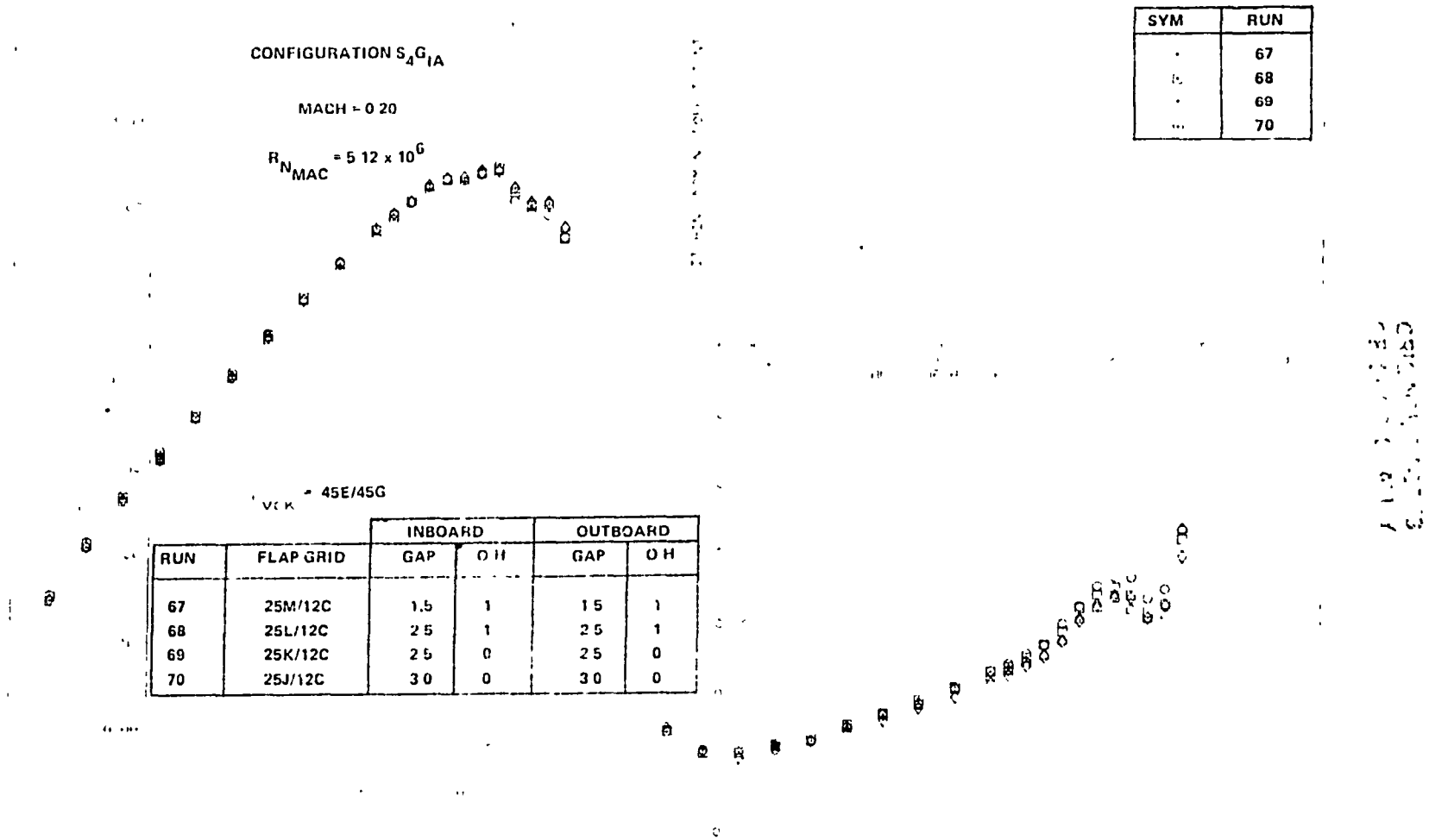

RUN	FLAP GRID	INBOARD GAP	INBOARD O H	OUTBOARD GAP	OUTBOARD O H
67	25M/12C	1.5	1	1 5	1
68	25L/12C	2 5	1	2 5	1
69	25K/12C	2 5	0	2 5	0
70	25J/12C	3 0	0	3 0	0

A LIFT AND PITCHING MOMENT

FIGURE 100 MAIN FLAP POSITION STUDY FOR TWO SEGMENT LANDING FLAPS WITH VCK

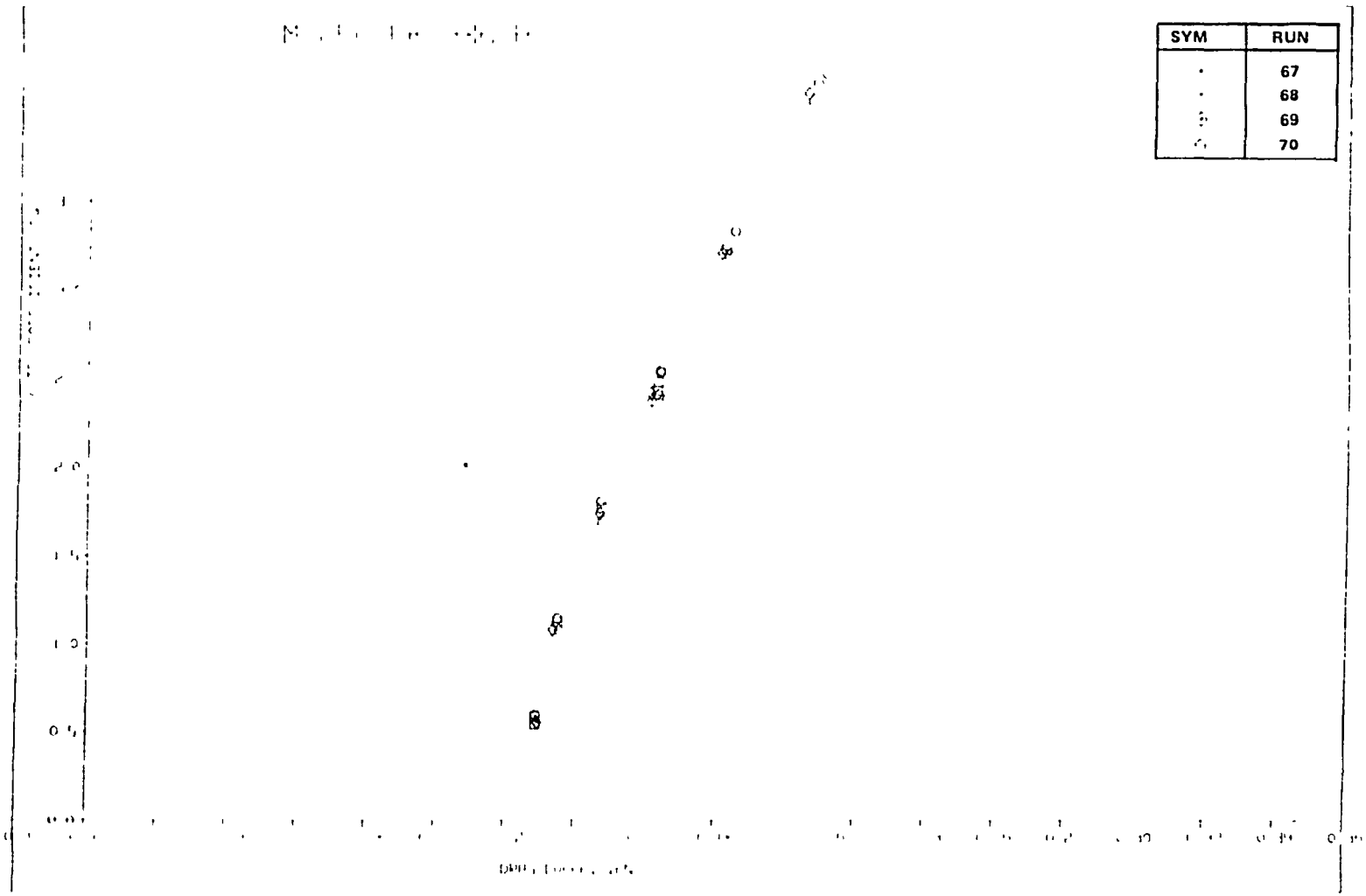

B. DRAG

FIGURE 100. MAIN FLAP POSITION STUDY FOR TWO-SEGMENT LANDING FLAPS WITH VCK (CONCLUDED)

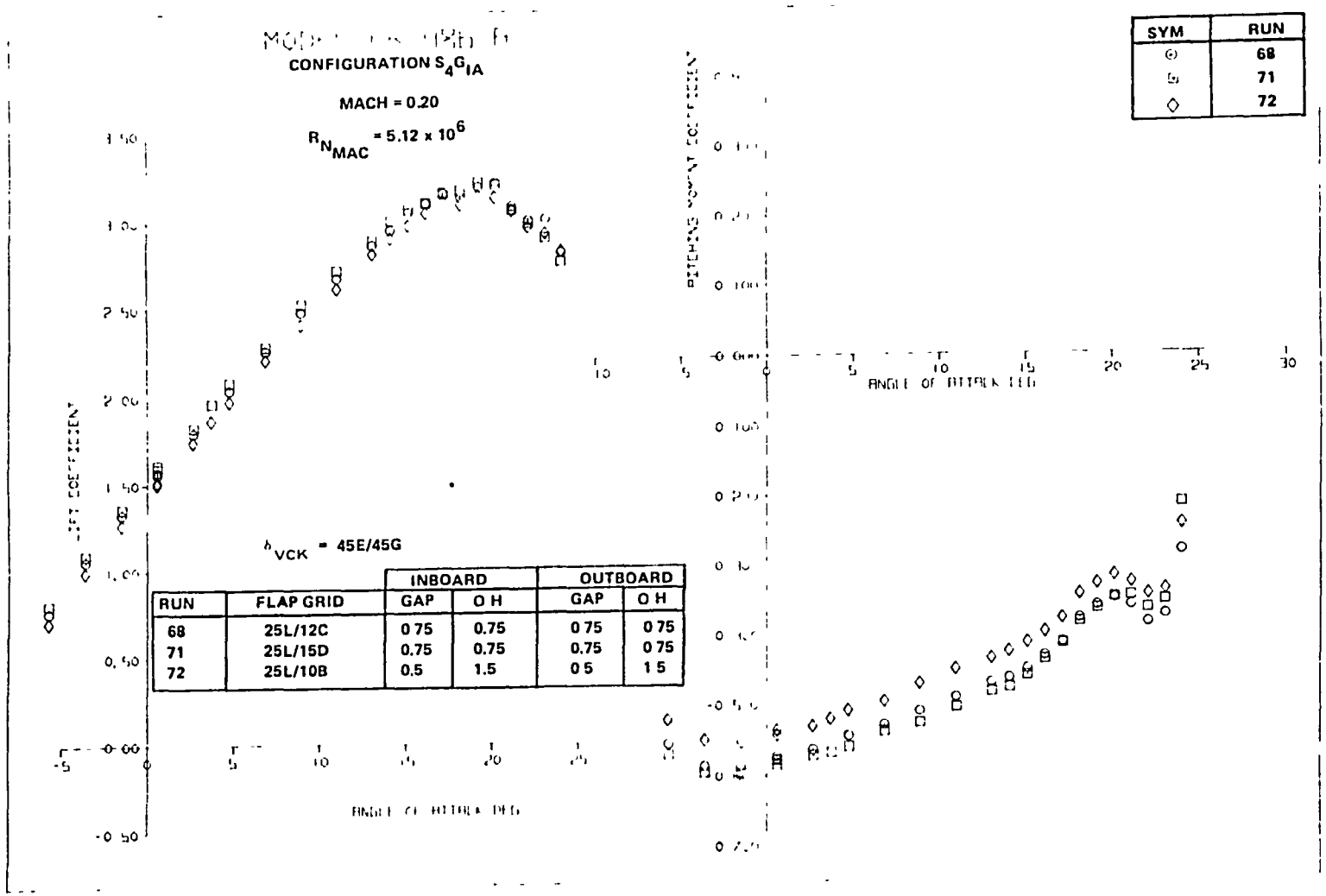

SYM	RUN
○	68
□	71
◇	72

RUN	FLAP GRID	INBOARD		OUTBOARD	
		GAP	O H	GAP	O H
68	25L/12C	0 75	0.75	0 75	0 75
71	25L/15D	0.75	0.75	0.75	0 75
72	25L/10B	0.5	1.5	0 5	1 5

A. LIFT AND PITCHING MOMENT

FIGURE 101. AFT FLAP DEFLECTION STUDY FOR TWO-SEGMENT LANDING FLAPS WITH VCK

ORIGINAL PAGE IS
OF POOR QUALITY

ORIGINAL PAGE IS
OF POOR QUALITY

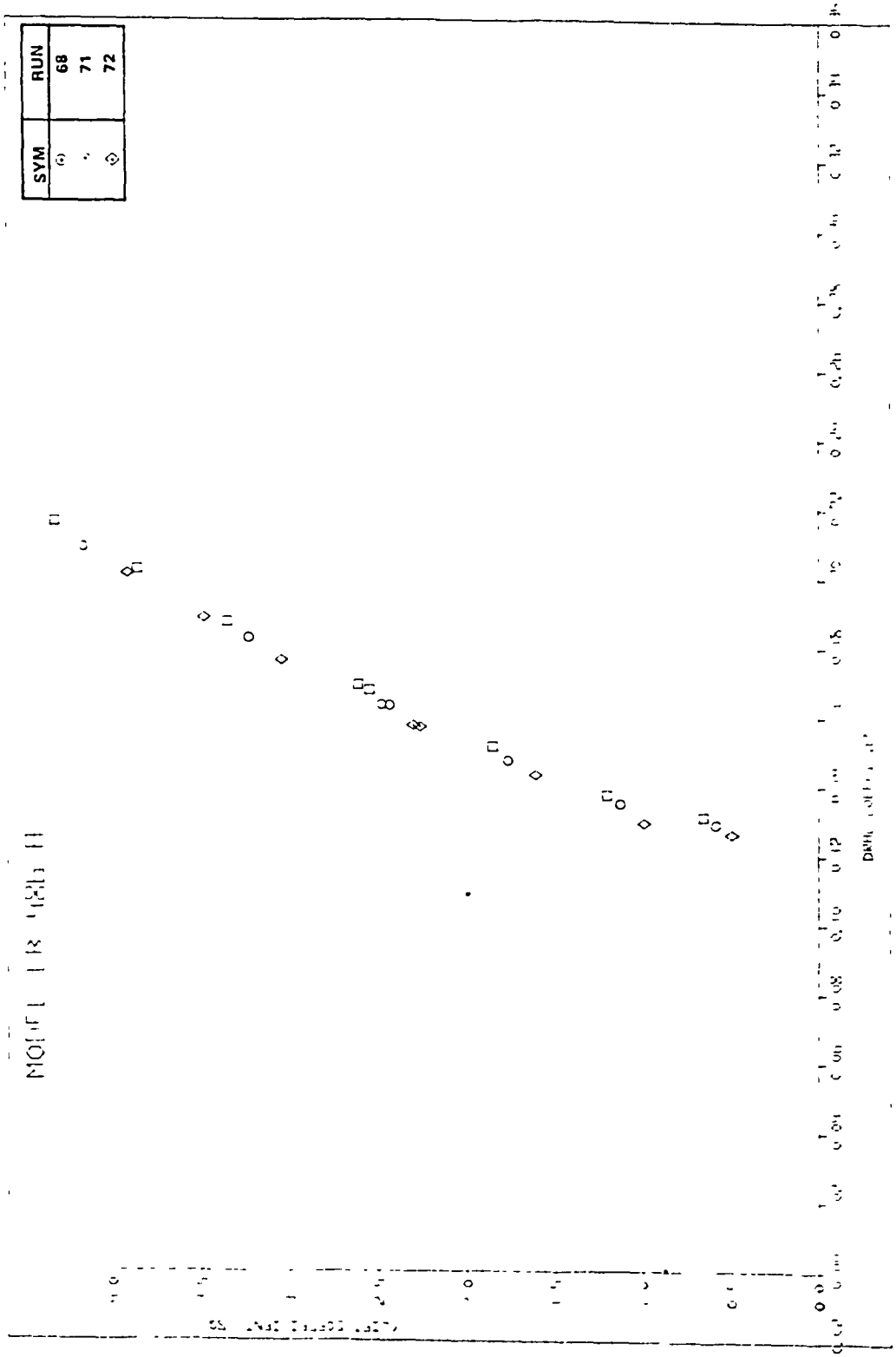

B. DRAG

FIGURE 101. AFT FLAP DEFLECTION STUDY FOR TWO-SEGMENT LANDING FLAPS WITH VCK (CONCLUDED)

ORIGINAL PAGE IS
OF POOR QUALITY

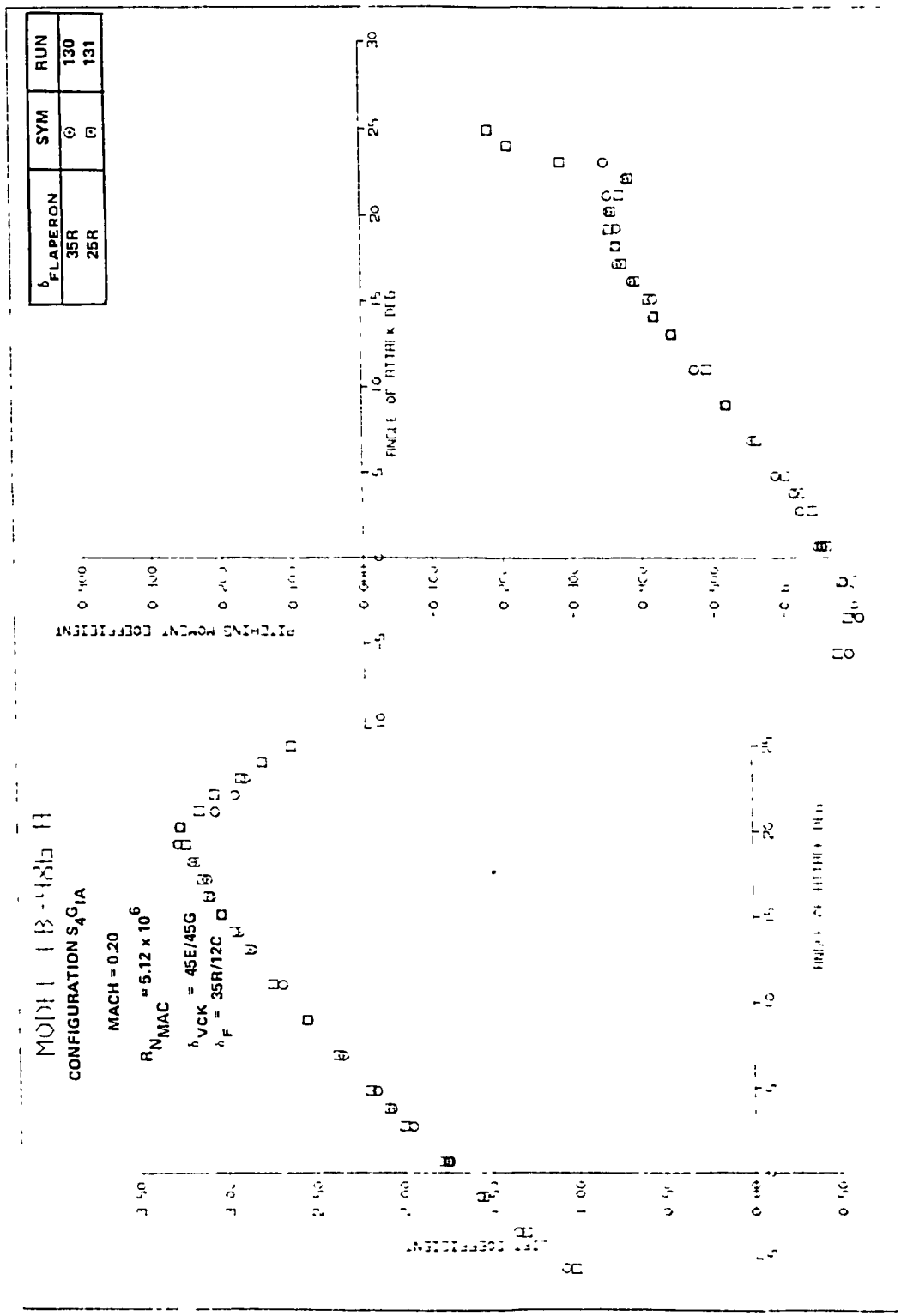

A. LIFT AND PITCHING MOMENT

FIGURE 102. FLAPERON DEFLECTION STUDY FOR TWO-SEGMENT LANDING FLAPS

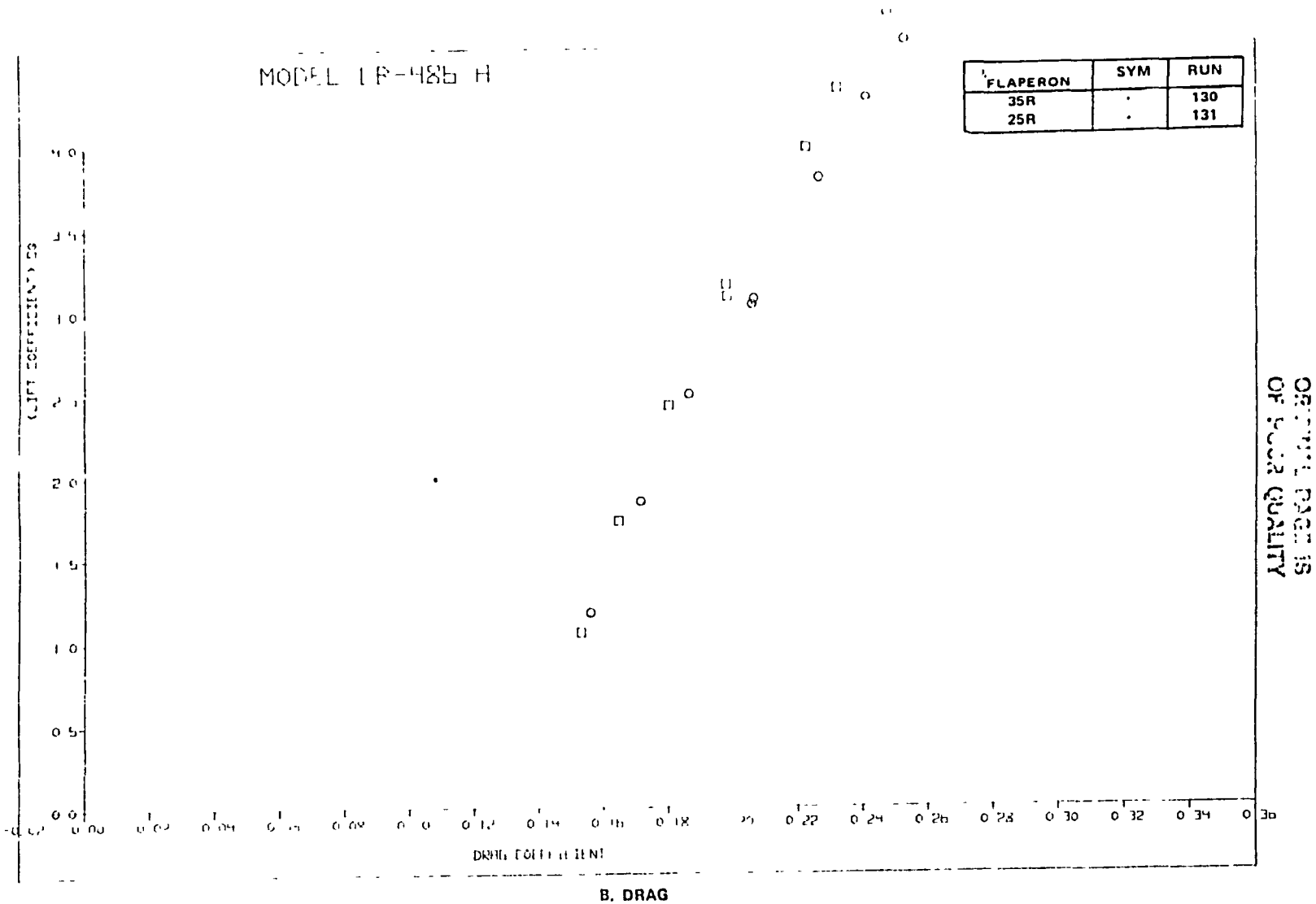

B. DRAG

FIGURE 102. FLAPERON DEFLECTION STUDY FOR TWO-SEGMENT LANDING FLAPS (CONCLUDED)

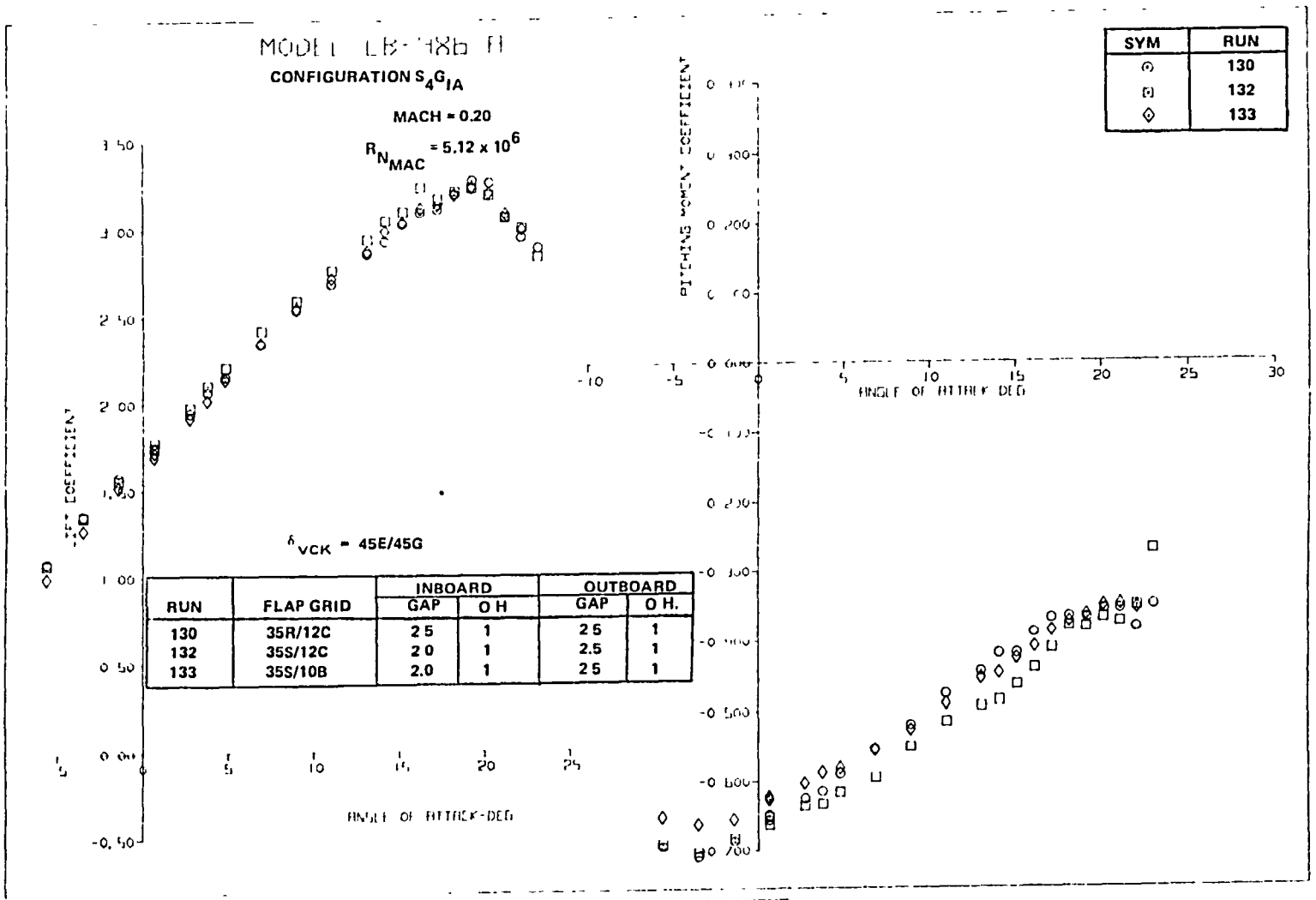

A. LIFT AND PITCHING MOMENT

FIGURE 103. MAIN FLAP POSITION AND AFT FLAP DEFLECTION STUDIES FOR TWO-SEGMENT FLAPS WITH VCK

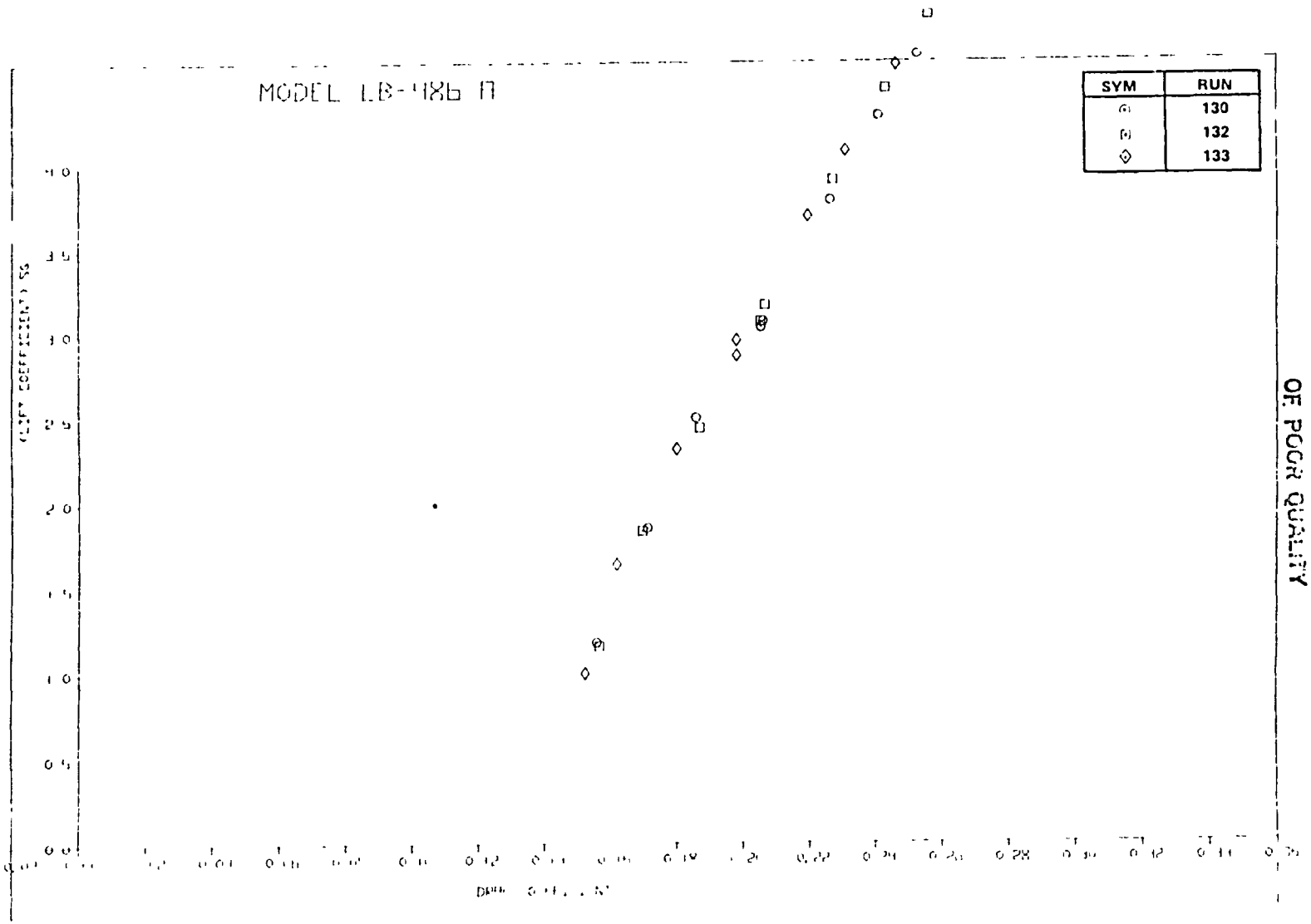

B DRAG

FIGURE 103. MAIN FLAP POSITION AND AFT FLAP DEFLECTION STUDIES FOR TWO-SEGMENT FLAPS WITH VCK (CONCLUDED)

OF POOR QUALITY

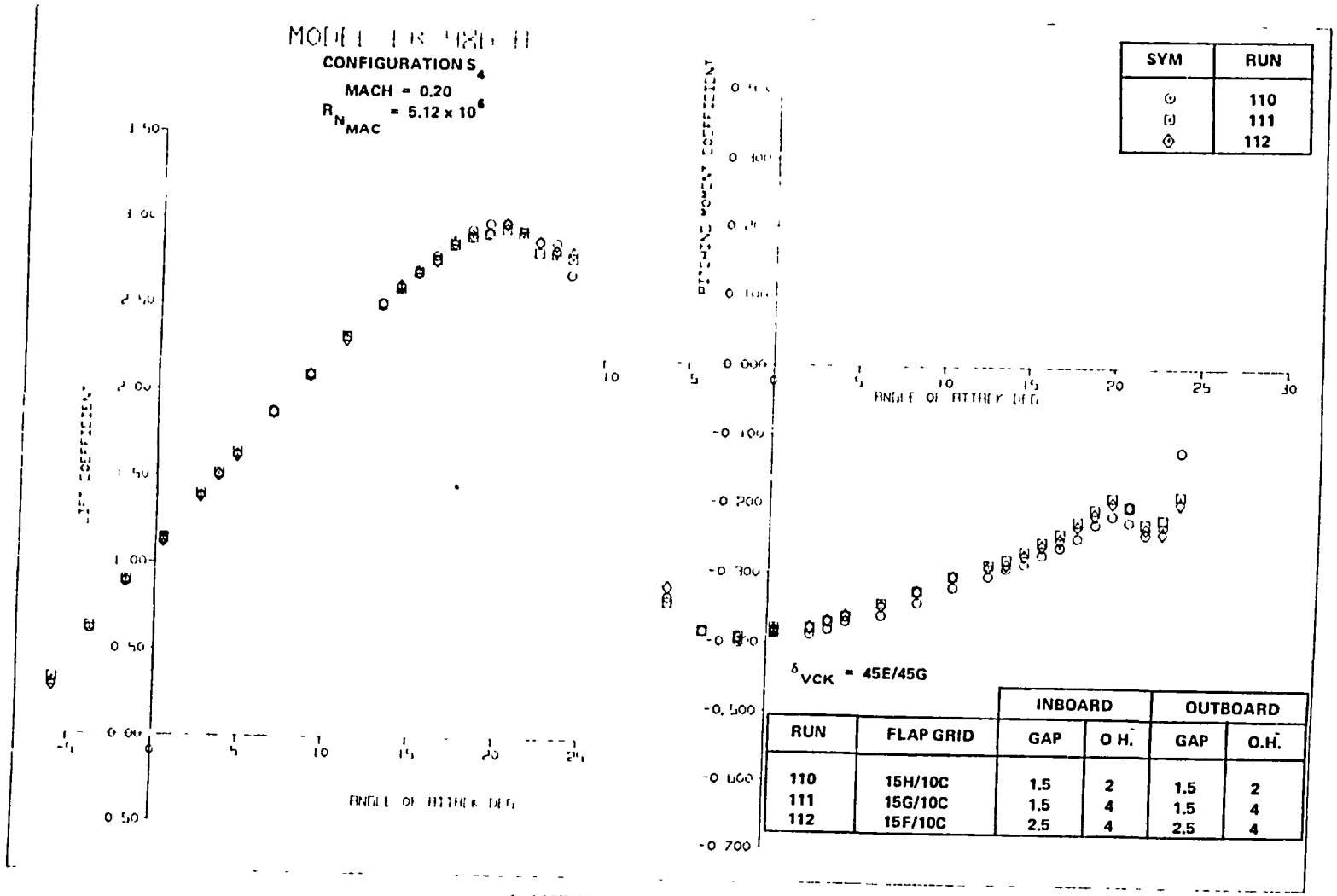

A. LIFT AND PITCHING MOMENT

FIGURE 104. MAIN FLAP POSITION STUDY FOR TWO-SEGMENT TAKEOFF FLAPS WITH VCK

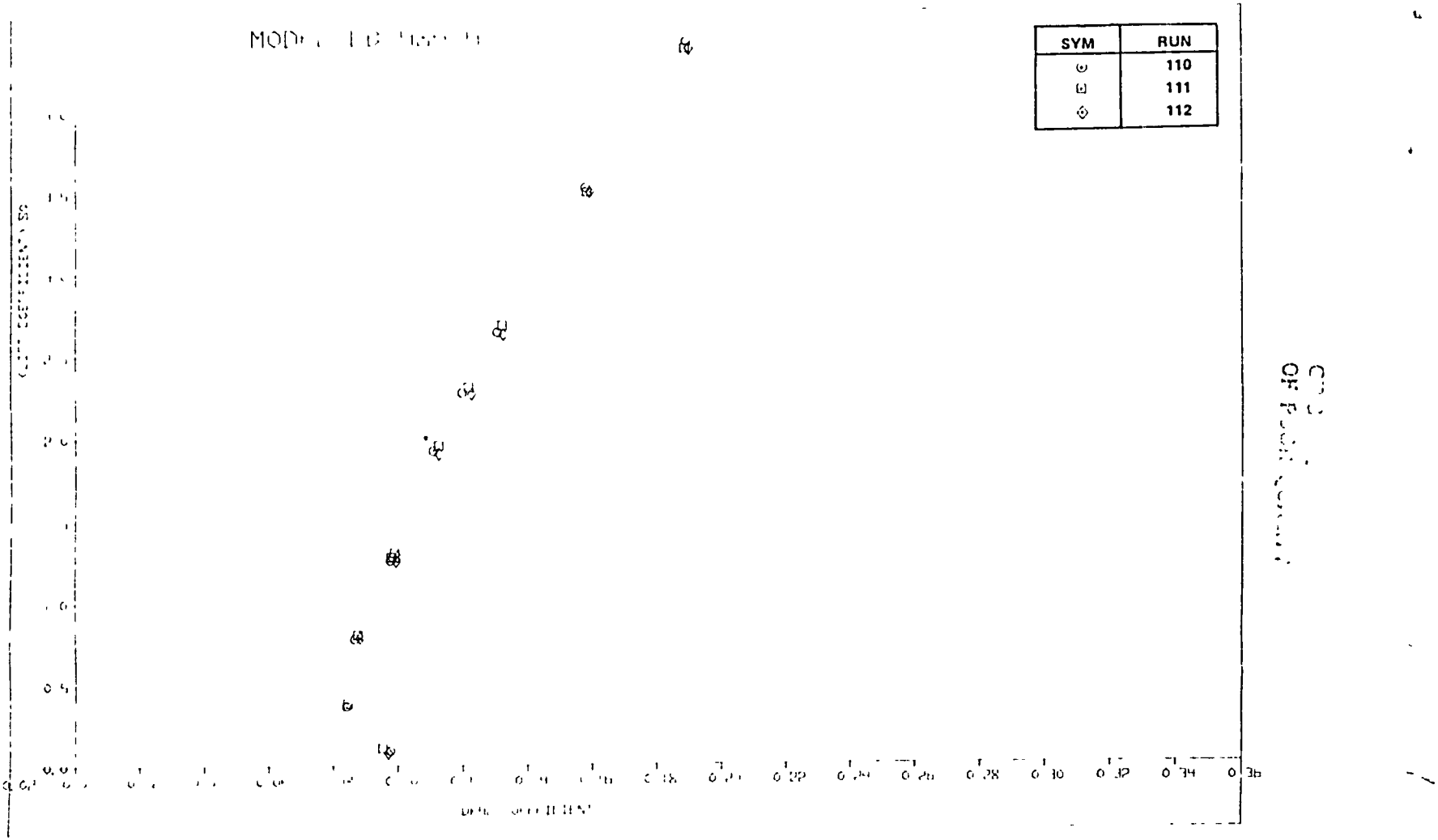

B. DRAG

FIGURE 104. MAIN FLAP POSITION STUDY FOR TWO-SEGMENT TAKEOFF FLAPS WITH VCK (CONCLUDED)

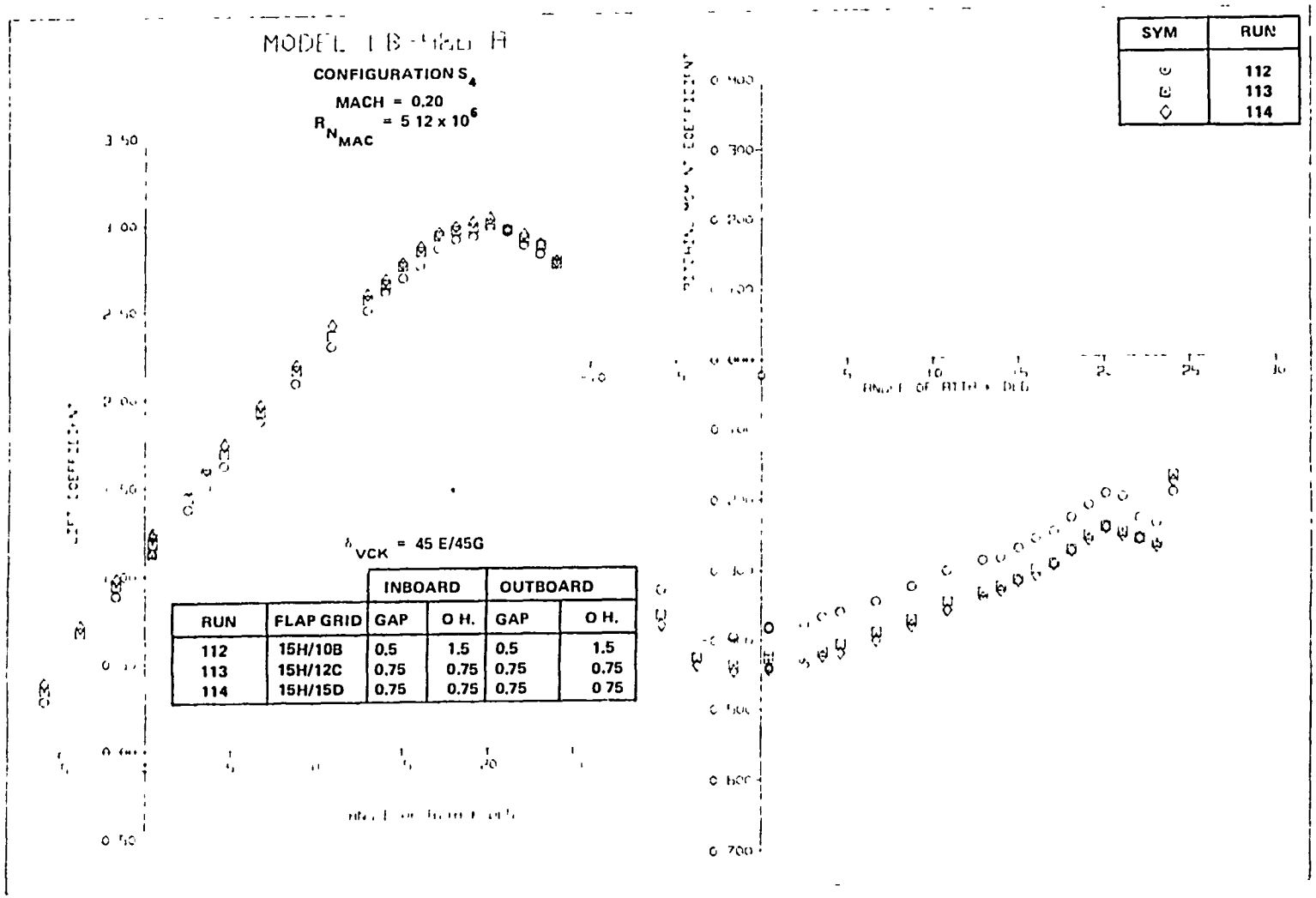

RUN	FLAP GRID	INBOARD GAP	INBOARD O H.	OUTBOARD GAP	OUTBOARD O H.
112	15H/10B	0.5	1.5	0.5	1.5
113	15H/12C	0.75	0.75	0.75	0.75
114	15H/15D	0.75	0.75	0.75	0.75

A. LIFT AND PITCHING MOMENT

FIGURE 105 AFT FLAP DEFLECTION STUDY FOR TWO-SEGMENT TAKEOFF FLAPS WITH VCK

ORIGINAL PAGE IS
OF POOR QUALITY

ORIGINAL PAGE IS
OF POOR QUALITY

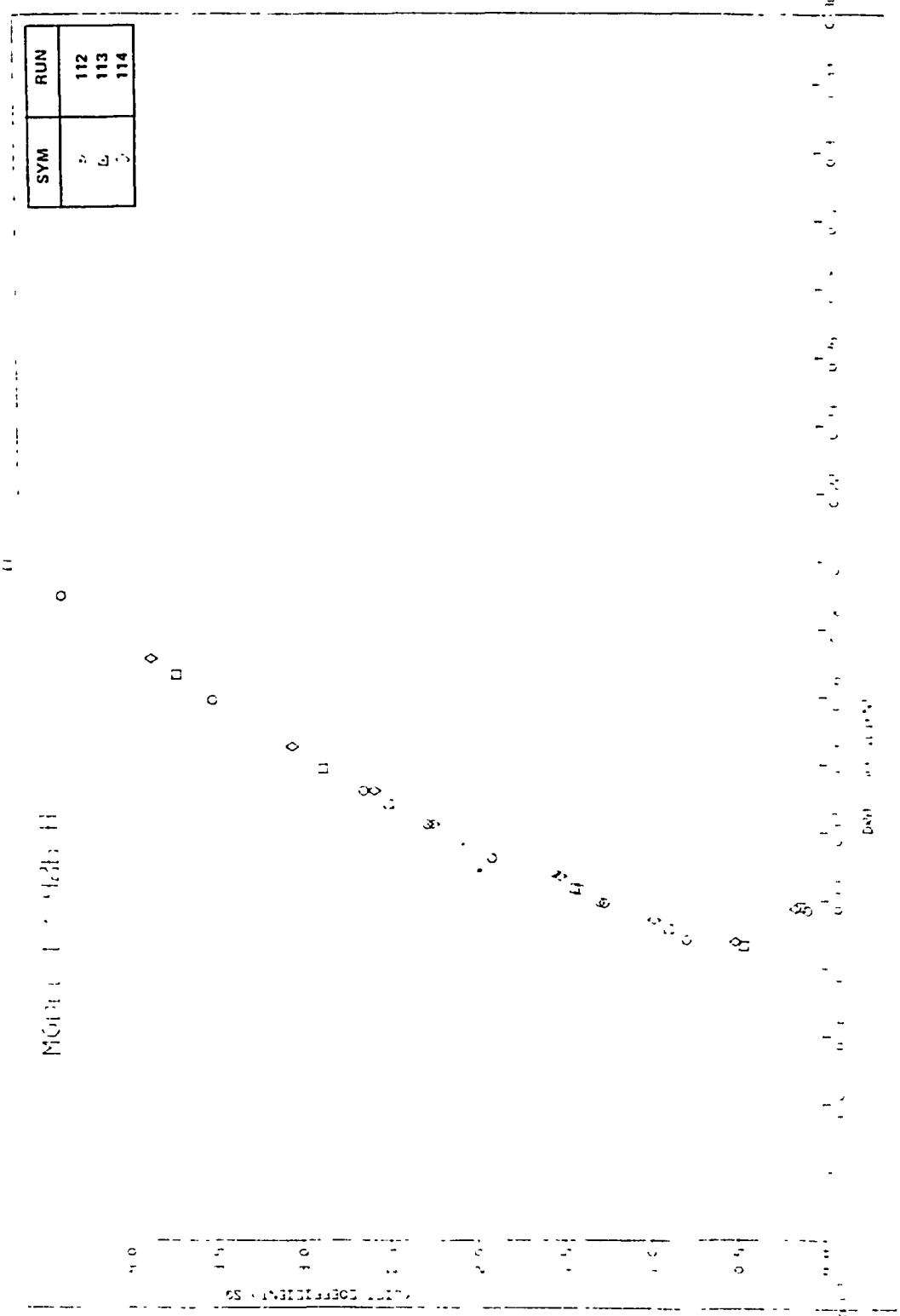

B. DRAG

FIGURE 105. AFT FLAP DEFLECTION STUDY FOR TWO-SEGMENT TAKEOFF FLAPS WITH VCK (CONCLUDED)

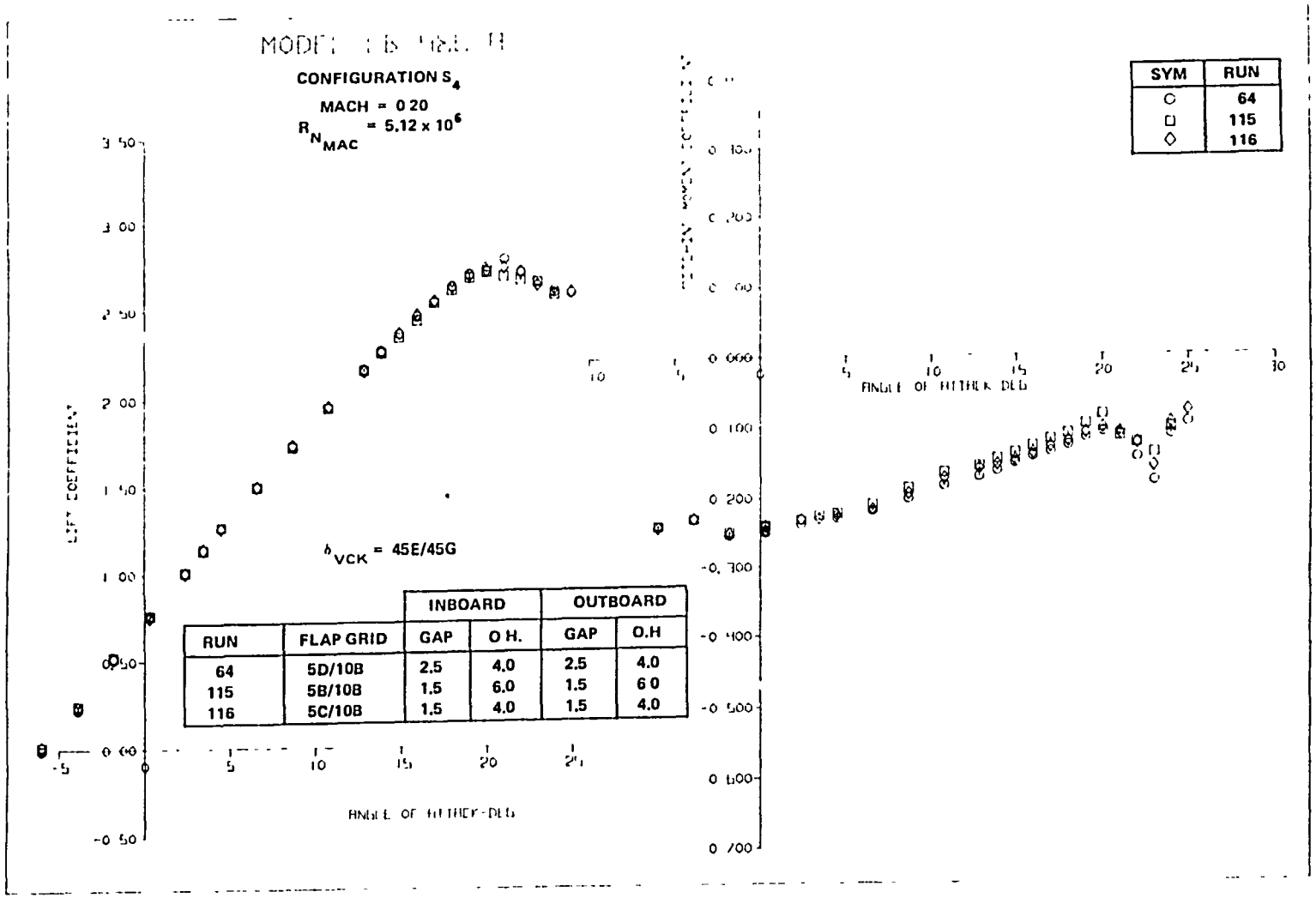

A. LIFT AND PITCHING MOMENT

FIGURE 106. MAIN FLAP POSITION STUDY FOR TWO-SEGMENT TAKEOFF FLAPS WITH VCK

ORIGINAL PAGE IS
OF POOR QUALITY

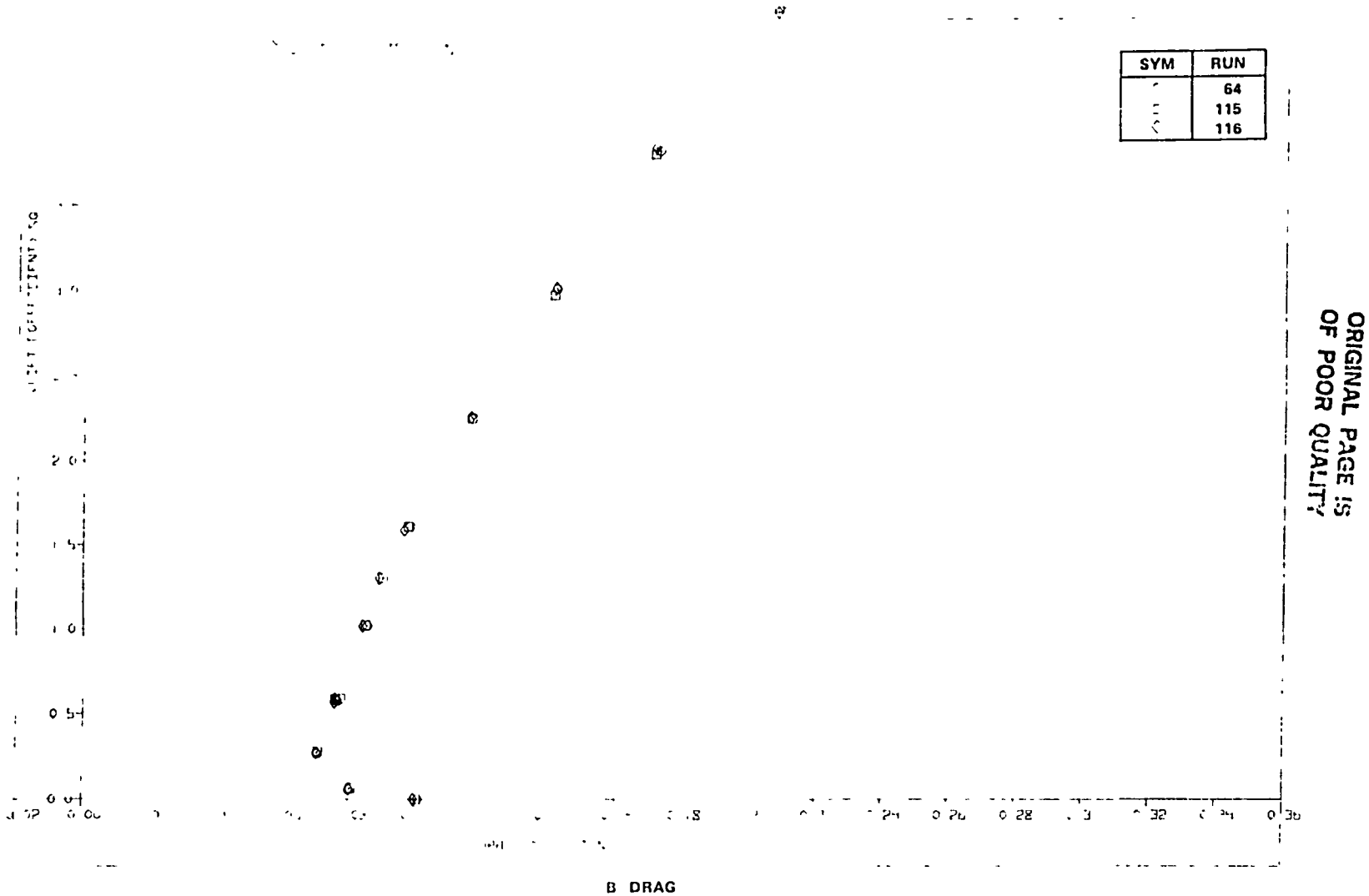

ORIGINAL PAGE IS
OF POOR QUALITY

FIGURE 106. MAIN FLAP POSITION STUDY FOR TWO-SEGMENT TAKEOFF FLAPS WITH VCK (CONCLUDED)

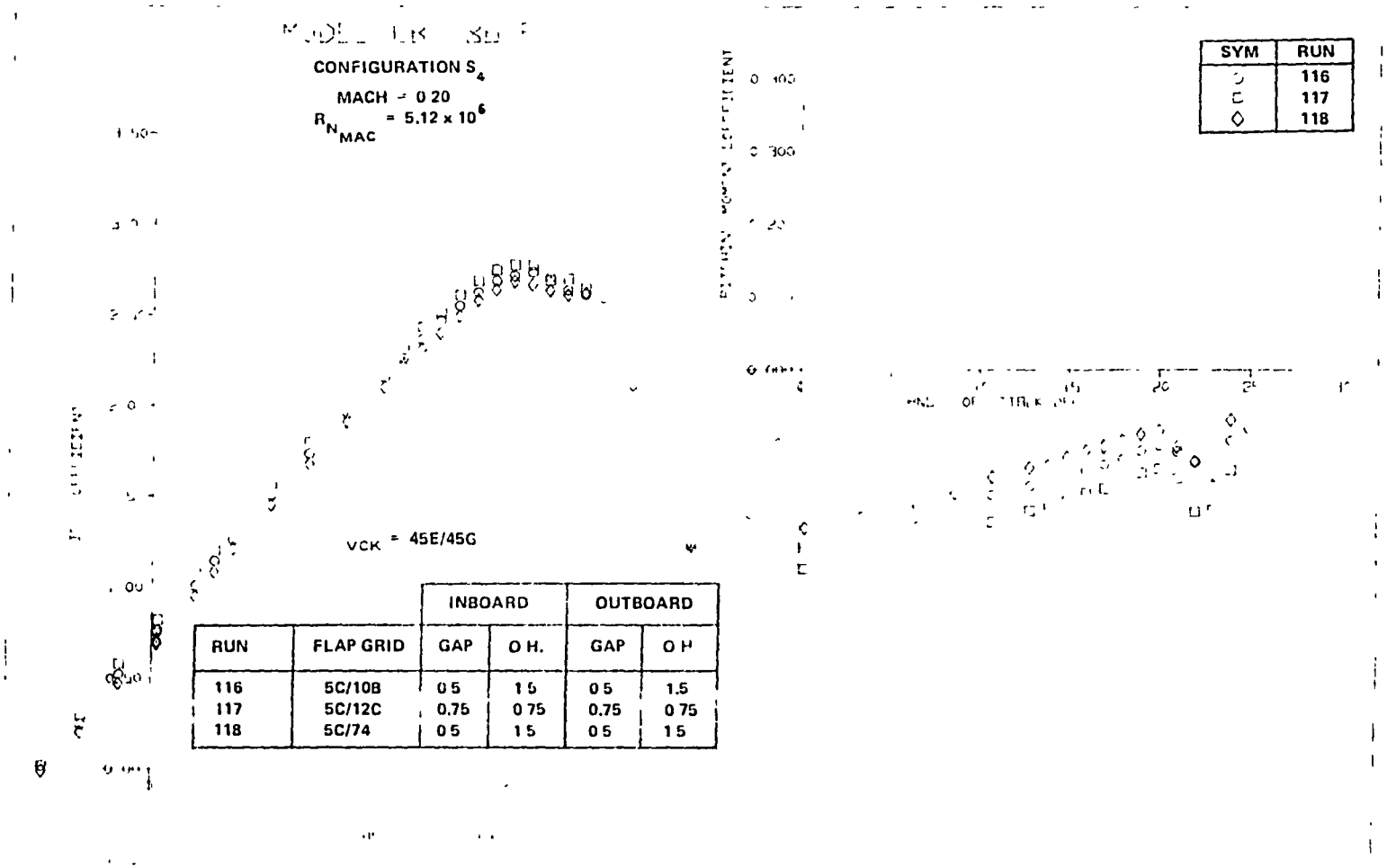

RUN	FLAP GRID	INBOARD GAP	INBOARD O H.	OUTBOARD GAP	OUTBOARD O H
116	5C/10B	0 5	1 5	0 5	1.5
117	5C/12C	0.75	0 75	0.75	0 75
118	5C/74	0 5	1 5	0 5	1 5

A LIFT AND PITCHING MOMENT

FIGURE 107 AFT FLAP DEFLECTION STUDY FOR TWO SEGMENT TAKEOFF FLAPS WITH VCK

ORIGINAL PAGE IS
OF POOR QUALITY

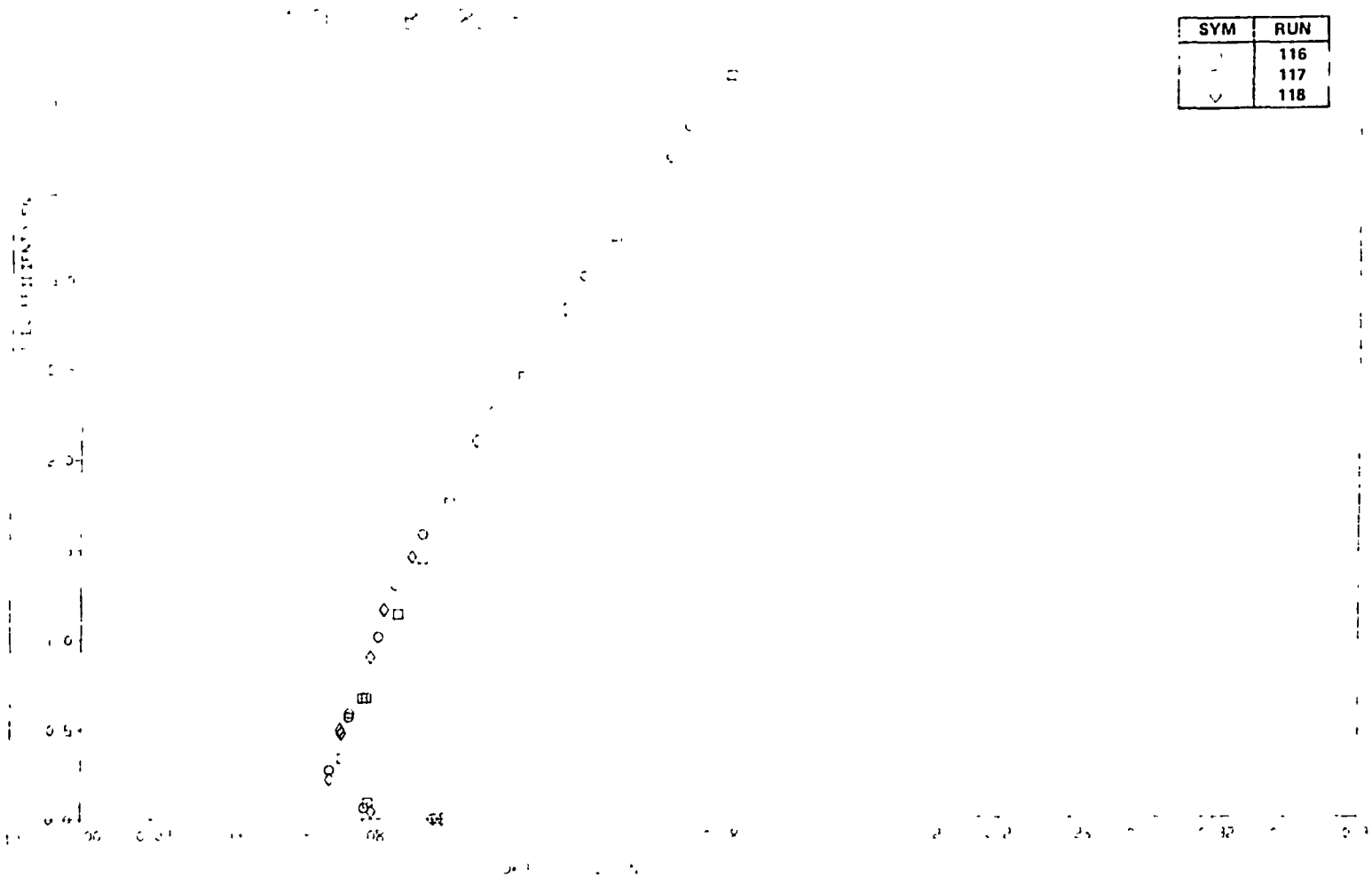

FIGURE 107. AFT FLAP DEFLECTION STUDY FOR TWO-SEGMENT TAKEOFF FLAPS WITH VCK (CONCLUDED)

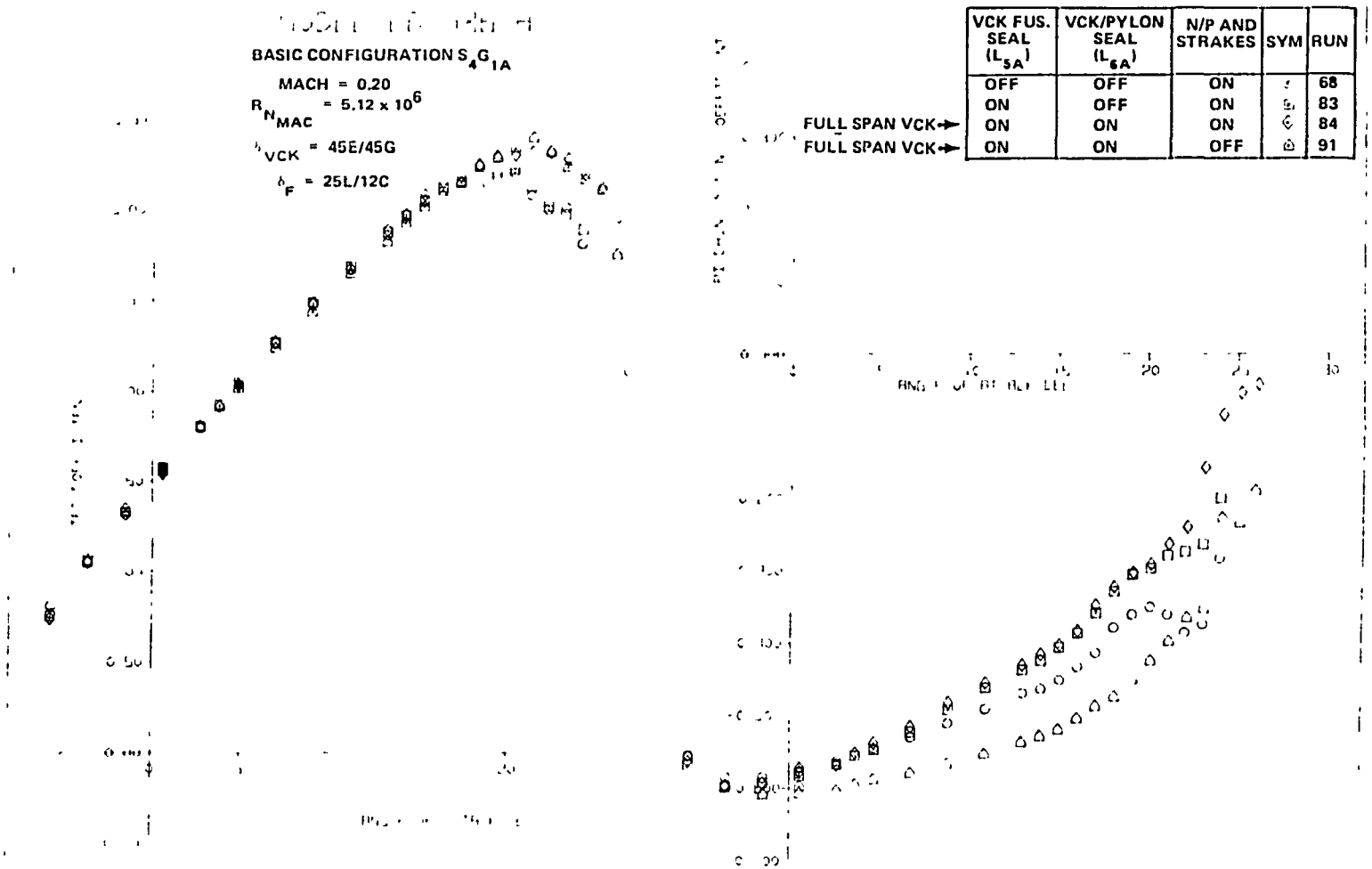

VCK FUS. SEAL (L_{5A})	VCK/PYLON SEAL (L_{6A})	N/P AND STRAKES	SYM	RUN
OFF	OFF	ON		68
ON	OFF	ON		83
ON	ON	ON		84
ON	ON	OFF		91

A. LIFT AND PITCHING MOMENT

FIGURE 108. EFFECT OF VCK SPAN AND NACELLES, PYLONS, AND STRAKES ON AERODYNAMIC CHARACTERISTICS FOR TWO-SEGMENT LANDING FLAPS

ORIGINAL PAGE IS
OF POOR QUALITY

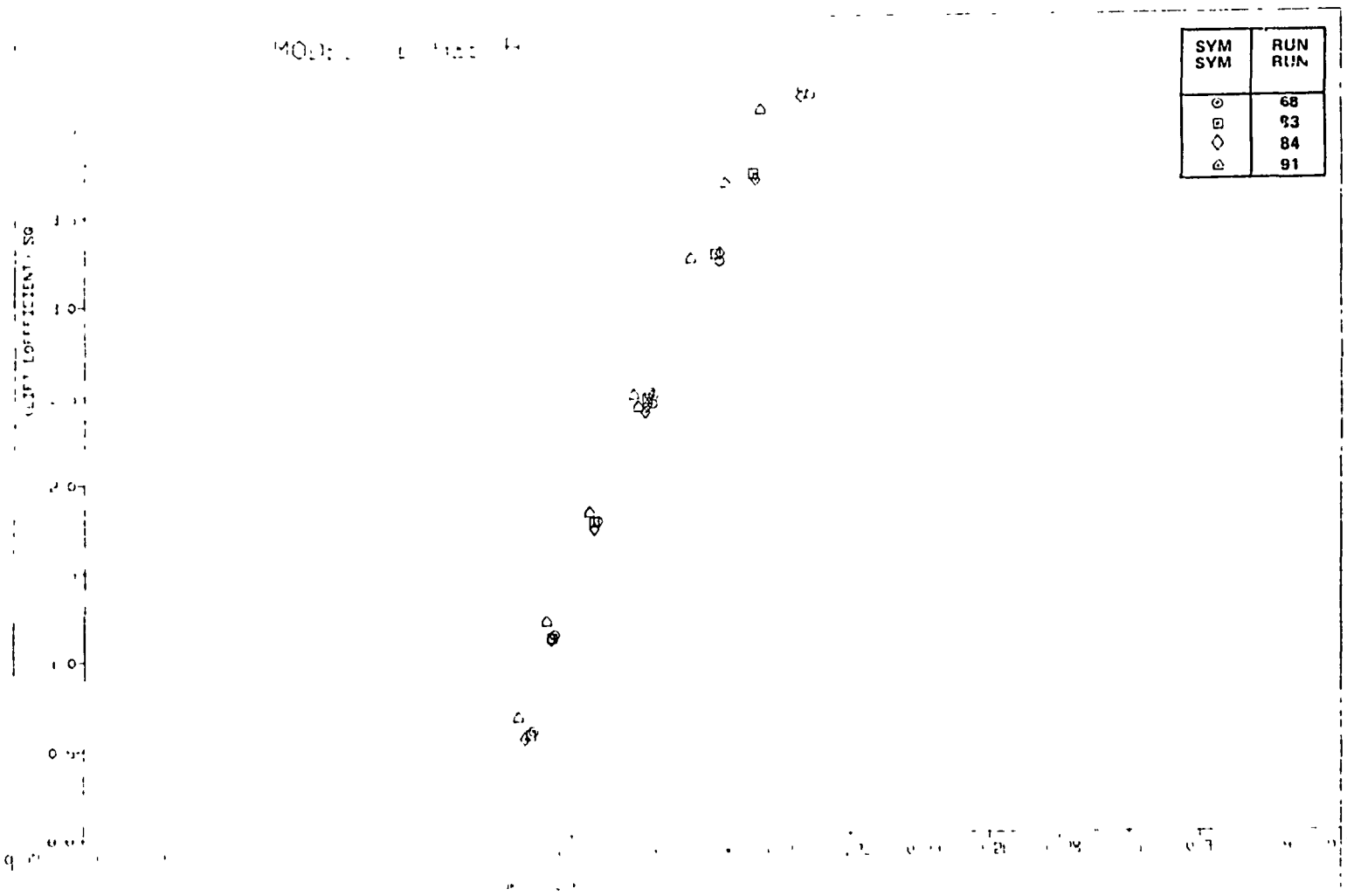

FIGURE 108. EFFECT OF VCK SPAN AND NACELLES, PYLONS, AND STRAKES ON AERODYNAMIC CHARACTERISTICS FOR TWO-SEGMENT LANDING FLAPS (CONCLUDED)

ORIGINAL PAGE IS
OF POOR QUALITY

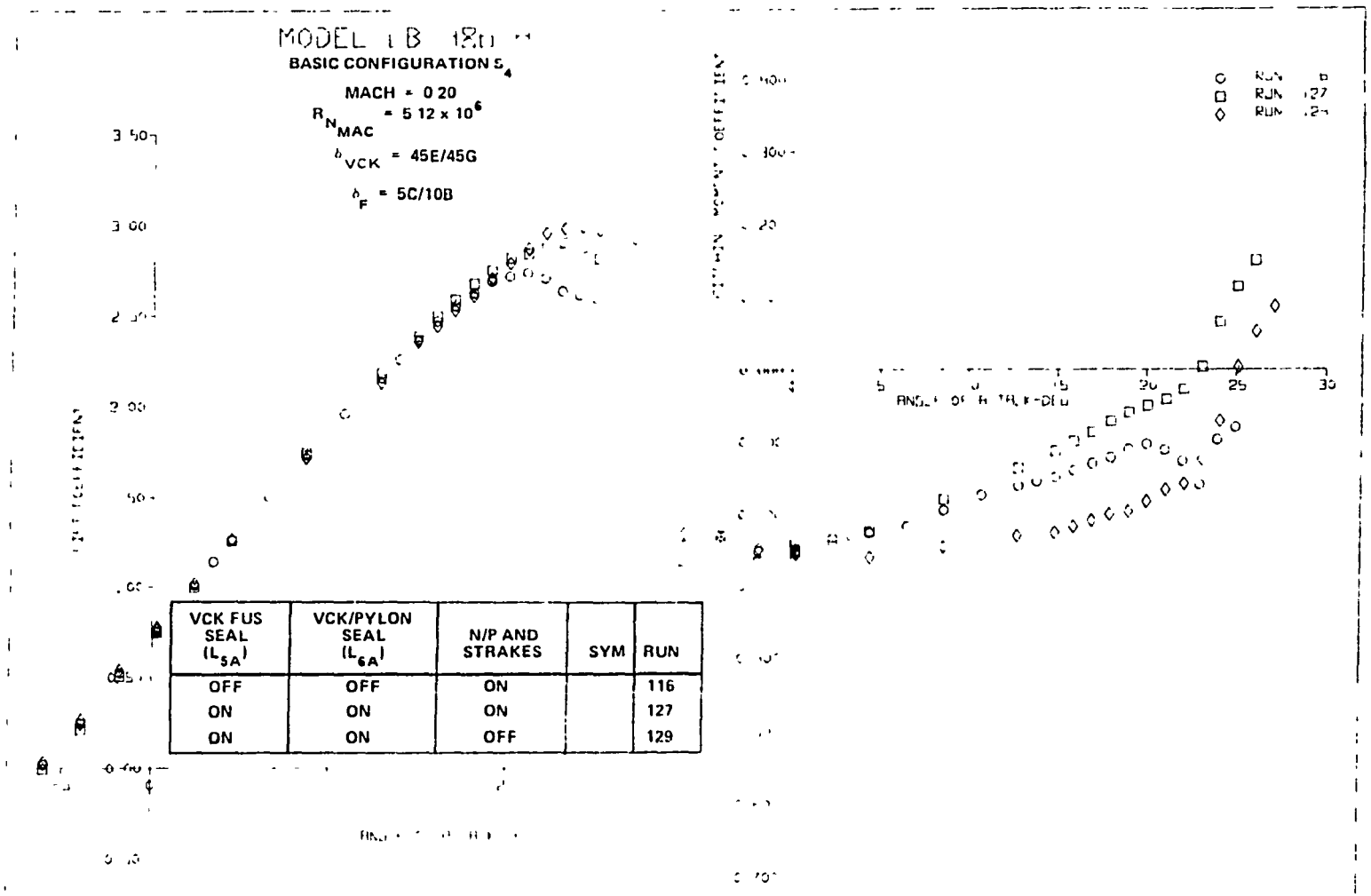

VCK FUS SEAL (L_{5A})	VCK/PYLON SEAL (L_{6A})	N/P AND STRAKES	SYM	RUN
OFF	OFF	ON		116
ON	ON	ON		127
ON	ON	OFF		129

A LIFT AND PITCHING MOMENT

FIGURE 109. EFFECT OF VCK SPAN AND NACELLES, PYLONS, AND STRAKES ON AERODYNAMIC CHARACTERISTICS FOR TWO SEGMENT TAKEOFF FLAPS

ORIGINAL PAGE IS
OF POOR QUALITY

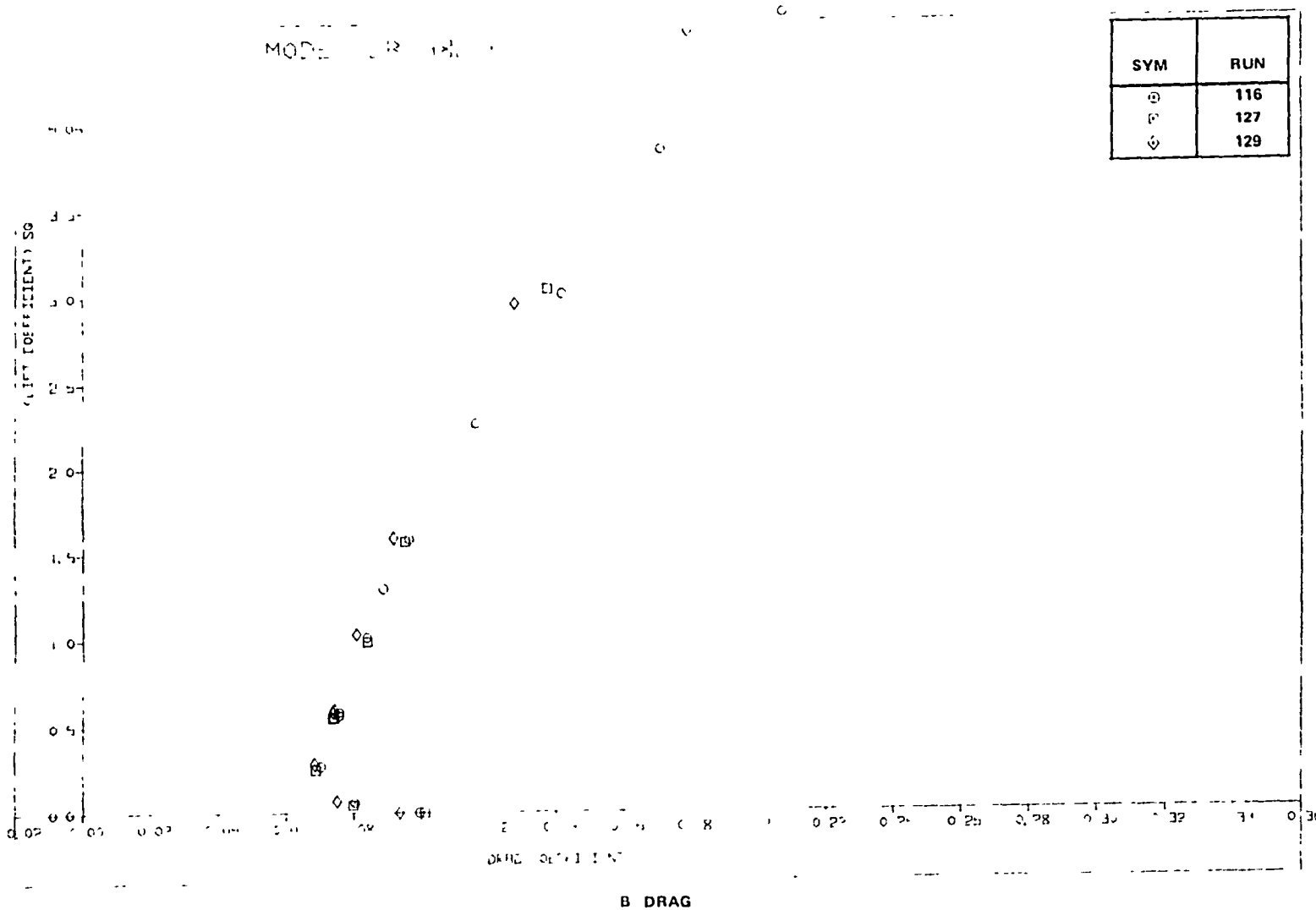

FIGURE 109. EFFECT OF VCK SPAN AND NACELLES, PYLONS, AND STRAKES ON AERODYNAMIC CHARACTERISTICS FOR TWO-SEGMENT TAKEOFF FLAPS (CONCLUDED)

ORIGINAL PAGE IS
OF POOR QUALITY

Reynolds Number Effects on VCK with Two-Segment Flap (Tail-Off). - The influence of Reynolds number variation on the longitudinal aerodynamic characteristics with two-segment landing and takeoff flaps is shown in Figure 110 and 111. A sizable shift in pitching moment is indicated for the landing and takeoff flap configurations at the lowest Reynolds number condition. The basic trend of the pitching moment at angles of attack near stall is not significantly changed by the reduction in Reynolds number. A reduction in $C_{L_{MAX}}$ of 0.16 for the flap deflections is also shown in Figures 110 and 111.

VCK with Two-Segment Flaps and Horizontal tail. - Figures 112 to 114 present the characteristics of the VCK with two-segment landing and takeoff flaps with the horizontal tail, and the effect of Reynolds number. Characteristics shown in Figure 112 indicate nose down pitching moment for the -15^{o} and -5^{o} horizontal incidences near $C_{L_{MAX}}$. Post stall pitch

characteristics are again influenced by the tip separation, and a reduction in stability is indicated at the highest angles.

Figure 113 shows, for the VCK with two-segment landing flaps, a change in Reynolds number ($R_{N_{MAC}} = 5.12 \times 10^{6}$ to $R_{N_{MAC}} = 1.14 \times 10^{6}$) does not alter the basic character of the pitching moment trends.

Single-Slot Flap Optimization. - Results of the optimization of this trailing edge device were presented in Figures 115 through 118 for flap deflections of 35^{o}, 25^{o}, 15^{o}, and 5^{o}. The pitch trends for each flap deflection were similar for the various grid positions. As the flap deflection was reduced, more favorable pitch characteristics after $C_{L_{MAX}}$ were obtained. Positions selected from this study were: 25K/0, 15G/0, and 5A/0 (see Data Summary Section . . . for comparisons with two-segment flap system).

Inboard VCK Effects. - The inboard VCK was removed and the changes in the longitudinal aerodynamic characteristics are shown in Figure 119. A $C_{L_{MAX}}$ reduction of 0.46 and an abrupt nose down pitching moment after $C_{L_{MAX}}$ is indicated in Figure 119. Removal of the inboard VCK reduced the drag by 0.008.

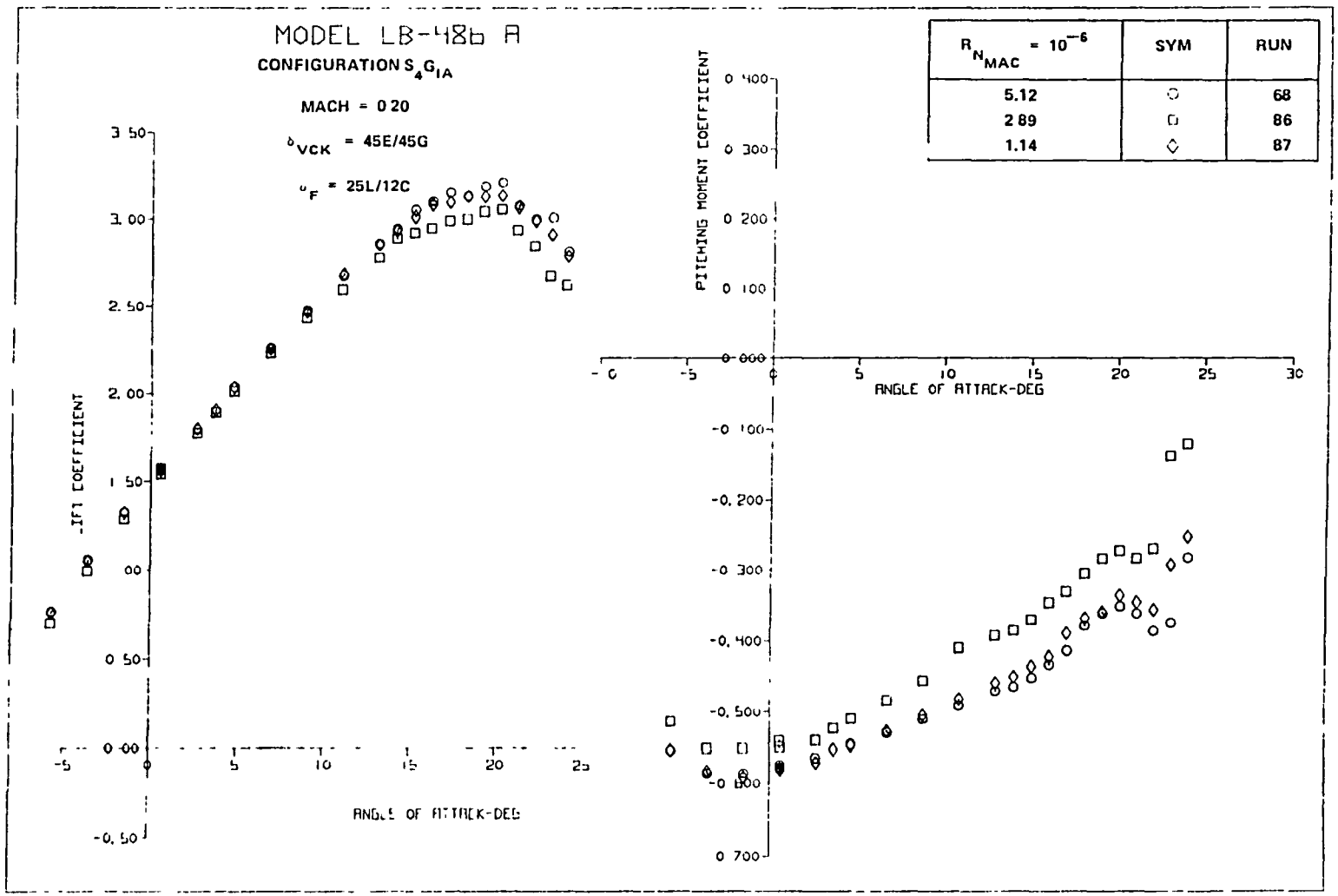

A LIFT AND PITCHING MOMENT

FIGURE 110 EFFECT OF REYNOLDS NUMBER ON AERODYNAMIC CHARACTERISTICS OF THE VCK WITH TWO SEGMENT LANDING FLAPS CONFIGURATION

ORIGINAL PAGE IS
OF POOR QUALITY

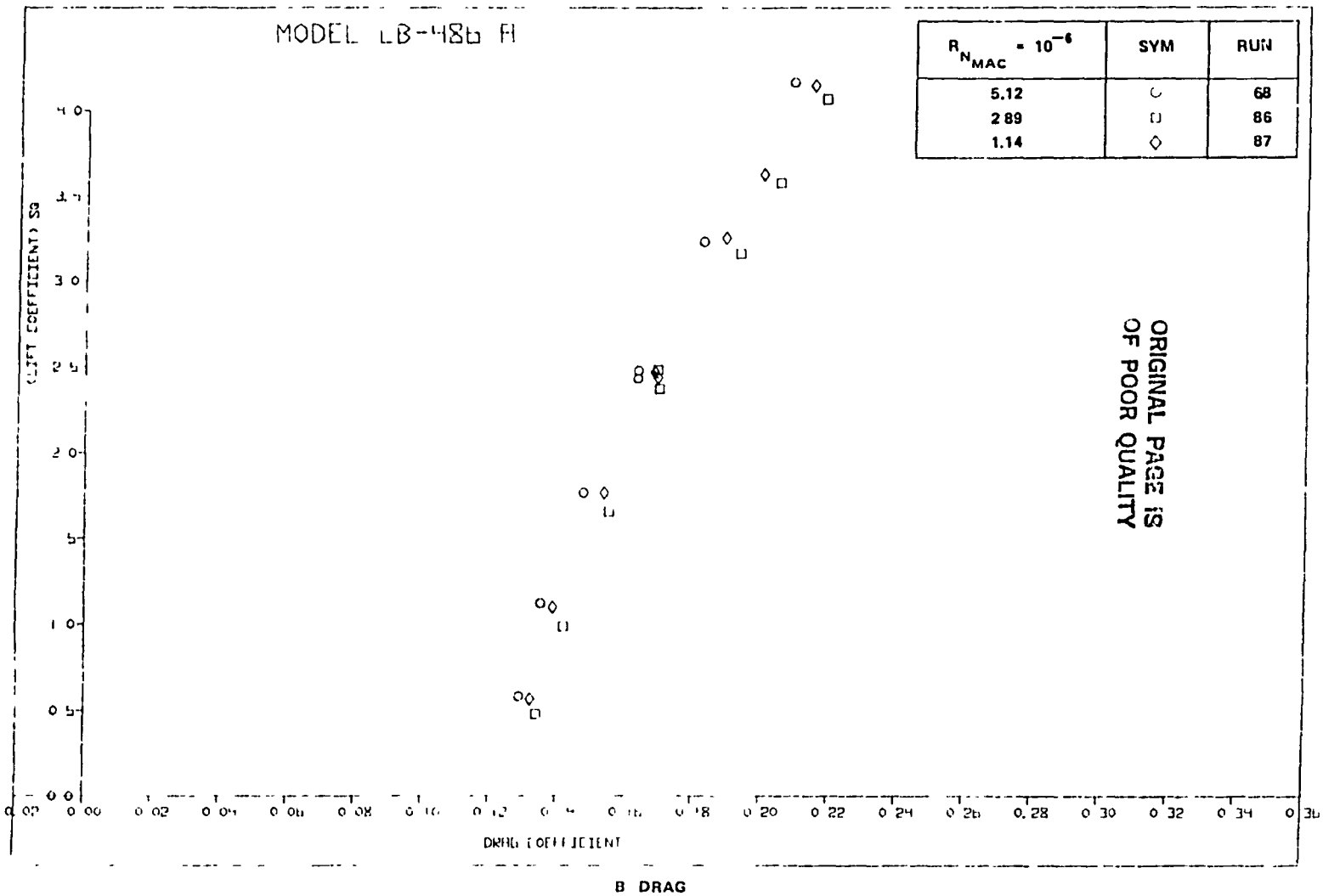

FIGURE 110. EFFECT OF REYNOLDS NUMBER ON AERODYNAMIC CHARACTERISTICS OF THE VCK WITH TWO SEGMENT LANDING FLAPS CONFIGURATION (CONTINUED)

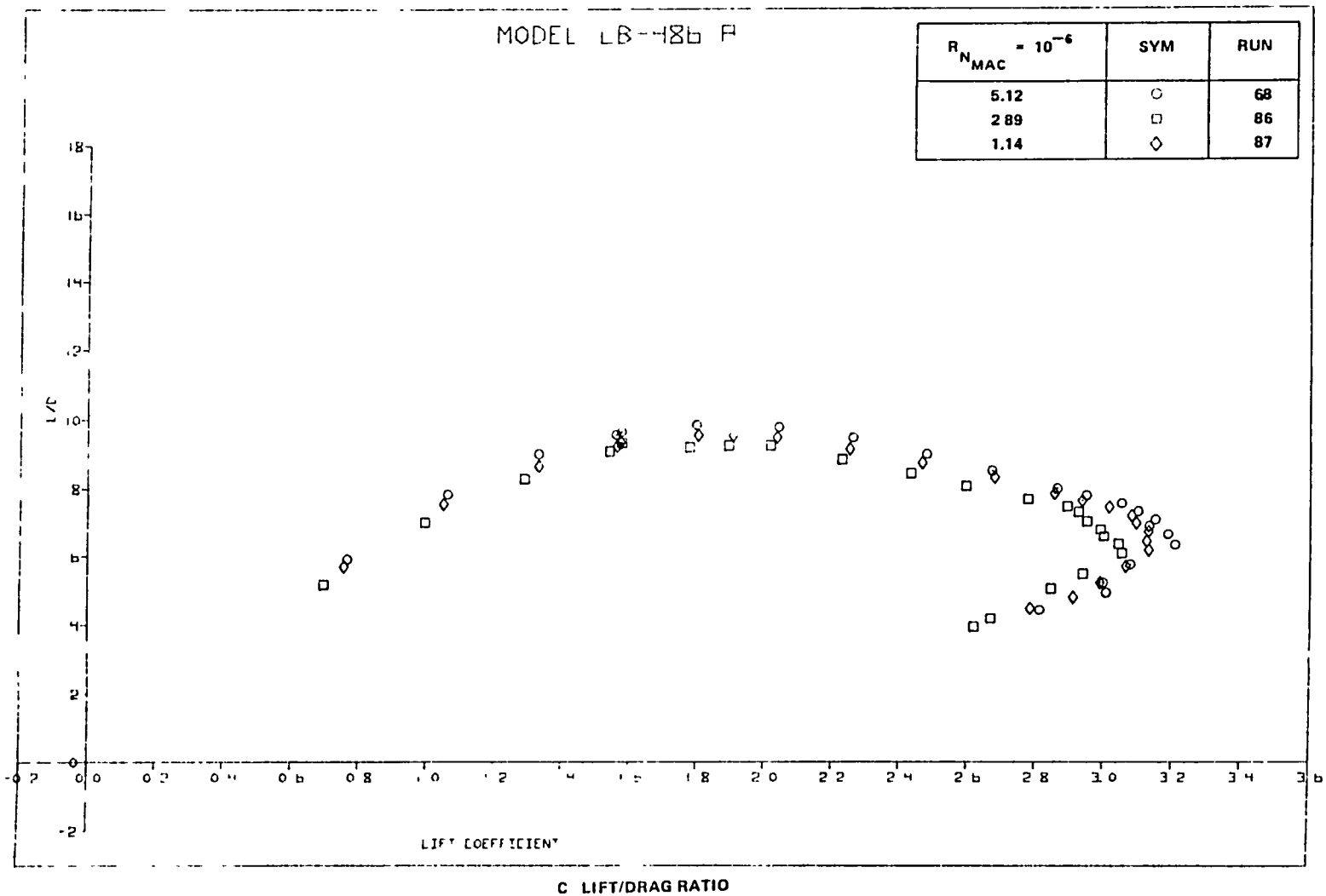

C LIFT/DRAG RATIO

FIGURE 110. EFFECT OF REYNOLDS NUMBER ON AERODYNAMIC CHARACTERISTICS OF THE VCK WITH TWO-SEGMENT LANDING FLAPS CONFIGURATION (CONCLUDED)

ORIGINAL PAGE IS
OF POOR QUALITY

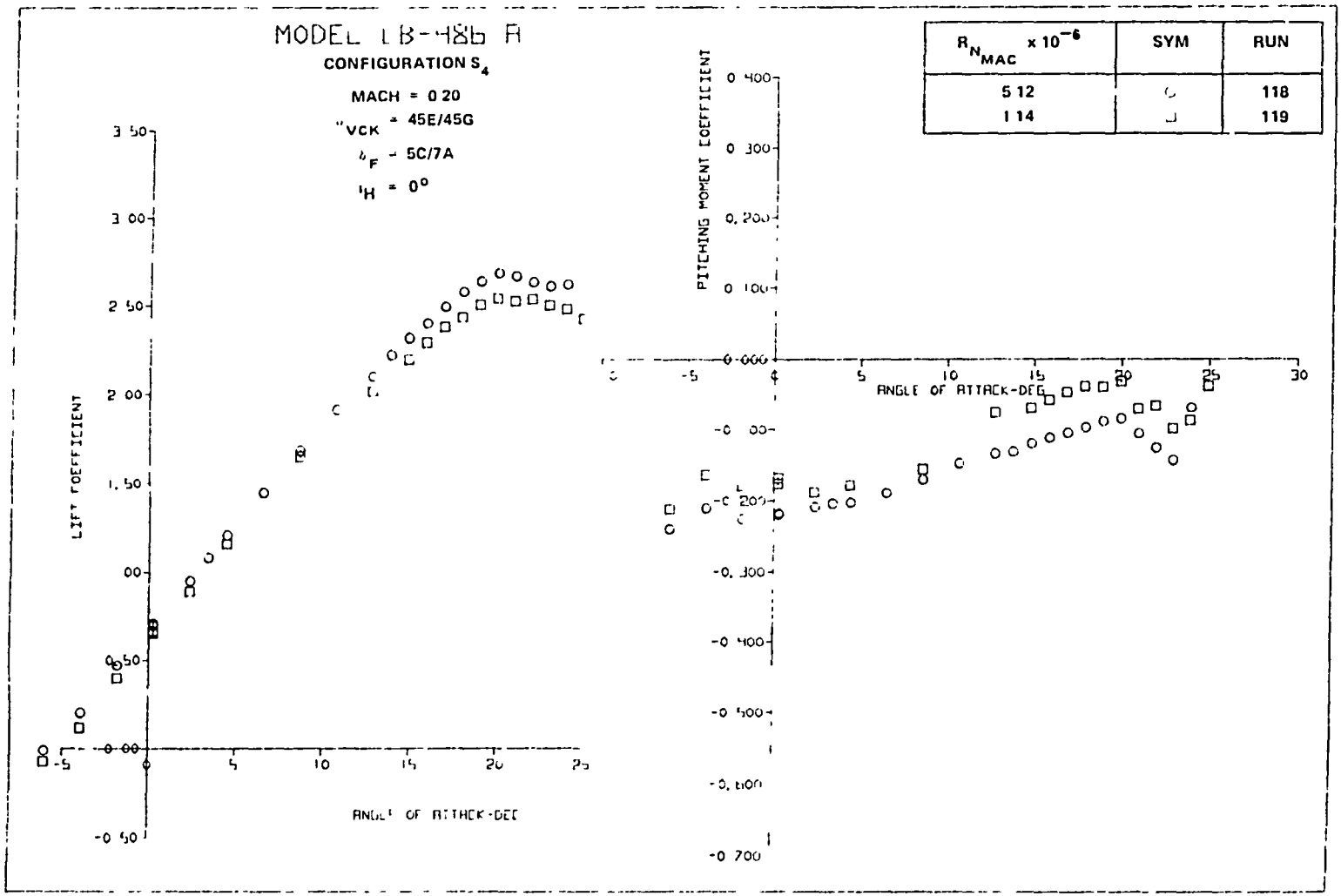

A LIFT AND PITCHING MOMENT

FIGURE 111 EFFECT OF REYNOLDS NUMBER ON AERODYNAMIC CHARACTERISTICS OF THE VCK WITH TWO-SEGMENT TAKEOFF FLAPS CONFIGURATION

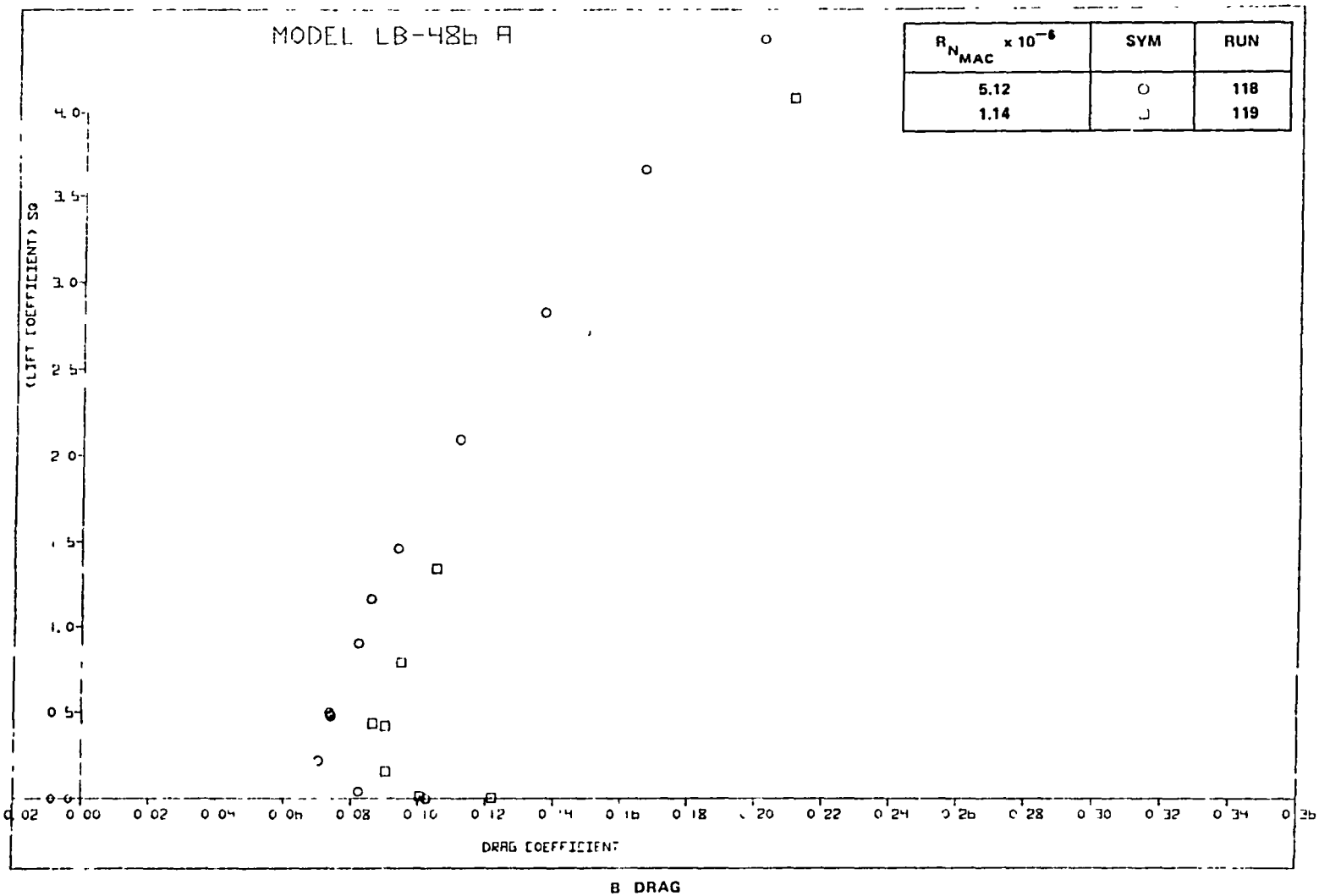

FIGURE 111. EFFECT OF REYNOLDS NUMBER ON AERODYNAMIC CHARACTERISTICS OF THE VCK WITH TWO-SEGMENT TAKEOFF FLAPS CONFIGURATION (CONTINUED)

ORIGINAL PAGE IS
OF POOR QUALITY

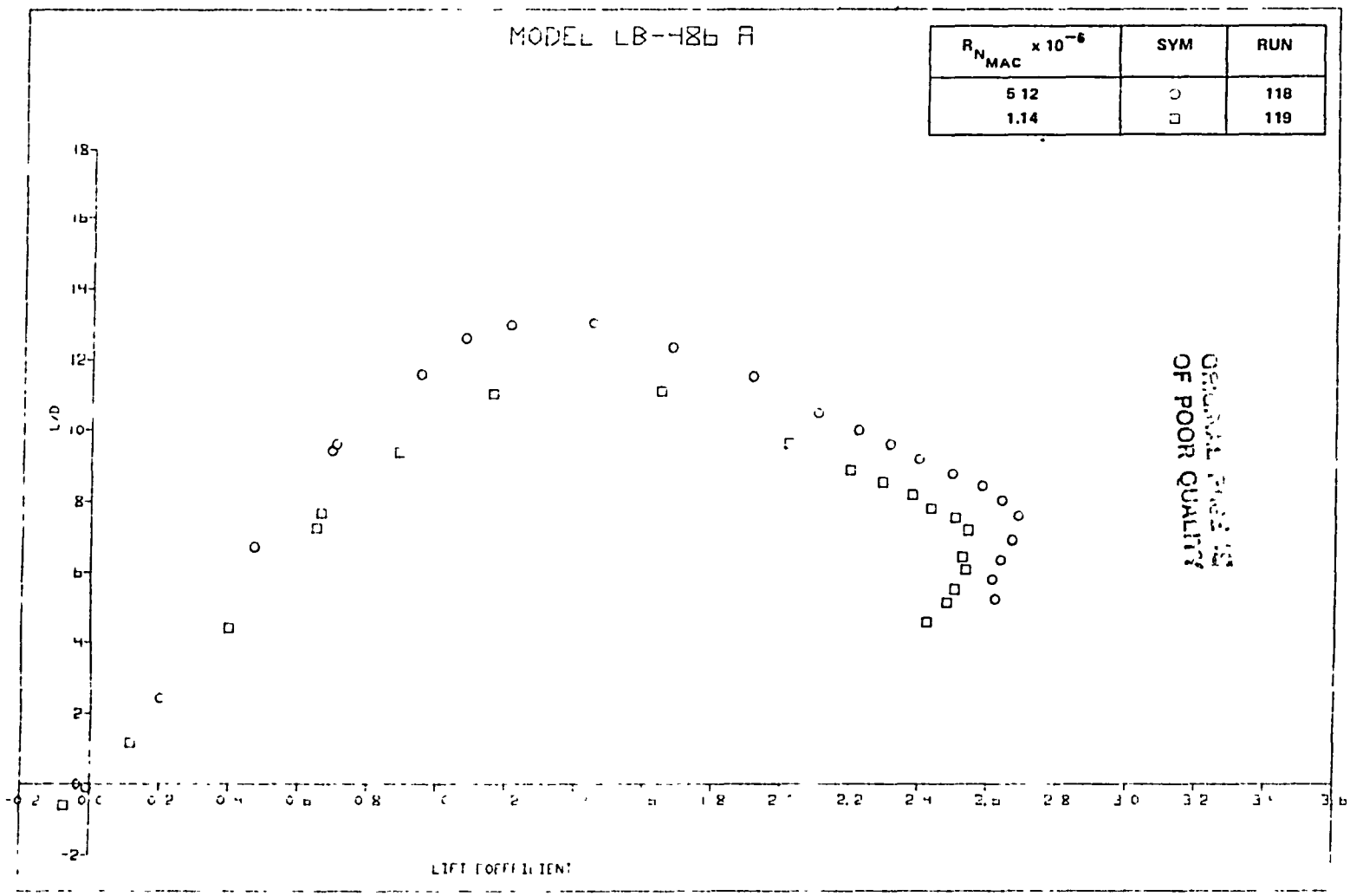

FIGURE 111. EFFECT OF REYNOLDS NUMBER ON AERODYNAMIC CHARACTERISTICS OF THE VCK WITH TWO-SEGMENT TAKEOFF FLAPS CONFIGURATION (CONCLUDED)

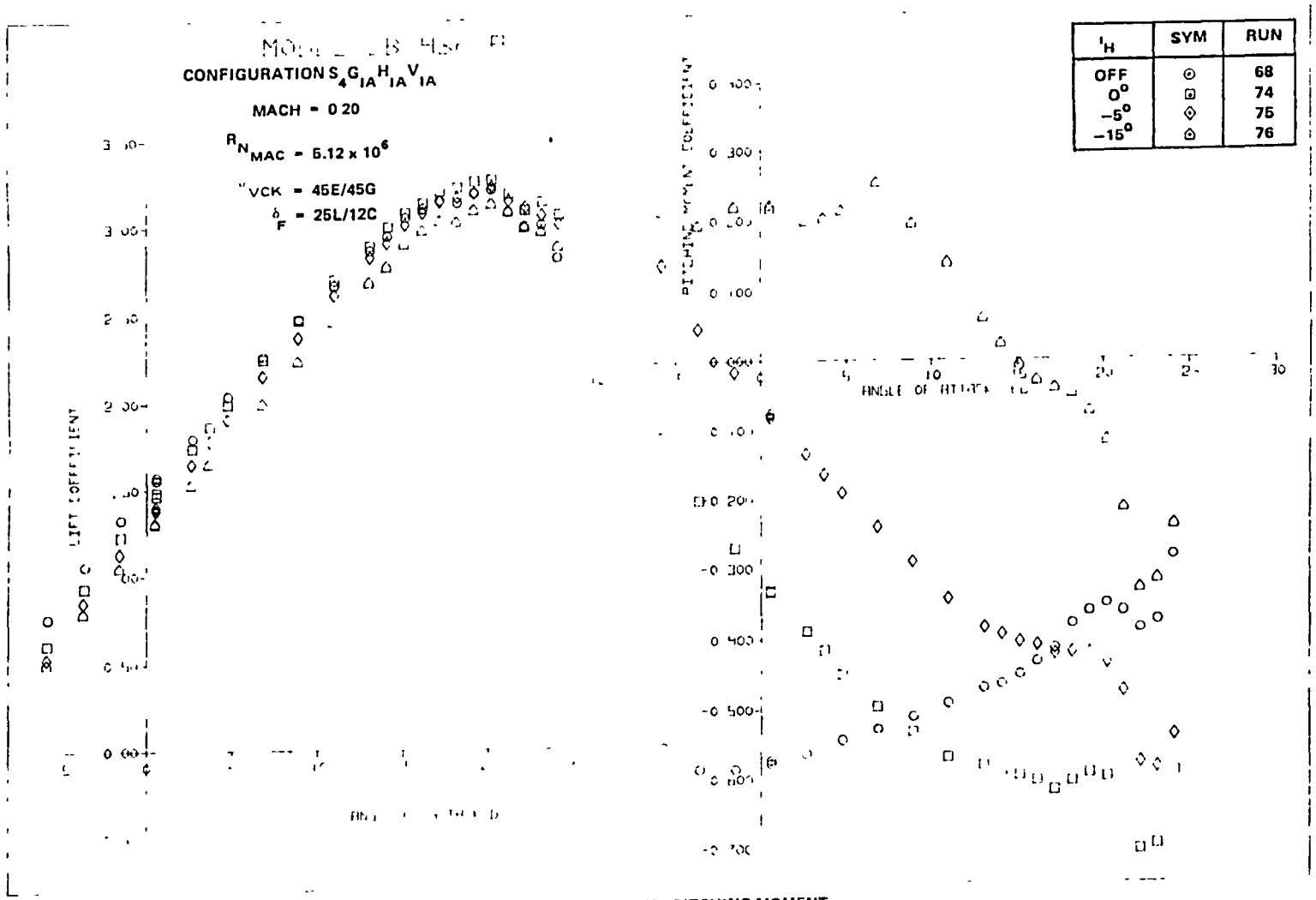

A LIFT AND PITCHING MOMENT

FIGURE 112. EFFECT OF HORIZONTAL TAIL DEFLECTION ON AERODYNAMIC CHARACTERISTICS OF THE VCK WITH TWO-SEGMENT LANDING FLAPS CONFIGURATION

PAGE IS
OF POOR QUALITY

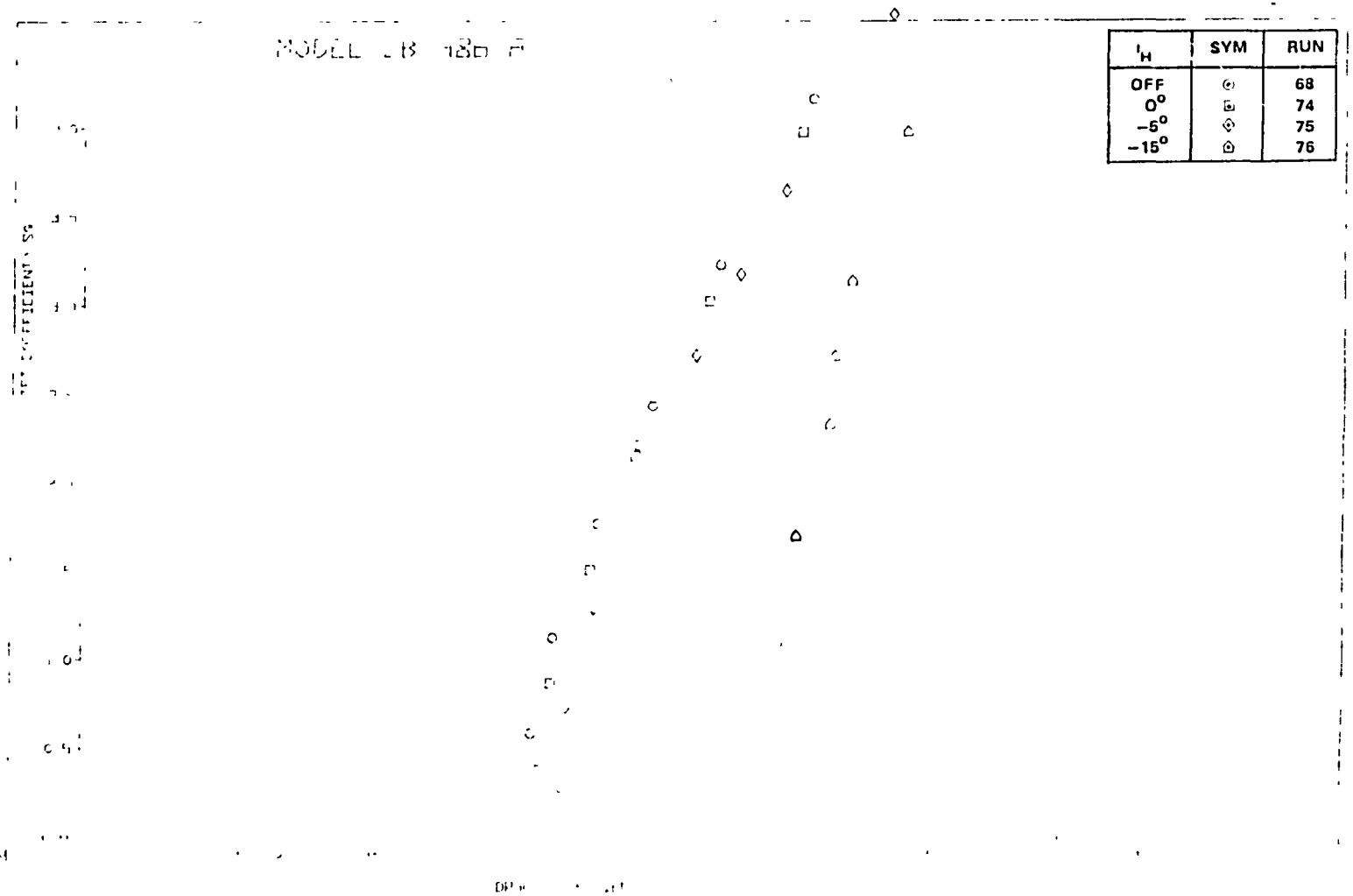

B. DRAG

FIGURE 112. EFFECT OF HORIZONTAL TAIL DEFLECTION ON AERODYNAMIC CHARACTERISTICS OF THE VCK WITH TWO-SEGMENT LANDING FLAPS CONFIGURATION (CONCLUDED)

ORIGINAL PAGE IS
OF POOR QUALITY

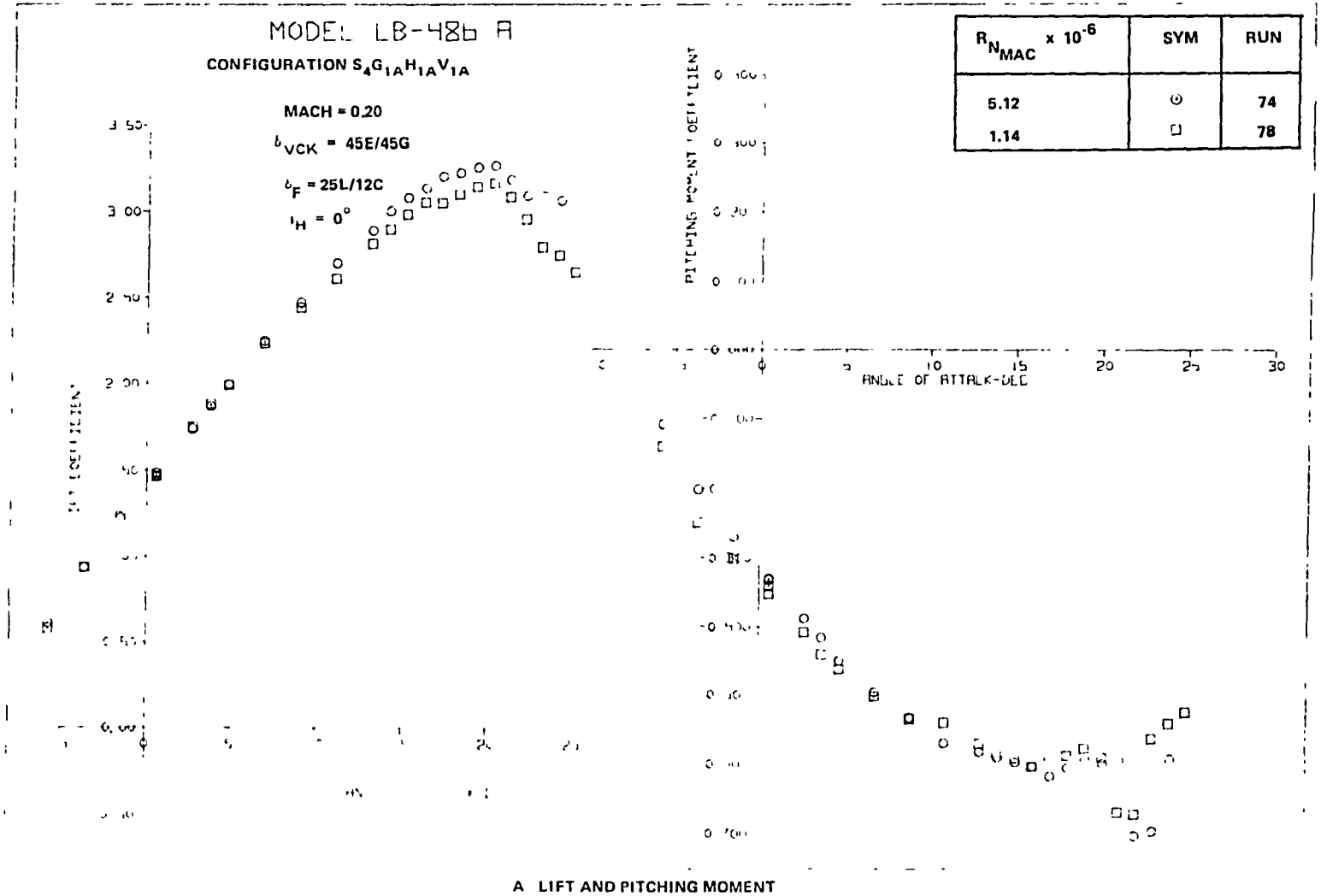

A LIFT AND PITCHING MOMENT

FIGURE 113. EFFECT OF REYNOLDS NUMBER FOR THE VCK WITH TWO-SEGMENT LANDING FLAPS (HORIZONTAL TAIL ON)

ORIGINAL PAGE IS
OF POOR QUALITY

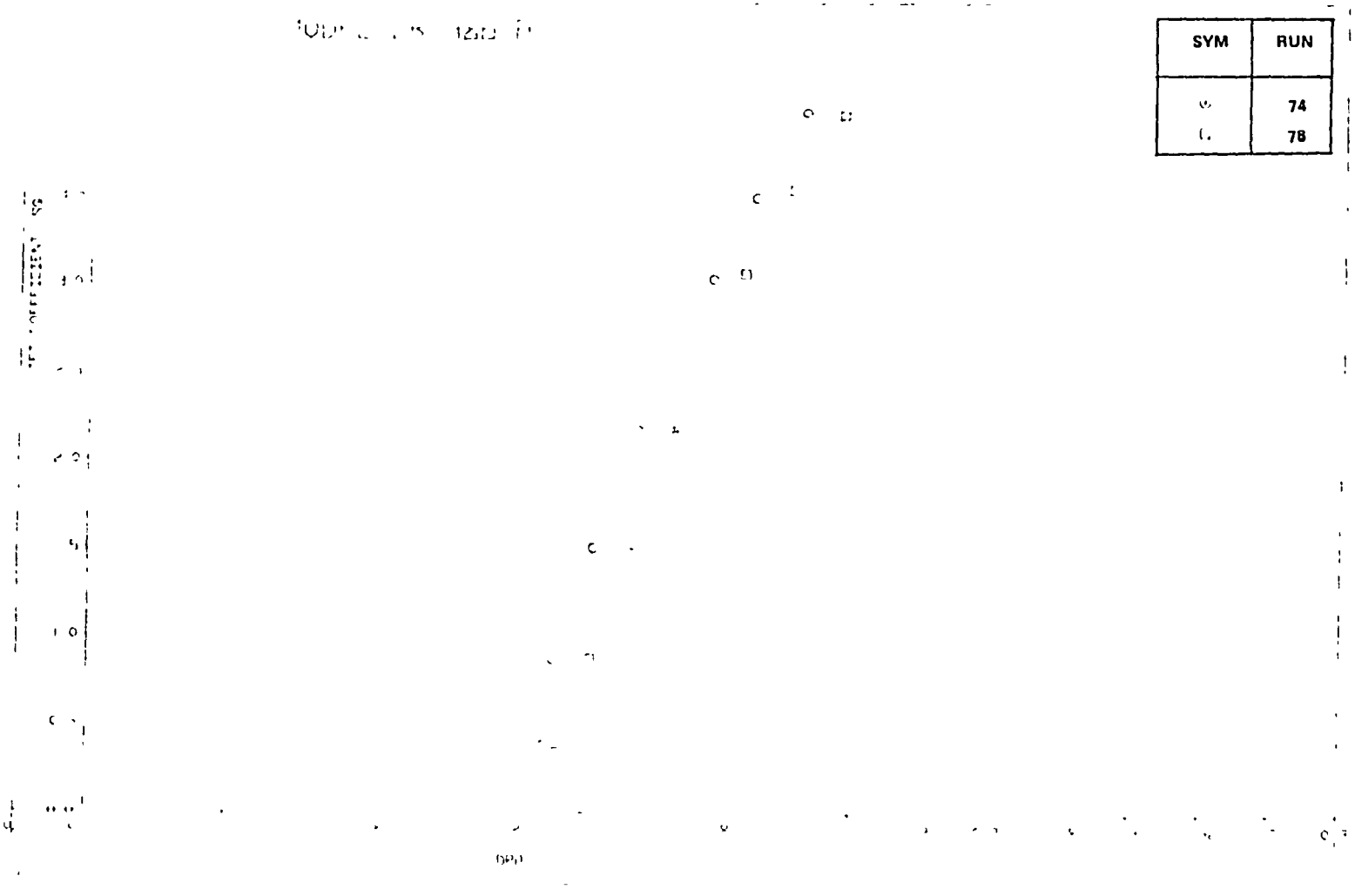

B DRAG

FIGURE 113 EFFECT OF REYNOLDS NUMBER FOR THE VCK WITH TWO-SEGMENT LANDING FLAPS (HORIZONTAL TAIL ON) (CONCLUDED)

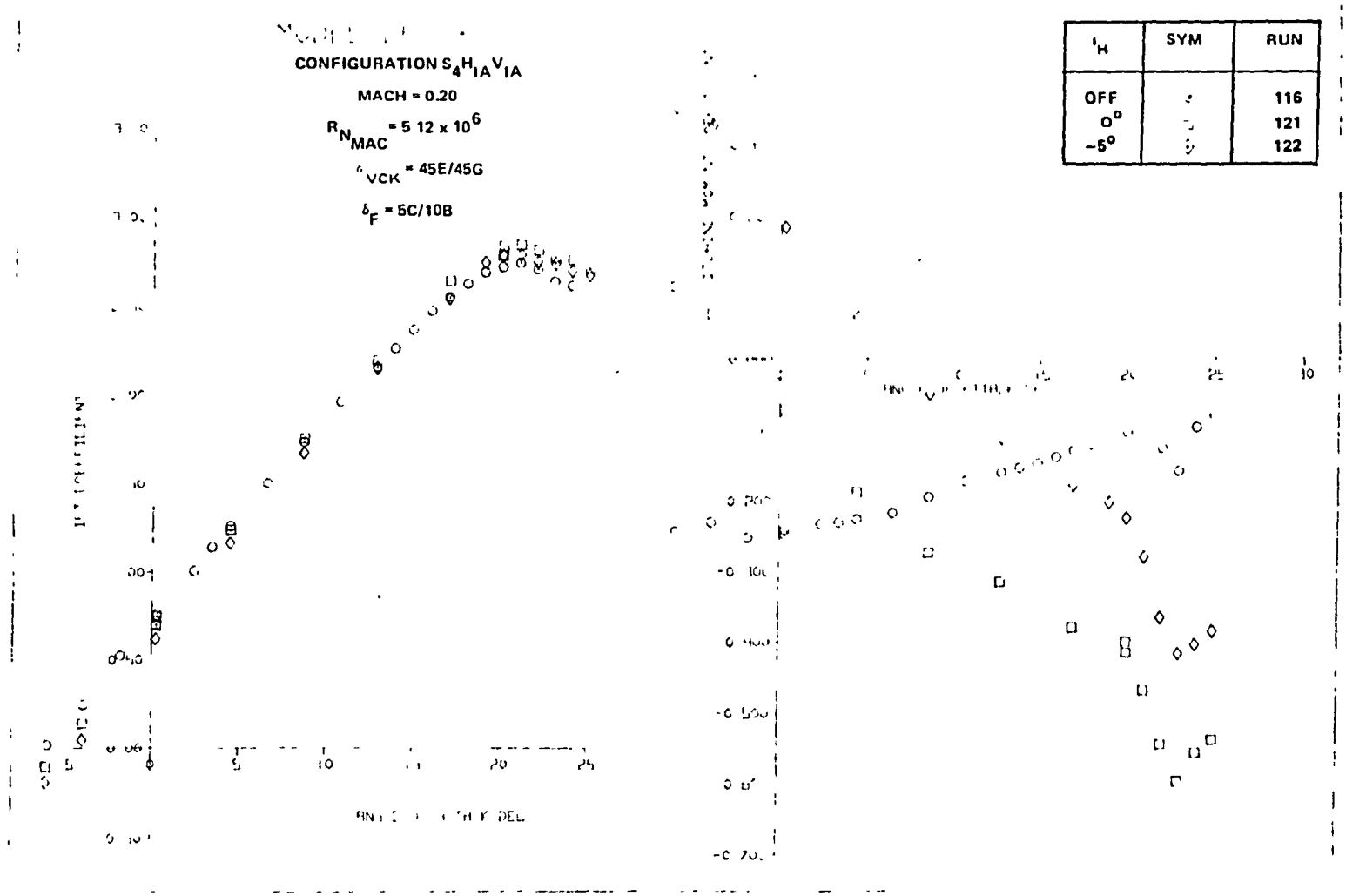

A. LIFT AND PITCHING MOMENT

FIGURE 114. EFFECT OF HORIZONTAL TAIL DEFLECTION ON AERODYNAMIC CHARACTERISTICS OF THE VCK WITH TWO-SEGMENT TAKEOFF FLAPS CONFIGURATION

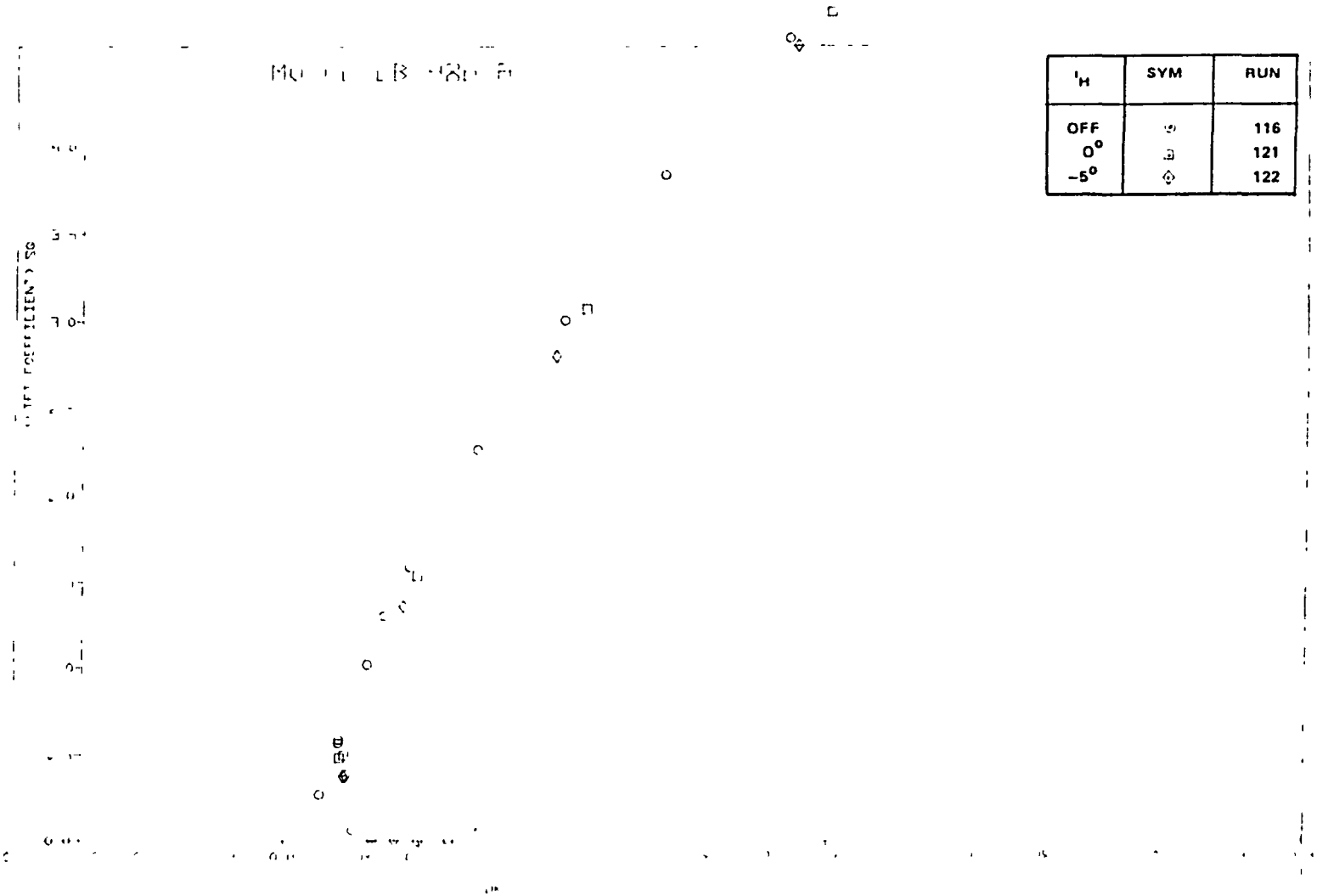

FIGURE 114 EFFECT OF HORIZONTAL TAIL DEFLECTION ON AERODYNAMIC CHARACTERISTICS OF THE VCK WITH TWO-SEGMENT TAKEOFF FLAPS CONFIGURATION (CONCLUDED)

ORIGINAL PAGE IS
OF POOR QUALITY

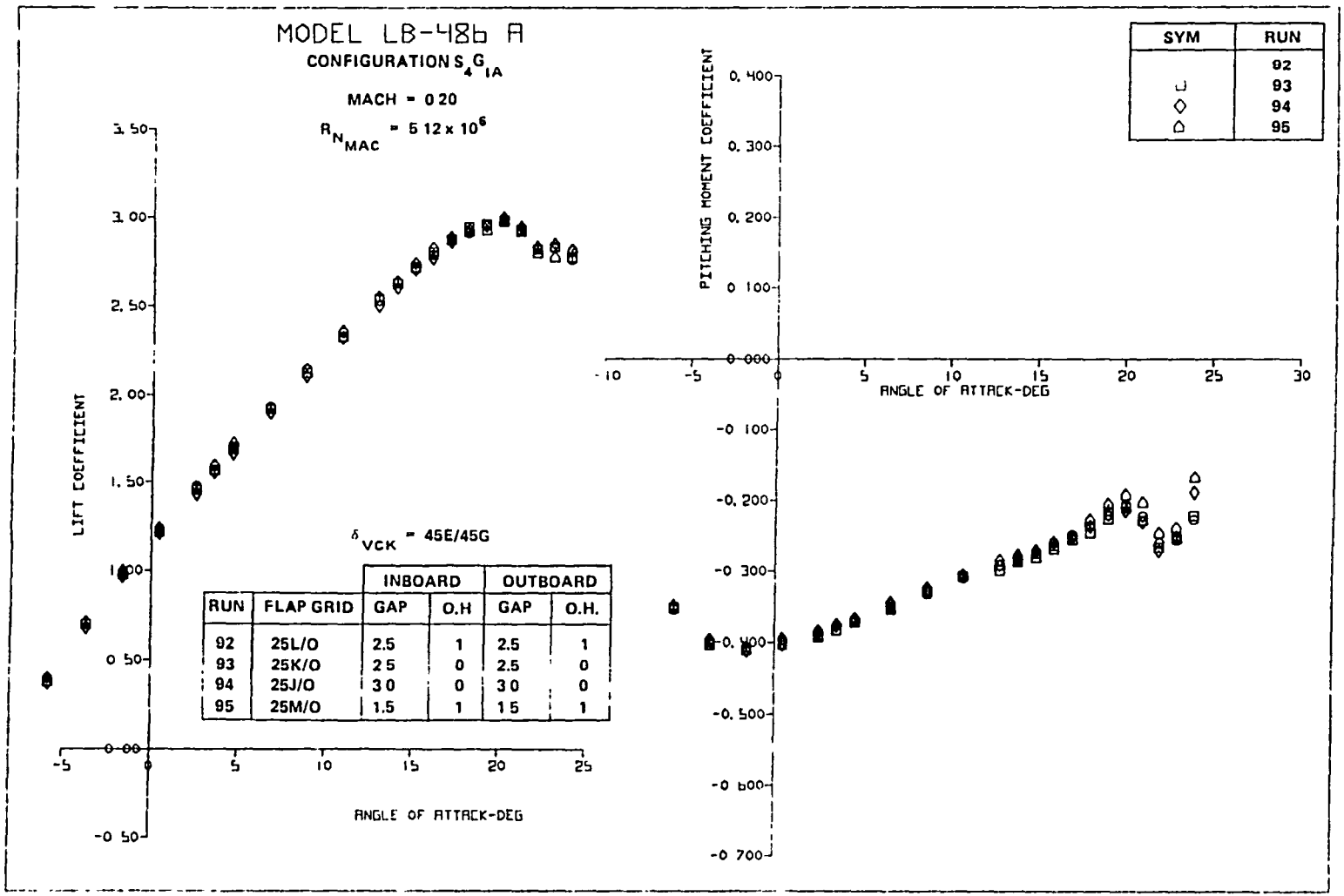

A LIFT AND PITCHING MOMENT

FIGURE 115. SINGLE-SLOT FLAP POSITION STUDY FOR LANDING FLAPS WITH VCK

ORIGINAL PAGE IS
OF POOR QUALITY

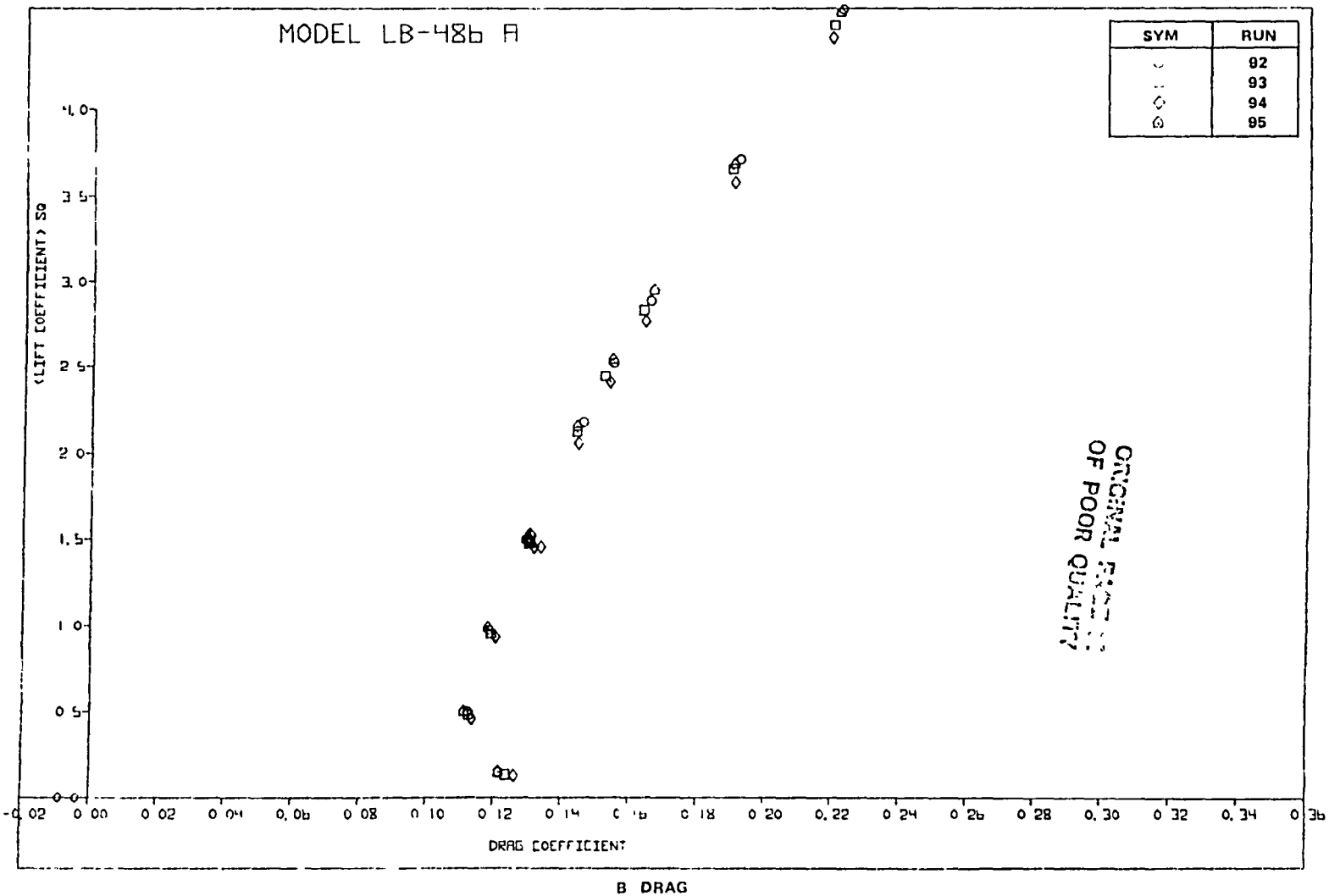

FIGURE 115. SINGLE-SLOT FLAP POSITION STUDY FOR LANDING FLAPS WITH VCK (CONCLUDED)

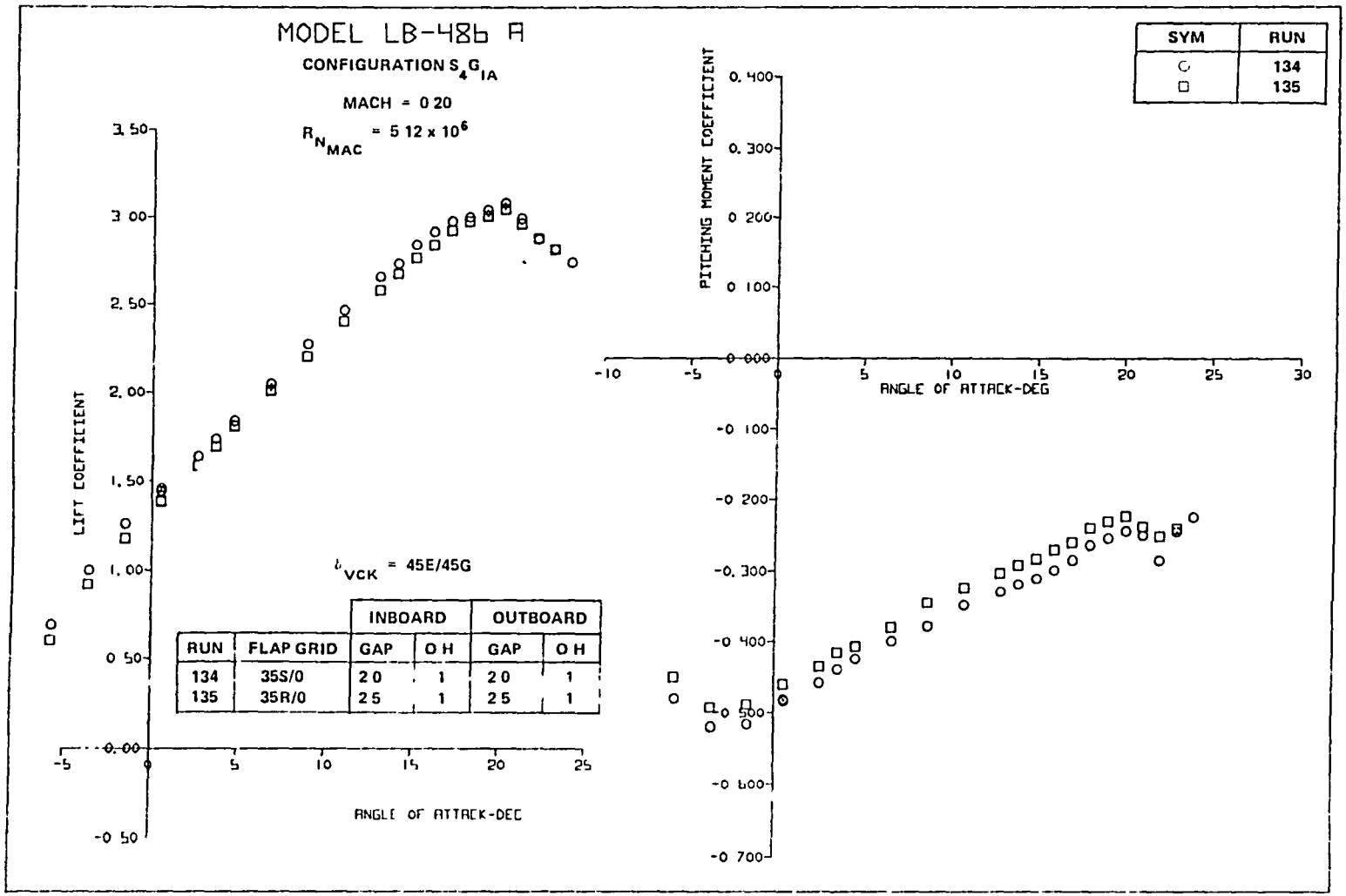

A. LIFT AND PITCHING MOMENT

FIGURE 116 SINGLE-SLOT FLAP POSITION STUDY FOR LANDING FLAPS WITH VCK

OF POOR QUALITY

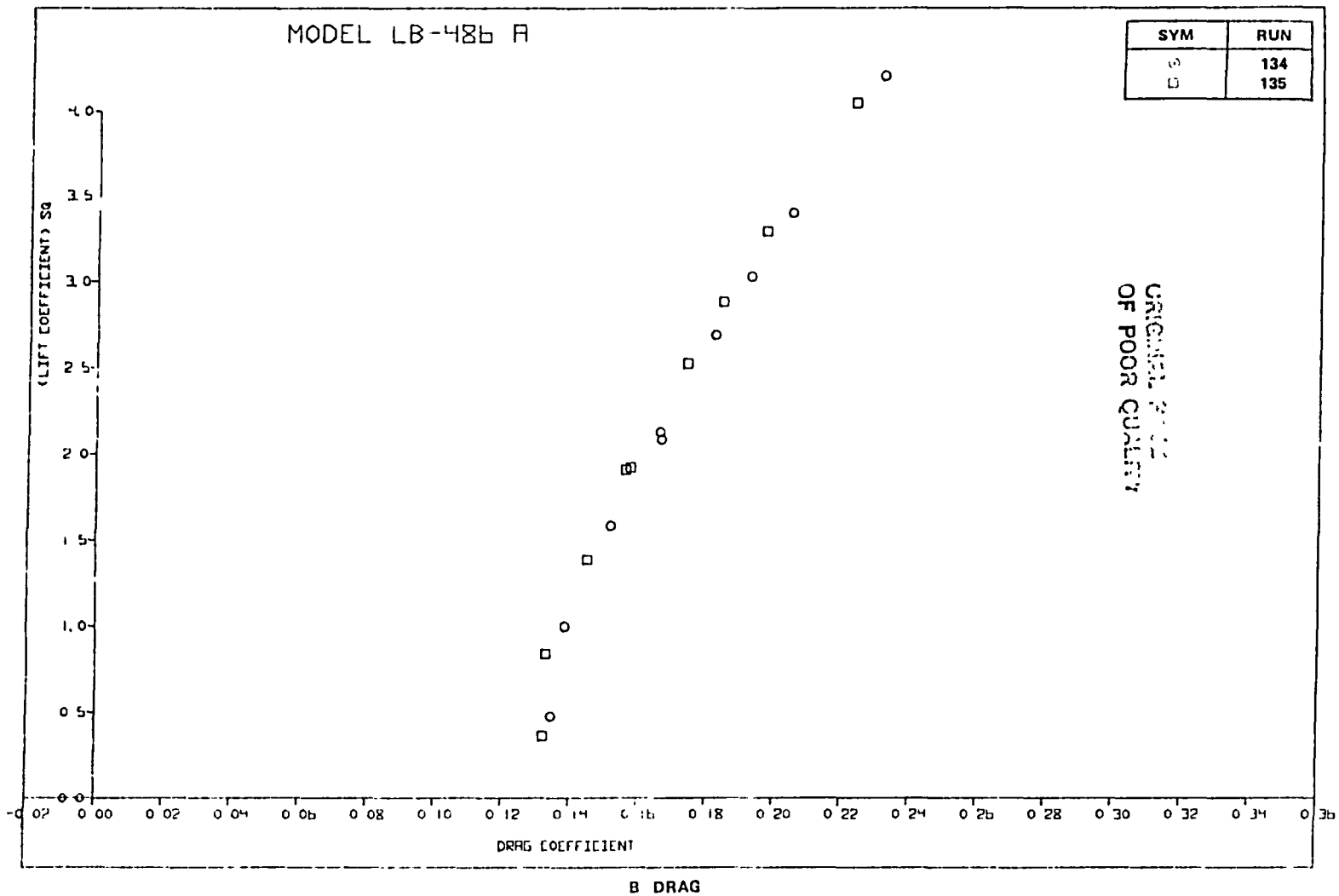

FIGURE 116. SINGLE-SLOT FLAP POSITION STUDY FOR LANDING FLAPS WITH VCK (CONCLUDED)

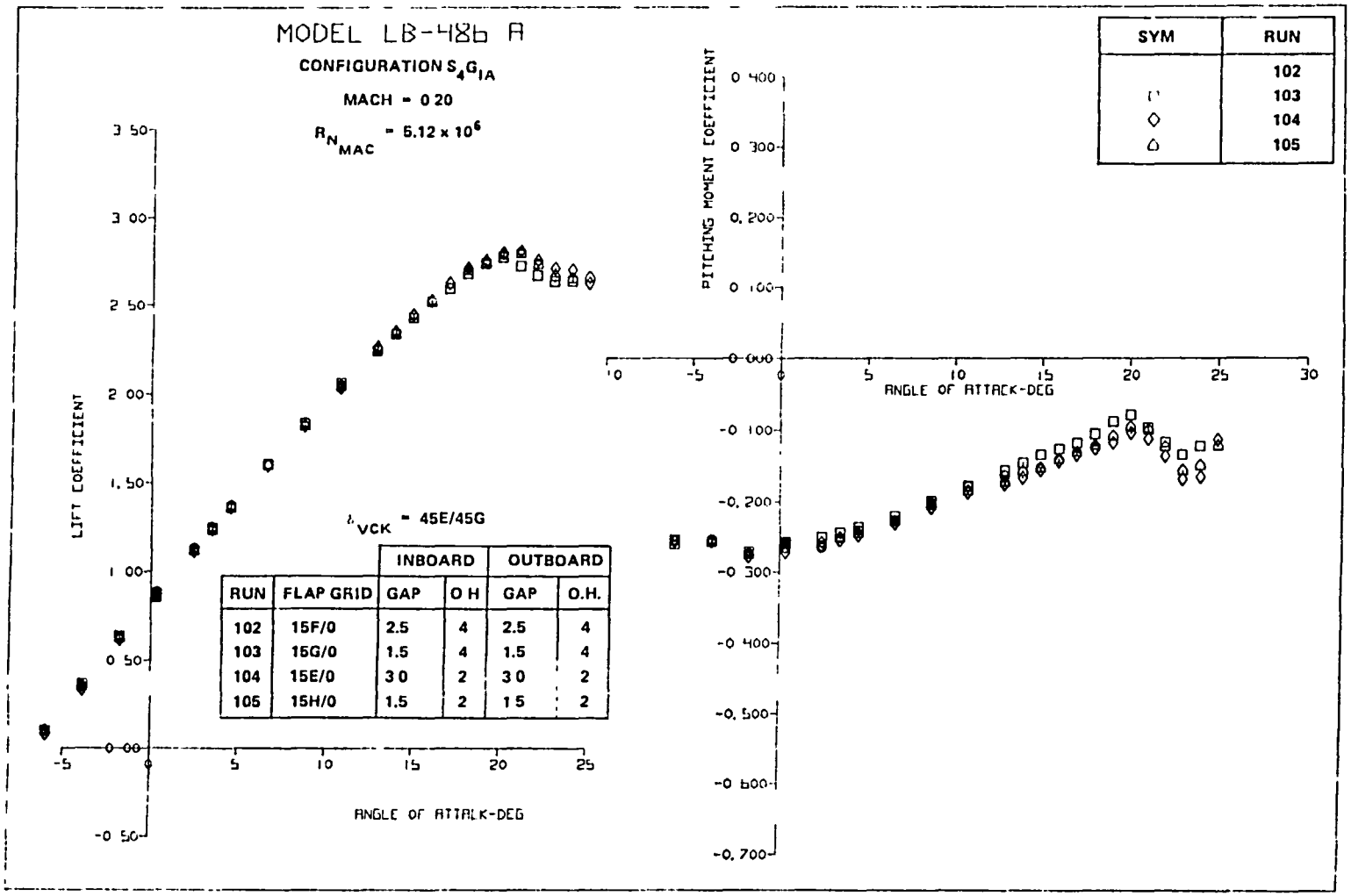

A. LIFT AND PITCHING MOMENT

FIGURE 117. SINGLE-SLOT FLAP POSITION STUDY FOR TAKEOFF FLAPS WITH VCK

ORIGINAL PAGE IS
OF POOR QUALITY

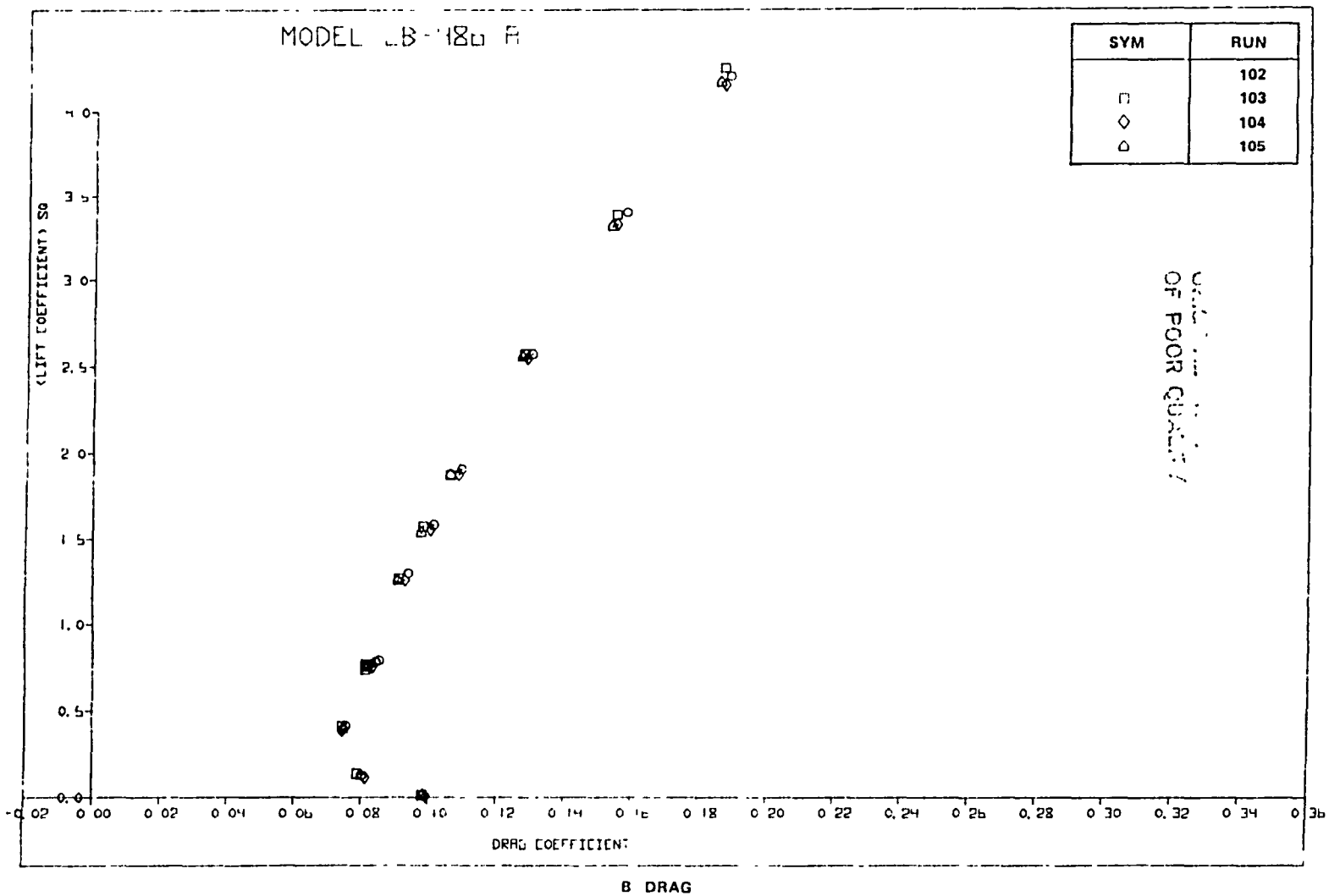

FIGURE 117. SINGLE-SLOT FLAP POSITION STUDY FOR TAKEOFF FLAPS WITH VCK (CONCLUDED)

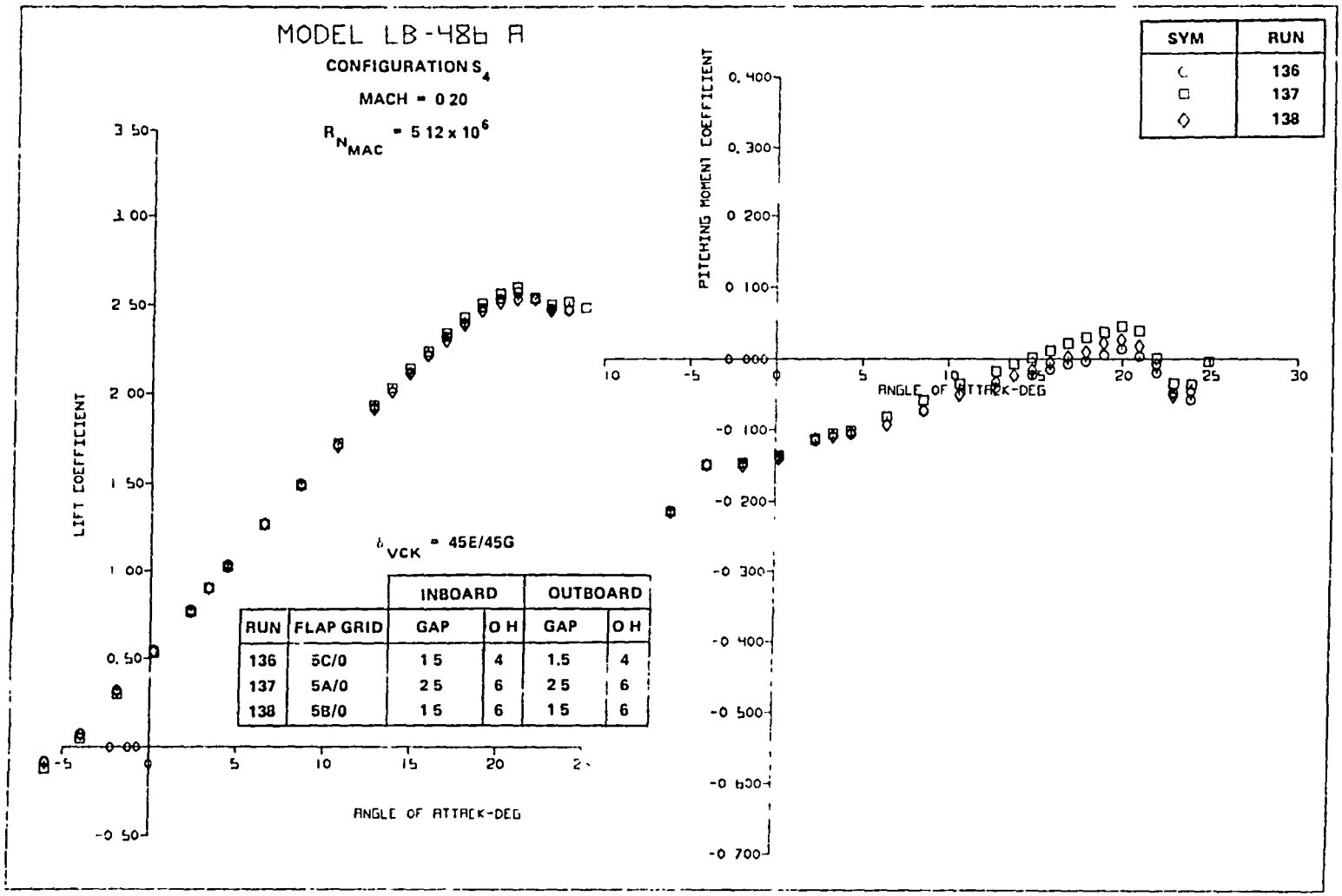

A LIFT AND PITCHING MOMENT

FIGURE 118. SINGLE-SLOT FLAP POSITION STUDY FOR TAKEOFF FLAPS WITH VCK

ORIGINAL PAGE IS
OF POOR QUALITY

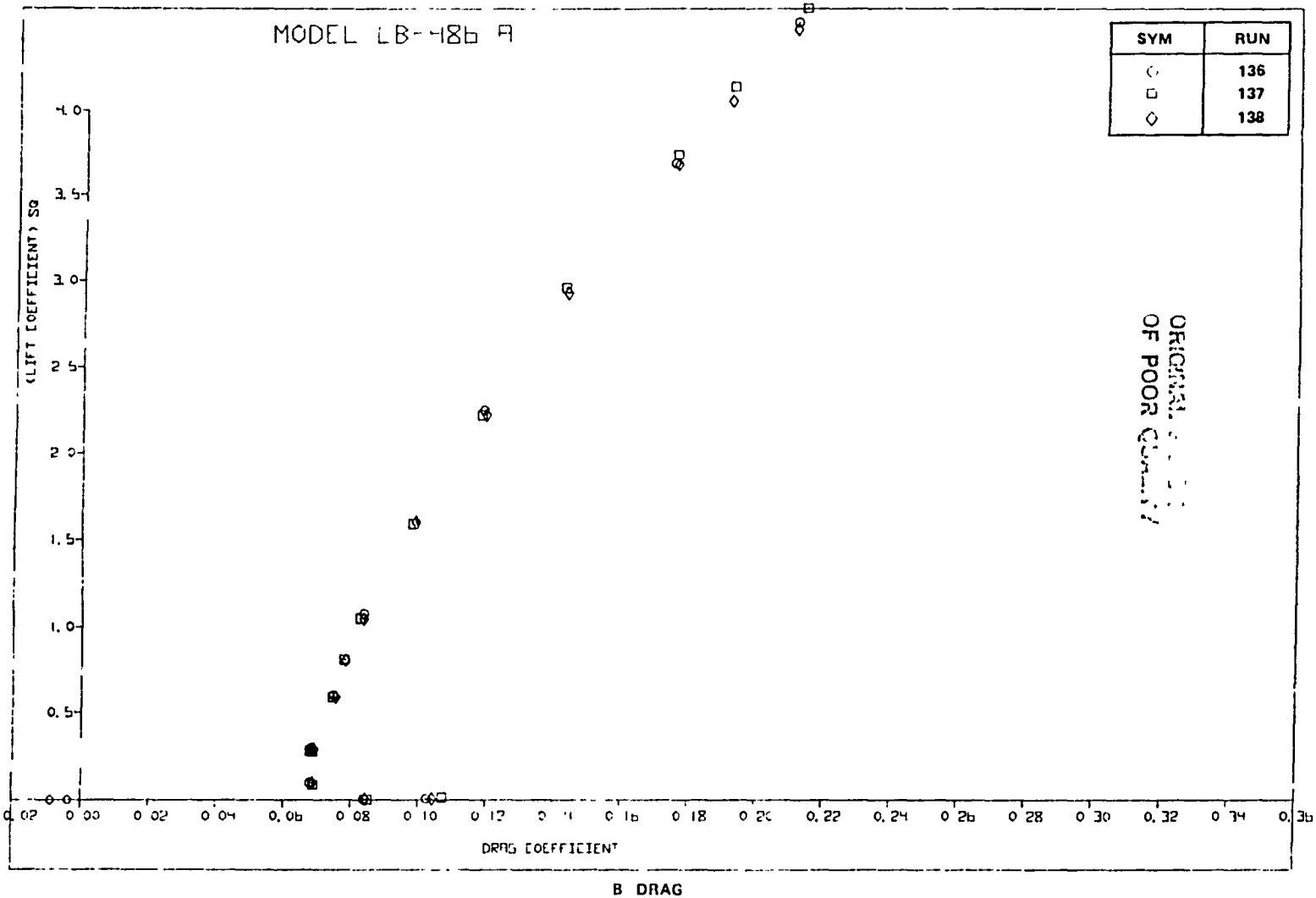

FIGURE 118. SINGLE-SLOT FLAP POSITION STUDY FOR TAKEOFF FLAPS WITH VCK (CONCLUDED)

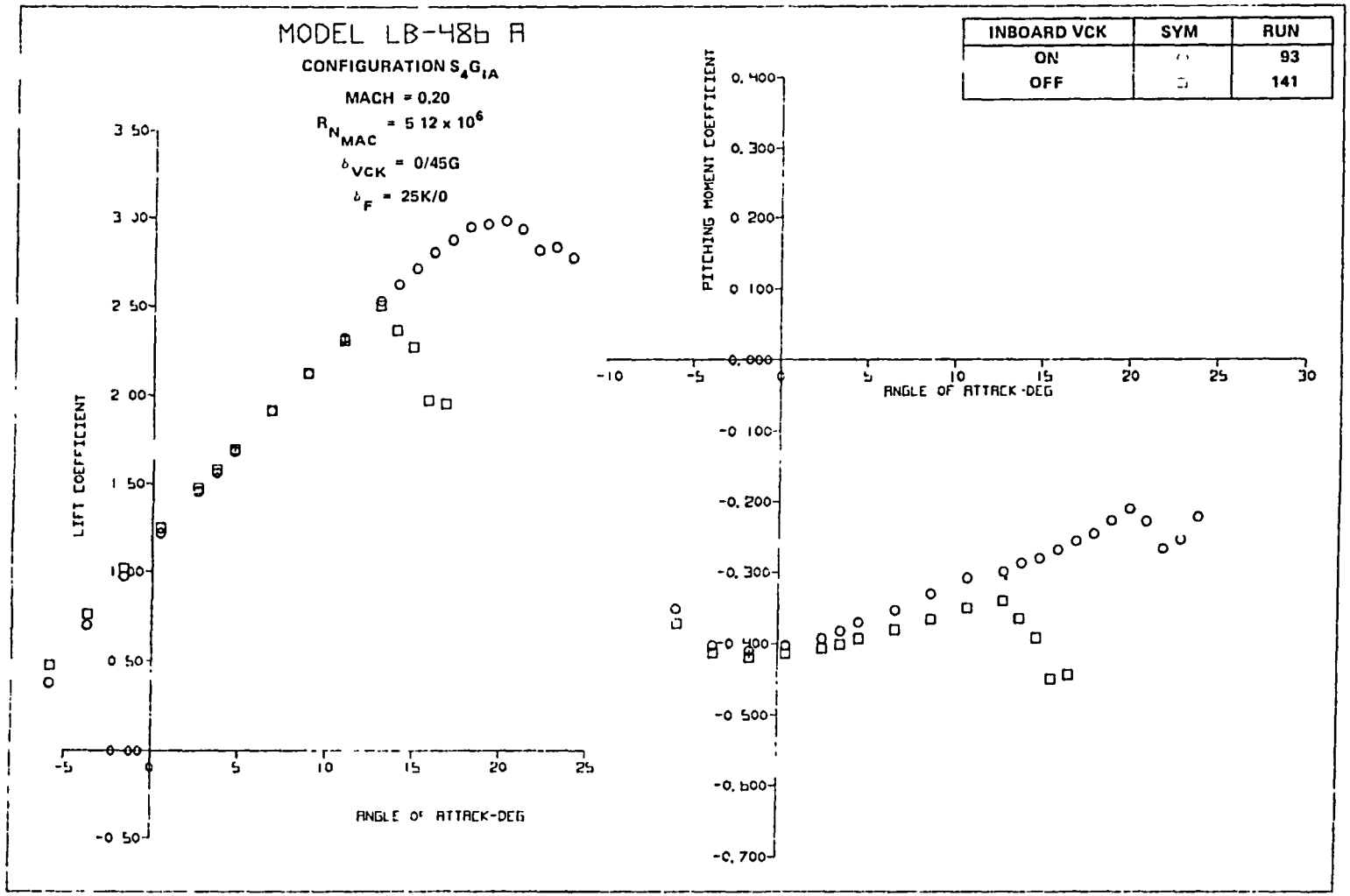

A LIFT AND PITCHING MOMENT

FIGURE 119 EFFECT OF INBOARD VCK REMOVAL ON AERODYNAMIC CHARACTERISTICS OF THE SINGLE-SLOT LANDING FLAPS WITH VCK CONFIGURATION

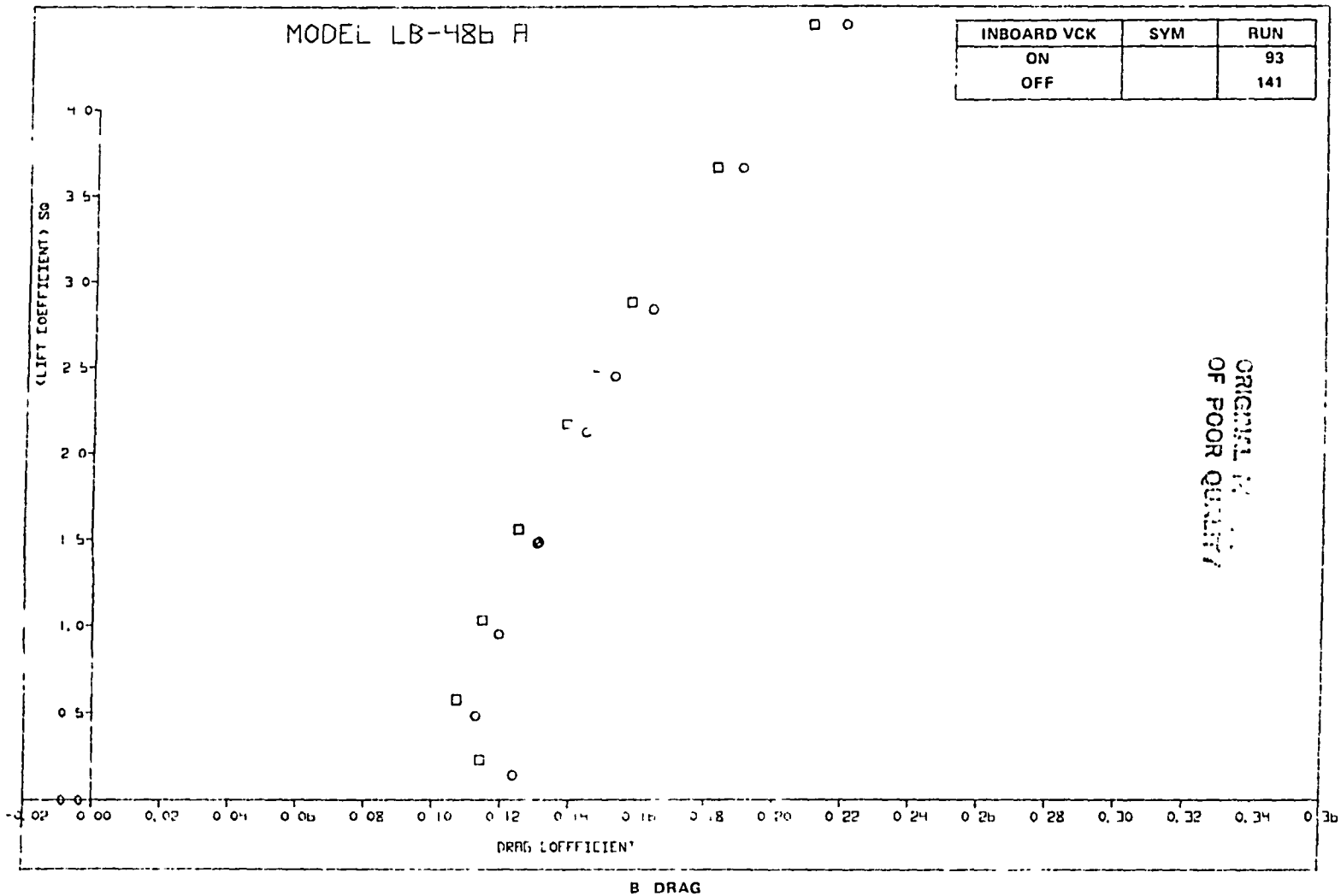

FIGURE 119. EFFECT OF INBOARD VCK REMOVAL ON AERODYNAMIC CHARACTERISTICS OF THE SINGLE SLOT LANDING FLAPS WITH VCK CONFIGURATION (CONCLUDED)

Reynolds Number Effects on VCK with Single-Slot Flap (Tail-Off). - The Reynolds number effect on VCK with single-slot landing and takeoff deflections is presented in Figures 120 and 121. A $C_{L_{MAX}}$ reduction of 0.16 was also obtained for the single slot configuration. The pitching moment shift is similar to the two-segment flaps.

VCK with Single-Slot Flap and Horizontal Tail. - The effect of horizontal tail deflection for landing and takeoff single-slot flap deflections is shown in Figures 122 and 123. The landing flaps pitching moment trends indicate some reduction in negative pitching moment prior to stall for $i_H = 0^o$. Takeoff flaps pitch characteristics are improved.

Slat Configuration

The slat with two-segment landing flaps configuration is shown in Figure 124. As mentioned previously, this configuration was evaluated with the optimized flap system defined in the previous VCK studies.

Slat Landing and Takeoff Optimization. - A slat deflection and position survey was evaluated with the two-segment flap system. Figure 125 presents the slat $25^o/35^o$ position study. A $C_{L_{MAX}}$ of 3.008 was obtained. The basic tail-off pitching moment trends indicate positive pitch increments prior to $C_{L_{MAX}}$, and no significant effect due to the change in slat position. The drag values show a slight reduction in drag for the small gap and overhang (Gap = 1.5%, O.H. = -1%). Figure 126 presents the sectional lift values for the two configurations. The significant trends from these plots at the high angles of attack are the lift loss at the 50- and 72-percent span stations, and the almost constant sectional lift values near the stall for the two inboard span stations.

The effect of slat position for the $15^o/25^o$ slat deflection is shown in Figure 127. The $C_{L_{MAX}}$ increased to 3.2, but the pitch characteristics are similar to the $25^o/35^o$ slat deflection. Near the 1.3 V_S condition, the difference in drag due to the change in slat position is small. Figure 128 illustrates the sectional lift values for the small gap and O.H. position. Results are similar to the $25^o/35^o$ slat results. Some improvement is noted in the sectional lift variation at 90-percent span station with the 25^o outboard slat deflection. Figure 129 presents the chordwise pressure distribution for Run 154 for angle of attack conditions prior to, and after $C_{L_{MAX}}$.

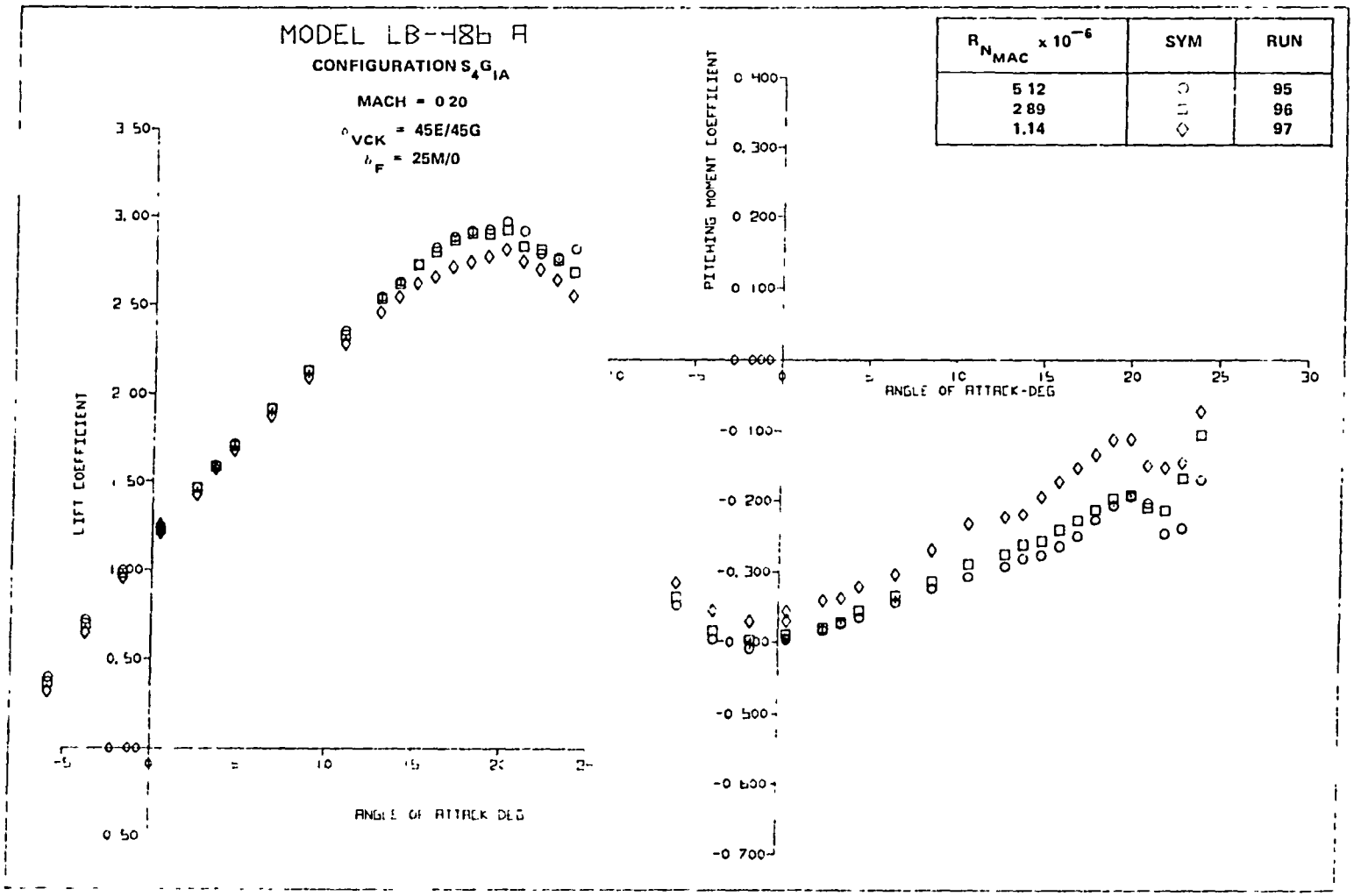

A LIFT AND PITCHING MOMENT

FIGURE 120. EFFECT OF REYNOLDS NUMBER ON AERODYNAMIC CHARACTERISTICS OF THE VCK WITH SINGLE-SLOT LANDING FLAPS

ORIGINAL PAGE IS OF POOR QUALITY

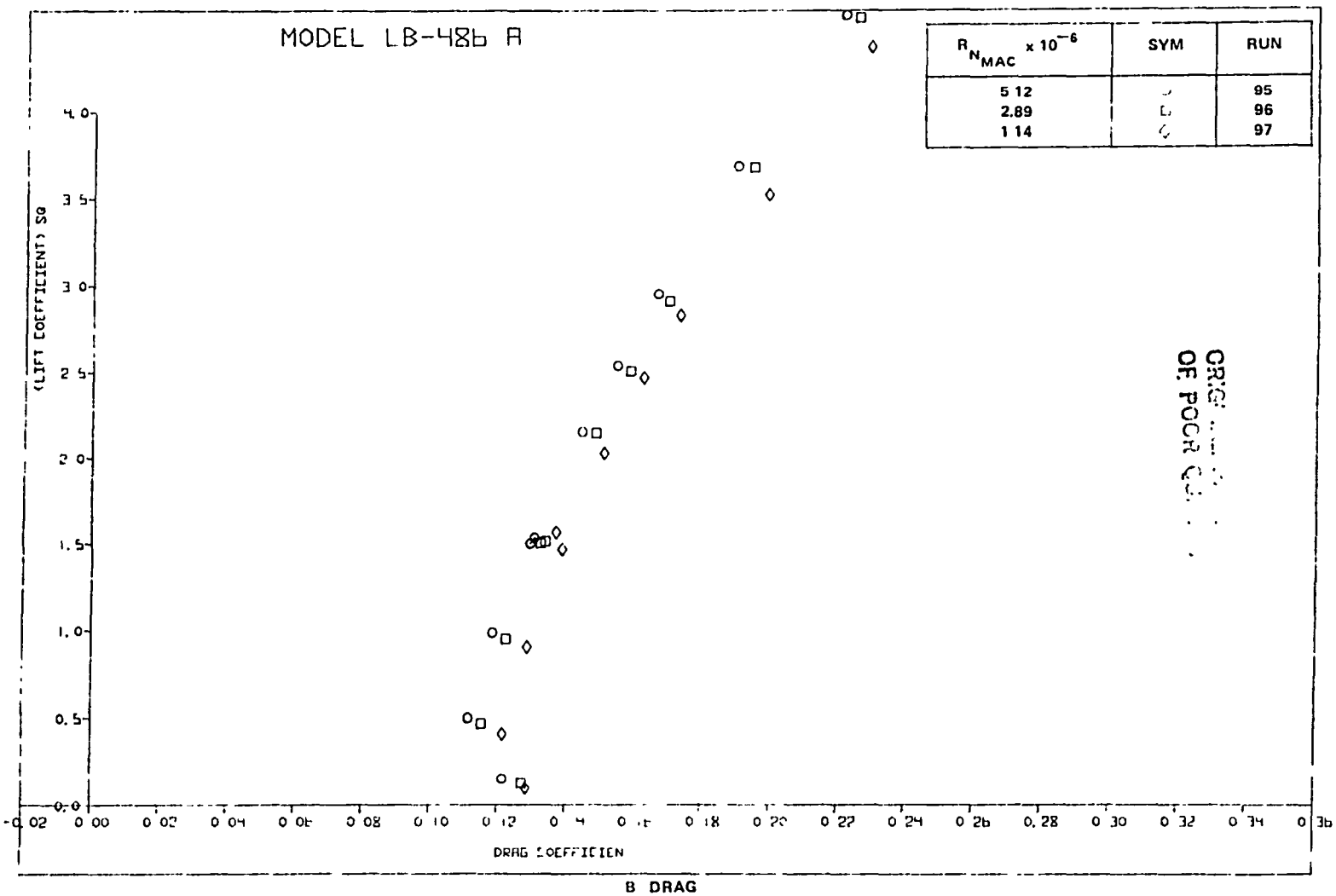

FIGURE 120 EFFECT OF REYNOLDS NUMBER ON AERODYNAMIC CHARACTERISTICS OF THE VCK WITH SINGLE-SLOT LANDING FLAPS (CONTINUED)

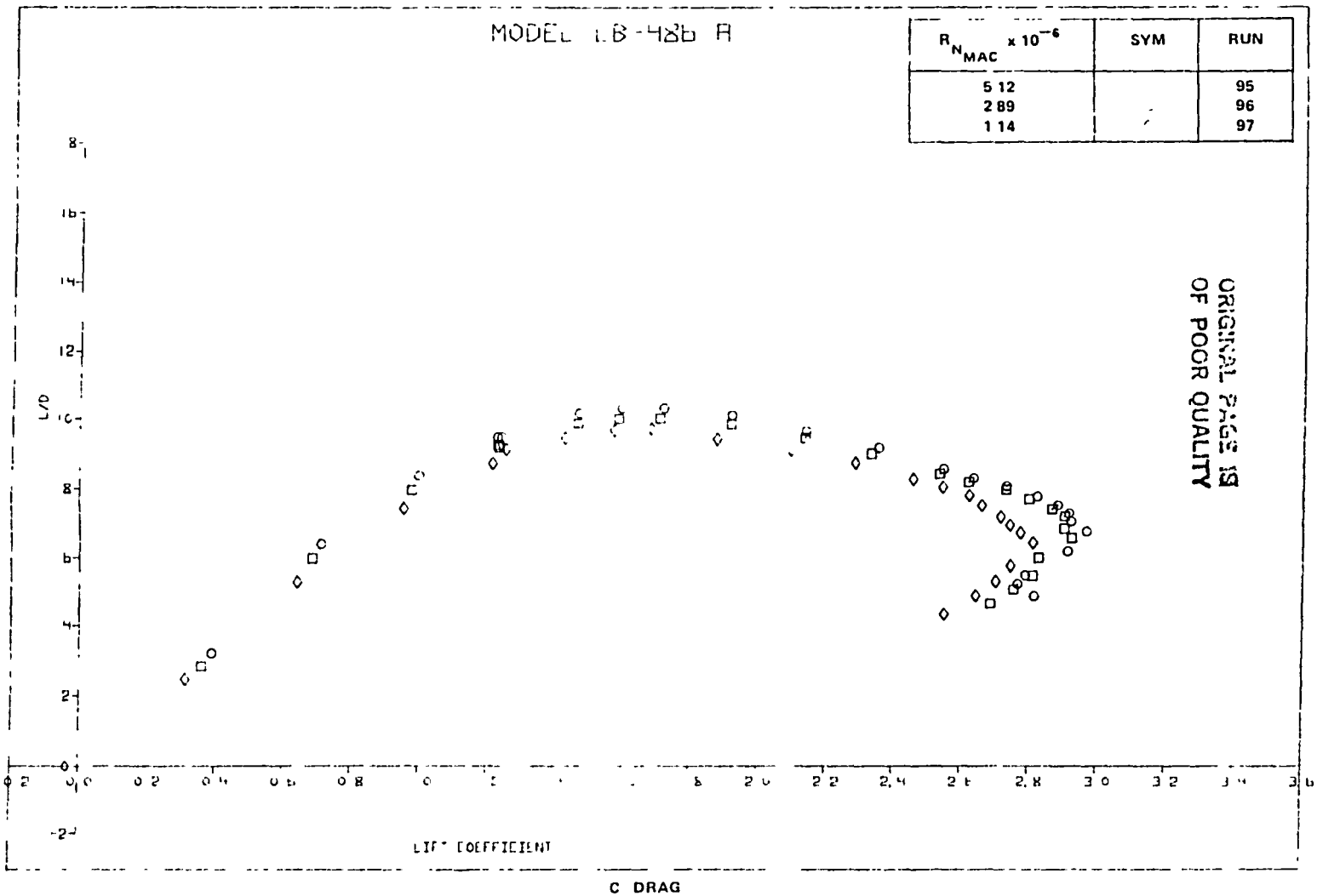

ORIGINAL PAGE IS
OF POOR QUALITY

FIGURE 120. EFFECT OF REYNOLDS NUMBER ON AERODYNAMIC CHARACTERISTICS OF THE VCK WITH SINGLE-SLOT LANDING FLAPS (CONCLUDED)

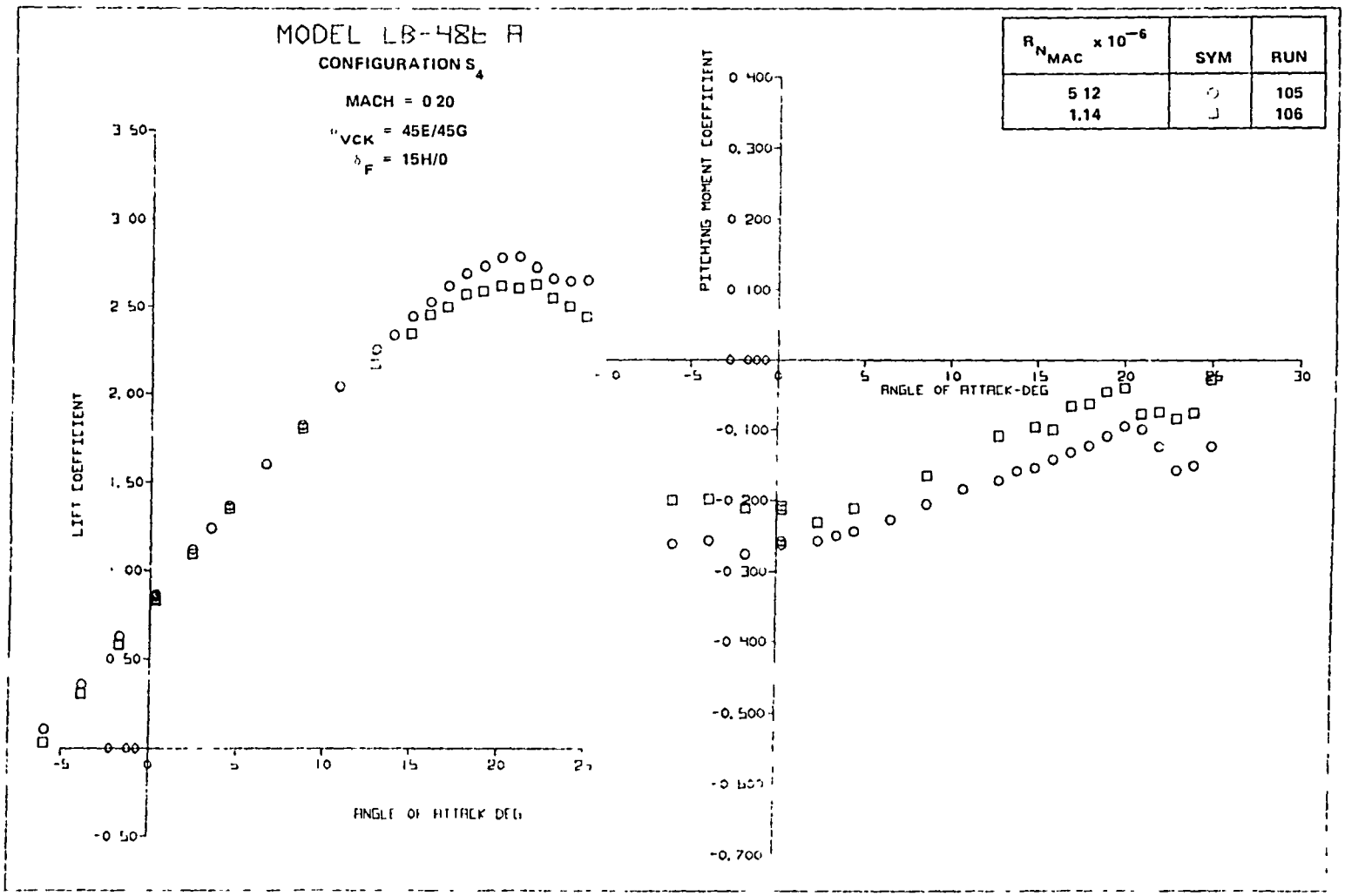

A LIFT AND PITCHING MOMENT

FIGURE 121. EFFECT OF REYNOLDS NUMBER ON AERODYNAMIC CHARACTERISTICS OF THE VCK WITH SINGLE-SLOT TAKEOFF FLAPS CONFIGURATION

ORIGINAL PAGE IS OF POOR QUALITY

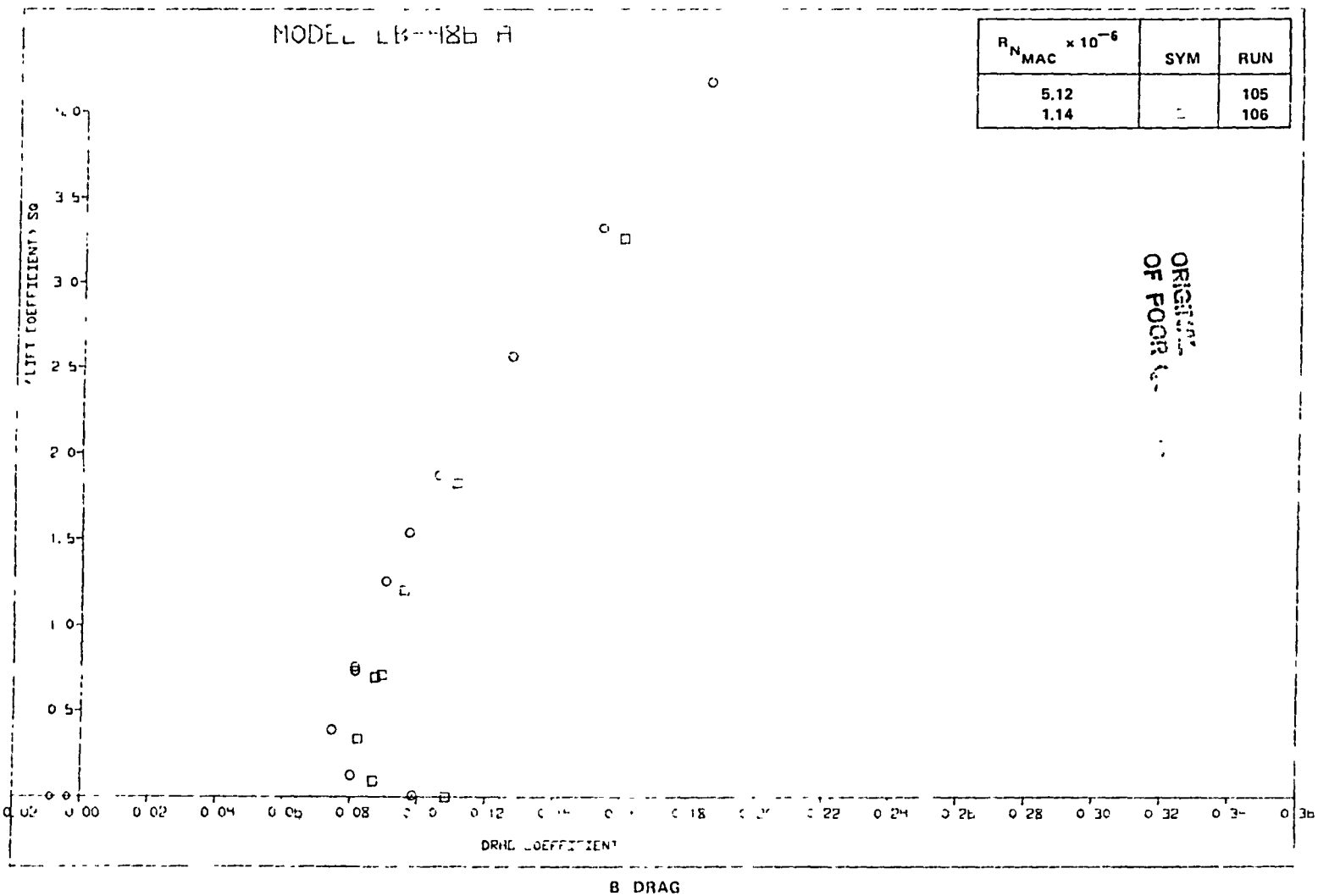

FIGURE 121 EFFECT OF REYNOLDS NUMBER ON AERODYNAMIC CHARACTERISTICS OF THE VCK WITH SINGLE SLOT TAKEOFF FLAPS CONFIGURATION (CONTINUED)

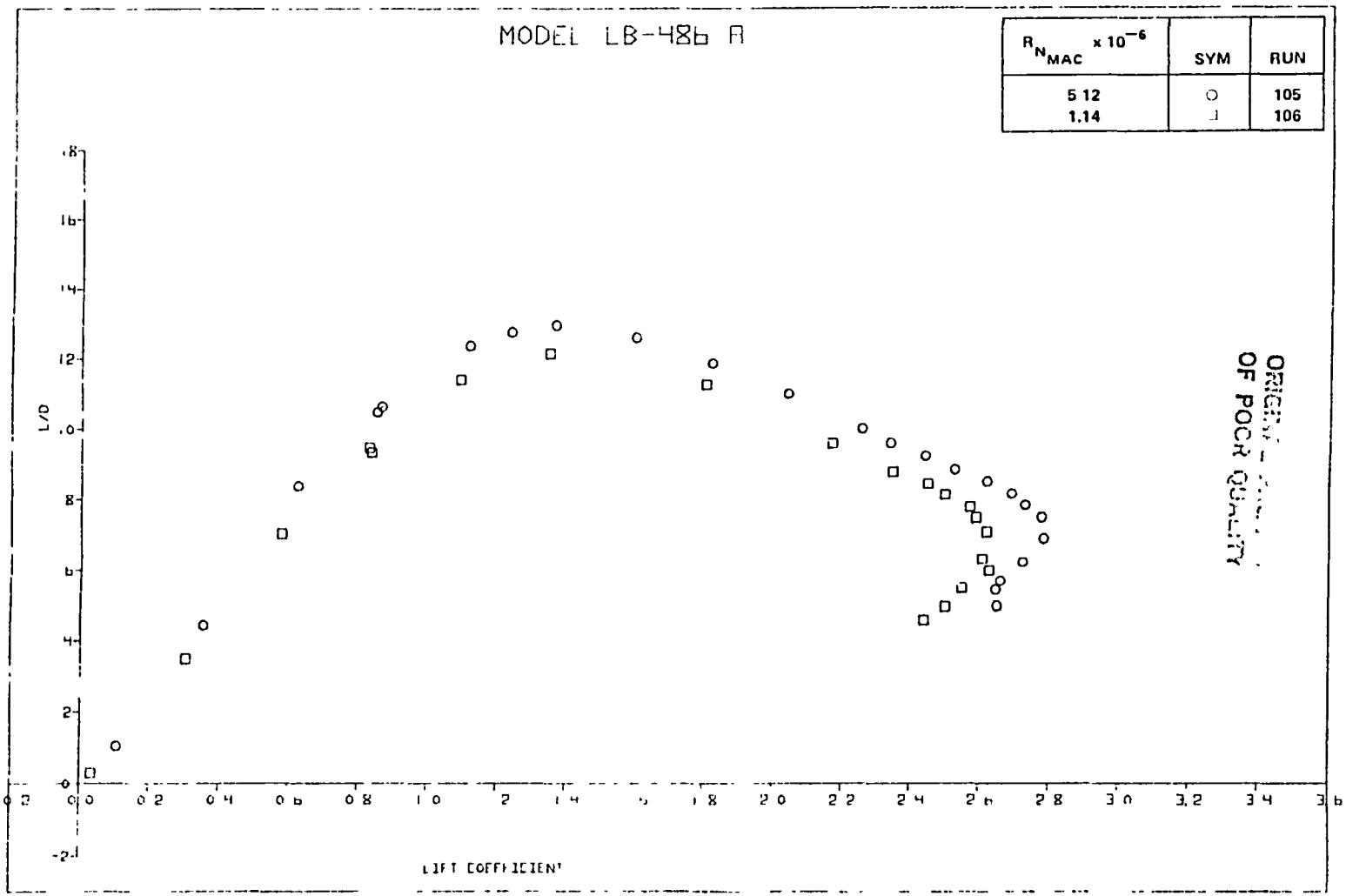

FIGURE 121. EFFECT OF REYNOLDS NUMBER ON AERODYNAMIC CHARACTERISTICS OF THE VCK WITH SINGLE-SLOT TAKEOFF FLAPS CONFIGURATION (CONCLUDED)

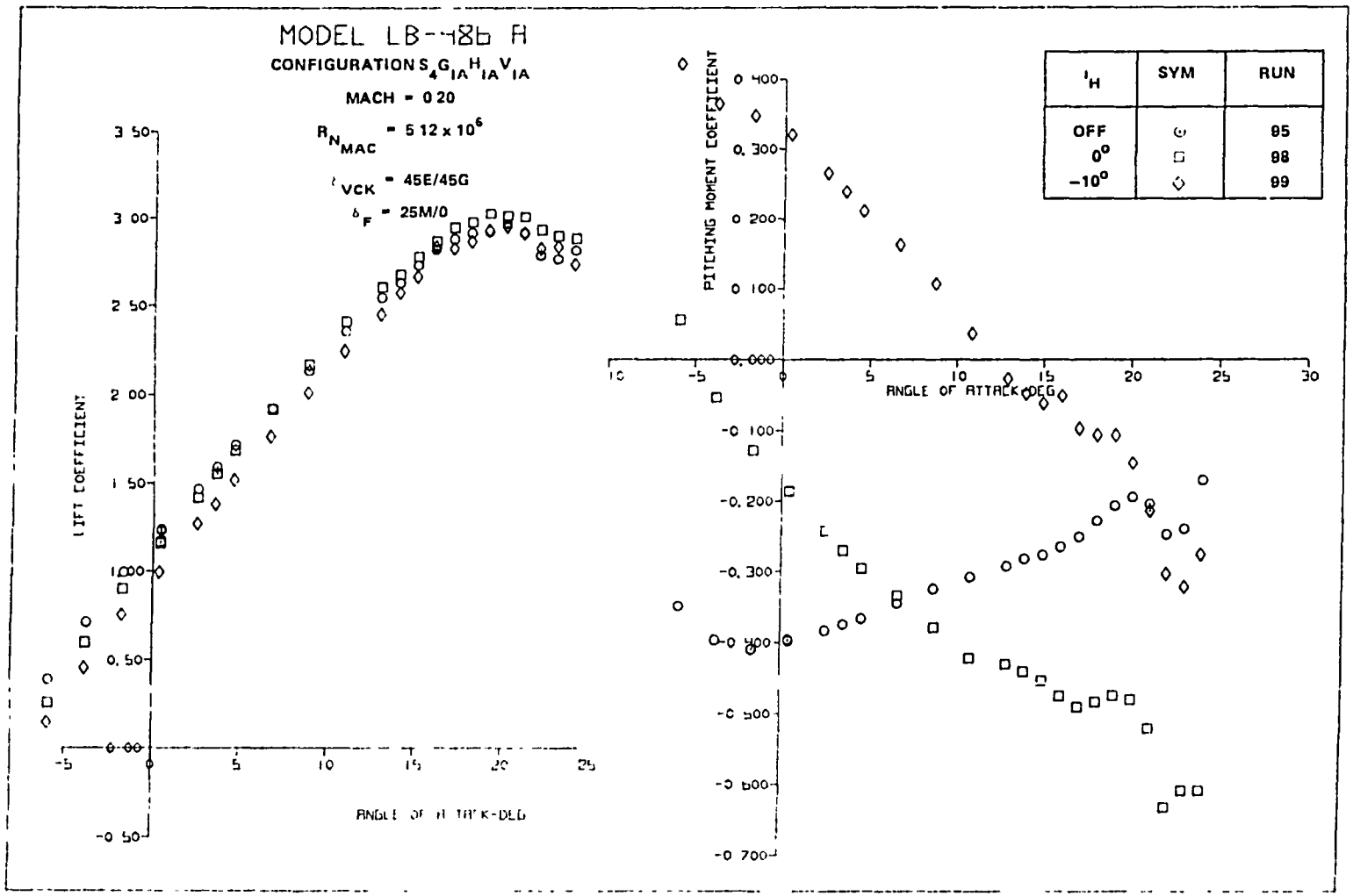

A LIFT AND PITCHING MOMENT

FIGURE 122. EFFECT OF HORIZONTAL TAIL DEFLECTION ON AERODYNAMIC CHARACTERISTICS OF THE VCK WITH SINGLE-SLOT LANDING FLAPS CONFIGURATION

ORIGINAL PAGE IS OF POOR QUALITY

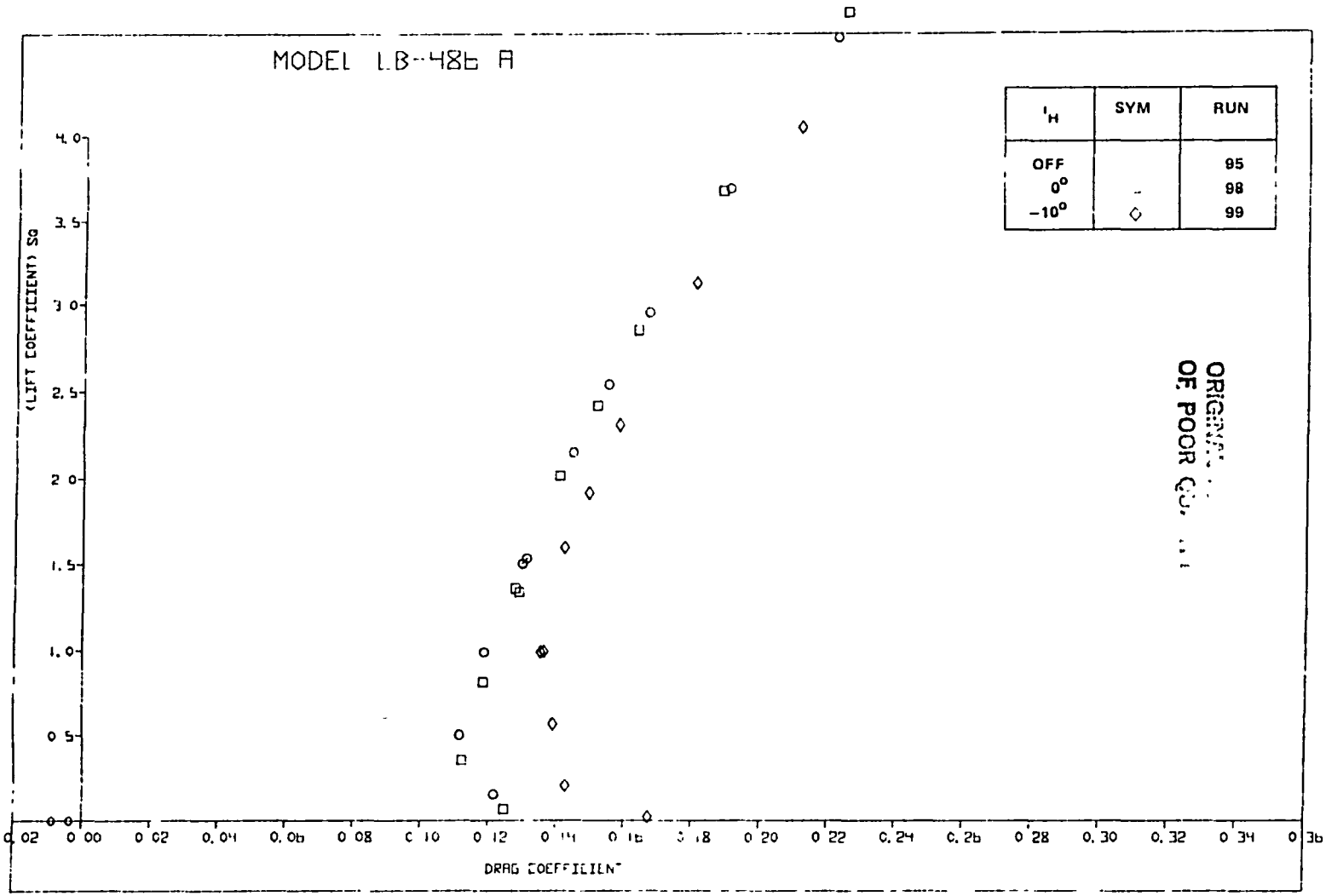

B DRAG

FIGURE 122. EFFECT OF HORIZONTAL TAIL DEFLECTION ON AERODYNAMIC CHARACTERISTICS OF THE VCK WITH SINGLE-SLOT LANDING FLAPS CONFIGURATION (CONCLUDED)

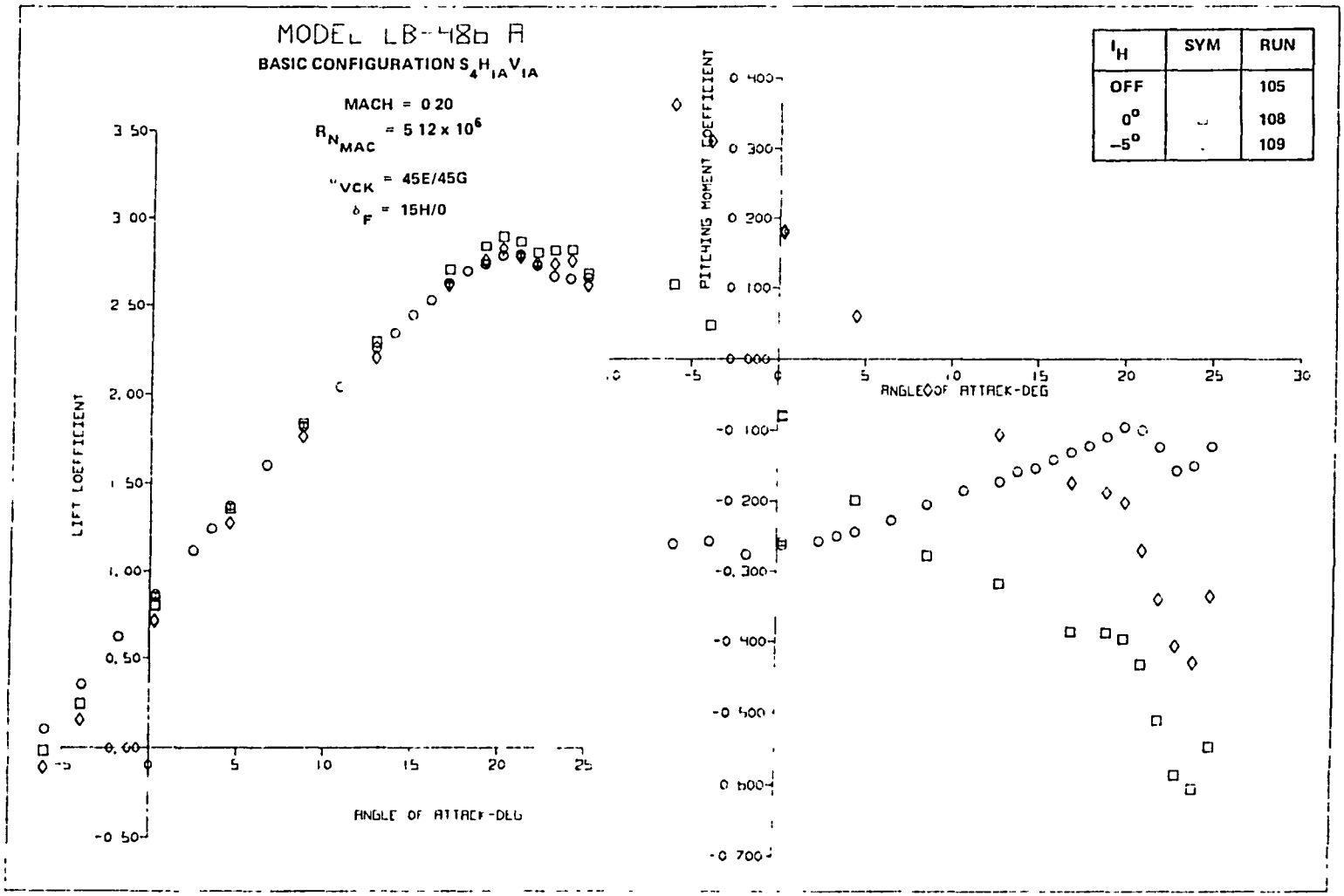

A LIFT AND PITCHING MOMENT

FIGURE 123. EFFECT OF HORIZONTAL TAIL DEFLECTION ON AERODYNAMIC CHARACTERISTICS OF THE VCK WITH SINGLE-SLOT TAKEOFF FLAPS CONFIGURATION

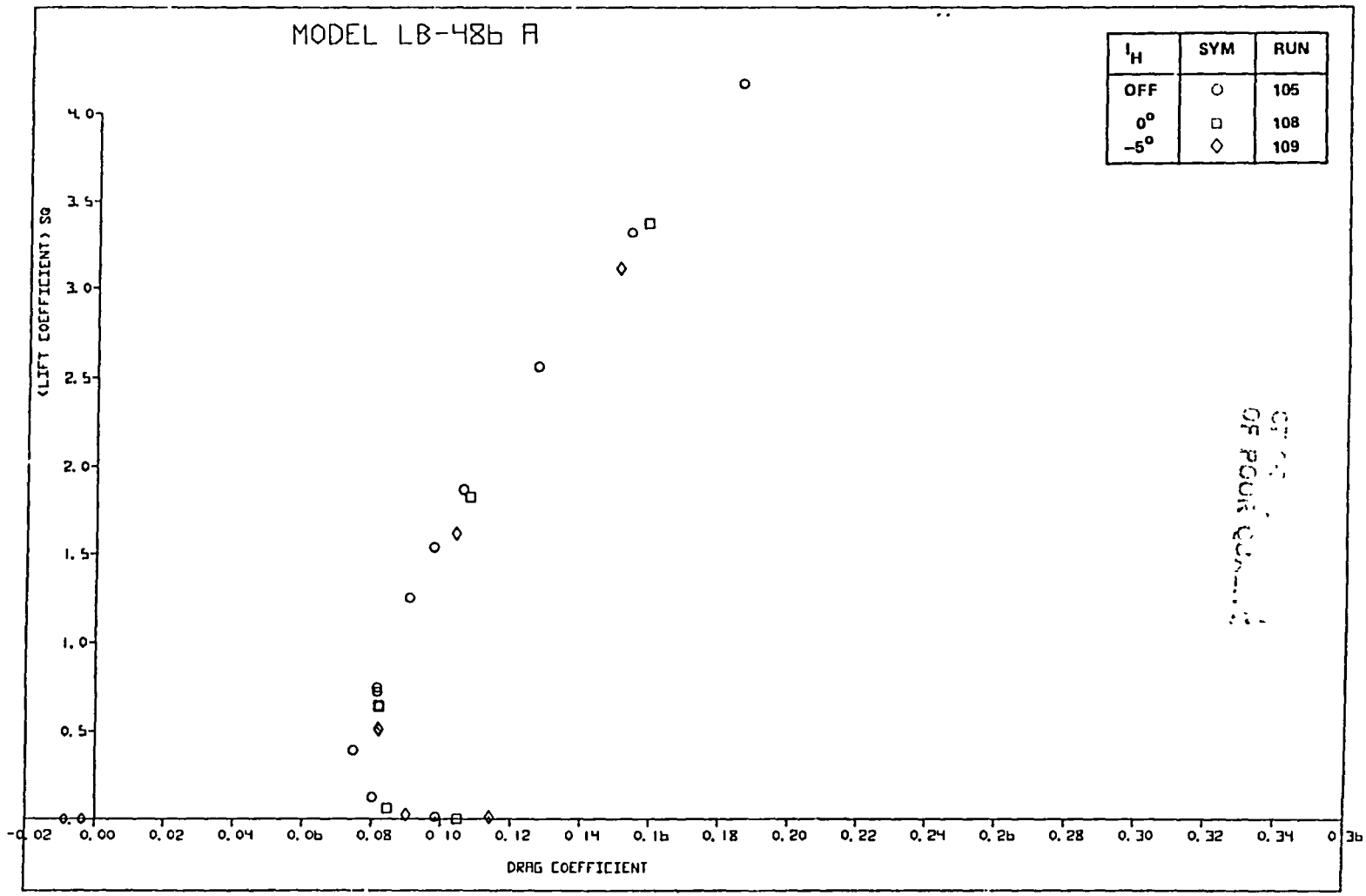

B. DRAG

FIGURE 123. EFFECT OF HORIZONTAL TAIL DEFLECTION ON AERODYNAMIC CHARACTERISTICS OF THE VCK WITH SINGLE-SLOT TAKEOFF FLAPS CONFIGURATION (CONCLUDED) —

ORIGINAL PAGE IS
OF POOR QUALITY

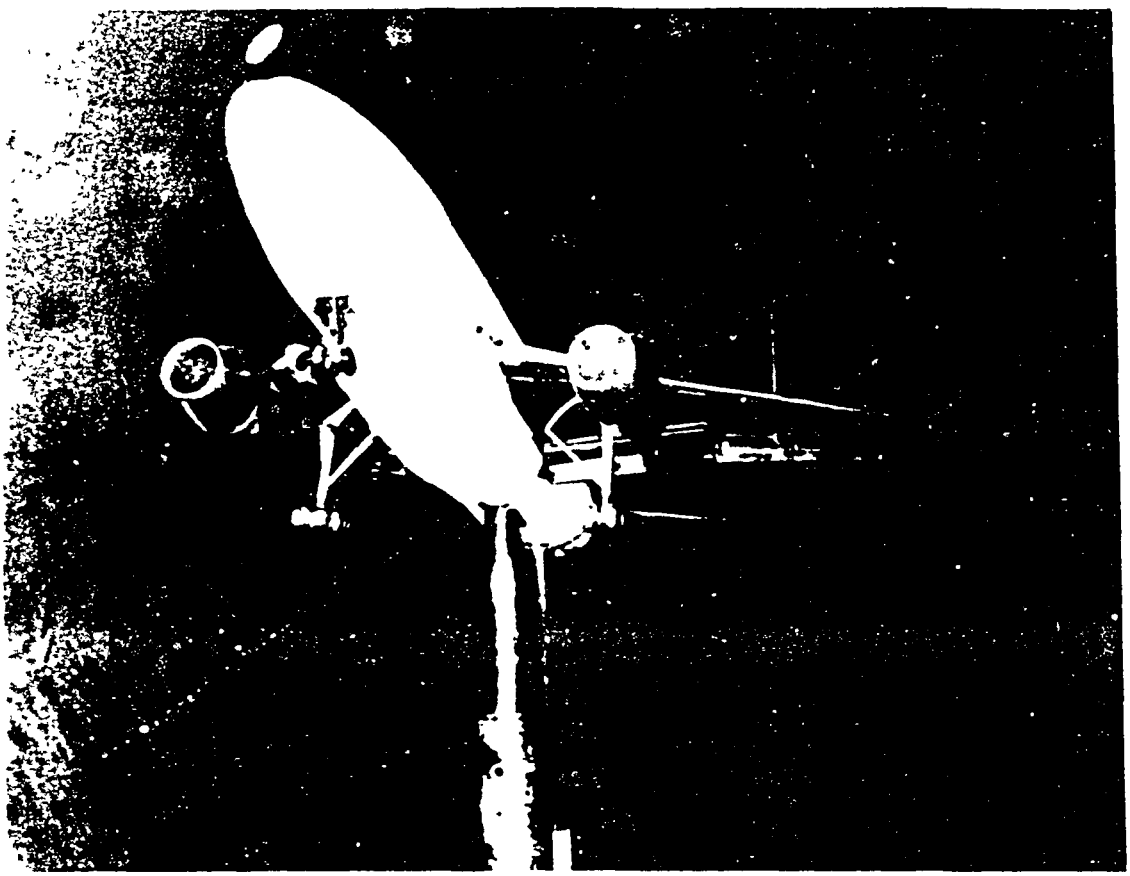

FIGURE 124. SLAT WITH TWO-SEGMENT LANDING FLAP CONFIGURATION

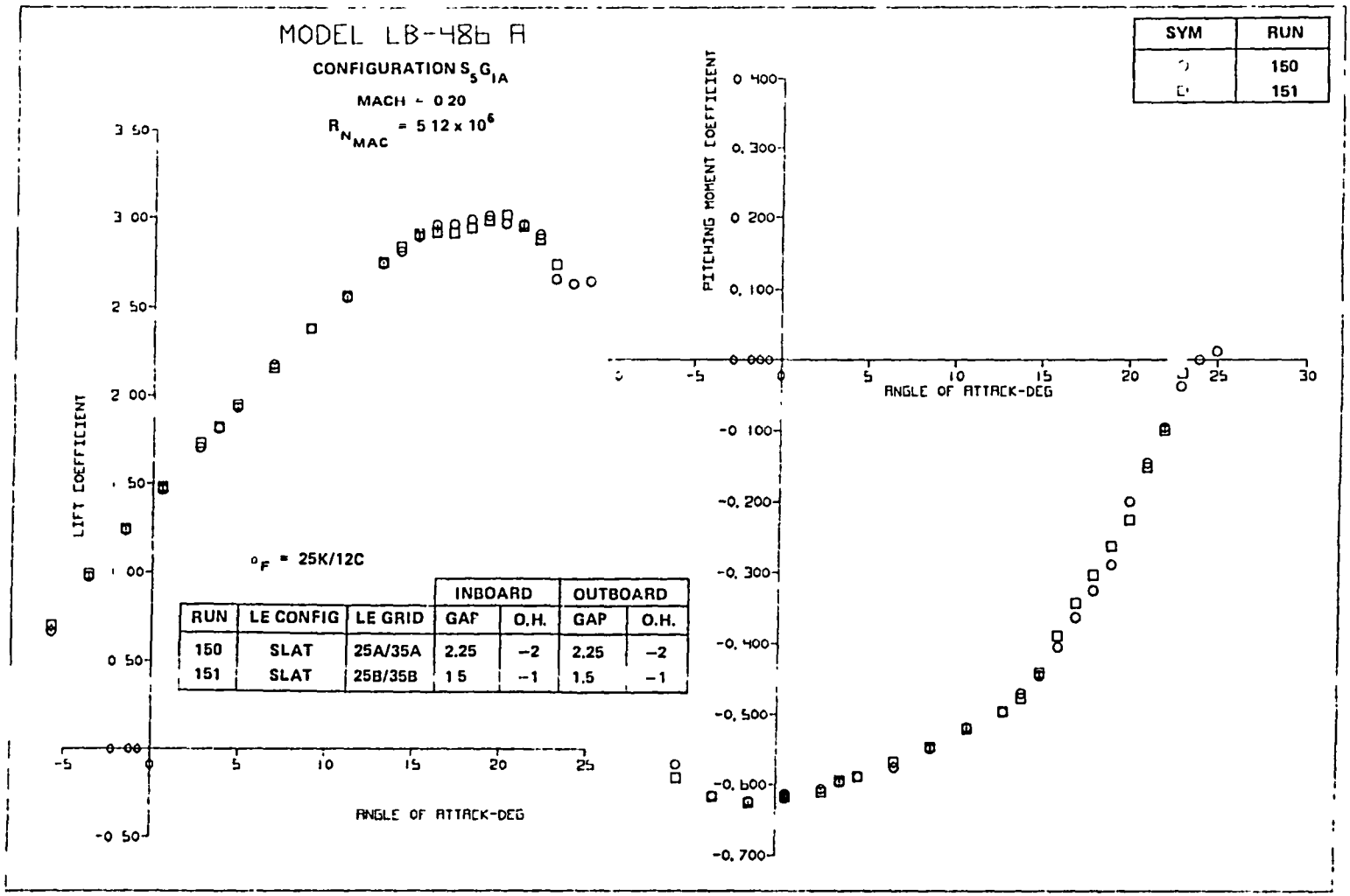

A LIFT AND PITCHING MOMENT

FIGURE 125. SLAT POSITION STUDY FOR LANDING FLAPS (δ_{SLAT} = 25°/35°)

OF POOR QUALITY

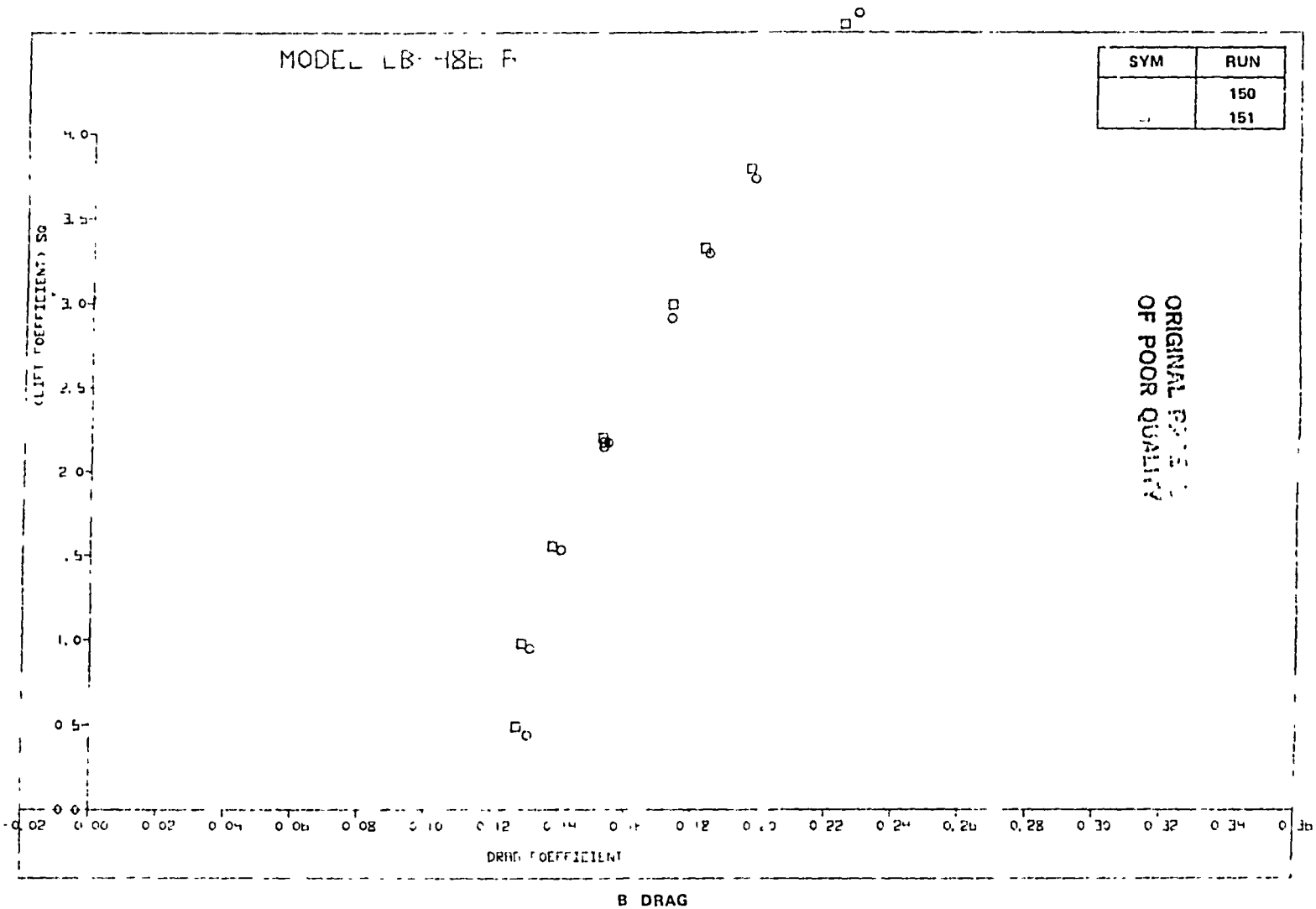

FIGURE 125 SLAT POSITION STUDY FOR LANDING FLAPS (δ_{SLAT} = 25°/35°) (CONCLUDED)

ORIGINAL PAGE IS
OF POOR QUALITY

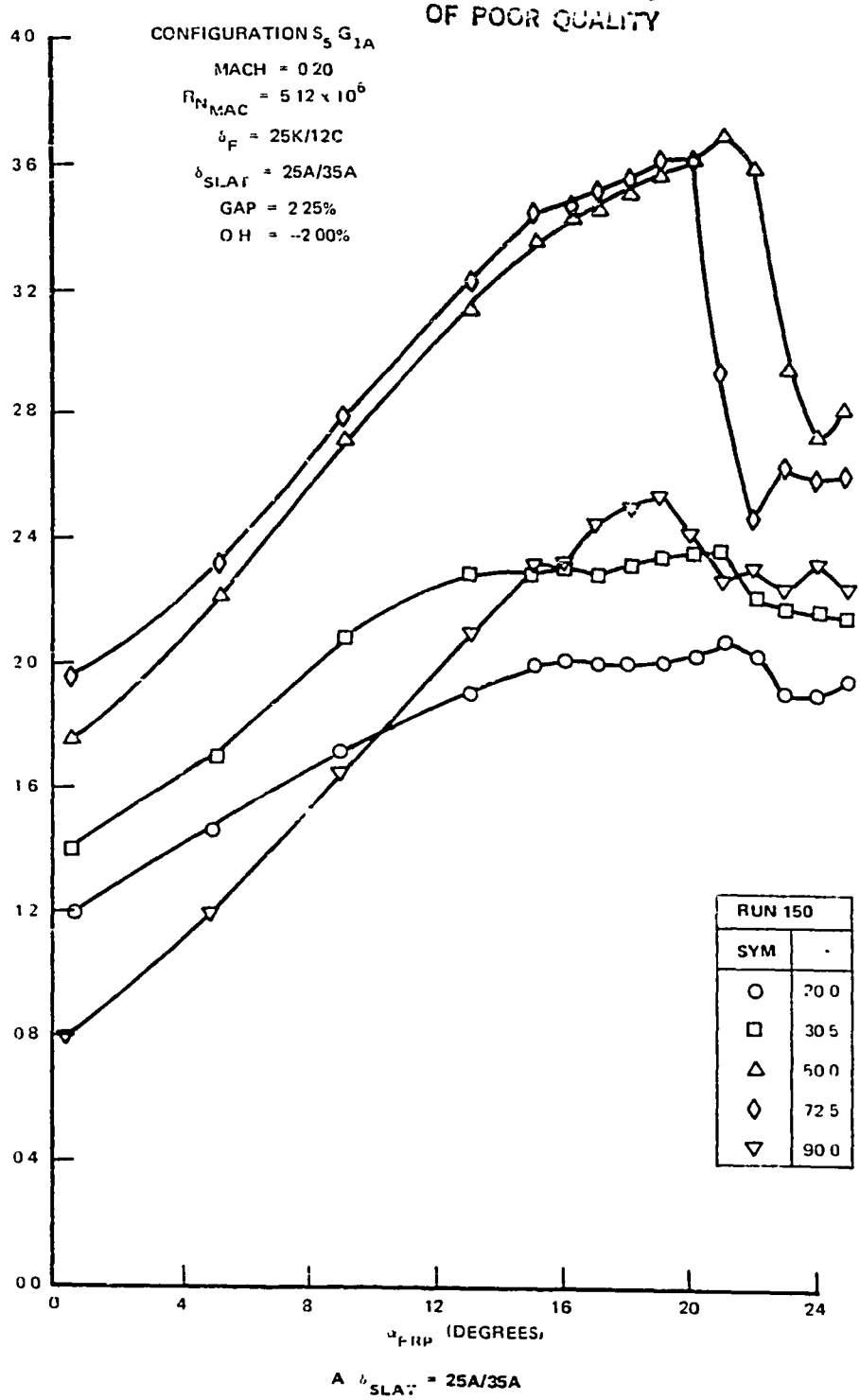

FIGURE 126. VARIATION OF SECTION LIFT COEFFICIENT FOR THE SLAT WITH TWO-SEGMENT LANDING FLAPS

ORIGINAL PAGE IS
OF POOR QUALITY

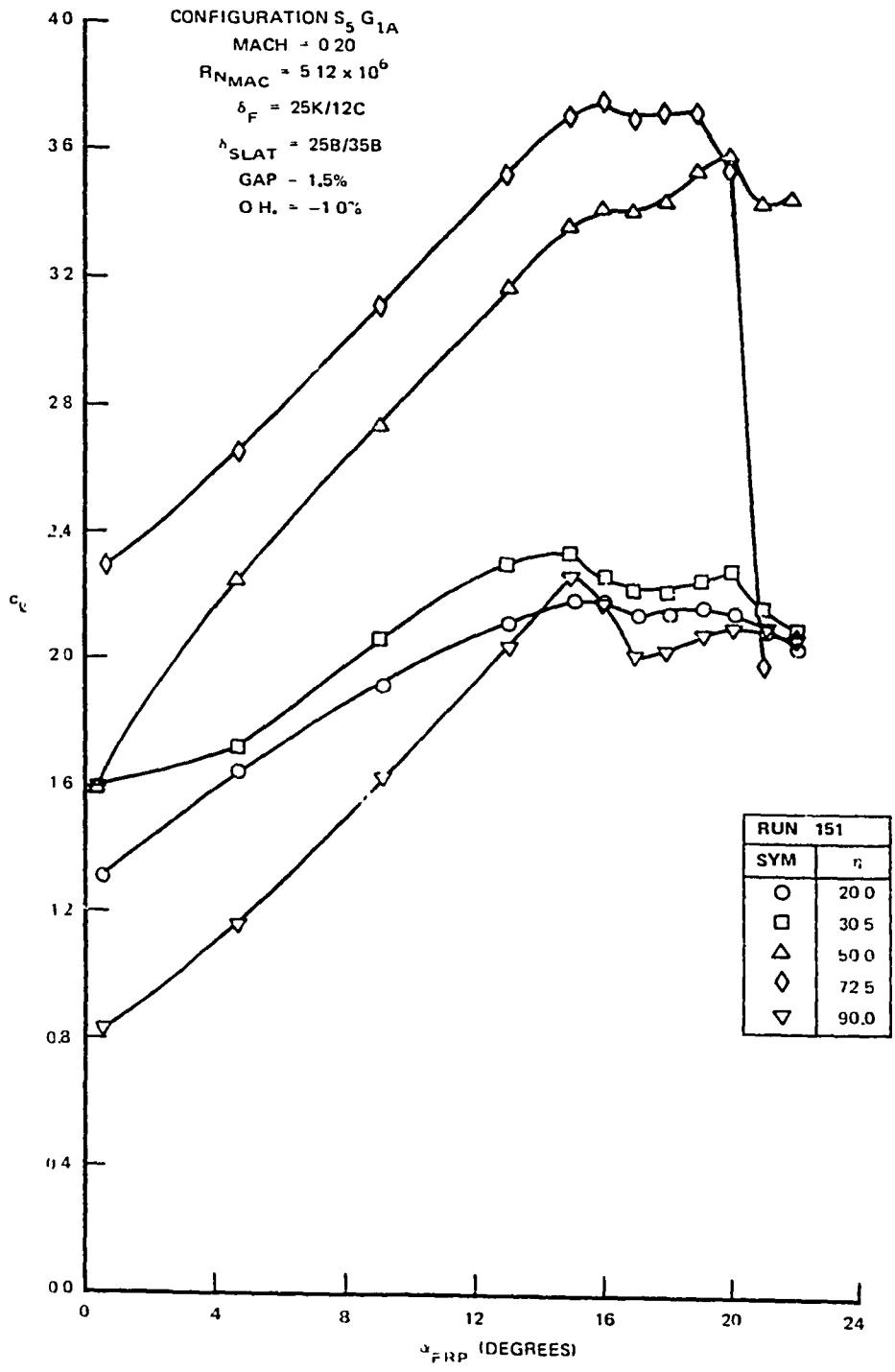

B. δ_{SLAT} = 25B/35B

FIGURE 126. VARIATION OF SECTION LIFT COEFFICIENT FOR THE SLAT WITH TWO-SEGMENT LANDING FLAPS (CONCLUDED)

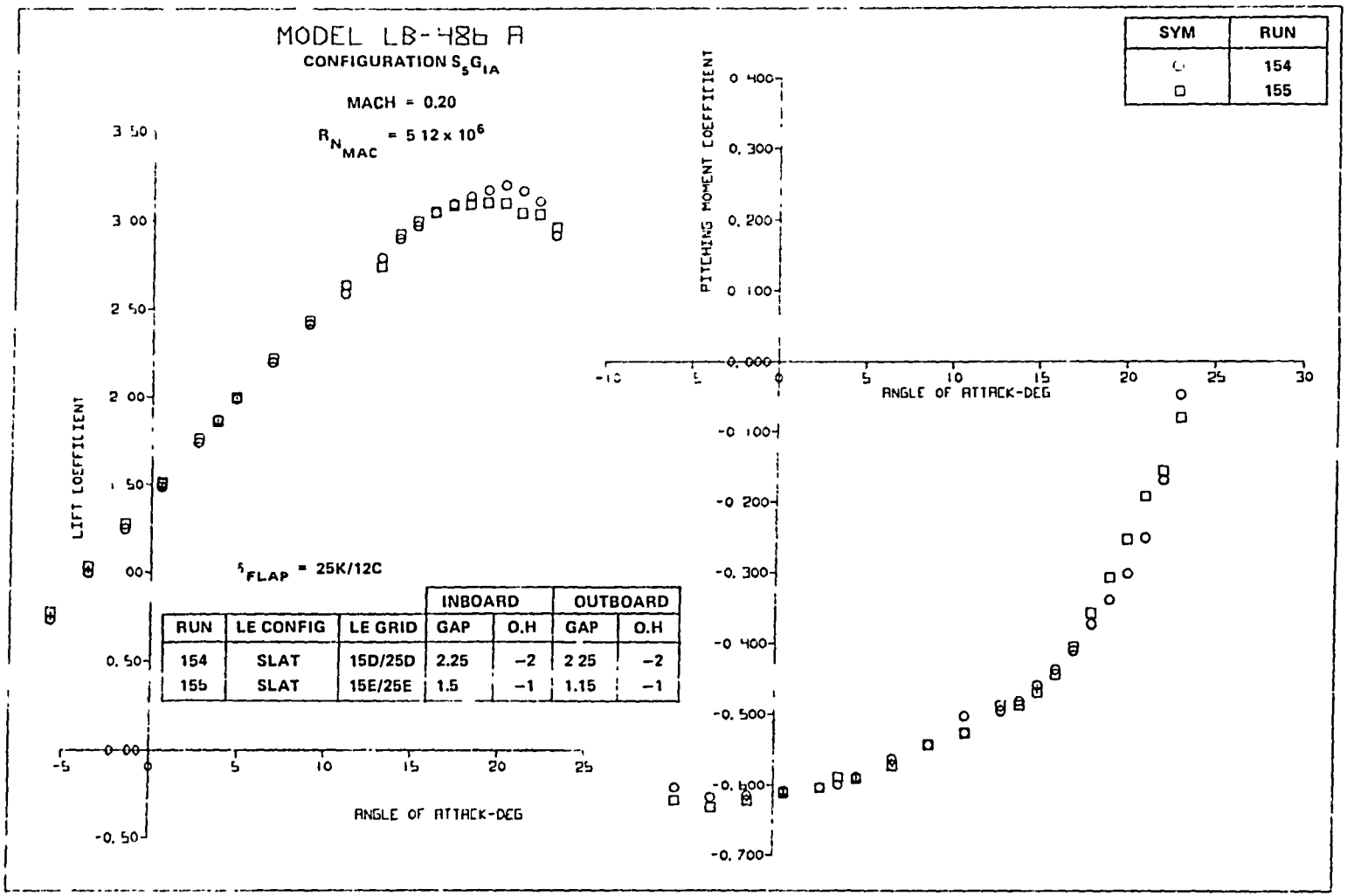

A. LIFT AND PITCHING MOMENT

FIGURE 127. SLAT POSITION STUDY FOR LANDING FLAPS (δ_{SLAT} = 15°/25°)

ORIGINAL PAGE IS OF POOR QUALITY

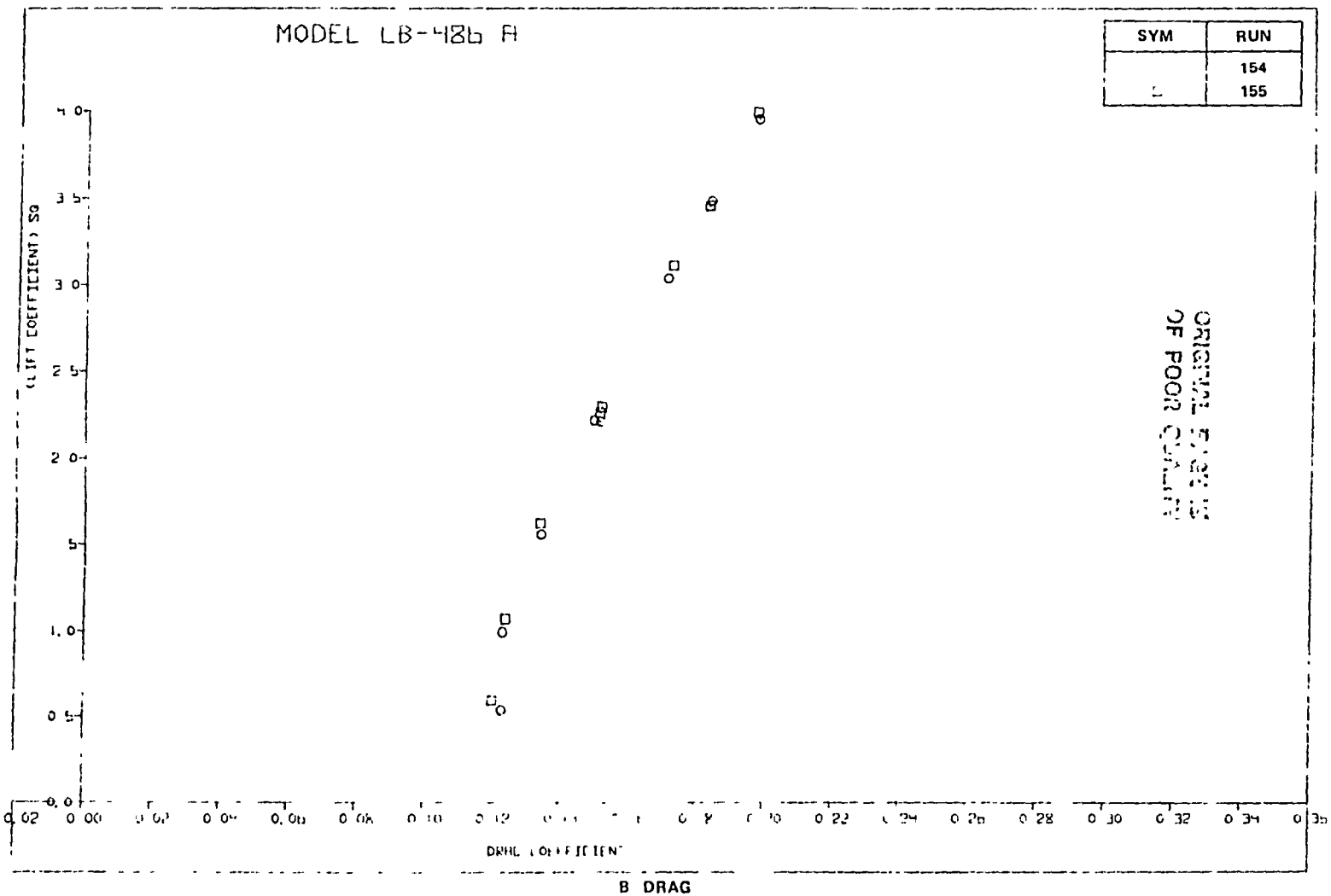

FIGURE 127. SLAT POSITION STUDY FOR LANDING FLAPS (δ_{SLAT} = 15°/25°) (CONCLUDED)

ORIGINAL PAGE IS
OF POOR QUALITY

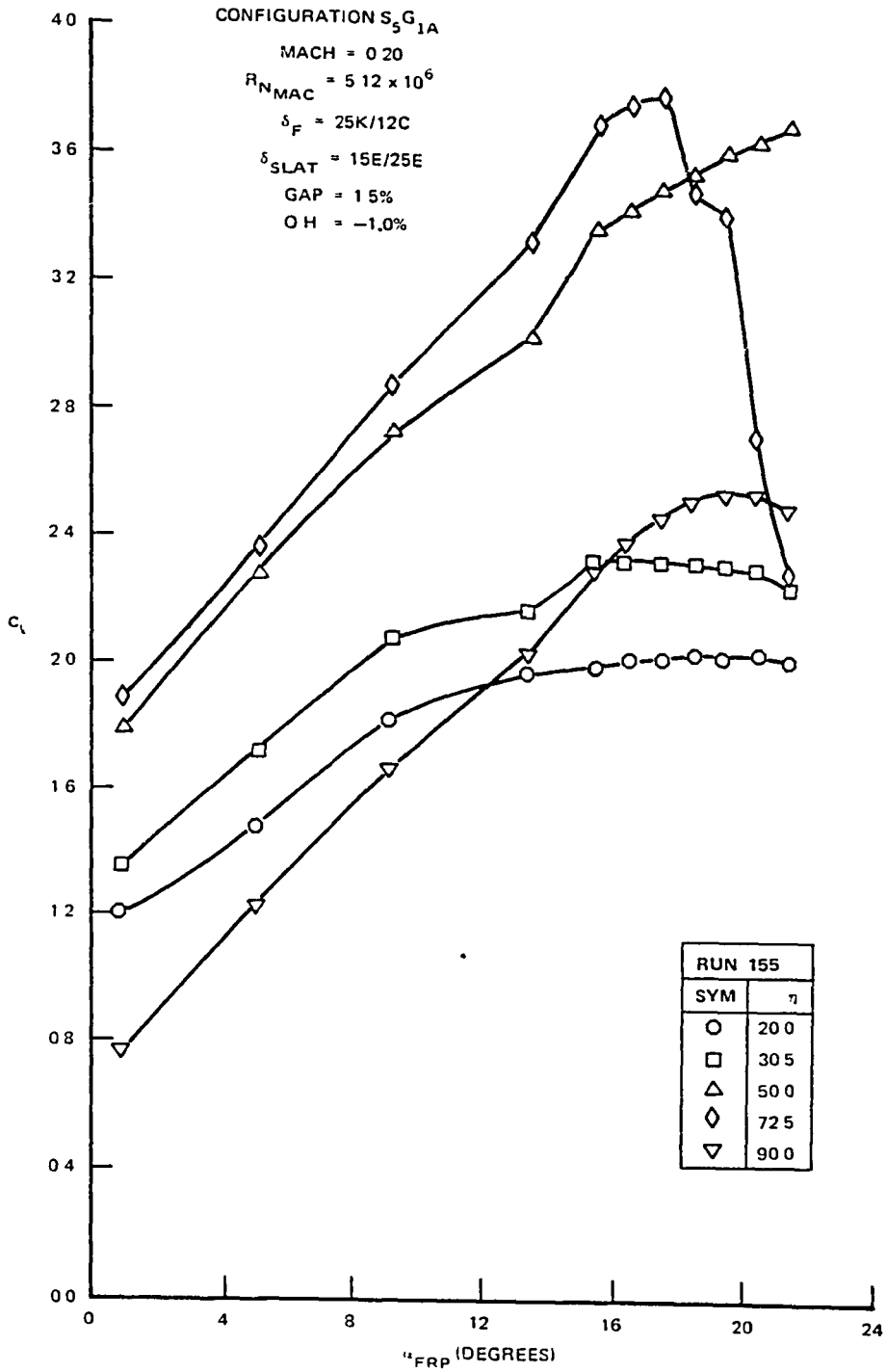

FIGURE 128. VARIATION OF SECTION LIFT COEFFICIENT FOR THE SLAT WITH TWO-SEGMENT LANDING FLAPS (δ_{SLAT} = 15E/25E)

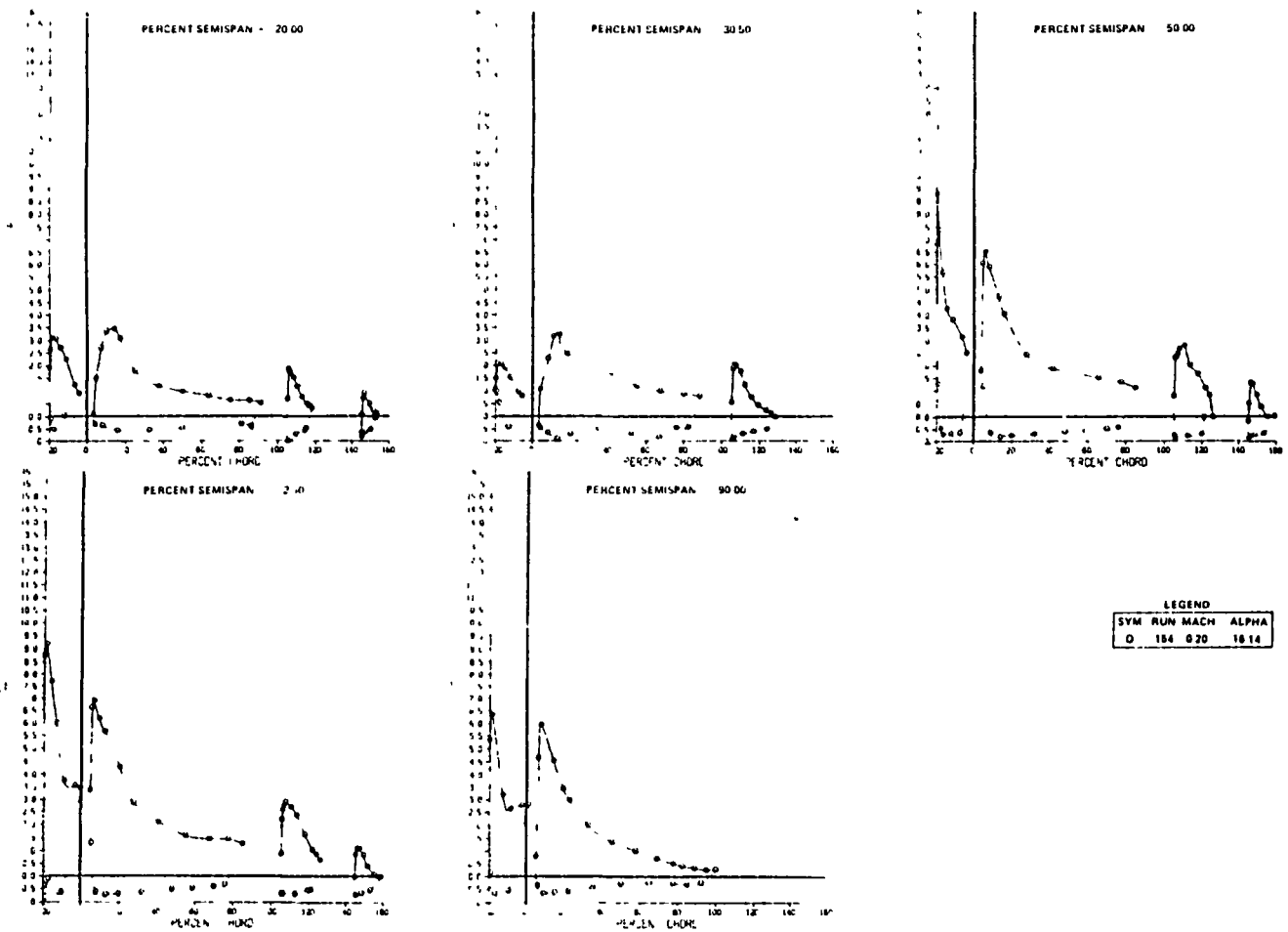

A_{FRP} = 16.14 DEG

FIGURE 129. EXPERIMENTAL CHORDWISE PRESSURE DISTRIBUTION FOR SLAT WITH TWO-SEGMENT LANDING FLAPS

ORIGINAL PAGE IS
OF POOR QUALITY

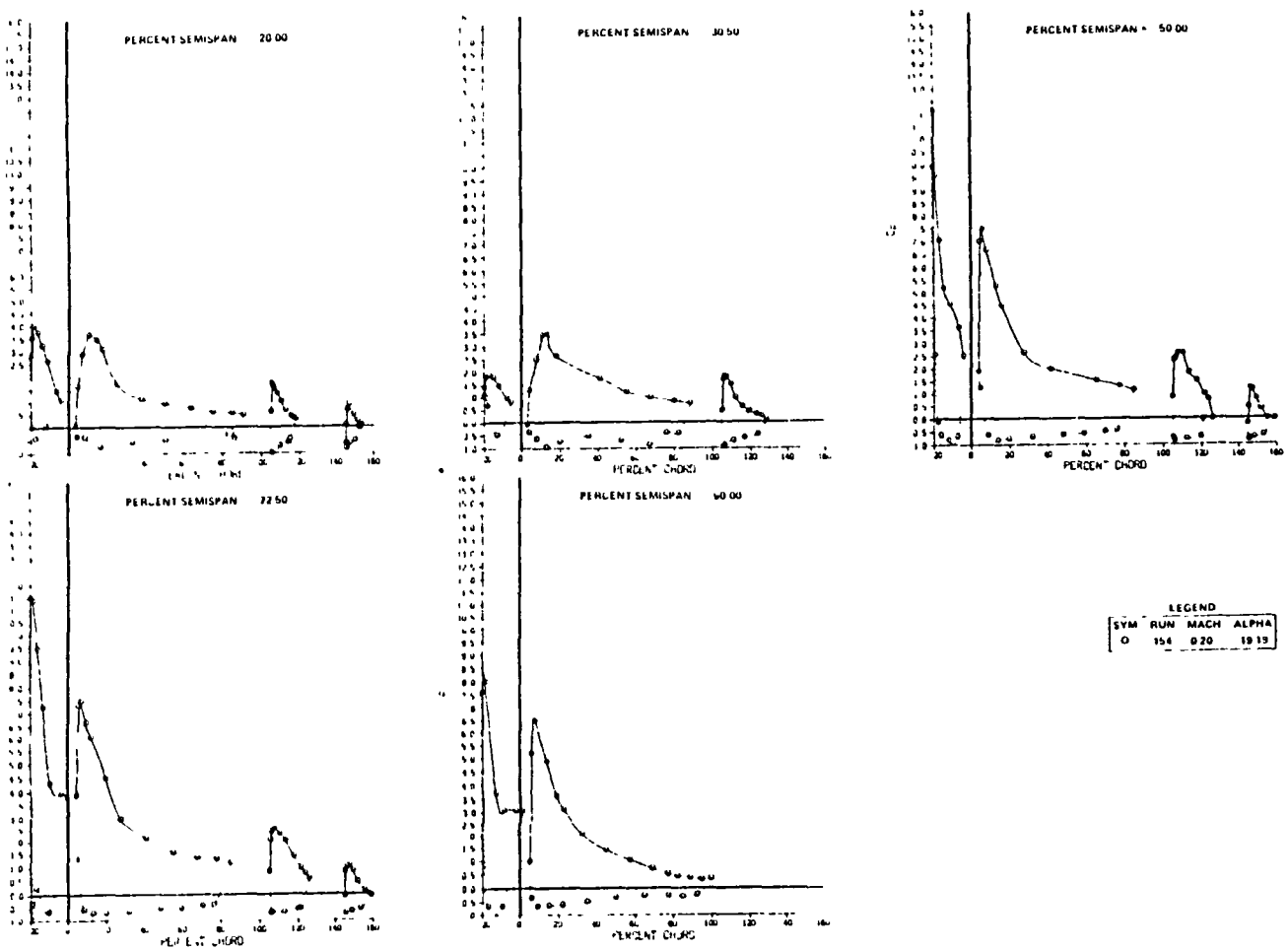

B α_{FRP} = 19 19 DEG

FIGURE 129. EXPERIMENTAL CHORDWISE PRESSURE DISTRIBUTION FOR SLAT WITH TWO-SEGMENT LANDING FLAPS (CONTINUED)

ORIGINAL PAGE IS
OF POOR QUALITY

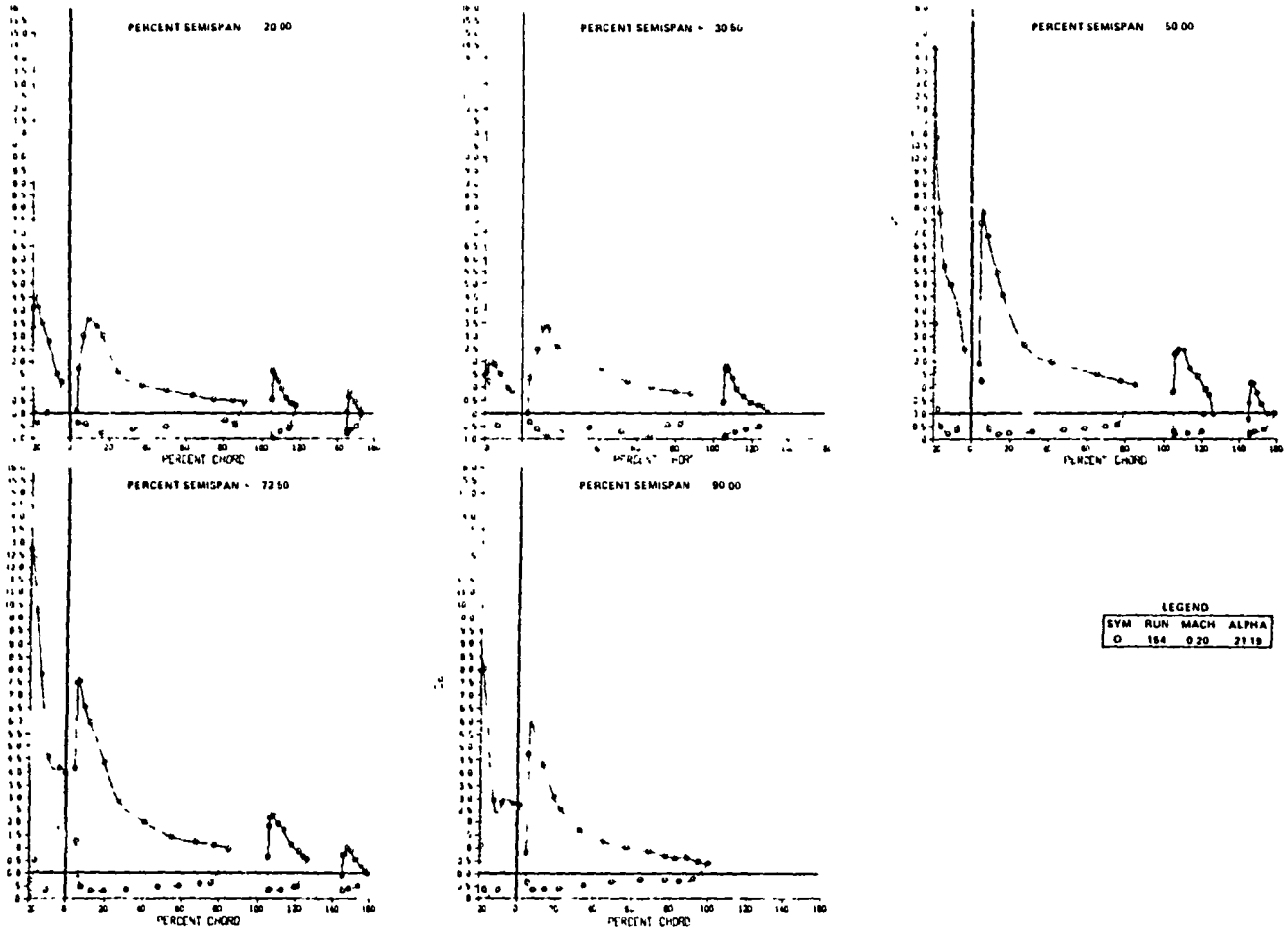

$C_{\alpha_{FRP}} = 21.19$ DEG

FIGURE 129 EXPERIMENTAL CHORDWISE PRESSURE DISTRIBUTION FOR SLAT WITH TWO-SEGMENT LANDING FLAPS (CONTINUED)

ORIGINAL PAGE IS
OF POOR QUALITY

ORIGINAL PAGE IS
OF POOR QUALITY

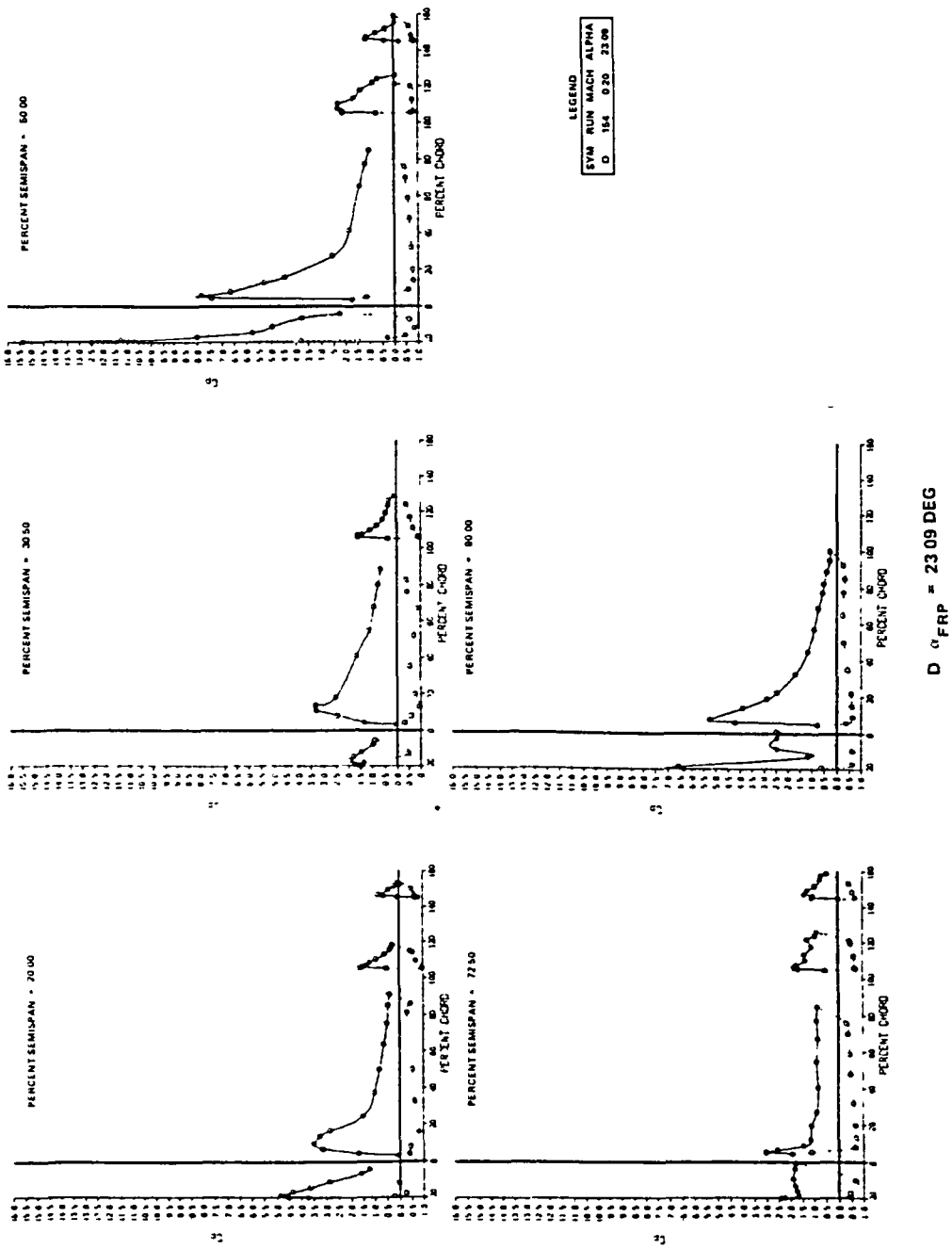

D α_{FRP} = 23.09 DEG

FIGURE 129. EXPERIMENTAL CHORDWISE PRESSURE DISTRIBUTION FOR SLAT WITH TWO-SEGMENT LANDING FLAPS (CONCLUDED)

A $C_{P_{MIN}}$ value of -15.4 is shown for the 50-percent span station (Figure 129D). This station remained attached for the angles of attack investigated. Also shown in Figure 129D are the attached flow at the 20-percent span station and the reduced lift at the 72.5-percent span station. Figure 130 shows the section lift variation with angle of attack for Run 154. The relatively constant lift at the higher angles of attack for the 20- and 30-percent span stations is readily apparent. Comparison of the 72.5-percent span station sectional lift characteristics for 25A/35A and 15D/25D (Figures 126A and 130), indicate a reduction in maximum lift and lift loss for the larger slat deflection.

Figure 131 presents the results of the slat position survey for the two-segment takeoff flap configuration. The largest $C_{L_{MAX}}$ was obtained with position 15D/25D (Gap = 2.25%, O.H. = 2%). Significant reduction in $C_{L_{MAX}}$ and increase in drag is shown for the large gap and overhang position (Run 174). The pitching moment trends are similar for the various grid positions.

The sectional lift values are shown in Figure 132. Reduced sectional lift values are indicated for the large gap and overhang position (Run 174) as expected. The small gap and overhang position (Run 175) results in the best sectional lift variation at 90-percent span station. Figure 133 illustrates the chordwise pressure distribution for Run 173 (Gap = 2.25%, O.H. = -2%). Noteworthy is the increase in loading for the 20-percent span station at angles of attack greater than $^{\alpha}C_{L_{MAX}}$. Examination of mini-tuft photographs for the inboard wing indicated significantly reduced tuft activity compared to the optimized VCK configuration. The large chord, and greater spanwise extent of the inboard slat (see Figures 49 and 50) resulted in significantly less lift loss at high angles of attack for this region of the wing. This is confirmed by the trends shown in Figure 134 for the 20-percent span station. Some reduction in the lift values at high angles of attack for the 90-percent span station is also noted. This would indicate, in a similar fashion to the landing slat and the VCK studies, that the reduced gap and overhang position is best for the most outboard region of the wing. Some reduction in lift at the 30-percent span station is noted at the higher angles of attack as well as a substantial reduction in lift for the 72.5-percent span station. Comparison of the cruise wing, slat extended flaps retracted (clean trailing edge configuration), and the

ORIGINAL PAGE IS
OF POOR QUALITY

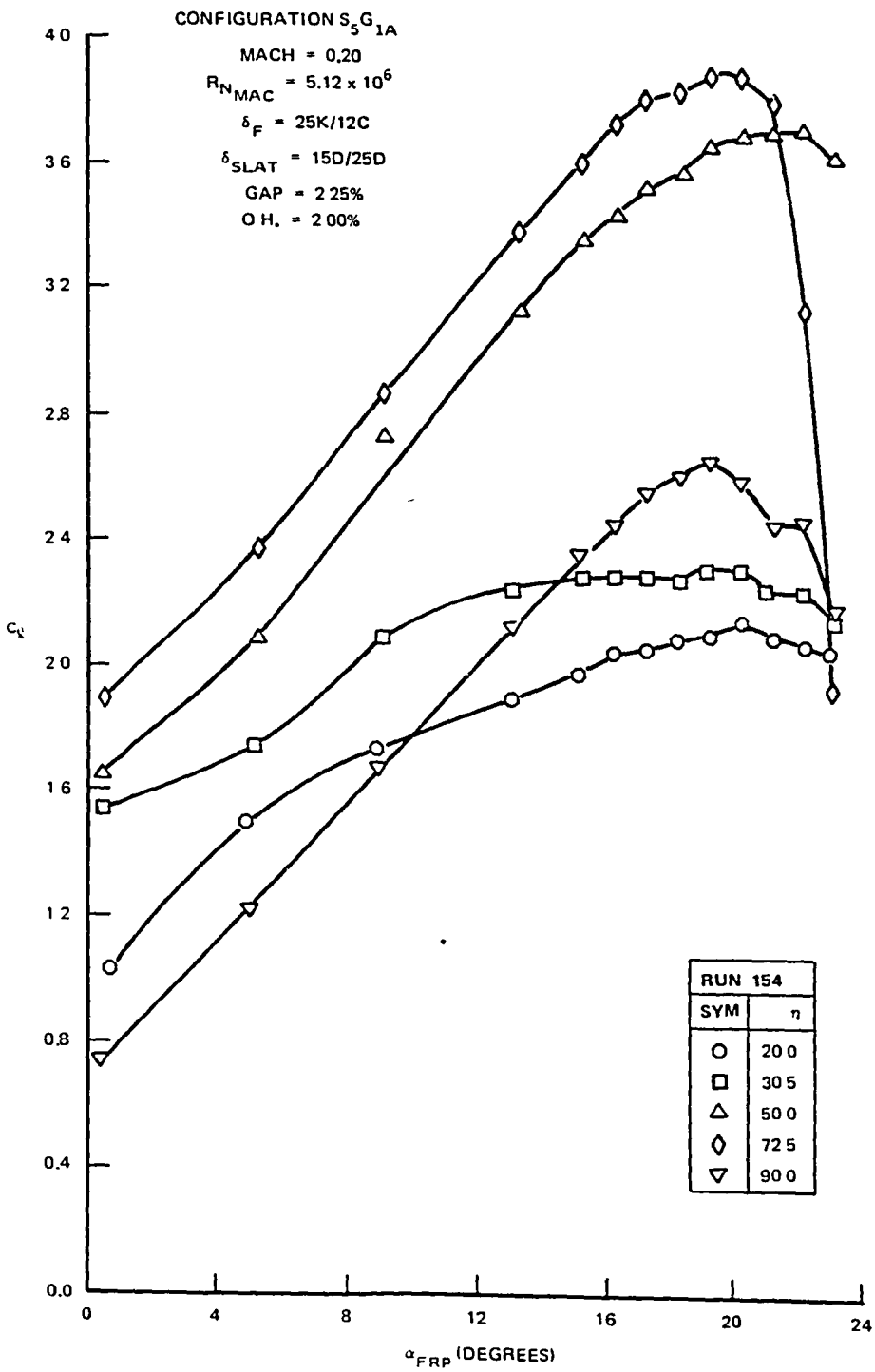

FIGURE 130. VARIATION OF SECTION LIFT COEFFICIENT FOR THE SLAT WITH TWO-SEGMENT LANDING FLAPS (δ_{SLAT} = 15D/25D)

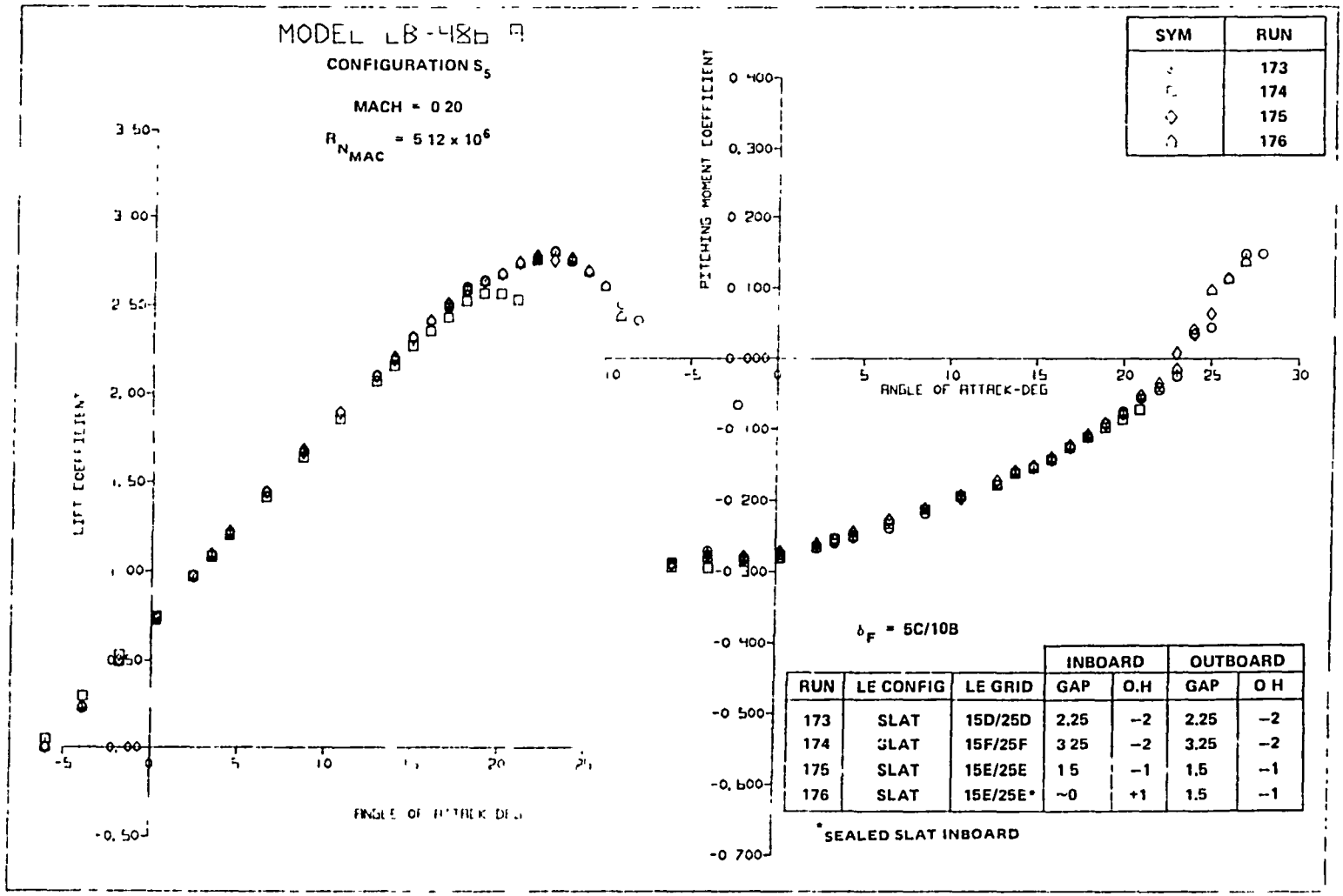

A LIFT AND PITCHING MOMENT

FIGURE 131. SLAT POSITION STUDY FOR TAKEOFF FLAPS (δ_{SLAT} = 15°/25°)

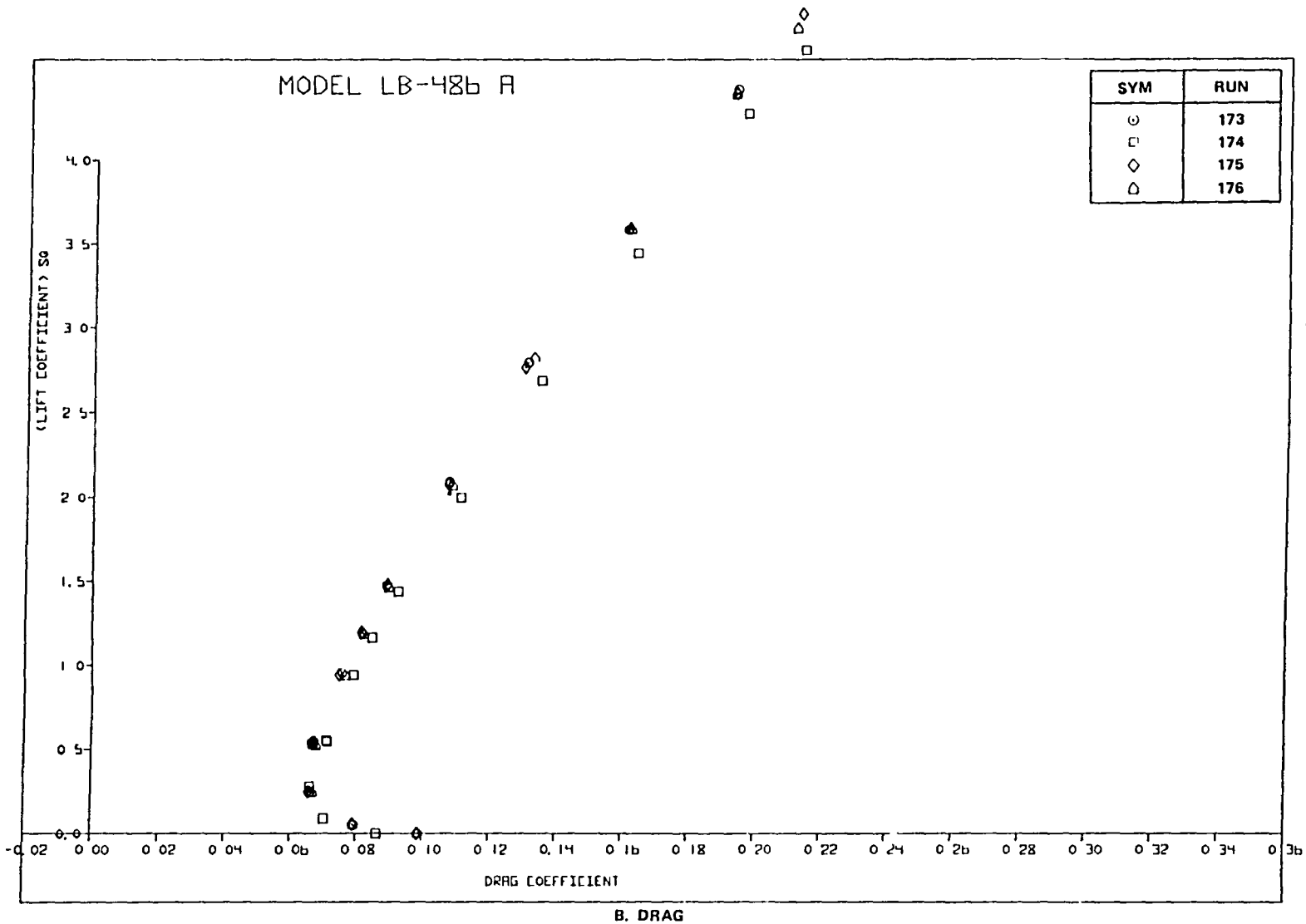

B. DRAG

ORIGINAL PAGE IS
OF POOR QUALITY

FIGURE 131. SLAT POSITION STUDY FOR TAKEOFF FLAPS (δ_{SLAT} = 15°/25°) (CONCLUDED)

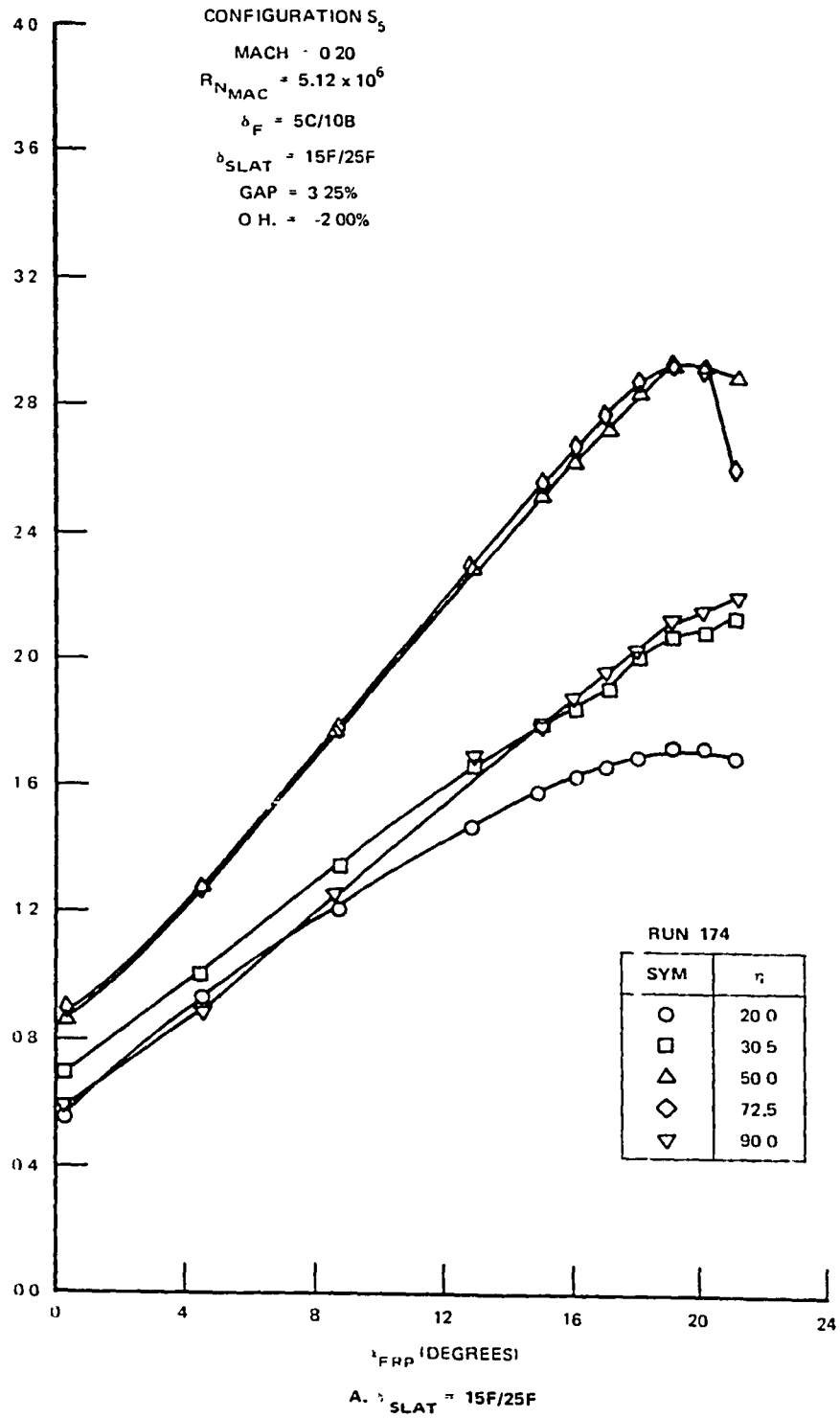

FIGURE 132. VARIATION OF SECTION LIFT COEFFICIENT FOR THE SLAT WITH TWO-SEGMENT TAKEOFF FLAPS

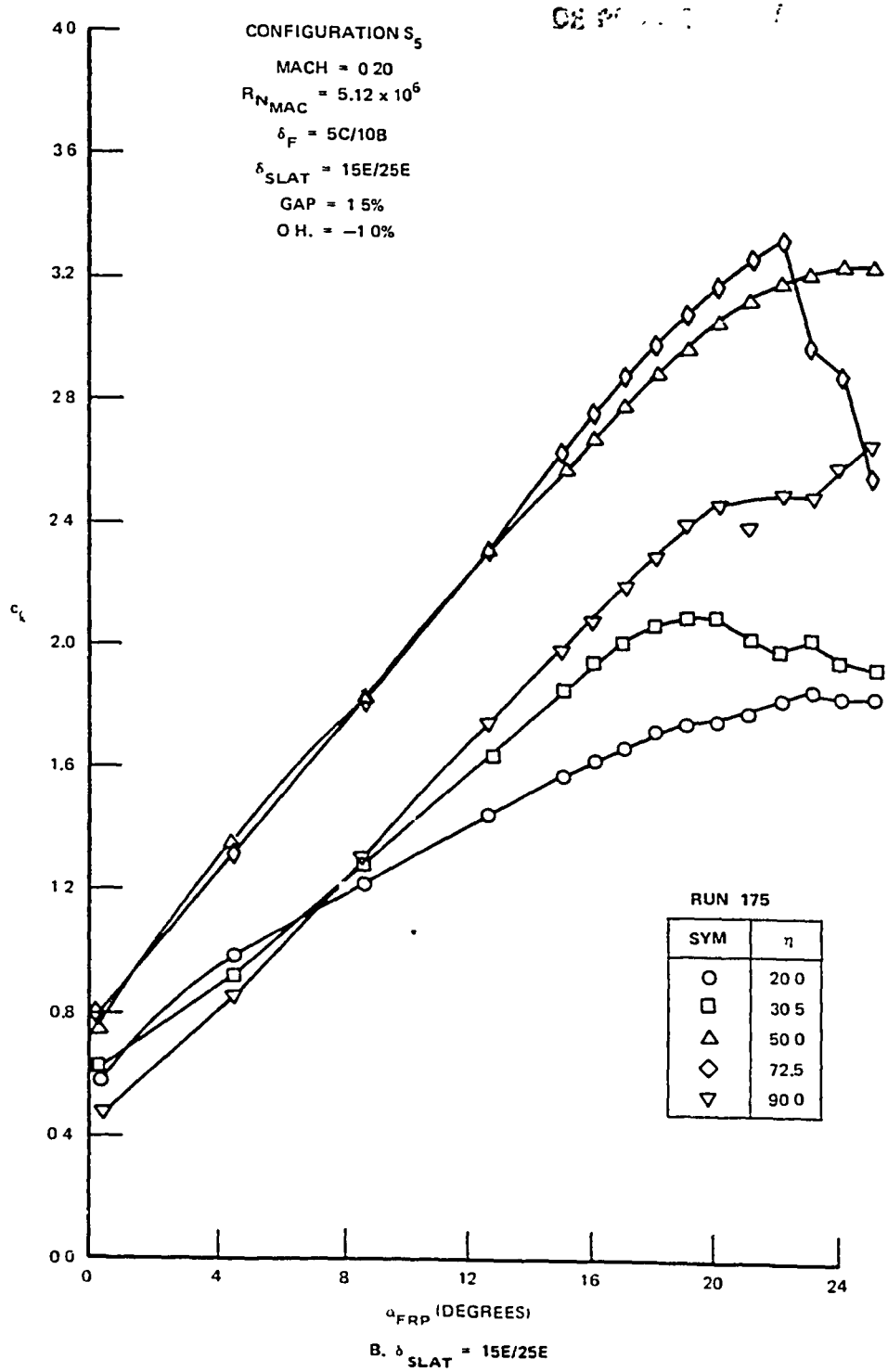

FIGURE 132. VARIATION OF SECTION LIFT COEFFICIENT FOR THE SLAT WITH TWO-SEGMENT TAKEOFF FLAPS (CONCLUDED)

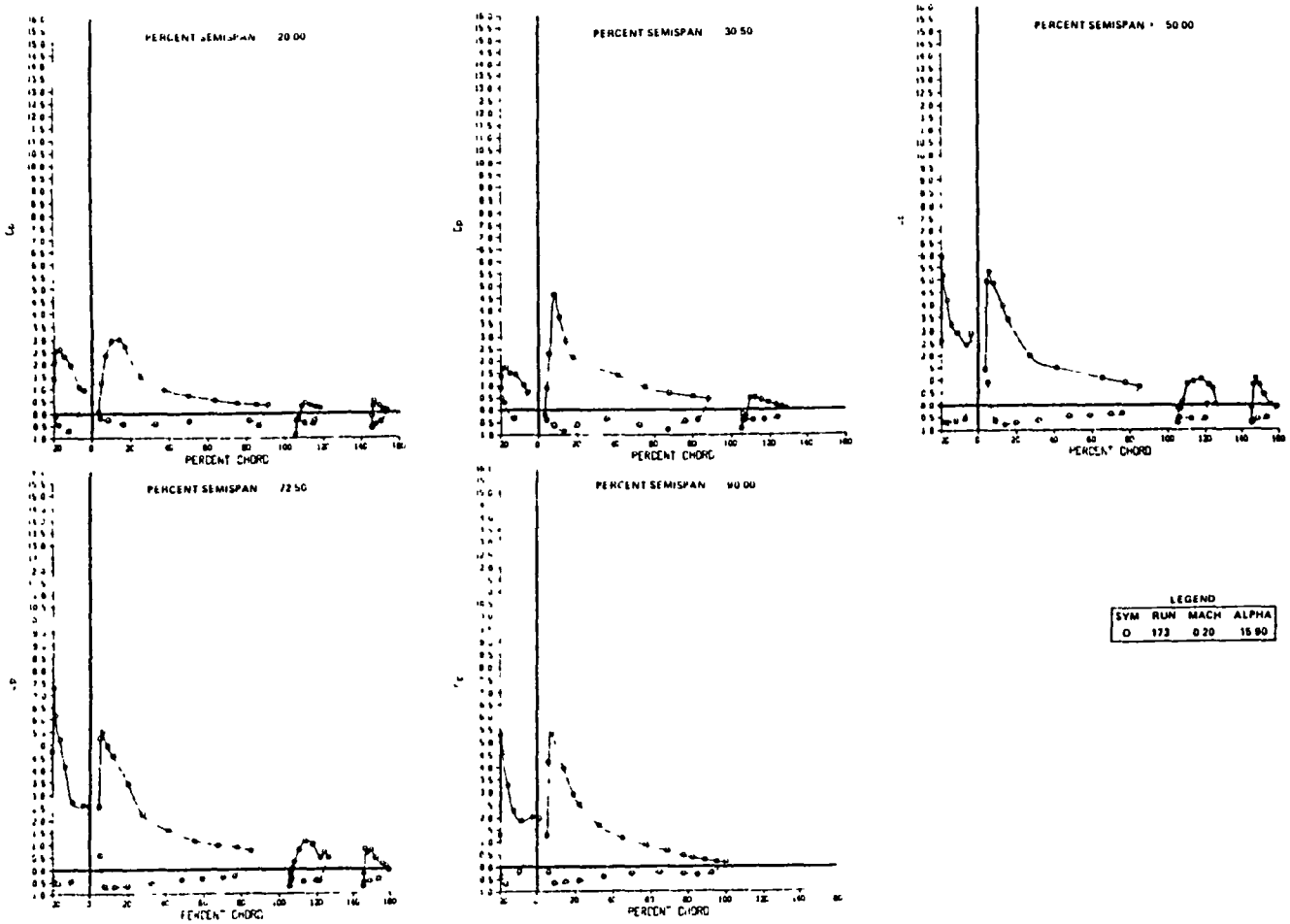

A $_{FRP}$ = 15.90 DEG

FIGURE 133 EXPERIMENTAL CHORDWISE PRESSURE DISTRIBUTION FOR SLAT WITH TWO-SEGMENT TAKEOFF FLAPS

ORIGINAL PAGE IS OF POOR QUALITY

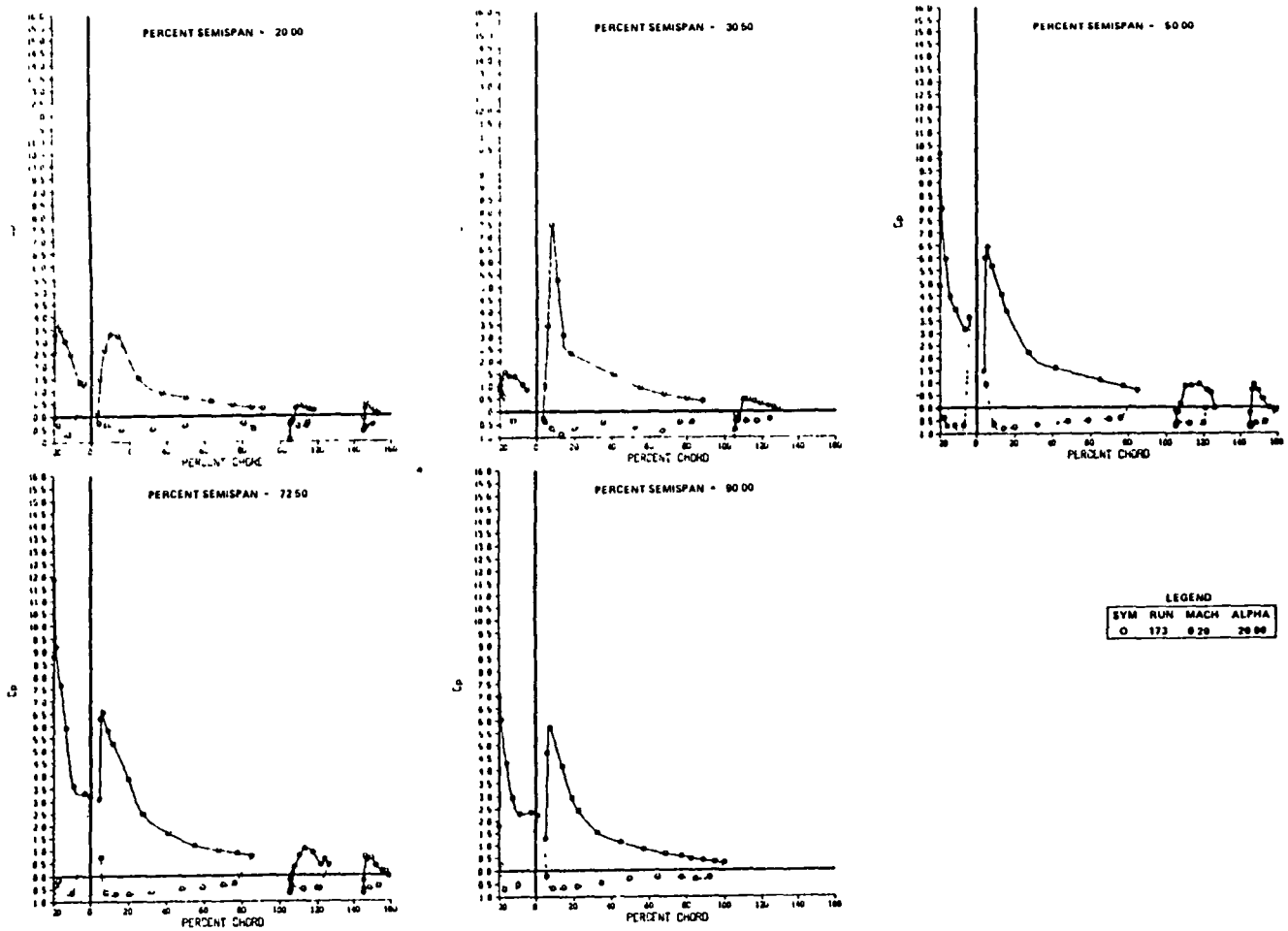

B. α_{FRP} = 20.00 DEG

FIGURE 133. EXPERIMENTAL CHORDWISE PRESSURE DISTRIBUTION FOR SLAT WITH TWO-SEGMENT TAKEOFF FLAPS (CONTINUED)

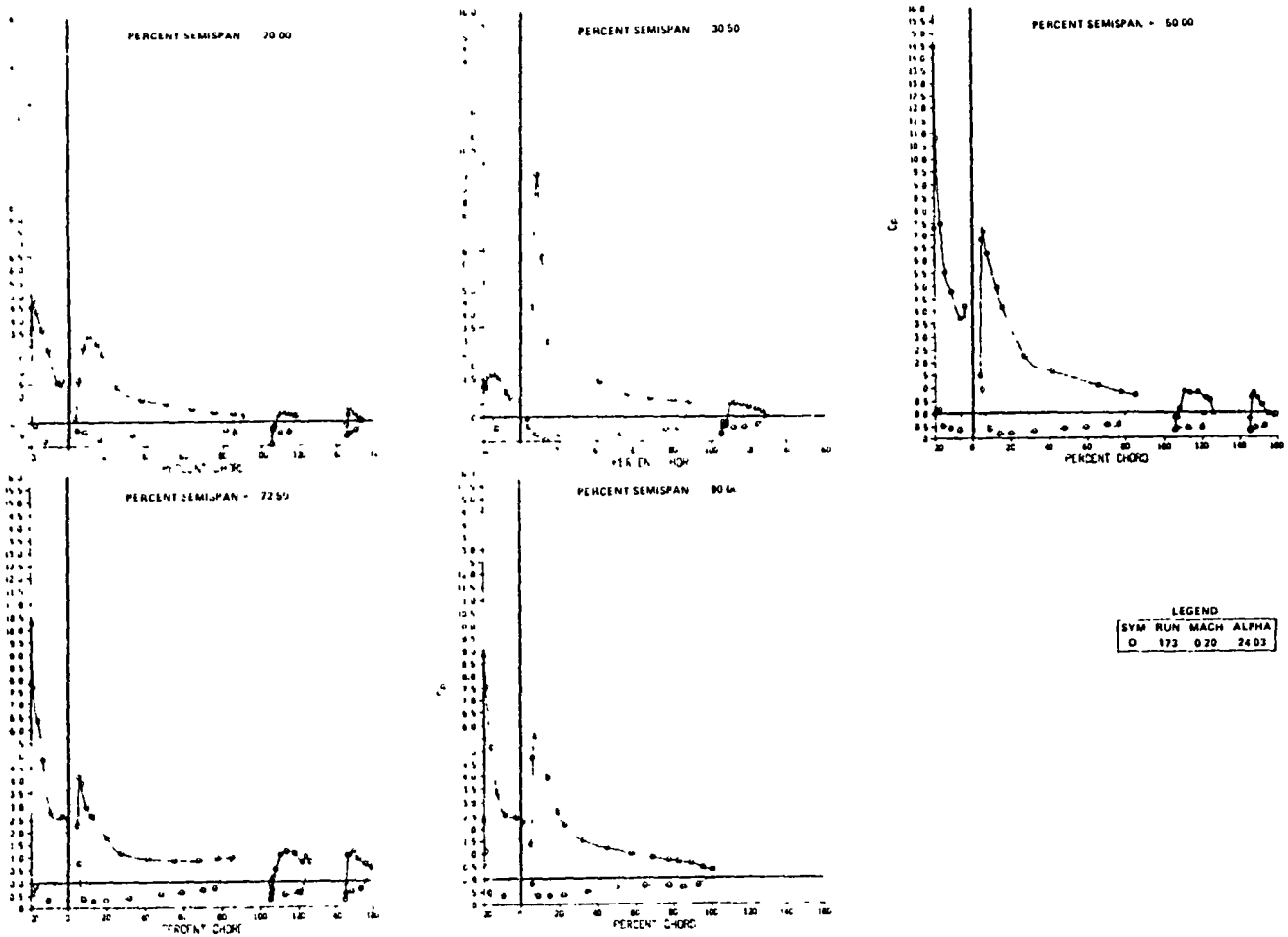

C_{FRP} = 24.03 DEG

FIGURE 133. EXPERIMENTAL CHORDWISE PRESSURE DISTRIBUTION FOR SLAT WITH TWO-SEGMENT TAKEOFF FLAPS (CONTINUED)

ORIGINAL PAGE IS
OF POOR QUALITY

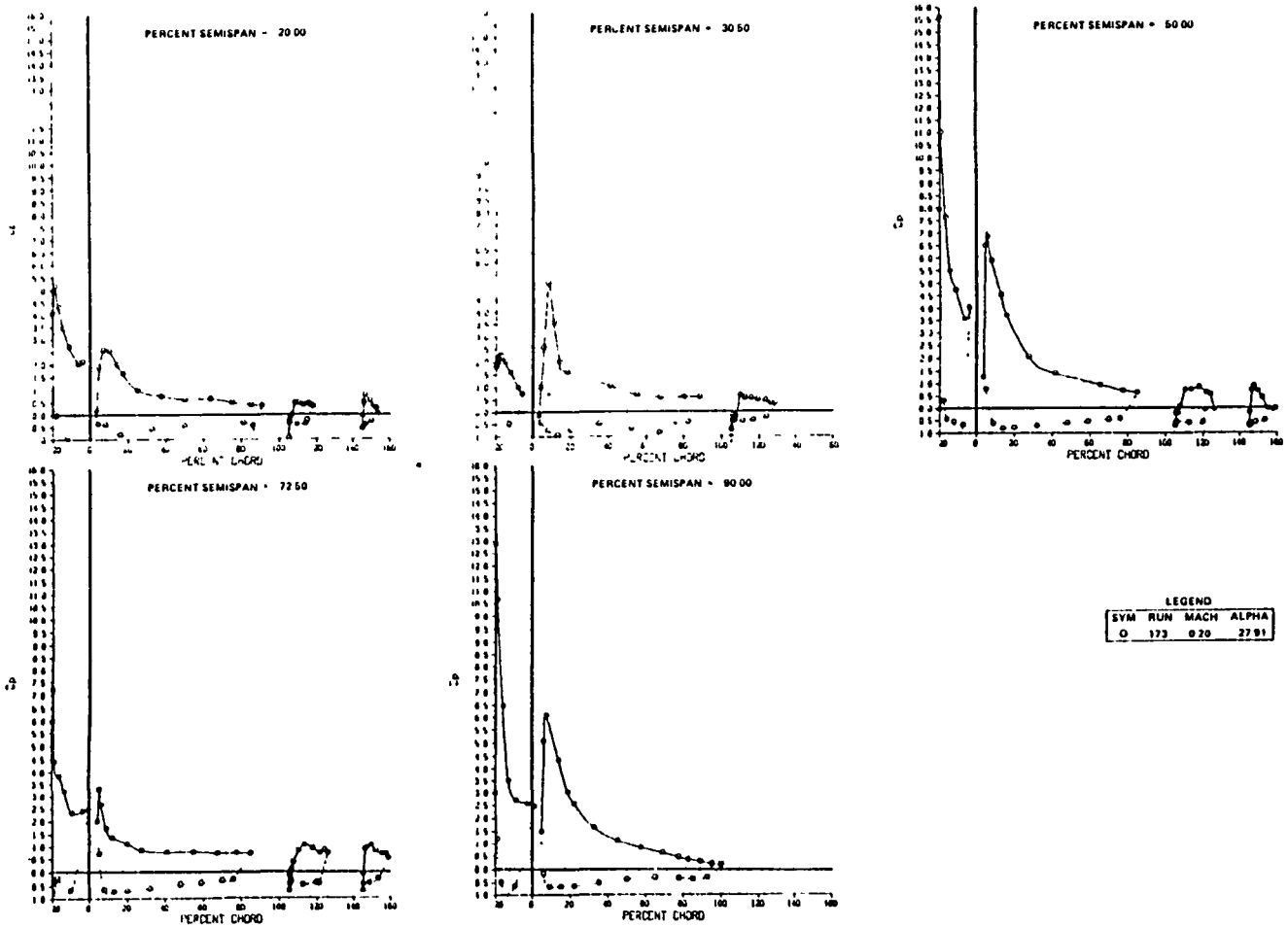

D. α_{FRP} = 27.91 DEG

FIGURE 133 EXPERIMENTAL CHORDWISE PRESSURE DISTRIBUTION FOR SLAT WITH TWO-SEGMENT TAKEOFF FLAPS (CONCLUDED)

ORIGINAL PAGE IS
OF POOR QUALITY

ORIGINAL PAGE IS
OF POOR QUALITY

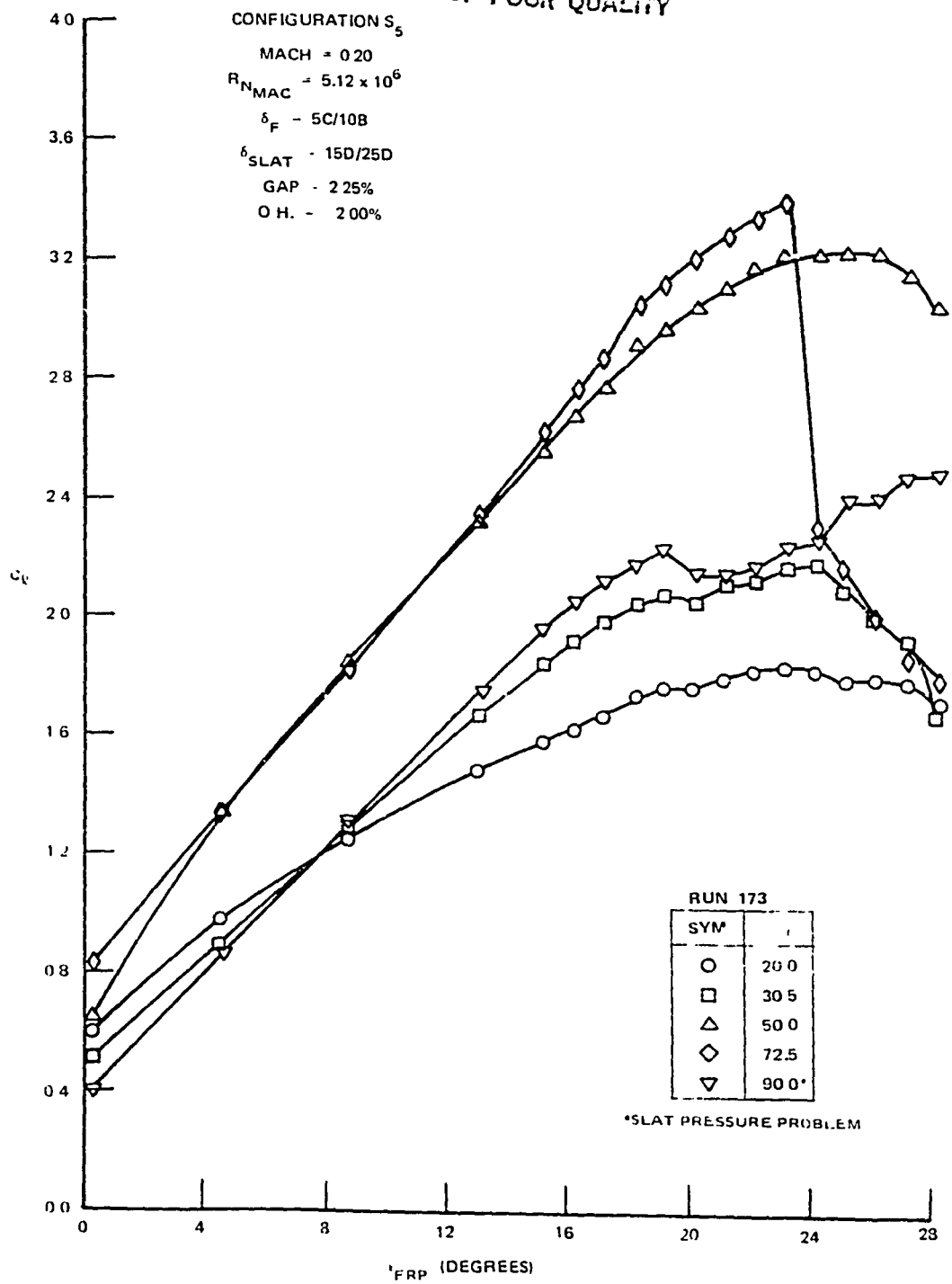

FIGURE 134 VARIATION OF SECTION LIFT COEFFICIENT FOR THE SLAT WITH TWO-SEGMENT TAKEOFF FLAPS (δ_{SLAT} - 15D/25D)

takeoff configurations just discussed, indicated significant reduction in L/D characteristics with slat deflected at the landing position. Improved L/D performance would appear possible with a sealed-slat configuration (slat trailing edge sealed at the WUSS surface) and this configuration should be evaluated in a future test program.

Mach Number Effects on Slat with Two-Segment Flap. - Figure 135 presents the influence of increasing Mach number on the lift, pitching moment, drag, and L/D characteristics. The $C_{L_{MAX}}$ reduction of 0.23 is indicated for an increase in Mach number from 0.20 to 0.32. The most significant differences in lift occurred at the angles of attack after $C_{L_{MAX}}$ was achieved. Increasing the Mach number also resulted in slightly larger lift values prior to $C_{L_{MAX}}$. Figure 135 also indicates that reduced stability occurs at the lower angle of attack for $C_{L_{MAX}}$ as the Mach number is increased. Small differences in drag and L/D are also shown in Figure 135. Analysis of the pressure data indicated local regions of supercritical flow on the outboard slat for 0.26 and 0.32 Mach numbers.

A similar comparison is shown in Figure 136 for the slat with two-segment takeoff flap configuration. The changes in lift and pitching moment due to increasing Mach number are similar to those for the landing configuration. A reduction in $C_{L_{MAX}}$ of 0.11 is shown for an increase in Mach number from 0.20 to 0.32. A slight reduction in drag, at a given lift coefficient, is also shown in Figure 136 and this results in slightly larger values of L/D.

Reynolds Number Effects on Slat with Two-Segment Flap. - The influence of a reduction in Reynolds number from the nominal test condition for the slat with two-segment landing flaps configuration is shown in Figure 137. $C_{L_{MAX}}$ reductions of 0.09 and 0.29 are shown for the intermediate and low Reynolds number test conditions ($R_{N_{MAC}} = 2.89 \times 10^6$ and $R_{N_{MAC}} = 1.14 \times 10^6$, respectively). A positive shift in pitching moment for angles of attack preceding $C_{L_{MAX}}$ is also shown for the low Reynolds number condition. As expected, for a given lift coefficient the drag increased and the L/D decreased with the reduction in Reynolds number. The tail-off L/D values at 1.3 V_S were 10.20, 9.85, and 9.60 for the high, intermediate, and low Reynolds number condition.

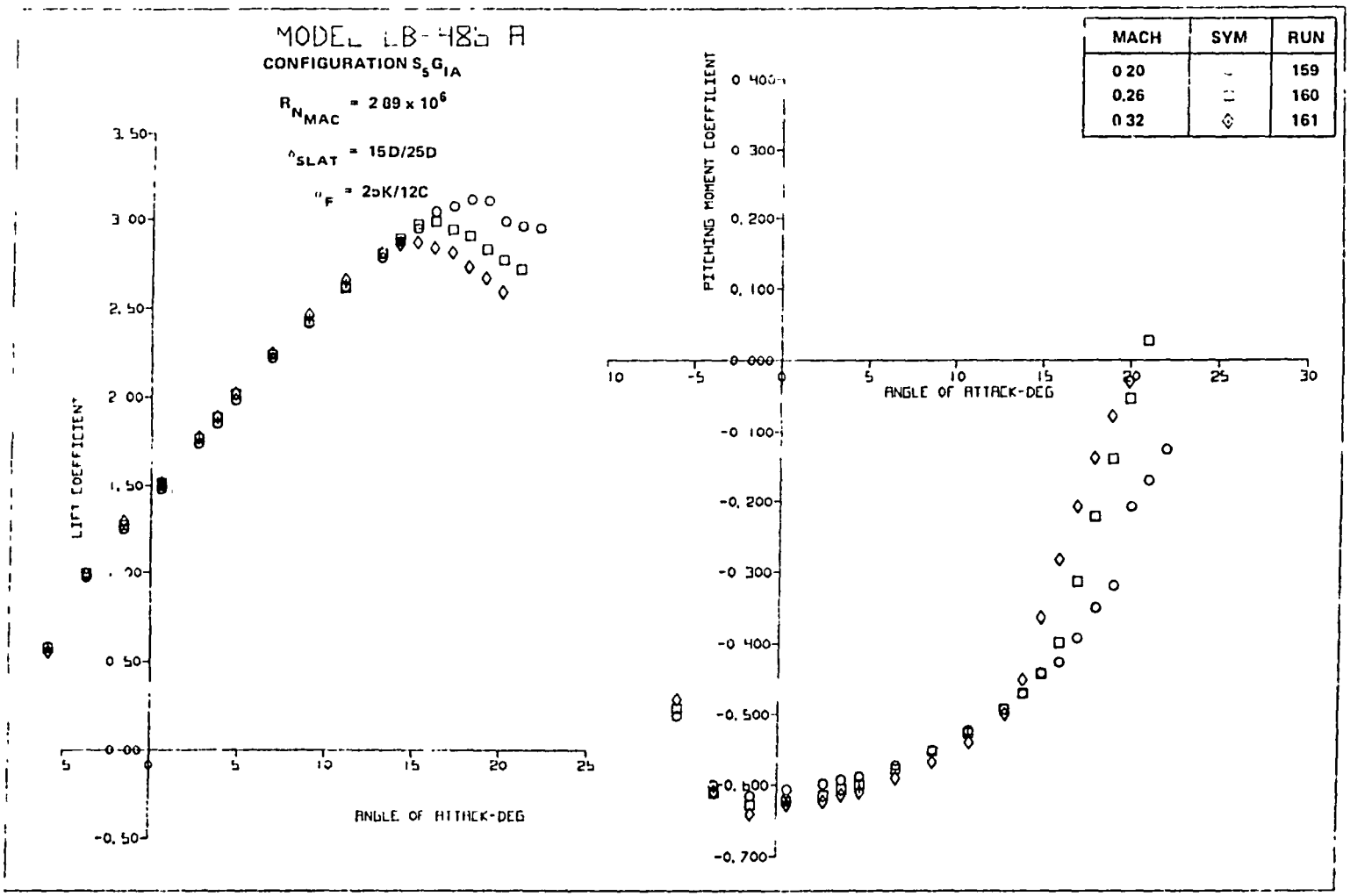

A LIFT AND PITCHING MOMENT

FIGURE 135. EFFECT OF MACH NUMBER ON AERODYNAMIC CHARACTERISTICS OF THE SLAT WITH TWO-SEGMENT LANDING FLAPS CONFIGURATION

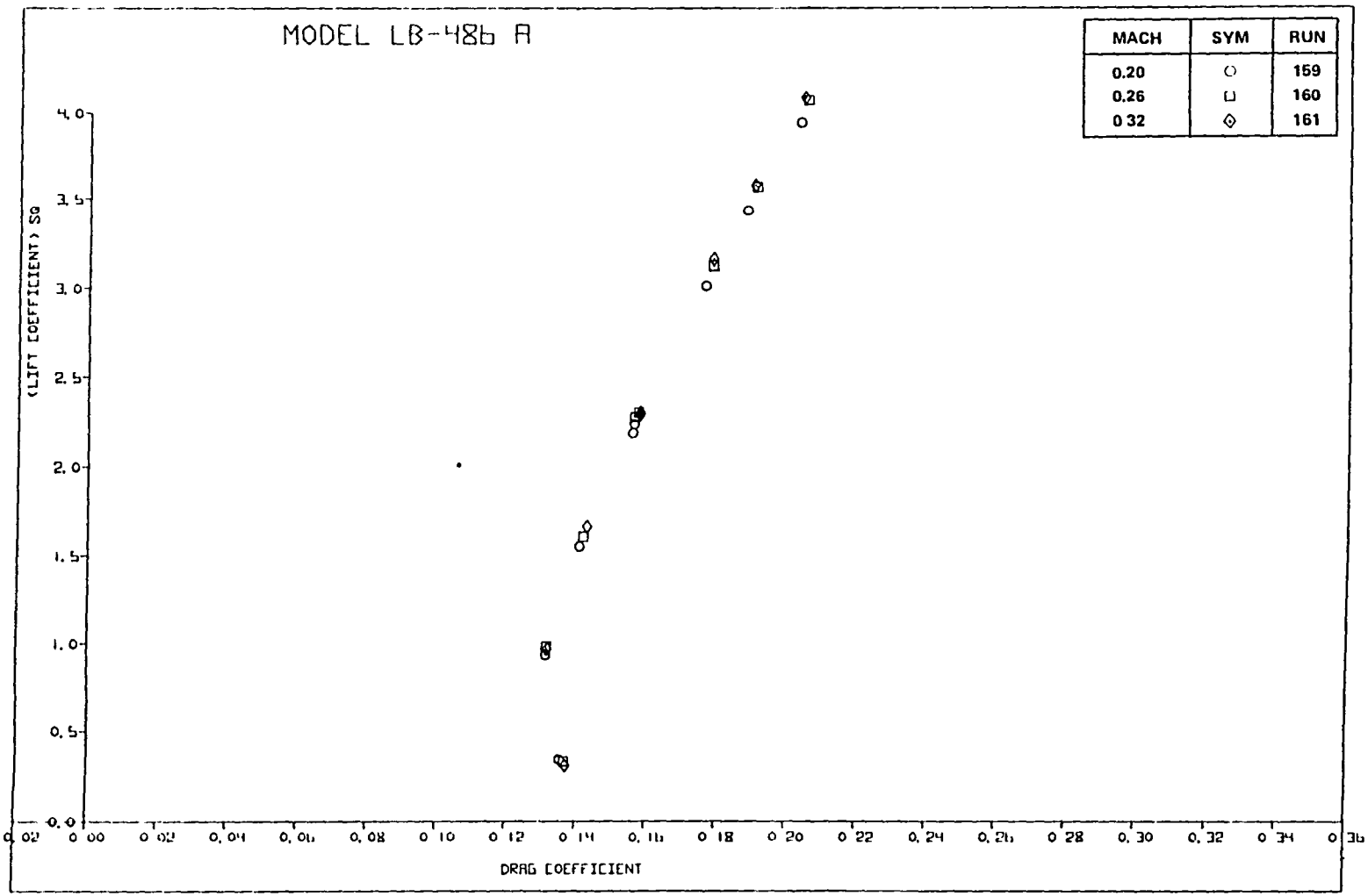

B. DRAG

FIGURE 135. EFFECT OF MACH NUMBER ON AERODYNAMIC CHARACTERISTICS OF THE SLAT WITH TWO-SEGMENT LANDING FLAPS CONFIGURATION (CONTINUED)

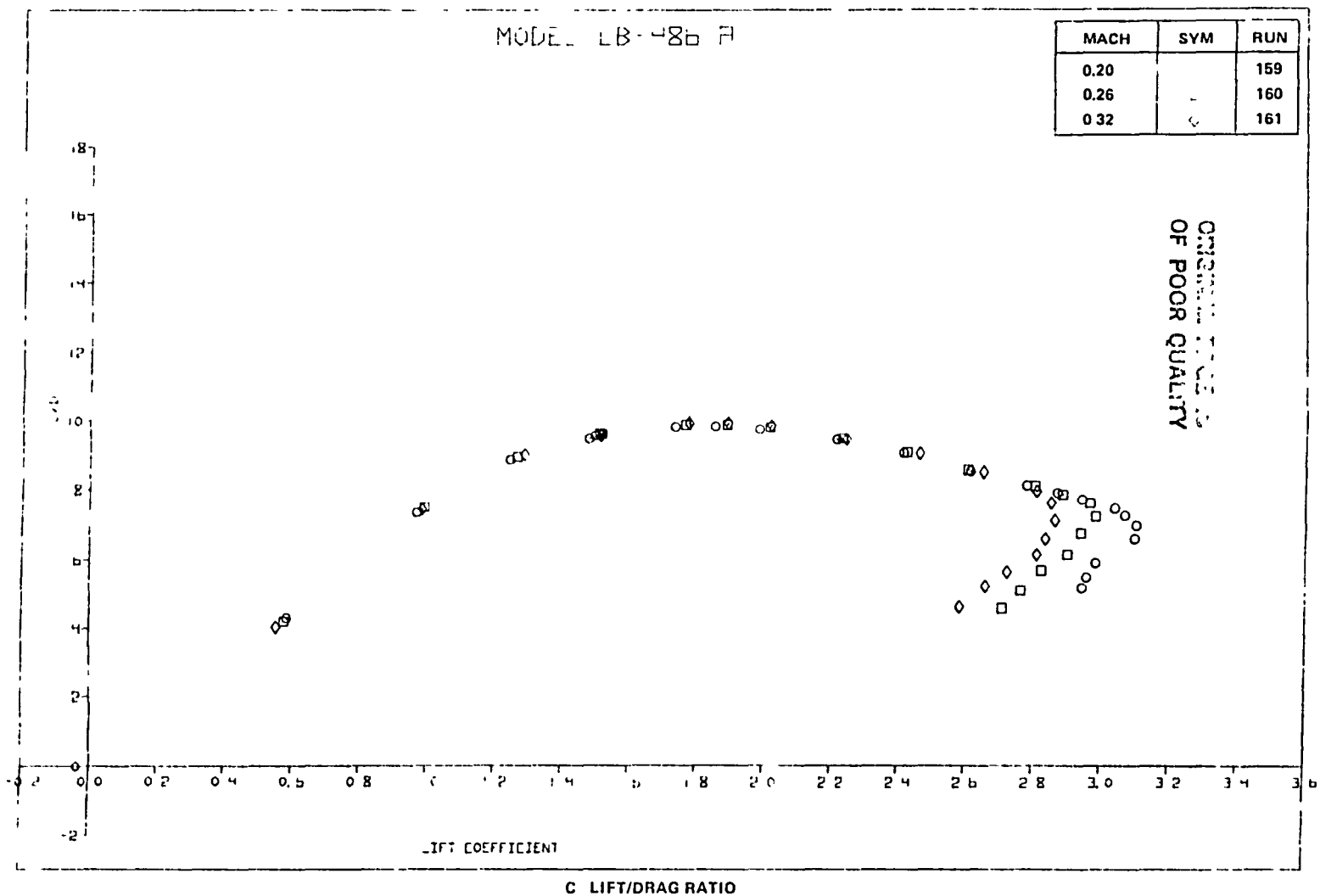

FIGURE 135. EFFECT OF MACH NUMBER ON AERODYNAMIC CHARACTERISTICS OF THE SLAT WITH TWO-SEGMENT LANDING FLAPS CONFIGURATION (CONCLUDED)

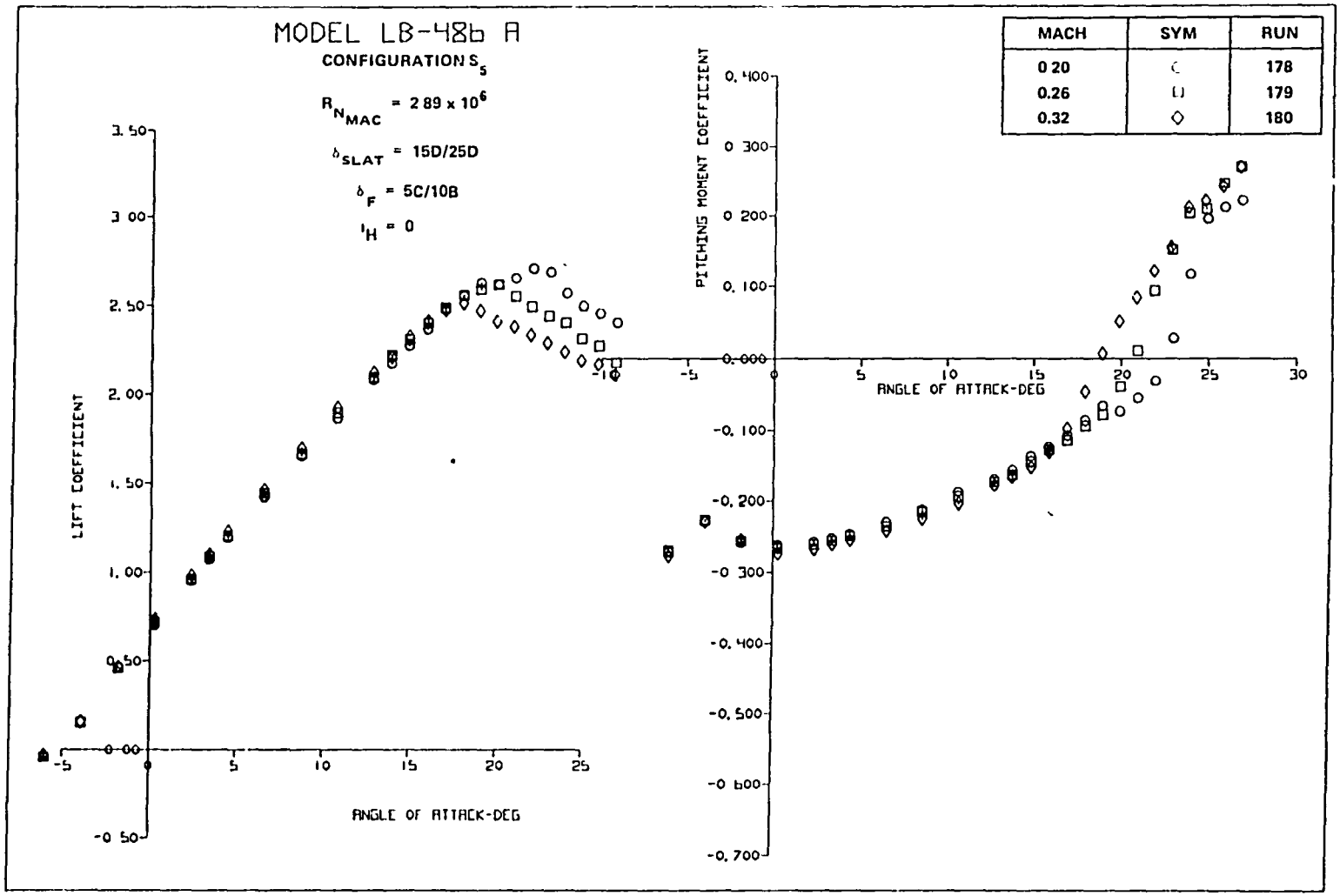

A. LIFT AND PITCHING MOMENT

FIGURE 136. EFFECT OF MACH NUMBER ON AERODYNAMIC CHARACTERISTICS OF THE SLAT WITH TWO-SEGMENT TAKEOFF FLAPS CONFIGURATION

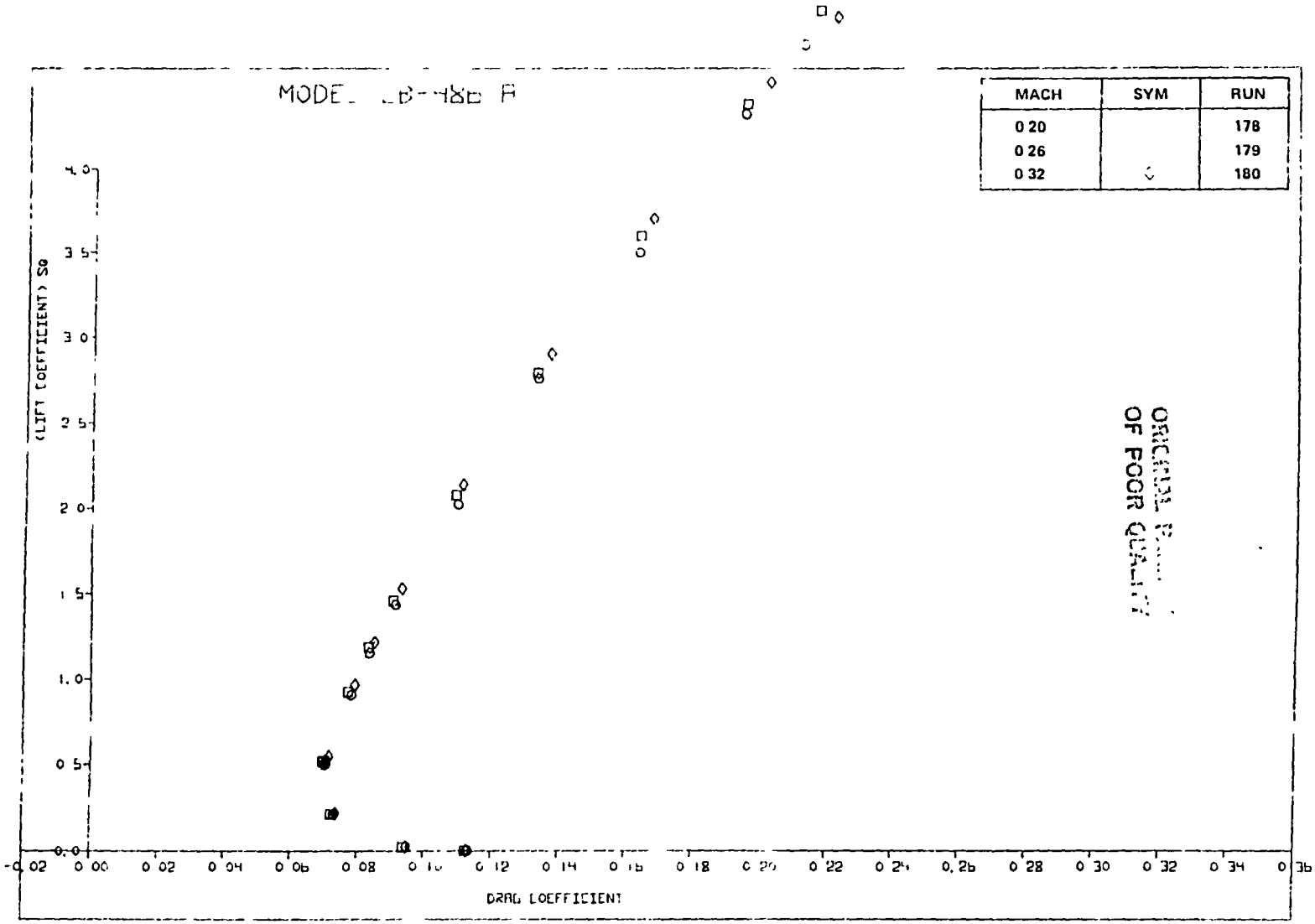

FIGURE 136 EFFECT OF MACH NUMBER ON AERODYNAMIC CHARACTERISTICS OF THE SLAT WITH TWO SEGMENT TAKEOFF FLAPS CONFIGURATION (CONTINUED)

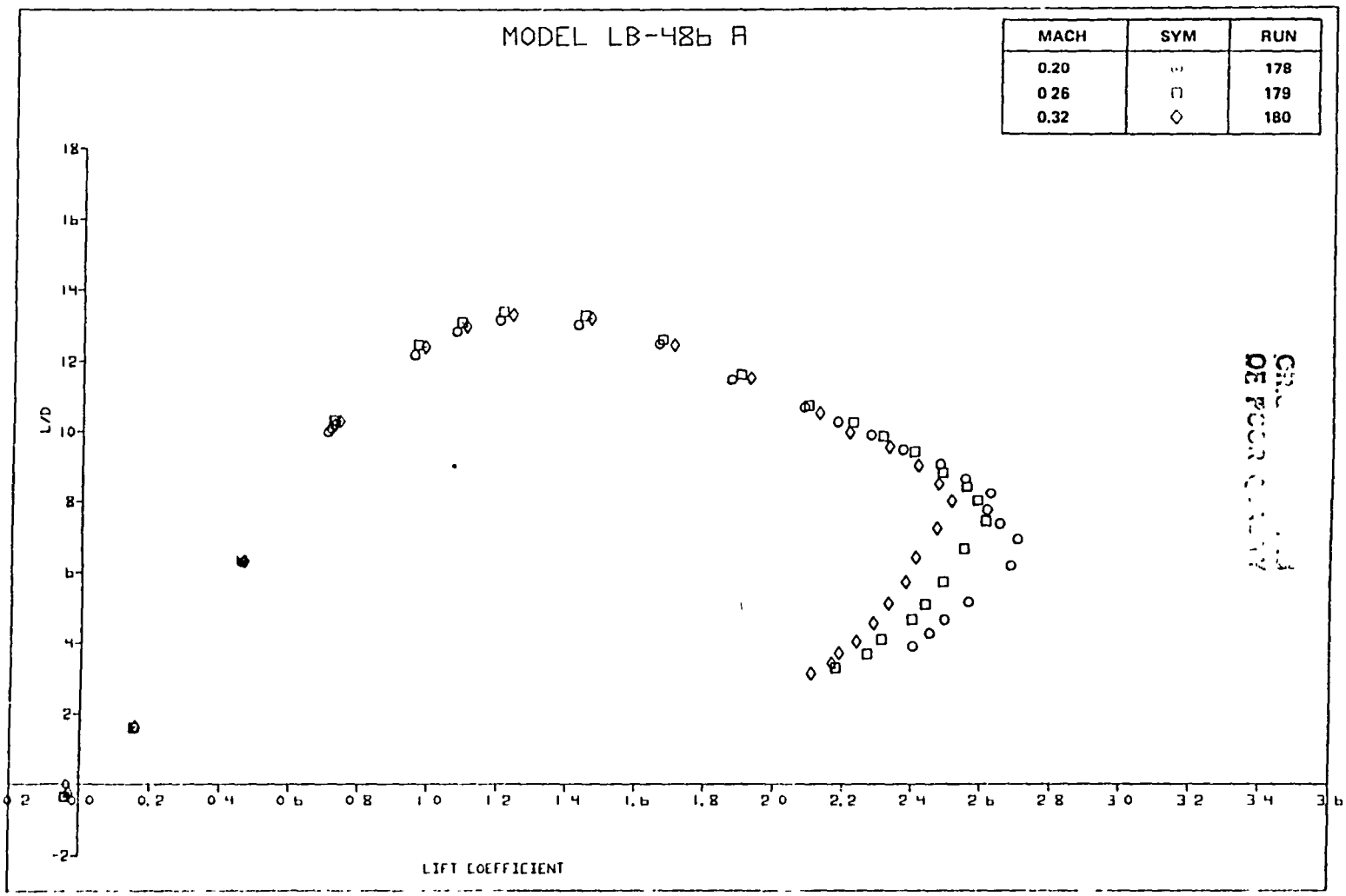

C. LIFT/DRAG RATIO

FIGURE 136. EFFECT OF MACH NUMBER ON AERODYNAMIC CHARACTERISTICS OF THE SLAT WITH TWO-SEGMENT TAKEOFF FLAPS CONFIGURATION (CONCLUDED)

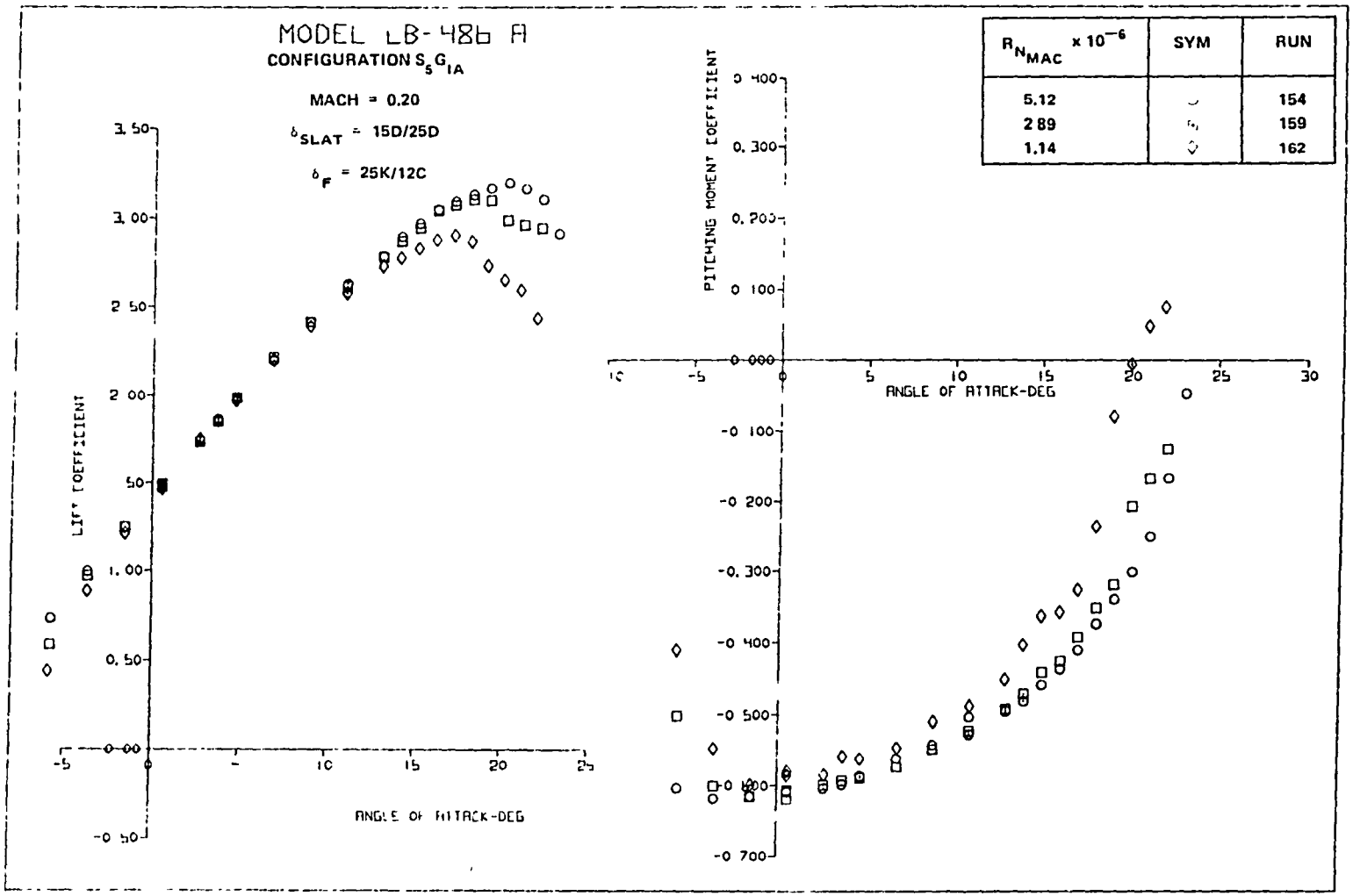

A. LIFT AND PITCHING MOMENT

FIGURE 137. EFFECT OF REYNOLDS NUMBER ON AERODYNAMIC CHARACTERISTICS OF THE SLAT WITH TWO SEGMENT LANDING FLAPS CONFIGURATION

ORIGINAL PAGE IS
OF POOR QUALITY

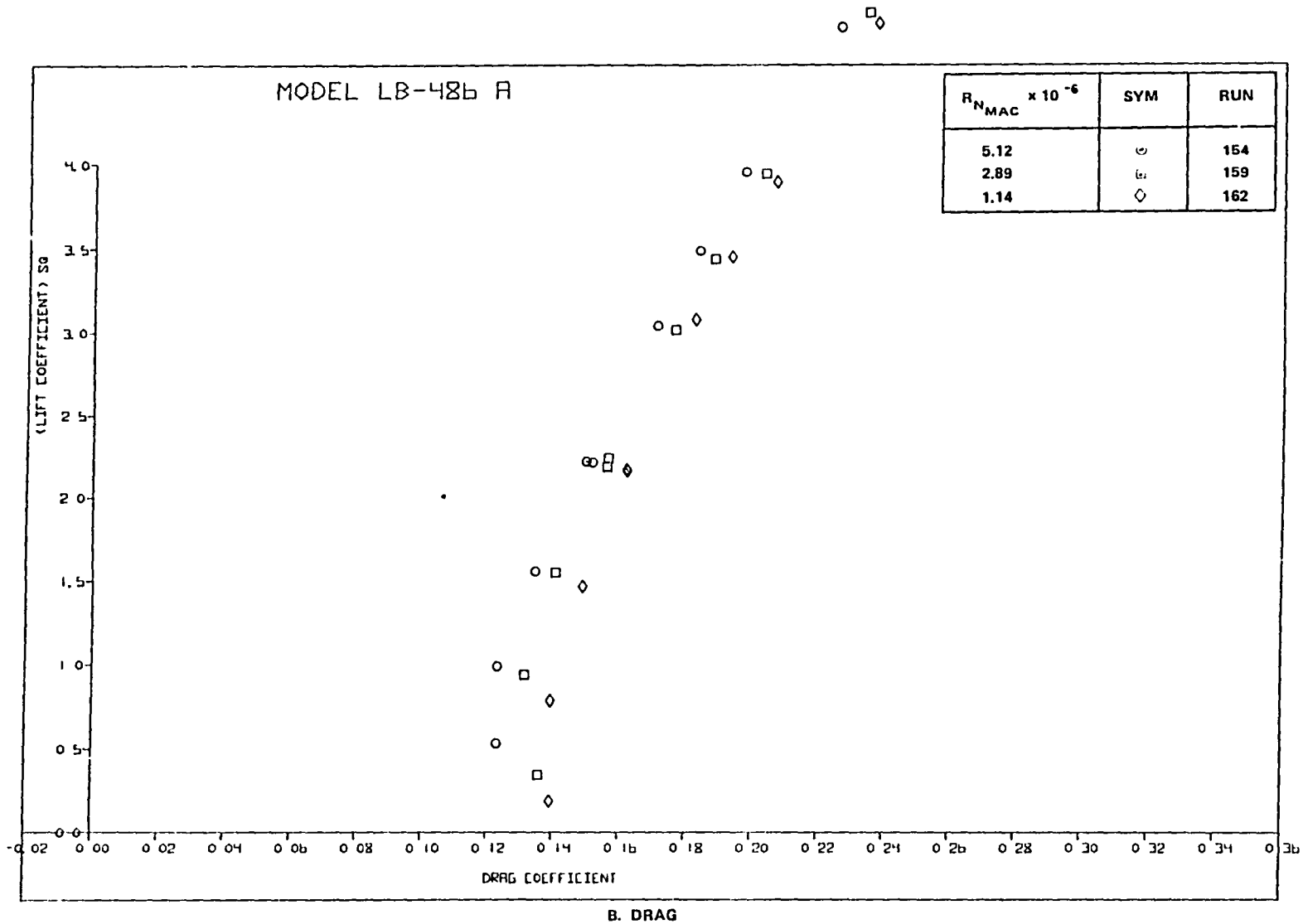

B. DRAG

FIGURE 137. EFFECT OF REYNOLDS NUMBER ON AERODYNAMIC CHARACTERISTICS OF THE SLAT WITH TWO-SEGMENT LANDING FLAPS CONFIGURATION (CONTINUED)

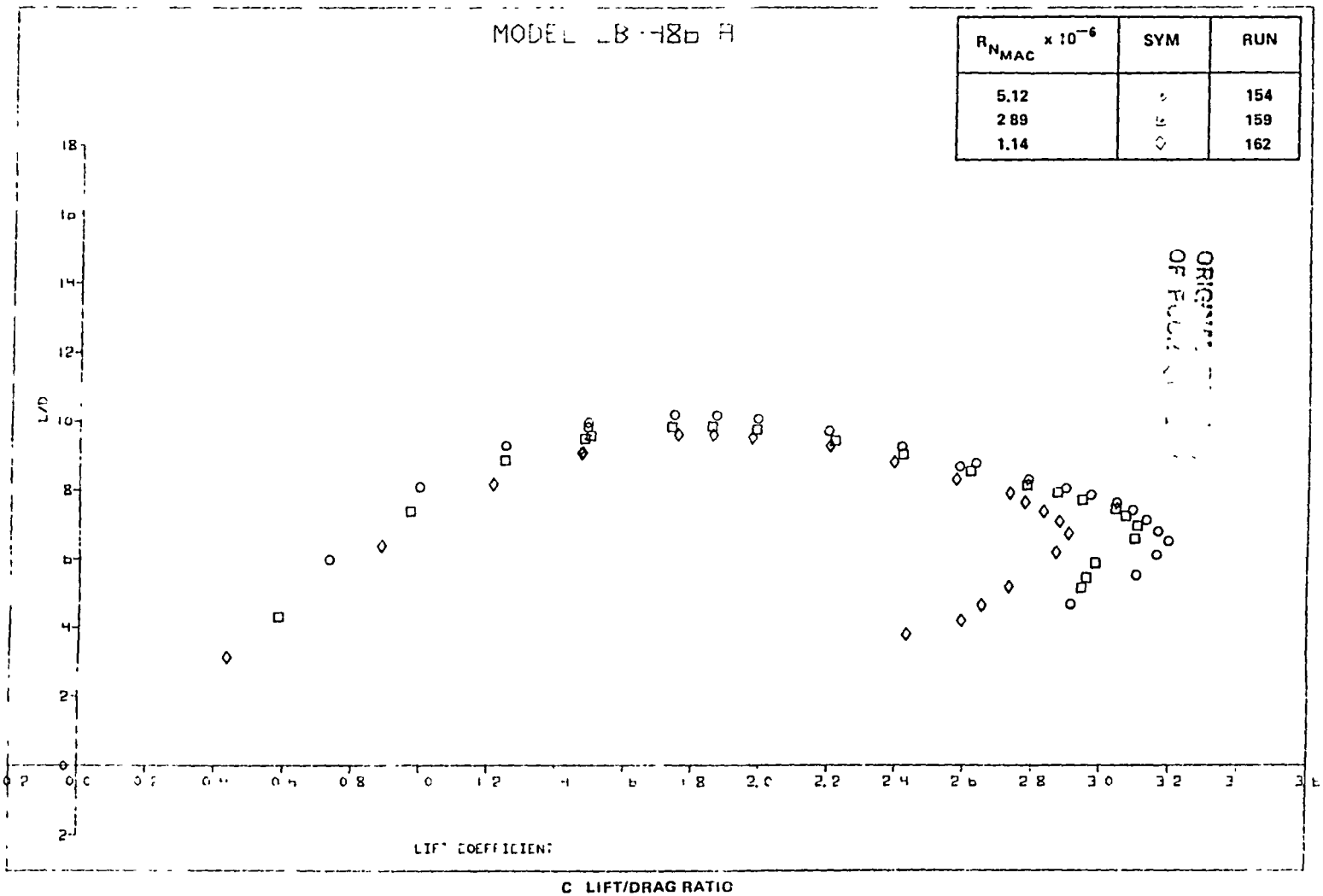

FIGURE 137 EFFECT OF REYNOLDS NUMBER ON AERODYNAMIC CHARACTERISTICS OF THE SLAT WITH TWO-SEGMENT LANDING FLAPS CONFIGURATION (CONCLUDED)

Reynolds number effects on the takeoff configuration longitudinal characteristics are shown in Figure 138. The reductions in $C_{L_{MAX}}$ were 0.10, and 0.30 for the intermediate and low Reynolds number. The effects of Reynolds number on the pitching moment characteristics are similar to the landing configuration. L/D values at 1.2 V_S are 11.55, 11.40, and 11.35 for the high, intermediate, and low Reynolds number. Comparison with the VCK configuration indicates a greater influence on $C_{L_{MAX}}$ due to a change in Reynolds number for the configuration with a slat leading edge device.

Slat with Two-Segment Flap and Horizontal Tail. - Figure 139 presents the high Reynolds number characteristics of the slat with two-segment landing flaps configuration with the horizontal tail attached. Reduced stability is indicated prior to $C_{L_{MAX}}$ for both stabilizer settings. Achievement of improved pitch characteristics will result from future tests with modifications to increase the lift loss inboard. The effect of Reynolds number on horizontal tail-on longitudinal characteristics is shown in Figure 140. A reduction in $C_{L_{MAX}}$ of 0.25 is indicated. At the reduced Reynolds number the basic trends of the pitch characteristics are similar, although the angle of attack for $C_{L_{MAX}}$ is reduced. Figure 141 presents the influence of the horizontal tail on the slat with two-segment takeoff flap deflection. Pitching moment trends are similar in character to those obtained with the landing flap deflection.

Slat with Single-Slot Flap Characteristics. - The influence of Reynolds number on the slat with single-slot flap configurations is shown in Figures 142 to 144. For the 25K/0 single-slot flap deflection, a $C_{L_{MAX}}$ of 2.95 and 2.77 is shown in Figure 142 for the high and low Reynolds number test condition. The resulting change in $C_{L_{MAX}}$ is 0.18. A reduced pitch stability for the angles of attack prior to $C_{L_{MAX}}$ is shown in Figure 143. A significant reduction in the pitching moment stability after $C_{L_{MAX}}$ is shown for the high Reynolds number condition. L/D values at 1.3 V_S were 10.5 and 9.9 for the high and low Reynolds number condition.

For the 15G/0 single-slot flap deflection, a $C_{L_{MAX}}$ of 2.71 and 2.50 shown in Figure 143 for the high and low Reynolds number condition ($C_{L_{MAX}}$ is 0.21). The Reynolds number effect on pitching moment is similar to the single-slot

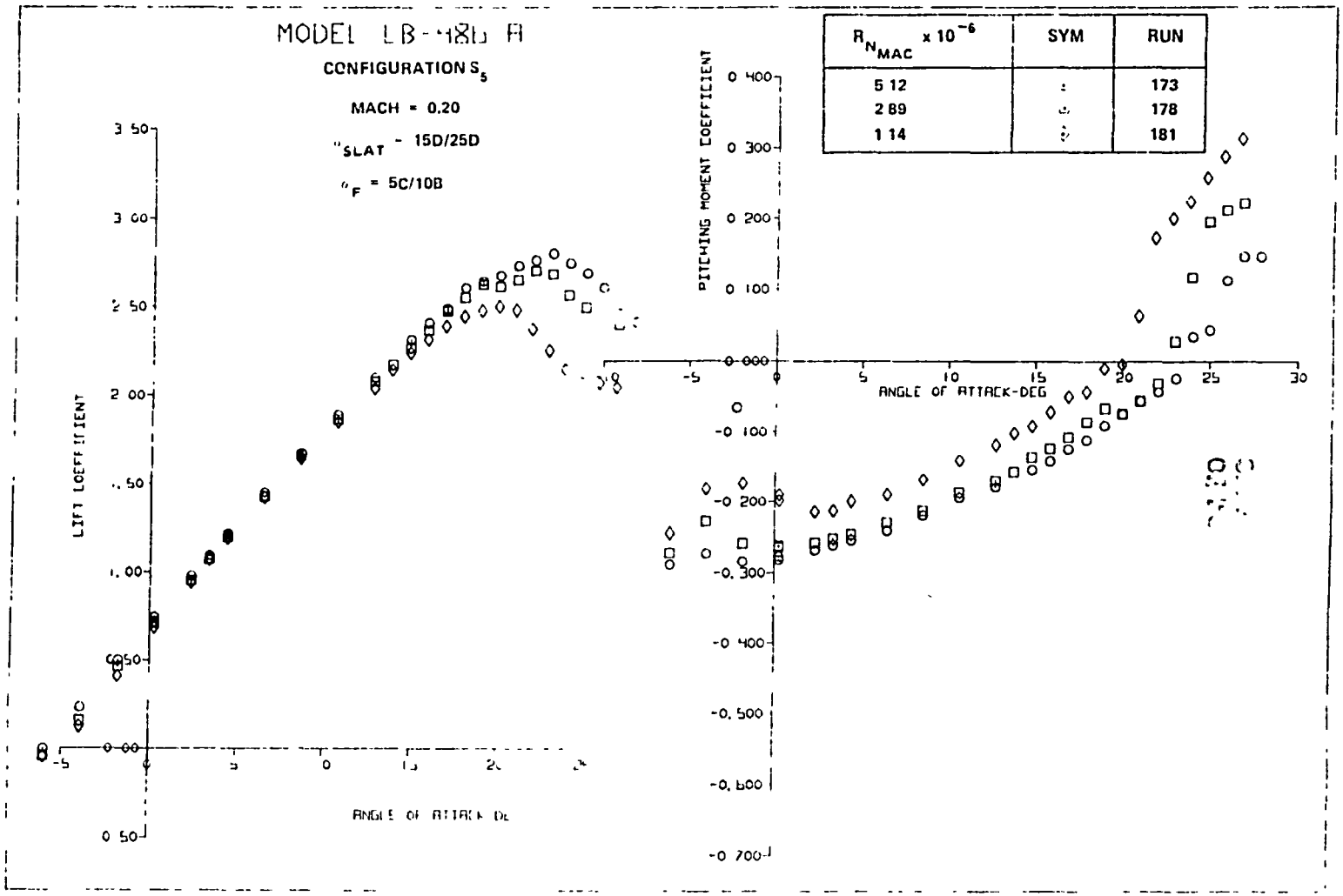

A LIFT AND PITCHING MOMENT

FIGURE 138. EFFECT OF REYNOLDS NUMBER ON AERODYNAMIC CHARACTERISTICS OF THE SLAT WITH TWO SEGMENT TAKEOFF FLAPS CONFIGURATION

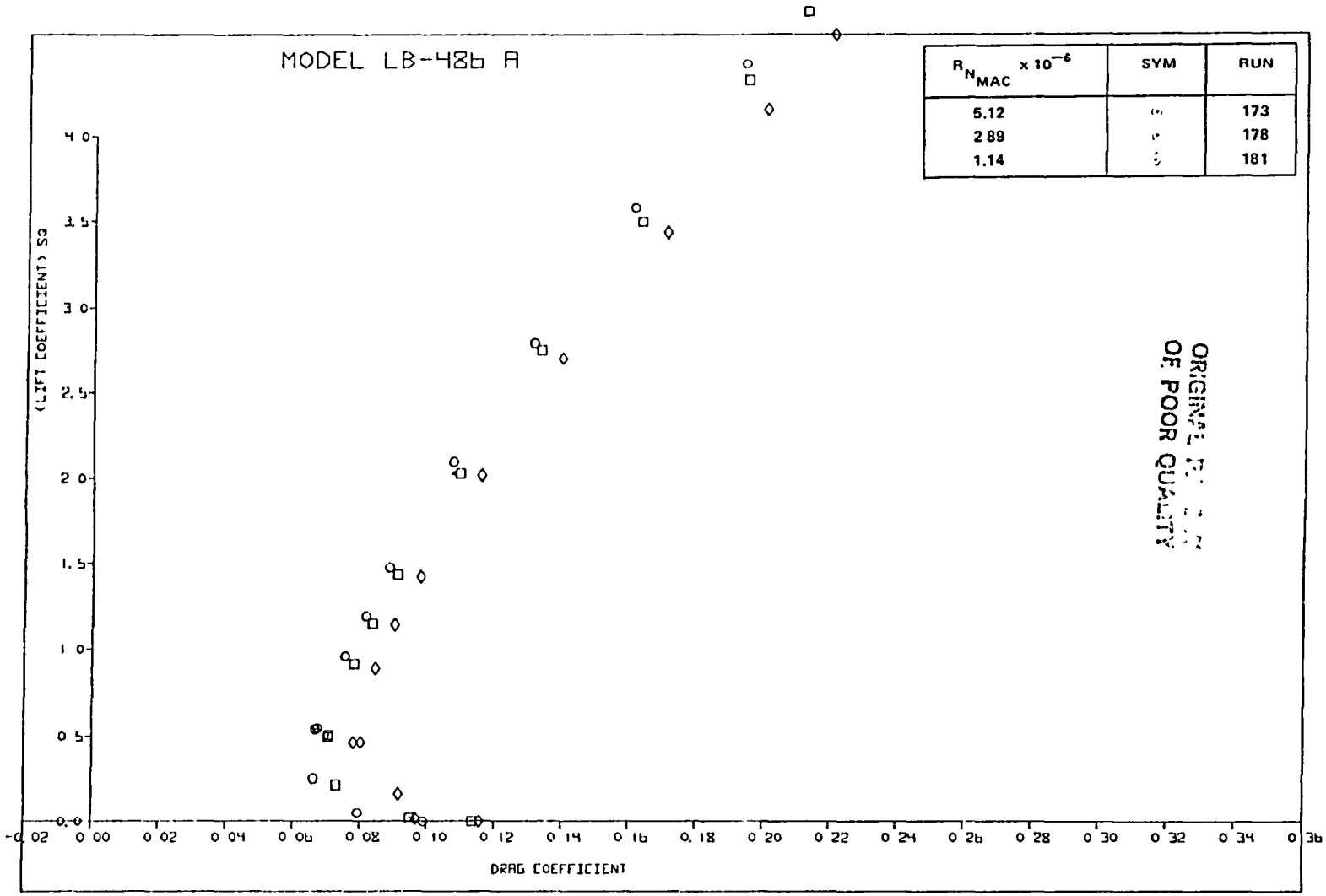

B. DRAG

FIGURE 138. EFFECT OF REYNOLDS NUMBER ON AERODYNAMIC CHARACTERISTICS OF THE SLAT WITH TWO-SEGMENT TAKEOFF FLAPS CONFIGURATION (CONTINUED)

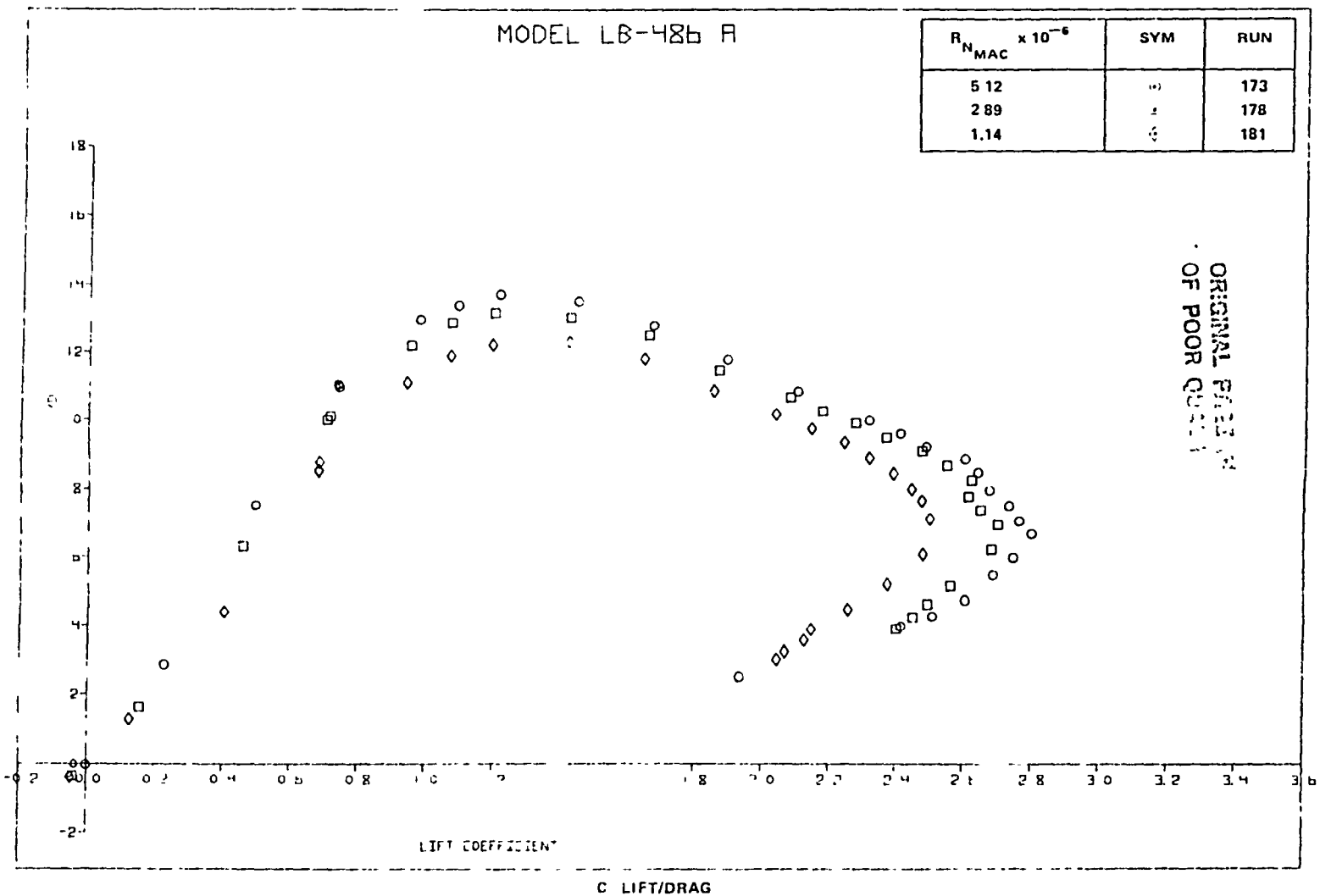

FIGURE 138. EFFECT OF REYNOLDS NUMBER ON AERODYNAMIC CHARACTERISTICS OF THE SLAT WITH TWO-SEGMENT TAKEOFF FLAPS CONFIGURATION (CONCLUDED)

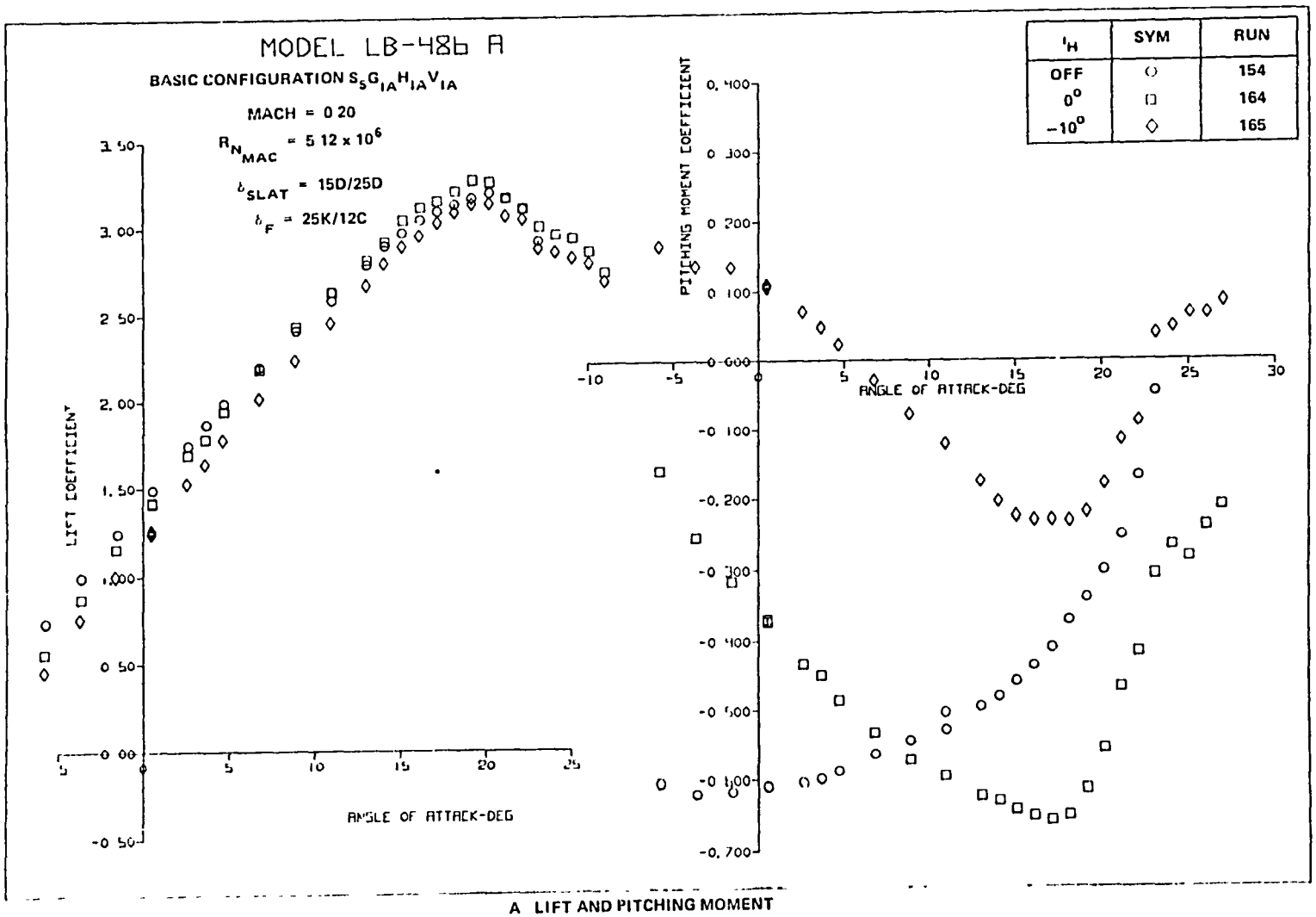

A LIFT AND PITCHING MOMENT

FIGURE 139. EFFECT OF HORIZONTAL TAIL DEFLECTION ON AERODYNAMIC CHARACTERISTICS OF THE [illegible] WITH TWO SEGMENT LANDING FLAPS CONFIGURATION

ORIGINAL PAGE IS OF POOR QUALITY

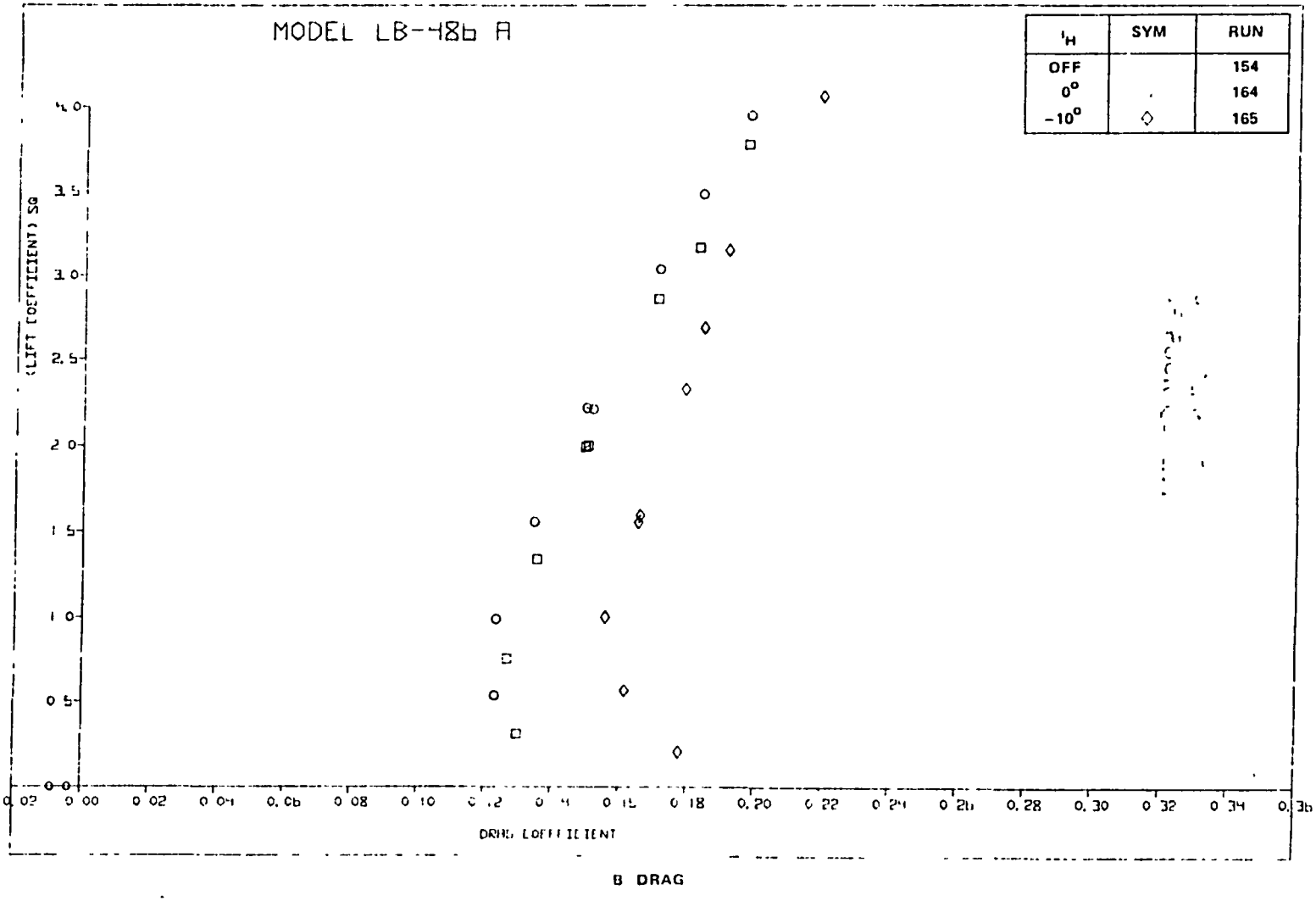

FIGURE 139. EFFECT OF HORIZONTAL TAIL DEFLECTION ON AERODYNAMIC CHARACTERISTICS OF THE SLAT WITH TWO-SEGMENT LANDING FLAPS CONFIGURATION (CONCLUDED)

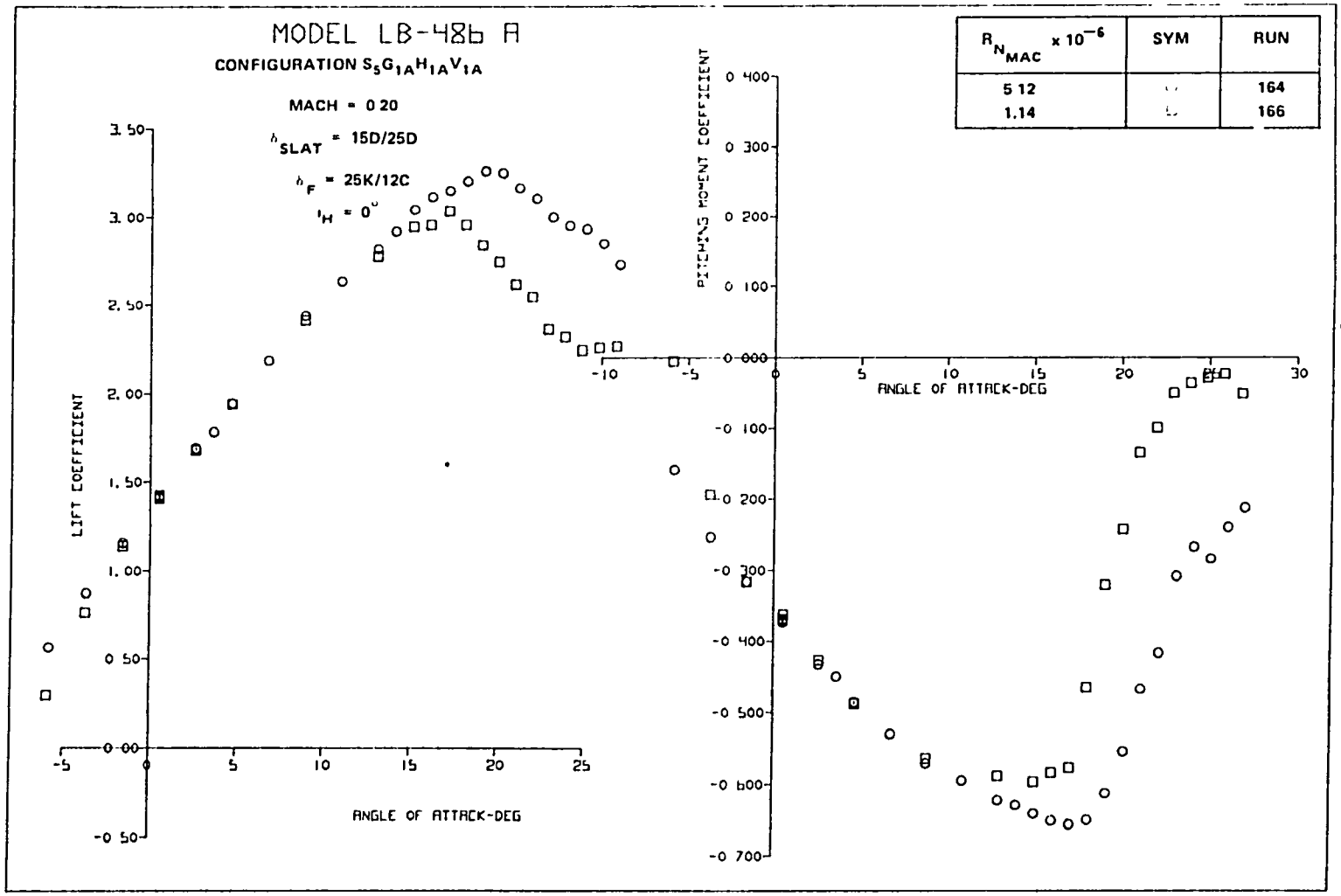

A. LIFT AND PITCHING MOMENT

FIGURE 140. EFFECT OF REYNOLDS NUMBER ON AERODYNAMIC CHARACTERISTICS OF THE SLAT WITH TWO-SEGMENT LANDING FLAPS CONFIGURATION (HORIZONTAL TAIL ON)

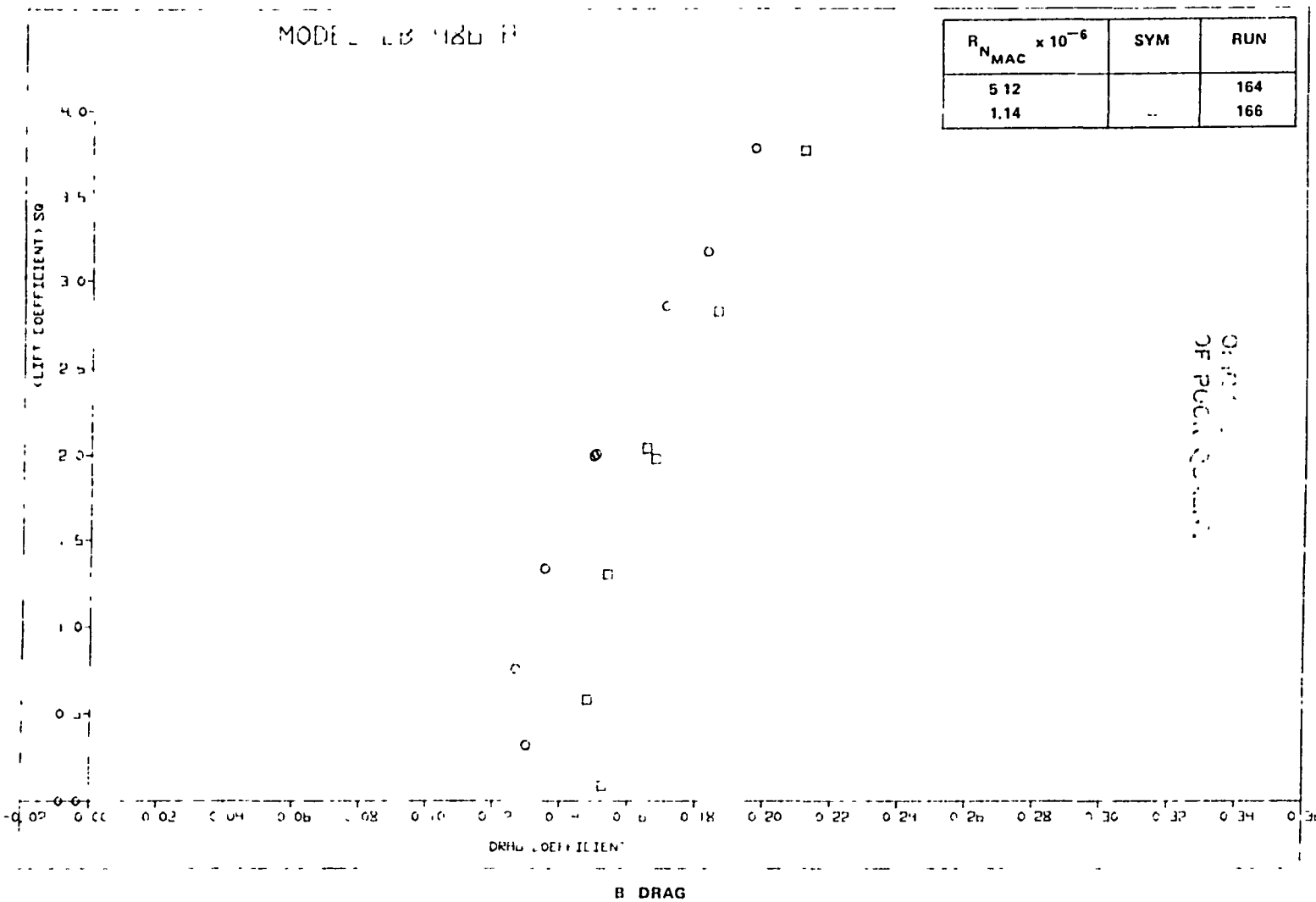

FIGURE 140. EFFECT OF REYNOLDS NUMBER ON AERODYNAMIC CHARACTERISTICS OF THE SLAT WITH TWO-SEGMENT LANDING FLAPS CONFIGURATION (HORIZONTAL TAIL-ON) (CONCLUDED)

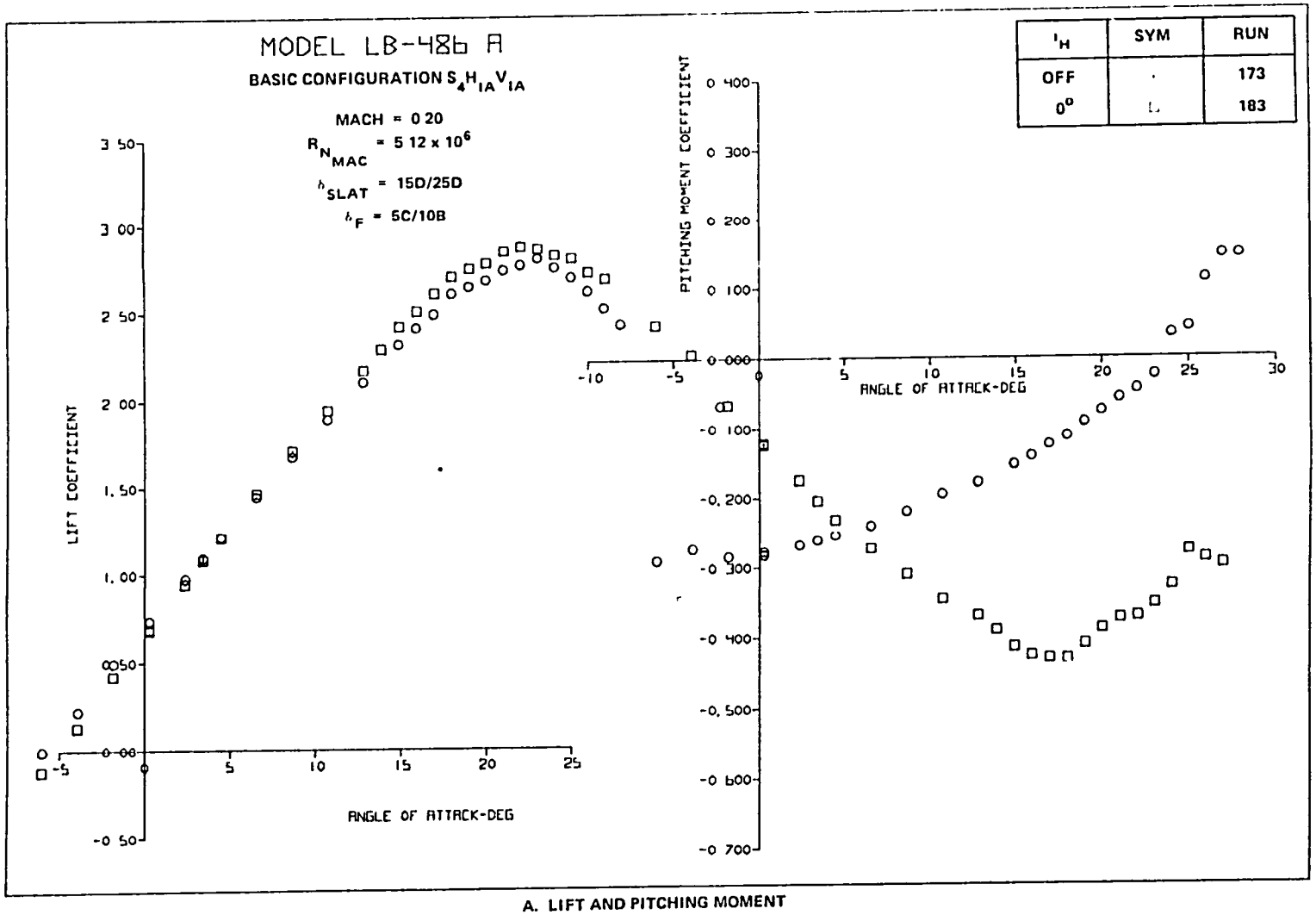

A. LIFT AND PITCHING MOMENT

FIGURE 141. EFFECT OF HORIZONTAL TAIL ON AERODYNAMIC CHARACTERISTICS OF THE SLAT WITH TWO-SEGMENT TAKEOFF FLAPS CONFIGURATION

ORIGINAL PAGE IS OF POOR QUALITY

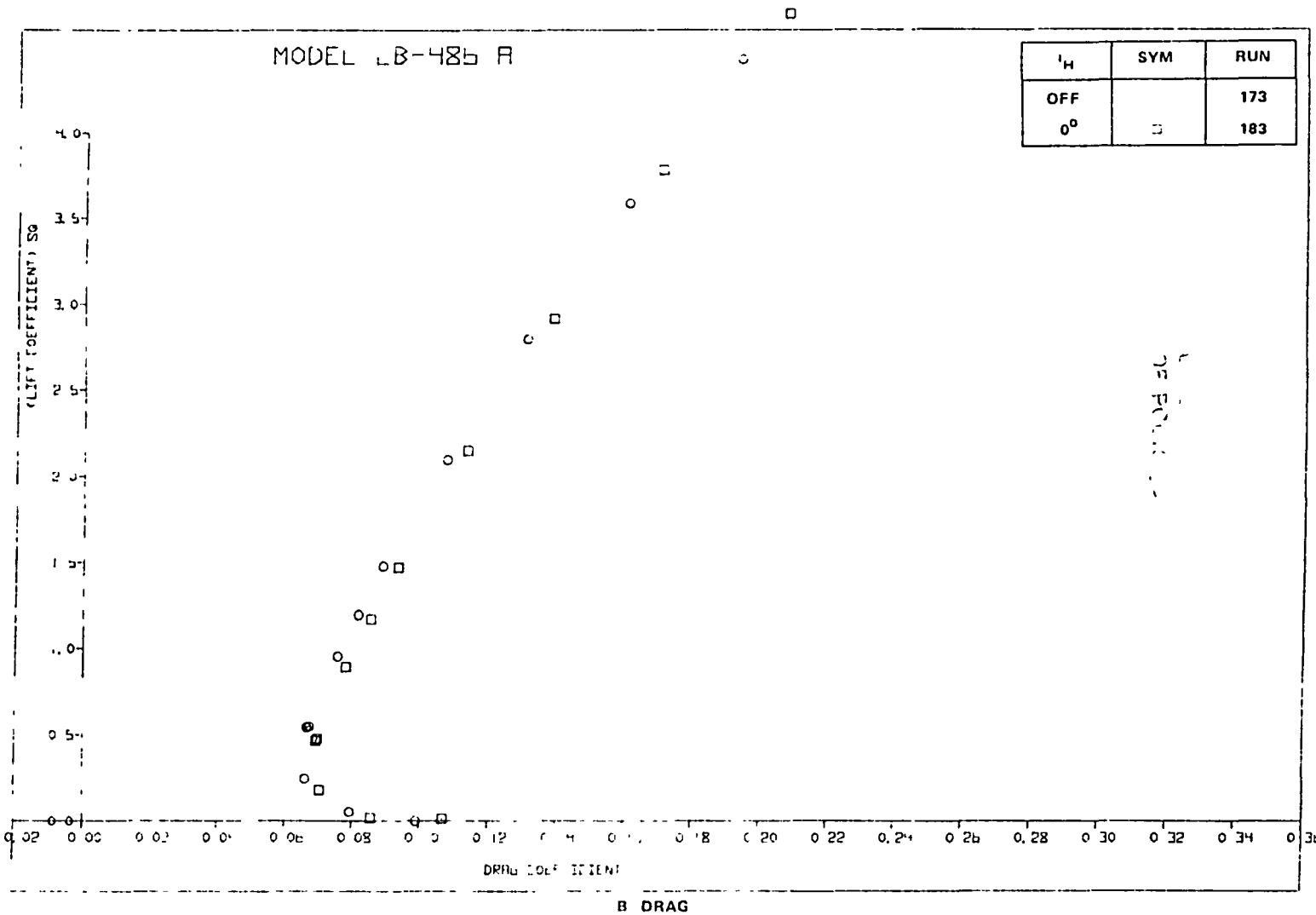

FIGURE 141. EFFECT OF HORIZONTAL TAIL ON AERODYNAMIC CHARACTERISTICS OF THE SLAT WITH TWO-SEGMENT TAKEOFF FLAPS CONFIGURATION (CONCLUDED)

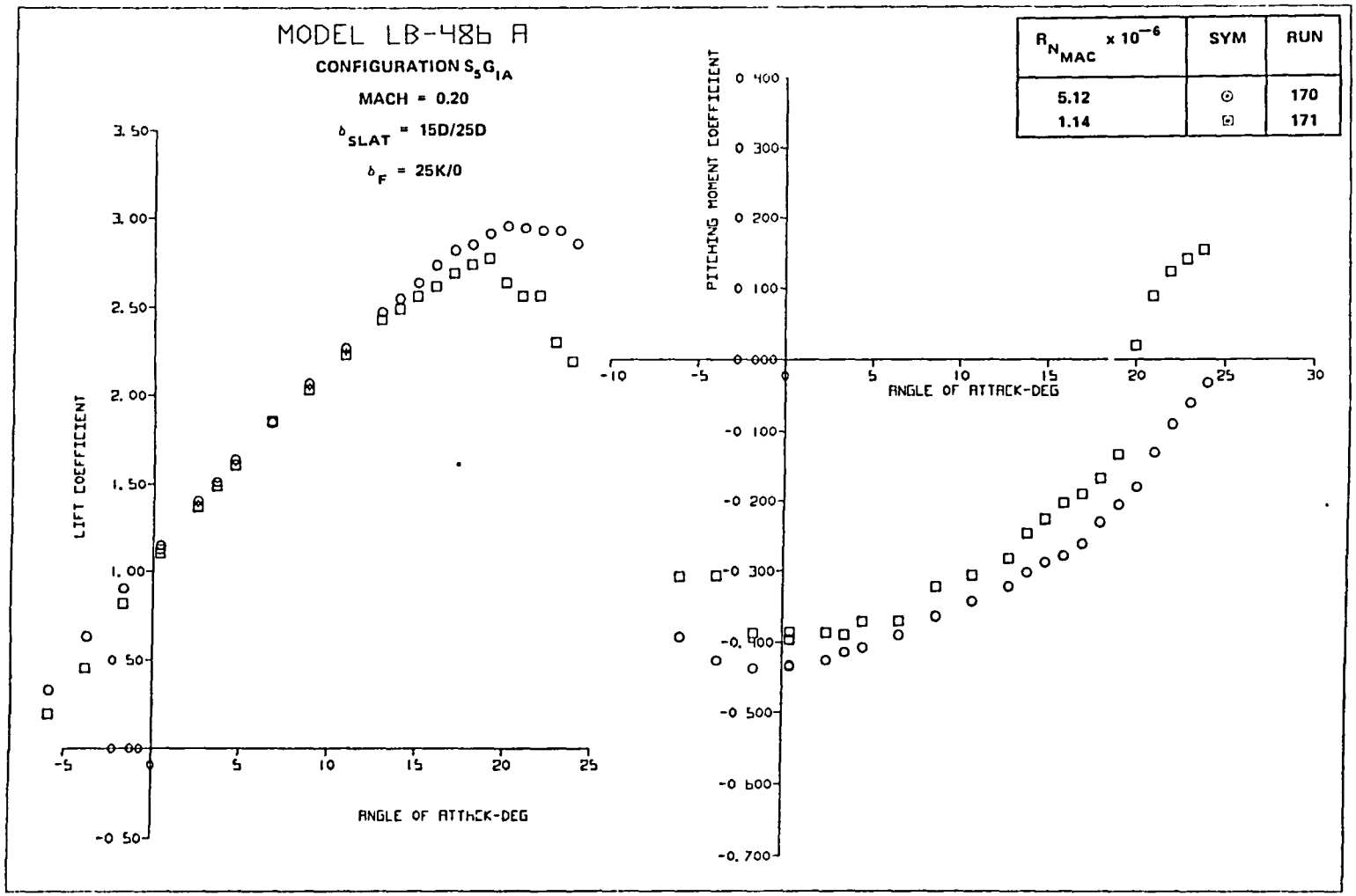

A. LIFT AND PITCHING MOMENT

FIGURE 142. EFFECT OF REYNOLDS NUMBER ON AERODYNAMIC CHARACTERISTICS OF THE SLAT WITH SINGLE-SLOT LANDING FLAPS CONFIGURATION

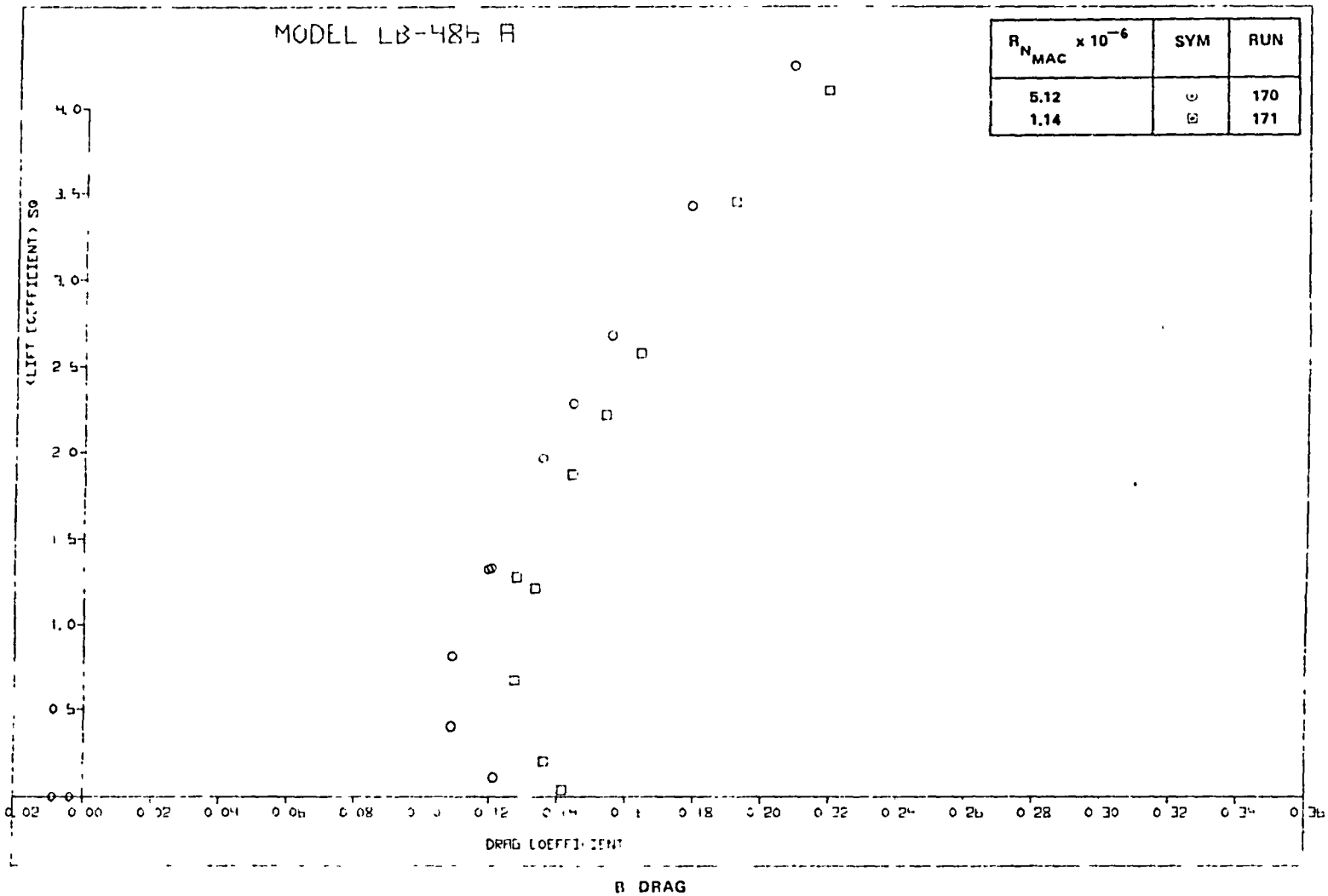

FIGURE 142 EFFECT OF REYNOLDS NUMBER ON AERODYNAMIC CHARACTERISTICS OF THE SLAT WITH SINGLE SLOT LANDING FLAPS CONFIGURATION (CONTINUED)

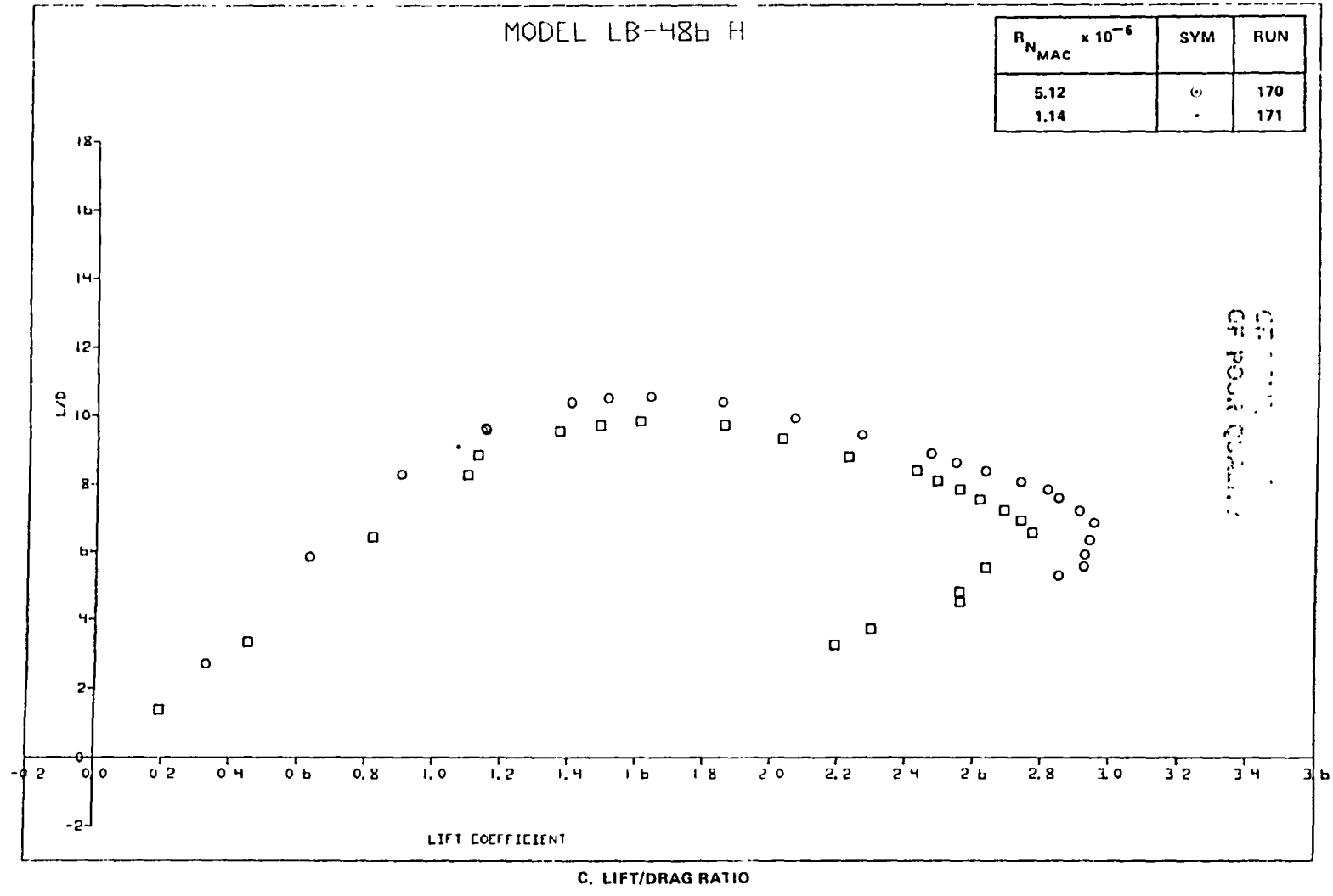

C. LIFT/DRAG RATIO

FIGURE 142. EFFECT OF REYNOLDS NUMBER ON AERODYNAMIC CHARACTERISTICS OF THE SLAT WITH SINGLE-SLOT LANDING FLAPS CONFIGURATION (CONCLUDED)

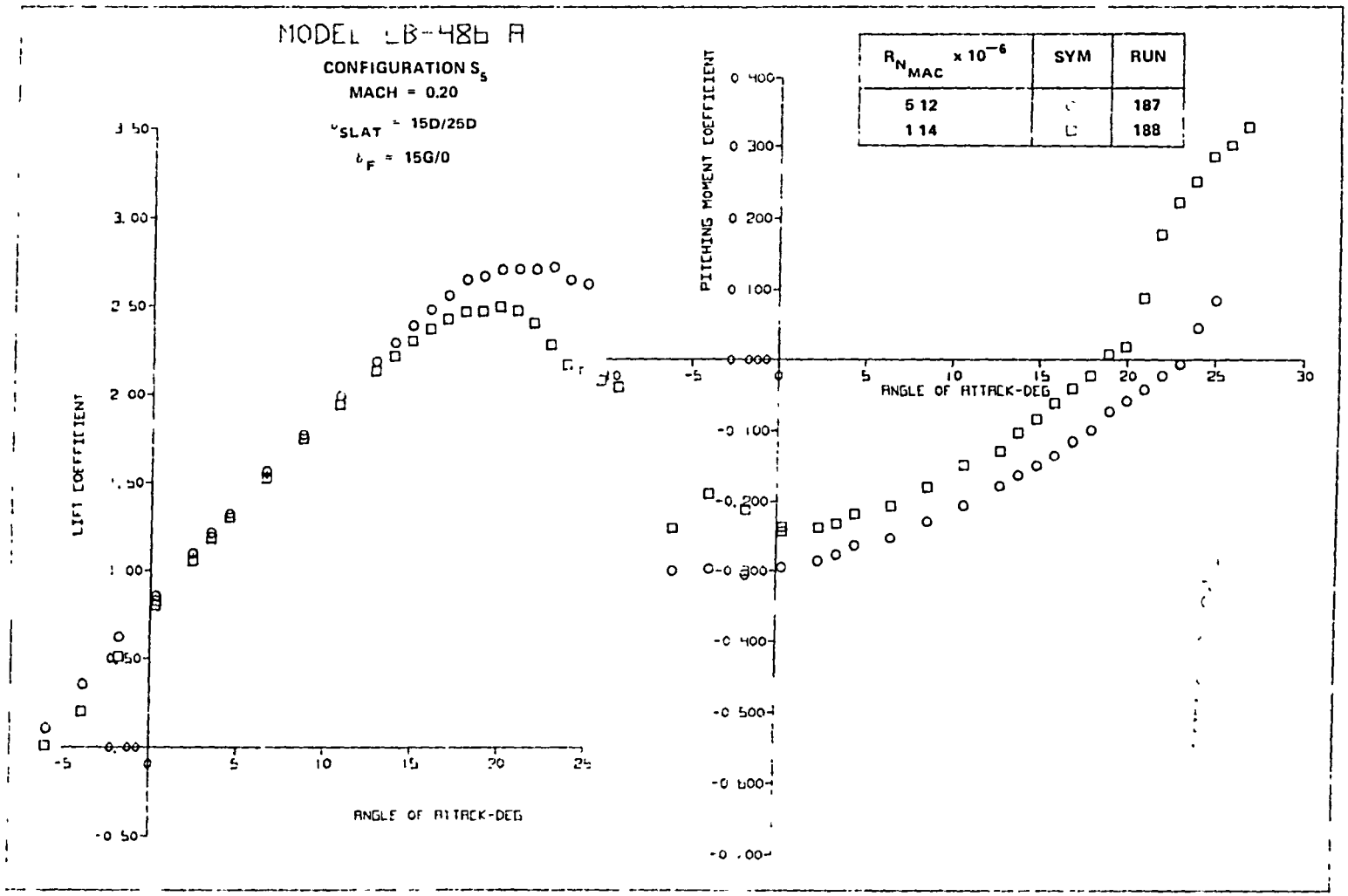

A LIFT AND PITCHING MOMENT

FIGURE 143. EFFECT OF REYNOLDS NUMBER ON AERODYNAMIC CHARACTERISTICS FOR THE SLAT WITH SINGLE-SLOT TAKEOFF FLAPS CONFIGURATION

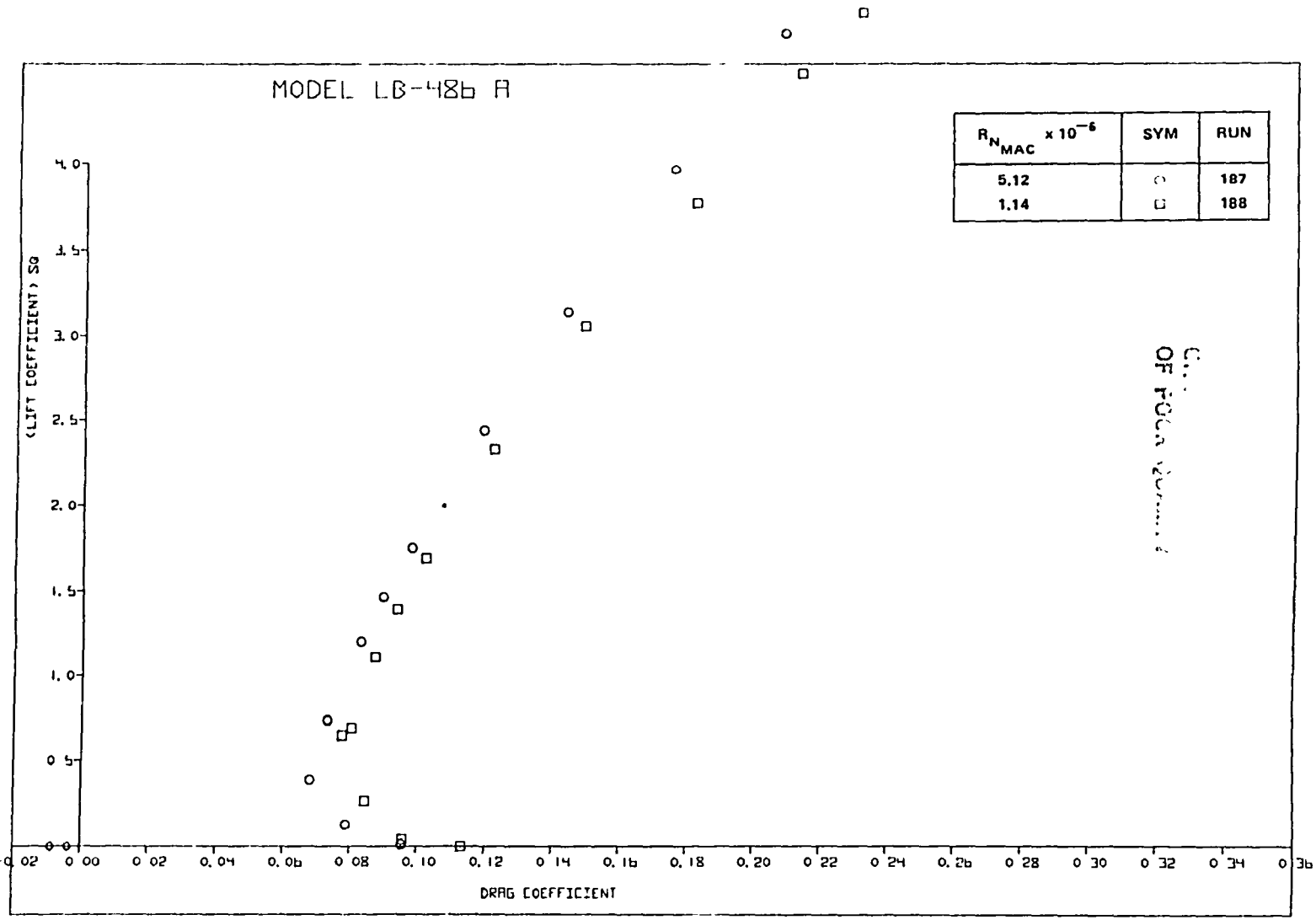

B. DRAG

FIGURE 143. EFFECT OF REYNOLDS NUMBER ON AERODYNAMIC CHARACTERISTICS FOR THE SLAT WITH SINGLE-SLOT TAKEOFF FLAPS CONFIGURATION (CONTINUED)

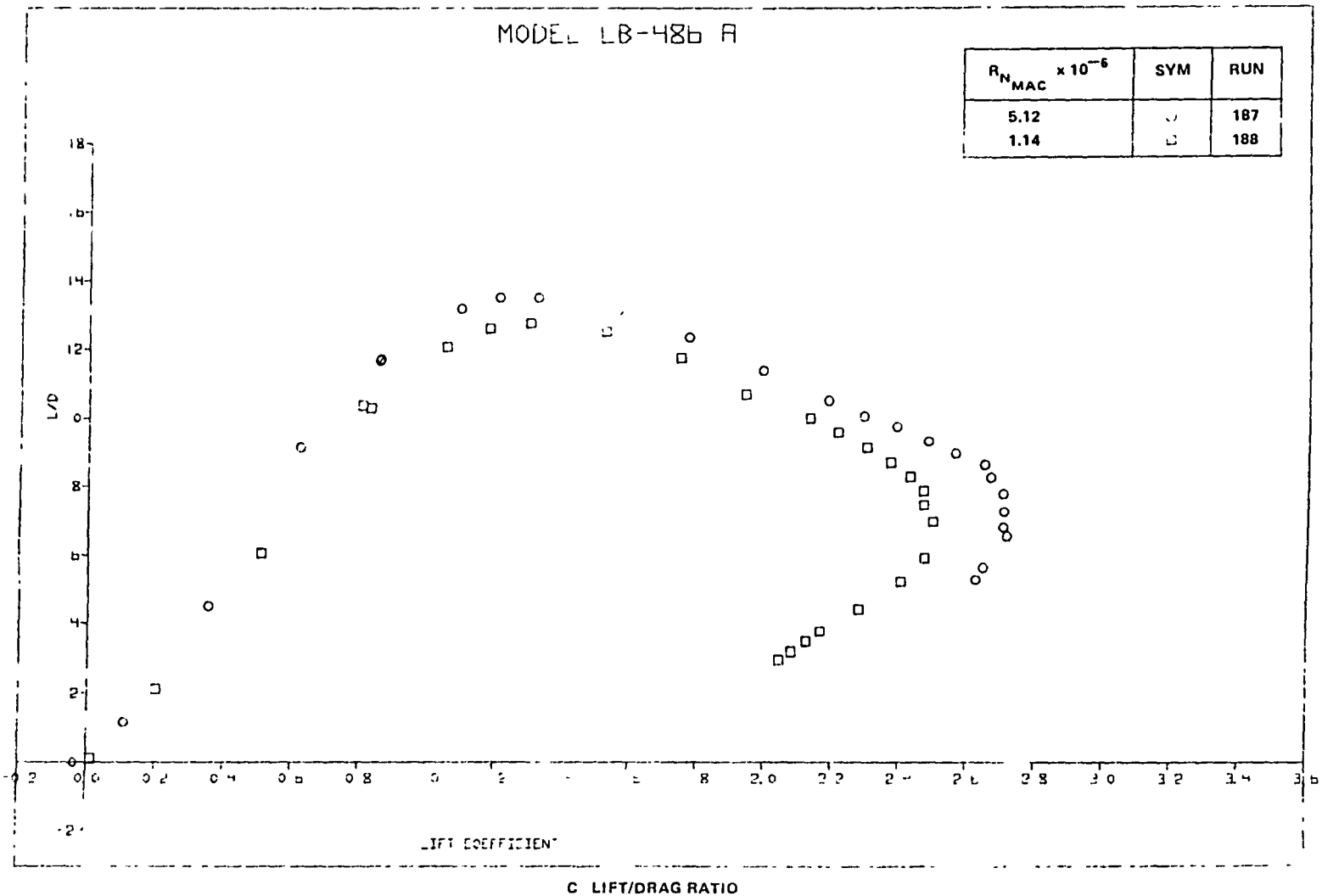

FIGURE 143 EFFECT OF REYNOLDS NUMBER ON AERODYNAMIC CHARACTERISTICS FOR THE SLAT WITH SINGLE SLOT TAKEOFF FLAPS CONFIGURATION (CONCLUDED)

ORIGINAL PAGE IS
OF POOR QUALITY

landing flap data. The L/D values at 1.2 V_S are 11.80 and 11.70 for the high and low Reynolds number test condition.

For 5A/0 takeoff flap deflection, $C_{L_{MAX}}$ values of 2.62 and 2.33 are shown in Figure 144. Figure 144 also shows a significant reduction in stability after $C_{L_{MAX}}$ is achieved for the high Reynolds number test condition. The corresponding L/D values at 1.2 V_S are 11.8 and 11.6 for the high and low Reynolds number condition.

The influence of the horizontal tail for the slat with the landing single-slot flap configuration is presented in Figure 145. Pitch characteristics near stall are similar in character to those obtained with the landing two-segment flap configuration.

Clean Leading Edge Configuration

The two-segment and single-slot aerodynamic characteristics with the leading edge device removed (cruise wing leading edge) are shown in Figures 146 and 147. For both flap systems, outboard leading edge separation occurs at decreasing angles of attack as the flap deflection is increased. Essentially similar values of wing leading edge $C_{P_{MIN}}$ values were indicated for the various flap deflections. Due to the expected outboard separation, only small gains in $C_{L_{MAX}}$ were obtained with increasing flap deflection. The flaps are very effective in increasing the lift at small angles of attack. The two-segment flap at 25K/12C achieved at $C_{L_{\alpha=0}}$ of 1.50. Two-segment and single slot $\Delta C_{L_{MAX}}$ and $C_{L_{\alpha=0}}$ increments (relative to the cruise wing) are presented in the Data Summary section.

Clean Trailing Edge Configuration

The influence of Reynolds number on the VCK with flaps retractd (clean trailing edge) configuration is shown in Figure 148. A $C_{L_{MAX}}$ of 2.56 for the high Reynolds number condition was obtained. The corresponding value at the low Reynolds number condition was 2.14. In comparison to the cruise wing configuration (Figure 73), the angle of attack for $C_{L_{MAX}}$ has been increased from 12.58° to 20.85°, the $C_{L_{MAX}}$ increased by 0.71, and favorable stability characteristics at $C_{L_{MAX}}$ was obtained for the VCK extended configuration at the high Reynolds number test condition. As with the takeoff and landing flap deflection, the low Reynolds number condition results in a positive pitch increment for most of the angle of attack range.

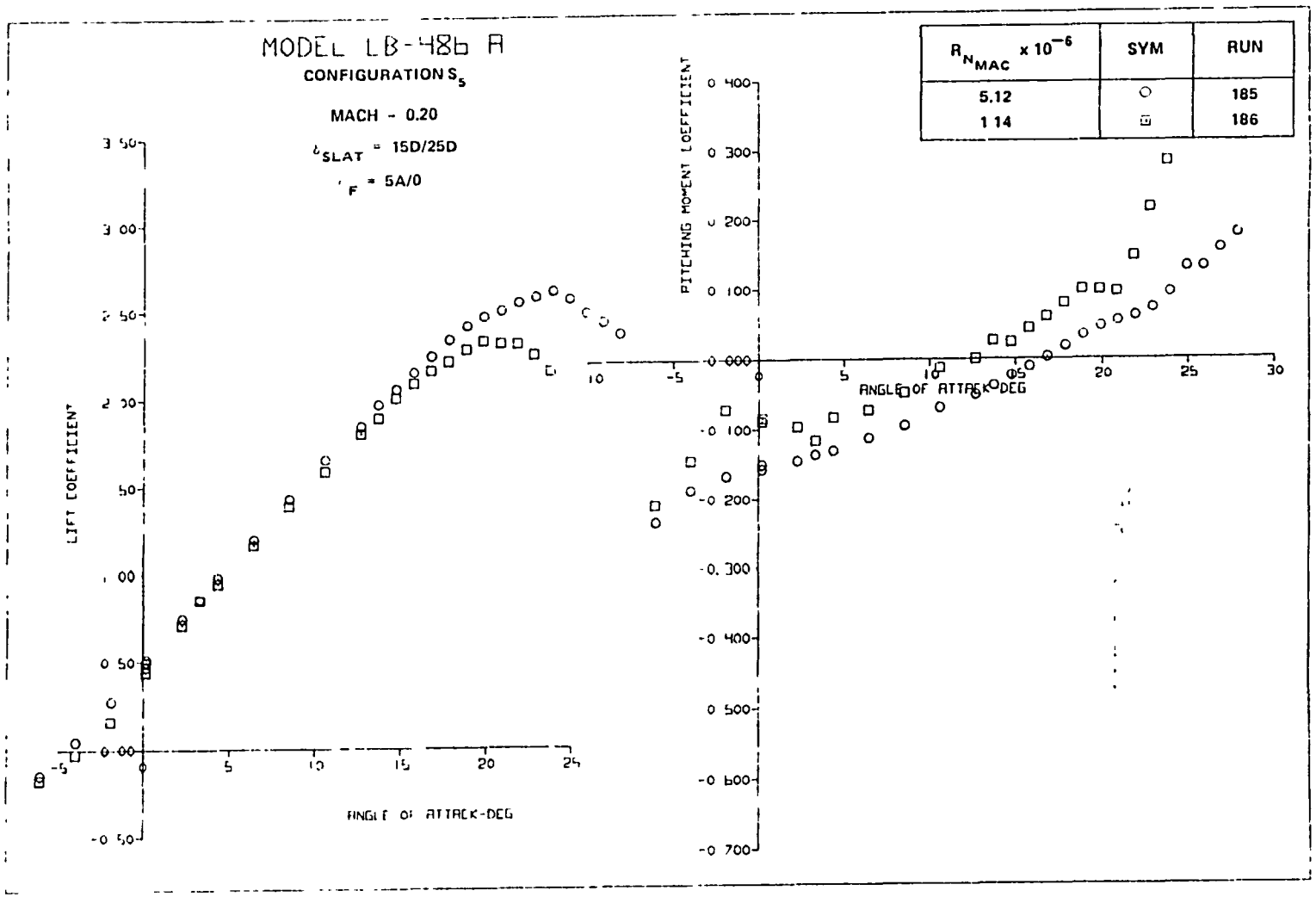

A LIFT AND PITCHING MOMENT

FIGURE 144. EFFECT OF REYNOLDS NUMBER ON AERODYNAMIC CHARACTERISTICS OF THE SLAT WITH SINGLE SLOT TAKEOFF FLAPS CONFIGURATION

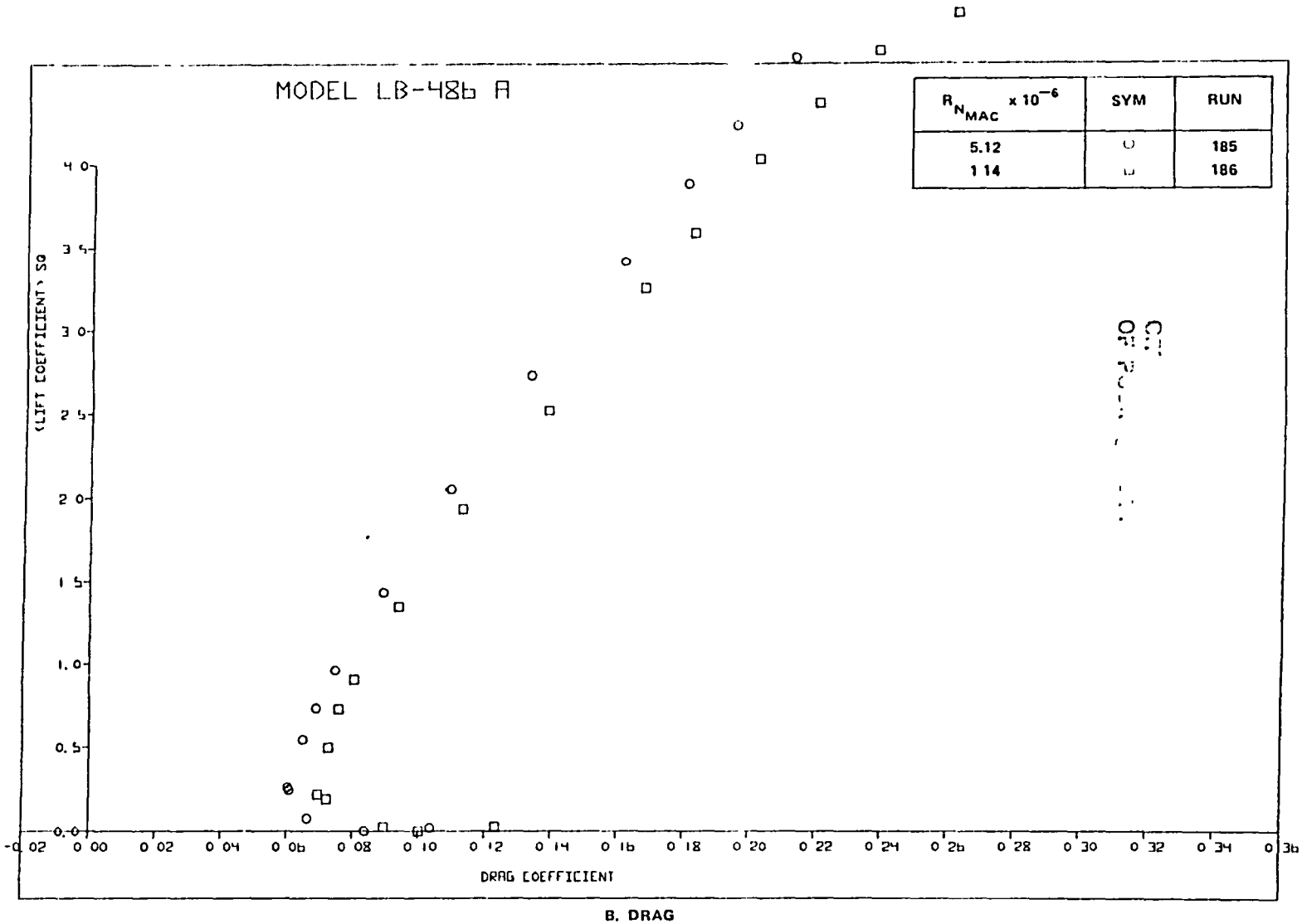

B. DRAG

FIGURE 144. EFFECT OF REYNOLDS NUMBER ON AERODYNAMIC CHARACTERISTICS OF THE SLAT WITH SINGLE-SLOT TAKEOFF FLAPS CONFIGURATION (CONTINUED)

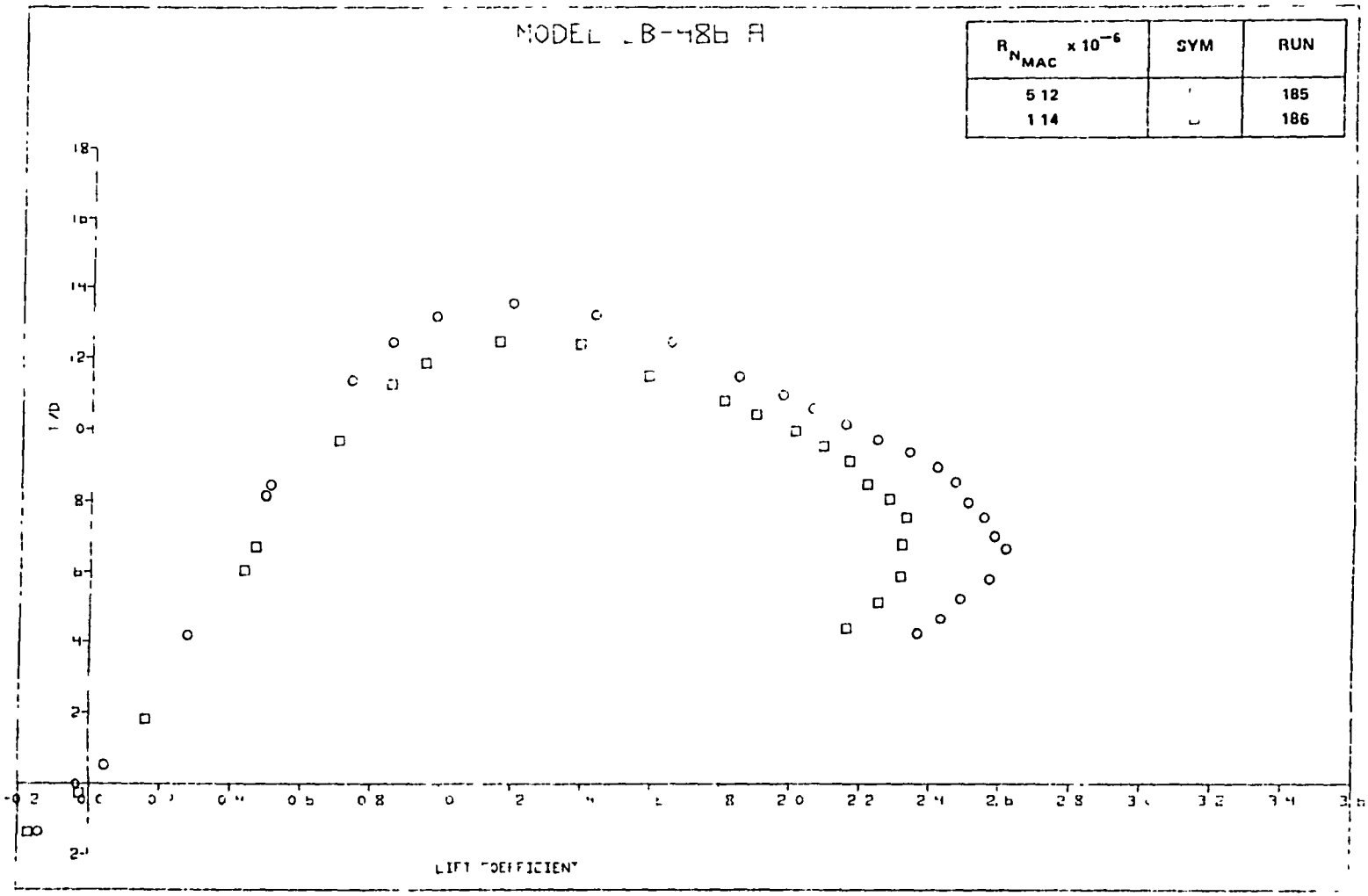

C LIFT/DRAG RATIO

FIGURE 144. EFFECT OF REYNOLDS NUMBER ON AERODYNAMIC CHARACTERISTICS OF THE SLAT WITH SINGLE-SLOT TAKEOFF FLAPS CONFIGURATION (CONCLUDED)

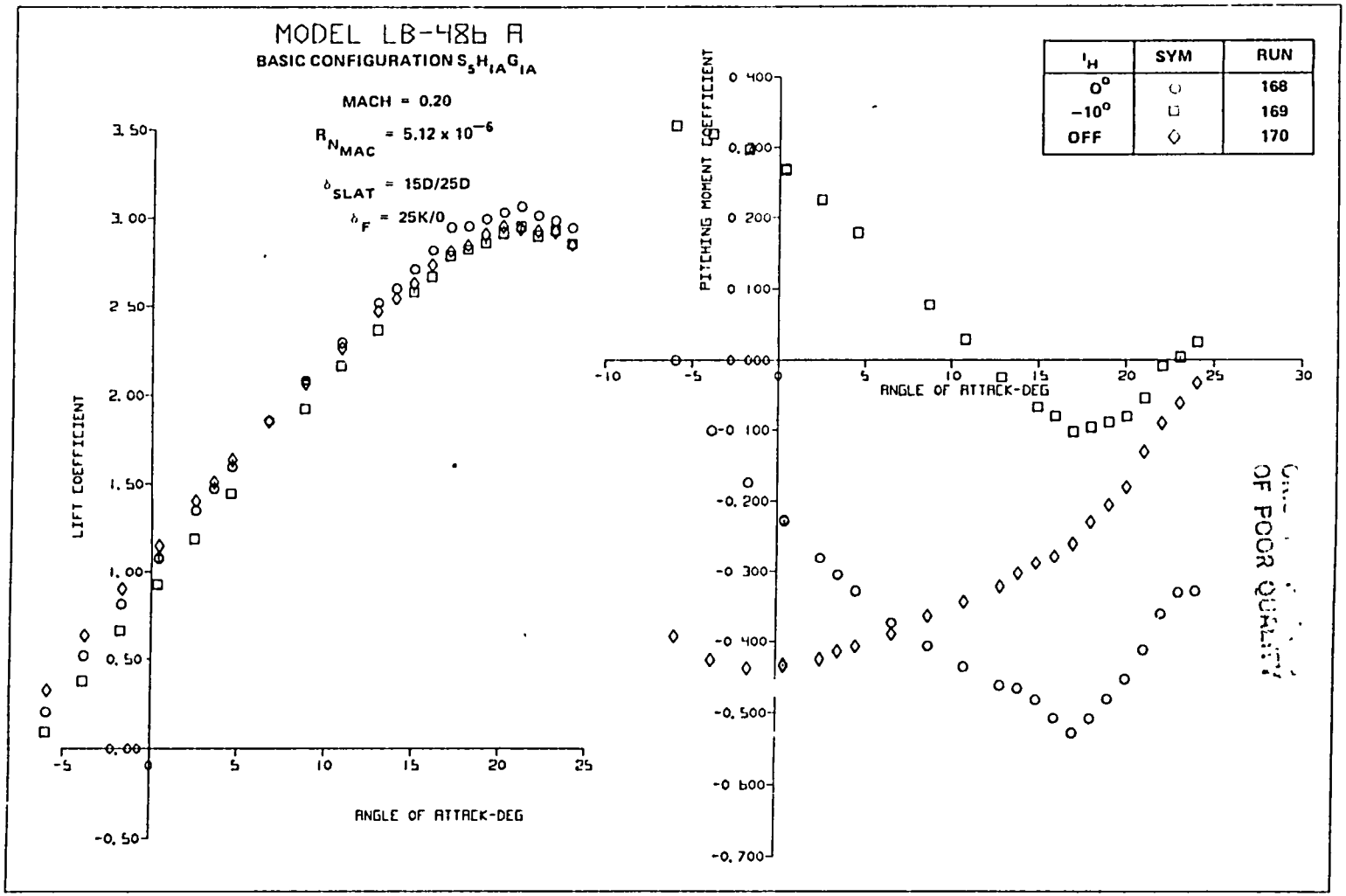

A. LIFT AND PITCHING MOMENT

FIGURE 145 EFFECT OF HORIZONTAL TAIL DEFLECTION ON AERODYNAMIC CHARACTERISTICS OF THE SLAT WITH SINGLE-SLOT LANDING FLAPS CONFIGURATION

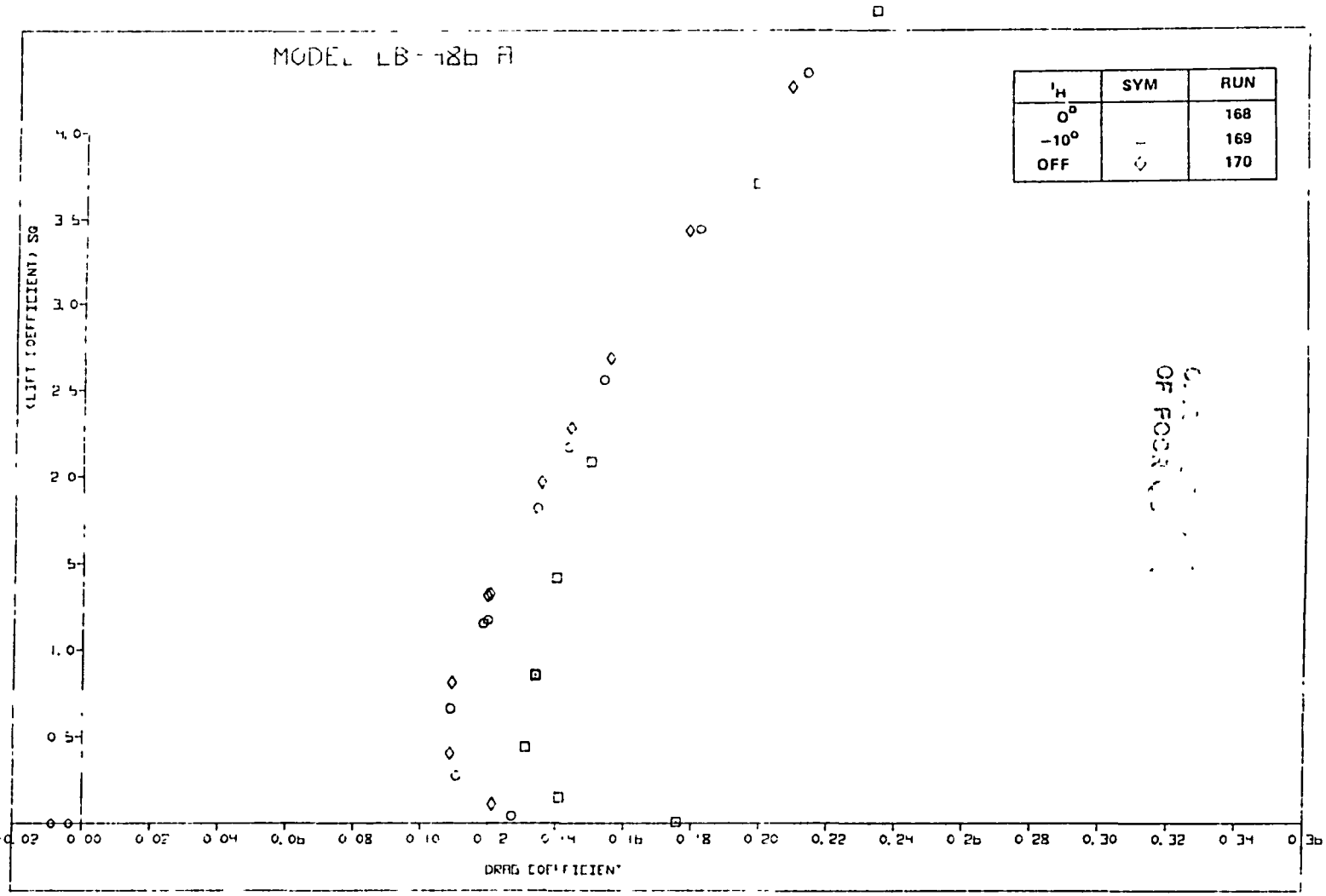

FIGURE 145. EFFECT OF HORIZONTAL TAIL DEFLECTION ON AERODYNAMIC CHARACTERISTICS OF THE SLAT WITH SINGLE-SLOT LANDING FLAPS CONFIGURATION (CONCLUDED)

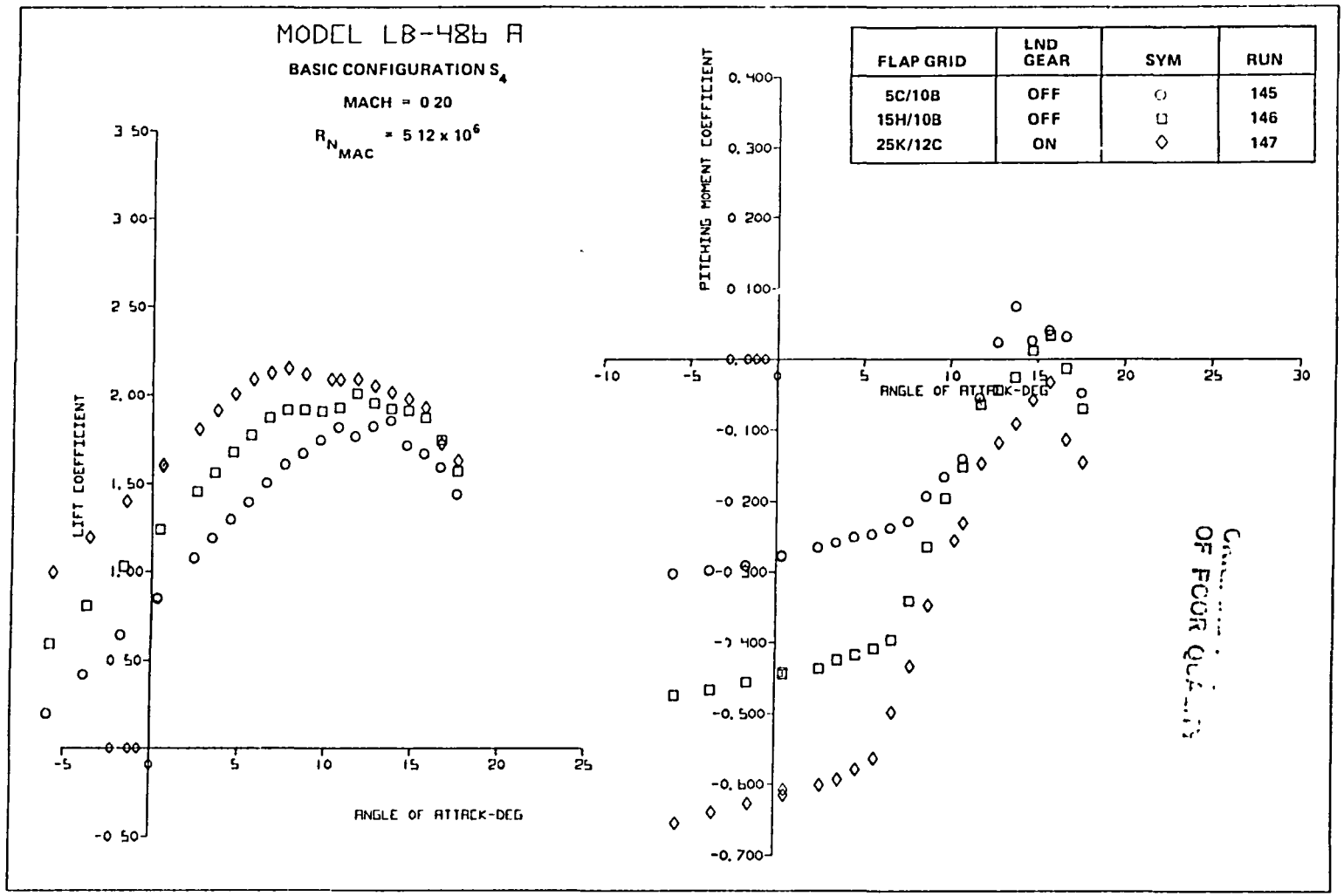

A LIFT AND PITCHING MOMENT

FIGURE 146. EFFECT OF TWO-SEGMENT FLAP DEFLECTION ON AERODYNAMIC CHARACTERISTICS WITH THE LEADING EDGE DEVICES REMOVED

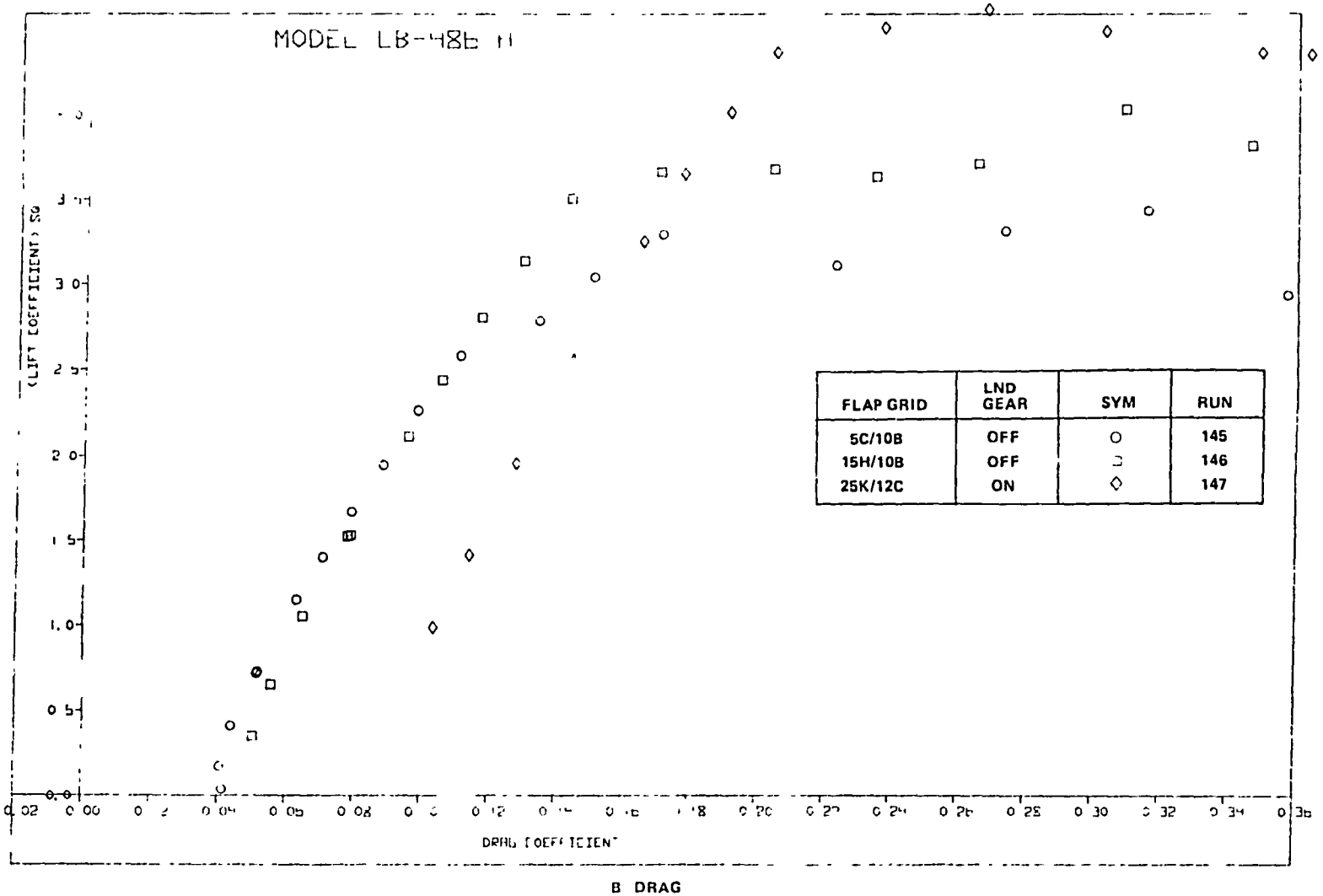

B DRAG

FIGURE 146 EFFECT OF TWO-SEGMENT FLAP DEFLECTION ON AERODYNAMIC CHARACTERISTICS WITH THE LEADING EDGE DEVICES REMOVED (CONCLUDED)

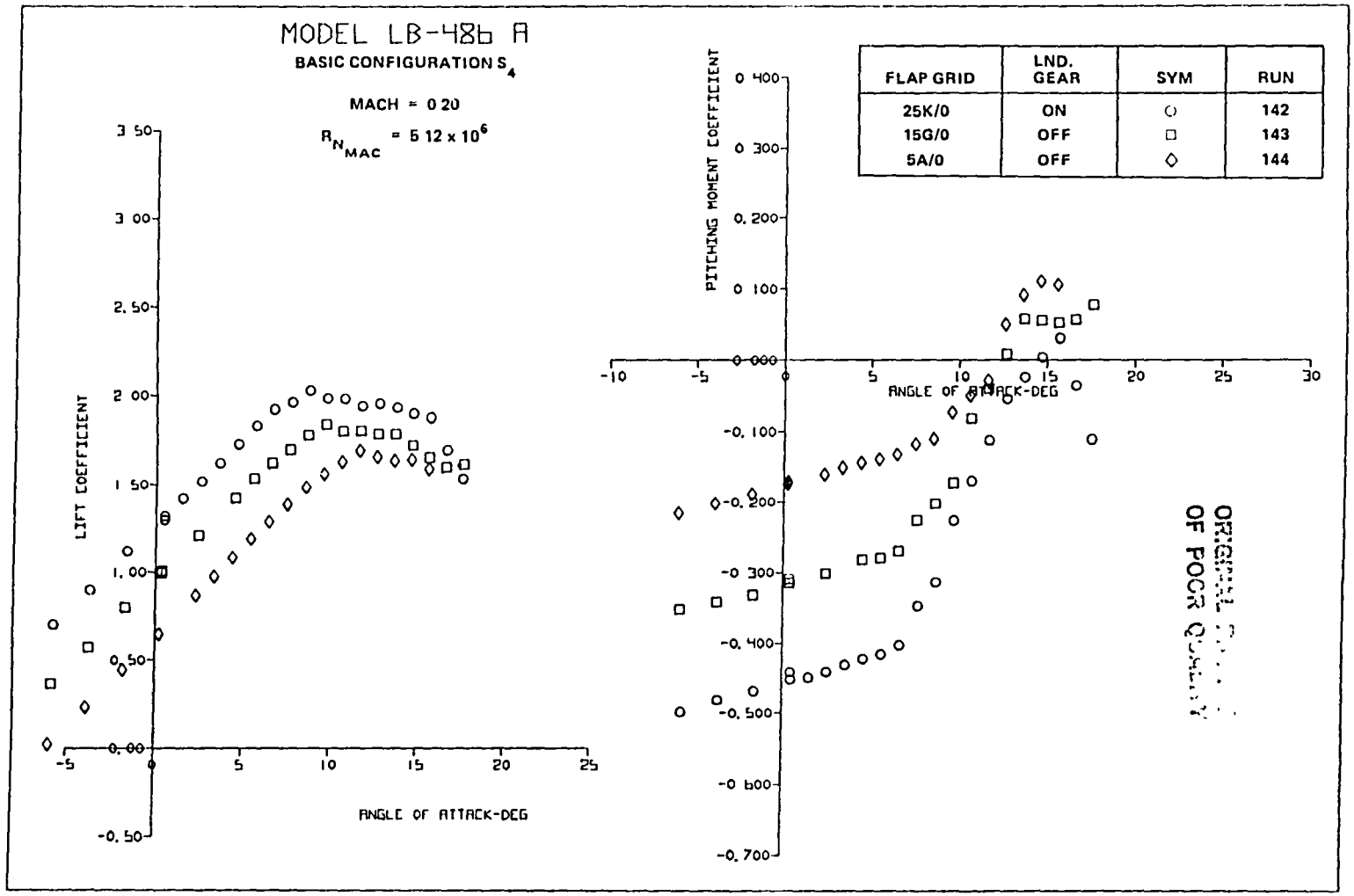

A. LIFT AND PITCHING MOMENT

FIGURE 147. EFFECT OF SINGLE-SLOT FLAP DEFLECTION ON AERODYNAMIC CHARACTERISTICS WITH THE LEADING EDGE DEVICES REMOVED

ORIGINAL PAGE IS OF POOR QUALITY

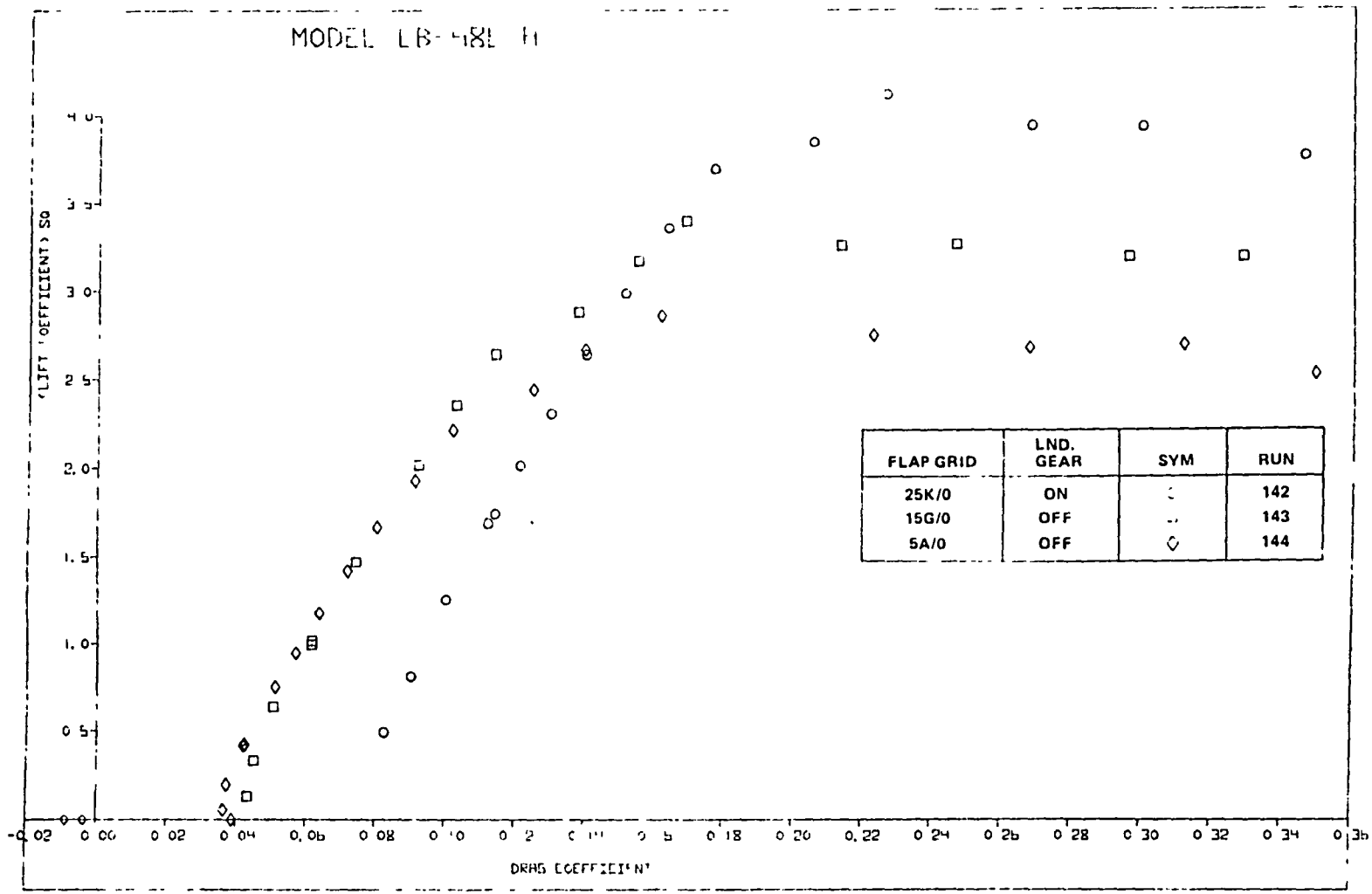

B DRAG

FIGURE 147. EFFECT OF SINGLE-SLOT FLAP DEFLECTION ON AERODYNAMIC CHARACTERISTICS WITH THE LEADING EDGE DEVICES REMOVED (CONCLUDED)

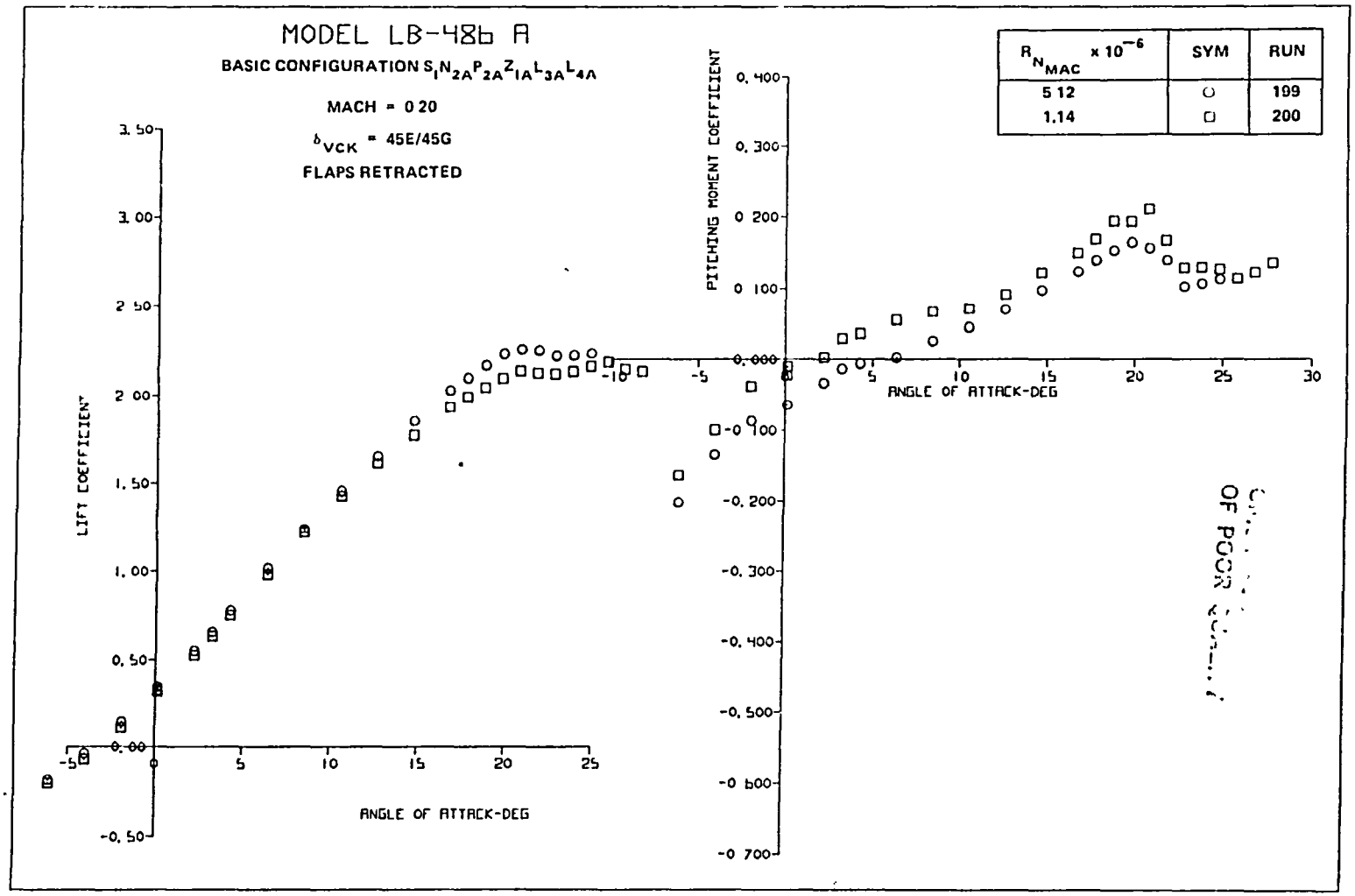

A. LIFT AND PITCHING MOMENT

FIGURE 148. EFFECT OF REYNOLDS NUMBER ON AERODYNAMIC CHARACTERISTICS OF THE FLAPS RETRACTED/VCK EXTENDED CONFIGURATION

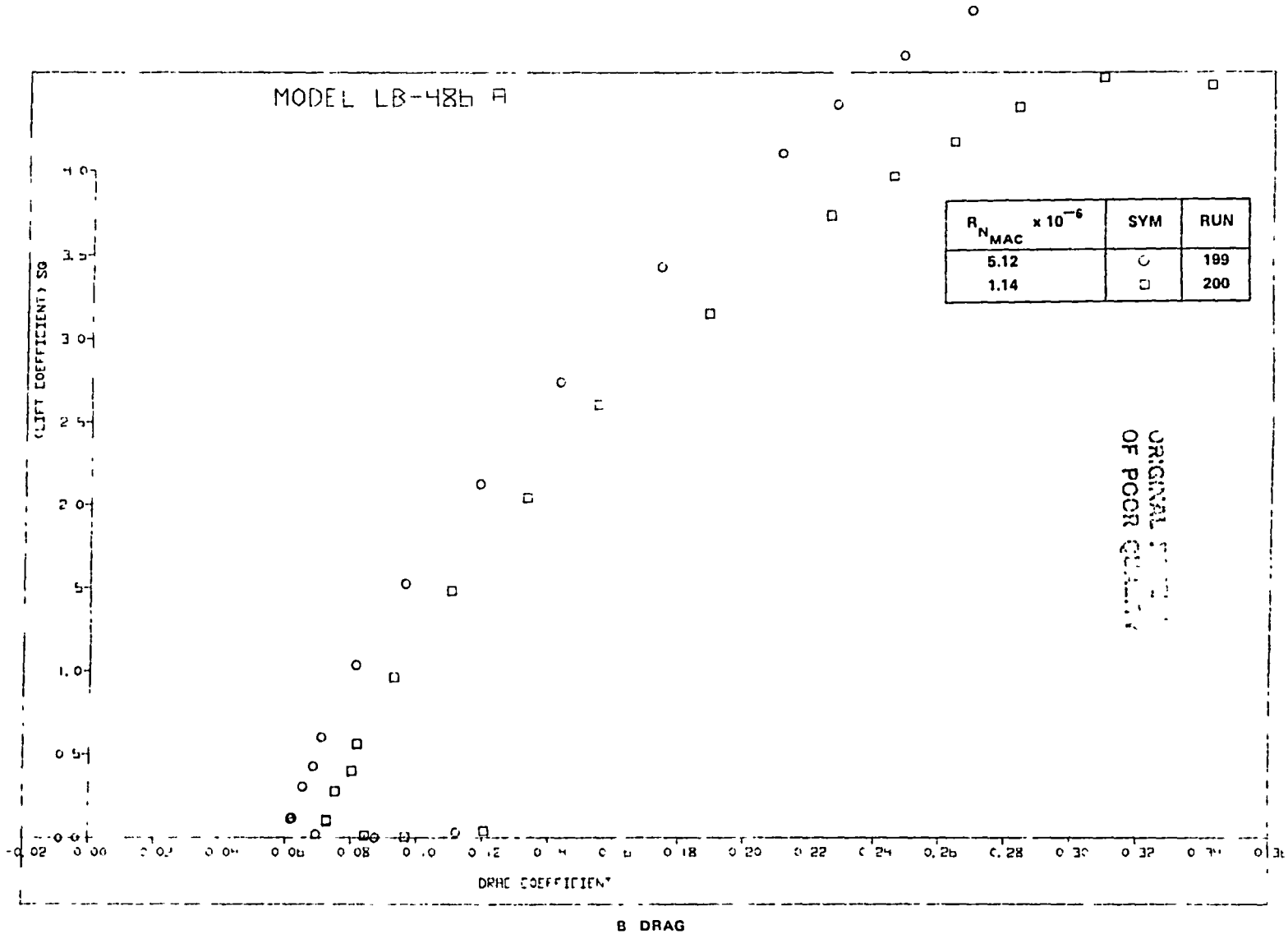

FIGURE 148. EFFECT OF REYNOLDS NUMBER ON AERODYNAMIC CHARACTERISTICS OF THE FLAPS RETRACTED/VCK EXTENDED CONFIGURATION (CONTINUED)

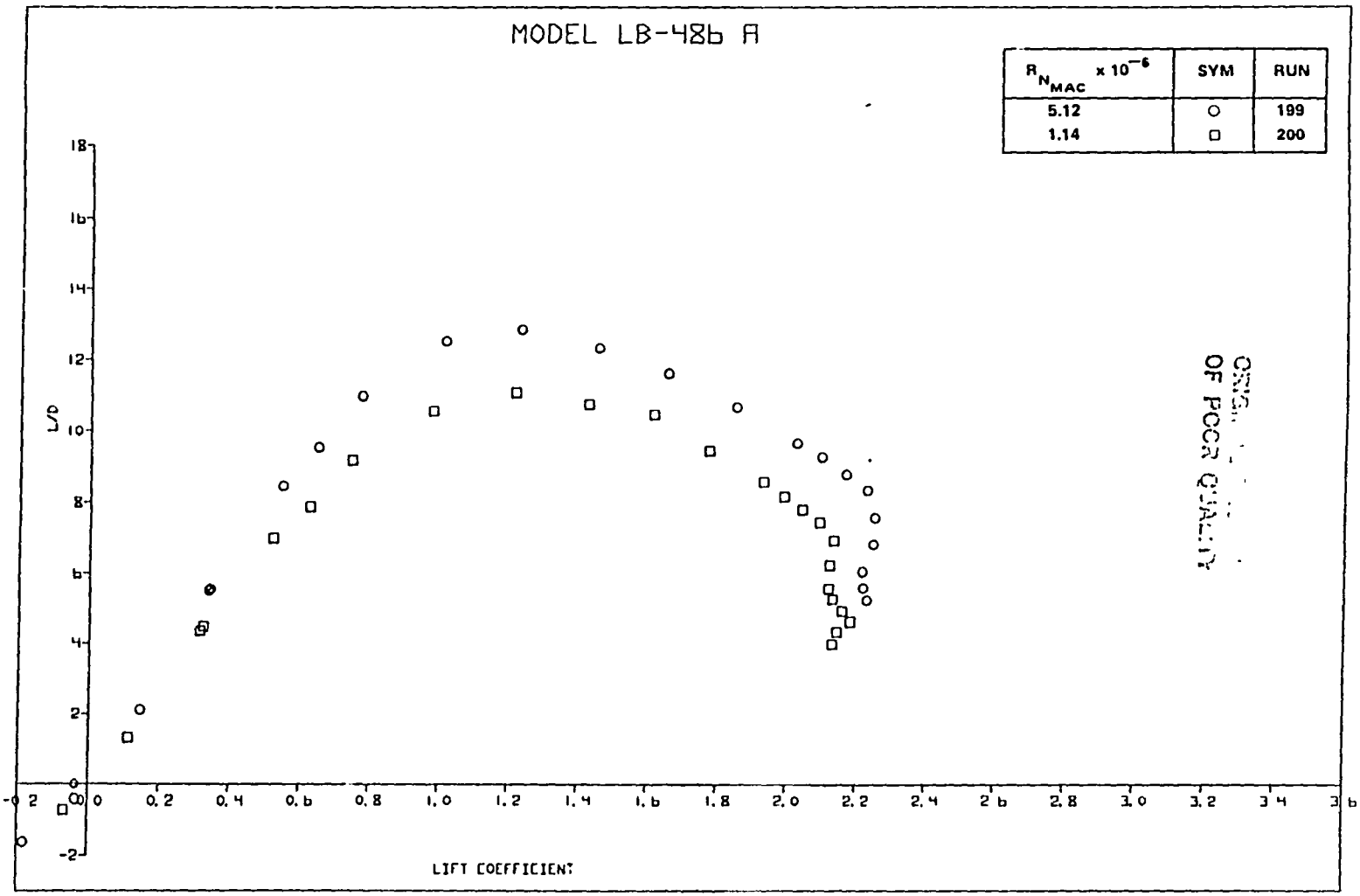

FIGURE 148. EFFECT OF REYNOLDS NUMBER ON AERODYNAMIC CHARACTERISTICS OF THE FLAPS RETRACTED/VCK EXTENDED CONFIGURATION (CONCLUDED)

ORIGINAL PAGE IS
OF POOR QUALITY

The basic trend of the pitching moment is similar for both Reynolds number. .tension of the VCK also reduced the L/D at 1.2 V_S to 11.0 (compared to 17.2 for the cruise wing configuration).

Figure 149 illustrates the slat with flaps retracted configuration. The effect of the horizontal tail on this configuration is shown in Figure 150. With the horizontal tail removed a $C_{L_{MAX}}$ of 2.30 was obtained, with an initial nose down pitching moment at $C_{L_{MAX}}$. The L/D at 1.2 V_S was 12.1 (a larger value than for the VCK extended configuration). Comparison of the cruise wing, flaps retracted, and takeoff and landing flap L/D characteristics, indicate improved takeoff performance may be possible by an alternate slat position. The L/D performance should be increased by means of a sealed slat configuration of reduced slat deflection, and this configuration is recommended for future experimental evaluation. Figure 150 also indicates, for the horizontal tail-on configuration, a reduction in stability prior, to stall, followed by nose-down pitching moment after

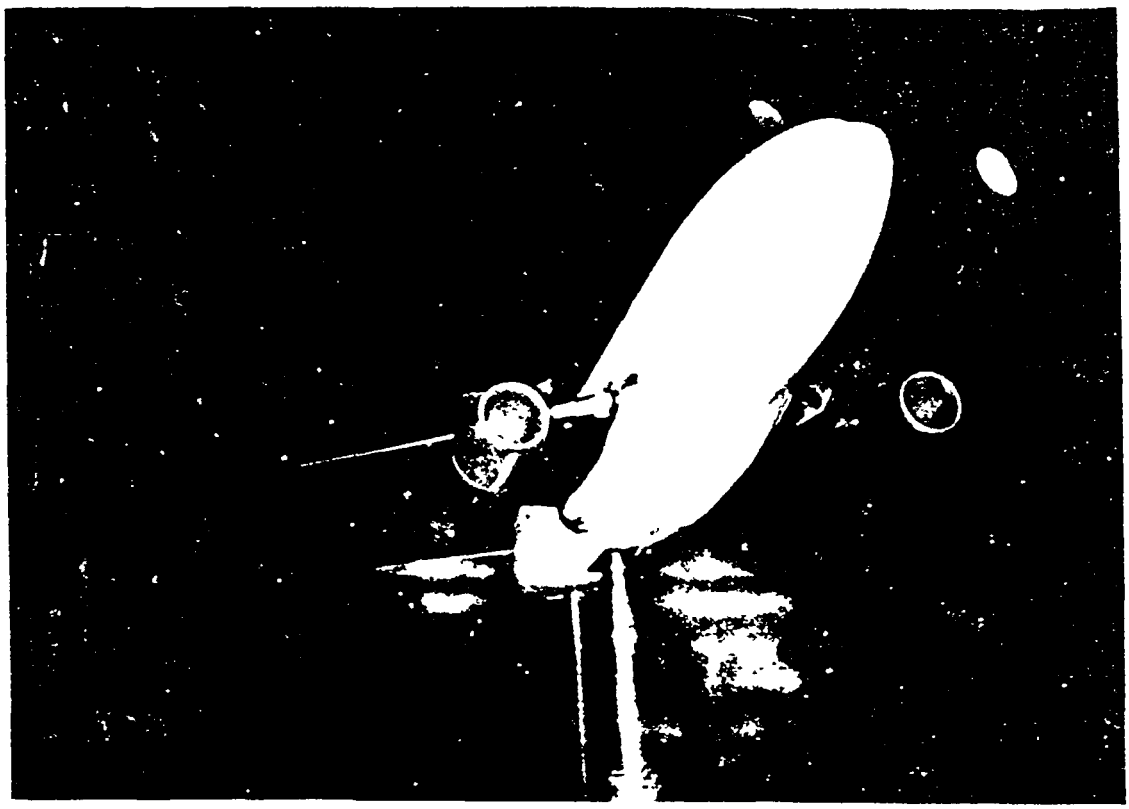

FIGURE 149. SLAT WITH RETRACTED FLAP CONFIGURATION

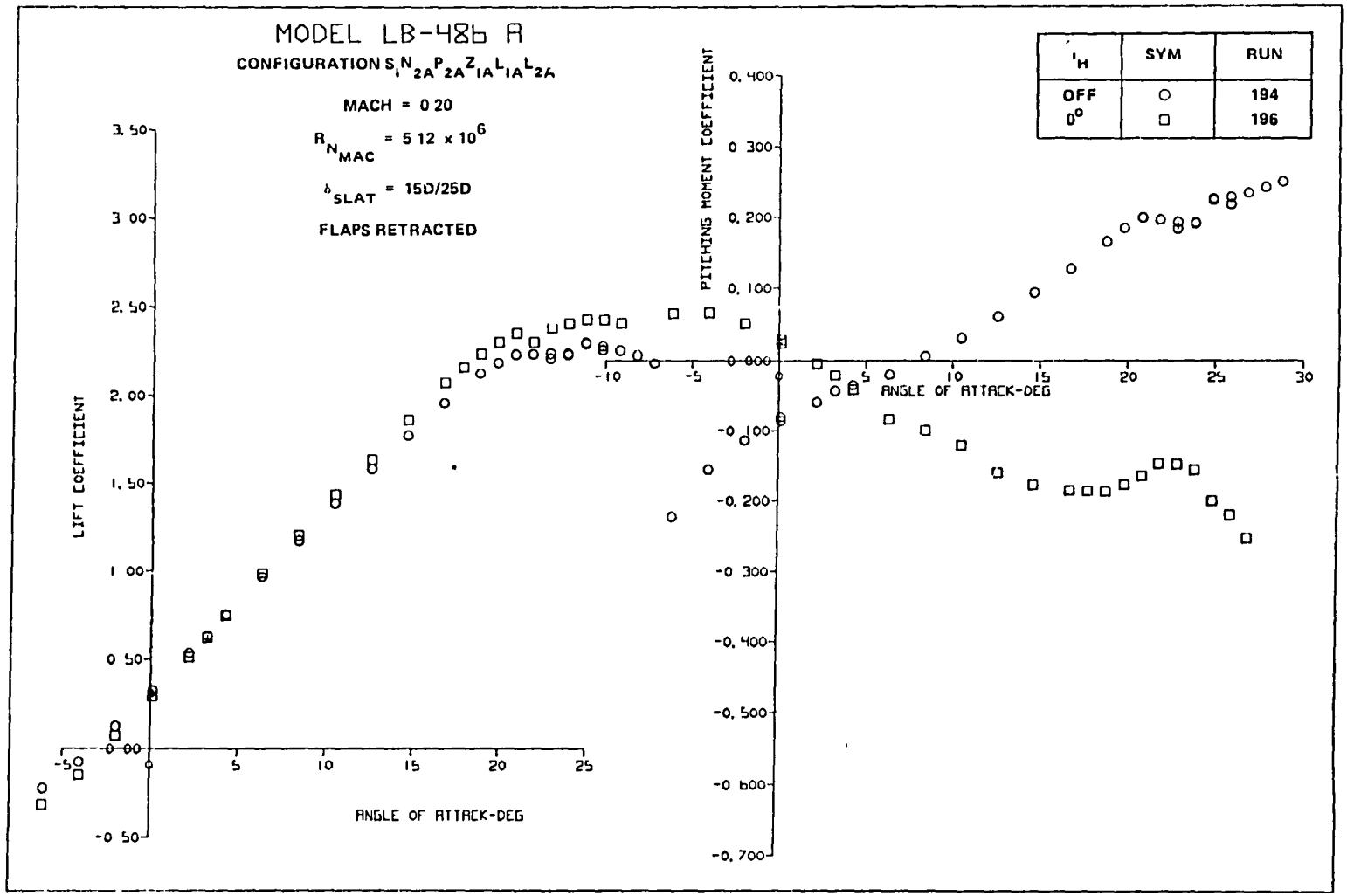

A. LIFT AND PITCHING MOMENT

FIGURE 150. EFFECT OF HORIZONTAL TAIL ON AERODYNAMIC CHARACTERISTICS OF THE FLAPS RETRACTED/SLAT EXTENDED CONFIGURATION

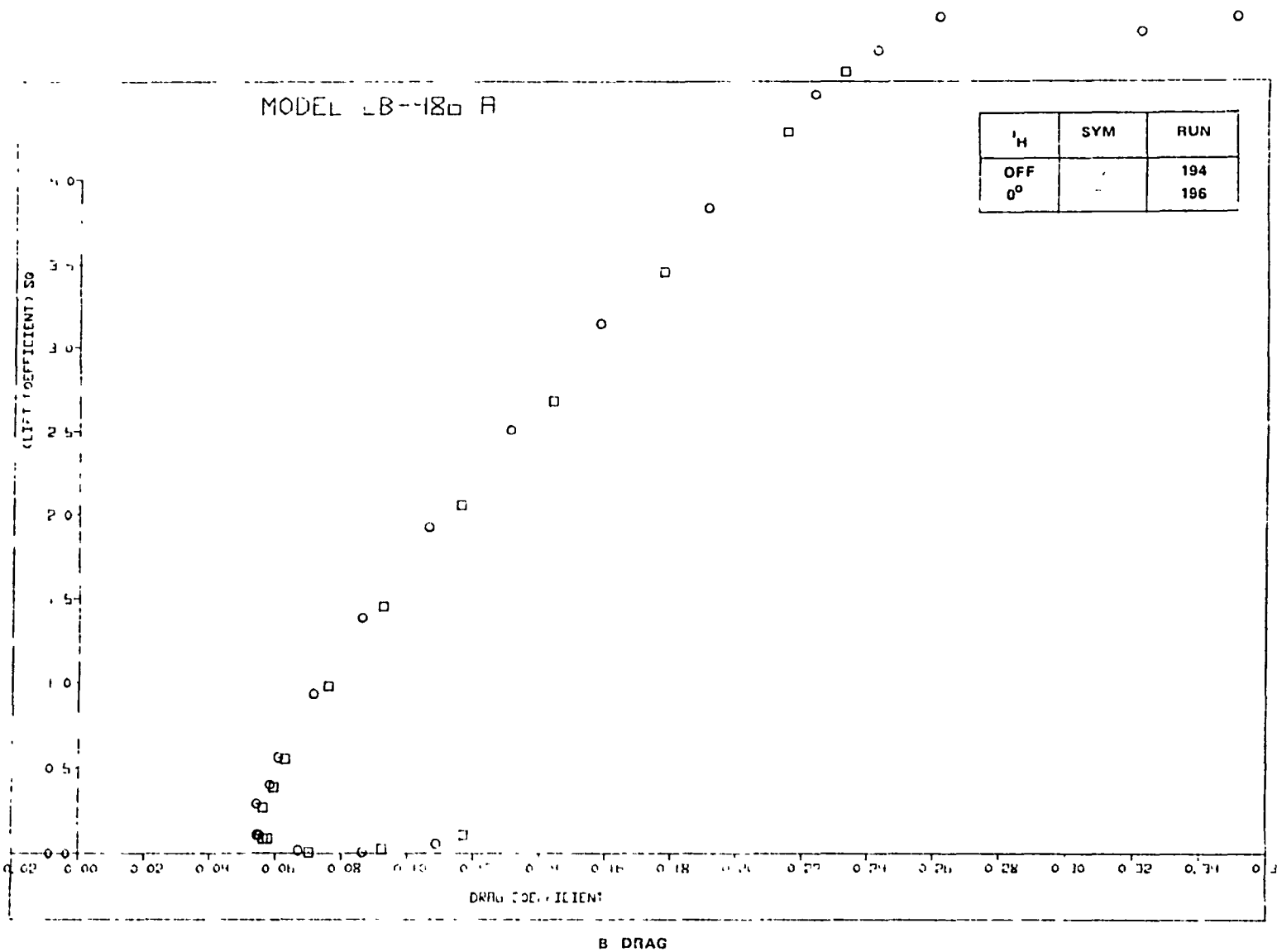

ORIGINAL PAGE IS
OF POOR QUALITY

FIGURE 150. EFFECT OF HORIZONTAL TAIL ON AERODYNAMIC CHARACTERISTICS OF THE FLAPS RETRACTED/SLAT EXTENDED CONFIGURATION (CONCLUDED)

$C_{L_{MAX}}$. Figure 151 shows the effect of a modified trim position for the inboard slat. The modified trim position was 2.54 cm (1.0 in) farther outboard than the basic slat trim near the fuselage. A small change in $C_{L_{MAX}}$ ($\Delta C_{L_{MAX}} = 0.027$), an increase in the angle of attack for $C_{L_{MAX}}$, and a small reduction in L/D at 1.2 V_S, is indicated in Figure 151. A substantial favorable change in the pitching moment characteristics is shown in Figure 151 for the high angles of attack. This revised trim position is also suggested for future testing with the deflected flap configurations.

Aileron and Spoiler Studies

Aileron effectiveness is presented for the cruise, takeoff, and landing configurations in Figures 152, 153, and 154, respectively. At pre-stall angles of attack, the aileron effectiveness is well-behaved for the cruise and landing configurations. The takeoff configuration data exhibit similar trends for most of the angle of attack range tested, but near the stall the effectiveness of the downgoing aileron is diminished.

The shape of the rolling moment curve with aileron deflection indicates for all flap settings that the negative deflections (TEU) are more effective than the positive (TED). In some cases, the incremental rolling moment obtained for negative aileron deflections was twice as large as the corresponding value for positive aileron deflection. These data were obtained in the NASA Ames 12-Foot Pressure Wind Tunnel at high Reynolds number conditions.

Spoiler effectiveness for the cruise, takeoff, and landing configurations is presented in Figures 155, 156, and 157, respectively. The spoiler data were obtained in the NASA Langley V/STOL Wind Tunnel at an atmospheric Reynolds number. The data indicate well-behaved characteristics for the three configurations with increasing effectiveness being shown for increased flap deflections. The spoiler arrangement consists of large chord panels compatible with space available aft of the rear spar and spoiler span corresponding to the flap span. This powerful spoiler configuration is needed because of the reduced roll rate capability associated with high-aspect-ratio wings.

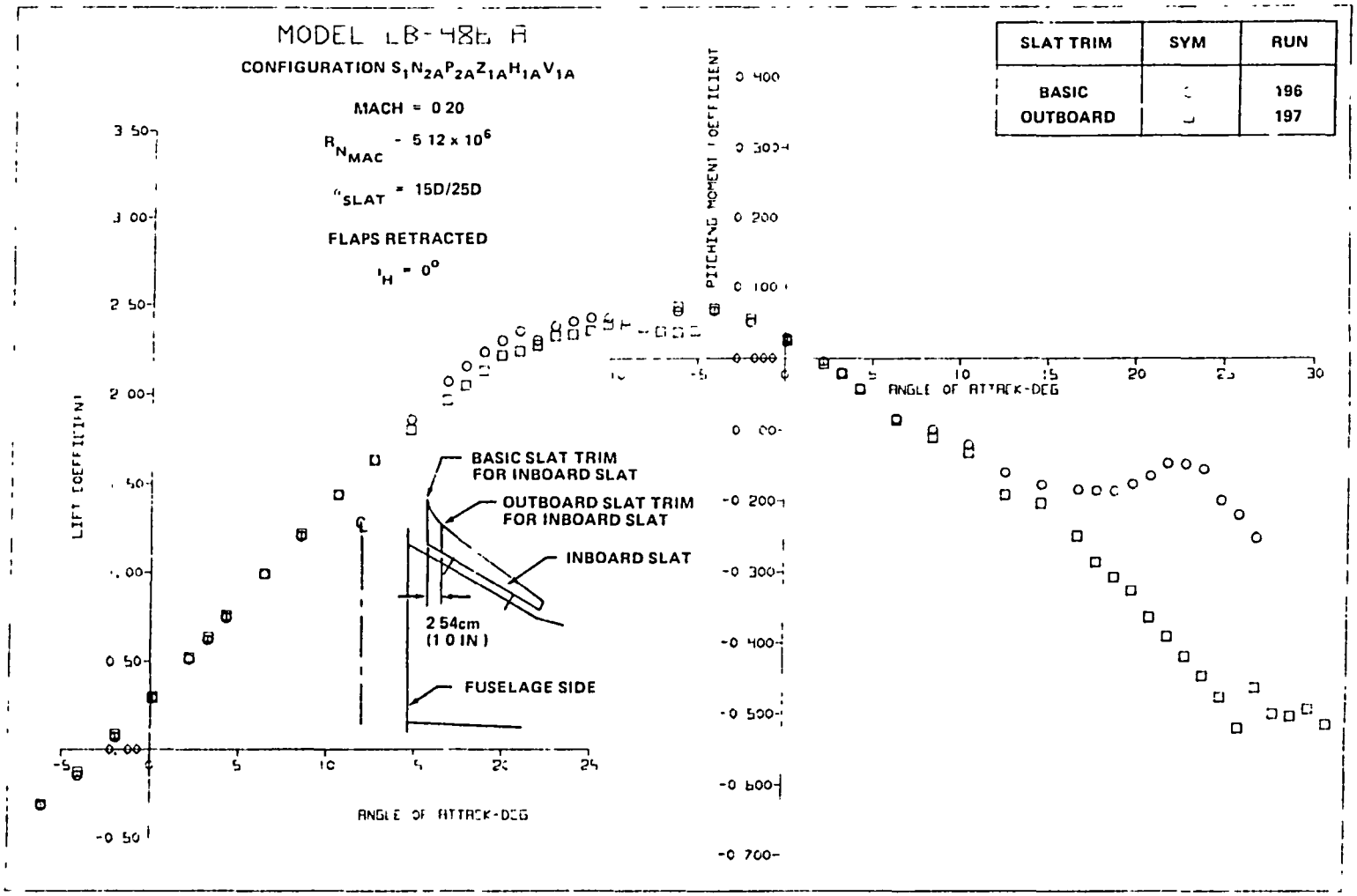

A LIFT AND PITCHING MOMENT

FIGURE 151 EFFECT OF INBOARD SLAT TRIM POSITION ON AERODYNAMIC CHARACTERISTICS OF THE FLAPS RETRACTED/SLAT EXTENDED CONFIGURATION (HORIZONTAL TAIL ON)

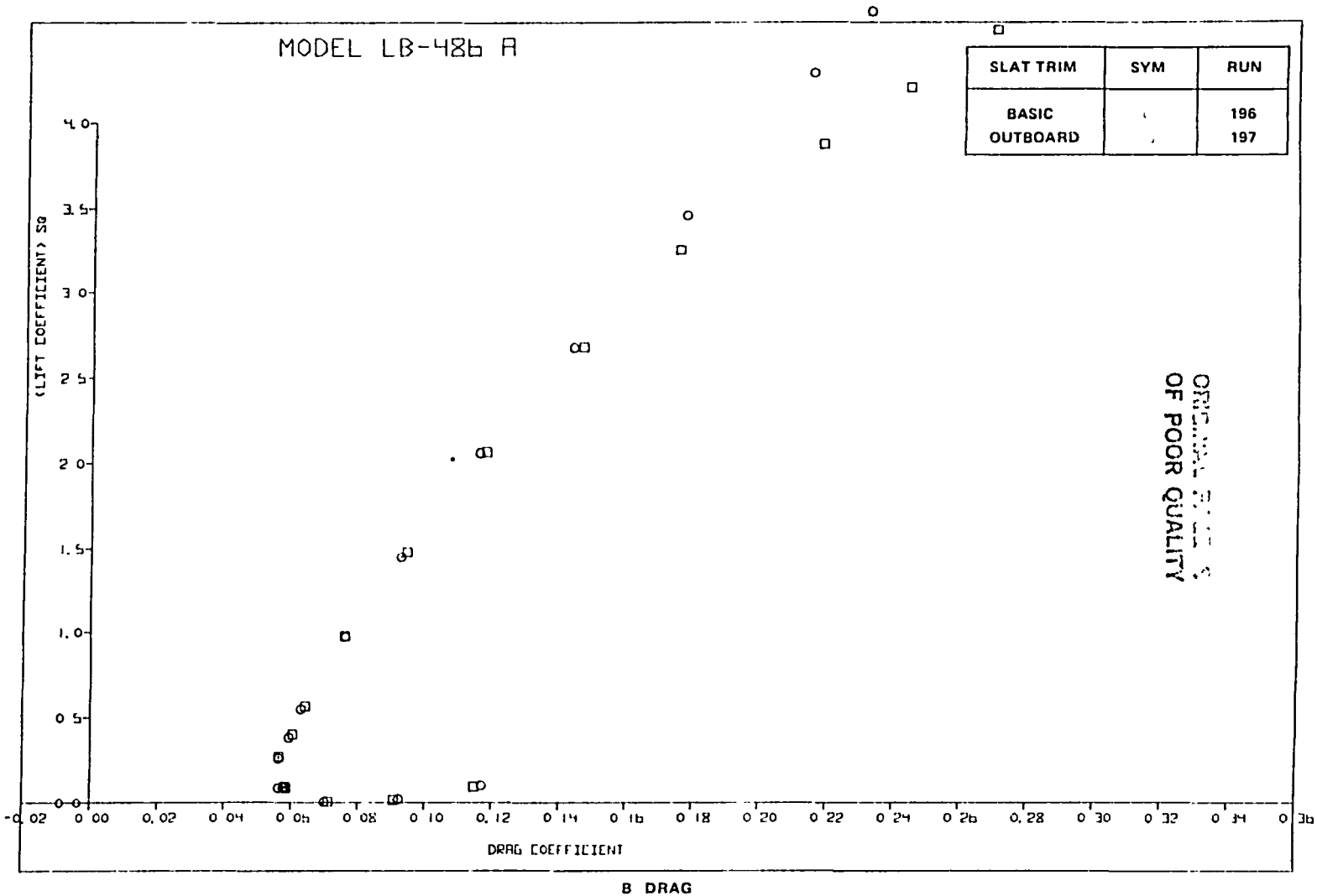

ORIGINAL PAGE IS
OF POOR QUALITY

FIGURE 151. EFFECT OF INBOARD SLAT TRIM POSITION ON AERODYNAMIC CHARACTERISTICS OF THE FLAPS RETRACTED/SLAT EXTENDED CONFIGURATION (HORIZONTAL TAIL-ON) (CONCLUDED)

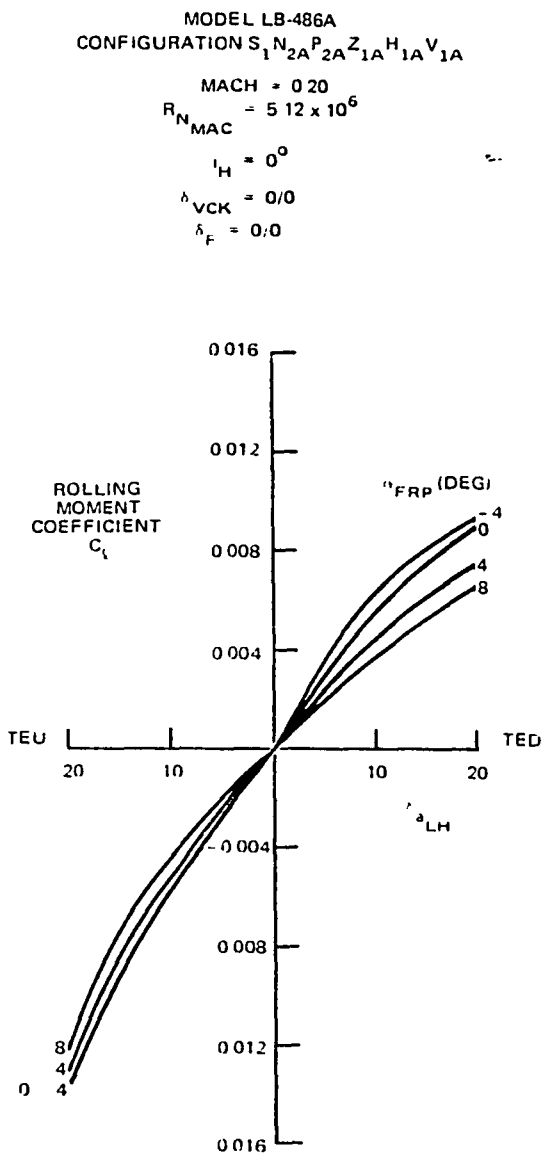

FIGURE 152. ROLLING MOMENT COEFFICIENT DUE TO AILERON DEFLECTION FOR CRUISE WING

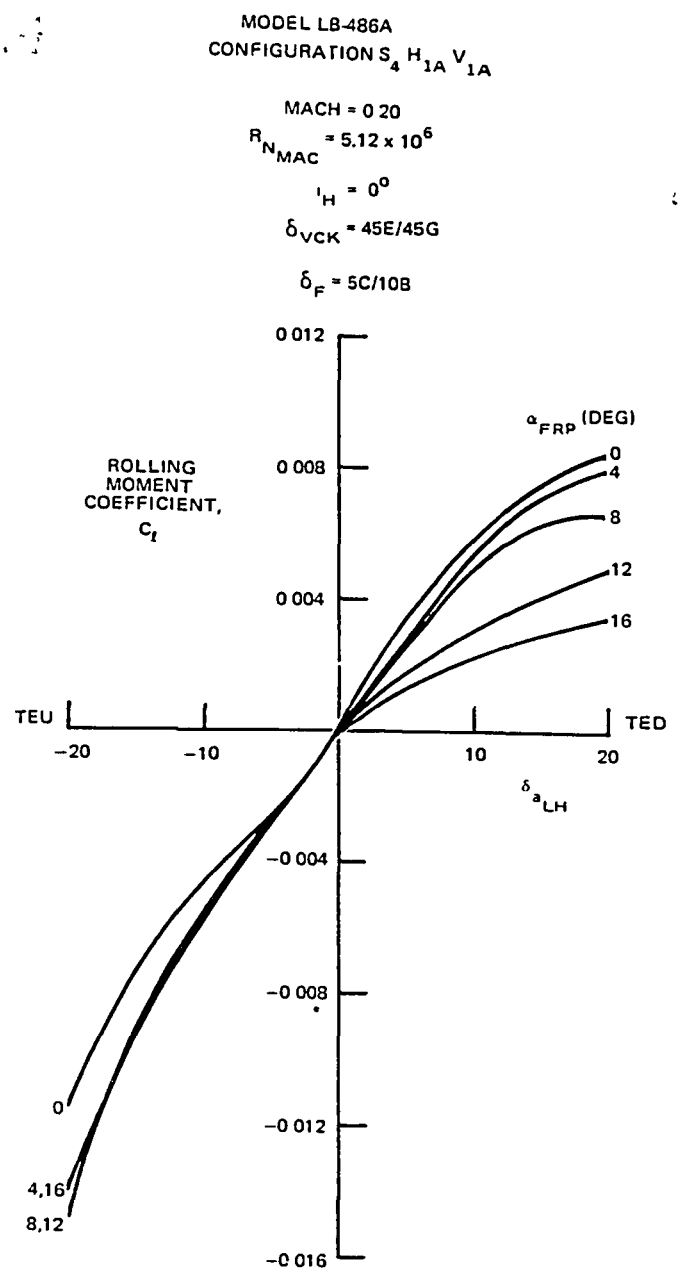

FIGURE 153. ROLLING MOMENT COEFFICIENT DUE TO AILERON DEFLECTION FOR VCK WITH TWO-SEGMENT TAKEOFF FLAPS

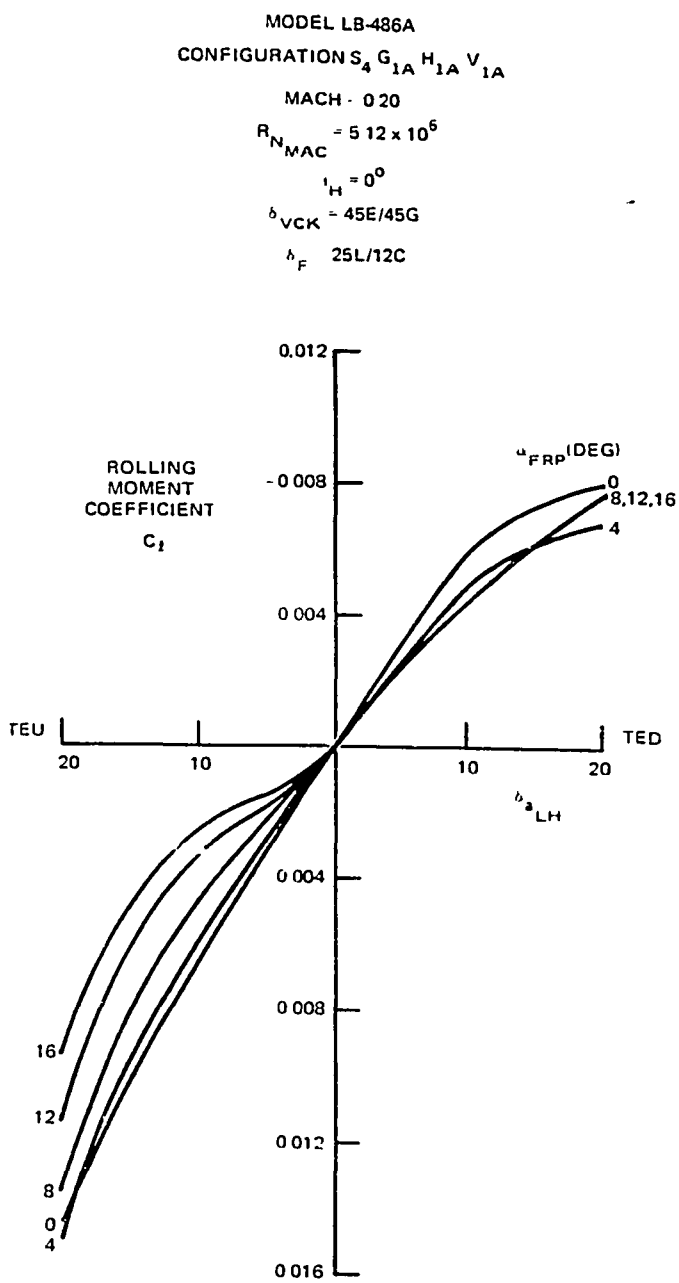

FIGURE 154. ROLLING MOMENT COEFFICIENT DUE TO AILERON DEFLECTION FOR VCK WITH TWO-SEGMENT LANDING FLAPS

ORIGINAL PAGE IS
OF POOR QUALITY

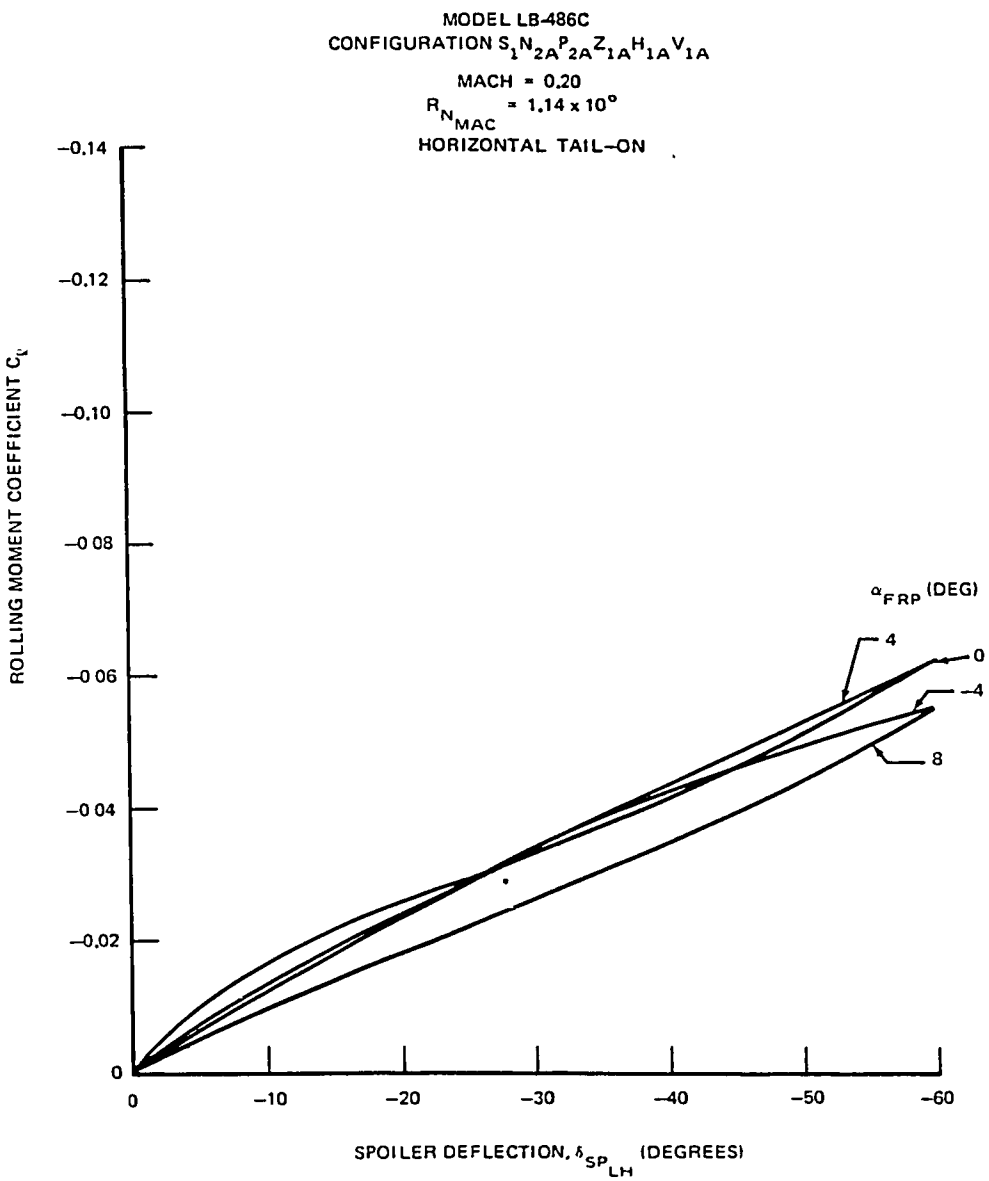

FIGURE 155. ROLLING MOMENT COEFFICIENT DUE TO SPOILER DEFLECTION FOR CRUISE WING

ORIGINAL PAGE IS
OF POOR QUALITY

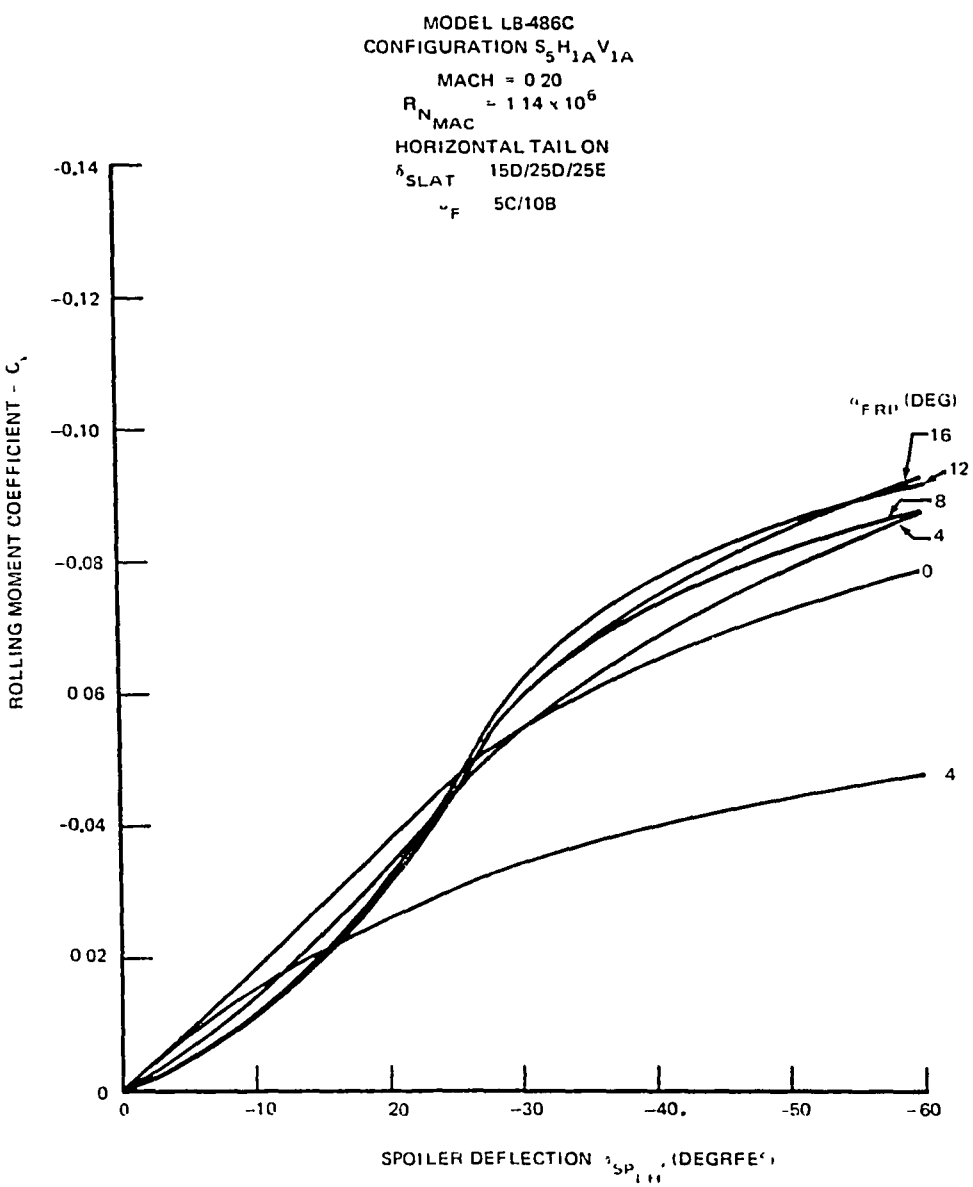

FIGURE 156. ROLLING MOMENT COEFFICIENT DUE TO SPOILER DEFLECTION FOR SLAT WITH TWO-SEGMENT TAKEOFF FLAPS

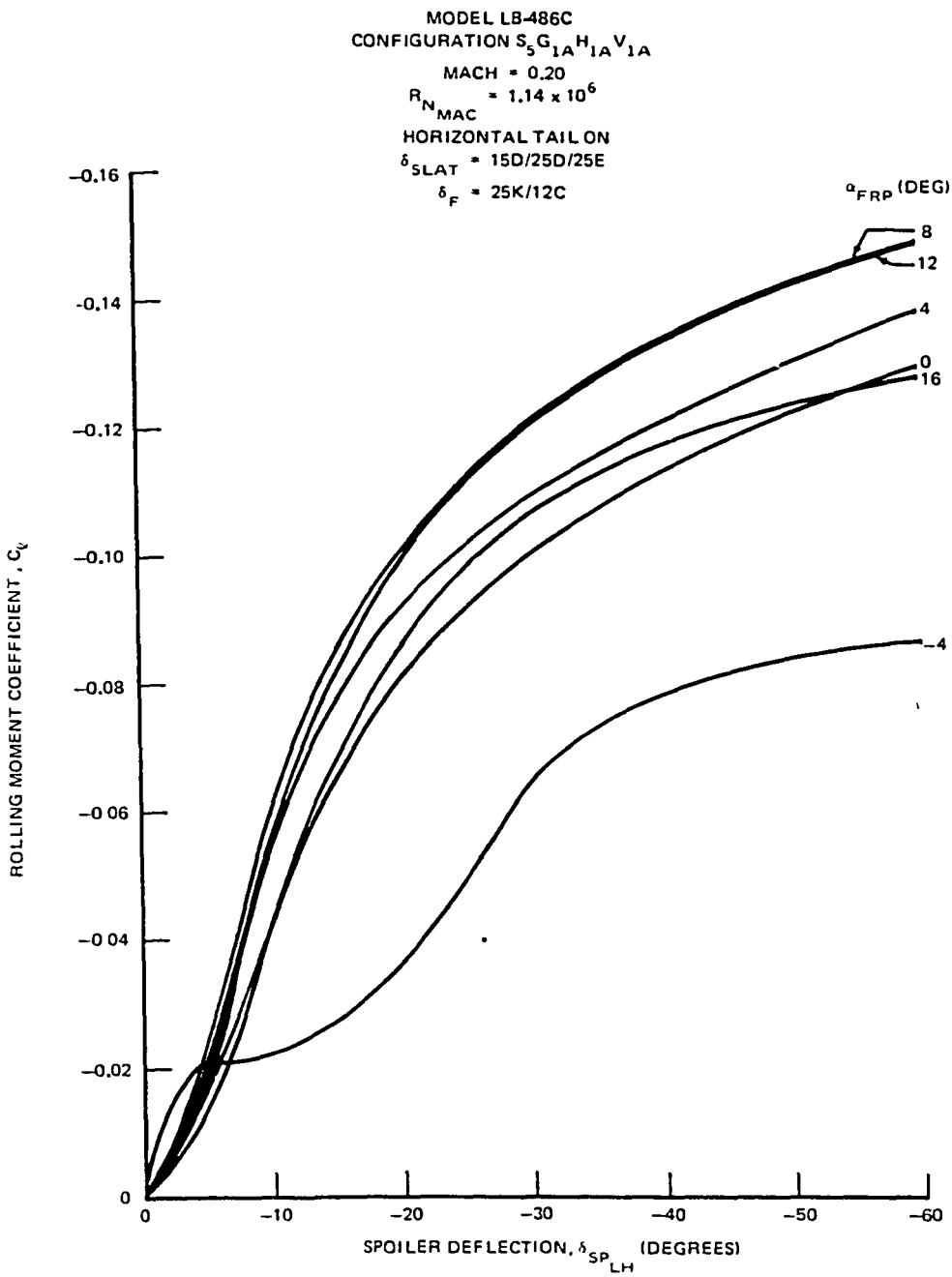

FIGURE 157. ROLLING MOMENT COEFFICIENT DUE TO SPOILER DEFLECTION FOR SLAT WITH TWO-SEGMENT LANDING FLAPS

The effect of symmetrical spoiler deflection for takeoff and landing flap deflection is shown in Figures 158 through 161. These results were obtained for out-of-ground-effect conditions. The large spoiler chord and spanwise extent is very effective in reducing the lift and increasing the drag for both flap deflections for a constant angle of attack (i.e., $\alpha_{FRP} = 0^{o}$). A significant positive pitching moment shift is also apparent for both the takeoff and landing configuration. While the reduction in lift and increase in drag would result in greater deceleration on the ground, the positive increment of pitching moment would tend to unload the nosewheel. The ground effect on pitching moment, lift, and drag, with the spoilers deflected should be obtained in a future test program.

Figure 160 indicates a reduction in C_{I} of 1.18 due to 30 degrees of spoiler deflection, and 1.56 for 60 degrees of spoiler deflection for the landing flap setting. Figure 161 shows an increase in drag of 0.135 is attained for the 60 degrees spoiler deflection at the landing flap deflection. A similar magnitude 0.143 is obtained with 30 degrees spoiler deflection with takeoff flap deflection (for aborted takeoff).

Landing Gear Studies

The effect of the landing gear on drag and $C_{L_{MAX}}$ is shown in Figure 162. The drag increment is reduced slightly with increasing C_{I} values. The increment in drag is very similar for the takeoff and landing flap deflections. The effect of the landing gear on $C_{L_{MAX}}$ for takeoff flap deflection is negligible (-0.002) and -0.076 for the landing flap deflections.

Data Summary & Comparisons of Leading & Trailing Edge High Lift Concepts

Figures 163 through 171 present the final tail-off lift, pitching moment and drag characteristics for the VCK and slat with two-segment flap configuration, and the VCK and slat with single-slot flap configuration. The data are for the nominal high Reynolds number condition and have been corrected for wall and strut effects.

Figure 171 presents a comparison of the wind tunnel tail-off $C_{L_{MAX}}$ between the current and DC-10 configurations. The current configuration high lift system was the VCK and two-segment flaps, and the DC-10 system was a slat

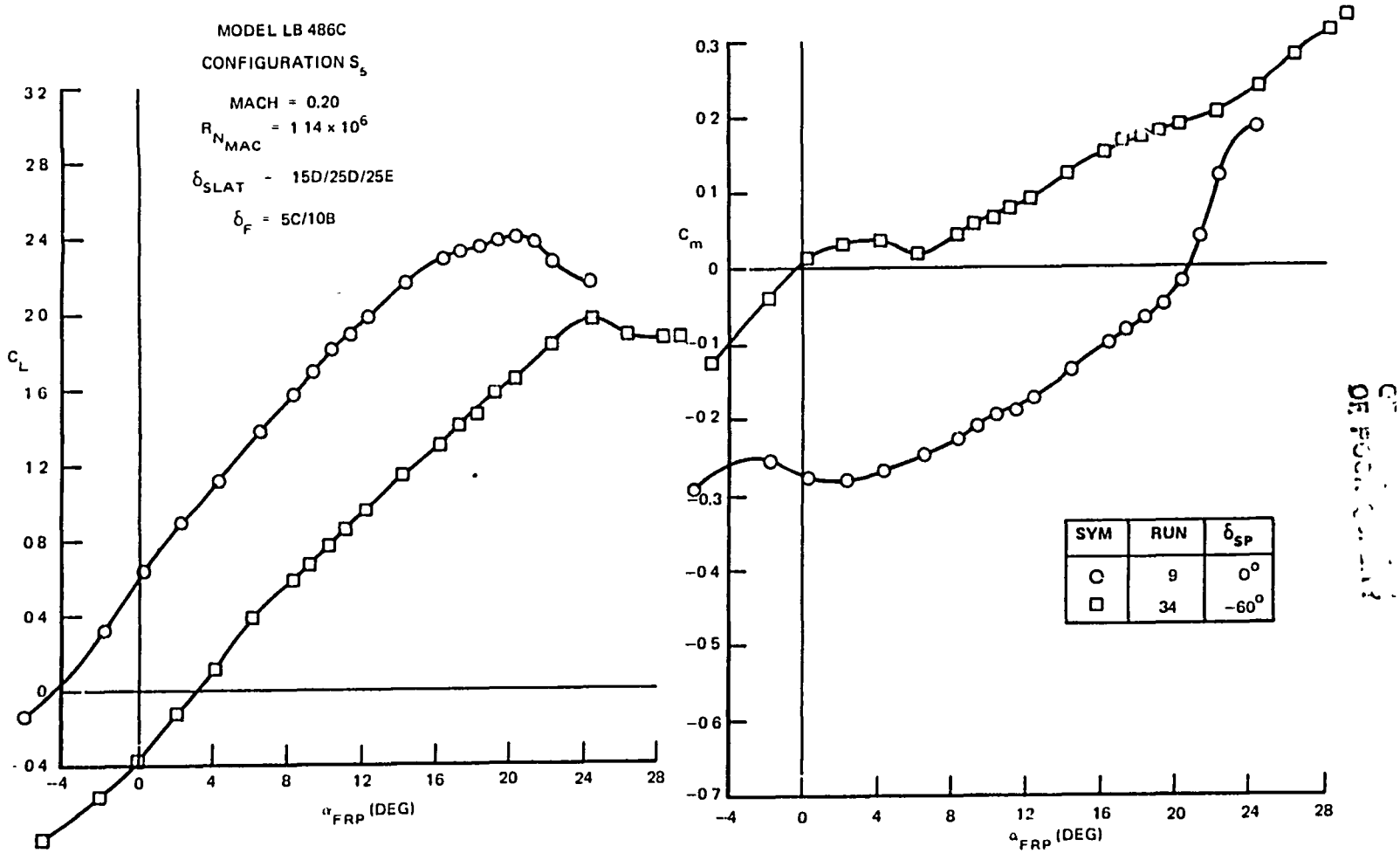

A. LIFT AND PITCHING MOMENT

FIGURE 158. EFFECT OF SYMMETRICAL SPOILER DEFLECTION ON AERODYNAMIC CHARACTERISTICS OF THE SLAT WITH TWO-SEGMENT TAKEOFF FLAPS CONFIGURATION

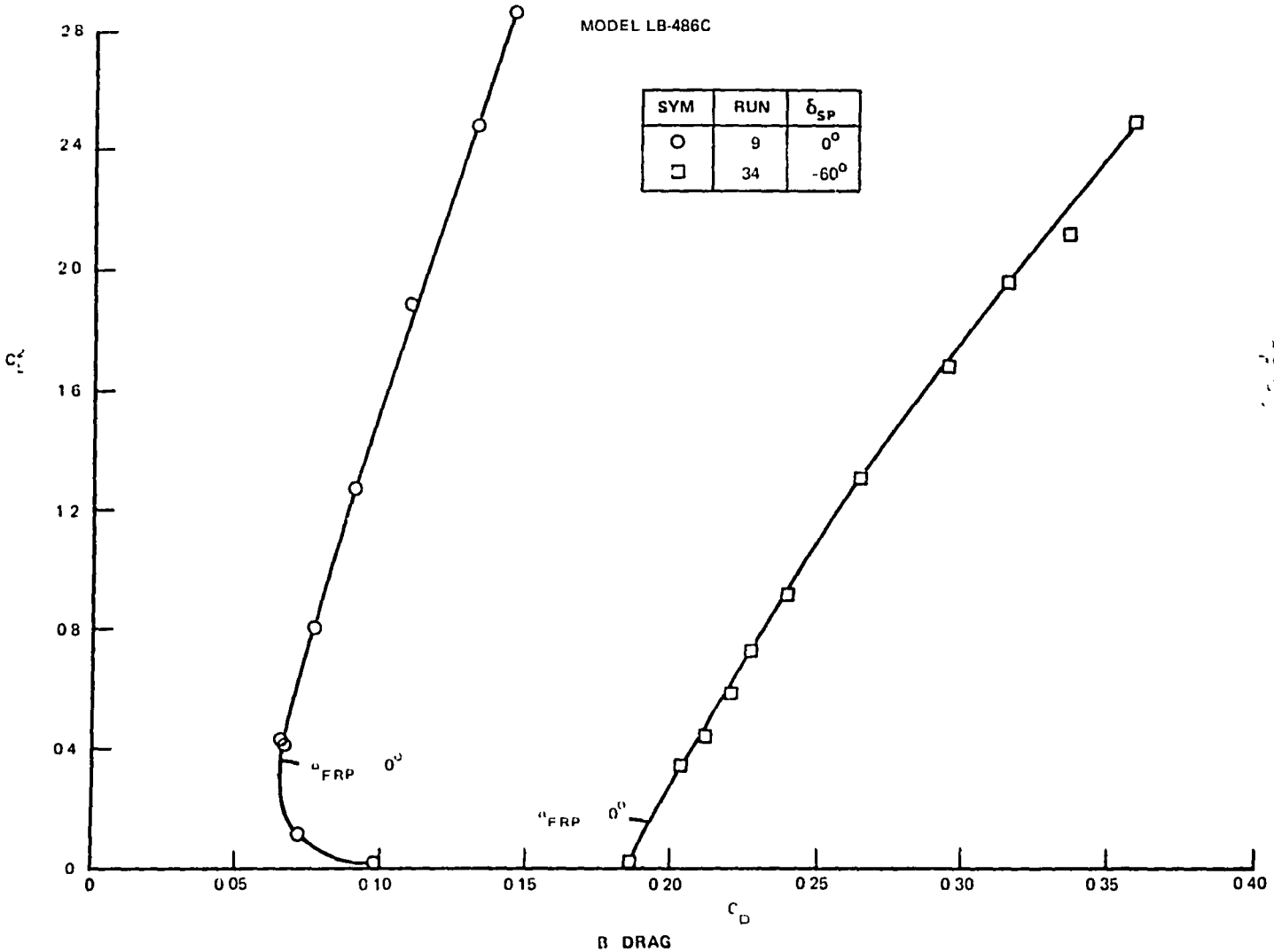

FIGURE 158. EFFECT OF SYMMETRICAL SPOILER DEFLECTION ON AERODYNAMIC CHARACTERISTICS OF THE SLAT WITH TWO SEGMENT TAKEOFF FLAPS CONFIGURATION (CONCLUDED)

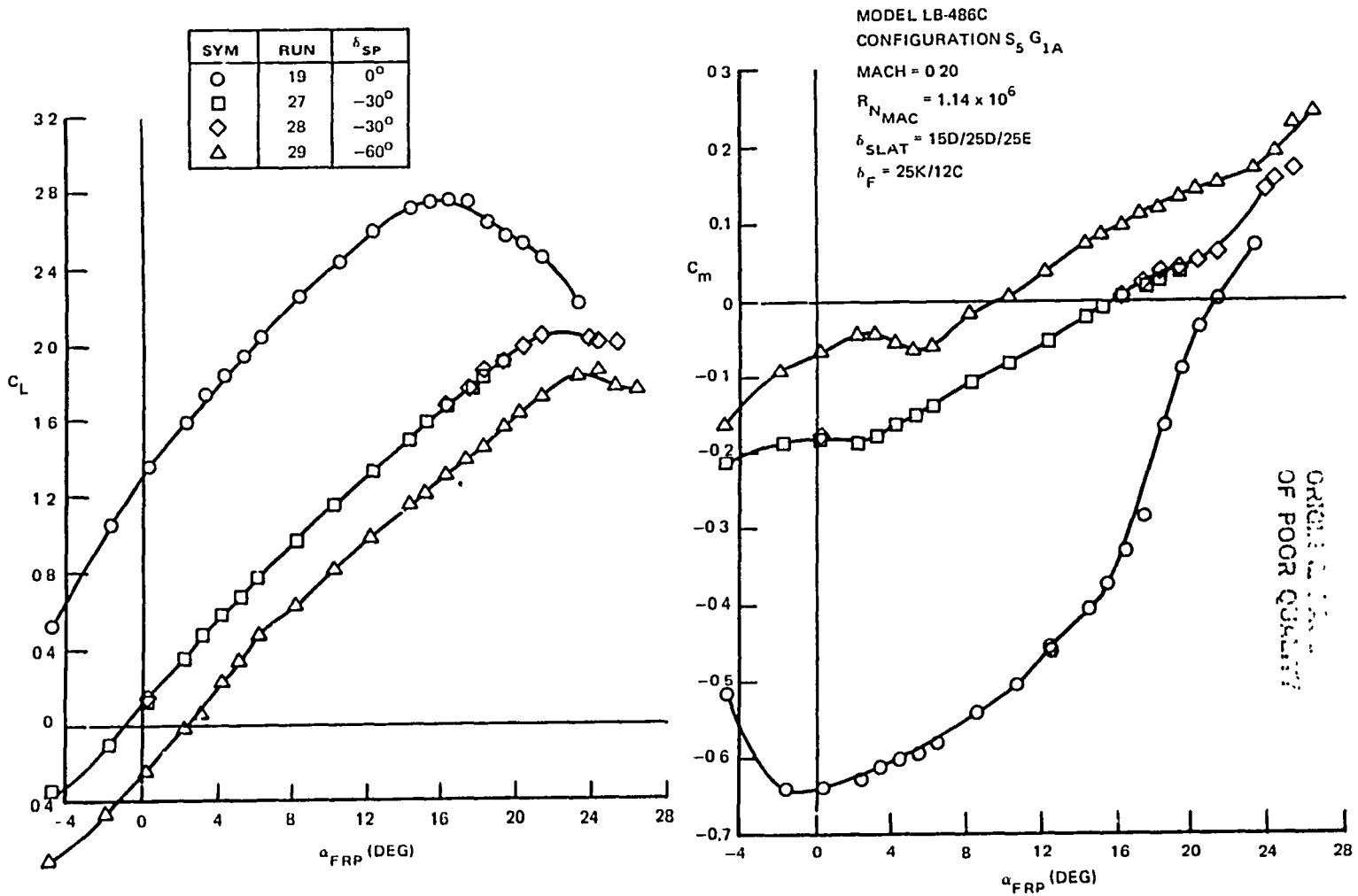

A. LIFT AND PITCHING MOMENT

FIGURE 159. EFFECT OF SYMMETRICAL SPOILER DEFLECTION ON AERODYNAMIC CHARACTERISTICS OF SLAT WITH TWO SEGMENT LANDING FLAPS CONFIGURATION

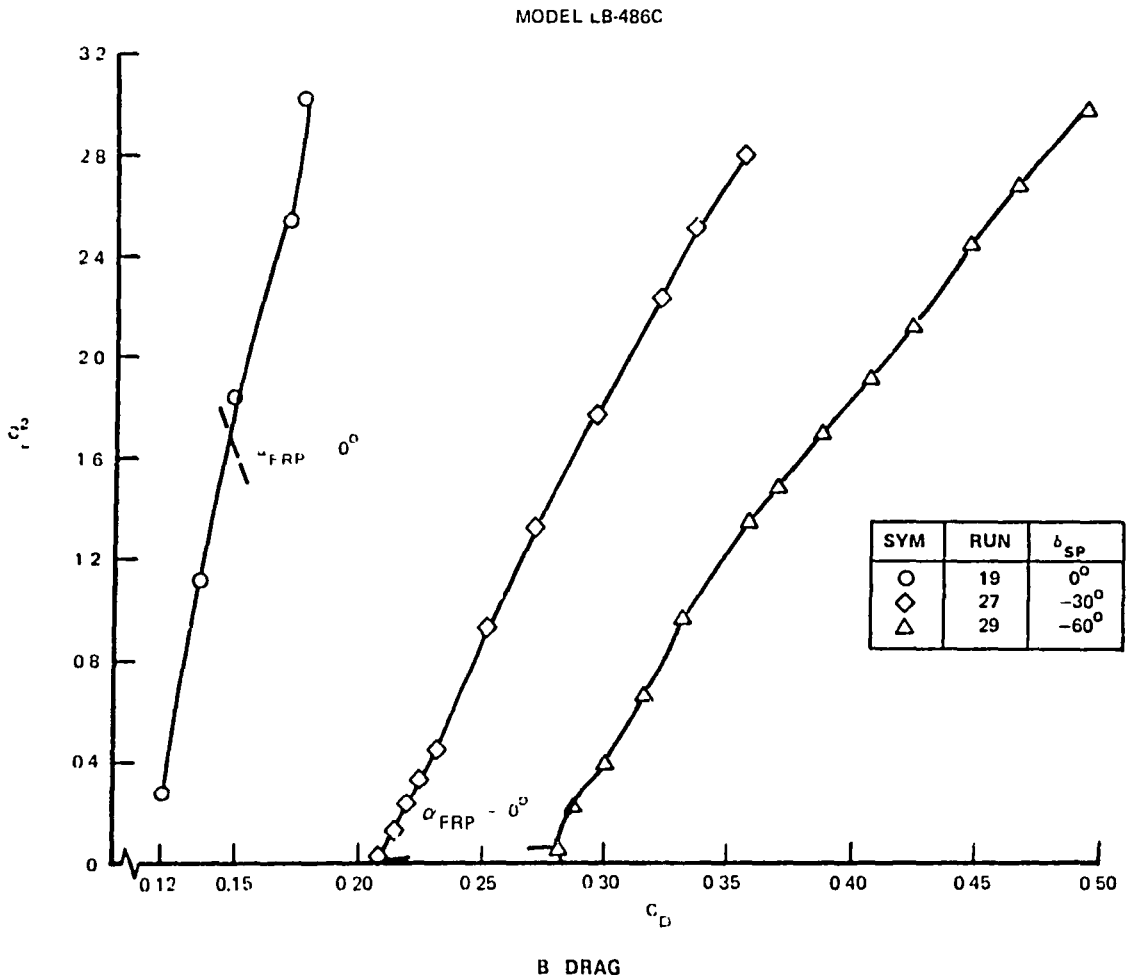

B DRAG

FIGURE 159 EFFECT OF SYMMETRICAL SPOILER DEFLECTION ON AERODYNAMIC CHARACTERISTICS SLAT WITH TWO SEGMENT LANDING FLAPS CONFIGURATION (CONCLUDED)

ORIG...
OF POOR ...

MODEL LB-486C
BASIC CONFIGURATION S_5
MACH = 0 20
$R_{N_{MAC}} = 1.14 \times 10^6$

δ_{SLAT} = 15D/25D/25E

SYM	δ_F	LND. GEAR
O	25K/12C	ON
□	5C/10B	OFF

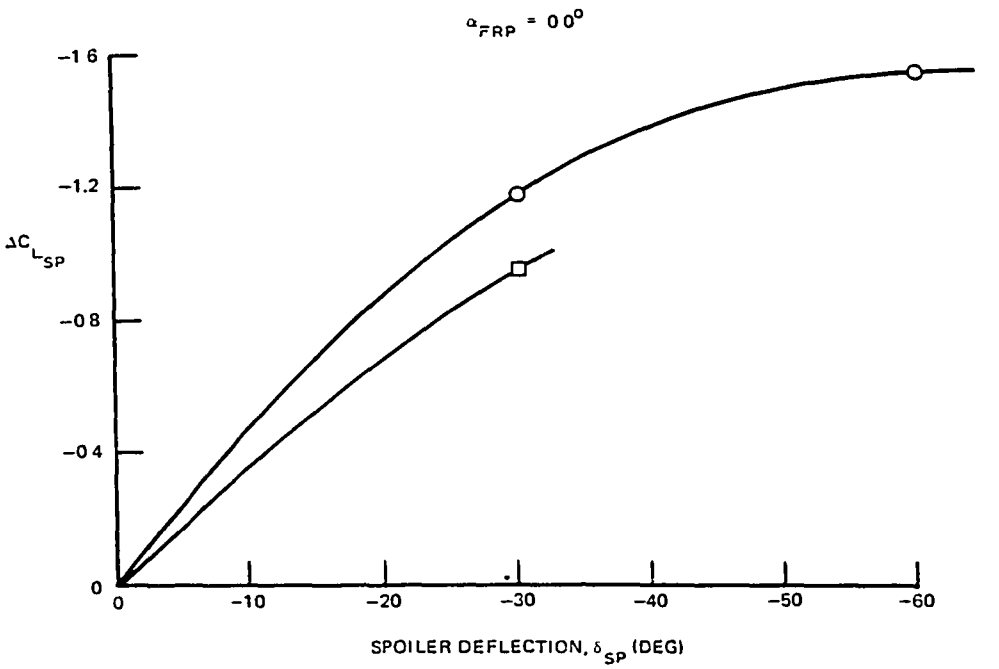

FIGURE 160. LIFT INCREMENT DUE TO SYMMETRICAL SPOILER DEFLECTION FOR SLAT WITH TWO-SEGMENT FLAP CONFIGURATION

MODEL LB-486C
BASIC CONFIGURATION S_5

MACH = 0.20

$R_{N_{MAC}} = 1.14 \times 10^6$

δ_{SLAT} = 15D/25D/25E

SYM	δ_F	LND. GEAR
○	25K/12C	ON
□	5C/10B	OFF

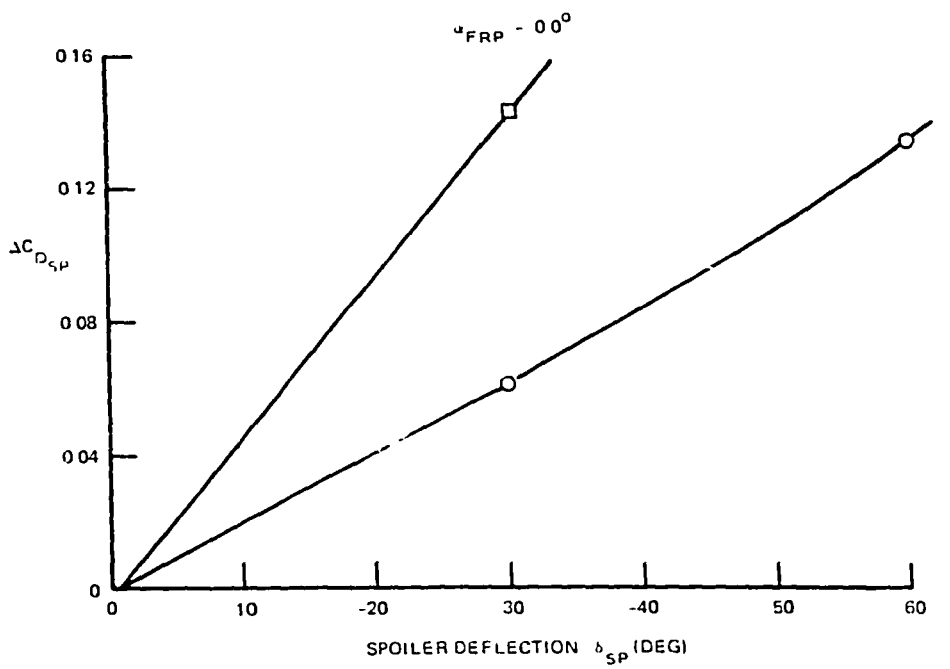

FIGURE 161. DRAG INCREMENT DUE TO SYMMETRICAL SPOILER DEFLECTION FOR SLAT WITH TWO-SEGMENT FLAP CONFIGURATION

ORIGINAL ...
OF POOR QU...

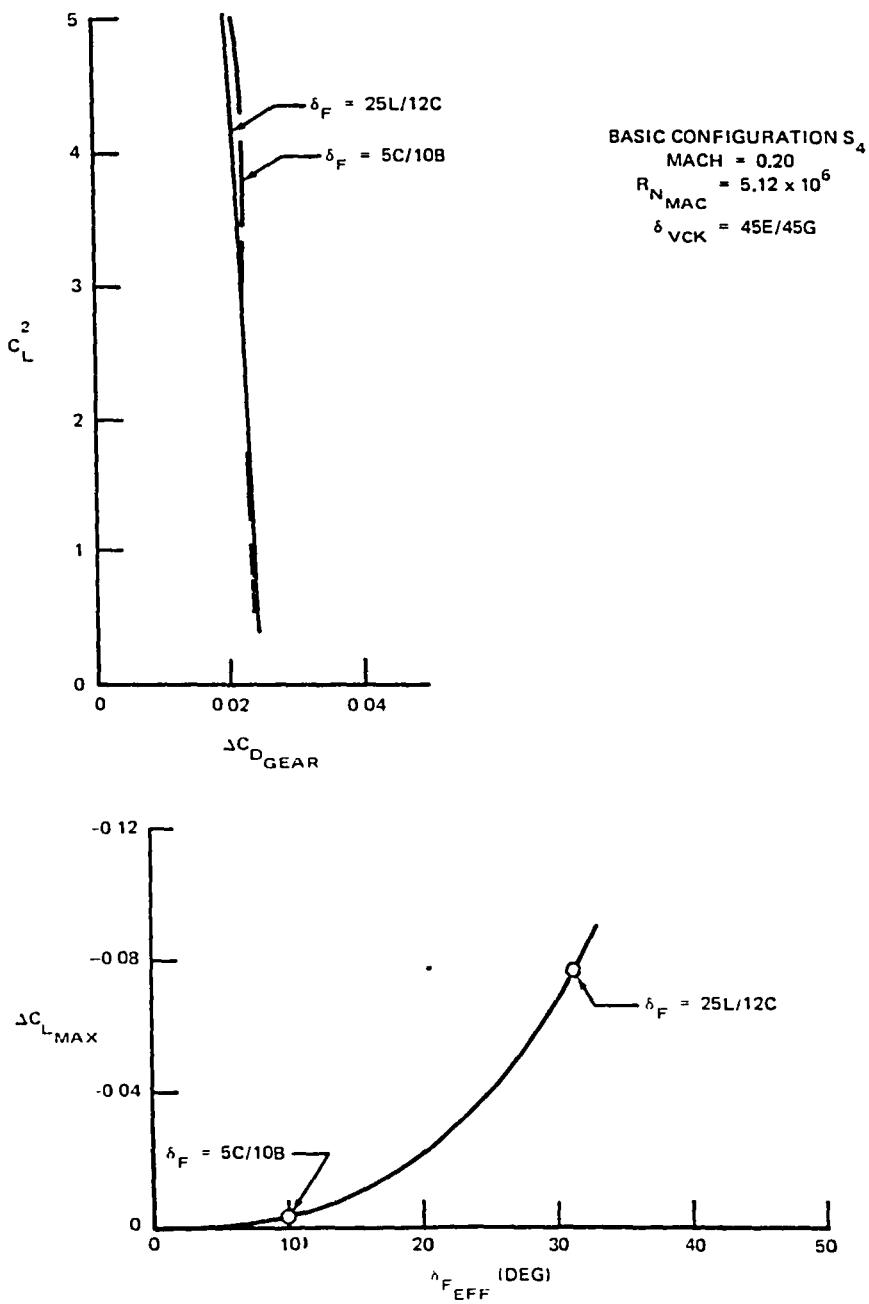

FIGURE 162. EFFECT OF LANDING GEAR ON DRAG AND $C_{L_{MAX}}$ FOR VCK WITH TWO-SEGMENT TAKEOFF AND LANDING FLAPS CONFIGURATIONS

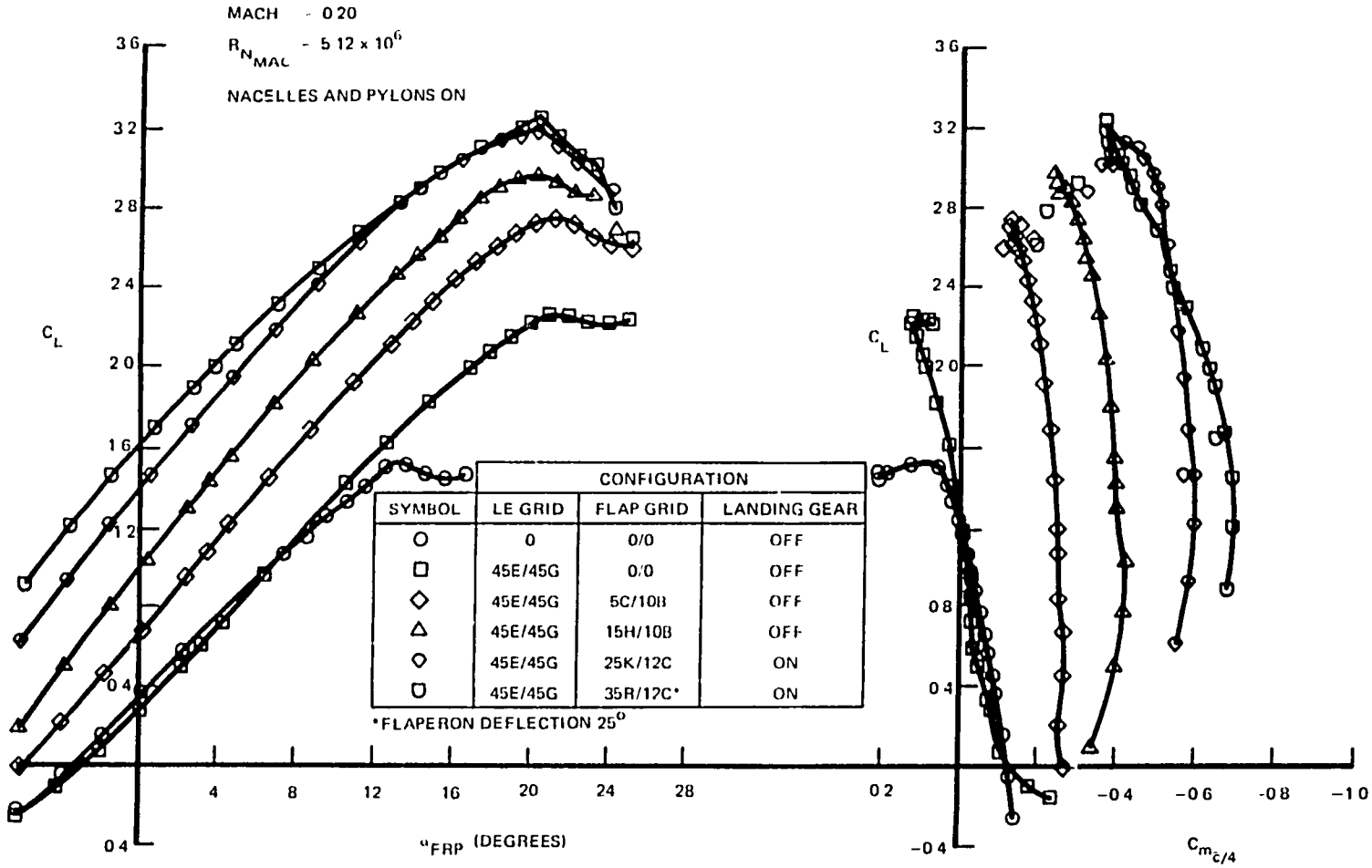

FIGURE 163. TAIL OFF LIFT AND PITCHING MOMENT CHARACTERISTICS FOR VCK AND TWO-SEGMENT FLAP CONFIGURATION

ORIGINAL PAGE IS
OF POOR QUALITY

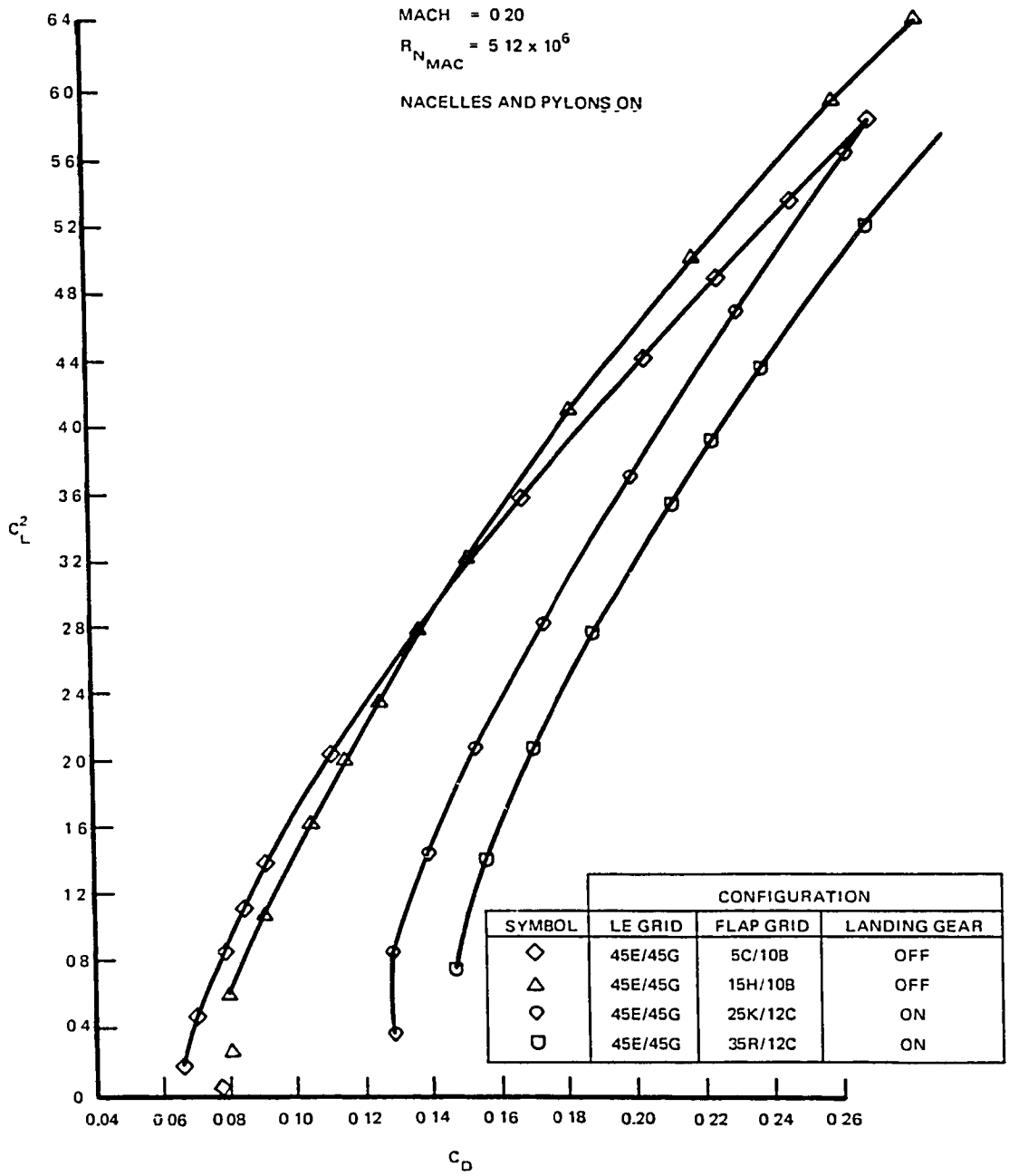

FIGURE 164. TAIL OFF DRAG CHARACTERISTICS FOR VCK AND TWO-SEGMENT FLAP CONFIGURATION

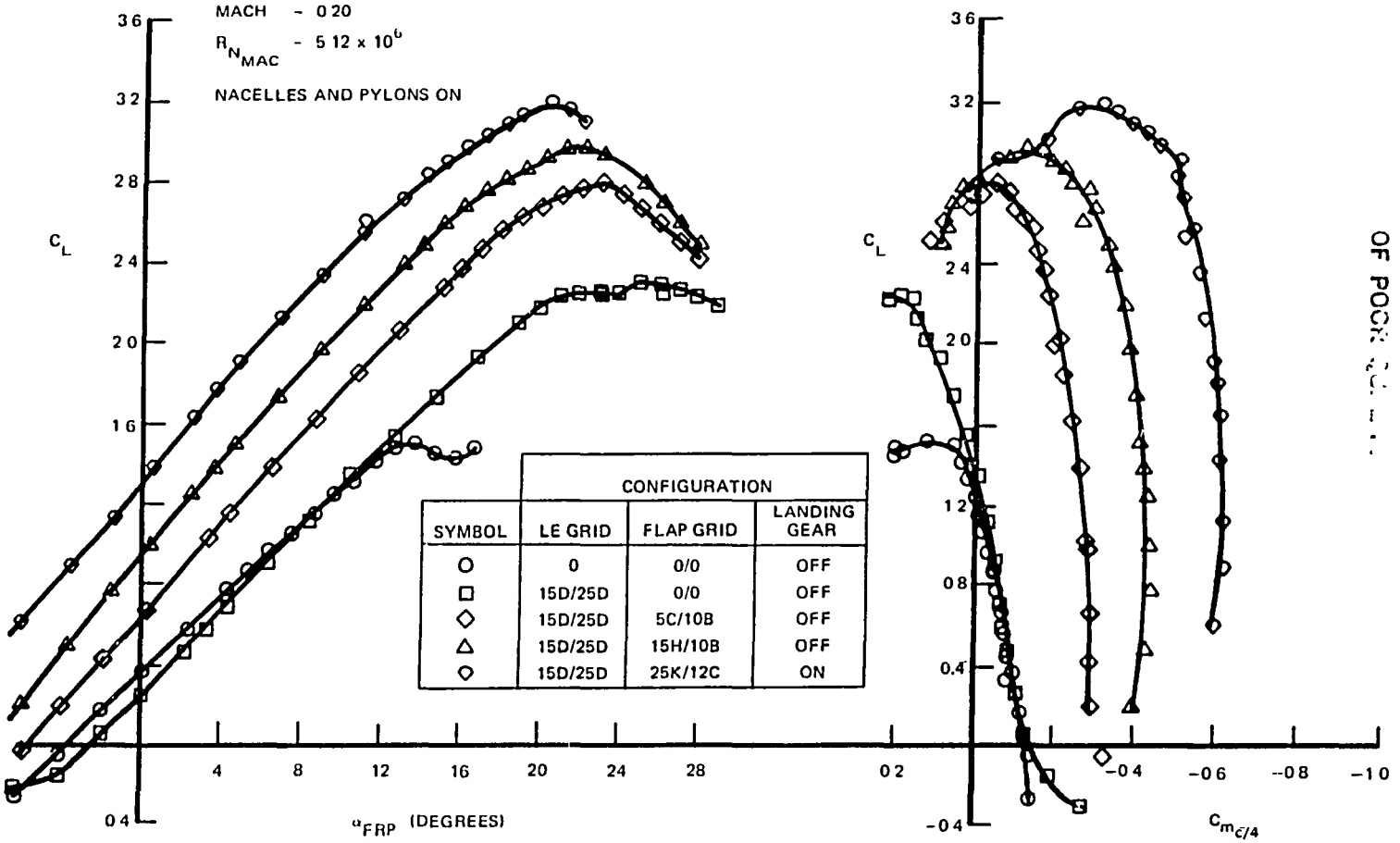

FIGURE 165. TAIL-OFF LIFT AND PITCHING MOMENT CHARACTERISTICS FOR SLAT AND TWO-SEGMENT FLAP CONFIGURATION

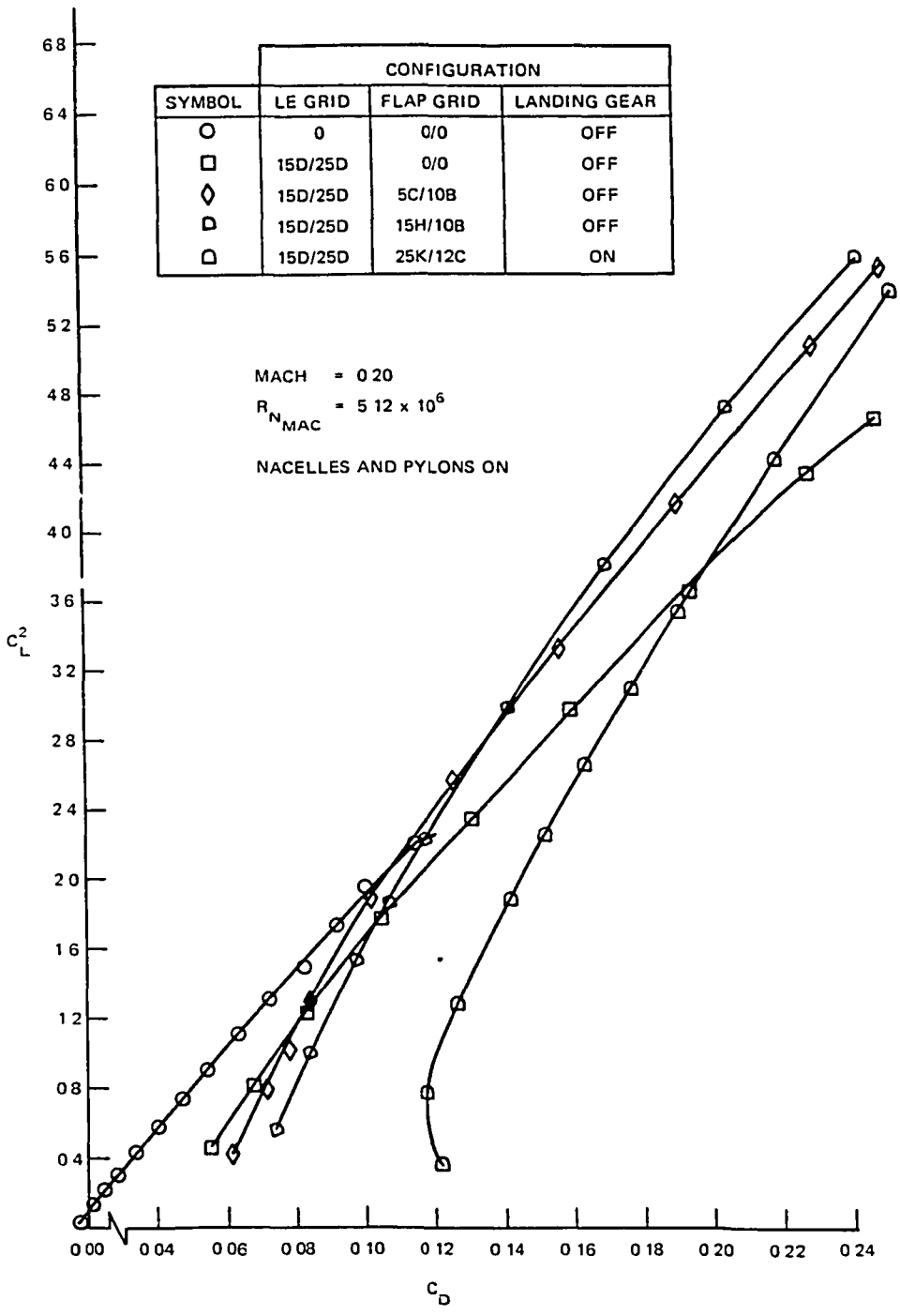

FIGURE 166. TAIL-OFF DRAG CHARACTERISTICS FOR SLAT AND TWO-SEGMENT FLAP CONFIGURATION

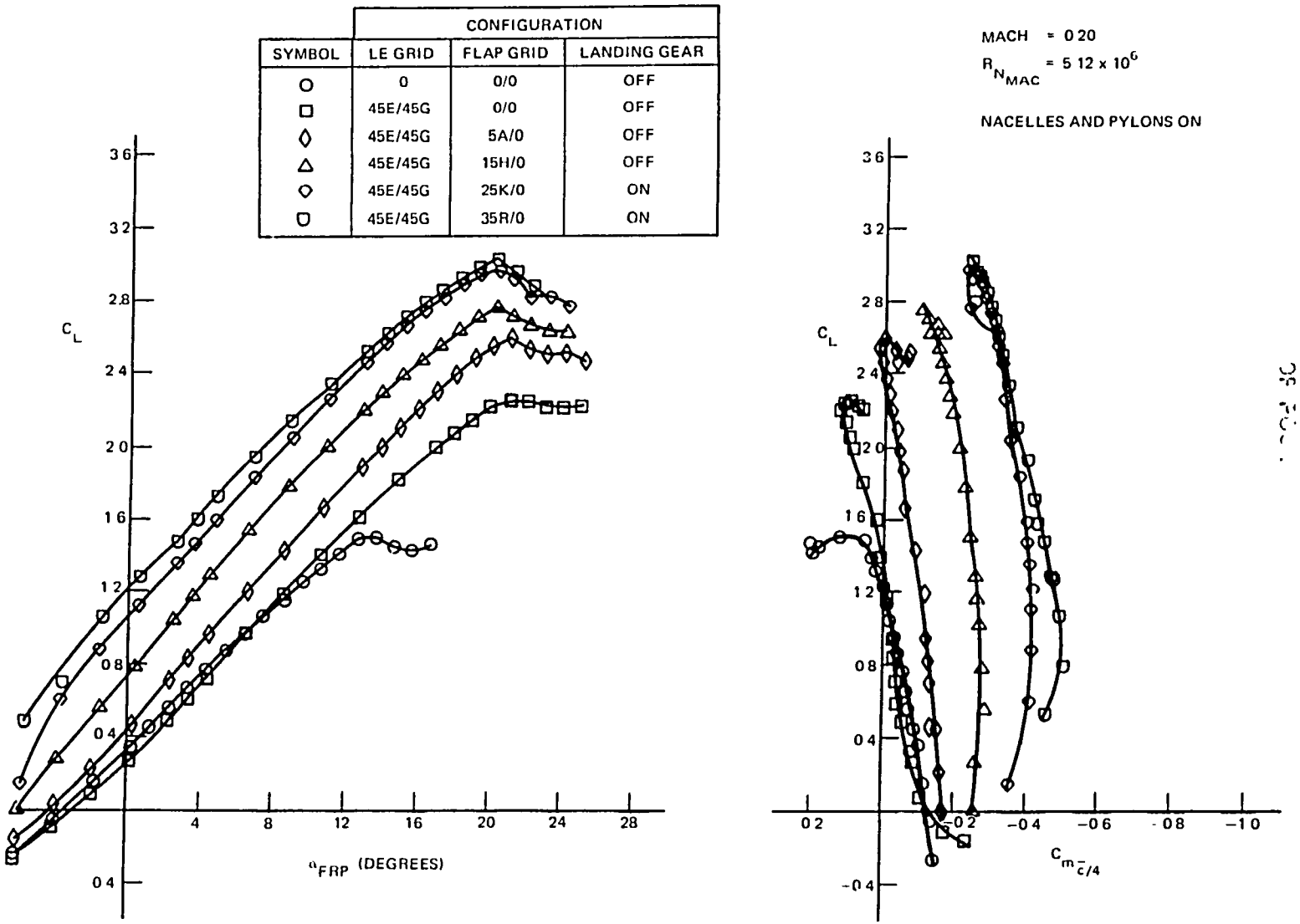

FIGURE 167. TAIL-OFF LIFT AND PITCHING MOMENT CHARACTERISTICS FOR VCK AND SINGLE-SLOT FLAP CONFIGURATION

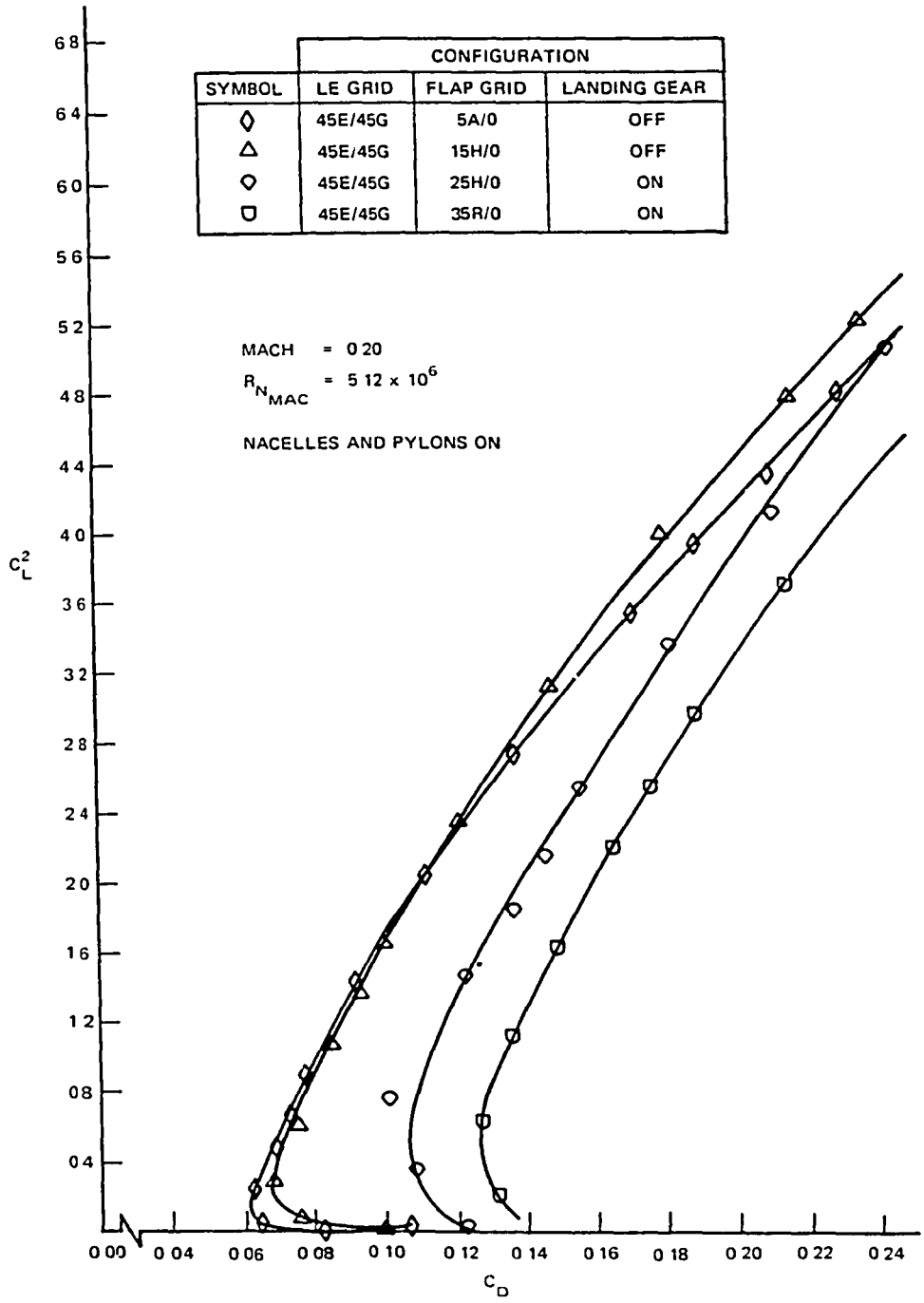

FIGURE 168. TAIL-OFF DRAG CHARACTERISTICS FOR VCK AND SINGLE-SLOT FLAP CONFIGURATION

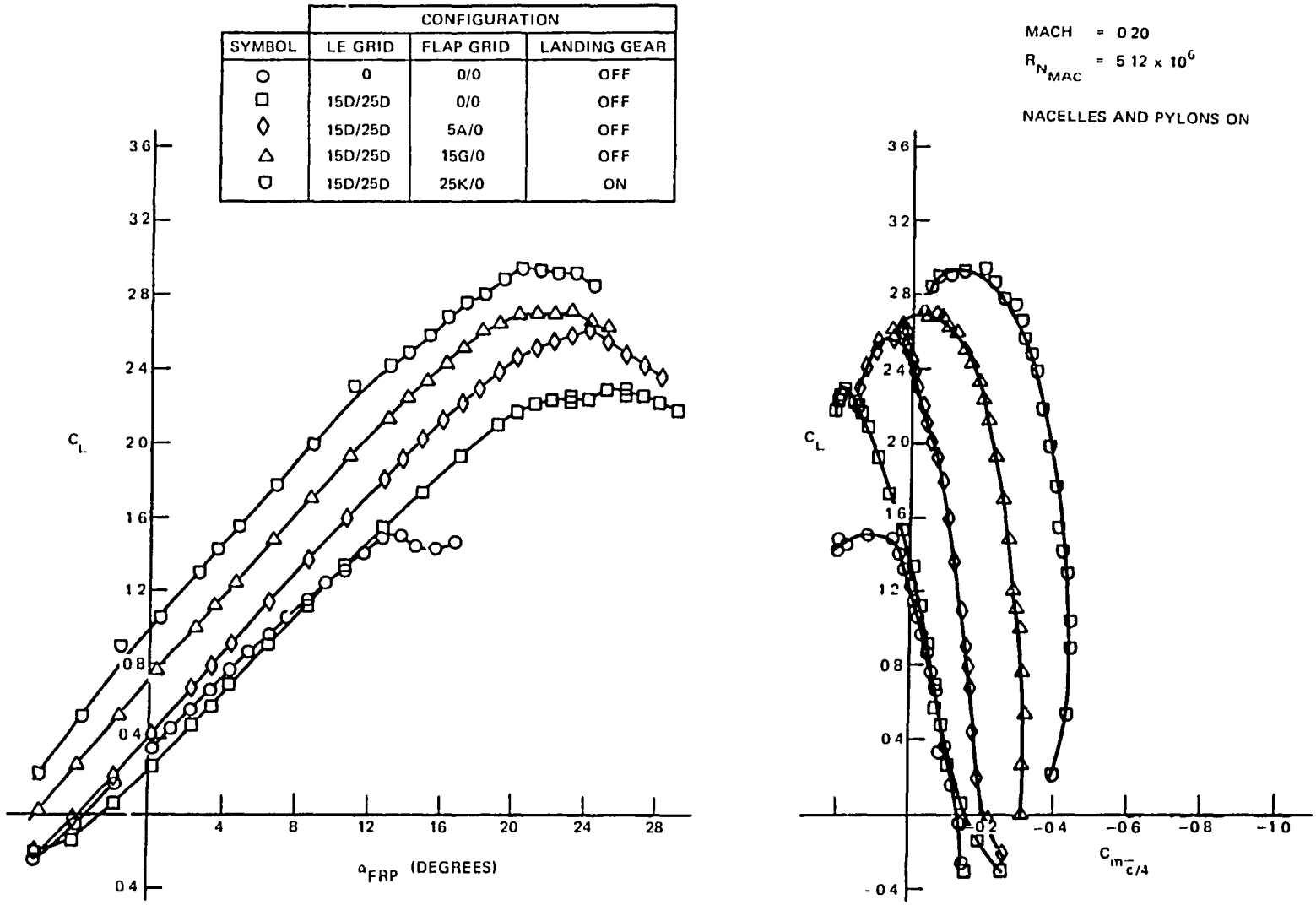

FIGURE 169. TAIL-OFF LIFT AND PITCHING MOMENT CHARACTERISTICS FOR SLAT AND SINGLE SLOT FLAP CONFIGURATION

ORIGINAL PAGE IS
OF POOR QUALITY

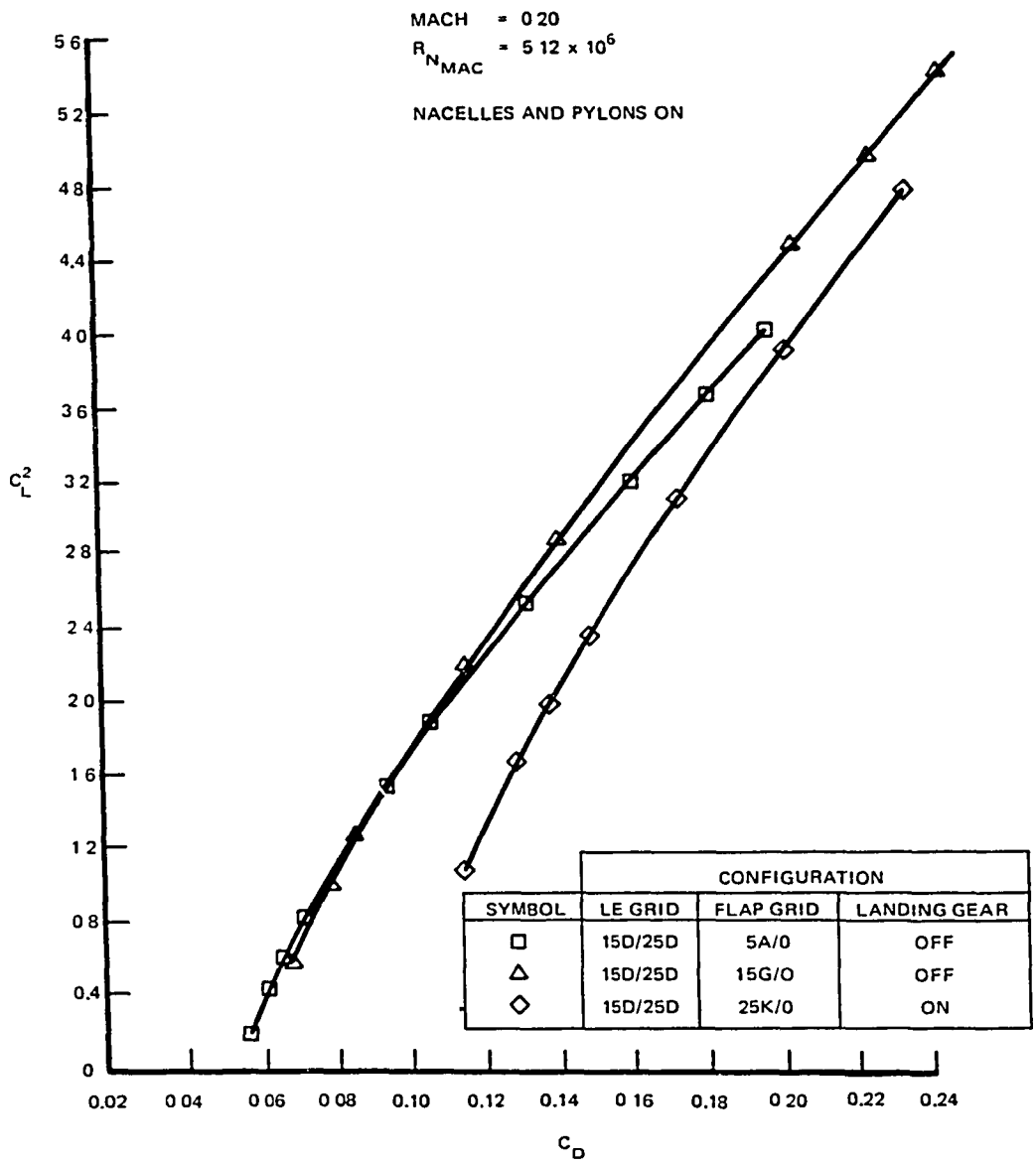

FIGURE 170. TAIL-OFF DRAG CHARACTERISTICS FOR SLAT AND SINGLE-SLOT FLAP CONFIGURATION

ORIGINAL
OF POOR QUALITY

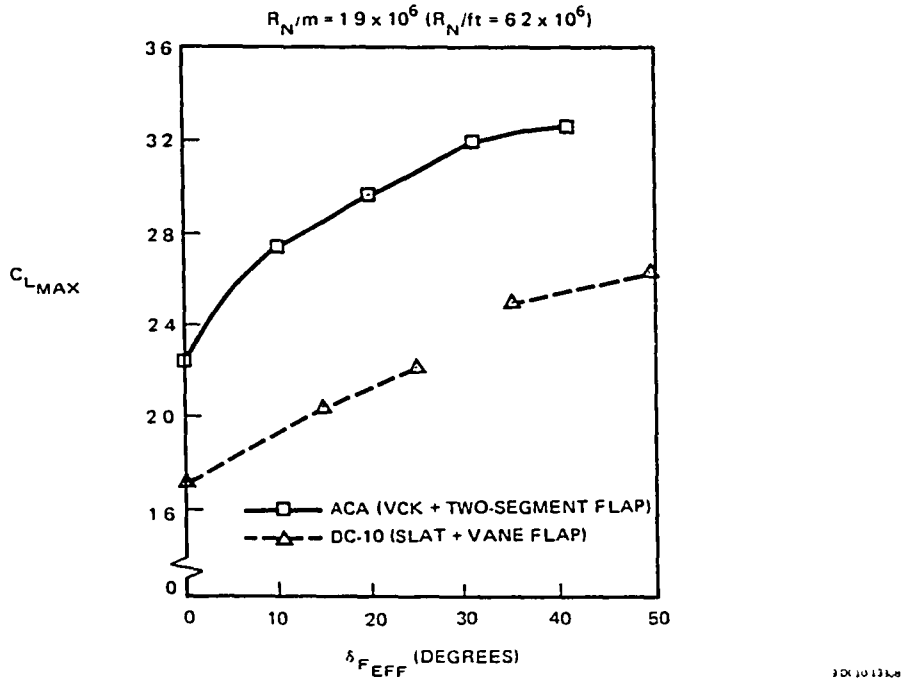

FIGURE 171. TAIL-OFF $C_{L_{MAX}}$ COMPARISON BETWEEN ADVANCED COMMERCIAL AIRCRAFT AND DC-10

and circular arc vane-flap system. Figure 171 indicates a significant improvement in $C_{L_{MAX}}$ for the high aspect ratio wing and advanced high lift system.

The VCK optimization was performed at takeoff and landing flap deflections with two-segment flap. The landing flap deflection was 25M/12C. The corresponding takeoff flap deflection for the VCK optimization was 5C/10B.

Results of the deflection and position surveys indicated that the smaller VCK deflection of 45 degrees obtained the best performance in terms of L/D and $C_{L_{MAX}}$. However, analysis of the surface pressure distributions showed that the VCK was over-deflected. Analysis also indicated that a larger gap for the inboard VCK was required to suppress a premature stall of the inboard region of the wing which reduced $C_{L_{MAX}}$. This premature inboard stall is thought to be an effect of the adverse merging of the VCK/Airfoil wake system with the flow over the flap. The flaperon section was especially sensitive to the leading edge device deflection and gap.

Increasing the gap permitted the inner wing sections to increase their maximum lift capabilty.

It was also noted that the outboard aileron region of the wing indicated poor trailing edge pressure recovery for most high lift configurations. This was due in part to the relatively low Reynolds number in this region but also due to the conflicting leading edge deflection and position requirements for the flapped and non-flapped portions of the outboard wing panel. For the flapped portion of the wing, the pressure recovery was only to the spoiler trailing edge velocity. This was a significantly higher velocity than freestream conditions due to the influence of the flaps. For the outboard aileron region (non-flapped), the pressure distribution on the wing has a more adverse recovery to freestream conditions from large suction peaks due to the adverse effects of sweep, aspect ratio and taper. Future tests will investigate differential leading edge device position for these two outboard regions.

From the VCK grid positions investigated, the final configuration selected for the VCK leading edge device was an inboard gap and overhang of 3.5 percent and -1.0 percent (VCK trailing edge one percent ahead of wing leading edge), and corresponding values for the outboard VCK were 2.5 percent and -1.0 percent. The VCK deflection was 45 degrees. This VCK configuration was selected by $C_{L_{MAX}}$, L/D and pitching moment characteristics.

Results of the slat deflection and grid survey indicated that, for $C_{L_{MAX}}$ and L/D characteristics, the minimum slat deflection of 15D/25D (inboard/outboard slat deflection) with a gap of 2.5 percent and overhang of -2.0 percent was the best overall configuration tested. With the original inboard slat spanwise extent, satisfactory pitch down at stall could not be obtained. Improved stalling characteristics were obtained for the flaps retracted configuration when the inboard slat was trimmed further out from the fuselage. This exposed more of the inner wing clean leading edge and resulted in more inboard wing stall. This slat modification did not cause a significant $C_{L_{MAX}}$ penalty. Further experimental optimization is required to improve the pitching moment and takeoff L/D characteristics.

With the VCK leading edge device, both the two-segment and single-slot flap were optimized at each of the flap deflections. For the two-segment flap system, the main flap grid was evaluated first and was followed by an aft flap deflection survey with the best main flap position. Results of the main flap position survey indicated relatively small changes in $C_{L_{MAX}}$, L/D, and pitching moment characteristics. From the optimization of the aft flap deflection at each main flap deflection, values of 5C/10B, 15/10B, and 25K/12C were the best compromise in terms of $C_{L_{MAX}}$, $C_{L_{\alpha=0}}$, L/D and pitching moment characteristics. At 35 degrees of main flap deflection the optimization indicated the flaperon was separated for most main flap grid positions. Reducing the flaperon deflection to 25 degrees while maintaining the inboard and outboard two-segment flap at 35R/12C improved the drag characteristics; however, this would not be a practical aircraft configuration. The single-slot flap optimization results indicated that for each flap deflection the aerodynamic characteristics were similar to those of the main flap grid study of the two-segment flap (i.e., not extremely sensitive to the grid position).

A comparison of the trimmed $C_{L_{MAX}}$ and $C_{L_{\alpha=0}}$ characteristics for the various high lift systems is shown in Figure 172. As noted previously, it is felt that the VCK was over-deflected and the resulting comparison shows the slat plus two-segment flap has the largest values of maximum lift coefficient. With the single-slot flap the differences between slat and VCK are reduced, with the slat being superior at small flap deflections and the VCK superior at the larger flap deflections.

The lift coefficient at zero angle of attack for the two-segment flap with the VCK is superior to that with the slat installed. On the other hand, very little difference is noted for the single-slot flap with either the VCK or the slat leading edge device. It can also be seen that the two-segment flap at landing deflections has a higher maximum lift capability than the single-slot flap regardless of the leading edge device.

Figures 173 through 180 present the trimmed lift and L/D characteristics for the VCK and slat with two-segment and single-slot flaps. A comparison of the various configurations at takeoff conditions is shown in Figure 181.

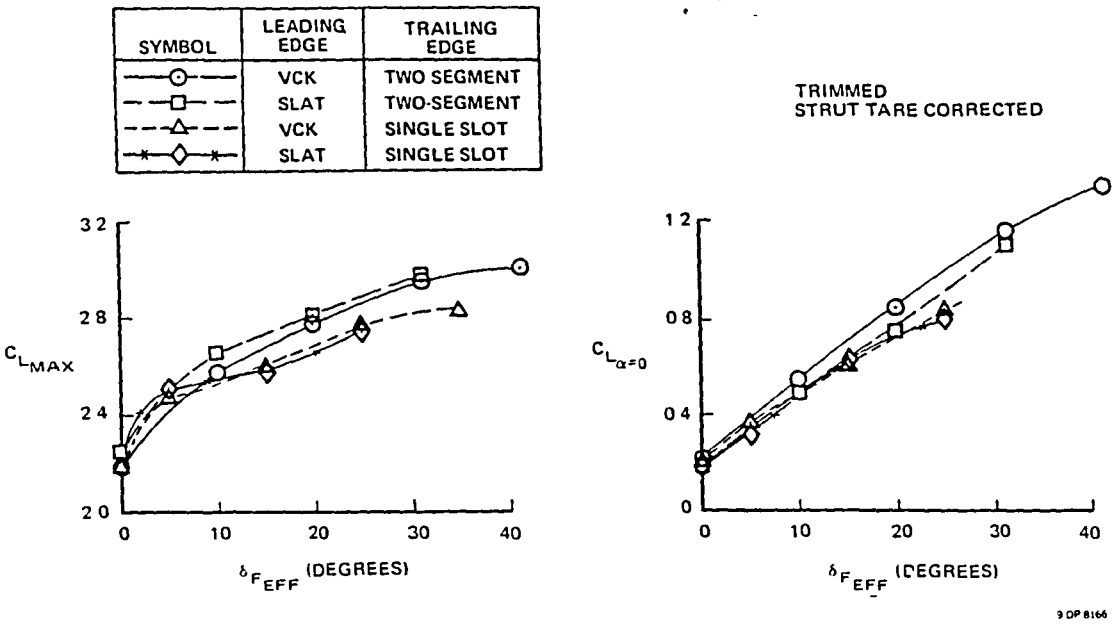

FIGURE 172. EFFECT OF LEADING AND TRAILING EDGE HIGH-LIFT CONFIGURATION ON $C_{L_{MAX}}$ AND $C_{L_{\alpha=0}}$

Due to overdeflection of the VCK, the slat shows superior performance at the lower C_L values. Only minor differences in the L/D envelopes are shown between the two-segment and single-slot flaps. The overall L/D values indicate that further optimization of the leading edge device positions for takeoff flap deflections could result in improved L/D characteristics.

A comparison of the two-segment and single-slot flap systems with the VCK at landing conditions is shown in Figure 182. For an equal C_L (i.e., equal approach speed) the two-segment flap system has a superior approach L/D. In fact, it is of interest to note that the two-segment and single-slot flaps (at deflections of 15/10 and 25/0, respectively) have the same approach C_L. For this C_L, the two-segment flap has a 16-percent improvement in approach L/D relative to the single-slot configuration.

Figure 183 presents the Reynolds number trends for the clean wing (i.e., flaps and leading-edge device retracted), and the slat and VCK with the two-segment flap system. These results are tail-off, nacelles and pylons on, and were obtained at a constant Mach number. The basic wing shows a

ORIGINAL IS
OF POOR QUALITY

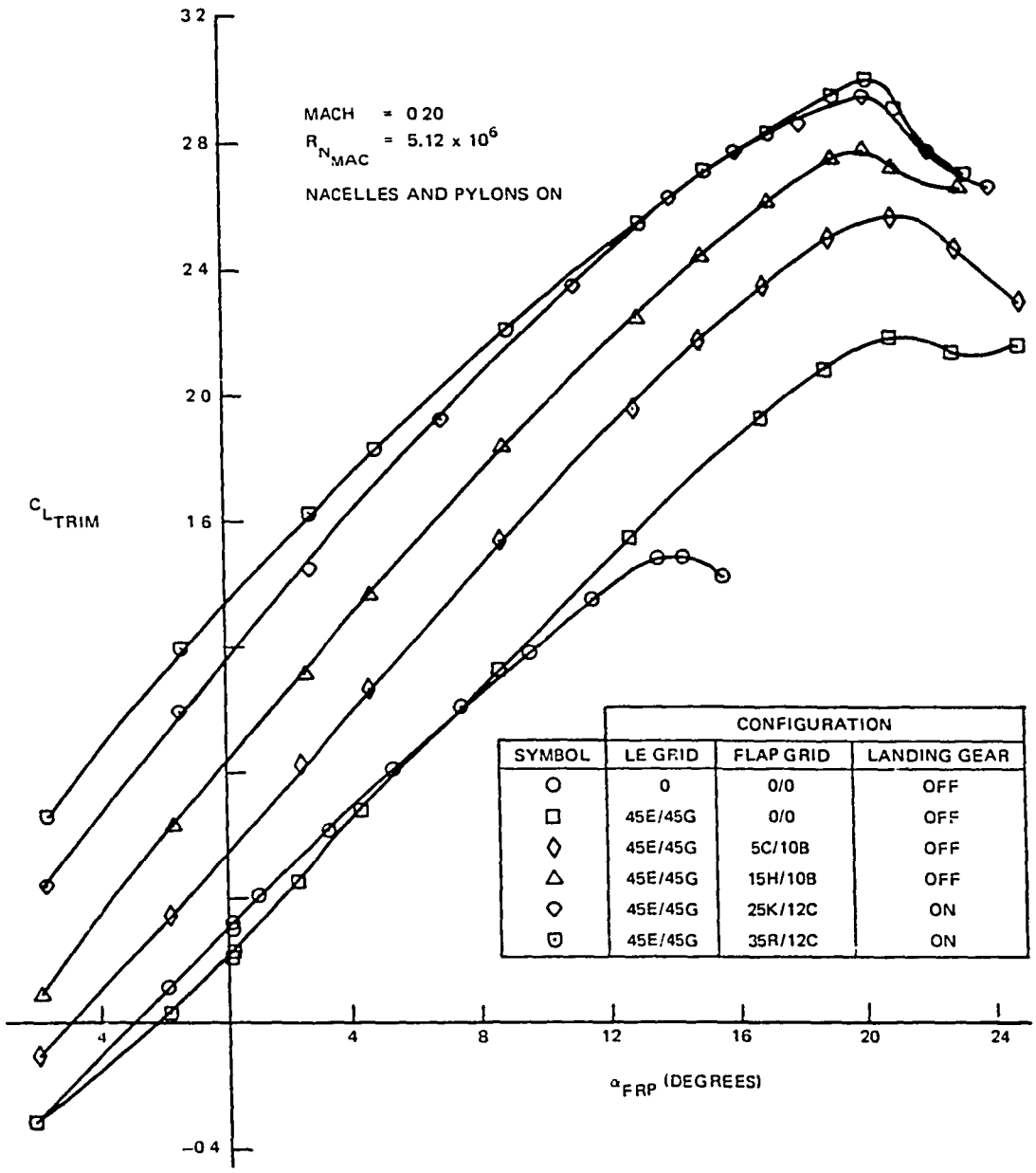

FIGURE 173. TRIMMED LIFT CURVES FOR VCK AND TWO-SEGMENT FLAP CONFIGURATION

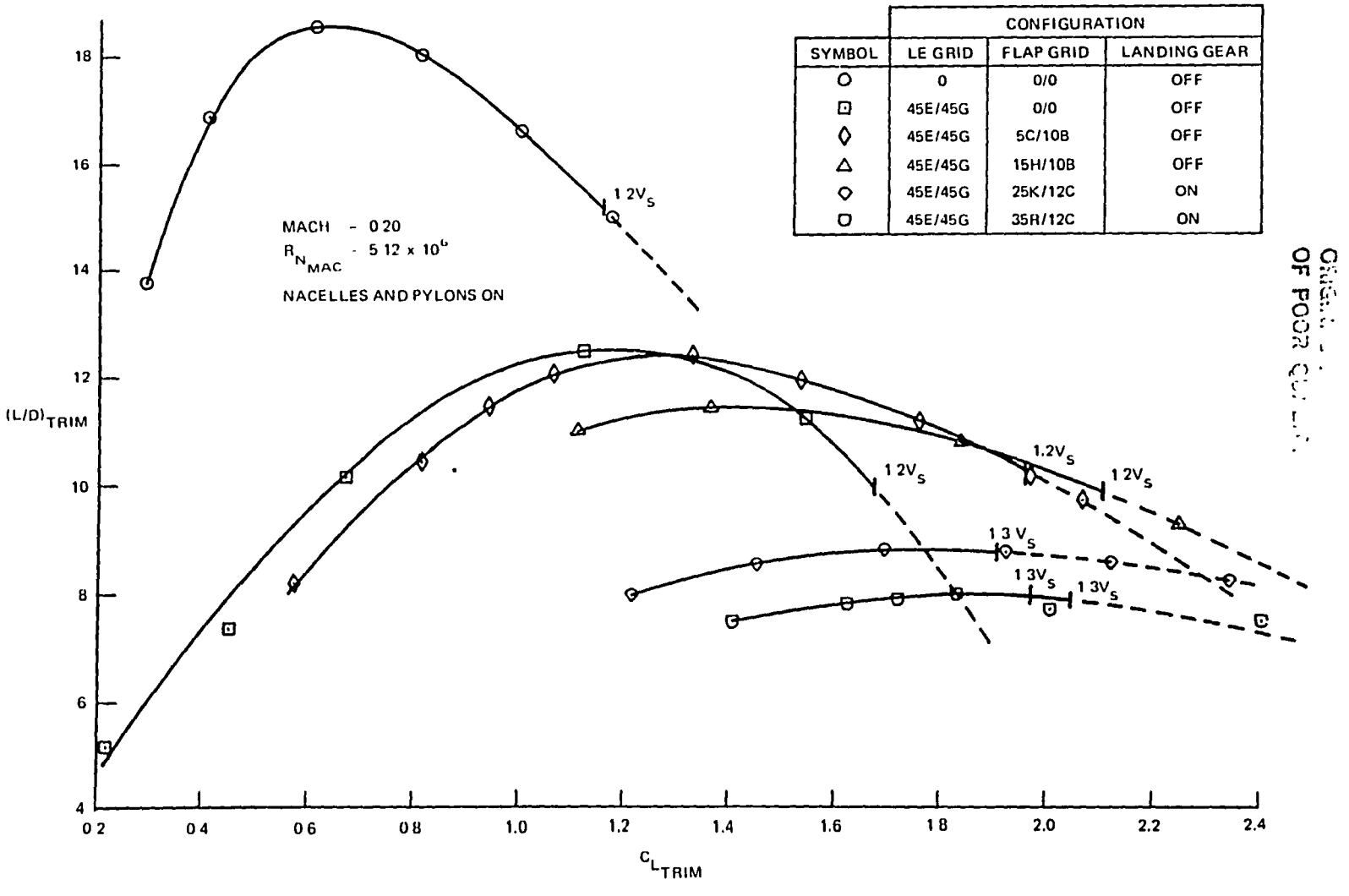

FIGURE 174. TRIMMED L/D CURVES FOR VCK AND TWO-SEGMENT FLAP CONFIGURATION

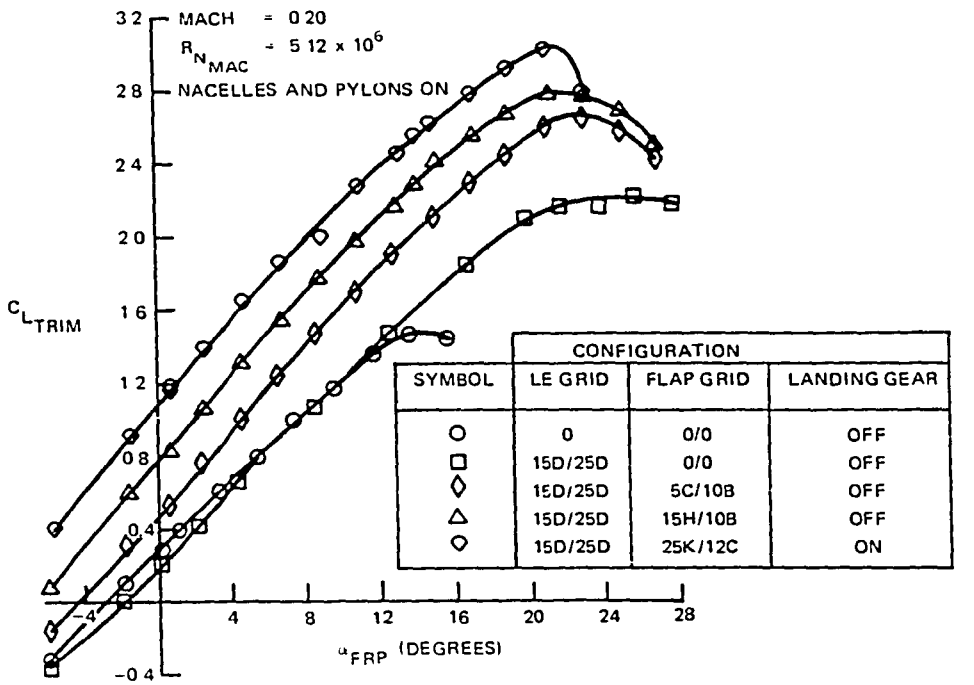

FIGURE 175. TRIMMED LIFT CURVES FOR SLAT AND TWO-SEGMENT FLAP CONFIGURATION

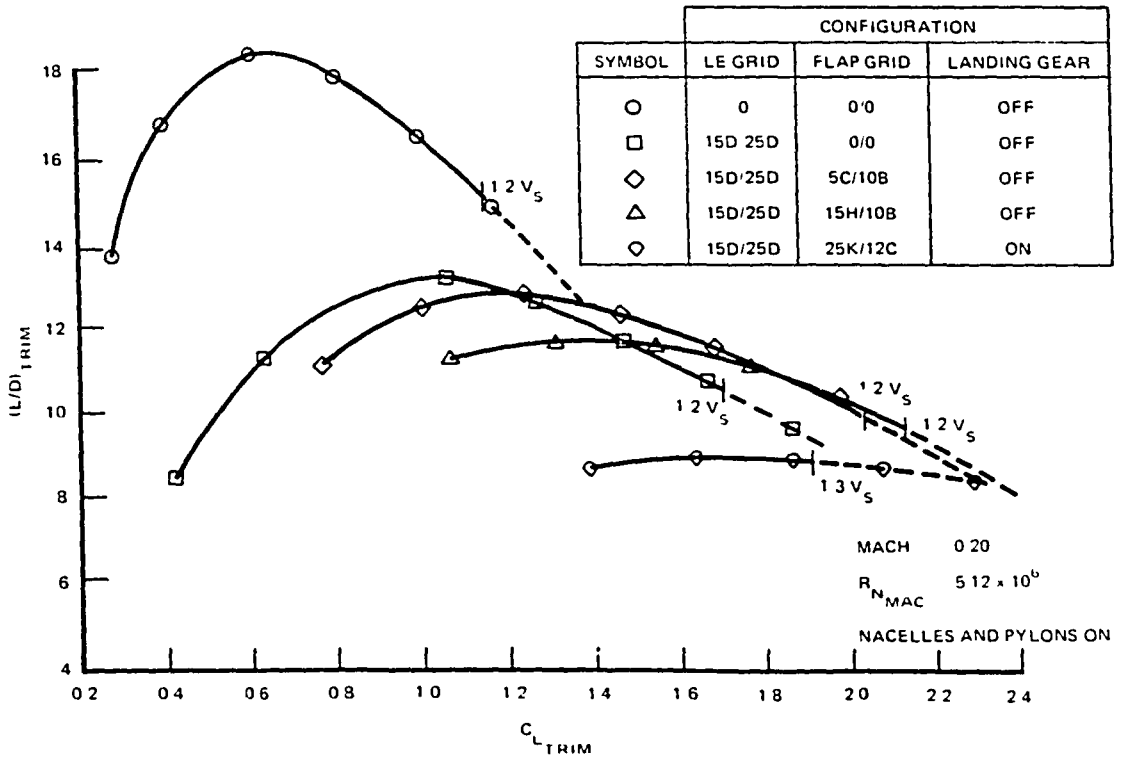

FIGURE 176. TRIMMED L/D CURVES FOR SLAT AND TWO-SEGMENT FLAP CONFIGURATION

ORIGINAL PAGE IS
OF POOR QUALITY

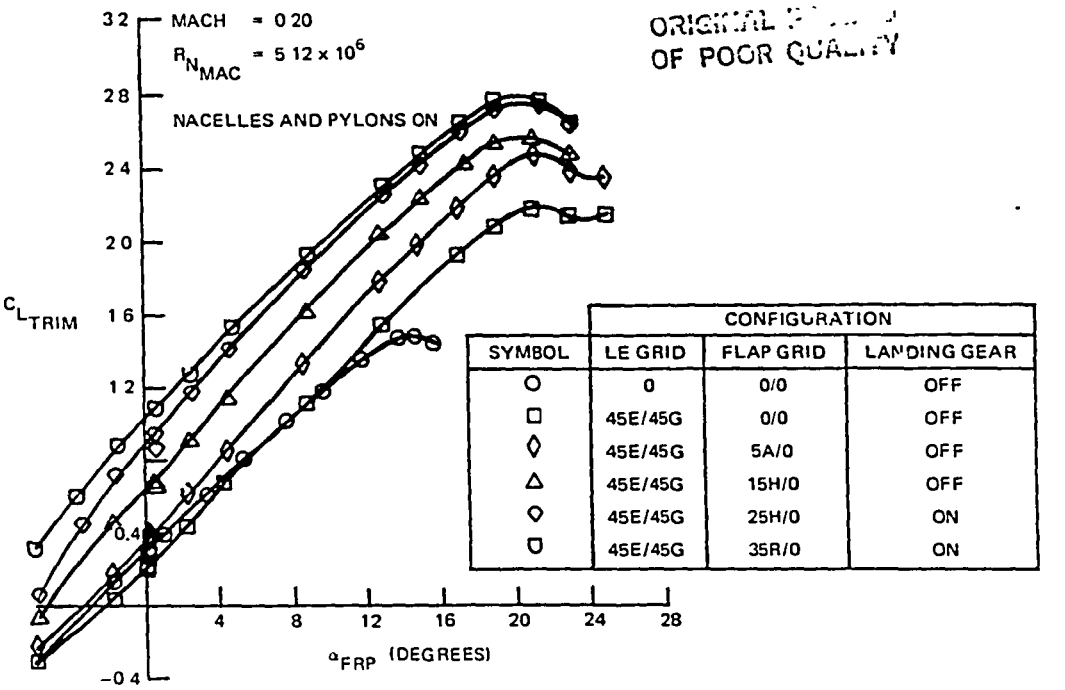

SYMBOL	CONFIGURATION		
	LE GRID	FLAP GRID	LANDING GEAR
○	0	0/0	OFF
□	45E/45G	0/0	OFF
◇	45E/45G	5A/0	OFF
△	45E/45G	15H/0	OFF
◇	45E/45G	25H/0	ON
▯	45E/45G	35R/0	ON

FIGURE 177. TRIMMED LIFT CURVES FOR VCK AND SINGLE-SLOT FLAP CONFIGURATION

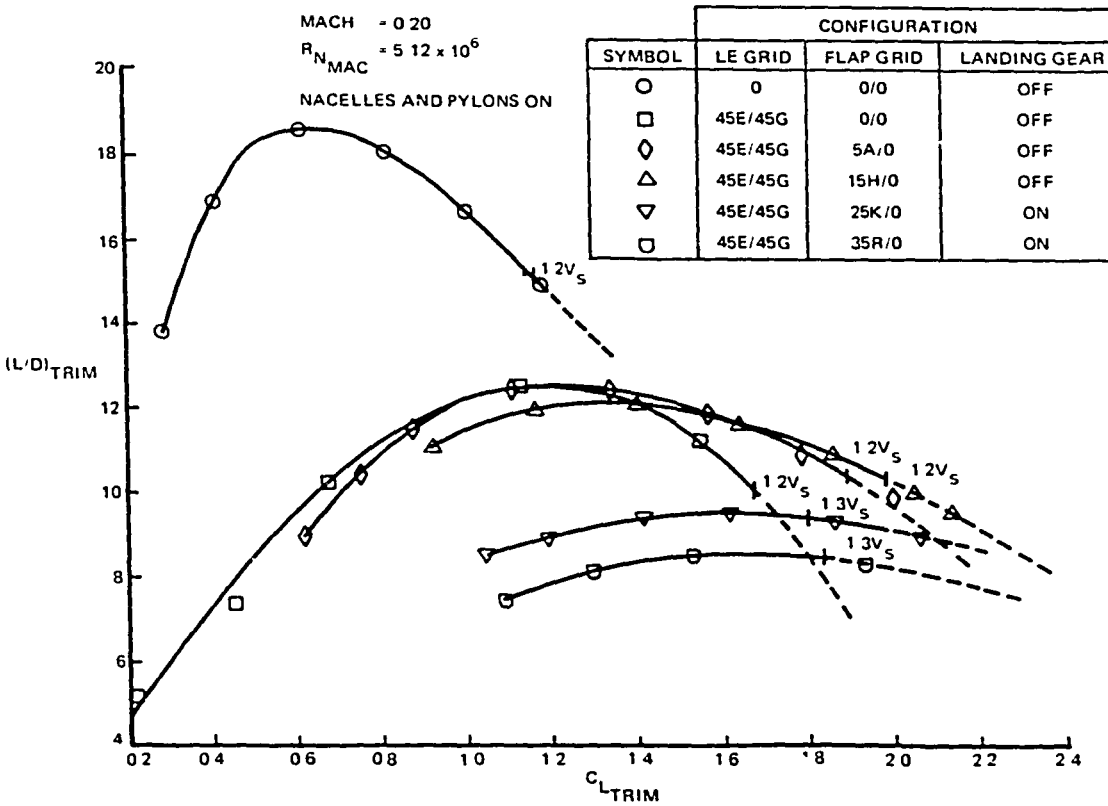

SYMBOL	CONFIGURATION		
	LE GRID	FLAP GRID	LANDING GEAR
○	0	0/0	OFF
□	45E/45G	0/0	OFF
◇	45E/45G	5A/0	OFF
△	45E/45G	15H/0	OFF
▽	45E/45G	25K/0	ON
▯	45E/45G	35R/0	ON

FIGURE 178. TRIMMED L/D CURVES FOR VCK AND SINGLE-SLOT FLAP CONFIGURATION

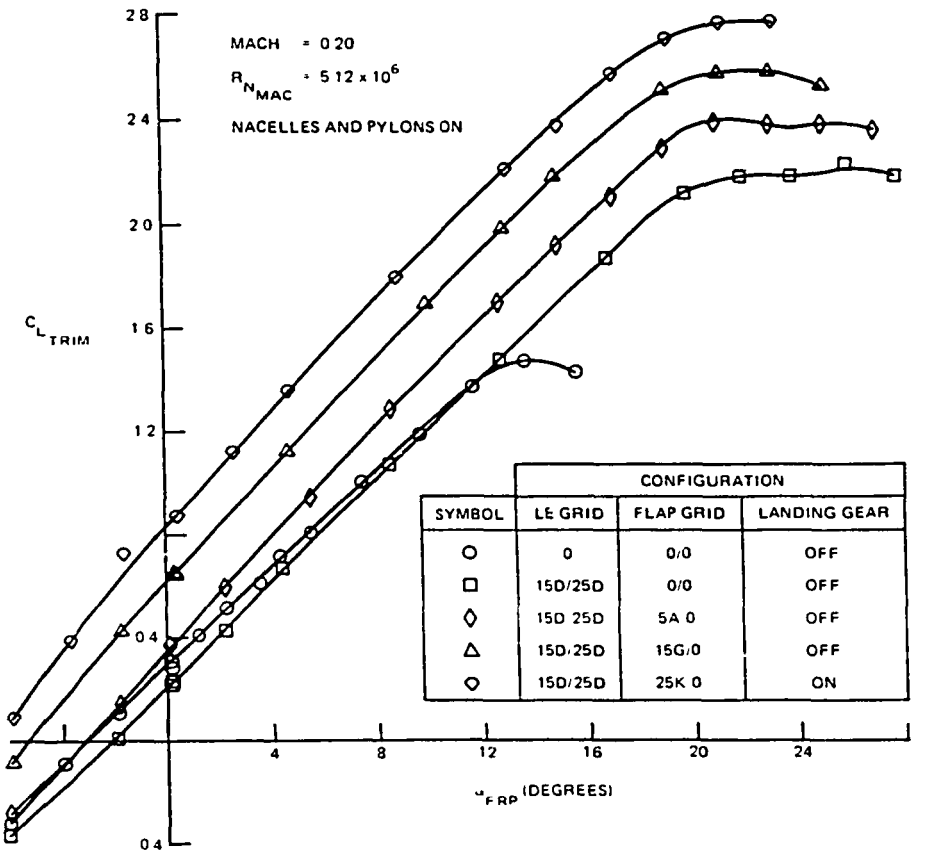

FIGURE 179. TRIMMED LIFT CURVES FOR SLAT AND SINGLE-SLOT FLAP CONFIGURATION

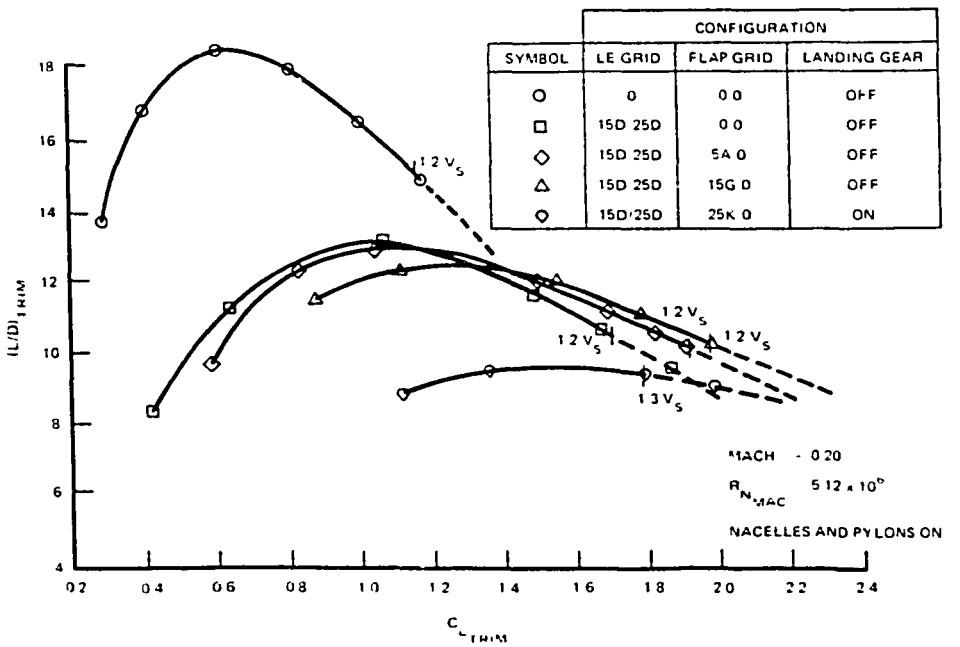

FIGURE 180. TRIMMED L/D CURVES FOR SLAT AND SINGLE-SLOT FLAP CONFIGURATION

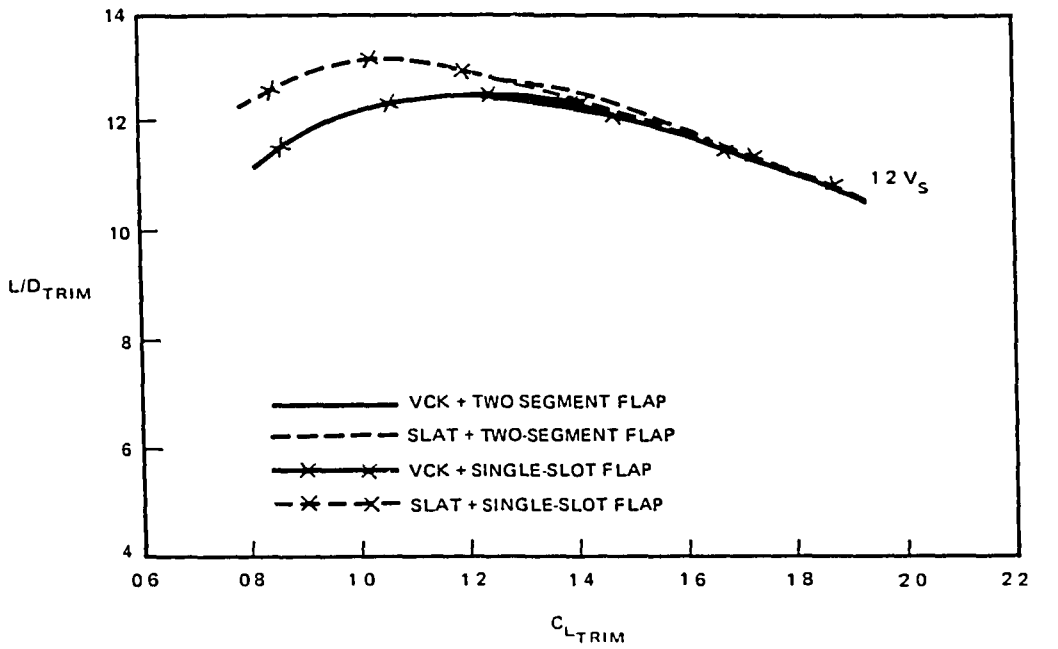

FIGURE 181. TRIMMED L/D COMPARISON FOR THE TAKEOFF CONFIGURATION

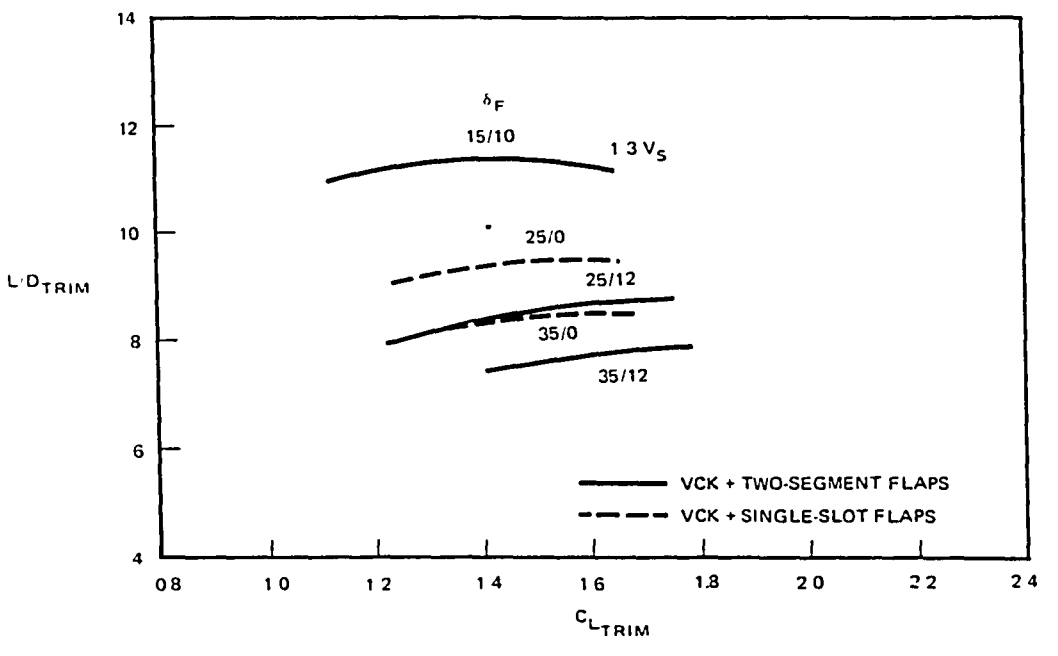

FIGURE 182 TRIMMED L/D COMPARISON BETWEEN TWO-SEGMENT AND SINGLE-SLOT FLAPS FOR THE LANDING CONFIGURATION

ORIGINAL
OF POOR

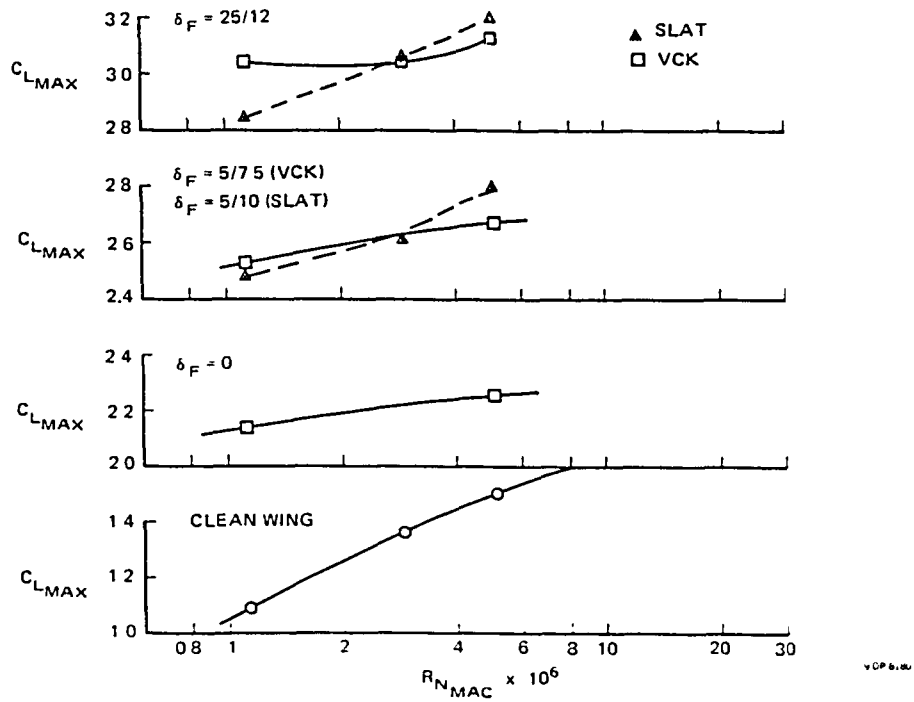

FIGURE 183. EFFECT OF REYNOLDS NUMBER ON VCK AND SLAT WITH TWO-SEGMENT FLAP SYSTEM (TAIL OFF)

signficant increase in $C_{L_{MAX}}$ as the Reynolds number is varied from atmospheric to maximum pressure conditions ($\Delta C_{L_{MAX}}$ = 0.42). Also noteworthy is the difference in variation between the VCK and slat configurations. The Reynolds number effect is much larger for the slat configuration. With the significantly reduced suction peaks of the VCK configuration, a smaller variation with Reynolds number would be expected. Mach number can also affect the high lift characteristics due to the large velocities about the leading-edge elements near stall. This is illustrated in Figure 184 for the clean wing and the slat with two-segment flaps at the takeoff setting. These results were obtained at a reduced Reynolds number due to tunnel operating limits. The clean wing shows a 0.1 reduction in $C_{L_{MAX}}$ as the Mach number is increased from 0.2 to 0.32. This increment increases to 0.14 for the takeoff flap setting. These trends are similar to those of current transport configurations.

The influence of the nacelle/pylon and VCK spanwise extent is shown in Figure 185. On the left-hand plot are the $C_{L_{MAX}}$ values obtained at high

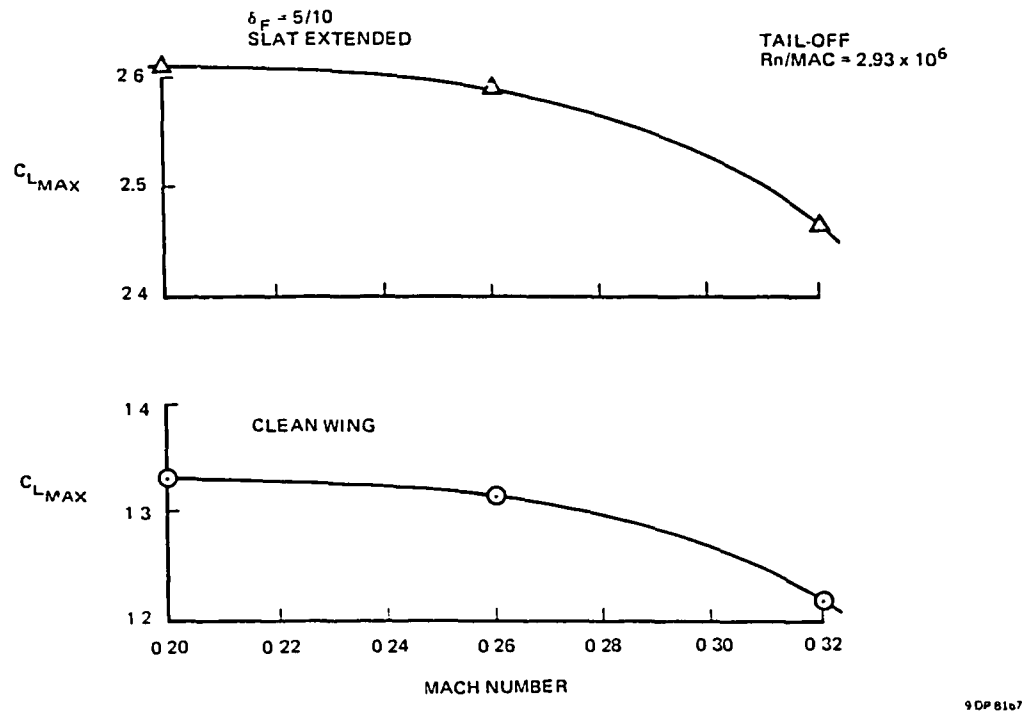

FIGURE 184. EFFECT OF MACH NUMBER ON SLAT WITH TWO-SEGMENT FLAP AND CLEAN-WING $C_{L_{MAX}}$

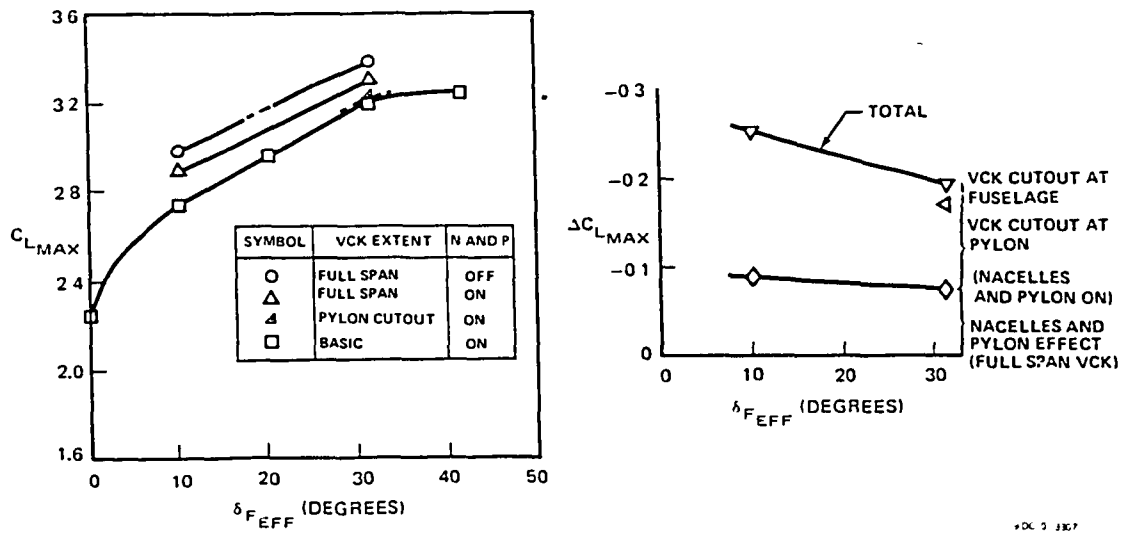

FIGURE 185. INFLUENCE OF NACELLE/PYLON AND VCK SPANWISE EXTENT ON TAIL-OFF $C_{L_{MAX}}$

Reynolds number with the horizontal tail removed. A full span VCK was tested both with and without the nacelle pylon group. The full span VCK was sealed at the fuselage side and continues uninterrupted across the pylon and extends to the wing tips. Also shown is the effect of the removal of the VCK piece in the area of the pylon, and finally, a portion of the VCK near the fuselage to obtain the basic configuration.

Figure 185 indicates a $C_{L_{MAX}}$ of 3.4 was obtained for the full span VCK with nacelles and pylon off at the two-segment landing flap setting. Addition of the nacelle pylon group to the full span VCK configuration resulted in a $C_{L_{MAX}}$ reduction approaching 0.1 as shown in the right-side of the Figure 185. Removal of the VCK in the region of the pylon resulted in a loss of another 0.1 in $C_{L_{MAX}}$. Finally, removal of the VCK near the side of the fuselage resulted in a 0.02 decrease in $C_{L_{MAX}}$. It is to be noted that as the $C_{L_{MAX}}$ decreased due to these changes, the pitch characteristics at stall were improving. This resulted from the nacelle pylon addition and the reduction in the inboard VCK extent which were promoting more inboard stall. At takeoff and landing flap deflections, the total $C_{L_{MAX}}$ reduction was 0.25 and 0.20, respectively.

COMPARISON OF EXPERIMENTAL DATA WITH ESTIMATED METHODS

Comparisons of theoretical and experimental results have been made for the cruise wing configuration W_{3B}. The theoretical results were calculated by the Giesing vortex lattice method (Reference 5) and the Douglas version of the Jameson-Caughey (FL022) three-dimensionial transonic flow program (Reference 3). The latter program includes an approximate fuselage simulation, an accelerated iteration step, and an iterated two-dimensional strip boundary layer solution.

Figure 186 presents the comparison of the theoretical and the experimental data. Two sets of experimental data are presented. The basic data have been corrected for wind tunnel wall effects, but not for the influence of the support system (tandem struts). The flagged symbols have been corrected for this effect. The strut tares were derived from an extensive experimental program detailed in Reference 6. The struts for the current configuration were placed further aft than for the previous experimental data base on which the strut tares were evaluated. A theoretical study utilizing the Douglas Three-Dimensional Lifting Neumann program (Reference 8) was performed to assess the significance of this further aft strut placement. This analysis, which included the effect of the strut wake system, indicated that the further aft placement of the system was not a significant factor. The theoretically predicted lift increment due to the strut system was in good agreement with the experimentally determined value. Figure 186 also shows the Neumann geometry for the configuration and the theoretical model of the strut and wake system.

Both the Giesing vortex lattice and Jameson results are in good agreement with the strut tare corrected experimental values. The test data were obtained at the nominal high Reynolds number condition in the Ames 12-Foot Pressure Wind Tunnel.

Comparisons of experimental and Jameson calculated wing pressures were generated and an example is presented in Figure 187. This comparison is for the 72.5-percent span location at the angle of attack for stall. Good agreement is shown between experiment and program calculations. Comparisons

OF POOR QUALITY

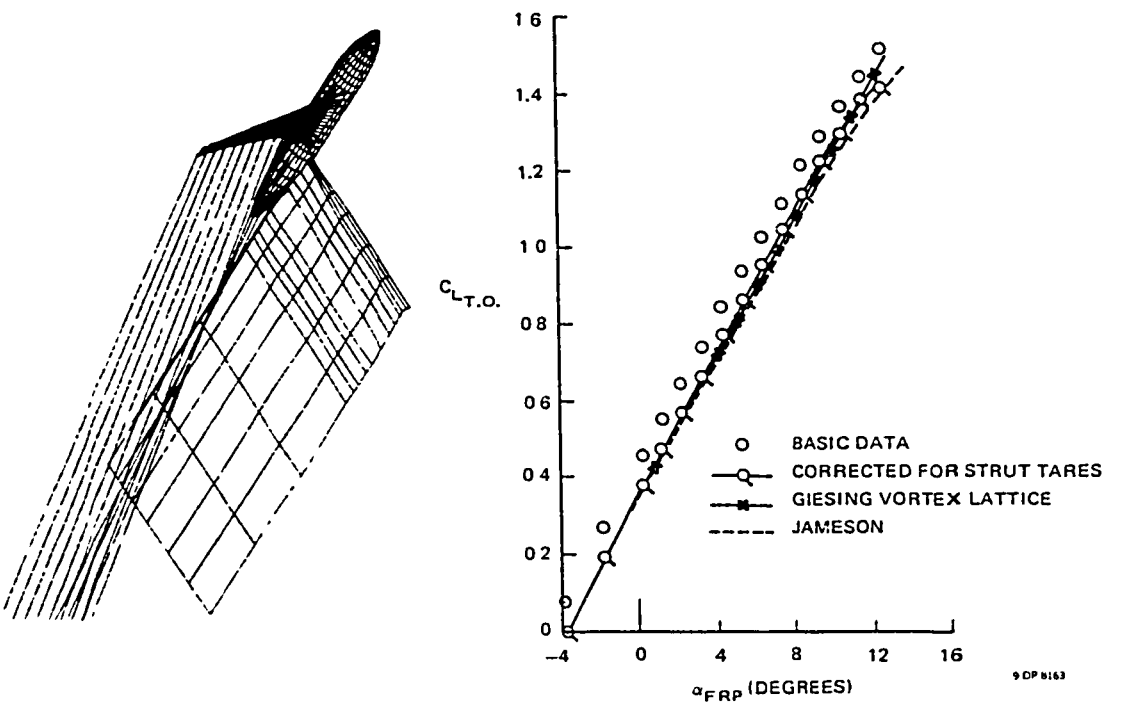

FIGURE 186. LIFTING NEUMANN GEOMETRY AND LIFT COMPARISON FOR THE CRUISE WING

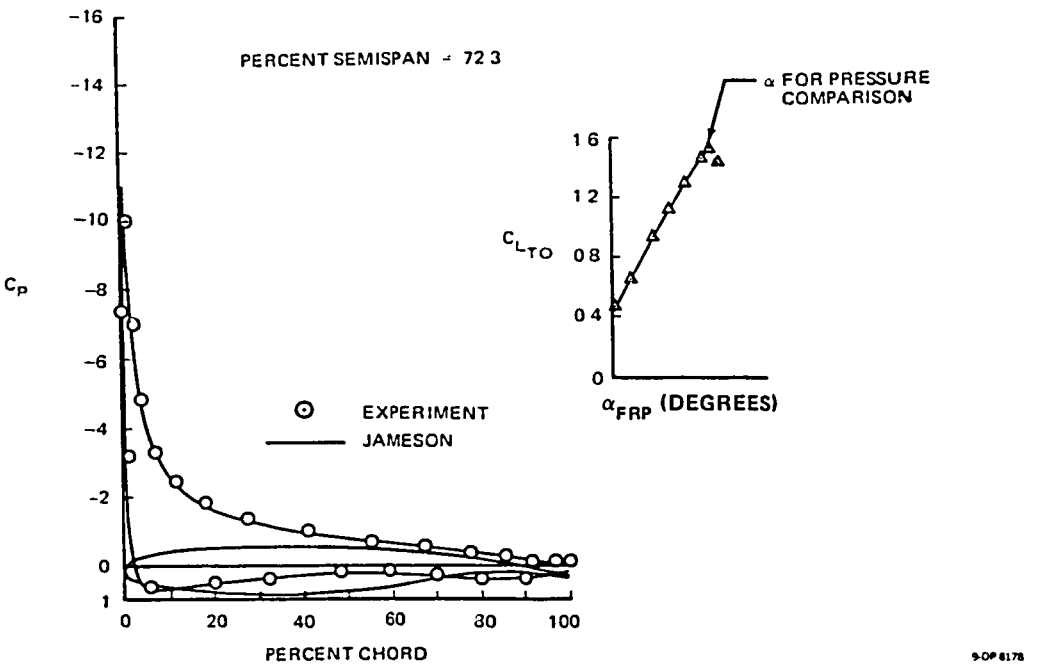

FIGURE 187. COMPARISON OF EXPERIMENTAL AND JAMESON CALCULATED PRESSURES

OF POOR QUALITY

at other angles of attack and other spanwise positions indicated similar agreement between experimental and calculated pressure distributions.

Comparisons of $C_{P_{MIN}}$ experimental values and the Jameson calculated values indicated the theoretical minimum pressures at the angle of attack for stall were within 0.8 of the experimental values. The Jameson program was predicting a more positive pressure. The resulting theoretical boundary layer characteristics indicated the initiation of a rapid forward shift in separation location over the outboard wing panel at angles of attack greater than the experimental stall angle.

A comparison of the spanwise variation of sectional lift coefficient for the Giesing vortex lattice, Jameson, and the Nonplanar Lifting Surface program (Reference 9) is shown in Figure 188. The theoretical methods are predicting very similar spanwise variations of sectional lift values. Good agreement between experiment and theory is shown for the inboard stations, but all theoretical methods overestimate the sectional lift values for the outboard span positions.

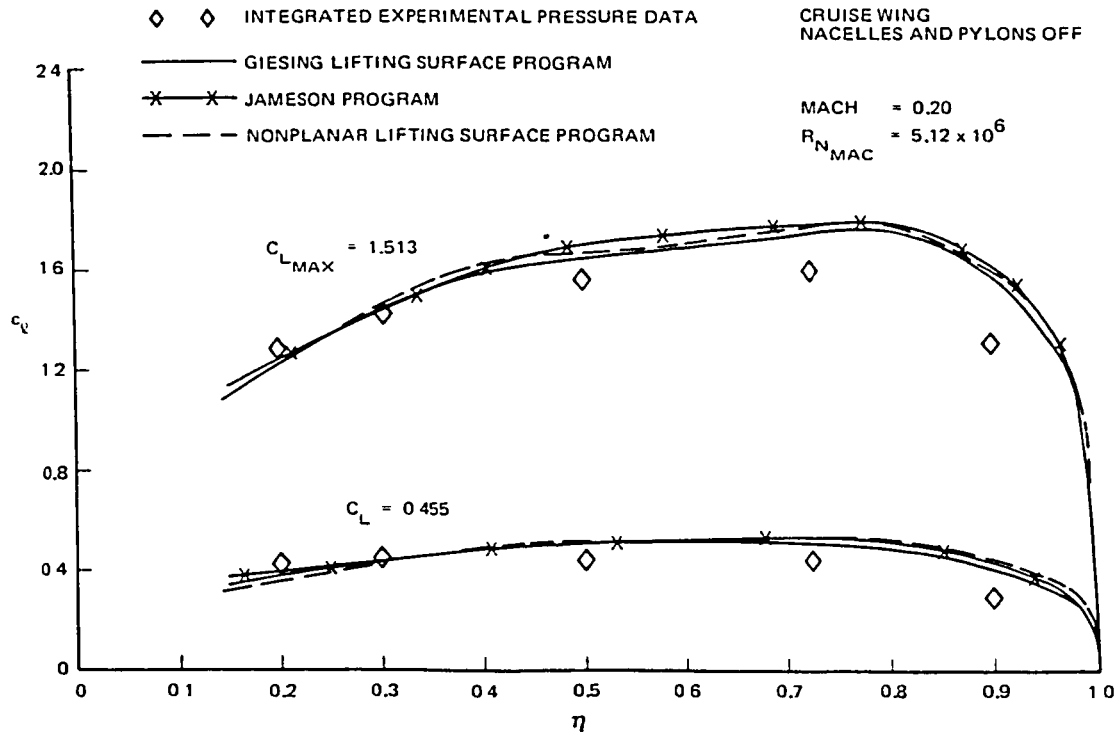

FIGURE 188. COMPARISON OF EXPERIMENTAL AND CALCULATED SPANWISE LIFT DISTRIBUTIONS

Figure 189 presents a comparison of experimental and estimated maximum lift increments for the VCK and the two-segment flap system. Also shown in Figure 189 is a comparison of the flap lift increment at zero degree angle of attack. Giesing calculated flap lift increments were essentially identical to the estimated values. The estimated VCK maximum lift increments were based on the two-dimensional and three-dimensional high lift experimental data base with corrections for local chord ratio. The maximum lift increments and $\Delta C_{L_{\alpha=0}}$ for the trailing-edge flap system were estimated by means of the two-dimensional experimental data base and methodology used successfully for current transport aircraft. The comparisons shown in Figure 189 indicate good agreement for these lift components. The flap lift increment is the difference between the clean leading edge with flap deflected and the basic cruise wing lift at zero degree angle of attack. The maximum lift increment for the VCK is the difference in $C_{L_{MAX}}$ with and without the VCK device for the various flap deflections.

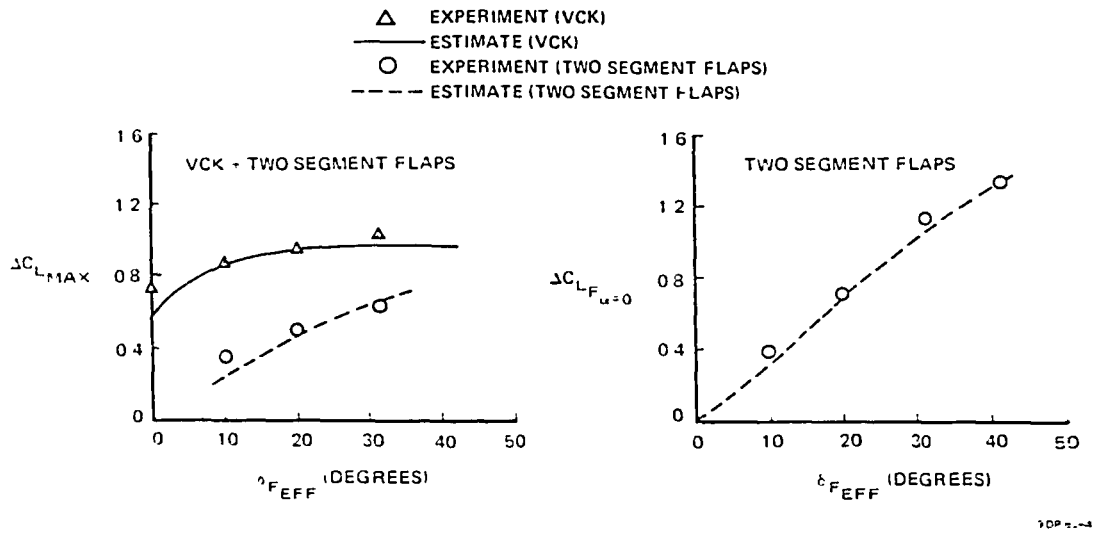

FIGURE 189. COMPARISON OF EXPERIMENTAL AND ESTIMATED MAXIMUM-LIFT INCREMENTS FOR VCK AND FLAPS, AND FLAP-LIFT INCREMENT AT ZERO ANGLE OF ATTACK

A trimmed $C_{L_{MAX}}$ comparison is presented in Figure 190. The predicted maximum lift values were estimated using an incremental buildup of the basic wing, trailing edge flaps, leading edge device, interference, and trim

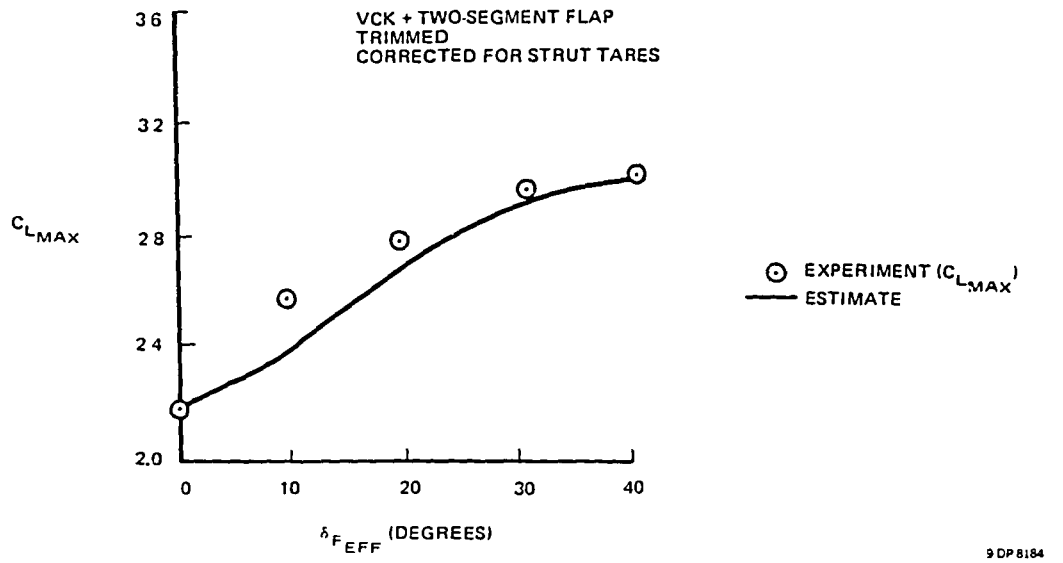

FIGURE 190. COMPARISON OF ESTIMATED AND EXPERIMENTAL $C_{L_{MAX}}$

penalties. The basic equation is as follows:

$$C_{L_{MAX}} = C_{L_{MAX}}{}_{CLEAN} + C_{L_{MAX}}{}_{FLAP} + C_{L_{MAX}}{}_{L.E.} + C_{L_{TRIM}} + C_{L_{MAX}}{}_{INTERFERENCE}$$

The clean wing maximum lift contribution is obtained from an estimation of the three-dimensional section lift distribution which first attains the estimated two-dimensional section maximum lift at some point along the span. The three-dimensional section lift distribution is predicted using lifting surface theory (Reference 5), and integration of this lift distribution yields the value of wing maximum lift. The values of maximum lift coefficient across the span are obtained from a correlation of two-dimensional wind tunnel data, which account for airfoil Reynolds number and geometry, including leading edge radius, maximum camber, and location of maximum camber and thickness. The trim lift penalty at $C_{L_{MAX}}$ is estimated for the appropriate center-of-gravity location using the relevant aircraft geometry and tail-off pitching moment at each flap setting. Miscellaneous interference penalties have been obtained from previous aircraft data and applied to the estimates. Such items as nacelles and pylons, leading-edge device cutouts, and effect of landing gear are included in this interference increment.

OF POOR QUALITY

The comparison shown in Figure 190 indicates good agreement at zero and maximum flap deflections. For the takeoff flap deflections, the estimated $C_{L_{MAX}}$ values are lower than the experimental data. The estimates are, in general, conservative for the VCK with two-segment flap configuration.

Figure 191 presents a comparison of experimental and estimated tail-off L/D characteristics for the VCK with two-segment flap configuration. The estimated tail-off L/D characteristics were obtained from drag polars based on an incremental buildup method similar to that used on current transport aircraft. Increments for parasite and induced drag of the flaps and VCK, nacelle drag, were applied to the estimated low-speed cruise configuration polar. The basic equation for the drag buildup is as follows:

$$C_D = \underbrace{C_{D_p} + \frac{C_L^2}{\pi AR e}}_{\text{Cruise Polar}} + C_{D_{PARASITE}}{}_{\text{FLAP + L.E.}} + \Delta C_{D_{INDUCED}}{}_{\text{FLAP}} + \Delta C_{D_{INDUCED}}{}_{\text{NACELLES}} + \Delta C_{D_{MISC}}$$

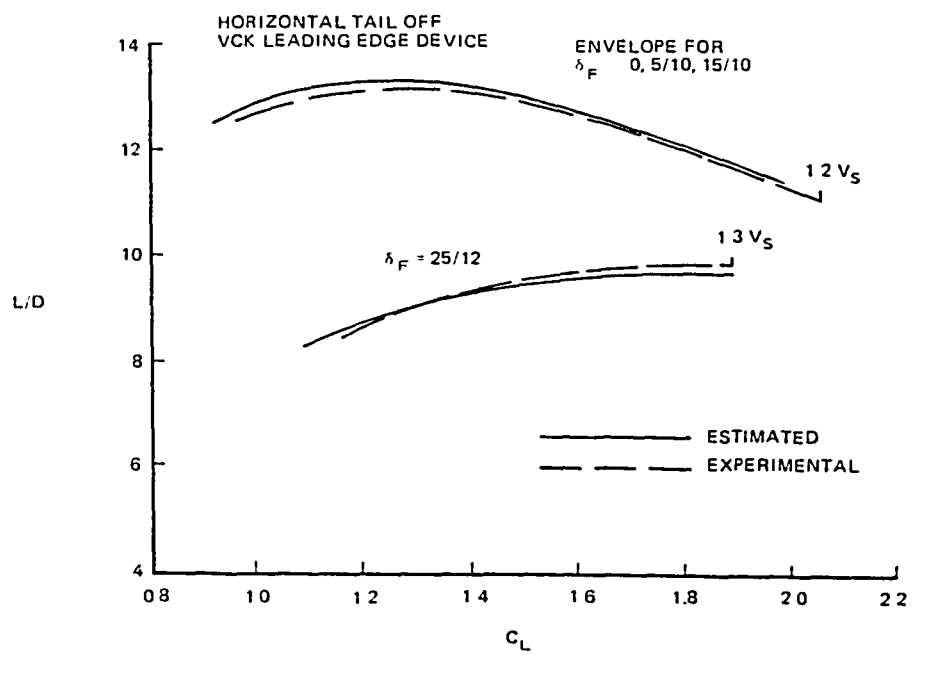

FIGURE 191. COMPARISON OF EXPERIMENTAL AND ESTIMATED L/D CHARACTERISTICS

ORIGINAL PAGE IS
OF POOR QUALITY

The parasite drag increment for the flap plus leading-edge device is based on previous three-dimensional test data for high lift configurations incorporating two-segment flaps, VCK, and slat geometries. Flap-induced drag increments relative to the clean wing were generated by the Giesing vortex lattice program (Reference 5) for the various flap settings. The nacelle-induced drag estimates are also based on the same method. The miscellaneous drag term includes the effect of the landing gear.

Good agreement between experimental and estimated L/D characteristics is shown in Figure 191 for the takeoff flap envelope and the 25/12 two-segment flap deflection.

Figure 192 shows a comparison of the span loading for the clean leading edge (no leading-edge device deployed) with the flaps deflected 15H/10B. The theoretical results were existing calculations at a slightly different flap deflection and without the nacelle and pylons. The shape of the span load distribution is predicted well by the Giesing method. The lift values, however, are somewhat overestimated.

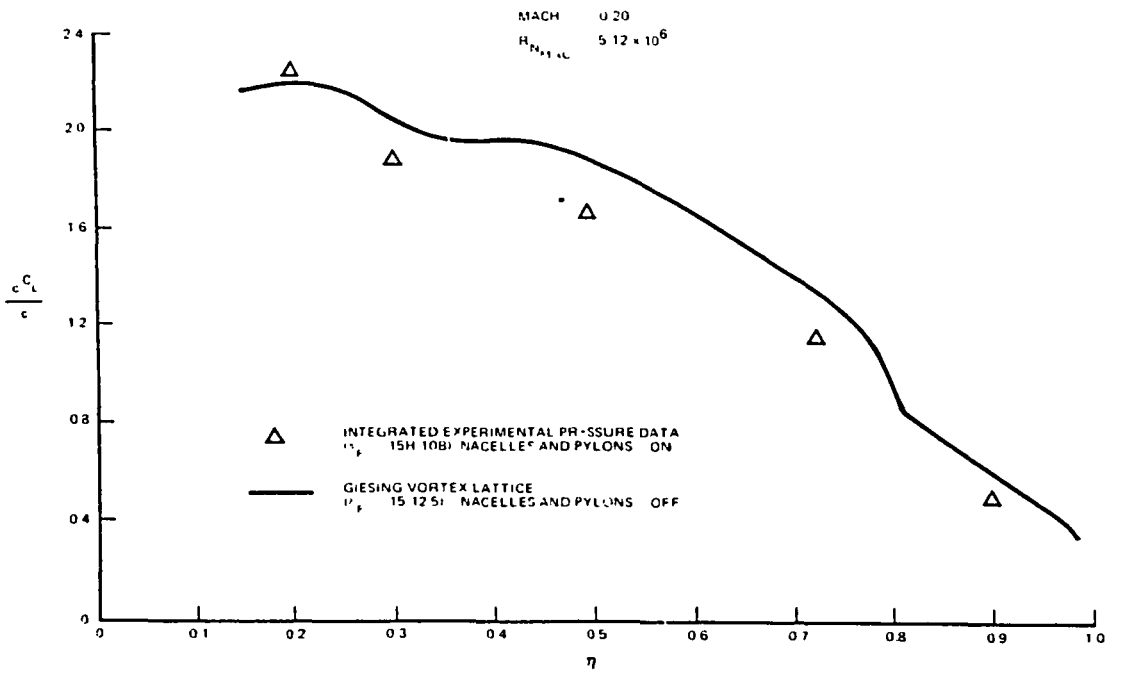

FIGURE 192. COMPARISON OF EXPERIMENTAL AND CALCULATED SPANWISE LIFT DISTRIBUTIONS (CLEAN LEADING EDGE WITH TWO-SEGMENT FLAPS)

PRECEDING PAGE BLANK NOT FILMED

CONCLUSIONS AND RECOMMENDATIONS

Conclusions

Results of the Phase I low-speed high lift tests have indicated significant aerodynamic performance improvements for the supercritical wing with advanced high lift systems. As with any new configuration, certain items require further development. This configuration is no different in this respect than other aircraft that have preceded it. Where improvements are desired, the means to achieve these goals seem available, and are contained in the recommendations. This combined NASA-Douglas research effort has helped to provide confidence in performance levels, established a comprehensive data base for analysis of developing methods, and highlighted future development areas.

The following conclusions can be drawn from the analysis of the test data:

1. The cruise wing achieved, for the high Reynolds number test condition, a trimmed $C_{L_{MAX}}$ of 1.5 and an L/D at 1.2 V_S of 15.0. Pitch characteristics indicated that outboard wing panel stall characteristics are influenced by changes in Mach and Reynolds number. The ongoing high-speed wing development has altered the span loading in a manner that will improve the stalling behavior.

2. The optimization of the leading-edge devices indicated superior $C_{L_{MAX}}$ and L/D performance for the slat configuration, whereas the pitch characteristics for the VCK were superior to the slat. The loading obtained on the VCK indicated that improved performance may be achieved by a reduction in VCK deflection. The superior VCK pitch characteristics resulted from an increased amount of inboard stall relative to the slat configuration and the ability of the VCK to prevent significant lift loss over the outboard wing. The VCK cutout at the nacelle pylon and the fuselage side contributed to the improved inboard VCK pitch characteristics. The best compromise between performance and stability and control for the VCK was obtained

with a 45° VCK deflection, and for the slat, the corresponding values were a 15° inboard and a 25° outboard deflection. Improvements in aerodynamic performance and pitch characteristics could result from further leading-edge device optimization studies.

3. Trailing-edge flap studies indicated that the changes in performance due to gap and overhang variations of the flap system were not as significant as the corresponding variations for the leading-edge devices. Optimization of the aft flap deflection, at each main flap deflection, resulted in the selection of 5C/10B, 15H/10B, and 25K/12C as the best compromise in terms of $C_{L_{MAX}}$, $C_{L\alpha=0}$, L/D, aircraft attitude, and pitching moment characteristics. As expected, the two-segment flap was superior in $C_{L_{MAX}}$ and flap lift increment. Trimmed polar comparisons indicated equivalent L/D envelopes for takeoff flap settings. For equivalent values of approach speed, the L/D values for the two-segment flap were superior to the single slotted flap. Improvement of the pitch characteristics may also be obtained in future studies by means of different flap deflection for the inboard and outboard sections (differential flap deflection).

4. Mach and Reynolds number effects were studied during the test program for selected configurations. The cruise wing $C_{L_{MAX}}$ was reduced 0.1 as the Mach number was increased from 0.20 to 0.32. The slat with two-segment flap was also evaluated for Mach number effects and the reduction in $C_{L_{MAX}}$, for the same increase in Mach number, was 0.14 and 0.24 for the takeoff and landing flaps, respectively. The cruise wing showed a significant increase in $C_{L_{MAX}}$ as the Reynolds number was varied from the atmospheric condition to the value at maximum pressure conditions ($R_{N_{MAC}} = 1.14 \times 10^6$ to $R_{N_{MAC}} = 5.12 \times 10^6$). The $C_{L_{MAX}}$ increase was 0.42 for this Reynolds number variation. The angles of attack for $C_{L_{MAX}}$ were changed by the Reynolds number variation, but the character of the stall was similar. For the high lift configurations, the effect of Reynolds number on the slat leading-edge configuration was much larger than for the VCK. This was true for both takeoff and landing

flap deflections. For the range of Reynolds number tested, typical values of the increase in $C_{L_{MAX}}$ were, for takeoff and landing two-segment flaps, 0.32 and 0.34 for the slat and 0.15 and 0.05 for the VCK. The change in Reynolds number did not alter the basic character of the pitching moment data. Angle of attack for $C_{L_{MAX}}$ and the magnitude of the pitching moment variation for poststall conditions were influenced by the Reynolds number change.

5. The effects of the nacelles, pylons, and VCK span interruptions at fuselage side and near the pylon were to reduce $C_{L_{MAX}}$. However, the pitch characteristics of the configuration were improved. The full-span VCK, without nacelles and pylons, achieved a $C_{L_{MAX}}$ of 3.4 with landing two-segment flap deflections. This $C_{L_{MAX}}$ was reduced to 3.2 with the normal VCK cutouts. The slat configuration was sealed in the area of the pylon and had an inboard trim position closer to the fuselage side. Improved pitch trends could result from increased outboard trim position (further from the fuselage and closer to the VCK spanwise position) and a revised trim over the pylon.

6. The clean leading-edge characteristics showed dramatically that the development of the leading-edge configuration was of equivalent importance to the development of the trailing-edge high lift system. Without the leading-edge device (clean leading-edge configuration), the $\Delta C_{L_{MAX}}$ with flap deflection was only 0.6. Achievement of large $C_{L_{MAX}}$ for these configurations requires significant leading-edge protection for the outboard wing panel.

7. The slat extended, flaps retracted pitching moment variation was improved significantly by a revised trim position for the inboard slat. This revised position was at an increased distance from the fuselage side. Future evaluation of this configuration for the flaps deflected case at high Reynolds number is expected to show improvements in the pitching moment trends.

8. Aileron effectiveness studies indicated that, for all flap settings, negative deflections (trailing-edge up) were more effective than positive (trailing-edge down) deflections. In some cases, the incremental rolling moment obtained with the negative aileron deflections reached values twice as large as the corresponding value for positive aileron deflections.

9. The effect of spoiler deflection on roll characteristics indicated improved effectiveness as the flap deflection was increased. Symmetrical spoiler deflection for takeoff and landing flap deflections showed the spoilers to be very effective in reducing lift and increasing drag.

10. The influence of the landing gear was shown to be negligible on $C_{L_{MAX}}$ at takeoff conditions, but resulted in a 0.076 reduction in $C_{L_{MAX}}$ for the landing flap configuration. The incremental drag due to the landing gear was essentially the same for takeoff and landing flap deflections.

11. The effects of the mini-tuft flow visualization technique on the low-speed high lift aerodynamic characteristics (including $C_{L_{MAX}}$, pitching moment, and drag) were not significant. The data did indicate a slight reduction in drag for the cruise wing and high lift configurations with the tufts mounted on the model.

Recommendations

Analysis of the data obtained has highlighted areas where continued efforts could result in further improvements of the technology. Items are suggested to improve the following low-speed aerodynamic characteristics: L/D for takeoff flap deflections, pitching moment for the high lift configurations, and improved lift and drag by replacement of the flaperon. The test items recommended for future studies include:

1. Sealed Slat Leading-Edge Configuration. - This configuration is primarily aimed at improving the takeoff L/D performance. This type of configuration has been successfully used in previous aircraft and although mechanically more complex, the existing L/D trends indicate the takeoff performance can be improved.

2. Reduced VCK Deflection. - Evaluation of $C_{P_{MIN}}$ for the VCK configuration indicated that the VCK, at the minimum deflection tested, may have been overdeflected. A reduced VCK deflection may result in lower profile drag and improved outboard wing panel characteristics.

3. Segmented Outboard Leading-Edge Devices. - Both the VCK and slat grid studies indicated that the flapped and nonflapped portions of the outboard wing achieved their best performance with different grid positions. Thus, the ability to position the leading edge device independently in these regions would result in improved lift, pitching moment, and drag. A cut near 80-percent semispan position for the leading-edge devices is recommended.

4. Revised Slat Trim. - Analysis of the test data indicated the existing inboard slat configuration did not result in appreciable lift loss at high angles of attack. A revised slat trim for the inboard slat (at a greater distance from the fuselage) was evaluated for the clean trailing-edge configuration (i.e., no flap deflection). This revised trim resulted in improved pitching moment characteristics with an acceptable penalty in $C_{L_{MAX}}$. This configuration is recommended for future study with the takeoff and landing configurations. Also, a revised trim in the area of the pylon (absence of pylon/slat sealing) should result in improved pitch characteristics.

5. Inboard Fixed Camber Krueger (constant chord). - As an alternate to the existing VCK and slat configurations, this device, of simpler mechanical design, has the potential of improving the stall characteristics for this configuration by means of a more rapid lift loss at the high angles of attack.

6. Large Chord Fixed Camber Krueger. - While some aerodynamic performance penalties may result, the magnitude of these penalties needs to be assessed with relationship to the reduced complexity of this leading-edge device.

7. Differential Flap Deflection. - Deflecting the inboard flap system to a larger angle than the outboard flap system is recommended for future testing to improve the stall characteristics.

8. Ground-Effect Aerodynamic Data. - At present, one area of aerodynamic data which is still lacking for this class of transport aircraft is the influence of ground effect. Test data of this type are required for the basic high lift configurations at high Reynolds number. Also required are the effect of large symmetrical spoiler deflections on the high lift characteristics with ground effect.

REFERENCES

1. Steckel, D.K.; Dahlin, J.A.; and Henne, P.A.: Results of Design Studies and Wind Tunnel Tests of High Aspect Ratio Supercritical Wings for an Energy Efficient Transport. NASA Contractor Report 159332, October 1980.

2. Sizlo, T.R.; Berg, R.A.; and Gilles, D.L.: Development of a Low-Risk Augmentation System for an Energy-Efficient Transport Having Relaxed Static Stability. NASA Contractor Report 159166, December 1979.

3. Taylor, A.B.: Advanced Aerodynamics and Active Controls for a Next Generation Transport. Douglas Paper 6696, March 1978.

4. Callaghan, J.G. and Beatty; T.D.: A Theoretical Method for the Analysis and Design of Multi-Element Airfoils. Journal of Aircraft, Vol. 9, No. 12, December 1972.

5. Giesing, J.P.: Lifting Surface Theory for Wing-Fuselage Combinations. McDonnell-Douglas Report DAC-67212, Vol. I, August 1968.

6. Callaghan, J.G.: Aerodynamic Prediction Methods for Aircraft at Low Speeds with Mechanical High Lift Devices. AGARD Lecture Series No. 67, Prediction Methods for Aircraft Aerodynamic Characteristics, May 1974.

7. Crowder, J.P.: Fluorescent Mini-Tufts for Non-Intrusive Flow Visualization. McDonnell-Douglas Report MDC-J7374, February 1977.

8. Hess, J.L: The Problem of Three-Dimensional Lifting Potential Flow and Its Solution by Means of Surface Singularity Distribution. Computer Methods in Applied Mechanics and Engineering, Vol. 4, No. 3, November 1974.

9. Goldhammer, M.I.: A Lifting Surface Theory for the Analysis of Nonplanar Lifting Systems. AIAA Paper 76-16, January 1976.

End of Document